THE
PHYSICAL REVIEW

A journal of experimental and theoretical physics established by E. L. Nichols in 1893

SECOND SERIES, VOL. 74, NO. 10 NOVEMBER 15, 1948

The Interaction of High Energy Neutrons and Heavy Nuclei

M. L. GOLDBERGER
Physics Department, University of Chicago, Chicago, Illinois
(Received July 20, 1948)

The interaction of high energy neutrons with heavy nuclei is studied under the assumption that the nucleus may be described by the statistical model. A detailed study is made of the energy transferred to the nucleus, the angular distribution of emerging particles, and the effective cross section for neutrons passing through nuclear matter. A summary of the results is given in the final section of the paper.

I. INTRODUCTION

THE 100-Mev neutrons produced by the Berkeley cyclotron[1] provide a powerful experimental tool for the study of the properties of heavy nuclei. Considerable work has already been done on the investigation of fission thresholds and nuclear reactions in heavy elements.[2] It is the purpose of this paper to investigate in detail the transfer of energy to the nucleus by high energy neutrons and to study the scattering of neutrons by heavy nuclei.

The general principles of high energy nuclear reactions have been described by Serber,[3] and the point of view presented by him will be adopted, for the most part, in this work. The main ideas enunciated by Serber are that one must consider individual nucleon-nucleon collisions in which a relatively small amount of energy is transferred on a single collision and that one must take into account the degeneracy of nuclear matter, i.e., effects due to the presence of nucleons other than the particular collision partner in question. This will be taken into account using the statistical model of the nucleus.[4] The experimentally measured neutron-proton cross section[5] will be used whenever possible, to characterize the individual collisions taking place inside the nucleus.

In Section II, the problem of the effective mean free path in nuclear matter is discussed in conjunction with a preliminary calculation of the scattering of nucleons by heavy nuclei. In Section III the energy transferred to the nucleus is studied in detail and the number and energy distribution of particles emitted "immediately" after a collision is discussed. (It should be noted that the problems discussed will not be those concerning what happens to the energy transferred to the nucleus, the results of which are usually described by the evaporation model.[3,6] The events of interest here are those which take place in the order 10^{-22} sec.) In Section IV the results are summarized and a discussion of the possibilities of experimental verification is given.

[1] Helmholz, McMillan, and Sewell, Phys. Rev. **72**, 1003 (1947).
[2] Cook, McMillan, Peterson, and Sewell, Phys. Rev. **72**, 1264 (1947).
[3] R. Serber, Phys. Rev. **72**, 1114 (1947).
[4] H. Bethe and R. Bacher, Rev. Mod. Phys. **8**, 83 (1936).
[5] Hadley, Kelly, Leith, Segrè, Wiegand, and York, Phys. Rev. **73**, 1114 (1948).
[6] P. Wolff and W. Heckrotte, Phys. Rev. **73**, 264 (1948).

II. THE EFFECTIVE MEAN FREE PATH IN NUCLEAR MATTER AND THE SCATTERING OF NEUTRONS BY HEAVY NUCLEI

A. The Mean Free Path

The first problem to be investigated is the mean free path of a nucleon when it is inside the nucleus. According to our model, we picture the nucleus as a mixture of two non-interacting, Fermi gases of neutrons and protons bound in a uniform potential of depth about 26 Mev, the highest filled state being at an energy of about -8 Mev. The maximum Fermi energies of the neutrons and protons are E_n and E_p, respectively, and are given by the well-known formula

$$E_F=(\hbar^2/2M)(3\pi^2N/V)^{\frac{1}{3}}, \tag{1}$$

where N is the number of neutrons or protons, V is the nuclear volume, and M is the mass of a nucleon. For simplicity, we shall assume that there is only one kind of particle inside the nucleus and use for the effective number of particles one-fourth the number of neutrons plus the number of protons. The reason for using only one-fourth the number of neutrons is that on the basis of an interaction consisting of one-half exchange and one-half ordinary forces which seems to be necessary to fit the observed neutron-proton scattering data[7] the total neutron-neutron cross section is about one-fourth the neutron-proton cross section. The exclusion principle will, however, be taken into account for the incident particle by demanding that the projectile as well as the target particle be outside the occupied sphere in momentum space after the collision. The radius of the sphere is given by

$$P=\hbar(3\pi^2N/V)^{\frac{1}{3}}. \tag{2}$$

It is easy to show that the most probable momentum transfer in a high energy nucleon-nucleon collision is of the order of $\hbar/r_0$, where r_0 is the range of nuclear forces. Since $\hbar/r_0P$ is of the order of $\frac{1}{2}$, a sizeable fraction of collisions are forbidden by the Pauli principle and thus the effective cross section is decreased. It is just this effect which will be computed.

Consider a neutron with energy E_0' incident upon a nucleus. Inside the nucleus it has an energy $E_0=E_0'+V_0$ where V_0 is the well depth.

[7] R. Serber, private communication.

It will be convenient to measure all momenta in units of P and all energies in units of $P^2/2M$, and this will be done throughout the paper. Let the momentum of the incident neutron (inside the nucleus) be $\mathbf{P}_0$ and that of one of the target nucleons be $\mathbf{P}_1$. It will be assumed that the cross section for a collision between $\mathbf{P}_0$ and $\mathbf{P}_1$, namely, $\sigma d\Omega\mathbf{p}_f$, is known. Here $d\Omega\mathbf{p}_f$ is an element of solid angle about the final projectile momentum $\mathbf{p}_f$ in the center of mass frame of the two collision partners. Obviously $p_f=p_0=|\mathbf{P}_0-\mathbf{P}_1|/2$ where $\mathbf{p}_0$ is the initial momentum in the center of mass frame. In general σ is a function of p_0 and the angle between $\mathbf{p}_0$ and $\mathbf{p}_f$. No assumption of the precise dependence will be made at this point. For convenience of expressing results in the laboratory frame, it is expedient to replace the element of solid angle by a three-dimensional volume element in momentum space. Let the momentum transfer in a collision be $\mathbf{g}$ where $\mathbf{g}=\mathbf{p}_f-\mathbf{p}_0=\mathbf{P}_f-\mathbf{P}_0$ and $\mathbf{P}_f$ is the final projectile momentum in the laboratory frame. The volume element transformation is as follows:

$$\sigma d\Omega\mathbf{p}_f=\sigma\frac{1}{p_f^2}\delta(p_f-p_0)d\mathbf{p}_f=\sigma\frac{1}{p_0^2}\delta(p_f-p_0)d\mathbf{g}, \tag{3}$$

where the last writing follows from the definition of $\mathbf{g}$ if $\mathbf{P}_1$ is regarded as fixed. $\mathbf{p}_f$ and $\mathbf{p}_0$ are now assumed to be expressed as functions of $\mathbf{g}$ and $\mathbf{P}_1$. The effective total cross section $\bar{\sigma}$ is then found by integrating the product of the relative velocity $|\mathbf{P}_0-\mathbf{P}_1|/M$ and the cross section over the allowed regions of $\mathbf{P}_1$ and dividing by the incident velocity P_0/M:

$$\bar{\sigma}=\frac{1}{P_0}\int d\mathbf{g}\int d\mathbf{P}_1N(\mathbf{P}_1)|\mathbf{P}_0-\mathbf{P}_1|\times\sigma(p_0,\mathbf{p}_0\cdot\mathbf{p}_f)\frac{1}{p_0^2}\delta(p_0-p_f), \tag{4}$$

where $N(\mathbf{P}_1)$ is the density of target nucleons in momentum space. The allowed regions of integration are confined to those values of $\mathbf{P}_1$, $\mathbf{g}$ such that the condition of having both the final momentum vectors of the collision partners lie outside the occupied sphere in momentum space is satisfied.

Before the evaluation of $\bar{\sigma}$ can be undertaken, an appropriate cross section must be chosen.

Since the problem of the mean free path is not the primary one in this paper and since it will be computed in another fashion in Section III the cross section will be taken here to be isotropic in the center of mass frame, i.e., $\sigma=\sigma_T/4\pi$, where σ_T is a total constant cross section. In the other calculation referred to, this crude assumption will be dropped.

A coordinate system appropriate for the calculation of $\bar{\sigma}$ is shown in Fig. 1. This computation of $\bar{\sigma}$ will be given in detail since most of the results may be directly applied to the angular distribution calculation (see Part B of this section). The construction for finding the allowed values of $\mathbf{P}_1$ such that for a given momentum transfer, $\mathbf{g}$, the target particle lies outside the occupied sphere after the collision is made as follows: Move a distance $\mathbf{g}$ from the filled momentum sphere parallel to $\mathbf{g}$ and draw a sphere of radius P with this point as center. The region above the auxiliary sphere and inside the original one defines the allowed values of $\mathbf{P}_1$ (see Fig. 1). The integrations over $\mathbf{P}_1$ are most easily carried out using a cylindrical coordinate system with center at $\mathbf{g}/2$ as shown. The limits on the $\mathbf{g}$ integration are forced by the δ-function appearing in the expression for $\bar{\sigma}$ together with the demand that $P_f>1$, i.e., that the projectile lie outside the filled region after the collision. They will be given explicitly below.

To proceed with the evaluation, all quantities must be expressed in terms of $\mathbf{g}$ and $\mathbf{P}_1$. The argument of the δ-function may be written in terms of the new variables ρ, z, φ by the use of the theorem

$$\delta(f(z)-0)=(\partial f/\partial z)^{-1}{}_{z=z_0}\delta(z-z_0), \tag{5}$$

where z_0 is the root of the equation $f(z_0)=0$. Using the relations $\mathbf{p}_f=\mathbf{p}_0+\mathbf{g}$ and $\mathbf{p}_0=|\mathbf{P}_0-\mathbf{P}_1|/2$, one finds easily

$$\begin{aligned} z_0&=-g/2+P_0\cos\eta,\\ (\partial f/\partial z)_{z=z_0}&=g/2P_0, \end{aligned} \tag{6}$$

where η is the complement of the angle between $\mathbf{g}$ and $\mathbf{P}_0$ (see Fig. 1). The fact that the contributing values of $\mathbf{P}_1$ lie on the plane $z=z_0$ is simply a statement of the physically obvious fact that the same specified momentum transfer parallel to $\mathbf{g}$ must be supplied by all target particles effective in scattering into $d\mathbf{g}$.

When every thing is written in terms of the above defined cylindrical coordinates, the z integration carried out, the expression for $\bar{\sigma}$ reduces to

$$\bar{\sigma}=\frac{N\sigma_T}{4\pi}\int d\mathbf{g}F(\mathbf{g}), \tag{7}$$

with

$$F(\mathbf{g})=\frac{3}{\rho_0\pi g}\int_0^{2\pi}d\varphi\int_{\rho_1}^{\rho_2}\rho d\rho \tag{8}$$

where the constant density in momentum space has been inserted. The limits ρ_1, ρ_2 depend on the values g and $\cos\eta$. Three cases must be considered:

$$\begin{aligned} &(1)\quad g\leqslant 2, && 0\leqslant z_0\leqslant 1-g/2,\\ &(2)\quad g\leqslant 2, && 1-g/2\leqslant z_0\leqslant 1+g/2,\\ &(3)\quad g\geqslant 2, && g/2-1\leqslant z_0\leqslant g/2+1. \end{aligned} \tag{9}$$

The corresponding values of ρ_1, ρ_2 are

$$\begin{aligned} &(1)\qquad \rho_1=(1-P_0^2\cos^2\eta)^{\frac{1}{2}},\\ &\qquad\qquad \rho_2=(1-(g-P_0\cos\eta)^2)^{\frac{1}{2}},\\ &(2)\text{ and }(3)\quad \rho_1=0\\ &\qquad\qquad \rho_2=(1-(g-P_0\cos\eta)^2)^{\frac{1}{2}}. \end{aligned} \tag{10}$$

The inequalities given in Eq. (9) completely define the region of integration in g, $\cos\eta$ space with the exception of the condition imposed by demanding that $P_f>1$. This yields the additional restriction

$$P_0-1\leqslant g\leqslant P_0+1,\ \cos\eta\leqslant(P_0^2+g^2-1)/2P_0g. \tag{11}$$

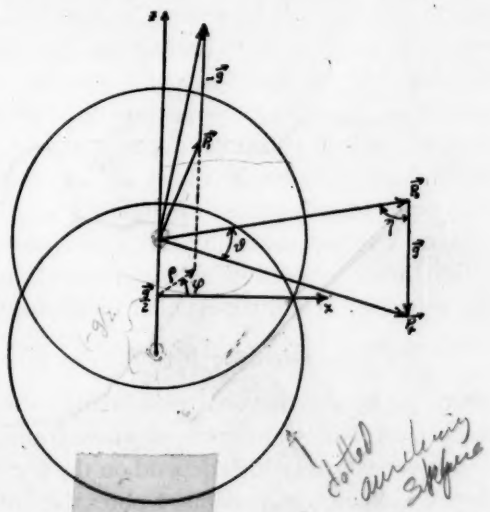

FIG. 1. Coordinate system used in computing the effective mean free path and the angular distribution of scattered particles.

$F(\mathbf{g})$ may be evaluated trivially; the result is

Case (1)

$$F(\mathbf{g})=(3/P_0)(2P_0\cos\eta-g), \tag{12}$$

Cases (2) and (3)

$$F(\mathbf{g})=(3/P_0g)\{1-(g-P_0\cos\eta)^2\}. \tag{13}$$

It is easy to see that $F(\mathbf{g})$ vanishes on the boundary lines $g=2P_0\cos\eta$, $g=P_0\cos\eta\pm1$. The line $\cos\eta=1/P_0$ marks the transition from Case (1) to Cases (2) and (3) and is an explicit manifestation of the exclusion principle.

The remaining integration over $\mathbf{g}$ is trivial, although rather tedious. The result for $P_0\geqslant\sqrt{2}$ is quite simple and is given by

$$\bar{\sigma}=N\sigma_T(1-7/5P_0^2). \tag{14}$$

The result for $P_0<\sqrt{2}$ is more complicated and will not be given. If the radius of the momentum sphere corresponds to 18 Mev, the potential well to 26 Mev, and the energy of the incident particle to 90 Mev outside the nucleus $\bar{\sigma}/N\sigma_T=0.78$. Assuming that the effective number of particles is 113 and the radius of the nucleus is 9×10^{-13} cm (corresponding to lead) and that the cross section σ_T is 0.064b (extrapolating the value of 0.083b at 90 Mev by a $1/E$ law) the mean free path is found to be 5.52×10^{-13} cm, whereas it would have been 4.3×10^{-13} cm with the neglect of the Pauli principle. It turns out that the isotropicity assumption underestimates the effect of the exclusion principle effect; the value of the effective cross section found in Section III, using a more realistic cross section, leads to a value of 6.20×10^{-13} cm.

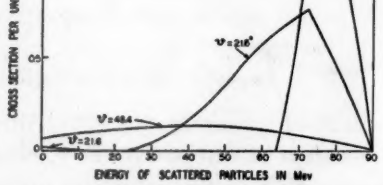

FIG. 2. Energy distribution of particles scattered from a heavy nucleus at fixed laboratory scattering angles. The energy of the incident neutron is 90 Mev. The discontinuous derivatives at the maxima result from the exclusion principle. The ordinate scale is in arbitrary units.

B. The Angular Distribution of Scattered Neutrons

The statistical model predicts that the angular distribution of neutrons scattered from a heavy nucleus will differ markedly from that expected qualitatively for high energy phenomena, namely, of strong forward scattering. Forward scattering implies small momentum transfers which, as was pointed out above, are very much reduced by the exclusion principle. Thus the angular distribution of scattered neutrons should show a pronounced dip in the forward direction. (Since the exclusion principle acts for the projectile, large momentum transfers are also discouraged, and there would be a corresponding dip in the backward direction.) It will be seen later that this is indeed the case. Another characteristic of the model is that for a fixed scattering angle there will be a distribution of energies among the scattered particles due to the motion of the target nucleons inside the nucleus.

The same assumption made in Part A of this section about having to deal with only one kind of particle will be made here. Two additional assumptions will be made: (a) The incident neutron makes only one collision inside the nucleus before escaping. This is not too good an assumption, as will be seen in Section III; however, the angular distribution is not greatly modified by the multiple collisions, as will be seen later. (b) The cross section for individual nucleon-nucleon collisions depends only on the momentum transfer involved in the collision. This point requires some discussion.

If one assumes that the Born approximation is valid, the cross section will be proportional to the square of a matrix element of the form

$$\langle\mathbf{p}_f|\,V\,|\mathbf{p}_0\rangle=\alpha f_1(\mathbf{p}_0-\mathbf{p}_f)+\beta f_2(\mathbf{p}_0+\mathbf{p}_f),$$

where $\mathbf{p}_f$, $\mathbf{p}_0$ are the final and initial momenta, respectively, in the center of mass frame, and α, β are constants which depend on the particular sort of exchange and ordinary potential mixtures assumed. The general characteristic of the angular distributions associated with f_1 and f_2 are

easily seen, since

$$f_1(\mathbf{p}_0-\mathbf{p}_f)\sim\int dr e^{i/\hbar(\mathbf{P}_0-\mathbf{P}_f)\cdot\mathbf{r}}U_1(\mathbf{r}),$$

$$f_2(\mathbf{p}_0-\mathbf{p}_f)\sim\int dr e^{-i/\hbar(\mathbf{P}_0+\mathbf{P}_f)\cdot\mathbf{r}}U_2(\mathbf{r}).$$

Evidently if the U's are reasonably well behaved f_1 will be large only when $\mathbf{p}_f\sim\mathbf{p}_0$ whereas f_2 will be large only when $\mathbf{p}_f\sim-\mathbf{p}_0$. Thus the angular distribution associated with f_1 is peaked in the forward direction, that of f_2 in the backward direction. As was pointed out at the beginning of this section, one would expect the effects of the exclusion principle to be prominent only in the case of very small or of very large momentum transfers. To see the effects, therefore, it will be sufficient to consider the case of small momentum transfer, in which case the most important contribution to be considered is that of the forward scattering, i.e., of $f_1(\mathbf{p}_0-\mathbf{p}_f)$. What shall be done in practice is to fit the experimentally measured neutron-proton angular distribution with a function $f_1(\mathbf{p}_0-\mathbf{p}_f)$ in the angular range of 0 to $\pi/2$ in the center of mass frame. It is, therefore, to be expected that the angular distribution in the heavy nucleus case will be correct only for angles somewhat less than $\pi/2$ in the laboratory frame since the transformation from the center of mass frame tends to concentrate the whole cross section in the forward direction. In Section III, the experimentally observed neutron proton cross section will be used.

The calculation proceeds exactly as that of $\bar{\sigma}$ in Part A, except that the integration over $\mathbf{g}$ is not carried out, since the differential effects are desired. Using the definition of $\mathbf{g}$ it is clear that $d\mathbf{g}=d\mathbf{P}_f$ where $\mathbf{P}_f$ is the final laboratory momentum of the scattered neutron. The cross section for scattering into $d\mathbf{P}_f$, namely, $\sigma_L d\mathbf{P}_f$, may be written as

Case (1)

$$\sigma_L d\mathbf{P}_f=\frac{3}{P_0}\sigma(\mathbf{p}_0-\mathbf{p}_f)\times\frac{P_0^2-P_f^2}{(P_0^2+P_f^2-2P_0P_f\cos\vartheta)^{\frac{1}{2}}}d\mathbf{P}_f, \quad (15)$$

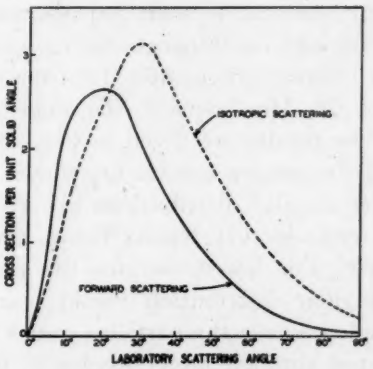

FIG. 3. Angular distribution of particles scattered by a heavy nucleus in the laboratory system assuming only a single collision inside the nucleus. The energy of the incident neutron is 90 Mev. Because of the symmetry of the neutron-proton scattering, these curves give also the distribution of recoil protons (see Section III). The ordinate scale is in arbitrary units and is not the same for the two curves.

Cases (2) and (3)

$$\sigma_L d\mathbf{P}_f=\frac{3}{P_0}\sigma(\mathbf{P}_0-\mathbf{P}_f)\times\frac{P_f^2-2P_fP_0\cos\vartheta+P_0^2P_f^2\sin^2\vartheta}{\{P_0^2+P_f^2-2P_0P_f\cos\vartheta\}^{\frac{1}{2}}}d\mathbf{P}_f, \quad (16)$$

where g and $\cos\eta$ in Eqs. (12) and (13) have been written in terms of (see Fig. 1) P_f and ϑ using

$$P_f^2=P_0^2+g^2-2P_0g\cos\eta,$$
$$g^2=P_0^2+P_f^2-2P_0P_f\cos\vartheta. \quad (17)$$

The regions of integration in P_f, $\cos\vartheta$ space follow in a straightforward fashion from Eq. (9), but the results are very complicated and will not be given. There is one modification of the region. The value of P_f must be greater than $(V_0)^{\frac{1}{2}}$ in order that the neutron be able to escape from the nucleus after suffering its collision.

The cross section chosen to fit the angular distribution in the region 0 to $\pi/2$ in the center of mass frame of neutron proton scattering at 90 Mev is

$$\sigma(\mathbf{p}_0-\mathbf{p}_f)=(\text{constant})/\{1.0714+(\mathbf{p}_0-\mathbf{p}_f)^2\}. \quad (18)$$

This cross section has no theoretical foundation and was taken only for simplicity of computation. The expressions for $\sigma_L d\mathbf{P}_f$ were evaluated for fixed values of the scattering angle ϑ, and

the energy spectra of scattered neutrons was found. Then the angular distribution was calculated. As a numerical example, neutrons with an energy of 90 Mev outside the nucleus were chosen. The results are given in Figs. 2 and 3. In Fig. 2 the energy spectra are shown, and in Fig. 3 the angular distributions are given, the isotropic cross-section results being given for comparison. For lower energies the maximum in the angular distribution would occur at a larger angle because the particles would have to be deflected through larger angles in order to transfer the requisite amount of momentum in a given collision. A further discussion of these results will be given in Section IV.

In addition to the inelastically scattered neutrons treated above, there will also be some neutrons scattered with no change in energy. This is scattering by the nucleus as a whole and corresponds to the well-known diffraction scattering. The importance of this effect is that the elastic scattering is confined primarily to small angles and would thus tend to erase the dip predicted by the statistical model (Fig. 3). It will be seen later that this complication does not provide an insurmountable barrier to the experimental measurement of the decreased forward scattering of the inelastically scattered neutrons. Nevertheless, it seems worth while to estimate the effect semiquantitatively.

To the approximation in which the nucleus is regarded as a completely black sphere of radius a (sticking probability unity), the differential cross section may be easily calculated to be

$$\sigma d\Omega = a^2 \left\{ \frac{J_1(ka\vartheta)}{\vartheta} \right\}^2 d\Omega,^8 \qquad (19)$$

where J_1 is the Bessel function, k is the wave number of the incident neutron, and ϑ is the scattering angle. This result is valid for $\vartheta \ll 1$. If a is taken to be 9×10^{-13} cm and k corresponding to 90 Mev, the first minimum occurs at about 11°. The approximation of sticking probability unity is a good one, as may be seen from the results of Section III.

III. MORE DETAILED CALCULATIONS

The problem to be considered in this section is that of calculating in some detail quantities such as the energy delivered to the nucleus in bombardment by high energy neutrons, the number of collisions suffered by the projectile, the angular distribution of scattered particles taking into account multiple collisions and, finally, the mean free path of a nucleon passing through nuclear matter. The statistical model will again be used to describe the nucleus; however, more attention will be paid to the fact that both neutrons and protons are present. The experimentally observed neutron-proton scattering cross section will be used whenever possible.

The approach to these problems will be primarily a classical one in the sense that the concept of a definite trajectory for the particles will be used and also that of a definite radius for the nucleus. This is a well justified approximation since the wave-length divided by 2π of a nucleon with an energy of 90 Mev is about $\frac{1}{2}\times10^{-13}$ cm, or eighteen times smaller than the nuclear radius. The method to be used has been developed by S. Ulam and J. von Neumann.[9] The fundamental idea of the method is the following: One follows in detail, collision by collision, the passage of a large number of particles through the nucleus until the particles either escape or lose sufficient energy to be captured. Evidently, if a sufficiently large number were chosen, an exact solution to the problem would be obtained. Whenever it is necessary to make a choice of a number of equally probable events, this choice will be made by a random process. The method can be most easily explained by actually describing the successive steps involved in following a particle.

The first problem to be faced is that of how far the nucleon travels into the nucleus before making a collision. One imagines that the nucleon has penetrated the nucleus; as far as this nucleon is concerned it is immersed in an infinite medium of nuclear matter. The geometry of the sphere will be taken into account later. Then the total interval from zero to infinity is divided into regions of equal probability. Evidently the division is made according to the law

$$p = e^{-x/\lambda}, \qquad (20)$$

[8] H. Bethe and G. Placzek, Phys. Rev. **57**, 1075 (1940).

[9] S. Ulam and J. von Neumann, Bull. Am. Math. Soc. **53**, 1120 (1947).

where p is the probability of penetrating a distance x from the surface without suffering a collision, and λ is the mean free path *not* taking account the Pauli principle (the particle does not know if the collision is to be forbidden until it tries to collide). The path lengths are found to be $x_n=\lambda \ln 1/p_n$, where p_n designates which one of the equally likely intervals in which the collision has taken place and is given by n/N where N is the total number of divisions of the total interval from zero to one ($0\leqslant n\leqslant N$). The value of p_n is chosen at random and a path length is obtained.

The next decision to be made is that of the momentum of the struck target particle. The whole allowed region of momentum space is divided into regions of equal probability, i.e., equal volume. The number of these divisions should be sufficient to cover the region in a reasonable representative way. Since the probability of making a collision with a particle in the ith region is proportional to $p_{ri}\sigma(p_{ri})$ where p_{ri} is the relative momentum and $\sigma(p_{ri})$ is the total cross section for a collision with relative momentum p_{ri}, it is clear that the appropriate division into equal probability intervals is obtained by computing the partial sums

$$s_n=\sum_{i=1}^{n} p_{ri}\sigma(p_{ri}) \Big/ \sum_{i=1}^{N_1} p_{ri}\sigma(p_{ri}),$$

where N_1 is the total number of divisions of the momentum space. Then a random number, m, between zero and one is chosen and if $s_n\leqslant m<s_{n+1}$ the collision is taken to be with a particle in region n.

Having decided on a collision partner, one must then find out the scattering angle. It is most convenient to work in the center of gravity system for this purpose. It is supposed that the differential cross section $\sigma(p_{ri},\vartheta)d\Omega$ is known. The appropriate values of ϑ_j are computed from

$$\frac{1}{\sigma(p_{ri})}\int_0^{\vartheta_j}\sigma(p_{ri},\vartheta)d\Omega=j/N_2, \qquad (21)$$

where $1\leqslant j\leqslant N_2$ and N_2 is the total number of intervals chosen for division. The final vector momenta of the collision partners are determined from the conservation laws. Then one must see if the collision is permitted by the Pauli principle. If it is permitted, the whole procedure is repeated for the two final particles until they have escaped from the physical sphere or been captured. If the collision is forbidden, the particle is given a new path length along its original trajectory.

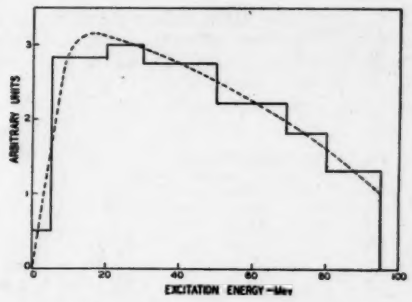

FIG. 4. Distribution of excitation energies of the residual nucleus immediately following the bombardment of a heavy nucleus by 86.6-Mev neutrons.

In the computations carried out in this paper, one hundred incident particles were followed. A greater number should, of course, be used, but if a greater number is chosen, the problem should be handled by a machine. The results obtained show some scattering but nevertheless indicate quite definite trends. The number of divisions used to obtain the path lengths was one thousand. The momentum sphere was divided into twenty regions and the scattering angles were divided into five regions from zero to $\pi/2$. The reason for going only to $\pi/2$ will be discussed immediately.

The choice of the differential cross section made here is based on the experimental fact that the neutron-proton scattering cross section is very nearly symmetric about $\pi/2$ in the center of mass system. This implies that the angular distribution of recoil protons is the same as that of the scattered neutrons. The convention was therefore made that only scattering angles less than $\pi/2$ in the center of mass frame would be considered; since targets and projectiles are treated on an equal footing, all possibilities are included. There is one important simplification resulting from this choice: Only one curve need be constructed for the determination of the scattering angles since the cross section may be chosen as a universal function of the momentum transfer, g, irrespective of the relative momentum

TABLE I. Results for 100 incident particles, of which 15 pass through the nucleus without collision. Energetics of the particles produced by the 85 which make successful collisions. All energies are in Mev.

No. particles emerging	No. of cases	Average excitation energy of residual nucleus	Average energy distribution of emerging particles decreasing energy 1	2	3
0	4	94.5			
1	58	41.6	45.0		
2	21	35.2	27.2	16.0	
3	2	40	14.5	9.5	6.5

$(g=\sqrt{2}p_r \sin\vartheta/2)$. It turns out that, on the basis of an interaction consisting of one-half ordinary forces and one-half exchange forces, which fits the experimental data,[7] the neutron-neutron scattering angular distribution has the same form as the neutron-proton; consequently the neglect of the difference between these types of collisions is justified. The exact form chosen is that given in Section II, Eq. (18). Further account of the presence of both neutrons and protons was taken by setting the minimum energy for escape from the nucleus at 14.5 Mev above the Fermi energy, an average between the neutron and proton barriers.

The energy dependence of the total cross section is taken to be inversely proportional to the relative energy, and the magnitude was fitted to the experimental result of 0.083b at 90 Mev. This has the consequence that $p_r\sigma(p_r)$ averaged over the momentum distribution is just $P_0\sigma(P_0)$,

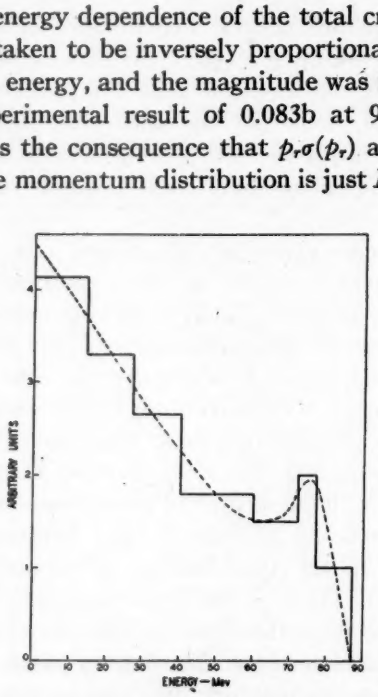

FIG. 5. Energy distribution of particles emerging at all angles immediately after the bombardment of a heavy nucleus by 86.6-Mev neutrons.

where P_0 is the projectile momentum, and provides a check on the method used to select the collision partners.

The actual calculations were carried out primarily by graphical means; analytical calculations would have required an exhorbitant amount of time if done with ordinary desk computing machines. The calculation described here required about two weeks full-time work by two people. The energy of the incident particles was taken to be 86.6 Mev, the depth of the potential hole to be 26 Mev, the maximum Fermi energy to be 18 Mev, and the nuclear radius to be 9.0×10^{-13} cm.

The mean excitation energy of the residual nucleus was found to be 42.5 Mev. The distribution of excitation energies is shown in Fig. 4; this curve represents 85 particles. The average number of collisions suffered by a particle escaping with more than 15 Mev is two, although about half the particles have only one collision. Note that these emerging particles may be target particles. The total energy distribution of all particles emerging at all angles is shown in Fig. 5; this curve represents 105 particles. The angular distribution of all emerging particles with energies greater than 15 Mev is shown in Fig. 6; this curve includes particles which have suffered up to five collisions before emerging and represents 76 particles. A further breakdown of the data is given in Table I. The effective cross section was found for particles with energies of 113 and 66 Mev inside the nucleus. The fractions of the total cross section at these energies are 0.69 and 0.32, respectively. It was found that 15 particles pass through the nucleus without a collision; an exact calculation based on a mean free path of 6.20×10^{-13} cm predicts 17 such events. It is interesting to note that the total cross section for lead found experimentally,[2] namely, 4.53b, agrees quite well with the value $0.85\times2\pi a^2$ which yields, with $a=9.0\times10^{-13}$, 4.32b. Of particles emerging with an energy greater than 15 Mev, 36 had suffered one collision, 29 had two collisions, eight had three collisions, five had four collisions, and one had five collisions. The intervals on the block diagrams were chosen so as to give a reasonably smooth curve and should not be regarded as giving a measure of the statistical accuracy involved.

Since each curve represents about 100 particles, the intervals on the diagrams represent from 10 to 15 particles.

IV. SUMMARY AND DISCUSSION OF RESULTS

(a) The theoretical angular distributions shown in Figs. 3 and 6 show that the expected dip in intensity in the forward direction for scattering high energy neutrons from heavy nuclei occurs over a relatively small angular interval; the interval is so small, about 25°, that experimental measurements will be difficult, although probably not impossible. It is interesting to note that the inclusion of multiple scattering does not radically change the angular distribution; this is due to the high number of single scatterings and to the fact that the double scatterings are strongly correlated to the single scatterings. The complication of the background of elastically scattered neutrons does not provide serious difficulty because of the fact that the distribution of recoil protons should be essentially the same as that of the scattered neutrons; one need, therefore, measure only the protons. In Fig. 2, the energy distribution of particles emerging at various angles is shown.

(b) The mean free path in nuclear matter for a neutron with energy 90 Mev outside the nucleus computed on the assumption of isotropic scattering in the center of mass system is 5.52×10^{-13} cm, whereas that computed using the observed angular dependence is 6.20×10^{-13} cm.

(c) The distribution of excitation energies of nuclei bombarded with 86.6-Mev neutrons is calculated (Fig. 4). The average excitation energy is 42.5 Mev. This energy will be distributed among the nucleons, and the subsequent behavior could be described by the evaporation model. The total energy distribution of emerging particles is shown in Fig. 5. The peak at the high energy end is believed to be real; it represents the large number of particles which suffer only one collision before escaping from the nucleus.

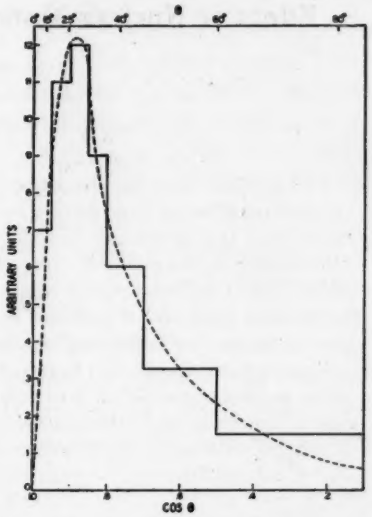

FIG. 6. Angular distribution of particles emerging from the nucleus taking into account multiple scattering (compare Fig. 3). The cosine of the laboratory scattering angle is given in the lower scale and the actual angle in the upper scale.

ACKNOWLEDGMENTS

The author wishes to express his gratitude to Dr. E. Fermi, who suggested this problem, for his frequent advice and encouragement. Thanks are also due G. F. Chew who shared the work in the tedious calculations and contributed essentially to all parts of this paper.

Effect of Nuclear Motion on the Fine Structure of Hydrogen

G. BREIT AND G. E. BROWN
Yale University, New Haven, Connecticut*

(Received July 26, 1948)

The problem is re-examined from the point of view of the Hamiltonian applicable to two charged particles and accounting for effects of order v^2/c^2, where v is the velocity. The work differs from that of Bechert and Meixner in that the energy of the Dirac's electron in a central field is taken as the reference point. The solution is carried out in terms of an eight-component rather than a four-component approximation to the 16-component wave function. The result is the same for practical purposes as that of Darwin for the prequantum-mechanical problem and of Bechert and Meixner for the four-component approximation. The energy formula is affected only by the original Bohr reduced mass correction to the term value and also by a term which is independent of the particular fine structure component and depends only on the principal quantum number. Bethe's electrodynamic shift is, therefore, not obscured to within terms of relative order $\alpha^2(m/M)$ by effect of nuclear motion.

I. INTRODUCTION

THE effect of nuclear mass motion on the fine structure of hydrogen has been calculated by Bechert and Meixner.[1] Related considerations have been made by Lowen.[2] The increased importance of the fine structure as a test of views on quantum electrodynamics[3] has made it desirable to re-examine the question. The work of Bechert and Meixner leaves one with a partial feeling of dissatisfaction because it employs the four-component approximation to the 16-component two-particle wave equation. It is not clear without further proof that this approximation is adequate for the present problem. While it is true that for a single particle the reduction from 4 to 2 components yields results for the energy which are correct to relative order α^2, it does not follow without further proof that the perturbing effect of the mass correction can be treated by an extension of the same method. One might be especially doubtful about the meaning of such a calculation if one recalls that the Dirac and Schroedinger wave functions are represented by different powers of the distance r at the origin.

The calculation of Bechert and Meixner amounts to the carrying out of the following two steps: (a) such a rearrangement of terms in the four-component wave equation that the explicit introduction of the reduced mass becomes possible and the non-relativistic Schroedinger equation with reduced mass can be used as the zeroth-order approximation to the problem; (b) the evaluation of the expectation value of the difference between the two-particle Hamiltonian and the zeroth approximation. The relative order of the difference is $(m/M)\alpha^2$, and the first-order perturbation theory suffices. The general scheme is doubtless beyond criticism. It is clear, however, that the application of first-order perturbation theory can have only a formal significance if the wave function is strongly affected by the difference between the actual and the approximate Hamiltonian. Since the Schroedinger function is a poor approximation to the Dirac function at short distances the question arises as to whether the application of first-order theory in the arrangement of terms chosen by Bechert and Meixner has more than a formal meaning, whether the perturbation method converges, and if it converges whether the convergence is rapid enough to make the result significant. A certain degree of optimism is, of course, necessary regarding absence of mathematical difficulties, and the questions raised above would probably be out of order if it were not for the fact that it is

* Assisted by the Office of Naval Research, project NR 024–055.

[1] K. Bechert and J. Meixner, Ann. d. Physik **22**, 525 (1935).

[2] I. S. Lowen, Phys. Rev. **51**, 190 (1937). Lowen's results are closely related to those of the present paper. This is especially true of his Eq. (14a). Lowen did not carry the calculation far enough to make it possible to make comparisons with experiment except for the 1*s* term.

[3] H. A. Bethe, Phys. Rev. **72**, 339 (1947); Julian Schwinger, Phys. Rev. **73**, 415 (1948); Willis E. Lamb, Jr. and Robert C. Retherford, Phys. Rev. **72**, 241 (1947); J. E. Mack and N. Austern, Phys. Rev. **73**, 1233 (A) (1948).

known that for small r the probability of finding an electron per unit volume behaves very differently with distance according to the Dirac and the Schroedinger equations and if the assumption of being able to expand the Dirac functions in terms of their non-relativistic approximations were not a part of the usual development of first-order perturbation theory. It is not clear that the large values of the ratio of Dirac electron density to the Schroedinger density can be accounted for by a series with a reasonably small number of terms or that the difference between the actual and the zero-order wave functions has a negligible effect on the final estimate of the mass correction. Some of these questions are still unclear, but it is believed that the matter is somewhat more soundly understood as a result of the present work.

An additional reason for undertaking it is the desirability of being able to see the answer in such a form that the exact solution of Dirac's equation for a fixed nucleus is approached as a limit for $M=\infty$. This is not the case for Bechert and Meixner's calculations, although it is the aim of Lowen's reductions. The latter are not carried, however, to the point of estimating the effects on the energy. It is obviously better to be able to carry out the development in such a way as to have the energy appear as the Dirac energy for $M=\infty$ because by doing so one is in a better position to obtain a theoretical understanding of the problem for cases of high atomic number Z. It may be mentioned that for small values of r the usual reduction of the 16-component equation to the four-component form requires modification and that for this reason the 4-component approach appears to be questionable. It derives an energy value by changing the wave equation close to $r=0$ and in a sense also the boundary condition at $r=0$.

In addition, it appears pertinent that the extra terms brought into the Hamiltonian by the nuclear motion have to be taken into account to the second order of perturbation theory. It is true that with Bechert and Meixner's arrangement of the calculation only first-order perturbation theory is used. This is the result of employing the non-relativistic Hamiltonian for reduced mass as the zeroth approximation and removing terms from the Hamiltonian which can give rise to effects of relative order m/M. The Bechert-Meixner work thus amounts to the calculation of the expectation value of the Hamiltonian employing the wave function of the non-relativistic reduced mass problem. A justification for employing this rather than another wave function is easy to give for the four-component treatment because for it effects of relative order m/M are removed from the perturbing Hamiltonian. The fact that the whole argument depends on this property of the four-component approximation and that the 16- or 8-component equations appear to require the consideration of second-order effects when one takes infinite nuclear mass as a starting point also suggested a re-examination of the problem.

NOTATION

m = electronic mass
M = mass of proton
e = electronic charge
Z = atomic number
$\hbar$ = Planck's $h/2\pi$
c = velocity of light
$\alpha = e^2/\hbar c$
E = energy of system in rest mass system $-Mc^2$
$r_e = (x_e, y_e, z_e)$ = coordinates of electron
$R_M = (x_M, y_M, z_M)$ = coordinates of proton
$r = r_e - R_M$
$p_e = (\hbar/i)(\partial/\partial x_e, \partial/\partial y_e, \partial/\partial z_e)$
$p_M = (\hbar/i)(\partial/\partial x_M, \partial/\partial y_M, \partial/\partial z_M)$
α, β = the four matrices, α_1, α_2, α_3, α_4, of Dirac. These matrices operate on the spin coordinates of the electron; $\beta = \rho_3$
n = principal quantum number
$a_H = \hbar^2/me^2$ = Bohr radius
T = non-relativistic kinetic energy
Ry = absolute value of energy of ground state of hydrogen for $M=\infty$; $Ry = e^2/2a_H$
ψ = four-component wave function for Dirac's equation
W = energy of single electron according to Dirac's equation
L = azimuthal quantum number
$\langle A \rangle$ = expectation value of operator A.

II. THE 8-COMPONENT EQUATION

The 16-component equation is equivalent to a set of two simultaneous equations on two four-component functions. In addition one has to add

to the energy the expectation value of an operator Y which represents the combined effect of the magnetic interaction and a correction for the effect of retardation on the electrostatic energy. The representation can be chosen in such a way that the equations have the form[4]

$$(\mathcal{E}+2Mc)+(\sigma_M\mathbf{p}_M)\Psi=0,\quad \mathcal{E}\Psi+(\sigma_M\mathbf{p}_M)\Phi=0, \tag{1}$$

where

$$\mathcal{E}=p_0+\alpha\mathbf{p}_e+\beta mc, \tag{1.1}$$

with

$$p_0=(E+e^2/r)/c. \tag{1.2}$$

In order to simplify the formulas the nuclear charge is taken to be e. In order to change results to a nuclear charge Ze, the quantities e^2, α should be replaced, respectively, by Ze^2, $Z\alpha$. The subscript M refers to the nucleus. The vector matrix σ_M has components having the form of Pauli's three spin matrices. The functions Ψ, Φ have two indices, the first of which is the Dirac four-valued spin index for the electron and the second of which is the two-valued spin index of the proton. The matrices α, β operate on the first index; σ_M operates on the second. The operator Y is

$$Y=(e^2/2r)[(\alpha\alpha_M)+(\alpha\mathbf{r})(\alpha_M\mathbf{r})/r^2] \tag{1.3}$$

in the original 16-component representation. In the notation used in the present paper α_M converts Φ into Ψ, Ψ into Φ, and after this operates like σ_M. The calculation will be carried out with an attempt at not making the assumption that the velocity of the electron is small until the final stage of the calculation. The operator α will be left, therefore, in Y and will be considered accurately. It is realized that Y is only accurate to order v^2/c^2 and that at this point the gain in accuracy is questionable. The contribution of Y is of the last highest order of quantities considered here and its effect vanishes for $M=\infty$. For hydrogen it does not matter whether the effect of Y is evaluated accurately or not. Since it turned out to be just as easy to calculate the expectation value accurately as approximately, the accurate evaluation will be used almost up to the end of this paper. The replacement of Y by something better requires a more thorough investigation. One of the objects here is to provide accurate forms of the answer for the approximate theory so as to make it easier to see in what way the physical effects that are approximately represented by Y can be treated more satisfactorily.

From the first of the two Eqs. (1) one finds

$$\Phi=-[1-(\mathcal{E}/2Mc)+\cdots](\sigma_M\mathbf{p}_M)\Psi/(2Mc). \tag{1.4}$$

The condition

$$(\mathbf{p}_e+\mathbf{p}_M)\Psi=(\mathbf{p}_e+\mathbf{p}_M)\Phi=0 \tag{1.5}$$

will be imposed on the wave function so as to have the total momentum equal to zero. The partial differential equations thus obtained show that each of the 16 components depends only on the relative coordinates $\mathbf{r}$. The operator $\mathbf{p}_e$ is the same for this wave function as the operator

$$\mathbf{p}=(\hbar/i)(\partial/\partial x,\ \partial/\partial y,\ \partial/\partial z). \tag{1.6}$$

Substitution of Eq. (1.4) into the second of the two Eqs. (1) gives the following equation on linearizing in σ_M and omitting terms in σ_M which contribute only to the hyperfine structure,

$$[\mathcal{E}-p^2/2Mc+\mathcal{E}_1]\Psi=0, \tag{1.7}$$

where

$$\mathcal{E}_1=\mathbf{p}\mathcal{E}\mathbf{p}/4M^2c^2. \tag{1.8}$$

One has

$$\mathcal{E}_1\Psi=p^2\mathcal{E}\Psi/4M^2c^2+\mathcal{E}_2\Psi \tag{1.81}$$

where

$$\mathcal{E}_2=he^2(\mathbf{pr})/(4iM^2c^2r^3). \tag{1.82}$$

The first two terms of Eq. (1.7) give an approximate wave equation which corrects the energy for the kinetic energy of the nucleus and includes, therefore, effects on the energy of the system to the first order of m/M. If the equation were exact then the first part of $\mathcal{E}_1$ in Eq. (1.81) would be equivalent to an addition to the energy operator of

$$-(cp^4/8M^3c^3) \tag{1.83}$$

which for small Z is of relative order

$$\frac{1}{4}\left(\frac{m}{M}\right)^3\frac{\alpha^2}{n^2} \tag{1.84}$$

[4] The arrangement of the calculation is similar to that in G. Breit and R. E. Meyerott, Phys. Rev. **72**, 1023 (1947) and G. Breit, Phys. Rev. **39**, 616 (1932). Equation (1) of the present paper does not include magnetic interaction and retardation effects. The expectation value of an operator called Y is used later in order to take into account these interaction effects, in accordance with the view that this is the proper way of employing the 16-component equation. A justification of this view is given in the (1932) paper quoted in this footnote.

and is negligible. The first-order effect of $\mathfrak{L}_2$ on the energy is obtained by taking the expectation value of $-c\mathfrak{L}_2$. For light nuclei this is

$$\begin{aligned}\langle -c\mathfrak{L}_2\rangle &\cong (\hbar^2e^2/4M^2c^2)\int_r^\infty \Psi_S(d\Psi_S/dr)4\pi dr \\ &\cong -\hbar^2e^2\Psi_S^2(0+)/2M^2c^2 \\ &= -Ry(m/M)^2\alpha^2/n^3.\end{aligned} \tag{1.85}$$

Here the subscript S on Ψ indicates the nonrelativistic Schroedinger approximation, the lower limit of integration is designated by r, and the notation $0+$ indicates that Ψ_S is evaluated for the small value r. The reason for putting the matter in terms of this notation should now be explained. The operator $\mathfrak{L}_2$ arose in the step between Eq. (1.8) and Eq. (1.81) as the result of interchanging the positions of $\mathfrak{L}$ and $\mathbf{p}$. The whole term $\mathfrak{L}$ came in as a consequence of the presence of $-\mathfrak{L}/2Mc$ in the brackets of Eq. (1.4). At distances of the order e^2/Mc^2 it is no longer satisfactory to stop with the second term in the brackets of Eq. (1.4) because then the potential energy and Mc^2 are of the same order. Carrying out the integration from $r=0$ to ∞ would not have much meaning, therefore. A second reason for employing the notation $0+$ is the convenience of not having to bring in the difference represented essentially by the factor $\exp[-(\alpha^2/2)\log r]$ between the larger of the two Dirac functions and the Schroedinger function Ψ_S. The small value of α does not make the integral diverge and the factor $\exp[-(\alpha^2/2)\log r]$ changes by $\sim$0.3 percent when r changes by a factor e. It changes, therefore, by roughly 2 percent between e^2/mc^2 and e^2/Mc^2 and is thus practically constant between the point at which the two terms of Eq. (1.4) are sufficient and the point at which the approximation of the larger Dirac radial function by the corresponding Schroedinger function becomes good up to values of r considerably greater than the Bohr radius. The right side of Eq. (1.85), while larger than the expression in Eq. (1.84), is, nevertheless, negligible.

It remains to consider the effect of the term in p^2 which enters Eq. (1.7). To the first order it brings in a correction of the order (m/M) of the term value. It gives besides effects of order $(m/M)^2$, $(m/M)\alpha^2$ and higher order terms. Effects of order $(m/M)^2\alpha^2$ and those of higher order will be neglected. Corrections of order $(m/M)^2$ cannot differ from the $(m/M)^2$ effects for the Schroedinger equation and are therefore taken care of by the second term in the Taylor expansion of the factor $[1+(m/M)]^{-1}$ in the original Bohr reduced mass correction. It is further seen that there are no correction terms of order $(m/M)^2\alpha$. In fact the process of expansion of the eigenvalue of Eq. (1.7) into a Taylor series in (m/M) is equivalent to the employment of the Rayleigh-Schroedinger perturbation method with $p^2/2M$ as the perturbing term in the Hamiltonian. The power $(m/M)^2$ is obtained in the second-order perturbation energy which is given by the standard expression

$$E_2=\Sigma_f|H_{if}'|^2/(E_i-E_f), \tag{1.9}$$

where i, f refer to initial and final states, respectively. The difference in E_2 caused by changing from the Schroedinger to the Dirac equation consists in three effects: (a) The presence of the negative energy part of the spectrum for E_f in the Dirac case; (b) Differences in E_i-E_f for $E_f>0$; (c) Differences in the numerator of the formula for $E_f>0$. It is well known that the relativity effect on E_f can be represented by a Taylor series in even powers of α. The effect (b) is, therefore, only that of causing the appearance of α^2 rather than α. An examination of the formulas of Darwin and Gordon[5] for the wave functions shows that here too all effects are free of the first power of α and that the effect (c) is, therefore, also harmless. The only place where the first power of α has the appearance of entering explicitly in Gordon's formulas is in the ratio $C_0^{(1)}/C_0^{(2)}$. It enters, however, through

$$(\alpha E/mc^2)/[1-(E/mc^2)^2]^{\frac{1}{2}}=n'+(k^2-\alpha^2)^{\frac{1}{2}}, \tag{1.91}$$

where n' and $|k|$ are both integers. The quantity k_0 in these formulas may be thought at first sight to contain the first power of α. This quantity occurs, however, only in the combination k_0r and, since

$$k_0r=(r/a_H)\{\alpha^2+[n'+(k^2-\alpha^2)^{\frac{1}{2}}]^2\}^{-\frac{1}{2}}, \tag{1.92}$$

the effect of relativity through k_0 is describable as a change of linear scale which is free of the

[5] C. G. Darwin, Proc. Roy. Soc. **A118**, 654 (1928); W. Gordon, Zeits. f. Physik **48**, 11 (1928).

first power of α. For E_f in the continuous positive energy spectrum one can make E_f the same for the Dirac and Schroedinger cases. The first-order radial equations,

$$\begin{cases}(p_0+mc)f-\hbar[g'+(1+k)g/r]=0,\\(p_0-mc)g+\hbar[f'+(1-k)f/r]=0,\end{cases} \quad (1.93)$$

give the Schroedinger equation identically if one replaces the coefficient p_0+mc of f by $2mc$. For values of $|E_f-E_i|$ of the order of the ionization potential and for $r>a_H$ the effect of relativity is thus describable as a change in f/g of the order $(E-mc^2)/mc^2$ which is of the order α^2/n^2. For distances of the order e^2/mc^2 the fractional effect on f/g is of the order of 50 percent. The volume within which this is the case is of the order $(e^2/a_Hmc^2)^3=\alpha^6$, however, and this effect is negligible. For $E_f\sim mc^2$ the relativistic f/g is again appreciably (of the order of 50 percent) different from the non-relativistic value. Here, however, the final state f is practically that of a free electron for which p^2 is diagonal in the non-relativistic approximation. One expects, accordingly, the whole effect to be small. In fact the number of states f in the energy interval mc^2 for a one-dimensional problem in the interval 0 to R is $\sim(R/\pi c\hbar)mc^2$. The effect of the short wave-length of the final state is to bring in a factor of the order $(\hbar/mc)/a_H=\alpha$ into each matrix element. Besides the normalization factor for the continuum is of the order $(a_H/R)^{\frac{1}{2}}$ of what it is for the ground state. The whole contribution is therefore of the order

$$mc^2(R/\pi c\hbar)(2m/2M)(T^2/mc^2)\alpha^2(a_H/R)\sim(m/M)\alpha^3Ry, \quad (1.94)$$

where the dependence on n is not considered since the whole is negligible. The relativistic value is of the same order as that just considered and effect (c) is negligible. The consideration of effect (a) is essentially similar to that just made for the continuum, with the additional simplification of larger energy denominators and the fact that for $|E_f+mc^2|\sim Ry$ the large initial g_i pairs off with a small final g_f. This brings in an extra factor α in each matrix element which takes the place of the factor $(\hbar/mc)/a_H$, which was discussed in connection with Eq. (1.93). Effect (a) is, therefore, also negligible. No terms of order $(m/M)^2\alpha$ are seen to be present in the second-order perturbation energy, and it suffices to use the non-relativistic value $-(m/M)Ry/n^2$ for this correction. It remains, therefore, to evaluate the expectation values of $p^2/2M$ and of the part of Y which does not depend on nuclear spin orientation.

III. EVALUATION OF EXPECTATION VALUES

Neglecting the second term in the expansion of Φ/Ψ, one obtains an equivalent operator Y' which contains σ_M quadratically. Linearizing in the σ_M and throwing away the spin dependent part, one is left with

$$Y''=(e^2/4Mc)[(\mathbf{p}\boldsymbol{\alpha})r^{-1}+r^{-1}(\boldsymbol{\alpha}\mathbf{p})+(\mathbf{pr})(\boldsymbol{\alpha}\mathbf{r})r^{-3}+r^{-3}(\boldsymbol{\alpha}\mathbf{r})(\mathbf{rp})]. \quad (2)$$

The expectation value of this quantity and of $p^2/2M$ will be calculated. Following Dirac it is convenient to introduce the operators

$$\epsilon=(\boldsymbol{\alpha}\mathbf{r})/r, \quad k=\beta[(\mathbf{L}\boldsymbol{\sigma})+1], \quad (2.1)$$

and to recall that the meaning of Dirac's angle-dependent canonical transformation is that the application of ϵ, k, β, to the Dirac four-component wave function amounts[6] to the operation on the column matrix

$$\begin{pmatrix}f\\g\end{pmatrix} \quad (2.2)$$

$$\epsilon=\begin{pmatrix}0, & -i\\ i, & 0\end{pmatrix}, \quad k=k\begin{pmatrix}1 & 0\\0 & 1\end{pmatrix}, \quad \beta=\begin{pmatrix}1 & 0\\0 & -1\end{pmatrix}, \quad \cdots, \quad (2.3)$$

where k is used interchangeably for the operator and its eigenvalue. It follows directly from the above form for ϵ that

$$\langle(\mathbf{pr})(\boldsymbol{\alpha}\mathbf{r})r^{-3}+r^{-3}(\boldsymbol{\alpha}\mathbf{r})(\mathbf{rp})\rangle=2\hbar\int_0^\infty(gf'-fg')rdr. \quad (2.4)$$

The normalization is here such that

$$\int_0^\infty(g^2+f^2)r^2dr=1.$$

Also it follows from the wave equation that

$$\langle(\mathbf{p}\boldsymbol{\alpha})r^{-1}+r^{-1}(\boldsymbol{\alpha}\mathbf{p})\rangle=-2\langle p_0+\beta mc\rangle, \quad (2.5)$$

[6] P. A. M. Dirac, Proc. Roy. Soc. **A117**, 611 (1928); The quantum number j of Dirac's article is called k here. His k is called L.

and hence again, by means of Eq. (2.3) as well as Eq. (2.4),

$$\langle Y''\rangle = -(e^2/2Mc)\int_0^\infty [(p_0+mc)f^2 + (p_0-mc)g^2+\hbar(fg'-gf')]rdr. \quad (2.6)$$

Multiplying the two Eqs. (1.93) by f and g, respectively, there results a relation which enables one to eliminate the derivatives and one obtains

$$\langle Y''\rangle = -(e^2/Mc)\left\{\int_0^\infty (p_0+mc)f^2 + (p_0-mc)g^2rdr - \hbar I\right\}, \quad (2.7)$$

with

$$I = k\int_0^\infty fgdr. \quad (2.8)$$

Again one has for the one-electron function ψ

$$p^2\psi = (\alpha\mathbf{p})^2\psi = -(\alpha\mathbf{p})(p_0+\beta mc)\psi = -(p_0-\beta mc)(\alpha\mathbf{p})\psi = (p_0{}^2-m^2c^2)\psi, \quad (3)$$

and hence

$$\langle p^2/2M\rangle = (1/2M)\int_0^\infty (p_0{}^2-m^2c^2)(f^2+g^2)r^2dr. \quad (3.1)$$

One has the helpful relations[7]

$$W = mc^2\int_0^\infty (g^2-f^2)r^2dr, \quad (4)$$

$$mc = \int_0^\infty p_0(g^2-f^2)r^2dr, \quad (4.1)$$

where the value of E for $M=\infty$ is denoted by W and $cp_0 = W+e^2/r$. It follows from these two relations that

$$\int_0^\infty (W+e^2/r)(g^2-f^2)r^2dr = mc^2, \quad (4.2)$$

and hence

$$\int_0^\infty (e^2/r)(g^2-f^2)r^2dr = (m^2c^4-W^2)/mc^2. \quad (4.3)$$

[7] The derivation of these equations is given in Appendix I. The object in introducing these relations is to express $\langle p^2/2M\rangle$ in terms of W and also only quantities which have to be evaluated only approximately. Equation (4) is analogous to the virial theorem. Equations (4) make it possible to express $\langle e^2/r\rangle$ in terms of W.

The factor e^2 and the combination $mc(f^2-g^2)$ under the integral sign of Eq. (2.7) are expressible by means of Eq. (4.3). Performing this substitution one has

$$\langle Y''\rangle = (m^2c^4-W^2)/Mc^2+[-W\langle e^2/r\rangle - \langle e^4/r^2\rangle + e^2c\hbar I]/Mc^2. \quad (4.4)$$

Again Eq. (3.1) gives

$$\langle p^2/2M\rangle = (W^2-m^2c^4)/2Mc^2 + [W\langle e^2/r\rangle + \langle e^4/2r^2\rangle]/(Mc^2). \quad (4.5)$$

Adding the last two equations one has

$$E_1 = \langle (p^2/2M)+Y''\rangle = \{-(W^2-m^2c^4)/2 + [-\langle e^4/2r^2\rangle + e^2c\hbar I]\}/Mc^2. \quad (4.6)$$

The quantity $W\langle e^2/r\rangle$ which occurs in Eqs. (4.5), (4.6) disappeared on addition. This was arranged on purpose so as not to have to evaluate corrections of order α^2 to $\langle e^2/r\rangle$. The deviation of the relativistic wave functions from their nonrelativistic approximations is taken into account implicitly in the value of W and appears besides in the terms $\langle e^2/2r^2\rangle$ and $c\hbar I$. The latter two terms will be seen to contribute only amounts of relative order $(m/M)\alpha^2$, and it will suffice to evaluate them without correcting for higher powers of α.

For a Coulomb field it will be seen that the terms in square brackets cancel in the nonrelativistic limit of small nuclear charge. In fact the well-known hydrogenic value of $\langle r^{-2}\rangle$ gives

$$(1/Mc^2)\langle e^4/2r^2\rangle = (m/M)\alpha^2Ry/[n^3(L+\tfrac{1}{2})]. \quad (5)$$

The integral I occurs[6] in the theory of hyperfine structure and has the value

$$I = (\hbar/2mc)\{-kg^2(0+)/2+\langle k(1+k)/r^3\rangle\} \quad (5.1)$$

in the approximation of small nuclear charge. The notation $0+$ means that g is evaluated at $r\sim e^2/mc^2$. The first term in braces is

$$-4\pi k\Psi_g{}^2(0), \quad (5.2)$$

and it vanishes except for s terms. One has, besides,

$$k(k+1) = L(L+1), \quad (5.3)$$

and for a Coulomb field

$$\langle r^{-3}\rangle = 1/[a_H{}^3L(L+\tfrac{1}{2})(L+1)n^3], \quad (5.4)$$

$$\Psi_g{}^2(0) = 1/[\pi n^3a_H{}^3]. \quad (5.5)$$

Hence

$$I=(\alpha/2)\langle r^{-2}\rangle, \tag{5.6}$$

so that the square bracket in Eq. (4.6) vanishes. The cancellation is a consequence of the equality of $\langle r^{-2}\rangle$ and $a_H L(L+1)\langle r^{-3}\rangle$ for a Coulomb field. The result is simply

$$E_1=-(W^2-m^2c^4)/(2Mc^2), \tag{6}$$

which can also be written as

$$E_1=-(m/M)(W-mc^2) -(m/4M)(\alpha^2/n^2)\,|\,W-mc^2\,|, \tag{6.1}$$

which is identical in form with the results of Darwin as well as Bechert and Meixner.

As has been discussed in the introduction, the meaning of the result is somewhat different from those previously obtained because it is expressed as a correction to Dirac's W rather than an approximation to it. This is only partially satisfying because Y'' is good only to order v^2/c^2 and one cannot be sure of the applicability of the second term in Eq. (6.1) for heavier nuclei.

The reasons explained in the introduction make one more certain, however, of the applicability of the answer. To within terms of order $(m/M)^2\alpha^2$ the latter may be written as

$$E-mc^2=(W-mc^2)/[1+(m/M)] -(m/4M)(\alpha^2/n^2)\,|\,W-mc^2\,|. \tag{7}$$

One may conclude that it is probably appropriate to apply Bethe's electrodynamic shift correction to the above formula for comparison with experimental values of the Lamb effect. It may be noted especially that there are no terms of order $(m/M)\alpha Ry/n^2$ which would be a serious effect, since $(m/M)\alpha Ry=1.3\times10^4 mc/s$.

The considerations carried out above apply directly only to an idealized proton having a magnetic moment $eh/2Mc$. The magnetic moment of the proton may be described phenomenalogically, however, by adding to the Hamiltonian terms involving the electromagnetic six vector in the manner proposed by Pauli as a mathematical possibility for uncharged particles. Attributing to the extra Pauli-like terms a physical significance only through their expectation values, one finds that nothing essential is changed in the reasoning which gave Eq. (6). It is still possible to start with Eq. (1). The terms independent of relative spin orientations of proton and electron are still represented by Eq. (2), and the remaining steps leading to Eq. (6) remain unchanged.

APPENDIX I

Some useful relations for the Dirac functions

Equations (4), (4.1) of the text do not seem to have been recorded in the literature. Equation (4) is a generalization of the virial theorem for the Schroedinger equation. To derive it one can start with the radial equations (1.93) and perform the similarity transformation

$$r=(1+\theta)r',$$

where θ is an arbitrary real number which will be made to have small positive values. The equations which result from the substitution are brought back to their original form on multiplication with $1+\theta$. Only now r' occurs everywhere in place of r and, $(1+\theta)E$, $(1+\theta)mc^2$ replace E, mc^2. Making θ small and recalling that the eigenvalue of an equation cannot depend on whether the independent variable is called r or r', one sees that the perturbation energy $mc^2\begin{pmatrix}-1 & 0\\ 0 & +1\end{pmatrix}\theta$, in the sense of Eq. (2.2), has caused a change in the eigenvalue of magnitude θE. Application of first-order perturbation theory yields Eq. (4).

One also has on multiplying the two radial equations by $-f$, g, respectively, and adding

$$(p_0-mc)g^2-(p_0+mc)f^2+\hbar d(fg)/dr+2\hbar fg/r=0.$$

Multiplying by r^2 and integrating, one obtains Eq. (4.1). Another useful relation which follows from the second-order equations is

$$\int_0^\infty (p_0^2-m^2c^2)(f^2+g^2)r^2dr =\hbar^2\int_0^\infty [(dg/dr)^2+(df/dr)^2+k(k+1)g^2/r^2 +k(k-1)f^2/r^2]r^2dr.$$

This equation is not used in the paper, but since it was helpful in some preliminary considerations it is reproduced here for possible use of other workers.

Depolarization of Neutrons During Diffusion

SIDNEY BOROWITZ* AND MORTON HAMERMESH**
Department of Physics, New York University, New York, New York

(Received June 1, 1948)

A theoretical analysis is given of the depolarization to be expected when a plane, monochromatic, polarized beam of thermal neutrons is incident normally on a slab of finite thickness in which the neutrons are scattered isotropically and without capture. The problem reduces to the solution of an integro-differential equation of the Wiener-Hopf type. The equation is solved approximately by a method of G. C. Wick. Experimental possibilities for measuring the scattering amplitudes by this method even in the case where neutron-nuclear forces are not very spin-dependent, are excellent. The case where the capture cross section is different from zero is also included.

I. INTRODUCTION

SPIN dependence of the interaction between a neutron and a nucleus manifests itself in the difference of the scattering amplitude when the neutron and nuclear spins are parallel and the amplitude when they are anti-parallel. Inasmuch as a consistent theory of the nucleus should be able to predict this spin dependence, experimental determination of this difference gives us a valuable datum for testing such theories.

Such an investigation has been carried out in the case of the neutron-proton interaction by observing[1–3] the differences of the scattering cross sections for slow neutrons in the ortho and para modifications of the hydrogen molecule, and by making a theoretical analysis of these differences.[4,5] In this case, the large spin dependence of the neutron-proton force results in a substantial difference between the ortho and para cross sections. Decisive information could therefore be deduced without requiring experimental results of extreme accuracy. A similar theoretical analysis[6] for ortho and para deuterium indicates that accuracy of but a few percent in the measurement of the ortho and para cross sections would be necessary, under the best circumstances to get comparable information about the neutron-deuteron force. There is also the possibility if this force is not very spin-dependent, that the best experiment of this type would still be indecisive. For nuclei heavier than deuterium, experiments of this sort would be extremely difficult to perform.

More recently,[7] a determination of parallel and anti-parallel scattering amplitudes has been attempted by comparing the magnitude of the diffuse scattering with the interference peaks obtained when slow neutrons are scattered from crystals such as sodium hydride and sodium deuteride. In this case too, if the scattering amplitudes do not differ by much, the experimental accuracy required is beyond the limits of available techniques.

Another possibility for the experimental determination of the spin dependence of the interaction is to study the depolarizing effect of scattering processes on a beam of polarized neutrons. Experimentally, techniques for obtaining polarized neutron beams and for the analysis of their polarizations are well known.[8,9] Theoretically, the probability that a slow neutron will change its spin orientation in a single collision, has been calculated[10] and is given by:

$$Q=\tfrac{2}{3}(2i+1)^{-1}[(a_1-a_0)^2 i(i+1)]/[(i+1)a_1^2+ia_0^2], \quad (1.1)$$

* Present address: Physics Dept., Harvard University, Cambridge, Massachusetts.
** Present address: Argonne National Laboratory, Chicago, Illinois.
[1] L. Alvarez, K. S. Pitzer, Phys. Rev. **58**, 1003 (1940).
[2] F. G. Brickwedde, *et al.*, Phys. Rev. **54**, 266 (1936).
[3] R. B. Sutton, *et al.*, Phys. Rev. **72**, 1147 (1947).
[4] J. S. Schwinger and E. Teller, Phys. Rev. **52**, 286 (1937); J. Schwinger, Phys. Rev. **58**, 1004 (1940).
[5] M. Hamermesh and J. Schwinger, Phys. Rev. **71**, 678 (1947).
[6] M. Hamermesh and J. Schwinger, Phys. Rev. **69**, 145 (1946).
[7] E. O. Wollan and C. G. Shull, Phys. Rev. **73**, 830 (1948); C. G. Shull, *et al.*, Phys. Rev. **73**, 842 (1948).
[8] L. Alvarez and F. Bloch, Phys. Rev. **57**, 111 (1940).
[9] F. Bloch, M. Hamermesh, and H. Staub, Phys. Rev. **64**, 47 (1943).
[10] O. Halpern and M. H. Johnson, Phys. Rev. **55**, 898 (1939).

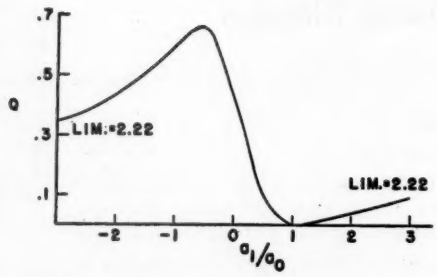

FIG. 1. Depolarizing factor Q as a function of the ratio of the scattering amplitudes when $i=1$.

where i=the spin of the interacting nucleus, a_1=the scattering amplitude for parallel spin, and a_0=the scattering amplitude for anti-parallel spin. $a_1=a_0$, implying no spin-dependence, has as a consequence $Q=0$ or no depolarization. This is clear since interactions which are not spin-dependent will produce no changes in spin orientation.

When several isotopes are present the depolarizing factor[10] is:

$$Q=\tfrac{2}{3}\sum_p |b_p|^2(2i_p+1)^{-1} \times\frac{(a_1{}^p-a_0{}^p)^2 i_p(i_p+1)}{(i_p+1)(a_1{}^p)^2+i_p(a_0{}^p)^2}, \quad (1.2)$$

where $|b_p|^2$ is determined by the relative abundance of the pth isotope ($\sum_p |b_p|^2=1$). The total scattering cross section[10] is:

$$\sigma_n=4\pi(2i+1)^{-1}[(i+1)a_1{}^2+ia_0{}^2], \quad (1.3)$$

when only one isotope is present, and is given[10] by:

$$\sigma_n=4\pi\sum_p |b_p|^2(2i_p+1)^{-1} \times[(i_p+1)(a_1{}^p)^2+i_p(a_0{}^p)^2], \quad (1.4)$$

when there is more than one isotope. A combination of two measurements, namely total scattering and Q is sufficient to determine the scattering amplitudes when only one isotope is present. This is no longer true when there are several isotopes.

The statement that the scattering amplitudes are determined by two measurements when only one isotope is present must be qualified. In Fig. 1, we have a plot of Q *vs.* a_1/a_0 when $i=1$. Except when a_1/a_0 is equal to 1 or $-\frac{1}{2}$, a determination of Q does not determine a_1/a_0 uniquely. In addition, the absolute sign of either amplitude cannot be found from these two measurements. In fact, no experiment in which the spin of the scattering nucleus is arbitrarily oriented in space will yield more information.[6]

If a_1-a_0 is small, the resultant depolarization for a single collision may not be measurable. It has been suggested,[6] therefore, that the cumulative effect of several depolarizing collisions be observed in order to determine the value of Q. This paper is concerned with the theoretical analysis of such an experiment. This technique will be most valuable when Q is in the neighborhood of zero, i.e., when a_1/a_0 is approximately 1. It is only in this region that our method is of interest. For a_1/a_0 considerably different from one, the depolarization in a single scattering process will be sufficiently large to enable determination of Q. In Fig. 2 we show the behavior of Q in this region for $i=1$.

II. FORMULATION OF THE PROBLEM

Specifically, we shall consider the following situation: a plane monochromatic beam of completely polarized (spins all pointing in some direction, p) slow neutrons, traveling in the positive z direction, is incident at $z=0$ on an infinite slab of amorphous scattering material perpendicular to the z axis and of thickness h. The neutrons are assumed to be scattered isotropically, in the laboratory system of coordinates. They are sufficiently slow so that no inelastic collisions are possible. We assume further, that no energy changes occur on collision, and for the moment we shall neglect capture. Physically this corresponds to a situation in which we are dealing with the interaction between a thermal neutron beam and a heavy nucleus, or with the interaction with a light nucleus such as deuterium which is combined in a heavy molecule whose other elements do not contribute to the scattering.

As the neutrons diffuse through the scatterer, the beam will become partially depolarized. In the material there will be two competing processes in the depolarization: Those neutrons whose spins point in the negative p direction will have a probability Q for spin reversal on collision, with a resultant increase in the polarization. Those neutrons whose spins are oppositely directed, will undergo depolarizing collisions with the same probability. At the outset, it should be

made clear that if the scatterer were infinitely thick, the emergent beam would be completely depolarized no matter what the value of Q since the depolarization process tends to equalize the populations of the two spin states. Thus, it is essential to consider a scatterer of finite thickness. Let:

$N^+(z, \mu)$ = the number of neutrons per unit volume whose spins point in the positive p direction and are traveling in a direction given by $\mu = \cos\theta$, in the angular range $d\mu$ (θ is the angle made with the positive z axis).

$N^-(z, \mu)$ = the number of neutrons per unit volume whose spins point in the negative p direction and are traveling in the direction given by μ, in the angular range $d\mu$.

V = the neutron speed.

l = the scattering mean free path.

If the time of collision is small compared to the time between collisions, then the transport equation for this process yields the following:

$$\frac{dN^+}{dt} = -\frac{V}{l}N^+(z, \mu, t) + \frac{V}{2l}\int_{-1}^{+1} N^+(1-Q)d\mu' + \frac{V}{2l}\int_{-1}^{+1} N^-Qd\mu', \quad (2.1)$$

and

$$\frac{dN^-}{dt} = -\frac{V}{l}N^-(z, \mu, t) + \frac{V}{2l}\int_{-1}^{+1} N^-(1-Q)d\mu' + \frac{V}{2l}\int_{-1}^{+1} N^+Qd\mu'. \quad (2.2)$$

The factor $\frac{1}{2}$ which appears before the integral sign is a normalization factor for the isotropic scattering function $1/4\pi$ and is determined by the condition

$$1/4\pi\int_0^{2\pi}\int_{-1}^{+1} Nd\mu' d\phi = 1.$$

We consider a steady state and for this case, we have:

$$\mu\frac{\partial N^+}{\partial z} + \frac{1}{l}N^+ = \frac{1}{2l}\int_{-1}^{+1} N^+(1-Q)d\mu + \frac{1}{2l}\int_{-1}^{+1} N^-Qd\mu', \quad (2.3)$$

and

$$\mu\frac{\partial N^-}{\partial z} + \frac{1}{l}N^- = \frac{1}{2l}\int_{-1}^{+1} N^-(1-Q)d\mu' + \frac{1}{2l}\int_{-1}^{+1} N^+Qd\mu'. \quad (2.4)$$

The problem reduces to the solution of a coupled system of integro-differential equations with appropriate boundary conditions. Equations (2.3) and (2.4) may be simplified by adding and subtracting them to give:

$$\mu\frac{\partial\sigma}{\partial z} + \sigma = \frac{1}{2}\int_{-1}^{+1}\sigma d\mu', \quad (2.5)$$

$$\mu\frac{\partial\Delta}{\partial z} + \Delta = \frac{\alpha}{2}\int_{-1}^{+1}\Delta d\mu', \quad (2.6)$$

where we have introduced the mean free path 1, as the unit of length and set

$$\sigma = N^+ + N^-,$$
$$\Delta = N^+ - N^-,$$
$$\alpha = 1 - 2Q.$$

Equations (2.5) and (2.6) are integro-differential equations of the Wiener-Hopf type. They arise from problems dealing with the radiative equilibrium of stellar atmospheres.[11] In most prob-

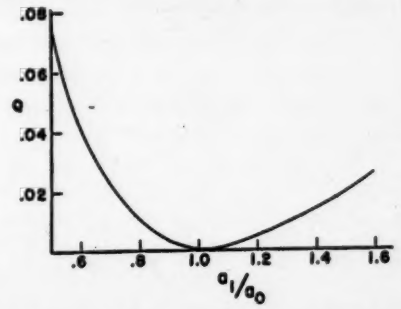

FIG. 2. Depolarizing factor Q as a function of the ratio of the scattering amplitudes when $i = 1$, and the ratio = 1.

[11] E. Hopf, "Mathematical problems of radiative equilibrium," *Cambridge Tracts*, No. 31 (1934); N. Wiener and E. Hopf, Berliner Ber. Math. Phys. Klasse, 696 (1931).

lems of interest to the astrophysicist the atmosphere is taken to have an infinite depth. As pointed out in I, we are obliged to deal with scatterers of finite thickness.

In order to facilitate the application of our special boundary conditions, we introduce into (2.5) and (2.6) the following transformations:

$$\sigma = J + \delta(\mu - 1)e^{-z/\mu}, \tag{2.7}$$

$$\Delta = I + \delta(\mu - 1)e^{-z/\mu}. \tag{2.8}$$

$\delta(\mu)$ = Dirac delta function; and

$$\int_{-1}^{+1} f(\mu')\delta(\mu' - \beta)d\mu' = f(\beta).$$

This gives for Eqs. (2.5) and (2.6)

$$\mu\frac{\partial J}{\partial z} + J = \frac{1}{2}\int_{-1}^{+1} J d\mu' + \tfrac{1}{2}e^{-z}, \tag{2.9}$$

and

$$\mu\frac{\partial I}{\partial z} + I = \frac{\alpha}{2}\int_{-1}^{+1} I d\mu' + \frac{\alpha}{2}e^{-z}. \tag{2.10}$$

Inasmuch as most detectors for slow neutrons measure neutron densities rather than flux, we will express our principal results in these terms. We will indicate later how these expressions are changed to represent the flux. Accordingly we define the polarization density as

$$P(z) = \int_{-1}^{+1} \Delta d\mu' \Big/ \int_{-1}^{+1} \sigma d\mu', \tag{2.11}$$

and are looking for $P(d)$, where d = thickness of the scatterer in units of mean free path ($=h/l$).

Our boundary conditions are:

at $z=0$;

$$\left.\begin{aligned} \sigma(0,\mu) &= \delta(\mu-1); \quad J(0,\mu)=0 \\ \Delta(0,\mu) &= \delta(\mu-1); \quad I(0,\mu)=0 \end{aligned}\right\} \mu>0; \tag{2.12}$$

at $z=d$;

$$\left.\begin{aligned} \sigma(d,\mu) &= 0; \quad J(d,\mu)=0 \\ \Delta(d,\mu) &= 0; \quad I(d,\mu)=0 \end{aligned}\right\} \mu<0. \tag{2.13}$$

The boundary condition (2.12) is an expression of the fact that a completely polarized plane beam is incident normally on the scatterer. Condition (2.13) states that after transmission, the vacuum returns no neutrons to the scatterer.

III. SOLUTION OF THE PROBLEM

The exact solution of the Wiener-Hopf equation for a finite thickness of scatterer has not yet been found. Inasmuch as our problem will not lead to significant results unless the slab is finite, we must resort to an approximate method of solving (2.9) and (2.10). The method we have used is one originally proposed by G. C. Wick[12] and which has been subsequently used and developed by S. Chandrasekhar.[13] The principle of the method is to replace the integral which appears on the right side of (2.9) and (2.10) by a polynomial, and thus reduce the integro-differential equation to a system of first-order differential equations. The special polynomial used is the one originally proposed by Gauss[14] in his quadrature method of approximating integrals:

$$\int_{-1}^{+1} I(z,\mu')d\mu' \cong \sum_{\substack{i=-n \\ n\neq 0}}^{n} a_i I(z,\mu_i) = \sum_{\substack{i=-n \\ n\neq 0}}^{n} a_i I_i. \tag{3.1}$$

The coefficients are the Christoffel[15] numbers which satisfy the conditions:

$$\sum_{i=1}^{n} a_i = 1; \quad a_i = a_{-i}. \tag{3.2}$$

The μ_i is determined in the nth approximation as solution of the equation $P_{2n}(\mu)=0$, where $P_{2n}(\mu)$ is the spherical harmonic of order $2n$. The solution of Eq. (2.10) by this method is found by letting

$$I_i = g_i e^{-\lambda z}, \tag{3.3}$$

for the homogeneous part and adding the particular solution

$$I_i = (\alpha/2)\Gamma e^{-z}/(1-\mu_i), \tag{3.4}$$

where

$$\Gamma = 1 \Big/ \left(1 - \alpha\sum_{i=1}^{n}\frac{a_i}{1-\mu_i^2}\right). \tag{3.5}$$

The complete approximate solution for I_i is

$$I_i = \sum_{p=1}^{n}\frac{L_p e^{-\lambda_p z}}{1-\mu_i\lambda_p} + \sum_{p=1}^{n}\frac{L_{-p}e^{\lambda_p z}}{1+\mu_i\lambda_p} + \frac{\alpha}{2}\frac{\Gamma e^{-z}}{1-\mu_i}, \tag{3.6}$$

[12] G. C. Wick, Zeits. f. Physik 121, 702 (1943).
[13] S. Chandrasekhar, Astrophys. J. 100, 76 (1944); S. Chandrasekhar, Astrophys. J. 106, 142 (1947).
[14] Riemann-Weber, *Diff. Gleichungen der Physik*, I (Dover Publications, New York), p. 394.
[15] A. N. Lowan, N. Davids, and A. Levenson, Bull. Am. Math. Soc. 48, 739 (1942).

where λ_p is determined by the equation

$$\alpha\sum_{i=1}^{n}\frac{a_i}{1-\mu_i^2\lambda^2}=1. \tag{3.7}$$

Equation (2.9) is solved in much the same way, except that in this case, (when $\alpha=1$) $\lambda=0$ identically satisfies (3.7) because of (3.2). The solution in this case is

$$J_i=b\left\{\sum_{p=1}^{n-1}\frac{M_p e^{-\zeta_p z}}{1-\mu_i\zeta_p}+\sum_{p=1}^{n-1}\frac{M_{-p}e^{\zeta_p z}}{1+\mu_i\zeta_p}+z-\mu_i+R\right\}+\frac{1}{2}\frac{\gamma e^{-z}}{1-\mu_i}, \tag{3.8}$$

where

$$\gamma=1\Big/\left(1-\sum_{i=1}^{n}\frac{a_i}{1-\mu_i^2}\right), \tag{3.9}$$

and ζ_p is a solution of the equation

$$\sum_{i=1}^{n}a_i/(1-\mu_i^2\zeta^2)=1, \tag{3.10}$$

which is different from zero.

The boundary conditions (2.12) and (2.13) now give the following system of linear equations for the determination of L_p, L_{-p}, M_p, M_{-p}, b and R.

$$\sum_{p=1}^{n}\frac{L_p}{1-\mu_i\lambda_p}+\sum_{p=1}^{n}\frac{L_{-p}}{1+\mu_i\lambda_p}+\frac{\alpha}{2}\frac{\Gamma}{1-\mu_i}=0 \qquad (i=1, 2\cdots n); \tag{3.11}$$

$$\sum_{p=1}^{n}\frac{L_p e^{-\lambda_p d}}{1+\mu_i\lambda_p}+\sum_{p=1}^{n}\frac{L_{-p}e^{\lambda_p d}}{1-\mu_i\lambda_p}+\frac{\alpha}{2}\frac{\Gamma e^{-d}}{1+\mu_i}=0 \qquad (i=1, 2\cdots n); \tag{3.12}$$

$$b\left\{\sum_{p=1}^{n-1}\frac{M_p}{1-\mu_i\zeta_p}+\sum_{p=1}^{n-1}\frac{M_{-p}}{1+\mu_i\zeta_p}-\mu_1+R\right\}+\frac{1}{2}\frac{\gamma}{1-\mu_i}=0 \quad (i=1, 2\cdots n); \tag{3.13}$$

$$b\left\{\sum_{p=1}^{n-1}\frac{M_p e^{-\zeta_p d}}{1+\mu_i\zeta_p}+\sum_{p=1}^{n-1}\frac{M_{-p}e^{\zeta_p d}}{1-\mu_i\zeta_p}+d+\mu_i+R\right\}+\frac{1}{2}\frac{\gamma e^{-d}}{1+\mu_i}=0 \quad (i=1, 2\cdots n). \tag{3.14}$$

IV. CALCULATIONS

The particular virtue of the method outlined above for approximating the solution of the Wiener-Hopf equation is that the convergence is so rapid. In most cases, in dealing with an infinite scattering atmosphere the second approximation gives results within 1 percent accuracy. In estimating the accuracy of our solutions in the various approximations, it was not possible to compare them with an exact solution. We have assumed that convergence to the exact solution was uniform, and if the difference between the nth and $n+1$th approximation is sufficiently small, we consider the $n+1$th result to be exact.

A. First Approximation

If one writes Eq. (3.3) in the first approximation, one has:[12]

$$\frac{1}{\sqrt{3}}(\partial I_1/\partial z)+I_1=\frac{\alpha}{2}I_1+\frac{\alpha}{2}I_{-1}, \tag{4.1}$$

$$-\frac{1}{\sqrt{3}}(\partial I_{-1}/\partial z)+I_{-1}=\frac{\alpha}{2}I_1+\frac{\alpha}{2}I_{-1}. \tag{4.2}$$

The total density is $I=I_1+I_{-1}$. I_1 may be considered to be the density moving to the right and I_{-1} may be considered that moving to the left. One can eliminate I_{-1} from (4.1) by differentiating with respect to z, then substituting for $\partial I_{-1}/\partial z$ from 4.2 and for I_{-1} from (4.1). In the same way one can eliminate I_1 and one gets for I, I_1, and I_{-1} the following:

$$(\tfrac{1}{3})\partial^2 I/\partial z^2+(\alpha-1)I=0, \tag{4.3}$$

which is the diffusion equation.

To gain some insight into the applicability of the first approximation, one starts with an exact equation such as (2.6) and expands the unknown function in spherical harmonics.

$$I=\frac{1}{4\pi}\sum_n(2n+1)P_n(\mu)I_n(z), \tag{4.4}$$

(we call the variable I instead of Δ). Resubstituting (4.4) into (2.6) we get:

$$\sum_n(2n+1)\mu P_n(\mu)\frac{\partial I_n}{\partial z}+\sum_n(2n+1)P_n(\mu)I_n=\alpha I_0. \tag{4.5}$$

TABLE I. Christoffel numbers and zeros of the spherical harmonics used in the various approximations.

First approximation		Third approximation	
a_1	1	a_1	0.467914
μ_1	0.577350	a_2	0.360762
Second approximation		a_3	0.171324
a_1	0.652145	μ_1	0.238619
a_2	0.347855	μ_2	0.661209
μ_1	0.339981	μ_3	0.932470
μ_2	0.861136		

First we integrate (4.5) from -1 to $+1$, and get

$$\partial I_1/\partial z+I_0=\alpha I_0, \tag{4.6}$$

then we multiply by μ and integrate from -1 to $+1$. Then this gives:

$$2\partial I_2/\partial z+\partial I_0/\partial z+3\partial I_1/\partial z=0, \tag{4.7}$$

since $\mu^2=(2P_2+P_0)/3$. Neglecting I_2 and substituting for I_1 from (4.7) into (4.6), we have:

$$\tfrac{1}{3}(\partial^2 I_0/\partial z^2)+(\alpha-1)I_0=0, \tag{4.8}$$

which is the diffusion equation again. Thus we see that if the distribution function is spherically symmetric, the Wiener-Hopf equation corresponds to the diffusion equation. Attempting to solve (4.8) instead of (2.8) means that we are assuming that the contributions to the solution of the higher terms in the expansion in spherical harmonics are negligible. This assumption corresponds exactly to using the first approximation in our approximate method.

For the particular boundary conditions that we are considering here, the distribution at $z=0$ is far from spherically symmetric. After several collisions it will be closer to spherical symmetry. We may expect therefore that the true transmitted density will be given more closely by the first approximation, the thicker the scatterer.

B. Calculation of Experimental Quantities

Having solved Eqs. (3.10) through (3.13) it remains to be seen how the experimentally measured quantities, i.e.,

$$\Delta_0(d)=\int_0^1 \Delta(d,\mu')d\mu',$$

and

$$\sigma_0(d)=\int_0^{+1} \sigma(d,\mu')d\mu',$$

depend on the values of L_p, L_{-p}, M_p, M_{-p}, b and R. By Eqs. (2.8), (3.6), (3.7), (3.5), (3.1), and (3.2) we have:

$$\begin{aligned}\Delta_0(d)&=\int_0^1 \Delta(d,\mu')d\mu'=\int_{-1}^{+1} Id\mu'\\&\quad+\int_{-1}^{+1}\delta(\mu'-1)e^{-z/\mu'}d\mu'\\&\cong\sum_{\substack{i=-n\\ n\neq 0}}^{n} a_i\sum_{p=1}^{n}\frac{L_p e^{-\lambda_p d}}{1-\mu_i\lambda_p}\\&\quad+\sum_{\substack{i=-n\\ n\neq 0}}^{n} a_i\sum_{p=1}^{n}\frac{L_{-p}e^{\lambda_p d}}{1+\mu_i\lambda_p}+\frac{\alpha}{2}\sum_{\substack{i=-n\\ n\neq 0}}^{n}\frac{a_i\Gamma e^{-d}}{1-\mu_i}\\&=2\sum_{p=1}^{n}L_p e^{-\lambda_p d}\sum_{i=1}^{n}\frac{a_i}{1-\mu_i^2\lambda_p^2}\\&\quad+2\sum_{p=1}^{n}L_{-p}e^{\lambda_p d}\sum_{i=1}^{n}\frac{a_i}{1-\mu_i^2\lambda_p^2}\\&\quad+\alpha\Gamma e^{-d}\sum_{i=1}^{n}\frac{a_i^2}{1-\mu_i^2}.\end{aligned}$$

$$\Delta_0(d)=\frac{2}{\alpha}\{\sum_{p=1}^{n}(L_p e^{-\lambda_p d}+L_{-p}e^{\lambda_p d})\}+\Gamma e^{-d}. \tag{4.9}$$

In a similar way we find that:

$$\begin{aligned}\sigma_0(d)&=\int_0^1\sigma(d,\mu')d\mu'\\&=2b\{\sum_{p=1}^{n-1}(M_p e^{-\lambda_p d}+M_{-p}e^{\lambda_p d})\\&\qquad+d+R\}+\gamma e^{-d}.\end{aligned} \tag{4.10}$$

For the sake of completeness, we include expres-

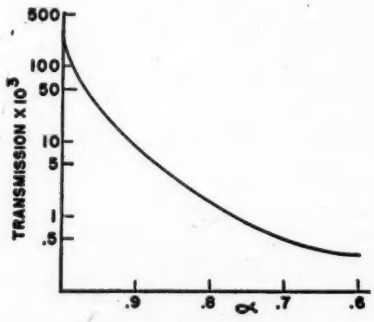

FIG. 3. Transmitted density as a function of $1-2Q$ in the second approximation when $d=10$ (mean free paths).

sions for the albedo (reflection coefficient) from a finite plate:

$$\Delta_0(0)=\int_{-1}^{0}\Delta(0,\mu')d\mu'$$
$$=-\frac{2}{\alpha}[\sum_{p=1}^{n}(L_p+L_{-p})]+\Gamma-1, \quad (4.11)$$

$$\sigma_0(0)=\int_{-1}^{0}\sigma(0,\mu')d\mu'$$
$$=2b[\sum_{p=1}^{n-1}(M_p+M_{-p})+R]+\gamma-1. \quad (4.12)$$

If a deep detector is used one would measure currents rather than densities. We therefore include the currents corresponding to Eqs. (4.9) to (4.12).

$$\int_0^1\sigma(d,\mu')\mu'd\mu'=-\tfrac{1}{3}b; \quad (4.13)$$

$$\int_{-1}^{0}\sigma(0,\mu')\mu'd\mu'=-\tfrac{1}{3}b-1; \quad (4.14)$$

$$\int_0^1\Delta(d,\mu')\mu'd\mu'=\left(\frac{2}{\alpha}-2\right)$$
$$\times\left\{\sum_{p=1}^{n}\left(\frac{L_pe^{-\lambda_pd}}{\lambda_p}-\frac{L_{-p}e^{\lambda_pd}}{\lambda_p}\right)\right\}$$
$$+(1-\alpha)\Gamma e^{-d}. \quad (4.15)$$

$$\int_{-1}^{0}\Delta(0,\mu')\mu'd\mu'=\left(\frac{2}{\alpha}-2\right)$$
$$\times\left\{\sum_{p=1}^{n}\left(\frac{L_p}{\lambda_p}-\frac{L_{-p}}{\lambda_p}\right)\right\}+(1-\alpha)\Gamma-1. \quad (4.16)$$

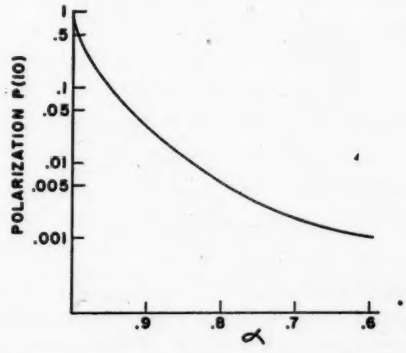

FIG. 4. Polarization as a function of $1-2Q$ in the second approximation for $d=10$ (mean free paths).

TABLE II. Solution of the equation $\alpha\sum_{i=1}^{n}a_i/1-\mu_i^2\lambda^2=1$ for various α's.

	1st approx.	2nd approx.		3rd approx.		
α	λ_1	λ_1	λ_2	λ_1	λ_2	λ_3
1		1.972027	—	3.202945	—	1.225211
0.95	0.387298	2.01257	0.379497	3.24943	0.37948	1.23255
0.9	0.547723	2.05519	0.525560	3.29669	0.52500	1.24087
0.8	0.774597	2.14577	0.711876	3.39312	0.71045	1.26096
0.7	0.948686	2.24183	0.834508	3.49150	0.829085	1.28609
0.6	1.09545	2.34138	0.922637	3.591195	0.900563	1.31067

C. Results

Using the values tabulated in Tables I and II, the transmitted density was calculated in the second approximation for $d=10$ (mean free paths), from $\alpha=0.6$ to $\alpha=1.0$. Formulas (4.9) and 4.10 were used for this calculation after having found L_p, L_{-p}, M_p, and M_{-p}, by solving (3.10)–(3.13). The values of Γ and γ are found from Eqs. (3.7) and (3.9). The results are shown in Fig. 3. The polarization $P(10)$ as defined by (2.11), if found in the case of no capture, by dividing the value of $\Delta_0(10)$ for a particular α, by the value of $\sigma_0(10)[=299\times10^{-3}]$. Thus the value of $P(10)$ for $\alpha=0.9$, is found by dividing 9.33×10^{-3} by 299×10^{-3}. This depolarization curve is shown in Fig. 4.

To test the accuracy of the second approximation for this thickness, both the diffusion and third approximation were calculated for $\alpha=0.9$ and compared.

	1st approx.	2nd approx.	3rd approx.
$\Delta_0(10)$	9.21×10^{-3}	9.334×10^{-3}	9.337×10^{-3}

It is thus seen (assuming uniform convergence as indicated above), that the second approximation is excellent, and the diffusion approximation more than adequate. The error in the first approximation is approximately given by $\Delta\alpha/\alpha=0.005$ percent which corresponds to an error in Q of ~0.05 percent if we assume that $Q\sim0.05$.

These results point to excellent experimental possibilities since the beam is depolarized by a factor of 30 when Q changes from zero to 0.05. This involves, however, the measurement of a neutron density after the polarized beam intensity has been reduced by a factor of 10,000. If a strong neutron source is not available, it may be advisable to reduce the thickness of the scatter-

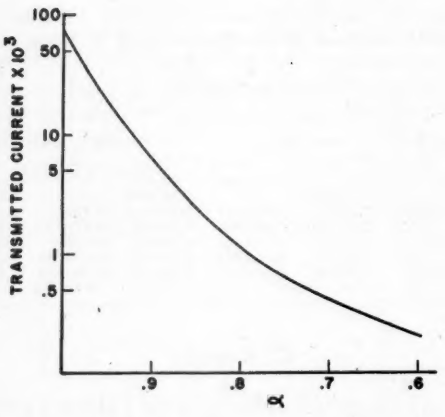

FIG. 5. Transmitted current as a function of $1-2Q$, second approximation, $d=10$ (mean free paths).

ing slab. This will increase the transmitted density, but at a sacrifice in the amount of depolarization.

To check the accuracy of the various approximations for the smaller thicknesses, we have calculated the transmitted densities in the first and third approximations for $d=5$. The results are:

	1st approx.	2nd approx.	3rd approx.
$\Delta_0(5)$	0.133	0.1249	0.1253

As is to be expected, the diffusion approximation is not as good as it was for $d=10$. In fact it is no longer adequate since the error in α is now approximately 0.25 percent corresponding to an error in Q of 2.5 percent again assuming that $Q\sim0.05$. The second approximation still seems to be remarkably good. In Table III, we have included a summary of some typical results which can be evaluated on the basis of the calculation which we have made.

For the sake of completeness, we have included too the curves in the second approximation for the transmitted current (Fig. 5), the reflected density (Fig. 6), and the reflected current (Fig. 7).

It may be remarked at this time that although we have neglected capture in this analysis, this restriction is by no means necessary. The effect of including capture is to change the fundamental Eqs. (2.7) and (2.8) as follows: in (2.7) the factor $\frac{1}{2}$ on the right is changed to $\beta/2$,[16] where β is the ratio of the total mean free path (capture +scattering) to the scattering mean free path; in Eq. (2.6) the factor α is changed to $\epsilon=(1-2Q)\beta$. Figure 3 can still be used to draw a new polarization curve. For example when $\beta=0.99$ and $Q=0.05$, the transmitted density for $\beta=0.99$ is read from Fig. 4 to be 160×10^{-3}. The transmitted density for $\epsilon=0.99(1-0.1)=0.891$ is again read from Fig. 3 and is equal to 8×10^{-3}. The polarization is therefore $8/160=0.05$ when $Q=0.05$. The rest of the curve is plotted the same way. It should be noted that distances are now measured in terms of total mean free paths, $1/l_{\text{tot.}}=1/l_{\text{cap.}}+1/l_{\text{scatt.}}$.

TABLE III. Summary of calculations for 5 and 10 mean free paths for two typical values of Q.

		5 mean free paths			
		Calculation accuracy		% error in Q when error in measurement of P is 1%	Intensity down approx.
Q	Polarization	1st approx. (%)	2nd approx. (%)		
0.025	0.62	—	—	16.3	330
0.05	0.27	2.5	0.06	3.7	330
		10 mean free paths			
0.025	0.16	1.2	0.001	1.9	10,000
0.05	0.03	0.05	0.001	0.28	10,000

V. SUMMARY AND CONCLUSIONS

We have described and analyzed an experiment suitable for the measurement of the difference between the two scattering amplitudes in the neutron-nucleus interaction. The techniques required for the experiment are the production and analysis of polarized neutron beams. The accuracy of determination of a_1-a_0 (or a_1/a_0) will depend on the accuracy of measuring polari-

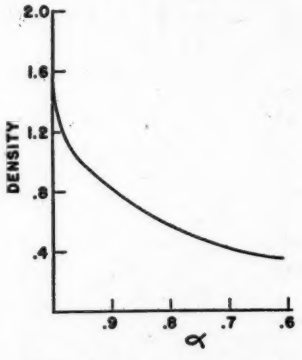

FIG. 6. Reflected density as a function of $1-2Q$, second approximation, $d=10$ (mean free paths).

[16] O. Halpern, R. Luneburg, and O. Clarke, Phys. Rev. 53, 173 (1938).

zations of neutron beams of relatively low density, and on the magnitude of the depolarizing factor Q.

Referring to Table III, we can see that for each value of Q, which must be determined approximately by some previous experiment, there will be an optimum value of scattering thickness. On the one hand, the thickness must not be so large as to completely depolarize the beam. On the other hand, the thickness must not be so small that a small error in the measurement of the depolarization will result in a large error in Q.

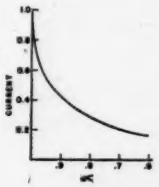

FIG. 7. Reflected current as a function of $1-2Q$, second approximation, $d=10$ (mean free paths).

PHYSICAL REVIEW VOLUME 74, NUMBER 10 NOVEMBER 15, 1948

A Direct Determination of the Energy of the He³ Nucleus from the D−D Reaction

HAROLD V. ARGO
Institute for Nuclear Studies and Department of Physics, University of Chicago, Chicago, Illinois

(Received August 2, 1948)

The energy of the He³ nuclei emitted at 90° to the incident deuteron beam in the D−D reaction has been measured directly by deflecting them through a 90°, 15-cm radius, cylindrical electrostatic analyzer. The He³ ions were detected by allowing them to eject secondary electrons from the first plate of a 12-element electron multiplier tube. Thus the ions were not required to traverse any foil or window material between the heavy ice target and the point of their detection.

The corrections to be applied to the electrostatic analyzer were experimentally investigated and when applied to the kinetic energies deduced from the observed critical deflecting voltages, give a Q value of 3.30 ± 0.01 Mev for this reaction.

INTRODUCTION

THE D−D reaction yielding a neutron and a He³ nucleus has been studied by observing the recoil He³ nuclei obtained when a beam of deuterons impinges on a thick target of D_2O ice. The energy of the He³ ions emitted at 90° to the incident deuteron beam was measured by deflecting them 90° with an electrostatic analyzer, and the ions were counted with an electron multiplier tube* of the type developed by J. S. Allen.[1] From the knowledge of the energy of the incident deuteron and the energy of the He³ nucleus emitted at 90°, one has from conservation of energy and momentum the energy released in the reaction

$$D^2+D^2\rightarrow He^3+n+Q, \qquad (1)$$

$$Q=E_D+4E_{He}, \qquad (2)$$

where Q is the energy released, E_D is the kinetic energy of the incident deuteron, and E_{He} is the kinetic energy of the He³ nucleus emitted at 90° in the laboratory system.

APPARATUS

The deuteron beam was accelerated by a Cockcroft-Walton voltage quadrupling circuit of conventional design employing a low voltage arc source developed by S. K. Allison.[2] Accelerating voltages up to 400 kv could be attained. This voltage was measured by a resistance stack of approximately 10^{10} ohms in series with a sensitive galvanometer. The current through the resistance stack was known to 0.1 percent accuracy, and the resistance to about 0.2 percent. The beam

* The construction of the electron multiplier tubes for this work was assisted by the Joint Program of the Office of Naval Research and the Atomic Energy Commission.

[1] J. S. Allen, Phys. Rev. **55**, 336 (1939); **55**, 966 (1939).

[2] S. K. Allison, Rev. Sci. Inst. **19**, 291 (1948).

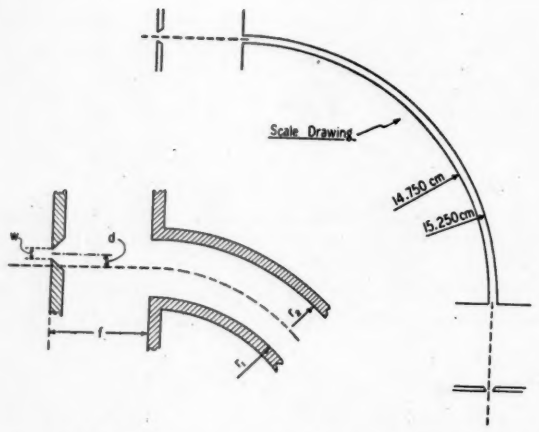

FIG. 1. Schematic illustration of the 15-cm electrostatic analyzer showing the entrance and exit slits.

was accelerated along a 3.0-meter path. At the end of this path an electromagnet was used to deflect the beam horizontally through an angle of 15°. This served to separate the deuteron beam from the other components present. One had the choice of either the atomic deuterium beam or the molecular deuterium beam which, of course, gave deuterons of one-half the accelerating voltage energy. The two beams were of comparable intensity.

The target was placed 100 cm from the deflecting magnet and was insulated electrically from the rest of the system. A $\frac{1}{4}$-in. diameter beam stop immediately in front of the target served to limit the beam, and for monitoring purposes a beam current integrator of conventional design measured the beam strength on the target.

The target was a layer of D_2O ice on a copper slug in good thermal contact with a liquid nitrogen reservoir. The target was laid down continuously during operating by feeding D_2O vapor into the target chamber by means of a $\frac{1}{8}$-in. I.D. tube connecting a small bottle of D_2O water with the target chamber. This technique was adopted at the suggestion of S. K. Allison to insure having a clean surface layer of D_2O on the target at all times. Three liquid nitrogen traps were used to reduce the pressure of oil vapor in the system. One trap was placed directly in the target chamber, and the remaining two were placed in the throats of the two six-inch oil diffusion pumps in the large system.

The plane of the target made an angle of 45° with the incident beam and 45° with a vertical line. The entrance slits to the electrostatic analyzer (Fig. 1) were 9.65 cm directly below the target and had a slit width of 3.0 mm.

The electrostatic analyzer used was a new one developed by S. K. Allison[3,4] (Fig. 2). Two cylindrical aluminum plates separated by 0.50 cm deflect the ions through 90°. The average radius of the two plates is 15 cm, and the radii have been held to within ±0.001 cm. The plates are supported on a single quartz post 1.5 inches in diameter, placed at their center of curvature, and the diameter of the cylindrical post has been held to a tolerance of ±0.0001 inch. Both the position and the width of the entrance and exit slits are adjustable externally.

The entrance and exit slits were placed 5.0 cm from the ends of the deflecting plates of the analyzer. With this arrangement, the fraction of particles collected from a monoenergetic source located at the target is given by

$$(h\Delta r)\Big/\left(4\pi\left(l_1+\frac{\pi r}{4}\right)\left(l_1+l_2+\frac{\pi r}{2}\right)\right), \quad (3)$$

where h is the height of the entrance into the

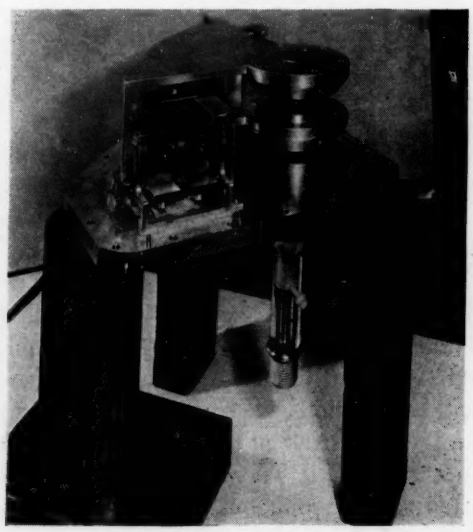

FIG. 2. Photograph of 15-cm electrostatic analyzer with outer shell removed, showing the two concentric cylindrical deflector plates supported by the quartz post. The entrance slit mechanism is in front of the deflector plates.

[3] S. K. Allison and H. V. Argo, Phys. Rev., in press.
[4] Allison, Skaggs, and Smith, Phys. Rev. **54**, 171 (1938).

electron multiplier tube, one inch in this case; Δr is the separation of the two analyzer plates; r is the mean radius of the two analyzer plates; l_1 is the distance from the target to the entrance end of the plates, 14.65 cm in this case; and l_2 is the distance from the exit end of the plates to the entrance of the electron multiplier tube, which is 12.5 cm. The solid angle factor, as expressed in (3), is calculated to be 6×10^{-5}.

The analyzer does not have perfect resolution,[4] that is, a monoenergetic point source of particles located at the target will not have an infinitely sharp line for its energy spectrum when viewed through the analyzer. Instead, it will have a triangular shaped distribution, as shown in Fig. 3, where E is the energy of the particles coming from the monoenergetic source, and δE is the half-width, or limit of resolution, of the instrument. For slits of equal width w, δE is given by the relationship

$$\delta E/E=w/r, \tag{4}$$

where r is the mean radius of the analyzer. With a slit width of 3.0 mm and a radius of 15 cm, the limit of resolution for this instrument is 2.0 percent in energy.

Let E be the kinetic energy, in electron kilovolts, of an ion traversing a circular orbit between the cylindrical electrodes, the orbit being concentric with the plates. Then

$$E=(z|V_2-V_1|)/(2(\log r_2-\log r_1)), \tag{5}$$

where

r_2, r_1 are the radii of the outer and inner plates, respectively,

z is the number of electronic charges carried by the ion,

$|V_2-V_1|$ is the numerical value of the difference in potential between the plates, expressed in kilovolts.

Using the dimensions of the present instrument, we obtain

$$E=15.00|V_2-V_1|z. \tag{6}$$

Various authors[5] have discussed the equations of the non-circular orbits and the focal properties of the device. Consider a source emitting monoenergetic ions of kinetic energy E_A. Let the source be located outside the analyzer, at distance f from the plane containing the entrance to the cylindrical channel. A divergent bundle of ionic rays, leaving this source and passing through the analyzer, is brought to a focus at a distance f' from the exit plane, which may be deduced from the two following expressions

$$[(f-g)(f'-g)]^{\frac{1}{2}}=\frac{r_1+r_2}{2\sqrt{2}\sin(\varphi_m\sqrt{2})}, \tag{7}$$

$$g=(r_1+r_2/2\sqrt{2})\cot(\varphi_m\sqrt{2}). \tag{8}$$

In these equations, φ_m is the angular length of the path between the plates, in our case, $\pi/2$. The important special case $f=f'=f_0$ is given by

$$f_0=\frac{r_1+r_2}{2\sqrt{2}}\frac{1+\cos(\varphi_m\sqrt{2})}{\sin(\varphi_m\sqrt{2})}. \tag{2}$$

Using the constants of our analyzer, we obtain $f_0=5.29$ cm.

The design of the analyzer was such that the disposition of slits, vacuum walls, etc., that would affect the stray electric field was the same (actually, the two dispositions were mirror images) at the entrance and exit of the cylindrical channel. In these measurements, the distance f (see Fig. 1) was held at 5.0 cm, close to the value of f_0, for both entrance and exit slits.

Protons scattered at 90° from a 312-kev beam were used to adjust the instrument. In order to

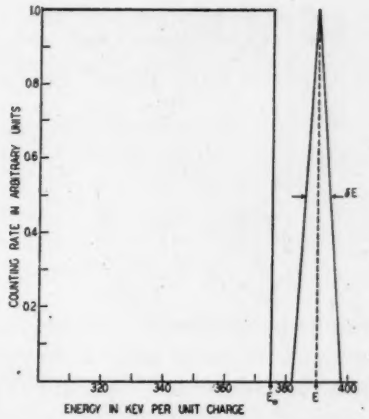

FIG. 3. "Step function" energy distribution of He^{3++} nuclei coming from D_2O ice target as predicted by simple theory. E_0 is the upper energy limit of the spectrum. Also shown is the triangular-shaped energy "window" of the electrostatic analyzer.

[5] A. L. Hughes and V. Rojansky, Phys. Rev. **34**, 284 (1929); R. Herzog, Zeits. f. Physik **89**, 447 (1934); A. J. Dempster, Phys. Rev. **51**, 67 (1936); F. T. Rogers, Jr., Rev. Sci. Inst. **11**, 19 (1940).

TABLE I. Test of the correction $P(\bar{r})$ using deuterons from $Be^9(p, d)Be^8$; incident proton energy about 266 kv; slit widths 0.20 cm; half-width at half-maximum of deuteron peaks, 2.5 percent *vs.* 1.3 percent expected from slit widths.

Arrangement	Deflecting kilovolts for maximum counting rate	E from Eq. (5) kev	$P(\bar{r})$	E_A kev
$V_1=0$	$V_2=+39.36$	590.4	+19.7	610.1
$V_2=0$	$V_1=-42.29$	634.4	−21.2	613.2

obtain protons homogeneous in energy, the primary beam was scattered from a very thin film of gold, which had been evaporated onto the polished surface of a beryllium button. The energy spectrum of the scattered protons shows a sharp, high peak from the gold at 312(196/198) kev, with a low, continuous distribution from the underlying beryllium having an upper energy limit slightly below 312(8/10) kev. Such scattered spectra are further discussed in another paper from this laboratory.[6]

Referring to Fig. 1, both slits were set with the width w at 0.05 cm, and various values of d were tried, keeping d the same for the entrance and exit slits, until a position was found in which the counting rate for protons scattered through the device was a maximum. In order to find this position, it was necessary, at each value of d which was tried, to

(a) maximize the counting rate as a function of deflecting kilovolts,

(b) maximize the counting rate as a function of target position.

Operation (a) is called for because of the following considerations. The effective radius $\bar{r}$, at which the narrow pencil of rays defined by the two slits passes through the cylindrical channel, is a function of the d of the slits. In order to cause the central ray in the pencil to traverse this orbit, the deflecting voltage must have such a value that E, calculated from Eq. (5), is given by

$$E=E_A+P(\bar{r}), \tag{10}$$

where $P(\bar{r})$ is the gain in energy resulting from the action of the electric field on the ions in passing from the grounded target to a point between the plates of the analyzer at distance $\bar{r}$ from the axis. Thus the deflecting voltage required to maximize the ion beam is a function of d.

[6] H. A. Wilcox, Phys. Rev. (to be published).

Operation (b) consisted in moving the target in order to be certain that any trend in the maxima from operation (a) was not due to inhomogeneities in the numbers of protons scattered from the various target areas coming in line with the changing slit positions.

In measuring the He^3 ions, the centers of the slits were left in the positions located as above; it was, however, necessary to open the slits to a width of 0.3 cm in order to obtain sufficient counting rates. With such an adjustment, it seems clear that the effective radius $\bar{r}=\frac{1}{2}(r_1+r_2)$, and that the value of $P(\bar{r})$ is $\frac{1}{2}z(V_1+V_2)$.** Since the object of the experiments is to determine E_A, not E, it is necessary to apply the "correction" $P(\bar{r})$.

The following experiment was performed to test the validity of this correction. A thin target of metallic beryllium evaporated onto polished nickel was bombarded by protons, and the deuterson from the reaction $Be^9(p, d)Be^8$ were deflected through the analyzer.[7] Two different arrangements of V_1 and V_2 were used, and it was ascertained that the correction produced the same value E_A from both. The data are given in Table I. It is seen that the application of the correction brings the two values together to within 0.5 percent.

The data of the experiments on He^3 ions were taken with the outer plate of the analyzer at ground potential and the inner plate supplied with a negative high potential.

The high voltage source for the electrostatic analyzer consisted of a 540-cycle generator with a simple half-wave rectifier having a 0.1-mf capacitor, and giving a continuously variable output up to 50 kv. The voltage was measured by means of a wire-wound resistance stack of 20(10)[6] ohms at ±0.1 percent, and a 1.5-ma meter calibrated to better than 0.1 percent accuracy. An electrostatic voltmeter was used as a check.

After passing through the electrostatic analyzer the ions were detected by a twelve-electrode electron multiplier tube in the manner already described in detail by L. del Rosario.[7]

** Using this value of the mean potential at the arithmetic mean radius is an obvious, but legitimate, approximation.

[7] See L. del Rosario, Phys. Rev. **74**, 304 (1948).

In brief, the impulse from the collecting electrode of the multiplier tube was fed into a cathode follower and preamplifier of unit gain, and thence into a pulse amplifier, discriminator, and scaler. The discriminator bias was set to accept a minimum pulse height of 0.010 volt from the multiplier tube. The pulse amplifier had a gain of approximately 500.

THEORY OF THICK TARGET YIELD

Since the He^3 ions coming from the thick target at 90° are not monoenergetic, one observes an energy spectrum. Some analysis is necessary to determine the energy of the nascent He^3 ions from this spectrum. Those He^3 ions produced deep in the target are due to deuterons which have been slowed down by their passage through the outer layers of D_2O ice. The He^3 ions will be degraded in energy in passing back out through the ice. Thus the nascent energy will be intimately related to the front edge of the energy spectrum.

The slowing down of low energy He^4 and D^2 ions while passing through gold foils has been measured in this laboratory by H. A. Wilcox.[6] Assuming that the molecular stopping power is the sum of the atomic stopping powers, and that the relative atomic stopping powers as given by Cork[8] hold for these low energies, one can use the results of Wilcox to get the slowing down of D^2 and He^4 ions in D_2O ice. Assuming that two isotopic ions of the same velocity have very nearly the same rate of energy loss, one can then get the rate of energy loss of He^3 in D_2O ice. Assuming a Q value for this reaction of 3.31 mev, after T. W. Bonner,[9] and an incident energy of 329 kev for the deuterons, one has for the nascent energy of the He^3 ions

$$E_{He}=\tfrac{1}{4}(Q-E_D)=745 \text{ kev}. \qquad (11)$$

From Wilcox's data one gets for the rate of energy loss of D^2 ions of 329-kev energy passing through D_2O ice

$$dE/d\tau \sim 270 \text{ kev/mg/cm}^2,$$

and for He^3 ions of 745-kev energy passing through D_2O ice

$$dE/d\tau \sim 990 \text{ kev/mg/cm}^2,$$

where τ is the path length in mg/cm². These loss rates are reasonably constant in the neighborhood of these energies. Thus one can easily find the energy of the deuterons as a function of the path length they have traversed in D_2O ice. From formula (11) above, one then finds the energy of the nascent He^3 nuclei as a function of the depth in the target at which they were produced. In the energy range which interests us, the energy of the deuteron is a linear function of the amount of material it has traversed, and since the energy of the nascent He^3 nucleus is a linear function of the energy of the deuteron producing it, the curve of energy of nascent He^3 *versus* the point of origin in the target will be a straight line for a considerable range of energy below the upper limit. Table II gives the above argument in a numerical form.

TABLE II. Estimated energies *vs.* depth in target for emergent He^3 ions.

τ mg/cm² traversed to point of creation of He^3	Deuteron energy in kev at point where He^3 originates	Energy in Mev of nascent He^3	Energy in Mev of He^3 emerging from target
0	329	0.745	0.745
0.00733	327	0.745_{75}	0.738_5
0.0146	325	0.746_{25}	0.731_8
0.0220	323	0.746_{75}	0.725_0
0.0293	321	0.747_{25}	0.718_2
0.0366	319	0.747_{75}	0.711_5

Bennett, Mandeville, and Richards[10] have measured the angular distribution of the $D^2(d, n)He^3$ reaction in the energy range from 0.5 to 1.8 Mev, using a thin target of D_2 gas. Extrapolating their data to 0.330 Mev and calculating the yield of He^3 to be expected at 90° in the laboratory system, one finds that a 3 percent decrease in the incident deuteron energy will decrease the yield by approximately 0.5 percent. As a first approximation we assume that the yield of He^3 in the ice target is independent of the position within the target, at least over the range of interest. Therefore, since the rate of energy loss of He^3 ions in D_2O ice is a constant in this energy region, one gets in first approximation that the

[8] J. M. Cork, *Radioactivity and Nuclear Physics* (Edwards Brothers, Inc., Ann Arbor, Michigan, 1946), p. 63.
[9] T. W. Bonner, Phys. Rev. 59, 237 (1941).
[10] Bennett, Mandeville, and Richards, Phys. Rev. 69, 418 (1946).

TABLE III. Results.

E_D	E_{He} (cf. E_A in Eq. (10))	Q (cf. Eq. (2))	Δ*	Weight
329 kev	741.5 kev	3.295 Mev	0.007 Mev	10
329	744.0	3.305	0.003	10
329	747.3	3.318	0.016	10
165.5	780.6	3.288	0.014	10
329	745.3	3.310	0.008	3
329	744.6	3.307	0.005	3

* Δ is the deviation from the mean.

emergent He^3 ions are uniformly distributed in energy over a sufficiently wide energy range to warrant treating the energy spectrum as a "step function."

The observed spectrum will be this "step function" as seen through the electrostatic analyzer, which has, effectively, a triangular shaped energy window of 2.0 percent half-width in energy. In Fig. 3, $\delta E = 0.02E$. E_0 is the energy of the front edge of the step function, and E is the energy the analyzer is set to transmit. The ordinate represents the number of ions coming from the target at 90°. As the "window" of the analyzer is moved downward along the energy scale, the number of ions getting through the analyzer is proportional to the area of the triangular window that is overlapped by the step function energy spectrum. This analysis is readily carried out, giving as the observed energy spectrum the curve in Fig. 4. E_0, the upper limit of the energy distribution of the He^3 nuclei, occurs at 51 percent of the peak counting rate.

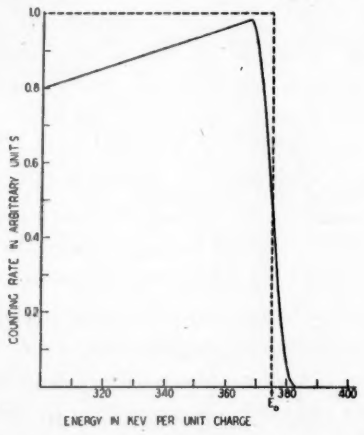

FIG. 4. The energy spectrum of Fig. 3 as observed through the electrostatic analyzer with a slit width of 3.0 mm. The dashed line is the assumed distribution and the solid line the observed distribution according to theory.

The observed curves are slightly more peaked, but have the same slope on the front edge as predicted by the above arguments. In the approximations which resulted in the step function yield from the target, the scattering of deuterons from the incident beam was neglected, as was the scattering of the He^3 nuclei from the emergent beam. The yield of the D−D reaction at 90° is not constant with energy as assumed, but drops off slightly as the energy decreases. In addition, contamination by oil and carbon of the D_2O layers below the surface layer has been ignored. All of these factors would tend to make the energy spectrum from the target have a more rapid drop off behind the front edge. A calculation using a "saw tooth" function was made, giving Fig. 5 as the predicted observable energy spectrum. The slope of the front edge remains essentially unchanged, while the peak intensity is reduced from 98 percent to 96 percent. E_0 occurs at 52 percent of the peak counting rate.

As the front of the observed and predicted curves is relatively steep, E_0 is well defined. After a comparison of the theoretical with the experimental curves, E_0 was chosen to be that energy corresponding to 52.5 percent of the peak counting rate.

RESULTS

Figure 6 shows a curve of the type obtainable with this arrangement. This particular curve is of interest because it shows both the He^{3++} and

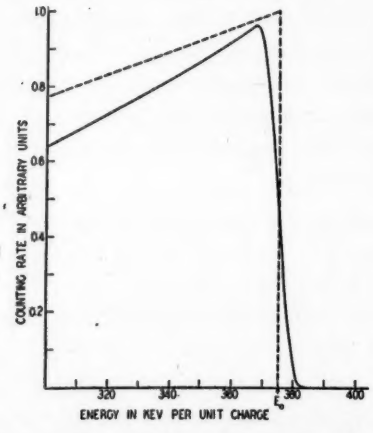

FIG. 5. A "saw tooth" energy distribution of He^{3++} nuclei coming from thick D_2O ice target as observed through the electrostatic analyzer with a slit width of 3.0 mm. The dashed line is the assumed distribution and the solid line the observed distribution according to theory.

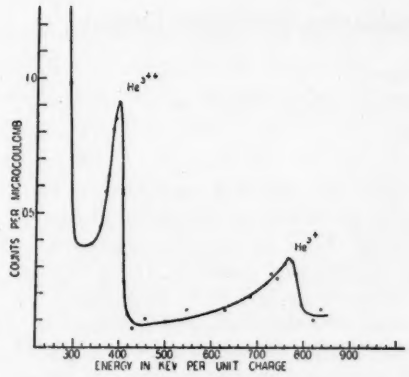

FIG. 6. A curve showing both the He^{3++} and He^{3+} ions coming from the D_2O ice target. The target was intermediate in thickness.

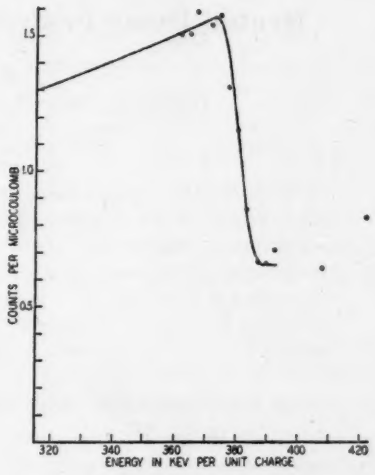

FIG. 7. A typical curve showing the high energy edge of He^{3++} particle distribution. The circles are experimental points, and the curve is that to be expected from theory. The abscissae are uncorrected energies per unit charge calculated from Eq. (5).

the He^{3+} peaks. The target in this instance was intermediate between a thick and a thin target, and the curve is not suitable for a quantitative measurement of energies.

As an illustration of the operating conditions a typical set of observations is included. For the curve shown in Fig. 7, the accelerating voltage was 329 kv, beam strength on target as measured by the beam current integrator was 10 μa, the current through the electromagnet to obtain a 15° deflection of the deuteron beam was 4.05 amperes, and the peak counting rate for He^{3++} ions was approximately 1.6 counts per microcoulomb. The counting periods were monitored at 500 microcoulombs on the target. The circles in the figure are the observed counting rates, while the smooth curve drawn through them is the theoretical one of Fig. 5 scaled to fit these data.

The peaks used for energy determinations in all cases were the He^{3++} ions, as these occur at one-half the analyzer voltage required to observe the He^{3+} ions, minimizing the natural background of the analyzer.

A total of six curves was obtained. They satisfy the criteria of having the slopes of their front edges agree with the theoretically predicted slope, and having a reasonable scattering of points so that smooth curves could be drawn through them. About an equal number of curves were rejected because of breaks in the front edges, scattering of points, and too gentle a slope. These troubles were attributed to changes in the target surface during the course of the run. A tabulation of the results appears in Table III. Because of a scattering of the observed points, the last two determinations were given a statistical weight of 3 as compared with a weight of 10 for the others. The resulting value of Q is 3.30 ± 0.01 Mev.

The best previous measurement of this energy release is due to T. W. Bonner,[9] who has measured the energy carried by the neutron by observing the recoil protons in a cloud chamber. This makes his result dependent upon the range energy relationship for protons. His result is $Q=3.31\pm0.03$ Mev, which is in agreement with the above value.

ACKNOWLEDGMENTS

The author would like to take this opportunity to thank Professor S. K. Allison for suggesting this measurement, and for his advice and assistance during the progress of the work. In addition, he wishes to thank the other members of this laboratory, M. L. Argo, W. R. Arnold, D. Bushnell, and G. W. Farwell for their kind assistance.

Neutral Decay Products of Cosmic Radiation at Great Depth

J. BARNÓTHY* AND M. FORRÓ*
Institute for Experimental Physics, University of Budapest, Hungary
(Received May 27, 1948)

The absorption curve of cosmic radiation was measured during a period of seven years in a coal mine at a depth of about 1000 m w.e. The shape of the curve and the counter-efficiency measurements suggest that the most penetrating component of cosmic radiation consists of non-ionizing or scarcely ionizing rays. It was found that the intensity decreases for inclined directions less than it would correspond to the thickness of the material and its temperature coefficient is positive. All these experimental evidences, together with the known fact that at 400 m w.e. depth the exponent in the intensity *versus* depth variation changes from 1.8 to 2.8, favor the view that the radiation present at 1000 m w.e. depth is formed at the decay of the mesons in the atmosphere. Neutrini or neutral mesons may account for the findings.

IN the present paper we summarize the results obtained in the course of seven years at 700 and 1000 m w.e. (water equivalent) depth, respectively, in the coal mine of Dorog, situated at 35 km NW from Budapest. Surveying now these experiments it is evident that more ingenious experiments could have been thought of than those we actually carried out. But we started in 1936 quite unprejudiced with the observations and only slowly arrived at the conclusion that the radiation must consist of neutral decay products of mesons. Further, we should stress that we have measured absorption curves at depths where others could merely confirm the presence of cosmic radiation. The extremely small intensities necessitated very long series of measurements.

DESCRIPTION OF THE APPARATUS

The measurements were performed with a method published in 1933.[1] The first circuit consists of a back-coupled amplifier (Fig. 1) which substitutes the slow voltage drops occurring during a discharge on the wire of the G-M counter with an impulse having a high initial steepness of 10^{-8} sec. The substituted impulse starts instantaneously when the voltage of the wire drops by merely 30 millivolts. The circuit can be adapted to the quenching of G-M counters filled with pure gases. The quenching is already established through the capacity formed by the auxiliary grid and the control grid, but its action can be promoted by a coupling condenser connected between the points 4 and 6. The coincidences are selected in the usual Rossi manner with a common plate resistor and the coupling elements $R\,C$ having a small time constant. A further back-coupled amplifier provides for sufficiently long impulses to operate a mechanical recorder. Only those details of the circuits will be here specified which are, according to our experience, important in measurements at great depth.

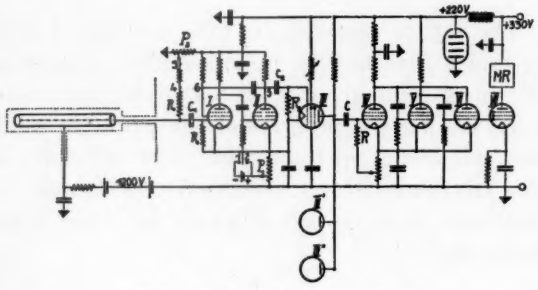

FIG. 1. Coincidence circuit.

The scarcely-ionizing nature of the radiation made it often necessary to register twofold coincidences, thus involving circuits with extremely high resolving power. However, on account of the slow motion of the electrons within the G-M counter, it is not safe to reduce for counters of 4 cm in diameter and argon+alcohol filling the resolving time below 10^{-6} sec.,[2] because otherwise more than ten percent of the genuine coincidences would be lost. For a coincidence time of 10^{-6} sec., however, the plate resistor of the valves *III*, *III'* $\cdots$ is, contrary to the Rossi circuit, small with respect to the inner resistance of the vacuum tubes. This might cause a con-

* Now at Barat College, Lake Forest, Illinois.
[1] J. Barnóthy, Naturwiss. **21**, 835 (1933).
[2] D. Nagy, Math. Fiz. Lapok **47**, 1 (1940).

siderable drop in the plate voltages even when only one of the valves is blocked. The selection of the coincidences is greatly facilitated if, for the valves *III*, *III'*, we use tetrodes without suppressor grids and make use of the secondary emission of the plates. If the potential of the screening grid is two to three volts higher than the plate voltage, a considerable secondary electron current will flow from the plate. When now one tube is blocked, it is sufficient that the plate voltage of the other tubes be raised by one to two volts in order to compensate the decrease of the plate current of the blocked tube through the decrease in the secondary currents from the plates of the other tubes.

Even if threefold coincidences are recorded, it is not advisible to choose the time constant of the coupling elements before the grid of valve *III* higher than 10^{-5} sec., because for the radiation observed at great depth the efficiency for twofold coincidences happens to be twenty times that of the threefold coincidences, in which case on account of the small total intensity a not negligible number of accidental coincidences might arise between the genuine twofold coincidences and the impulses of the third counter.

The theoretical resolving power of the circuit is limited by the ratio of the capacities of the electrodes and connecting wires to the steepness of the vacuum tubes. For resolving times up to 10^{-6} sec. commercial amplifier valves may be used. For other purposes when the utilizable resolving power is not limited by the use of gas-filled G-M counters, vacuum tubes with high steepness and small electrode capacities enable the extension of the resolving power to about 10^{-9} sec.

According to our measurements, a coincidence telescope in which every counter tray contains two G-M counters of 100 cm length, of 4 cm diameter, and filled with a mixture of argon+alcohol, when using for $R_0 = 100 M\Omega$ and a coincidence time $\vartheta = 1.4 \times 10^{-6}$ sec. the losses (listed in Table I) in the efficiency of the whole apparatus result on account of the slow reloading of the counter wires and on account of the coincidence time. The efficiency of our G-M counter for the radiation at sea level was better than 99 percent.

The high voltage of the G-M counters was supplied by a dry cell battery. The temperature within the locality during the whole year was within $\pm 1°$C constant. Consequently, an impulse-size regulator, commonly applied in our periodicity measurements, was here superfluous. Plate and filament storage cells, iron-hydrogen resistors and glow lamp stabilizers provided a constant voltage which did not appreciably drop even if the main electricity supply was switched off for several hours. The humidity in the mine amounted to 85–95 percent; consequently, waterproof boxes were used and the sensitive insulating parts of the apparatus were kept dry by heating or with P_2O_5.

TABLE I.

	Twofold coinc.	Threefold coinc.	Fourfold coinc.
On account of R_0	3%	4.5%	6%
On account of ϑ	6%	6 %	6%
Total loss	9%	10.5%	12%

The coincidences were recorded with a mechanical recorder and the distribution of the coincidences could be checked on a paper strap moved with constant velocity by clockwork.

MEASUREMENTS PERFORMED AT 730 m w.e. DEPTH

During two months of the year 1936 we measured at a depth of 730 m[3] two- and threefold coincidences in the positions illustrated in Fig. 2. The material immediately above the apparatus consisted of a coal layer. The arrangements *b–g* enabled us to determine the directional distribution of the radiation. The surface of the ground above the shaft was nearly level, the elevations nowhere exceeded 20 m, and with the help of a map giving the level lines in a ratio 1:25,000 and out of samples gathered from 30 different bores, we could establish the thickness and mass of the material above the apparatus for every part of

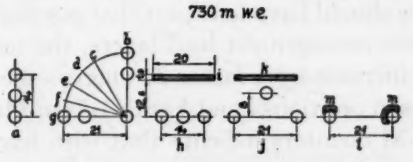

FIG. 2. Arrangements for the measurement of directional distribution and showers. Distances given in cm.

[3] J. Barnóthy and M. Forró, Zeits. f. Physik **104**, 744 (1937).

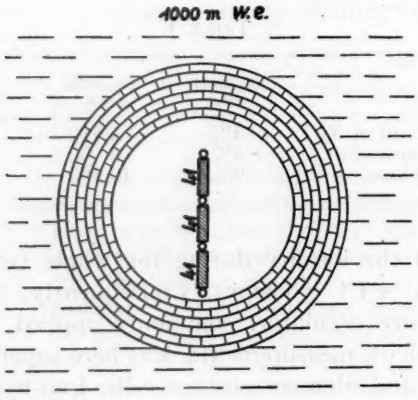

FIG. 3. Disposition of the counter-trays within the brick cylinder of the shaft.

its aperture with nearly as much accuracy as if the whole device had been submerged in water.

For the directional distribution we found (after subtracting as residual intensity that of position *g*):

$$D(\alpha)\times 10^6 = -0.2+3.7\cos^2\alpha - 1.0\cos^4\alpha$$

coinc./cm² hours, square degree.

The vertically incident radiation computable from this directional distribution yields the value:

$$J_v = 2.5\times 10^{-6} \text{ coinc./cm}^2\text{, hours, square degree.}$$

In all these measurements carried out deep underground below a dense material, the intensity due to cascade showers initiated by decay electrons of the mesons is negligible, merely knock-on secondaries and their cascade showers have to be considered. According to the computations of Bhabha,[4] the probability that a primary meson or proton of, say, $10^{11}-10^{12}$-ev energy should be accompanied by more than two secondary particles is in lead twice as much as in lighter materials, for instance, in coal. Therefore, we should have to expect that putting above a shower arrangement lead layers, the intensity would increase by a factor 2, whereas the observations in positions *i* and *k* with 1.5 cm Pb above the G-M counters indicate that with lead layer the intensity amounts merely to 40 percent of the intensity without lead. This suggests that the primary radiation cannot consist of mesons or other heavier charged particles.

From the measurements made in positions *l* and *m*, where twofold coincidences were registrated between horizontally placed G-M counters, first without lead and then with the counters surrounded by 1.5 cm Pb, we may reckon the range of the secondary particles to be 19 g/cm². This value is smaller than the range of the secondaries found with the same arrangement under a coal layer in our institute (48 g/cm²). The range of these secondaries establishes with sufficient certainty that the showers observed in the mine do not consist of coherent rays, able to penetrate through the deep earth layer.

A further noteworthy feature of the radiation is that the ratio of the horizontal intensity, i.e., of the shower intensity to the vertical intensity, is greater by a factor 4–6 in the mine than in our institute (120 m above sea level) under a coal layer. The arrangements *l* and *j* were able to detect showers with two to three particles. Assuming that the intensity from the horizontal direction is almost negligible, that the showers have the same directional distribution as the vertical radiation and, moreover, that the ratio of showers with three particles to those with two particles has the same value as the ratio of the showers containing two particles to those with only one particle, we can reckon from the respective counting rates the intensity of the shower particles arriving from the vertical direction to be:

$$J_s = 2.6\times 10^{-6} \text{ coinc./cm}^2\text{, hour, square degree.}$$

The amazing equality of this value of J_s with that of the vertical intensity J_v, together with the foregoing considerations, suggest that in the mine the penetrating radiation consists of non-ionizing rays, which are able to produce coincidences with the help of their ionizing secondaries. However, the secondaries and cascades can not be produced by knock-on electrons, but in nuclear collisions. This explains the fact that the number of secondaries decreases when the material above a shower arrangement is replaced by a material of higher atomic weight. At that time we assumed that the penetrating non-ionizing component consisted of neutrini created in air showers.

[4] H. J. Bhabha, Proc. Roy. Soc. **A164**, 257 (1928).

RADIATION MEASURED WITH TWOFOLD COINCIDENCES

In the subsequent measurements which we began at the end of 1937 at 1000 m w.e. depth, the apparatus was installed in a cylindrical side gallery of the mine (Fig. 3), which had a diameter of 2 m; it had a brick casing 60 cm thick. In every counter tray two parallel-connected G-M counters were mounted; thus the sensitive area was increased to 820 cm² and provision was made to place 120 cm of lead between the counter trays.

Suspecting the non-ionizing nature of the penetrating radiation, our aim first was to measure the efficiency of the radiation by determining the twofold and threefold coincidence rates. Table II contains the results. In case of the twofold coincidences it was important to determine separately the rate of accidental+shower coincidences. This was performed by placing the two counters in a horizontal plane as far apart as the narrow locality permitted, a huge lead block being placed between the counters. The number of accidental coincidences was computed from the coincidence time of the circuit to be 1.4 coinc./hour; in horizontal position we found 5.6 coinc./hour, thus 4.2 coinc./hour were due to showers.

For the ratio of the threefold to twofold coincidences we found the very low value of 4.7 p.c. The gas-filling of the G-M counters was equivalent to about 1 cm of air at N.T.P.; thus this radiation which is hardly able to produce a threefold coincidence has a specific ionization of 0.05 ion/cm air at N.T.P. G-M counters of 4 cm in diameter have, according to our measurements, 0.4 p.c. efficiency in detecting γ-rays from RaC. Although the specific ionization of the radiation exceeds the value we found for γ-rays, we can not discard the possibility that perhaps the apparent greater specific ionization is a consequence of the fact that it is able to create more energetic electrons. In order to investigate this point we have placed 11 cm of lead between the counters (second row in Table II), the efficiency was again very low, only 10 p.c., meaning that after 11 cm Pb this scarcely ionizing radiation is still present. This circumstance excludes its interpretation as being a γ-radiation. In this second set we have subtracted from the number of the twofold coincidences merely the number of the accidental coincidences, the number of the showers being now negligible, since the bottom counter was shielded from all sides by lead.

TABLE II.

Absorber	Distance of the counters	A Twofold coinc. per hour	B Threefold coinc. per hour	B/A Efficiency
0.4 cm Pb	24 cm	26.6±0.4	1.25±0.11	4.7 p.c.
11 cm Pb	24 cm	11.0±1.4	1.09±0.10	10 p.c.

The result that the intensity of the twofold coincidences decreases rapidly with absorber thickness whereas the intensity of the threefold coincidences does not, seems to indicate that two kinds of penetrating radiation are present at 1000 m depth—one, scarcely ionizing and not able to produce a threefold coincidence, and another which gives rise to the threefold coincidences and which may be perhaps ionizing. Anyway, from the very slight decrease in the number of the threefold coincidences after inserting 11 cm Pb, we may infer that this radiation is also penetrating and moreover it cannot consist of electrons.

The properties of the scarcely ionizing radiation which is not able to produce a threefold coincidence were investigated by inserting thin lead layers between the counters of a twofold coincidence device. Lead blocks placed at both sides of the counters sufficiently insured the triggering of the counters by shower particles.

The intensity decreases rapidly (Fig. 4), indicating that the scarcely ionizing radiation has a high absorbability in lead. However, after a

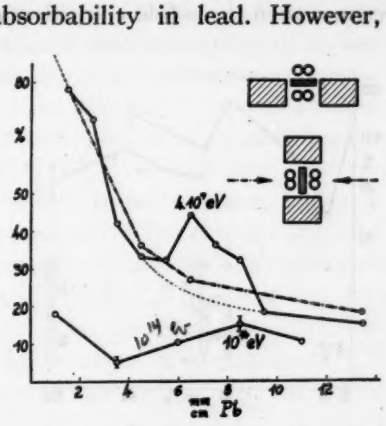

FIG. 4. Absorption curve of twofold coincidences in lead. For the upper curve the abscissae are expressed in mm Pb, for the lower curve in cm Pb.

TABLE III.

Absorber	Distance of the counters	Threefold coinc. per hour	Fourfold coinc. per hour	Efficiency
3 cm Pb	152 cm	0.099±0.008	0.087±0.009	88±10 p.c.
123 cm Pb	152 cm	0.088±0.009	0.058±0.008	66±10 p.c

minimum the intensity increases anew, reaches a maximum, whereafter it falls down. This part of the curve is very similar to the Rossi curve of showers, and obviously the absorption of the scarcely ionizing radiation is also due to the production of electron pairs and cascade showers.

The most striking thing, however, is that the absolute intensities and the slope of the absorption curve remains unchanged when the whole arrangement is turned through 90°, in which case only the incident rays coming sideways are able to trigger the counters. In Fig. 4 the dash-dot (–·–·–) line corresponds to this measurement. This result can be interpreted by assuming that the scarcely ionizing radiation is isotropic for the whole hemisphere. At first glance we might interpret this phenomenon by saying that the radiation is produced when secondary mesons stopped in the surrounding material suffer decay. This explanation is, however, not consistent with the small range and relatively high intensity of the scarcely ionizing radiation as compared to the small intensity of the secondary mesons. (See ratio of two-fold to three-fold coincidences). Anyhow, the isotropy of the radiation does not invalidate the previous findings of a directional distribution in our 1936 measurements, because then three-fold coincidences were recorded, thus not the directional distribution of this soft, scarcely ionizing component.

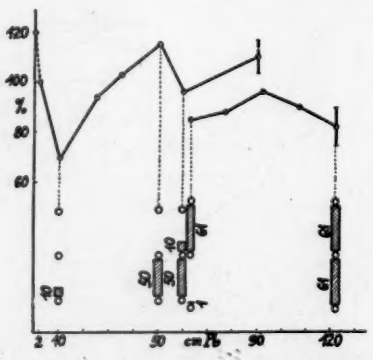

FIG. 5. Absorption curve of threefold coincidences in lead. Lead thickness varied either between bottom and middle counter, or between middle and top counter.

The measurements were extended for lead thicknesses up to 14 cm Pb; the lower curve in Fig. 4 indicates the results. The two curves were adjusted for the intensities at 1 cm Pb. The abscissa for the lower curve indicates thicknesses in cm Pb. Again the intensity decreases and has a subsequent increase. Very thin and moderately thick lead layers seem to provoke similar intensity variations. Therefore, it is very probable that at least two kinds of scarcely ionizing components are present, the first being absorbed in about 5 mm Pb, the second in about 5 cm Pb. If the absorption is due to cascade production, we may compute from the position of the maxima, in accordance with the cascade theory, the initial energy of such a shower: $l_{max}=\ln(E/E_i)$. (l_{max} measured in radiation units $=0.5$ cm, and $E_i=10^7$ ev for lead.) From the upper curve we find $E\doteq 4\times 10^7$ ev and from the lower curve $E=10^{14}$ ev. Hence the first scarcely ionizing component is much softer than the radiation producing the usual cascade showers at sea level. Whereas the high value for the second component renders it very improbable that this component should create electron showers, these secondaries must consist of heavier particles, obviously mesons.

RADIATION MEASURED WITH THREEFOLD COINCIDENCES

Our next purpose has been to determine the nature of the penetrating component giving rise to threefold coincidences. In case this component should consist of ionizing particles we might not expect to find a difference in the four- and threefold counting rates. Table III indicates the results. With 3 cm Pb between the counters, three of the four G-M counters were already shielded by 1 cm Pb. Thus it seems very likely that the number of the shower coincidences is, in both arrangements, negligible. The total efficiency difference between a threefold and a fourfold arrangement is, according to Table I, two p.c. The observed efficiency for the additional fourth G-M counter was with 3 cm Pb 88 p.c., a value equal to that found with the same arrangement in our institute. This apparently low efficiency is due to the fact that threefold coincidences are more

likely to respond to showers than fourfold coincidences. Hence, if 120 cm Pb were inserted between the counter trays, the efficiency decreased to 66 p.c. although now the thick lead layer excluded any effect of showers. This result indicates that the penetrating component cannot consist of ionizing particles alone. In order to investigate the nature of this component we measured its absorption in lead. In the upper curve of Fig. 5 lead was first placed gradually between middle and bottom counter and only when 50 cm Pb were reached was the additional lead placed between middle and top counter. The intensity decreases in the first 10 cm Pb very rapidly after passing through a minimum the intensity increases anew to reach nearly its original height after 30 cm Pb. A second drop is only observable when the additional lead was placed between top and middle counter. The shape of this absorption curve can in no case be explained by an ionizing radiation alone; we have rather to assume that a non-ionizing agent creates in the material above the apparatus, in clay, secondaries of about 10 cm Pb range. If less than 10 cm Pb are inserted, it can produce a discharge in all the three counters, whereas for greater lead thicknesses it can only discharge the two upper counters and consequently we observe a decrease of intensity. The creation of a further secondary in lead is now required for the production of a threefold coincidence. The number of the secondaries created in lead will increase with the thickness of the lead layer. Accordingly, the intensity increases for greater thickness. A second drop will occur when lead is placed between top and middle counter, because now a secondary created in clay, which was able to trigger both of the upper counters, is prevented from reaching the middle counter. A threefold coincidence can only occur when the non-ionizing radiation liberates a secondary ray above each of the counters. With the thickness of the upper layer, the number of the secondaries triggering the center counter increases, and a further rise in the intensity might result.

On the other hand, in the lower curve of Fig. 5, when 60 cm Pb was placed permanently between top and middle counter and only the thickness of the lead layer between middle and bottom counter was varied, we may remark that the intensity remains fairly constant.

TABLE IV.

Number of coinc.	Time in hours	coinc./ hour	Lead in cm	Intensity ±p.e.	
420	1648.2	0.245	2	100±3.4 p.c.	M_0
230	1125.7	0.191	7	78±3.7	
311	1665.6	0.175	12	71±2.9	m_1
273	1348.8	0.209	17	85±3.4	
268	1292.0	0.223	22	91±3.5	M_1
259	1402.9	0.200	27	82±3.2	
310	1613.1	0.182	32	74±2.7	
399	2012.9	0.187	37	76±2.7	
325	1916.9	0.164	42	67±2.6	m_2
294	1535.7	0.180	47	74±3.1	
306	1584.6	0.182	52	74±3.0	
126	592.3	0.209	57	85±5.2	M_2
254	1232.3	0.191	62	78±3.6	
191	918.5	0.185	67	76±4.2	
48	309.8	0.139	72	57±6.1	
50	334.8	0.137	77	56±5.8	m_3
145	1000.3	0.139	82	57±3.3	

Two interpretations can be offered for this behavior. Either the residual intensity after 60 cm Pb is due to an ionizing radiation, the non-ionizing radiation being stopped in 60 cm Pb—a circumstance which is highly improbable for a radiation which was able to penetrate 1000 m w.e.—or the lower lead absorbs about the same amount of secondaries arising from the upper lead block as are created in it anew.

After a short interruption the measurements were resumed in 1939 and were continued till wartime activities put an end to the whole enterprise. Unfortunately, our whole apparatus was destroyed during the siege. The only difference as compared to the previous sets was that now we placed simultaneously the same amount of lead between top and middle counters as between middle and bottom counters. Our aim was to determine with sufficient accuracy the exact shape of the absorption curve. Therefore, every point of the curve was measured several times. A total of 4209 coincidences were recorded in 21,734 hours. (In one of the series 70 cm of wood were placed above the counter trays.[5] However, it was seen later that this circumstance did not affect the results.) The data are collected in Table IV. The values of the intensity are corrected for a mean temperature of 6°C with a temperature effect of 1.0 percent per degree C.[6]

[5] J. Barnóthy and M. Forró, Zeits. f. tech. Physik **21**, 290 (1940); Phys. Rev. **55**, 870 (1939).
[6] M. Forró, Phys. Rev. **72**, 868 (1947).

TABLE V.

Max. −Min.	Intensity differences
M_0-m_1	29±4.5 percent
M_1-m_1	20±4.5
M_1-m_2	24±4.3
M_2-m_2	13±3.9
M_2-m_3	23±3.9

The differences between the maximum and minimum points are collected in Table V. For M_2 we used the mean intensity of the two arrangements with 57 and 62 cm Pb, because in the maximum position (57 cm Pb) less than 200 coincidences were recorded and further, since the intensity was practically constant for the last three points, we used for m_3 the mean of all three values. Except for M_2-m_2 in all other cases the intensity differences are greater than four times their probable error, and even in this latter case it is 3.3 times its error. Thus in the intensity variation the existence of two minima and two maxima can be seen.

INTERPRETATION OF THE ABSORPTION CURVE

The shape of this absorption curve cannot be interpreted by assuming an ionizing radiation. In order to obtain an analytic representation of the curve, let us assume that (1) the non-ionizing radiation produces secondaries of sharp range $=a/2$ in clay and of range $=a$ in lead (this proportion of the ranges was taken for the sake of simplicity); and (2) the probability of a secondary being produced along dx either in the material above the counters, or in the absorber between the counters, is dx/P, where P is the mean free path between the production of two such secondaries expressed in mass units. For the sake of simplicity let us assume that P is identical for clay and lead. We choose unit of length $=P$ and further $P=1$. The counters are separated by distances x.

If $x>a$, a threefold coincidence takes place whenever at least one secondary is produced in each of the three intervals of length $a/2$, or a, above or between the counters. For $x<a$ the intervals overlap and a coincidence may be caused by less than three independent secondaries. In particular for $x=0$ one secondary is sufficient to give rise to a coincidence.

TABLE VI.

Interval	dJ/dx
I. $0<2x<a/2$	$-2e^{-a/2}e^{-x}$
II. $a/2<2x<a$	$2e^{-x}(e^{-x}-e^{-a/2})$
III. $a<2x<2a$	$(1-e^{-a/2})e^{-x}(1-2e^{-x})$
IV. $2a<2x$	0

When x increases from 0 to a, we have to deal with four cases. The probability computations† yield the derivatives given in Table VI of the intensities within the respective intervals: Within interval I the intensity decreases; in II the intensity increases, reaches a maximum for $2x=a$; furthermore, a minimum must occur at the intersection of the intervals I and II, i.e., for $2x=a/2$; in III we find a minimum for $e^{-x}=0.5$ and in interval IV the intensity remains constant for all values of $x>a$.

We may infer that this theoretical curve is qualitatively in agreement with our experimental curve of Fig. 6 (except for the last decrease of intensity). The place of the first minimum (m_1) corresponds to the range of the secondaries created in clay; the first maximum (M_1) will occur when the total thickness of the two lead layers is equal to the range of the secondary produced in lead, and the second maximum (M_2) is reached when the thickness of each lead layer is equal to the range of the secondary created in lead. We conclude that the experimental curve can be obtained by assuming that a non-ionizing radiation produces ionizing secondaries in the material above the counters and in the absorber between the counters. In particular, it is necessary to assume secondaries of about 10 cm Pb range in clay and of 20 cm Pb range in lead. The secondaries must therefore be heavier particles, probably mesons.

The circumstance that the range of the secondary ray created in clay is smaller than the range of those created in lead can be interpreted by assuming that nuclear forces are responsible for the production of these secondaries. However, on account of the short range of nuclear forces the interaction will actually take place merely with the nucleons situated in the vicinity of the track of the penetrating, non-ionizing component. The

† We are indebted to L. Jánossy for a helpful discussion of this analysis.

total energy of the created meson is equal to the whole energy transferred to the nucleus. In a first approximation the number of the nucleons encountered by the non-ionizing radiation during its path through the nucleus is equal to $8N^{\frac{1}{3}}$ (N=atomic weight). Therefore, the mesons produced in clay will receive about half as much energy as those created in lead. A meson of range 10 cm Pb can be created with a total energy (rest energy+kinetic energy) of 3.4×10^8 ev, and if its range is 20 cm Pb, with 6×10^8 ev, these values being in the expected ratio. Every nucleon will receive about 10^7-ev energy.

In order to interpret the last decrease of the intensity after M_2, we have either to assume that the penetrating non-ionizing radiation is absorbed in 80 cm of lead, a circumstance which is—as we already mentioned—highly improbable, or the mechanism of the creation of secondaries is more complex than assumed hitherto. Perhaps according to the way the collision between non-ionizing radiation and atomic nuclei takes place, two or more kinds of secondaries with different ranges are produced in the different materials (clay, lead).

In our interpretation of the absorption phenomena we have hitherto only dealt with the two ionizing secondaries of 10- and 20-cm Pb range, created by the penetrating non-ionizing radiation in clay or in lead. A full understanding would, however, require taking into consideration the effect of the scarcely ionizing radiation. As seen, its intensity is 21 times higher in producing twofold coincidences than in threefold coincidences, suggesting the probability that it would discharge a single G-M counter is 450 times as great. Should this scarcely ionizing component be a permanent companion of the penetrating non-ionizing radiation, we would have to take into account, in interpreting the absorption curve, that the top counter tray and the counter in the middle for small lead thicknesses are almost always triggered by this component. At present, however, we have far too little experimental knowledge of its properties to be able to carry out such a quantitative analysis of the absorption curve.

INTENSITY *VERSUS* DEPTH VARIATION

Some light is cast upon the nature of the penetrating radiation by considering the intensity-depth dependence. According to the measurements of Ehmert,[7] Clay,[8] and V. C. Wilson,[9] the intensity decreases between 40 and 250 m w.e. inversely proportional to the 1.8 power of the depth; for still greater depth the exponent changes to 2.7. Represented on a logarithmic scale we may observe a bend at about 300–400 m w.e. The intensity variation before the bend corresponds, as known, to a meson intensity with an integral spectrum proportional to $E^{-1.7}$.

To explain the bend, we might think that the greater absorption below of thick layers is due to the circumstance that for such energies the radiative losses become more and more important. However, according to the cascade theory, only for a meson of 2.5×10^{12}-ev energy will the energy loss due to ionization be of the same order as the radiative loss. On the other hand, if only ionization losses are to be considered, a meson of 2×10^{11} ev would be able to reach a 500-m depth. Consequently, the bend of the absorption curve can not be explained by radiative losses. Since there does not seem to exist any reason preventing a meson of 2×10^{11} ev to reach 500 m, and nevertheless the intensity at 500 m does not correspond to a meson intensity, we infer, that in the primary meson spectrum, for reasons unknown hitherto, mesons with greater energies than 2×10^{11} ev are not present. (In a paper dealing with the origin of cosmic radiation,** we obtained the following expression for the integral

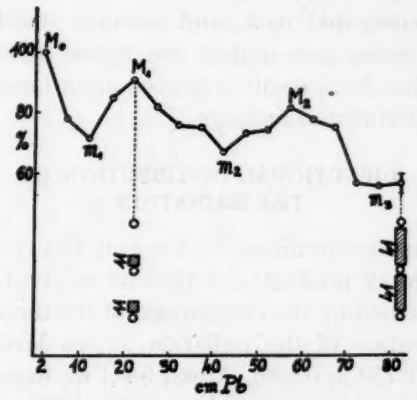

FIG. 6. Absorption curve of threefold coincidences in lead. Lead thickness varied simultaneously at both places.

[7] A. Ehmert, Zeits. f. Physik **106**, 751 (1937).
[8] J. Clay and A. Gemert, Physica **6**, 497 (1938).
[9] V. C. Wilson, Phys. Rev. **53**, 337 (1938).
** T. Barnóthy and M. Forró, Csill. Lapok **7**, 65 (1944).

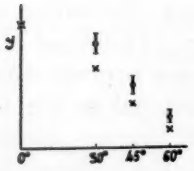

FIG. 7. Intensity found for various inclinations. o indicates the experimental values and × the values corresponding to the thickness of the material.

spectrum of fast mesons:

$$F_m = 2.3\times10^{-4}[(e^{-3W}/3W) - Ei(-3W) + 2Ei(-6W)],$$

where the energy is expressed in $W = E/2\times10^{11}$-ev units, and Ei denotes the exponential integral. This expression can account for the cut-off of the energy spectrum at about 2×10^{11} ev.)

Let us assume that the depth below 300 m w.e. is only reached by decay products of mesons and, further, that these decay products have constant energy losses. In this case the intensity will be proportional to the number of mesons disintegrated in the atmosphere:

$$J_D = \int_{E_{\min}}^{E_{\max}} \frac{J_0}{E^{2.7}}\left[1-\exp\left(-\frac{L\mu c^2}{c\tau E}\right)\right]dE \sim \frac{\text{const}}{E_{\min}{}^{2.7}} = \frac{\text{const}}{H^{2.7}},$$

(L = mean free path of the meson; μ = its mass; τ = its lifetime and H = thickness in w.e.). For all energies to be considered the exponent is small compared to 1, and we may develop in power series and neglect the higher terms. As seen, the above result is in good accordance with the experimental findings.

DIRECTIONAL DISTRIBUTION OF THE RADIATION

A further circumstance favoring the view that only decay products are present at great depth is furnished by the comparison of the directional distribution of the radiation at sea level with that at 730 m depth. At sea level we found with a counter telescope with aperture 10° in zenith-angle directions from a total of 4 million coincidences:***

$$D(\alpha)\times10^4 = 5.0 + 74.5\cos^2\alpha + 0.5\cos^4\alpha$$

coinc./cm², hour, square degree,

corresponding to

$$D(\alpha)\sim\cos^2\alpha.$$

For inclined directions the thickness of the material varies according to $1/\cos\alpha$. We should, therefore, expect to find a meson intensity varying like $E^{-1.7}$, i.e., a variation according to $\cos^{1.8}\alpha$. However, on account of the fact that in inclined directions the path of the mesons increases, the decay of the mesons will render the intensity decrease somewhat steeper. Actually it was found to vary like $\cos^2\alpha$.

At 730-m depth we found for the directional distribution[3]

$$D(\alpha)\times10^6 = 0.2 + 3.7\cos^2\alpha - 1.0\cos^4\alpha$$

coinc./cm², hour, square degree.

Hence,

$$D(\alpha)\sim\cos^{1.7}\alpha.$$

At first glance this slight difference in the exponent of the cosine seems to mean that the effect of the decay is less important for these more energetic mesons present at great depth. Consequently, we should infer that both directional distributions have to be attributed to the same kind of radiation, i.e., to mesons. However, according to the experimental data, at 730 m depth the intensity decreases with the -2.7 power of the depth, accordingly we should expect a directional distribution varying with $\cos^{2.7}\alpha$ instead of the actually found $\cos^{1.7}\alpha$.

Let us try anew to assume that great depth is only reached by decay products of mesons. Writing as before:

$$J_D = \int_{E_{\min}}^{\infty} \frac{\text{const}}{E^{2.7}}\left[1-\exp\left(-\frac{L\mu c^2}{c\tau E}\right)\right]dE = \text{const}\frac{L}{E_{\min}{}^{2.7}}.$$

For inclined directions the thickness of the material varies like $1/\cos\alpha$ and similarly $E_{\min}$ varies with $1/\cos\alpha$. But also the length of the trajectory L of the meson in the atmosphere is varying like $1/\cos\alpha$. Hence

$$J_D = \text{const}\times\cos^{1.7}\alpha,$$

in best accordance with the observed variation.

*** T. Barnóthy and M. Forró, unpublished results. See also Nature 144, 116 (1939).

THE ABSORPTION ANOMALY FOR INCLINED DIRECTIONS

The circumstance previously mentioned that in this particular shaft the thickness of the earth layer above the apparatus was known with great accuracy enables us to compare directly the intensities we measured with inclined counter telescopes with the results of V. C. Wilson[9] obtained with a vertical apparatus. For the sake of an exact computation we have divided the aperture of our counter telescope into 16 parts of equal length and have reckoned for every center line of these parts the mass of the material above it. Considering also the variation of the sensibility for rays striking the counter telescope at different angles, we could compute the intensities we should have found at different inclinations according to Wilson's measurements. In Fig. 7 the crosses correspond to the values computed from Wilson's observations and the circles to our actually found intensities. We may remark that in every inclined direction the directly measured intensity is higher than would correspond to the thickness of the material, meaning that at great depth the absorption anomaly has a reversed sign: the intensity decreases less than would correspond to the thickness of the layer. This peculiar behavior may be easily understood if we take into account that in inclined directions the mean path of the meson in air is longer, a greater number of mesons suffer disintegration, more decay products are formed; accordingly, the intensity of the decay products will be higher than would correspond to the thickness of the material.

This inverse absorption anomaly can be detected in Wilson's results. At several depths he measured with inclined counter telescope and observed that in all cases the intensity values did not fit his absorption curve, but were always higher. To account for this discrepancy Wilson assumed that the true mean thickness of the material did not correspond to that measured in the direction of the center line of his apparatus, but to thicknesses in directions tilted 7° less than the center line. He argued that on account of the breadth of the aperture of his telescope the surplus from directions above the center line exceeds the loss due to the greater thickness of the absorbing layer for more inclined directions. Although his argumentation is substantially correct, closer scrutiny reveals that the corrections to be applied are in each case much smaller than assumed by Wilson: for 45° inclination the correction is less than $\frac{1}{4}$ degree and even for 72° it amounts merely to one degree.

In Fig. 8 the crosses indicate in polar coordinates the intensities corresponding to the same thickness of material when measured with a vertical apparatus, the circles indicate the intensities actually measured by Wilson, and the squares the intensities we obtain if we take into account that the number of the decay products is, in consequence of the increased path of the mesons, greater for inclined directions.

POSITIVE TEMPERATURE EFFECT

Still another circumstance supports the view that only decay products of mesons are present at great depth. One of us[6] has found that a positive temperature dependence exists for the radiation present at 1000 m w.e. depth. The data collected during the investigations of the years 1939–43 were suitable for such an analysis, since it was possible to select nine different arrangements where observations were performed at the same place and with identical thickness of lead. However, they were repeated on three different occasions and each time the measurements were carried on for at least two–three weeks. For every arrangement the correlation between intensity and outer air temperature was computed. Although the individual values of the temperature effect have, on account of the small intensities, large standard errors, the mean value of these

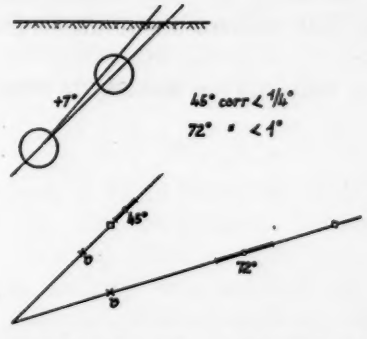

FIG. 8. Intensities for 45° and 72° inclination of the counter telescope. o is the measured values of Wilson, × the intensities corresponding to the thickness measured vertically and □ after correcting for greater number of decay-products in inclined directions.

nine individual results yields an effect:

$$+0.74\pm0.13 \text{ percent per degree C,}$$

a value exceeding six times its probable error, and therefore the existence of a positive temperature effect is established.

As known, the temperature effect of cosmic radiation at sea level has a negative sign—the rise in temperature tends to diminish the intensity. Blackett[10] offered an interpretation for this behavior by assuming that at higher temperature the atmosphere expands and the place where the mesons are produced is shifted upwards. Consequently, a larger number of mesons disintegrate before reaching sea level; the intensity will be lessened. Pursuing this argumentation we may infer that with higher temperature more decay products are formed. Accordingly, their intensity increases and we will observe a reversed, i.e., a positive, temperature effect for the decay products.

CONCLUSIONS

a. The shape of the absorption curve and the counter-efficiency measurements indicate that below 730 m w.e. depth the cosmic radiation consists—at least to a great extent—of non-ionizing or scarcely ionizing particles.

b. Three independent experimental evidences, namely, (1) the intensity *versus* depth variation, (2) the inverse absorption anomaly, and (3) the positive temperature effect, favor the view that great depth is reached merely by decay products of mesons.

The next question seeking an answer is to establish the nature of these non-ionizing decay products. Fast mesons might disintegrate into protons and neutrons. However, according to the theory of Hamilton, Heitler, and Peng,[11] only neutrons with extremely high energies (10^{14} ev) would be able to reach 1000 m depth. Conversely, the intensity *versus* depth variation indicates that if no mesons of higher energy than 2×10^{11} ev are present in the primary meson spectrum, no neutrons of the required energy can be formed.

The other alternative at our disposal is that the meson disintegrates into an electron and a neutrino. Several considerations seem to suggest that it is more likely that a meson of integer spin, 212 m_0 mass, and 2.17×10^{-6} sec. lifetime would disintegrate in the atmosphere into an electron and a "meso-neutretto." The latter neutral particle would have $\hbar/2$ spin, about 10^{-10} sec. lifetime, and 97 m_0 or $148m_0$ mass.[12]

To date we know theoretically far too little about neutrini and neutrettos and their possible interactions to be able to perform a more exact computation. We think it is up to the theoretical physicist to find significant differences in the behavior of neutretto and neutrino radiations, which would indicate a way to check this point experimentally and thus solve the problem of the nature of the penetrating component.

ACKNOWLEDGMENT

We wish to thank Mr. Z. Ozorai and D. Nagy for their help and assistance in taking the data. The Hungarian Board of Science and the Hungarian Academy of Science supported the investigations. We are greatly indebted to the managers, engineers, and miners of the Salgótarjáni Coal Mine Company for their kind cooperation in the use of the mine.

[10] P. M. S. Blackett, Phys. Rev. **54**, 973 (1938).

[11] Hamilton, Heitler, and Peng, Phys. Rev. **64**, 78 (1943).

[12] T. Barnóthy, Phys. Rev., in print; Nature **161**, 681 (1948).

Radioactive Isotopes of Ga and Ge

D. A. McCown,* L. L. Woodward,** and M. L. Pool
The Ohio State University, Columbus, Ohio

(Received July 19, 1948)

The radioactive germanium isotope of 1.65-day half-life has been produced by Zn(α,n), Ga(d,$2n$), and Ge(n,$2n$) reactions, but not by deuteron bombardment of germanium. This isotope is reassigned and placed at Ge^{69}. It decays with emission of positrons, x-rays, and gamma-rays. No evidence for the existence of the 195-day period has been found at Ge^{69} by deuteron bombardment of gallium. The characteristic x-ray lines of gallium from decay activity of the 11.4-day Ge^{71} have been photographed by a curved crystal camera. Deuteron bombardment of Ge^{76}, enriched electromagnetically to 70 percent, has given no evidence of a 9-day period at Ga^{74}. The half-life of Ge^{75}, produced by fast neutron bombardment of arsenic, is 1.37 ± 0.02 hours. The half-life of Ga^{67}, produced by alpha-particle bombardment of zinc, is 3.26 ± 0.02 days.

Ge^{71}

A RADIOACTIVE isotope of 11 days' half-life has been reported[1] in the germanium fraction from deuteron bombardment of both gallium and germanium and assigned to Ge^{71}. This isotope was found to decay by emitting electrons of about 0.6 Mev, and possibly by K-electron capture. No gamma-ray activity was observed. Other investigators[2] reported that they did not observe this 11-day activity in the germanium fraction.

In order to investigate further the 11-day germanium activity, gallium metal was bombarded with 10-Mev deuterons. Figure 1 shows the decay activity of the germanium fraction. An activity of 11.4 ± 0.1 days' half-life was found and measured over an interval of nine half-lives. Assignment of this activity may thus be made to Ge^{69} or Ge^{71}.

Additional information for assignment of this activity was obtained from germanium bombarded with deuterons. Figure 2 shows the decay activity of the germanium fraction. The existence of the 11.4-day period in the germanium fraction thus confirms the existence of this activity and assignment to Ge^{71}.

Decay measurements, as shown in both Figs. 1 and 2, indicate that this period decays entirely by K-electron capture. After the shorter periods had become negligible, cloud-chamber observations indicated only x-ray tracks. Figure 3 shows an aluminum absorption of the x-ray activity; any charged-particle radiation was removed by a magnetic field. A mass absorption coefficient of 34 cm^2/g is obtained, corresponding to a wave length of 1.35A. The wave-length of the gallium $K\alpha$ x-ray is 1.34A. No gamma-ray activity was observed in this period.

For further evidence of the K-capture process of decay of the 11.4-day period, an activated sample of GeO_2 from Oak Ridge was exposed to an 8-inch Cauchois curved crystal camera, having a mica crystal of 0.43 mm in thickness. During the 32-day exposure, decay measurements showed the x-ray activity to be decaying with the 11.4-day period. The film showed the presence of the Ga $K\alpha$ and Ga $K\beta$ x-ray lines. Identification was made by calibrating the film with the fluorescent K x-ray lines of Ga, Ge, As, and Se.

Ge^{69}

An activity of 30 ± 4 hours' half-life has been reported[2] in the germanium fraction from Ge(n,γ), Ge(n,$2n$), Ge(d,p), and Se(n,α) reactions. This activity was assigned to Ge^{71}. A 37-hour positron emitting activity has been found[3] in the germanium fraction from zinc bombarded with alpha-particles and assigned to

* Capt., U.S.A.F. Research under auspices of Air University, Maxwell Air Force Base, Montgomery, Alabama.
** Lt. Col., U.S.A.F. Research under auspices of Air University, Maxwell Air Force Base, Montgomery, Alabama.

[1] G. T. Seaborg, J. J. Livingood, and G. Friedlander, Phys. Rev. 59, 320 (1941).
[2] R. Sagane, G. Miyamato, and M. Ikawa, Phys. Rev. 59, 904 (1941).
[3] Wilfred B. Mann, Phys. Rev. 54, 649 (1938).

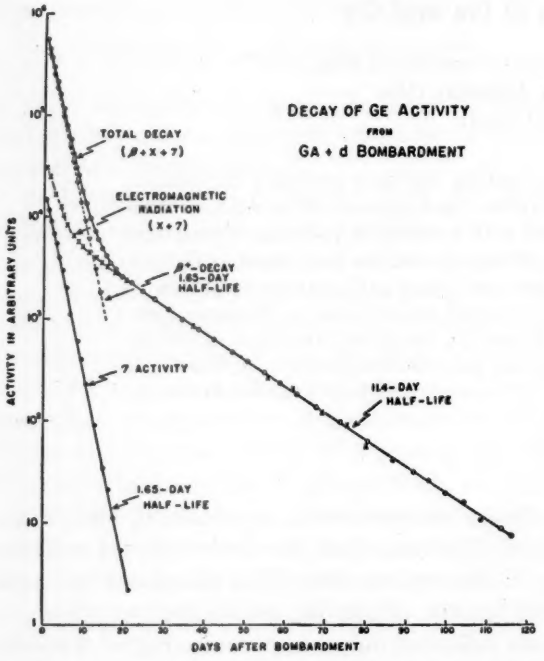

FIG. 1. Decay of Ge activity from deuteron bombardment of gallium. The 11.4-day x-ray and 1.65-day positron periods are shown.

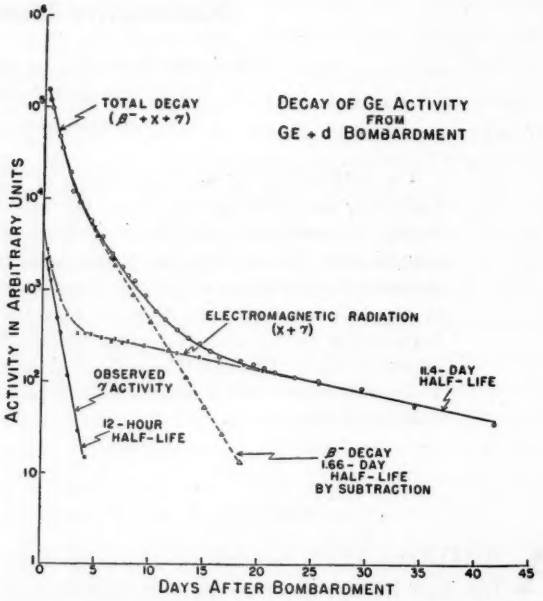

FIG. 2. Decay of Ge activity from deuteron bombardment of germanium. The 11.4-day x-ray and 1.66-day negative beta-activities are shown. The only gamma-activity present is that of the 12-hour period.

Ge^{69}. Subsequent investigators[1] reported a 40-hour activity in the germanium fraction from gallium bombarded with deuterons. This period, found to emit positrons of 1.2 Mev, was assigned to Ge^{71}. An activity of the same half-life was also produced by these workers from deuteron bombardment of germanium. They suggested that a long 195-day germanium period reported[3] in the germanium fraction from alpha-particle bombardment of zinc might possibly be due to Ge^{69}.

In order to clarify these conflicting interpretations and to determine the decay characteristics of this isotope of approximately 40 hours' half-life, a study was made of the short activity existing in the germanium fraction from deuteron bombardment of gallium.

Figure 1 shows a half-life of 1.65 ± 0.02 days, obtained over nine half-lives by subtraction of the electromagnetic radiation, $(x+\gamma)$, from the total activity, $(\beta+x+\gamma)$. This activity decays by the emission of positrons, x-rays, and gamma-rays.

Cloud-chamber observations immediately after chemical separation showed the presence of only positrons and x-rays. Aluminum absorption measurements of the positron activity, shown in Fig. 4, indicate a beta-end point of 0.433 g/cm² of aluminum, corresponding to an energy of 1.0 Mev as determined by the Sargent range-energy relation.

A lead absorption of the gamma-ray associated with the 1.65-day half-life, as seen in Fig. 5, indicates energies of 0.50 Mev and 1.22 Mev. The 0.50-Mev gamma-ray is due to annihilation radiation.

Subtraction of the γ-ray activity shown in Fig. 1 from the $(x+\gamma)$ activity indicates the

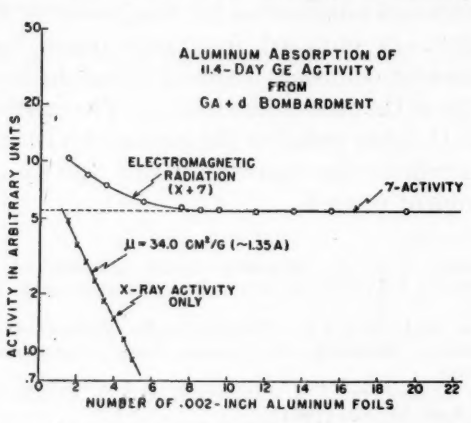

FIG. 3. Aluminum x-ray absorption of the 11.4-day x-ray period of Ge.

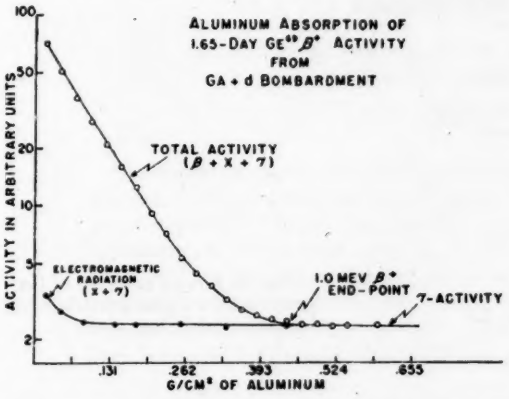

FIG. 4. Aluminum absorption curve of the 1.65-day positron activity in Ge showing 1.0-Mev end point.

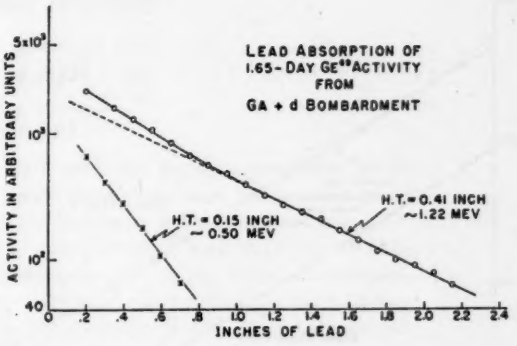

FIG. 5. Lead-absorption curve for the 1.65-day Ge^{69} period.

presence of x-rays in the 1.65-day period. From consideration of the amount of x-ray activity that would be expected from "bremsstrahlung" effect, it was concluded that this x-ray radiation was due to the K-capture process. The ratio of K-capture processes to positron emissions in the 1.65-day activity is 2 to 1. This value was obtained by multiplying the ratio of positron to x-ray activity by a factor giving the relative ionization produced by beta-radiation and x-ray radiation in the energy ranges involved.

This same positron activity of 1.65-day half-life has been produced in the germanium fraction from zinc bombarded with alpha-particles and from germanium bombarded with fast neutrons.

Figure 2 shows the existence of an activity of a similar half-life in the germanium fraction from deuteron bombardment of germanium. In this case, however, cloud-chamber observations indicated only negative beta-activity. This beta-negative emitting activity of As^{77} which is the daughter product of Ge^{77} has frequently been confused with the 1.65-day Ge^{69} activity. Since only the 11.4-day Ge^{71} has been produced by the (d,p) reaction on Ge^{70}, the positron emitting period of 1.65-day half-life in germanium therefore is assigned to Ge^{69}, and has been produced by $Ga(d,2n)$, $Zn(\alpha,n)$, and $Ge(n,2n)$ reactions.

Ge^{75}

A value of 1.48 hours has been reported[1] for the half-life of Ge^{75}, produced in the germanium fraction by fast neutron bombardment of arsenic. A small gamma-ray intensity was found associated with this activity. Other investigators[2] report a half-life of 1.37 hours and a beta-end-point energy of 1.10 Mev.

The decay activity of Ge^{75}, produced by fast neutron bombardment of arsenic, showed a single half-life activity of 1.37 ± 0.02 hours, measured over an interval of seven half-lives. No gamma-ray activity was observed.

Apparent longer half-life values of approximately 1.48 hours have also been obtained in the arsenic fractions from deuteron bombardments of germanium. This larger value is easily due to errors involved in subtraction of the longer periods.

Ga^{74}

An activity of about nine days' half-life has been reported[2] in the gallium fraction from deuteron bombardment of germanium and assigned tentatively to Ga^{74}.

In order to study the characteristics of this period, a sample of GeO_2, enriched from 6.5 percent to approximately 70 percent in isotope 76,† was reduced in a hydrogen furnace to metallic germanium, pressed into an aluminum target holder, and bombarded with deuterons. The gallium activity was chemically extracted.

No evidence of a long period in gallium was found, although the decay of this fraction indicated a certain amount of 14.1-hour Ga^{72} produced by the (d,α) reaction on the Ge^{74} isotope of reduced percentage. Hence the presence of a long period assigned to Ga^{74} seems improbable.[4]

† Supplied by the Y-12 plant, Carbide and Carbon Chemicals Corporation, through the Isotopes Division, U. S. Atomic Energy Commission, Oak Ridge, Tennessee.

[4] U. S. Atomic Energy Commission Abstracts of Declassified Documents, Vol. 11, No. 5, MDDC—1694A, p. 125.

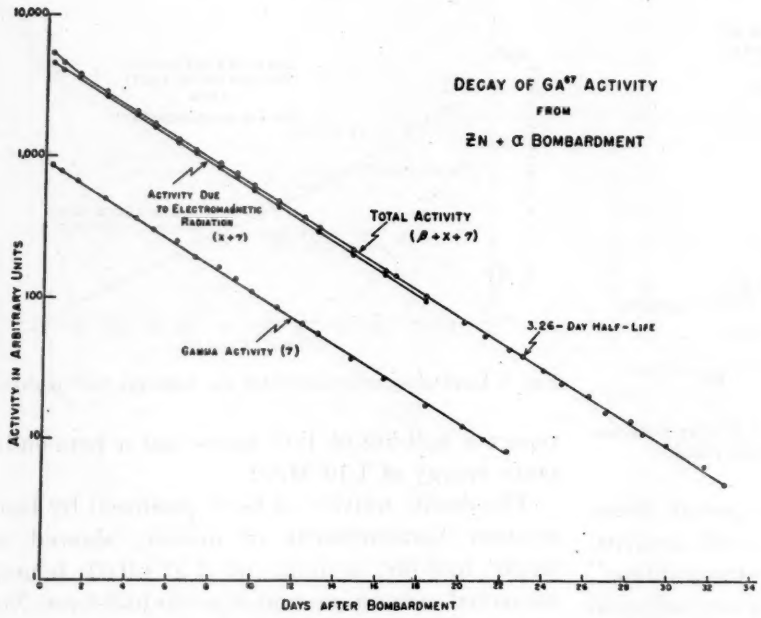

FIG. 6. Decay activity of Ga^{67} produced by alpha-particle bombardment of Hilger zinc.

Ga^{67}

A decay activity of 97 hours' half-life was first reported,[5] produced by bombardment of zinc with deuterons. No isotopic assignment was made. Later investigators[6,7] identified this period as that of Ga^{67}. From deuteron bombardment of zinc, a complete study[7] was made of the characteristic radiations of Ga^{67} activity, and its half-life was given as 83 hours.

Figure 6 shows the decay activity of the gallium fraction from alpha-particle bombardment of zinc. Since Hilger zinc was used and since a single activity was evident, the value of the half-life, determined over eight half-lives, is found to be 3.26 ± 0.02 days. Studies of the radiations emitted by this isotope are in agreement with those previously reported.[7]

[5] J. J. Livingood, Phys. Rev. **50**, 425 (1936).
[6] Wilfred B. Mann, Phys. Rev. **53**, 212 (1938). Luis W. Alvarez, Phys. Rev. **53**, 606 (1938).
[7] Luis W. Alvarez, Phys. Rev. **54**, 486 (1938).

DISCUSSION

As illustrated in Fig. 1, no evidence was found for existence of the 195-day Ge activity, reported at Ge^{69}. The production of this 195-day activity by the $Ga^{69}(d,2n)$ reaction must be less than 1/150 of the production of the 11.4-day activity by the $Ga^{71}(d,2n)$ reaction.

The relative reaction cross section for the production of the 11.4-day germanium activity by $Ga^{71}(d,2n)$ reaction to that of the 1.65-day germanium activity by $Ga^{69}(d,2n)$ is observed to be 10 to 1.

ACKNOWLEDGMENTS

The support received from the Ohio State University Development Fund and the Graduate School is gratefully acknowledged. Appreciation is also expressed to Mr. H. L. Finston and Mr. R. M. Dyer for their excellent chemical separations required in this work.

Radioactive Arsenic Isotopes

D. A. McCown,* L. L. Woodward,** and M. L. Pool
The Ohio State University, Columbus, Ohio

(Received August 4, 1948)

Simultaneous alpha-particle bombardments of Ge^{70}, enriched electromagnetically to 90 percent, and germanium of normal isotopic constituency have established the location of an arsenic activity of 76±3 days' half-life at mass number 73. Decay is by K-capture into Ge^{73}. The energy of the gamma-ray is about 0.10 Mev. The half-life of As^{74}, measured over 10 half-lives, is 17.5±0.1 days. Simultaneous deuteron bombardments of two selenium samples, enriched, respectively, in isotope 74 and 76, have established the location of the 1.08-day arsenic activity at mass number 72. A radioactive arsenic isotope of 2.08 days' half-life has been produced by deuteron bombardment of germanium and is assigned to As^{71}.

76-DAY As^{73}

In arsenic a 90-day half-life activity produced by deuteron bombardment of germanium has been reported.[1] This activity was assigned to As^{77} since negative beta-particles were thought to be emitted in the decay process. Later investigators,[2] by studying the radiations in a magnetic lens β-ray spectrometer, found a 0.052-Mev gamma-ray which was internally converted. K x-rays were also observed.

Results obtained by the last group above would indicate assignment of this activity to an arsenic isotope other than As^{77}. This statement is based on the fact that the location of As^{77} relative to stable isotopes would prohibit its decay by K-capture. The series of experiments described under this section were to establish the isotopic assignment and to study more completely the decay characteristics.

Figure 1 shows the decay activity of the arsenic fraction from deuteron bombardment of germanium. The measuring technique, which employed a Wulf Electrometer attached to a Freon-filled ionization chamber, was similar to that described previously.[3]

A half-life of 76 days is found. This activity decays entirely by emission of electromagnetic radiation. After the shorter half-lives had become negligible, cloud-chamber observations indicated no beta-activity, although x-ray ionization was observed.

Figure 2 shows an aluminum absorption of this x-ray activity. A mass absorption coefficient of 28.5 cm^2/g is obtained, corresponding to a wave-length of 1.27A. Since the wave-length of the Ge Kα x-ray is 1.25A, it is evident that the K-capture process takes place in the activity. This is further confirmed by the decay curves in Fig. 1, where it is seen that the total activity, $(\beta+x+\gamma)$ eventually becomes equal to the electromagnetic activity $(x+\gamma)$. An aluminum absorption measurement, made with an open ionization chamber, gave no evidence of low energy beta-activity.

A copper absorption measurement of the gamma-activity of this 76-day period indicates an energy of 0.10 Mev.

In Fig. 3 is shown the presence of this same activity produced in the arsenic fraction from germanium bombarded with 20-Mev alpha-particles. The value of the half-life, measured over four half-lives, is 76±3 days.

The fact that alpha-particle bombardment of germanium does produce this activity and that the activity decays by K-electron capture indicates that assignment can be made either to As^{73} or As^{76}.

For additional information on assignment of this 76-day period, GeO_2, enriched in isotope 70 from 21.2 percent to about 90 percent,*** and an

* Captain, U.S.A.F. Research under auspices of Air University, Maxwell Air Force Base, Montgomery, Alabama.

** Lieutenant Colonel, U.S.A.F. Research under auspices of Air University, Maxwell Air Force Base, Montgomery, Alabama.

[1] R. Sagane, S. Kojima, G. Miyamoto, and M. Ikawa, Proc. Phys. Math. Soc. Japan 21, 660, 728 (1939).

[2] L. Elliott, M. Deutsch, and A. Roberts, Phys. Rev. 63, 457 (1943).

[3] W. S. Cowart, M. L. Pool, D. A. McCown, and L. L. Woodward, Phys. Rev. 73, 1454 (1948).

*** Supplied by the Y-12 plant, Carbide and Carbon Chemicals Corporation, through the Isotopes Division, U. S. Atomic Energy Commission, Oak Ridge, Tennessee.

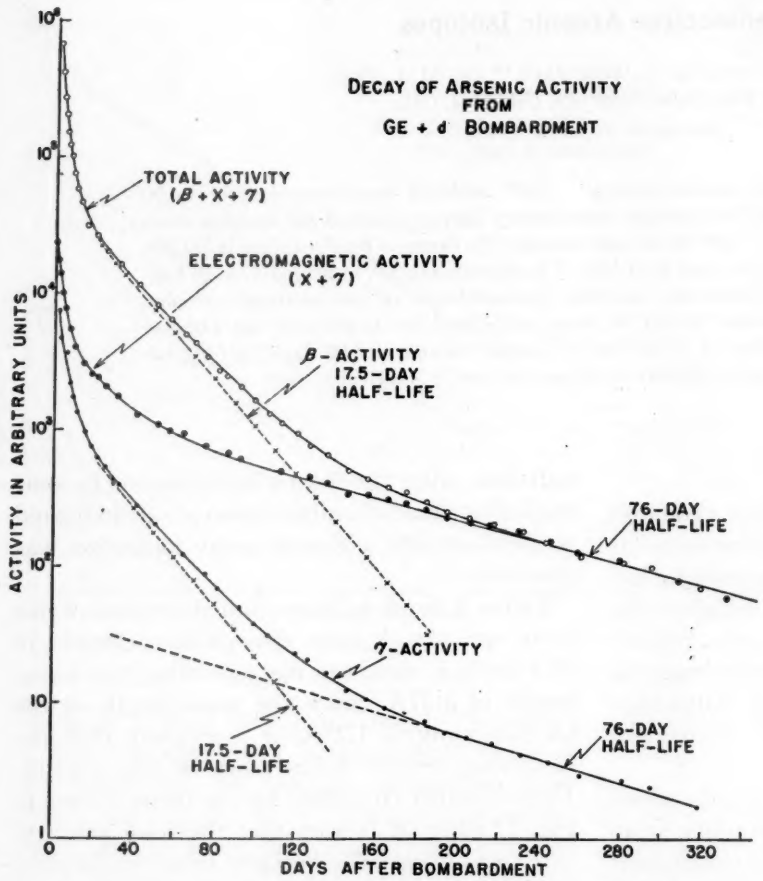

FIG. 1. Decay of As activity from deuteron bombardment of Ge. The 76-day and the 17.5-day activities are shown.

equal amount by weight of GeO_2 of normal isotopic constituency were bombarded simultaneously with alpha-particles. Decay measurements were made directly on the two activated samples.

The amount of 76-day activity appearing in the enriched Ge^{70} sample was approximately four times as great as that appearing in the ordinary Ge sample. Since stable Ge^{70} was approximately four times as abundant in the enriched Ge^{70} sample as in the ordinary Ge, it follows that this 76-day activity is produced from the stable Ge^{70} isotope. Hence the assignment of this activity, produced by the (α,p) reaction on Ge^{70}, is made to As^{73}.

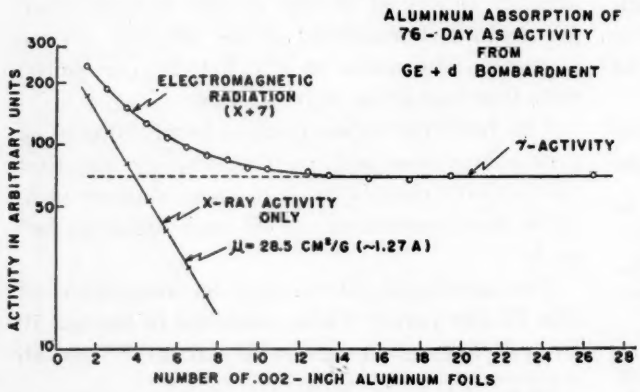

FIG. 2. Aluminum-absorption curve of the x-ray activity in the 76-day As period.

17.5-DAY As^{74}

An activity of 13.5 days' half-life has been reported[4] in arsenic, produced by fast neutron bombardment of As^{75}. This activity was assigned to As^{74}. β^+ and β^- emission were found. Other investigators[1] gave the half-life as 16 days and reported the end-point energy of the positive par-

[4] B. R. Curtis and J. M. Cork, Phys. Rev. **53**, 681 (1938).

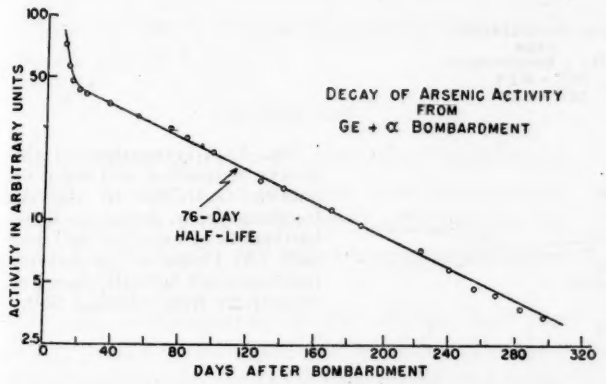

FIG. 3. Decay of As activity from alpha-particle bombardment of germanium. The value of the half-life for the long period is 76±3 days.

ticles to be 0.9 Mev and that of the negative to be 1.3 Mev.

Figure 1 shows the decay of the arsenic fraction from deuteron bombardment of germanium. The β-activity was obtained by subtraction of the electromagnetic radiation, $(x+\gamma)$, from the total radiation, $(\beta+x+\gamma)$. Subtraction of the γ-activity from the $(x+\gamma)$ activity gives no evidence of x-ray radiation. Beta-ray and gamma-energies were observed to be in agreement with values stated above.

Figure 4 shows the activity produced in the arsenic fraction from gallium bombarded with alpha-particles. Because this activity could be followed over a period of more than 10 half-lives, it is possible to assign a half-life value of 17.5 ±0.1 days.

1.08-DAY As^{72}

An investigation[5] has been made of the radiations emitted by the 1.08-day positron-emitting activity in arsenic, produced by bombardment of gallium with alpha-particles. A positron end-point energy of 2.78±0.10 Mev was reported along with a gamma-ray energy of 2.4 Mev. An alpha-particle bombardment of gallium fixes the location of this activity at As^{72} or As^{74}.

The bombardment of enriched stable Se isotopes should give sufficient information to make a mass number assignment of the activity. Two selenium samples, enriched,*** respectively, in

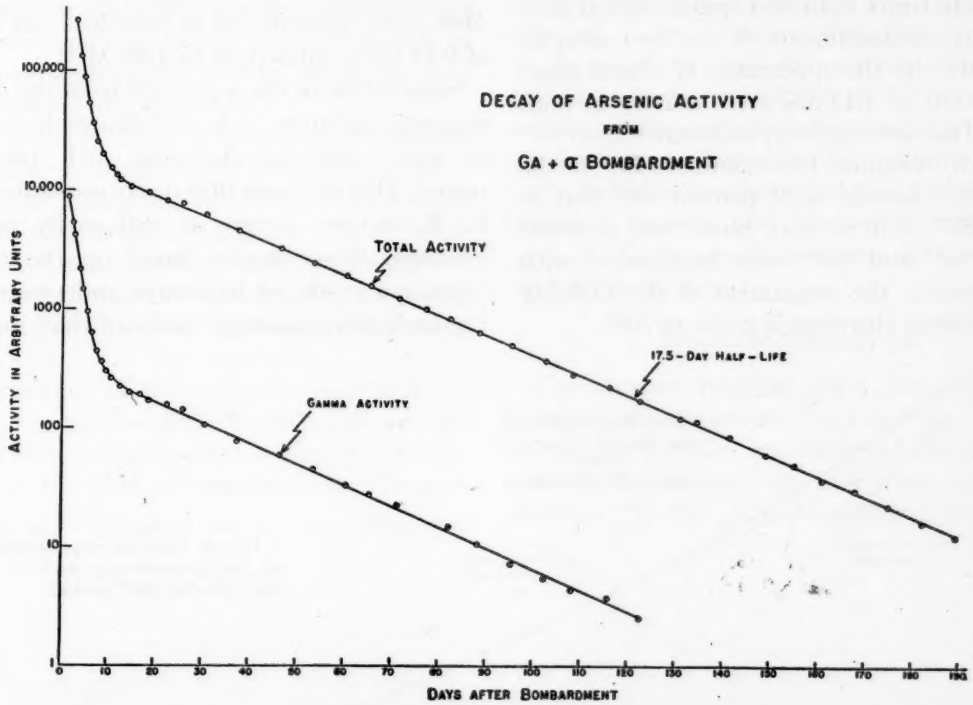

FIG. 4. Decay of As activity from alpha-particle bombardment of Ga. The value of the half-life for the long period is 17.5±0.1 days.

[5] A. C. G. Mitchell, E. T. Jurney, and M. Ramsey, Phys. Rev. 71, 825 (1947).

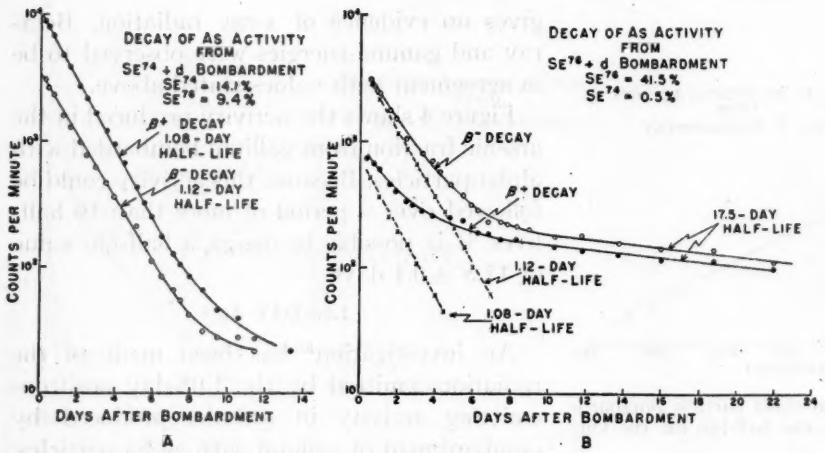

FIG. 5. A comparison of the decays of positive and negative beta-ray activities in the As fractions from deuteron bombardments of enriched Se^{74} and Se^{76}. (A) Decay of As activity from enriched Se^{74}; (B) decay of As activity from enriched Se^{76}.

Se^{74} from 0.9 percent to 14 percent and Se^{76} from 9.5 percent to 41.5 percent, were simultaneously bombarded with deuterons. A reversible electromagnetic field was used to measure[6] the positive and negative beta-decay activity of the two arsenic fractions.

Figure 5 shows these decay activities. The amount of 1.08-day positron activity in the arsenic fraction from enriched Se^{74} is seen to be considerably larger than that from enriched Se^{76}. Equivalent bombardments of the two samples are indicated by the appearance of almost identical amounts of 1.12-day As^{76} activity in both samples. This latter activity is obtained from Se^{78} by the (d,α) reaction. The amount of Se^{78} in the enriched Se^{74} sample is 21 percent and that in enriched Se^{76} is 16 percent. Since both enriched samples, Se^{74} and Se^{76}, were bombarded with equal intensity, the assignment of the 1.08-day arsenic activity therefore is made to As^{72}.

An aluminum absorption of the beta-activity indicated a beta-end-point energy of 2.8 Mev in agreement with that previously reported.

No evidence, however, was obtained of the 2.4-Mev gamma-ray energy reported above. Figure 6 shows a lead absorption measurement of the gamma-radiation in this activity. This absorption curve shows a gamma-ray of half-thickness in lead of 0.20 inch, equivalent to 0.60 Mev, and a gamma-ray of half-thickness in lead of 0.45 inch, equivalent to 1.40 Mev.

Subtraction of the γ-activity from the electromagnetic radiation, $(x+\gamma)$, indicates the presence of x-ray radiation decaying with the same period. This indicates that decay probably occurs by K-electron capture as well as by positron emission. Observations, based on the relative ionization produced by x-rays and positrons in the ionization chamber, indicate that the ratio

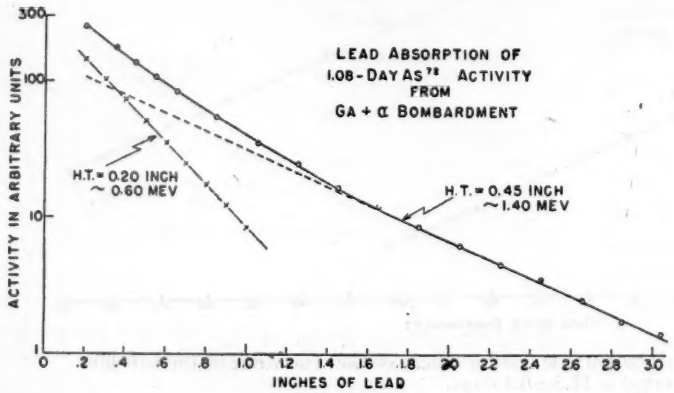
LEAD ABSORPTION OF 1.08-DAY As72 ACTIVITY FROM Ga + α BOMBARDMENT
H.T. = 0.20 INCH ~ 0.60 MEV
H.T. = 0.45 INCH ~ 1.40 MEV
ACTIVITY IN ARBITRARY UNITS
INCHES OF LEAD

FIG. 6. Lead-absorption curve of the gamma-ray activity in the 1.08-day As^{72} period.

[6] Submitted for publication elsewhere.

of the number of x-rays to positrons emitted is approximately 2 to 1.

2.08-DAY As^{71}

A positron activity of 2.08 days' half-life in arsenic, produced by deuteron bombardment of germanium, has been reported[7] and assigned to As^{73}. The positron end-point energy was found to be 0.6 Mev.

In the investigation of the 76-day As^{73} activity, produced by alpha-particle bombardment of germanium, no evidence was found of a 2.08-day period. Calculations based on the smallest detectable intensity of the 2.08-day activity, had it been present, and the saturation intensity of the 76-day activity show that the reaction cross section for formation of the 2.08-day to that of the 76-day activity must be less than 1 to 600.

Further attempts to find this activity of 2.08 days' half-life were made by investigating the shorter periods in the arsenic fraction from deuteron bombardment of germanium. Figure 7 shows the initial part of Fig. 1 on an expanded time scale.

Subtraction of the 17.5-day beta-activity from the total composite beta-activity indicates an activity of 2.08 days' half-life, measured over approximately four half-lives.

Subtraction of the γ-activity from the electromagnetic radiation, $(x+\gamma)$, gives the net x-ray activity. By subtracting the 76-day x-ray activity from the net x-ray activity, a second x-ray period of about 11.4 days' half-life is obtained. Subtraction of this 11.4-day activity gives only one other period, one of approximately 2 days' half-life.

The presence of the 11.4-day x-ray activity, presumed to be that of Ge^{71}, would indicate that this 2.08-day activity is that of radioactive As^{71}, formed by the (d,n) reaction on Ge^{70}. The reaction cross section for formation of the 2.08-day activity to that of the 11.4-day activity is observed to be approximately 1 to 1 as would be expected if the 11.4-day activity were formed by decay of the 2.08-day activity. Hence this 2.08-day activity is assigned to As^{71}.

This activity decays by K-capture and positron emission into Ge^{71}, then by K-capture into stable Ga^{71}. Relative intensities of x-ray activity to β-activity in this 2.08-day period indicate the ratio of K-capture to positron emission to be approximately 2 to 1.

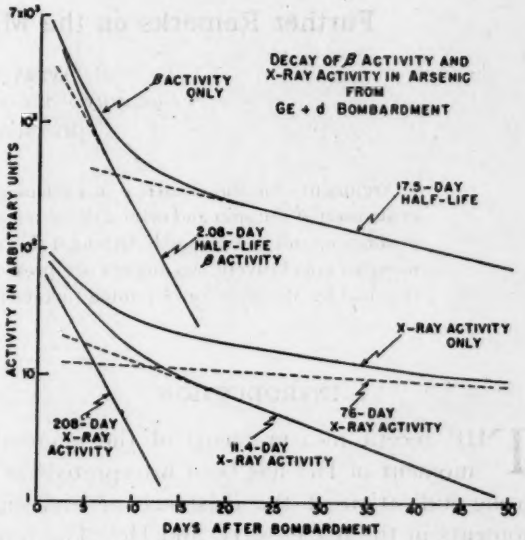
DECAY OF β ACTIVITY AND X-RAY ACTIVITY IN ARSENIC FROM GE + d BOMBARDMENT
β ACTIVITY ONLY
17.5-DAY HALF-LIFE
2.08-DAY HALF-LIFE β ACTIVITY
X-RAY ACTIVITY ONLY
76-DAY X-RAY ACTIVITY
2.08-DAY X-RAY ACTIVITY
11.4-DAY X-RAY ACTIVITY
ACTIVITY IN ARBITRARY UNITS
DAYS AFTER BOMBARDMENT

FIG. 7. The initial part of Fig. 1 showing the shorter half-life activities in the arsenic fraction from deuteron bombardment of Ge. The 2.08-day beta-ray activity, 2.08-day x-ray activity, and the 11.4-day x-ray activity are shown. Original data in Fig. 1.

ACKNOWLEDGMENTS

The support received from the Ohio State University Development Fund and the Graduate School is gratefully acknowledged. All chemical separations necessary in this work were ably performed by Mr. H. L. Finston and Mr. R. M. Dyer.

[7] R. Sagane, G. Miyamoto, and M. Ikawa, Phys. Rev. 59, 904 (1941).

Further Remarks on the Magnetic Moments of H^3 and He^3

R. AVERY AND R. G. SACHS
University of Wisconsin, Madison, Wisconsin
(Received July 21, 1948)

Arguments for the existence of exchange moments in these nuclei depend on an accurate evaluation of the spin and orbital contributions to the moments. Assumptions made in previous evaluations are re-examined. Although the results do *not* establish the existence of the exchange moment conclusively, arguments are presented which make the alternative appear to be less reasonable. Methods for obtaining further information on this question are discussed.

I. INTRODUCTION

THE recent measurement[1] of the magnetic moment of He^3 has been interpreted[2] as a strong indication of the existence of exchange moments in the nuclei of H^3 and He^3. The term exchange moment is meant to refer to any contribution to the magnetic moment of a system which cannot be accounted for by simply adding the spin and orbital moments of the nucleons making up the nucleus. On the basis of rather general assumptions concerning the nuclear wave functions, formulae have been given[3] for the spin and orbital contributions to the moments of these nuclei, and the failure of the formulae to agree with the measured values has led to the aforementioned interpretation. In view of the importance that may be attached to the existence of an exchange moment with regard to the understanding of nuclear interactions,[4,5] it seems necessary to investigate more fully the assumptions made in reference 3 in order to verify their validity.

The failure to obtain agreement occurs by a very small margin. This can be seen from Fig. 1, which displays both the linear relationship between the ^2P, ^4P and ^4D state probabilities imposed by the sum of the observed moments (see Eq. (1)) and the relationship required by the H^3 moment alone (Fig. 1 of reference 3). Agreement would correspond to the intersection of the curves referring to the same value of the ^4P probability. Although the curves fail to intersect, they almost intersect in the neighborhood of zero probability for the ^4D state if the ^2P and ^4P state probabilities are greater than 20 percent and 15 percent respectively. Small corrections, such as the effect of coulomb repulsion between protons on the He^3 wave function or relativistic corrections,[6] may overcome the difference. Therefore the experimental evidence does not conclusively establish the existence of the exchange moment. The alternative description requires, however, that the moments be understood in terms of a ground state for which the amplitudes of the ^2P and ^4P functions are much larger than that of the ^4D function. Such a description is objectionable on aesthetic grounds while the concept of an exchange moment is most acceptable in view of current ideas concerning nuclear forces. But this argument does not constitute a proof.

A more likely argument may be based on the results of rough binding energy calculations for the nuclei in question. These calculations[7] indicate that the introduction of any amount of P state decreases the binding even in the presence of a tensor interaction. Therefore it would seem that the conventional two-body interaction would lead to a wave function containing little or no P state. The best choice of wave function appears[8] to consist of about 96 percent ^2S state and 4 percent ^4D state. Now information con-

[1] H. L. Anderson and A. Novick, Phys. Rev. **73**, 919 (1948). The value used here is that presented at the Washington meeting of the American Physical Society, 1948.
[2] H. L. Anderson, Phys. Rev. **73**, 919 (1948).
[3] R. G. Sachs, Phys. Rev. **72**, 312 (1947). Fig. (2) of this paper is in error and therefore should not be used for the interpretation of any results.
[4] F. Villars, Phys. Rev. **72**, 256 (1947), F. Villars, Helv. Phys. Acta XX, 476 (1947), A. Thellung and F. Villars, Phys. Rev. **73**, 924 (1948).
[5] R. G. Sachs, Phys. Rev. **74**, 433 (1948).
[6] H. Primakoff, Phys. Rev. **72**, 118 (1947); G. Breit and I. Bloch, *ibid.* 135 (1947); and R. G. Sachs, *ibid.* 91 (1947).
[7] M. Goeppert-Mayer and R. G. Sachs, Phys. Rev. **73**, 185 (1948).
[8] E. Gerjuoy and J. Schwinger, Phys. Rev. **61**, 138 (1942).

cerning the ^2S, ^2P, ^4P, and ^4D state probabilities may also be obtained from the sum of the magnetic moments of the two nuclei by application of the formula[9]

$$\mu(H^3)+\mu(He^3)=\mu_p+\mu_n-2(\mu_p+\mu_n-\tfrac{1}{2}) \times(3^4D-^4P+2^2P)/3, \quad (1)$$

where ^2P, ^4P, and ^4D represent the probabilities in question. This formula is probably valid even in the presence of exchange currents since the exchange moments appear to be equal and opposite for the two nuclei.[5,10] If we insert the experimental value[11]

$$\mu(H^3)/\mu_p=1.066636\pm0.00001 \quad (2)$$

into Eq. (1) we obtain

$$\mu(He^3)/\mu_p=-0.7514+0.0906(3D-^4P+2^2P). \quad (3)$$

Now taking the values $^2S=0.96$, $^4D=0.04$, which are suggested by the binding energy calculations, we find

$$\mu(He^3)/\mu_p=-0.7623 \quad (4)$$

which is in agreement with the experimental[1] value

$$\mu(He^3)/\mu_p=-0.7618\pm0.0008. \quad (5)$$

Of course this agreement may be fortuitous, but one can at least argue that it is a remarkable coincidence. This argument would appear to provide sufficient justification for rejecting the P function in favor of the simpler interpretation until contradictory evidence is obtained from other sources.

Having accepted this conclusion, it is *not* now possible to fit the formulas of reference 3 to the observed moments. However, there are still simplifying assumptions in reference 3 that could conceivably lead to a large error in the formulas and thereby invalidate the argument for an exchange current. In particular there is the assumption that the wave functions have no angular dependence other than the minimum required to provide the necessary symmetry properties of the ^2S, ^2P, ^4P, and ^4D functions (see Eq. (35) of reference 3). As a consequence the cross term between the ^2S and ^2P functions in the theoretical expression for the magnetic moment vanishes. Since the amplitude of the ^2S function is presumed to be large, this term might be important for a very small but finite ^2P amplitude in the event that the original assumption were in error.

II. THE *S-P* CROSS TERM

The reason for making the particular choice of wave function which leads to no cross term is that the wave function always adjusts itself in such a way as to minimize the total energy. Any extra angular dependence would seem to increase the energy by adding to the kinetic energy. In order to demonstrate that this is indeed the case, we now consider the expression for the magnetic moment of H^3 which is obtained under the three assumptions:

(1) There is no exchange moment.
(2) The ground state is predominantly (96 percent) a ^2S function with a small (4 percent) admixture of ^4D function and an even smaller admixture of ^2P function.
(3) There is no limitation on the angular dependence of the ^2S and ^2P functions.

If the coefficients in the wave function are chosen in such a way as to give a maximum importance to the $^2S-^2P$ cross term, the expression for

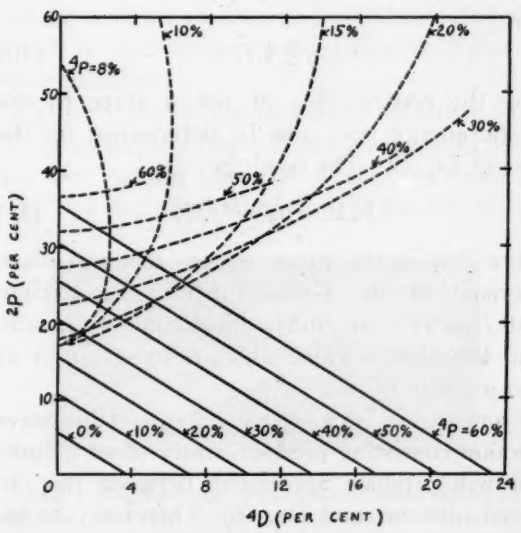

FIG. 1. Solid lines give relation between ^2P, ^4P, and ^4D state probabilities required to account for the sum of the observed moments of H^3 and He^3. Dashed lines give relation between probabilities required by H^3 moment alone on the basis of Eq. (43), reference 3.

[9] R. G. Sachs and J. Schwinger, Phys. Rev. **70**, 41 (1946).
[10] P. Morrison, Bull. Am. Phys. Soc. **23**, 28 (1948).
[11] H. L. Anderson and A. Novick, Phys. Rev. **71**, 372 (1947); Bloch, Graves, Packard and Spence, Phys. Rev. **71**, 373 and 551 (1947).

UNIVERSITY OF MICHIGAN LIBRARIES

the H^3 moment becomes[3]

$$\mu(H^3)=\mu_p-(4/3)^2P\mu_p-(2/3)D(2\mu_p+\mu_n)+(2/9)^2P+(1/3)D+I(^2PS)^{\frac{1}{2}}, \quad (6)$$

where

$$I=2/9\int\int\int(1-q^2)qf_3f_1'r^4\rho^4drd\rho dq. \quad (7)$$

ϱ is the distance between the neutrons, $\mathbf{r}$ the distance from the center of the neutrons to the proton and $q=(\mathbf{r}\cdot\varrho)/r\rho$. The functions f_1 and f_3 are the radial ^2S and ^2P functions and $f_1'=df_1/dq$. Since we are interested only in the case of a very small P state probability, the condition has been imposed that $^2P\leq 0.04$. In order that Eq. (6) lead to the observed value of $\mu(H^3)$ we find

$$I\geq 2.13. \quad (8)$$

It can be shown that if f_3 does not depend on q, the condition Eq. (8) cannot be satisfied by virtue of the normalization conditions on the radial functions. In order to obtain a maximum value of I with minimum angular dependence, we assume that f_3 has the same angular dependence as f_1, which has been taken to be

$$f_1=c_1[\exp(-\gamma^2q^2)f_0(r,\rho)], \quad (9)$$

where f_0 is a Gauss function. It is then found that $I\approx 4\gamma/9$. Thus if Eq. (8) is to be satisfied, then

$$\gamma\geq 4.7. \quad (10)$$

Now the contribution of the S state to the kinetic energy may also be determined on the basis of Eq. (9). The result is

$$\text{K.E.}=6\gamma^2\alpha\hbar^2/M, \quad (11)$$

where $2/\alpha$ is the mean square distance characteristic of the Gauss function f_0. Taking[7] $\alpha=0.7(mc^2/e^2)^2$ we find a kinetic energy greater than 400 Mev, a value which is too great by at least a factor of ten.

From this it is clear that no reasonable wave function consisting predominantly of an S function will produce agreement between the observed moment and Eq. (6). Therefore the exchange moment appears to be required to account for the observations if the ground state of H^3 contains only the S and D functions to an appreciable extent.

III. FURTHER EXPERIMENTAL POSSIBILITIES

Although the arguments for the existence of the exchange current appear to be rather convincing, they cannot be said to be conclusive. Corroborative experiments would be very desirable. One experiment which would appear to be most promising for this purpose is the accurate measurement of the hyperfine splitting of the ground state of tritium. In view of the explanation by A. Bohr[12] of the corresponding anomaly[13] for deuterium, the anomaly for tritium would be expected to depend to some extent on the nature of the moment, i.e., on the relative contributions of orbital and exchange moments. However, a rough estimate of the effect indicates that either explanation of the triton moment (i.e., exchange moment or large orbital moment) could lead to an anomaly in the hyperfine splitting of the order of five percent of the deuteron anomaly. Therefore a high degree of accuracy would seem to be required of both theory and measurements before this experiment will settle the question.

Additional information could be obtained from the photo-disintegration cross sections of H^3 and He^3 or the neutron and proton capture cross sections of the deuteron. These cross sections will depend on the nature of the H^3 or He^3 wave function.[14] Furthermore, the interaction of a nucleus with radiation is modified by the presence of exchange currents.[5] Consequently the cross sections for these radiative processes will depend in a detailed way on the nature of the exchange current.

This investigation was financed in part by the Wisconsin Alumni Research Foundation.

[12] A. Bohr, Phys. Rev. **73**, 1109 (1948).
[13] J. E. Nafe, E. B. Nelson, and I. I. Rabi, Phys. Rev. **71**, 914 (1947); D. E. Nagle, R. S. Julian, and J. R. Zacharias, Phys. Rev. **72**, 971 (1947).
[14] This point was called to the authors' attention independently by L. Schiff and H. Primakoff.

Inelastic Scattering of Protons from Light Nuclei

H. W. FULBRIGHT AND R. R. BUSH
Palmer Physical Laboratory, Princeton University, Princeton, New Jersey

(Received August 9, 1948)

A method has been developed for doing scattering experiments inside the vacuum chamber of an f-m cyclotron. The magnetic field of the cyclotron is used to analyze the scattered beam. The spectrum of the scattered particles is recorded on photographic plates, and lines corresponding to states of the scattering nucleus are found. Levels are reported for B, C^{13}, N^{14}, O^{16}, Mg, Al^{27}, and Ni.

I. INTRODUCTION

EXPERIMENTS which show that protons of energies up to 8 Mev can be scattered inelastically by certain nuclei have been made by a number of investigators.[1] The method has generally been to direct at the scatterer a collimated beam of approximately monoenergetic protons, then by means of range measurements or by use of an analyzer magnet to determine the energy distribution of the protons scattered through a known angle. The highest energy peak in the distribution curve corresponds to elastic scattering, and the lower energy peaks correspond to inelastic scattering. From the energy values of the peaks the positions of the corresponding nuclear energy levels can be calculated by use of the laws of conservation of energy and momentum. In this way portions of the energy level schemes of a number of naturally occurring isotopes have been obtained.

The experiments described below are of the same general sort, but are different in several respects: they are done inside the vacuum chamber of the cyclotron; no special equipment is required for collimating or analyzing the primary beam; the magnetic field of the cyclotron is used for analyzing the scattered beam; energies up to 17 Mev are used.

II. METHOD

The Princeton cyclotron is a 35-in. f-m machine with a single dee. The scattering camera (see Fig. 1 and Fig. 2) rests on the floor of the dee chamber, beneath the beam, in the region normally occupied by the second dee of a two-dee cyclotron. The scattering foil, which is both thin and narrow, is held vertical so that it intercepts the beam. Protons scattered slightly downward follow helical paths of small pitch. Some of them pass through the vertical slit and strike the horizontal photographic plate at a glancing angle of about 15°. Since the radius of the helix followed by a particular proton depends upon the momentum of that proton, a spectrum of the scattered beam is recorded on the plate. Ilford nuclear physics plates with 50-μ and 100-μ thick emulsions have been used so that the full range (up to about 1000μ) of most protons would be spent in the emulsion. Lines easily visible to the unaided eye, each corresponding to a state of the residual nucleus, are obtained with beam currents of half a microampere and exposure times of thirty minutes.

Figure 3 shows the spectrum obtained from platinum with a primary beam energy of 15 Mev. Only one proton line, the elastic line,[2] can be seen. The sharply defined line on the left lies in

FIG. 1. Small scattering camera and plate holder. The plate is covered with a 0.5-mil aluminum foil. The body of the camera is made of dural and the slit jaws are of copper.

[1] T. R. Wilkins and G. Kuerti, Phys. Rev. **57**, 1082(A) (1940); T. R. Wilkins and G. Wrenshall, Phys. Rev. **58**, 758 (1940); T. R. Wilkins, Phys. Rev. **60**, 365 (1941); R. H. Dicke and J. Marshall, Jr., Phys. Rev. **63**, 86 (1943); J. Chadwick, A. N. May, T. G. Pickavance, and C. F. Powell, Proc. Roy. Soc. **183A**, 1 (1944); H. Heitler, A. N. May, and C. F. Powell, Proc. Roy. Soc. **190A**, 180 (1947); K. E. Davis and E. M. Hafner, Phys. Rev. **73**, 1242(A) (1948).

[2] For brevity the expressions "elastic line" and "inelastic line" will be used throughout for lines produced by elastic and inelastic scattering, respectively.

UNIVERSITY OF MICHIGAN LIBRARIES

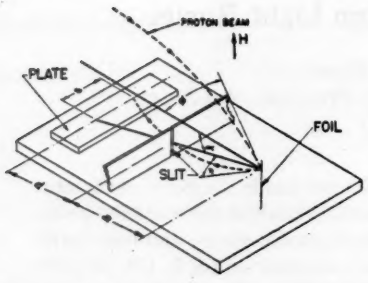

FIG. 2. Diagram of scattering arrangement. ($a \leqq d \leqq 5$ cm, s varies from 0.8 to 1.7 cm.)

a plane which passes through the slit and the scattering foil. Simple absorption measurements indicate that it is produced by soft, characteristic x-rays generated in the foil by the passage of the protons.[3] The x-ray line is a very useful reference mark in measuring the proton line deflections.

Calculations

The calculation of energies has been on a nonrelativistic basis throughout. If the deviation, s, of a line has been measured the corresponding proton kinetic energy can be calculated from the equation

$$E=(e^2/2mc^2)H^2R^2(1+\mu^2), \tag{1}$$

where

$$R^2=\left(\frac{a\cos\alpha}{2}\right)^2+\left(\frac{s}{2}+\frac{d(a+d)\cos^2\alpha}{2s}\right)^2$$

and

$$\mu=\frac{(a+d)\sin\alpha}{R\sin^{-1}[2sd\cos\alpha/(s^2+d^2\cos^2\alpha)]}.$$

H is the vertical component of magnetic field (assumed constant); e and m are the charge and rest mass of the proton; and s, α, a, and d are defined in Fig. 2.

Equation (1) is based on the assumption of a helical path which originates at the intersection of the foil with the median plane of the beam. The position of the median plane was determined by probe measurements. Since the variation of H over the paths of the particles was less than 0.5 percent, the value of H at the slit was chosen as a reasonable average for use in the calculations.

[3] Such x-rays have previously been observed. M. S. Livingston, F. Genevese, and E. J. Konopinski, Phys. Rev. 51, 835 (1937).

A useful approximation, which under our conditions is always accurate to within 0.8 percent, is

$$E=(e^2/2mc^2)(H\cos\alpha)^2[d(a+d)/2]^2\times[1/s^2+1/(a+d)^2+1/d^2]. \tag{2}$$

After the energies of the scattered proton groups have been calculated, the corresponding nuclear energy levels can be obtained by means of the laws of conservation of energy and momentum. The energy of the ith excited state is

$$E_{ei}=[(\beta-1)/\beta]E_0-[(\beta+1)/\beta]E_i+(2/\beta)(E_0E_i)^{\frac{1}{2}}\cos\theta, \tag{3}$$

where E_0 = energy of incident protons, E_i = energy of the ith group of inelastic protons, β = ratio of mass of scattering nucleus to proton mass, and θ = scattering angle. For the ground state, $E_{ei}=0$, and (3) may be solved for E_0 in terms of $E_i=E_{el}$, the energy of the elastically scattered protons:

$$E_0/E_{el}=1+2/(\beta-1)^2\times[\beta-\sin^2\theta-\cos\theta(\beta^2-\sin^2\theta)^{\frac{1}{2}}]. \tag{4}$$

It is an important advantage of this method that E_0 can be chosen from a continuous range of values (extending in our case from 5 to 17 Mev) by setting the position of the camera so that the foil intercepts the beam at an appropriate radius. Furthermore, the scattering angle can be set to have any value between 20° and 160°.

A special camera which has eight slits and eight photographic plates arranged around a common scattering foil was often used.

It can be seen from Fig. 2 that the scattering angle θ has three parts. The part η, between the tangent to the scattered beam and the line between the foil, slit, and plate, varies slightly from line to line, but ϕ is constant, set by means of a jig which holds the camera. α is fixed by the geometry of the camera and the height of the beam. The beam is assumed to be centered horizontally at the geometrical center of the cyclotron.

Limits of accuracy

From (2) it follows that if there are errors δH, δa, and δs in the measurements of H, a, and s, respectively, the largest expected fractional un-

certainty in the calculated energy of a line is

$$\delta E/E = 2\delta H/H + 4\delta a/a + 2\delta s/s, \quad (a \cong d). \quad (5)$$

In our experiments the maximum expected errors in the measured quantities are all about one percent, so the maximum expected error in the absolute value of each energy is 8 percent. $\delta H/H$ and $\delta a/a$ are the same for all lines on a single plate, while $\delta s/s$ is different for each line. $\delta H/H$ is almost entirely systematic. The maximum errors expected in the energy levels calculated from the line energies obtained from a single plate are about 7 percent E_0. Most of the results quoted below represent averages over many separate determinations. The accuracy of the method can be improved by refining techniques, particularly by the reduction of δa by more accurate setting of the foil.

The widths of the lines arise principally from foil and slit width, spread in energy of the incident beam, foil thickness, vertical extension of the incident beam, and scattering from the slit edges. The total width corresponds to about 0.3 Mev. An analysis of the widths of the elastic lines obtained with $E_0 = 6$, 9, and 15 Mev shows that the spread in energy at "half-maximum" for the incident beam is less than 0.1 Mev in each case, and that the foil and slit widths are mainly responsible for the observed line width.

Preparation of foils

All the metallic foils used were about 6 mils wide and between 1.0 and 0.1 mil thick. They were cut by means of a special tool consisting of two razor blades clamped together with an appropriate spacer. By this procedure, foils of magnesium, aluminum, iron, nickel, copper, and platinum were made. It was found that lampblack, amorphous boron, several oxides, and a number of other chemical compounds would adhere to platinum if applied in a water or alcohol paste. In this way boron, carbon, nitrogen, oxygen, and fluorine scatterers were made. A quartz fiber was used for the examination of silicon and oxygen.

The foils were cemented to "*C*" shaped holders which were clamped in the scattering camera, as shown in Fig. 1. An aluminum baffle plate (not shown) was provided to prevent primary protons which got past the foil from striking the foil holder.

TABLE I. Summary of energy levels found in B, C^{12}, N^{14}, O^{16}, Al^{27}, Si^{28}, and Ni.

Element	Incident energies E_0 (Mev)	Line intensity S = strong M = medium W = weak	Energy levels E_x (Mev)	Previously observed levels* (Mev)
B**	9.2, 15.6	*W*	2.2±0.3	2.1
	15.6	*S*	4.8±0.4	4.4
	15.6	*S*	6.5±0.3	5.8
	15.6	*W*	7.8±0.4	—
C^{12}	12.3, 15.0	*S*	4.4±0.2	4.3
	12.3, 15.0	*M*	5.5±0.3	—
	15.0	*W*	9.7±0.6	9.5
N^{14}	15.1	*M*	5.1±0.4	5.4
	15.1	*M*	6.7±0.4	6.6(?)
O^{16}	15.3	*S*	5.8±0.3	6.1, 6.3
	15.3	*S*	6.7±0.3	6.7(?)
	15.3	*W*	8.6±0.4	—
	15.3	*W*	9.7±1.0	10.5
Al^{27}	6.1, 9.6	*W*	0.9±0.2	0.87
	9.6	*W*	2.9±0.2	2.70
Si^{28}	15.3	*W*	4.6±0.3	—
Ni	15.3	*W*	3.8±0.4	—

* All the levels recorded in this column except those of aluminum were found by experimental means other than the inelastic scattering of protons (Hornyak and Lauritsen, reference 7).

** The calculation of energy levels for boron was based upon the assumption that the scattering nucleus had mass eleven. If any of the levels is due to B^{10}, the energy reported here will be somewhat high.

III. DISCUSSION OF RESULTS

The results obtained thus far are of the limited accuracy and resolving power indicated above. Furthermore, the scattering materials have not been analyzed for purity, and for this reason some small uncertainty exists in the assignment of the lines observed. It is hoped that experiments with separated isotopes of boron, magnesium, etc., can be made later. A summary of the present results is given in Tables I and II.

Boron

Foils consisting of a thin layer of amorphous boron (81.6 percent B^{11}, 18.4 percent B^{10}) on

FIG. 3. Photograph taken with a platinum scattering foil at $E_0 = 15.0$ Mev and $\theta = 162°$. No inelastic lines are seen.

UNIVERSITY OF MICHIGAN LIBRARIES

TABLE II. Summary of energy levels found in magnesium.

E_0(mean) (Mev)	R.M.S. deviation in E_0 (±Mev)	Line strength	E_{ex}(mean) (Mev)	R.M.S. deviation in E_{ex} (±Mev)	Number of observations	Estimated error (±Mev)
6.08	0.07	*M*	1.00	0.05	6	0.2
		M	1.58	0.03	6	0.2
9.64	0.20	*W**	0.59**	0.08	4	0.2
		S	1.33	0.06	10	0.2
		*W**	1.98	0.14	6	0.3
		*W**	2.64	0.02	3	0.3
		M	3.97	0.14	8	0.2
15.30	0.22	*S*	1.54	0.13	6	0.2
		S	4.17	0.05	8	0.2
		S	5.51	0.24	8	0.3
		M	7.32	0.30	7	0.3
		M	8.30***	0	2	0.4

* Observed only at $\theta=153°$ and 162°.
** Probably an elastic line due to oxygen contamination. See discussion under magnesium.
*** Observed only with small camera (Fig. 1).

platinum were prepared as described above. Exposures were made at $E_0=6$, 9, and 15 Mev with the single and multiple cameras. An example of the plates obtained is shown in Fig. 4a. Besides the elastic lines of platinum and boron, four other lines are found, the middle two being strong, the others weak. An examination of the plates under a microscope was made, and many short tracks presumed to be due to He^4 or He^3 nuclei were found. However, all the lines observed must have been caused by protons since they continued to appear when additional exposures were made with sufficient aluminum over the photographic plates to stop all the helium nuclei.

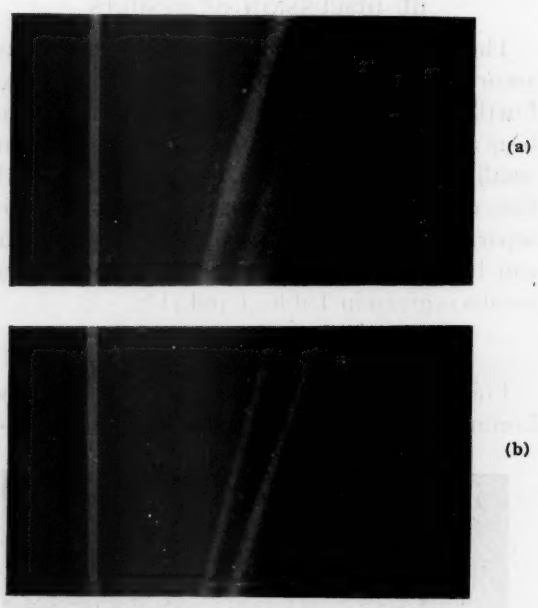

FIG. 4. (a) Photograph taken with boron on a platinum foil at $E_0=15.6$ Mev and $\theta=162°$. The vertical line on the far left is the x-ray line. The first slant line on the left is the platinum elastic line, and the next one is the boron elastic line. Beyond these are three inelastic lines, the first being quite weak. (b) Similar photograph taken with carbon on platinum foil at $E_0=15.3$ Mev and $\theta=162°$. Beyond the two elastic lines are two inelastic lines of carbon.

The intensity relationship of the various proton lines shows that the cross section for inelastic scattering from boron must be comparable with the cross section for elastic scattering. It is somewhat surprising that the (p,p) cross section is so large since the $B^{11}(p,\alpha)$ reaction is exothermic by 8.6 Mev, and the $B^{11}(p,n)$ reaction is endothermic by only 2.7 Mev. The threshold of the $B^{10}(p,n)$ reaction is 5.8 Mev.

Carbon

Foils were made by two methods: (a) a suspension of lampblack in ethyl alcohol was applied to a platinum foil, and (b) carbon was deposited on platinum by burning camphor. Three inelastic lines appeared when 12.3 and 15.0-Mev primary protons were used (see Fig. 4b). None of these appeared when the bombarding energy was 6 or 9 Mev. The corresponding energy levels are all assigned to C^{12} because of its 98.9 percent abundance.

Nitrogen

Foils of zirconium nitride on a platinum support were prepared by the method described in Section II. Multiple-angle exposures were made with incident energies of 6, 9, and 15.2 Mev. Inelastic lines were obtained only at 15.2 Mev. They were all attributed to scattering from nitrogen, chiefly because we have been unable to excite any well resolved levels in platinum, iron, copper, and nickel (except for a very weak line in nickel), while strongly excited levels have frequently been found in the lighter nuclei (see later discussion). The lowest level is calculated to lie at 5.1 ± 0.4 Mev, showing that we have not been able to find any evidence for an excited state in N^{14} below 4.7 Mev. This is interesting because of the prediction[4,5] that there should be

[4] E. Feenberg and E. Wigner, Phys. Rev. **51**, 95 (1937).
[5] R. Sherr, H. R. Muether, and M. G. White, Phys. Rev. (to be published).

an excited state of the N^{14} nucleus at about 2.4 Mev, having zero spin and corresponding to the ground state of C^{14}. The only definite experimental evidence that we know for such a level in N^{14} is the result of Sherr, Muether, and White,[5] which indicates that a gamma-ray of about 2.3 Mev is emitted by N^{14} as it decays to its ground state following the positron decay of O^{14}. Fowler, Lauritsen, and Lauritsen[6] reported a gamma-ray of 2.3 Mev from the $C^{13}(p,\gamma)$ process, but were unable to assign it to a transition between two particular states of N^{14}. The fact that the 2.3-Mev level is strongly excited in the positron decay process and only weakly at best by inelastic scattering makes further study of N^{14} desirable.

Oxygen and Silicon

Quartz fibers (SiO_2) of about 1.6-mils diameter were used in a number of exposures made with each scattering camera. Two elastic lines, two strong inelastic lines, and three weaker inelastic lines were found.

It was necessary to find a reason for assigning each line either to silicon or to oxygen. Three of the assignments were made by means of a test based upon the fact that the energy of a proton which has been scattered so as to leave the nucleus in a particular state depends upon the scattering angle. The laws of conservation of energy and momentum lead to the approximation

$$E_i(\theta)\cong E_i(\pi/2)+[2/(\beta+1)][E_i(\pi/2)E_0]^{\frac{1}{2}}\cos\theta,$$

which is good to within a few percent under our conditions. Thus experimental values of E_i plotted against $\cos\theta$ should give a straight line whose slope can be used to determine β. An example of the use of this method is illustrated in Fig. 5, where values of E_i for silicon and oxygen are shown plotted against $\cos\theta$. The scatter in points is considerable, but the method has indicated with a fair degree of certainty that oxygen should be assigned levels at 5.8 ± 0.3, 6.7 ± 0.3, and 8.6 ± 0.4 Mev, the first two of which have also been obtained with lead oxide scatterers. The method failed to give clear evidence for the assignment of the other two lines. Tentatively, a level at 9.7 Mev was assigned to oxygen and a level at 4.6 ± 0.3 Mev was assigned to silicon. The latter assignment

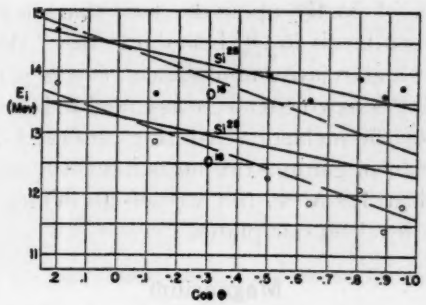

FIG. 5. Plot of energy of the two elastic groups of protons scattered from quartz (SiO_2) *vs.* the cosine of the scattering angle.

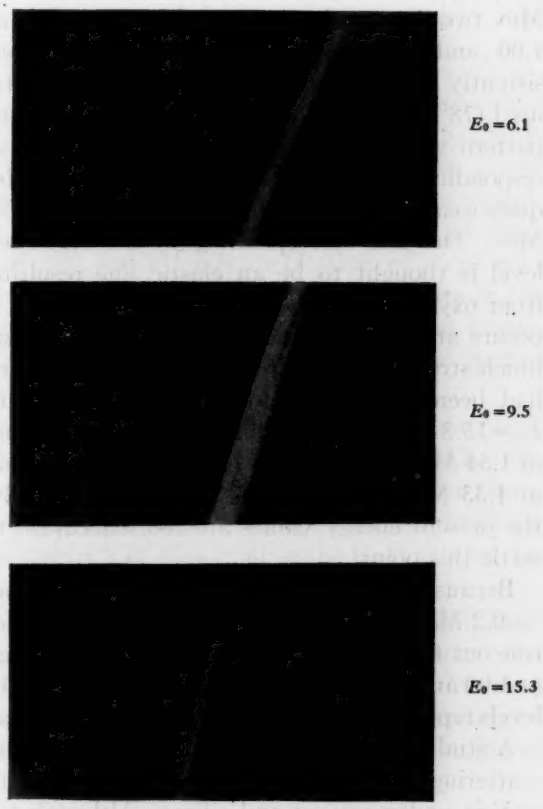

FIG. 6. Photographs taken with a magnesium scattering foil, at $\theta=162°$, and at the incident proton energies indicated in Mev at the right of each photograph. In the upper plate can be seen, from left to right, the elastic line and two inelastic lines. In the center picture are two inelastic lines barely resolved (these were clearly resolved in some of the plates), and another inelastic line on the far right. In the lower plate three additional lines may be seen. (In a number of the plates a line corresponding to $E_{ex}=1.54$ Mev was clearly resolved from the elastic line.)

[6] W. A. Fowler, C. C. Lauritsen, and T. Lauritsen, Rev. Mod. Phys. 20, 236 (1948).

UNIVERSITY OF MICHIGAN LIBRARIES

was based partly upon the fact that there are no known levels in O^{16} below 6.1 Mev.[7] Because of their high relative abundance, Si^{28} (94 percent) and O^{16} (99.8 percent) were assumed to be responsible for the inelastic scattering observed. Si^{28} is known from gamma-ray measurements[8] to have a level at 1.8 Mev, but we see no evidence for such a level on our plates.

Magnesium

The foils were made of commercial magnesium ribbon rolled to thicknesses ranging from 0.5 to 1.0 mil. Before being used they were washed in benzene and acetone.

Some of the pictures obtained are shown in Fig. 6. A summary of the results of all the magnesium pictures is given in Table II. With $E_0=6.1$ Mev two lines corresponding to energy levels at 1.00 and 1.58 Mev, respectively, were consistently found at all of the scattering angles used (78° to 162°). With $E_0=9.6$ Mev a different pattern was obtained with one strong line, corresponding to a level at 1.33 Mev, flanked by quite weak ones suggesting levels at 0.59 and 1.98 Mev. The line corresponding to the 0.59-Mev level is thought to be an elastic line resulting from oxygen impurity in the foil because (a) it occurs at the proper energy and (b) it appears much stronger in pictures made with foils which had been aged in air for several weeks. With $E_0=15.3$ Mev a single low lying level is found at 1.54 Mev. This may be the same as that found at 1.33 Mev with $E_0=9.6$ Mev. Unfortunately, the present energy values are too inaccurate to settle this point.

Because of the uncertainties in energy values (± 0.2 Mev), described in Section II, one cannot rule out the possibility that the calculated levels at 1.00 and at 1.33 Mev are identical, or that the levels reported at 1.58 and 1.98 Mev are identical.

A study of the variation of line energies with scattering angle was made as described in the section under oxygen and silicon. Although the measurements were too inaccurate for this test to be decisive, the evidence supports the belief that none of the stronger lines observed was the result of scattering from oxygen, nitrogen, or carbon. Examination of the plate under a microscope showed that none of the lines observed was composed of alpha-particle tracks. The other energetically possible reaction which might have caused complications is the (p,d) process. The threshold for the reaction $Mg^{24}(p,d)Mg^{23}$ is 13.3 Mev, so this reaction should not be of consequence here. The threshold for the reaction $Mg^{25}(p,d)Mg^{24}$ is 4.9 Mev, but the particular group of deuterons from this reaction which would leave Mg^{24} in its ground state would have appeared between the x-ray line and the elastic (p,p) line. Very few tracks of any sort appeared there. The threshold for the reaction $Mg^{26}(p,d)Mg^{25}$ is 9.8 Mev, so this reaction also is unimportant except possibly at the highest energy used. These arguments, along with the fact that the abundance of Mg^{25} and Mg^{26} is small (about 11 percent each), make it seem unlikely that any of the lines reported was due to a (p,d) reaction.

A definite assignment of the various levels to particular isotopes of magnesium on the basis of present results cannot be made, but there are several reasons to suspect that all the levels except possibly the weak ones at 2.0 and 2.6 Mev are due to Mg^{24}. First, the inelastic lines are about as strong as the elastic line. Second, the competing reaction $Mg^{24}(p,n)Al^{24}$ probably has a high threshold since Al^{24} has never been observed, while the reactions $Mg^{25}(p,n)Al^{25}$ and $Mg^{26}(p,n)Al^{26}$ have 4.7- and 3.6-Mev thresholds, respectively, and would be expected to compete strongly with the corresponding (p,p) reactions.

Dicke and Marshall,[1] using 6.9-Mev protons and a scattering angle of 135°, found a strongly excited level at 1.32 and weakly excited levels at 2.74 and 3.88 Mev. Wilkins' values are 1.37, 2.80, and 4.07 Mev. These probably correspond to our levels at 1.33 (and possibly 1.54), 2.64, and 4.17 Mev. It is known that gamma-rays of energies 2.76 and 1.38 Mev are consecutively emitted by Mg^{24} following the beta-decay of Na^{24},[9] so there must be a level at 4.14 Mev and another at either 2.76 or 1.38 Mev. Our level at 4.17 probably is the same as the 4.14-gamma-level, and it is possible that our 1.33 (and possibly 1.54) level is the same as the 1.38-gamma-

[7] W. F. Hornyak and T. Lauritsen, Rev. Mod. Phys. 20, 191 (1948).
[8] E. Bleuler and W. Zünti, Helv. Phys. Acta 20, 195 (1947).
[9] K. Siegbahn, Phys. Rev. 70, 127 (1946).

level, but the large uncertainty in our energy values makes the comparison difficult. It has not always been possible to excite by inelastic scattering, levels known from gamma-ray spectroscopy (cf. discussion under silicon, nitrogen, and iron). There is evidence for a 1.3-Mev level found in experiments on the inelastic scattering of 2.5-Mev neutrons,[10] but the results are not good enough statistically to eliminate the possibility that two levels might be found by that method.

Although quantitative data on the intensities of the various lines have not been obtained, it is clear from visual inspection of the plates that with fixed E_0 the intensities of most of the strong lines remain roughly constant with angle. However, the neighboring lines corresponding to levels at 4.17 and 5.51 Mev show a relative variation which is clearly evident. For $E_0=15.3$ Mev and $\theta=90°$ their intensities are about equal, while at $\theta=162°$ that corresponding to 4.17 Mev of excitation is more intense, and at $\theta=78°$ the intensities are just reversed.

Aluminum

Two lines were found in the Al^{27} spectrum corresponding to levels at 0.9 ± 0.2 and 2.9 ± 0.2 Mev in good agreement with the results of Davis and Hafner[11] and Dicke and Marshall.[1]

Iron, Nickel, Copper, and Fluorine

When foils of iron, nickel, and copper were examined with $E_0=9$ and 15 Mev, a broad band of proton tracks appeared in each case. Figure 7 shows a typical picture obtained with iron. The proton band may be due to inelastic scattering, giving a number of unresolved overlapping lines, or it may be due to a three-particle disintegration of the compound nucleus, or to both. In the case of copper it is likely that some of the protons were from the $Cu^{63}(p,pn)Cu^{62}$ reaction, because the yield from this process was found to be large when 16-Mev protons were used to bombard a thick target.[12] The high energy edge of the proton band of copper corresponds to a first excited level at about 1.7 Mev. Values of 6.6 and 5.8 Mev were found for iron and nickel, respectively. In addition to the broad band, nickel pictures showed a very weak line corresponding to a level at 3.8 ± 0.4 Mev.

FIG. 7. Photograph taken with an iron scattering foil at $E_0=14.9$ Mev. and $\theta=162°$.

Sodium fluoride and strontium fluoride scatterers gave patterns similar to those obtained with iron, with a "threshold" of about 5.0 Mev. This figure is too low to apply to the (p,pn) process in either sodium or fluorine, because calculations based on the known masses of Na^{23}, Na^{22}, F^{19}, and F^{18} indicate Q values of about -12 and -10 Mev, respectively. The masses of the iron, nickel, and copper isotopes are not known well enough for similar calculations to be applied to their cases.

It is known from beta-ray spectrographic work that Fe^{56} (92 percent) has levels at 0.845, 2.65, and 2.98 Mev.[13] We find no evidence for them, but this is not surprising since the (p,n) threshold for Fe^{56} is 5.47 Mev,[13] while the Coulomb barrier is higher, about 6.8 Mev.

We wish to thank Professors M. G. White and R. Sherr, and H. R. Muether for permission to use their results on N^{14} before publication. We also wish to acknowledge the stimulating interest of members of this laboratory and the assistance of the cyclotron staff.

This work was assisted by the joint program of the office of naval research and the atomic energy commission.

[10] R. N. Little, R. W. Long, and C. E. Mandeville, Phys. Rev. **69**, 414 (1946).

[11] K. E. Davis and E. M. Hafner, paper presented at the New York meeting of the American Physical Society, January 1948.

[12] A two-minute bombardment produced a strong 10.5-minute copper activity presumed to be due to Cu^{62}. Roughly speaking, the yields from the $Cu^{63}(p,pn)Cu^{62}$ and $Cu^{63}(p,n)Zn^{63}$ reactions were equal.

[13] L. G. Elliot and M. Deutsch, Phys. Rev. **64**, 321 (1943).

UNIVERSITY OF MICHIGAN LIBRARIES

Delayed Neutrons from U^{235} After Short Irradiation*

F. DE HOFFMANN, B. T. FELD,** AND P. R. STEIN***
University of California, Los Alamos Scientific Laboratory, Los Alamos, New Mexico

(Received June 10, 1948)

The decay curve of the delayed neutrons from U^{235} after an approximately 10-millisecond irradiation is measured for times from 0.2 second to 10 minutes. This curve is resolved into 5 periods, and their relative intensities are determined. When the data are converted to the conventional case of infinite irradiation, we may represent the decay curve on a relative basis by the following formula where t is in seconds.

$$N(t)=0.076\exp(-t/0.52)+0.279\exp(-t/2.5)+0.297\exp(-t/7.9)+0.294\exp(-t/32.4)+0.054\exp(-t/79.9).$$

Indications of a 6-millisecond delayed neutron period are found. These 6-millisecond period neutrons seem to amount to only 2 percent of the delayed neutrons when irradiated to saturation.

I. INTRODUCTION

At the end of 1944, O. R. Frisch *et al.* built a chain-reacting assembly nicknamed "The Dragon" at Los Alamos Laboratory. The essential feature of Frisch's device was that a slug of active material[1] was made to fall through a core of active material in such a fashion that momentarily a chain reaction sustained by the neutrons emitted instantaneously in fission (prompt neutrons) alone took place. This gave rise to an intense burst of neutrons lasting a very short time; for example, the bursts lasted some milliseconds and gave rise to about 10^{14} neutrons per burst.

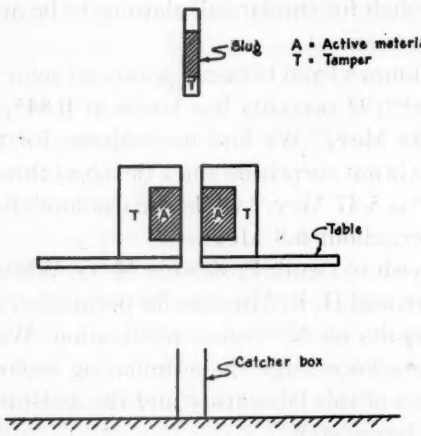

FIG. 1.

Delayed neutron periods of U^{235} had been measured by this time or were being worked on by several investigators,[2] but all these measurements were made with rather long irradiation times. In consequence, the resolution of the shorter periods was questionable. The dragon, or drop experiment as it was also called, was the first opportunity to realize exceedingly short irradiations of U^{235} and then measure the decay curve of the delayed neutrons.

II. EXPERIMENTAL ARRANGEMENT

A. General Set-Up

In the drop experiment essentially three different assemblies were used. Such an assembly is sketched in Fig. 1 (not to scale). The "slug" contained about 10 percent of the active material. The three assemblies shall be referred to as assembly *I*, *II*, and *III*. Their essential characteristics as they affect this investigation are given in Table I.

It will be noted that assemblies *I* and *II* used a BeO reflector and consequently, in addition to the delayed neutrons, neutrons after the main pulse were produced by the $\gamma-n$ reaction in Be.

There were essentially two places where delayed neutrons could be detected: (a) near the core (i.e., on the "Table") or, (b), near the

* This work was completed on April 6, 1945, and filed as a classified report of the Los Alamos Scientific Laboratory. The results only of this work were reported previously as a Letter to the Editor in this journal (Phys. Rev. 73, 636 (1948)).

** Now at Massachusetts Institute of Technology.

*** Now at Harvard University.

[1] By active material is meant a mixture of U^{235} and moderator.

[2] Snell, Nedzel, Ibser, Levinger, Wilkinson, and Sampson, Phys. Rev. 72, 541 (1947); W. C. Redman and D. Saxon, Phys. Rev. 72, 570 (1947); Hughes, Dabbs, Cahn, and Hall, Phys. Rev. 73, 111 (1948).

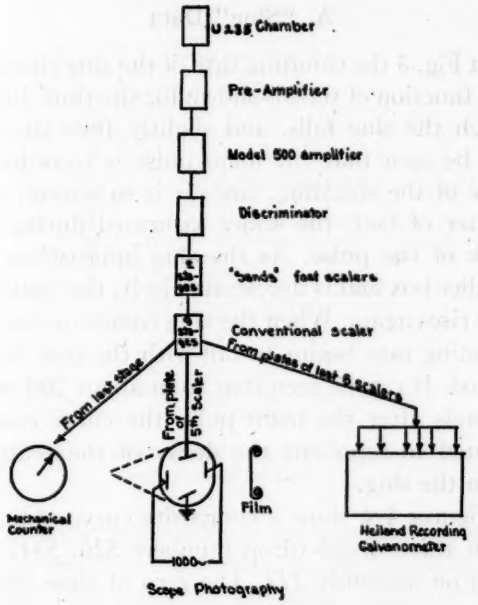

FIG. 2.

catcher box. If one observes the decay curve by means of a neutron-detecting device on the table, it has the advantage that one can record immediately after the main burst is past; i.e., from about 10 milliseconds on. The disadvantage of the table position is that it presents a distorted picture of the decay curve, since the core and reflector form a highly multiplicative system even without the slug; in addition, the neutrons from the $\gamma-n$ reaction of the fission product γ's on the Be further distort the decay curve.

A chamber which is placed near the catcher box and measures delayed neutrons emitted from the slug does not so distort the decay curve, but it does not permit the measurement of the source sooner than about 200 milliseconds after the main pulse, the time required for the slug to arrive and come to rest in the catcher box.

In consequence of the above considerations it was decided to measure the true decay curve from 200 milliseconds on out by measuring the delays emitted from the slug in assembly *III*, where no $\gamma-n$ reaction or multiplicative system would interfere.

To obtain an idea about possible delay periods in the region between several milliseconds and 200 milliseconds, a neutron detector was located on the table in all three assemblies with the clear understanding that it might give a somewhat distorted picture but would show up any important effects.

TABLE I. Characteristics of the assemblies.

Assembly No.	Neutron reflector	Effective width B of main pulse
I	BeO	~3 milliseconds
II	BeO—sheet of Cd between core and tamper	~3 milliseconds
III	Graphite and polythene	~11 milliseconds

B. Neutron Detecting and Recording Equipment

The chambers used throughout were two flat U^{235} fission chambers[3] filled with an argon+CO_2 mixture and using electron collection for rapid response.

For measurements on the slug, a chamber was placed close to the catcher box and surrounded by 2 to 3 inches of paraffin. The top and sides were covered with cadmium and paraffin to stop the neutrons emitted from the core on the table.

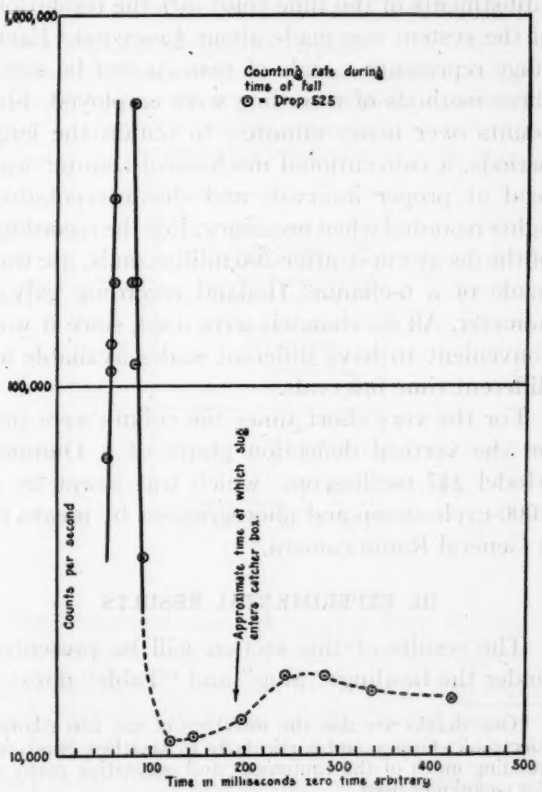

FIG. 3.

[3] Constructed by H. Daghlian and M. Holloway.

UNIVERSITY OF MICHIGAN LIBRARIES

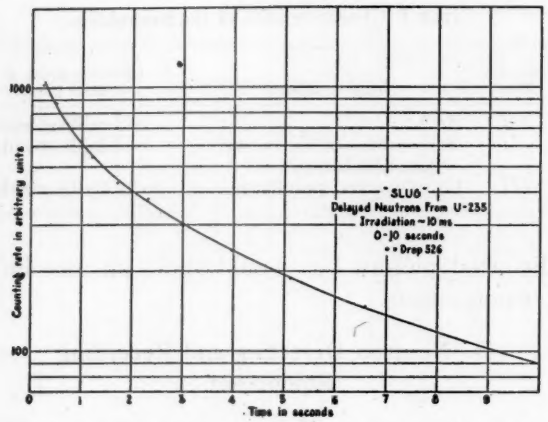

FIG. 4.

The table chamber was placed in different positions on the three assemblies. In assembly *I* and *II* it was placed at the interface of core and reflector; in assembly *III*, it rested on the outside of the polythene reflector.

The amplifying and recording arrangement is depicted in a block diagram in Fig. 2. By suitable adjustments of the time constants the resolution of the system was made about $\frac{1}{2}\mu$-second.[4] Each stage represents a scale of two. As can be seen, three methods of recording were employed. For counts over many minutes, to obtain the long periods, a conventional mechanical counter was read at proper intervals and the interpolation lights recorded when necessary. For the recording of the decay curve after 200 milliseconds, use was made of a 6-channel Heiland recording galvanometer. All six channels were used, since it was convenient to have different scales available at different time intervals.

For the very short times the counts were put on the vertical deflection plates of a Dumont Model 247 oscilloscope, which was swept by a 1000-cycle sweep and photographed by means of a General Radio camera.[5, 6]

III. EXPERIMENTAL RESULTS

The results of this section will be presented under the headings "Slug" and "Table" data:

A. "Slug" Data

In Fig. 3 the counting rate of the slug chamber as a function of time is shown for the time during which the slug falls, and slightly thereafter. It can be seen that the main pulse is recorded in spite of the shielding, since it is so strong; as a matter of fact, the scaler saturated during the peak of the pulse. As the slug approaches the catcher box and is decelerated in it, the counting rate rises again. When the slug comes to rest the counting rate begins to fall with the true decay period. It can be seen that from about 200 milliseconds after the main pulse the curve can be trusted to represent the decay of the neutrons from the slug.

Figures 4–6 show a composite curve obtained from three drops (drop numbers 526, 534, and 537) on assembly *III*. The zero of time chosen corresponds to the midtime of the main pulse.

Drops 526 and 537 were normalized to match drop 534. The arbitrary scale chosen for the *Y* axis is thus counts/second on drop 534. The conversion factors for the other drops were:

$$(534)/(526) = 1.22 \times 10^{-1},$$
$$(534)/(537) = 1.251 \times 10^{-2}.$$

That is, the observed intensities were multiplied by these factors in order to obtain one curve for all three measurements.

Since some of these counting rates were quite high, a counting loss correction was applied. This figure was obtained experimentally by making

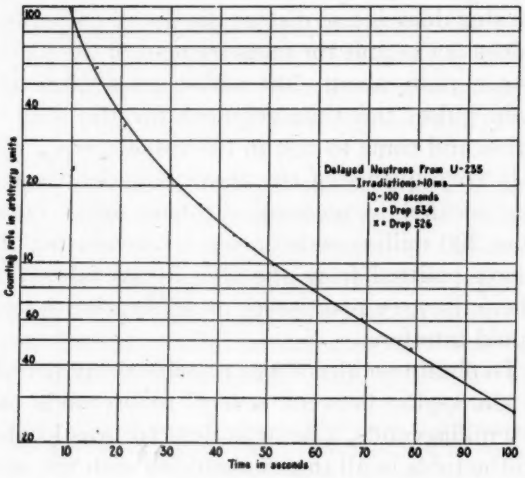

FIG. 5.

[4] Our thanks are due the members of the Los Alamos Electronics Group, and particularly to Matthew Sands for building much of the equipment and suggesting many of the techniques used.

[5] See Appendix for further details.

[6] We are greatly indebted to B. Brixner for help in all photographic aspects of the problem.

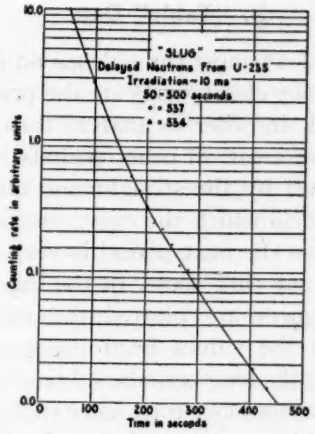

FIG. 6. (The symbol appearing at the bottom of the ordinate should read 0.01.)

the assembly supercritical and allowing the neutron intensity to rise with a period of about one second. This exponentially rising intensity was recorded and plotted on semilog paper; the deviation from a straight line gives the counting loss correction. In the drops 526, 534, and 537 the counting rate was never greater than 60,000 counts/sec., where the correction was 3 percent.

For drops 526 and 534 the records were taken from the Heiland camera, whereas drop 537 was recorded by reading the mechanical counter.

A small background resulting from the presence of a Po-Be source in the assembly was checked before each drop and deducted. The

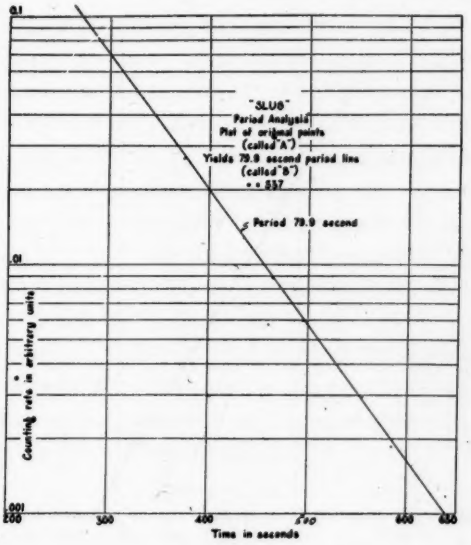

FIG. 7.

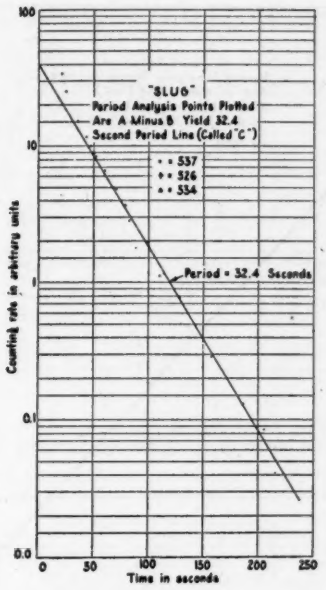

FIG. 8.

effect of delayed neutrons excited by preceding drops was always negligible.

The accuracy of the plotted points is as follows:

Drop 526: 2048 counts for each point.
Drop 534: 3000–8000 counts for each point.
Drop 537: up to 300 seconds—each point represents 15 seconds counting; after 300 seconds—each point represents 30 seconds counting.

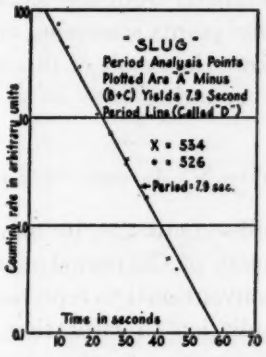

FIG. 9.

The smoothed curve drawn on Figs. 4–6 was the curve that best fitted these points. Supporting evidence not presented here was gained from several additional drops, which showed temporary breakdown of the scalar system but were trustworthy in certain limited time regions.

The analysis into periods was performed by using the *smoothed* curve and "peeling" succes-

UNIVERSITY OF MICHIGAN LIBRARIES

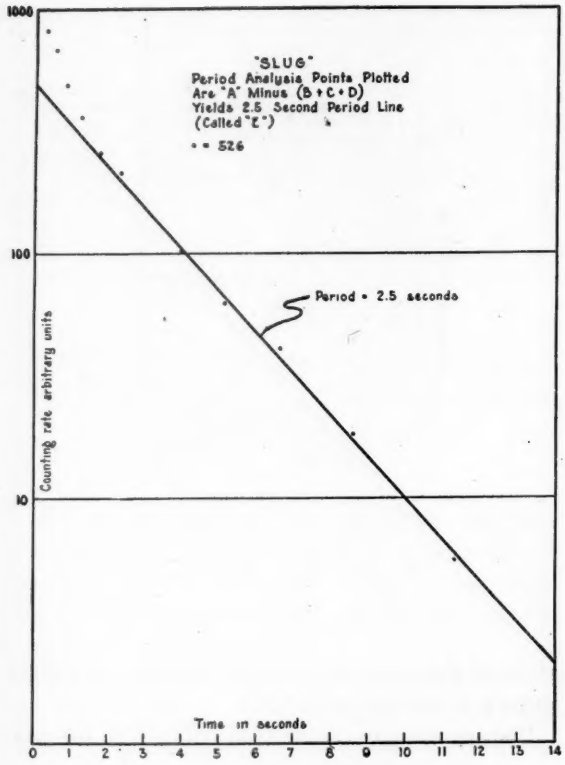

FIG. 10.

sive periods in the conventional fashion. Figures 7–11 serve to illustrate this process and show the period lines obtained from the smoothed curve with the *original* points scattering around it.

Table II shows the result of this analysis. We represent the counting rate as a function of time by

$$N(t)=\sum_i A_{0i}\exp(-t/\tau_i),$$

where 200 milliseconds $<t<$ 10 minutes. A_{0i} is thus the intensity of the period τ_i at zero time.

Since it is conventional to represent this curve in case of irradiation to saturation, we convert our relative intensities to this standard. Since our irradiation was infinitely short compared with any of the periods in Table I, we merely have to form the product $A_{0i}\tau_i$ to achieve this purpose. The column entitled r_i normalizes the products $A_{0i}\tau_i$ so that $\sum_i r_i=1$. The probable errors indicated on the periods obtained are guesses based on the "peelings" as shown and on evidence from the analysis of drops not presented here.

B. "Table" Data

Figures 12–14 show three drops on assemblies *I* and *II*. They clearly indicate the presence of a short period. In order to analyze this portion of the curve we treat all other periods as a single one, as shown by the straight and almost horizontal line into which the curve merges. This is justified since the next period is very long compared with our time scale. In the insert of each of these figures are plotted the experimental points with the values from the straight line, representing the long periods, subtracted off. The points are rather inaccurate since each represents only 64 to 320 counts, save that the long-period line is much better established. Appropriate counting rate corrections were applied, but these were difficult to ascertain accurately for such enormous counting rates and were really guesses for rates above 200,000 counts/second. The average value of the period is 6.3 ± 1 milliseconds.

Figure 15 shows two samples of the type of curves obtained with assembly *III*. The left side, i.e., the rise of the main burst, was plotted for one drop only. The short period is much less in

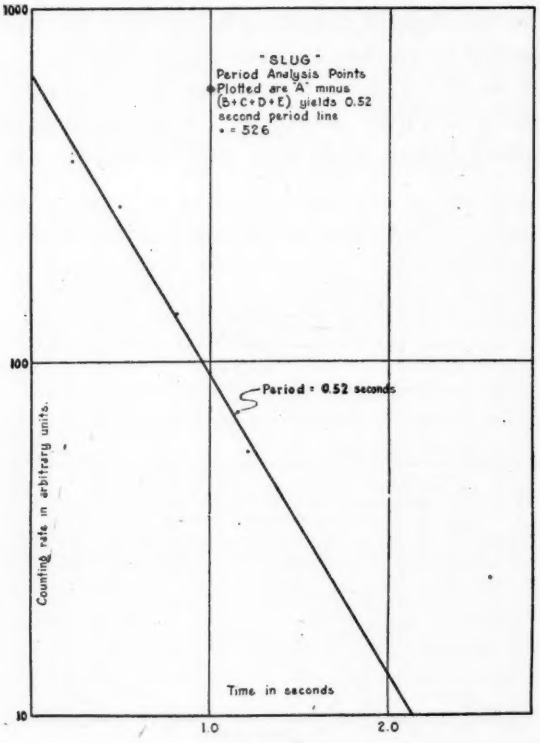

FIG. 11.

evidence here. However, this is to be expected since the main pulse is much broader and hence the short period would have decayed considerably by the time at which it becomes possible to observe it. The dotted curves indicate the intensity expected on the basis of a 6.3-millisecond period with an intensity averaged from Figs. 12–14, and it is seen to agree reasonably well with the observed points.

In calculating the curve, allowance was made for the different length of irradiation in the different assemblies. The rise and fall of the neutron intensity during the main burst corresponds to a Gaussian[7] function $\exp(-t^2/B^2)$, where B is the equivalent width of the burst as given in Table I. If a neutron emitter of period τ is produced by such an irradiation, the activity at the time $t(t^2 \gg B^2)$ is $A_0 \exp(-t/\tau) \exp(B^2/4\tau^2)$, where A_0 is the initial activity which would be produced by an infinitely short irradiation of the same integrated intensity. The correction factor $\exp(B^2/4\tau^2)$ is 1.02 for $\tau=6.3$ milliseconds and $B=3$ milliseconds (assemblies *I* and *II*), and 1.275 for $\tau=6.3$ milliseconds and $B=11$ milliseconds (assembly *III*). Hence the intensity of the short period was multiplied by $1.275/1.02 = 1.25$ before constructing the dotted line in Fig. 15.

The fact that all these assemblies indicate a short period of about the same length and intensity makes it seem unlikely that it should be spurious. If it were, for instance, caused by neutrons which have been diffusing in the neutron reflector for some time, it should be most prominent in assembly *III*, in which thermal neutrons are very important, and least in assembly *II*, in which they hardly contribute to the reaction. If it were caused entirely by a $\gamma-n$ reaction in the BeO tamper, it should be absent in assembly *III*. On the other hand, γ-rays of a similar period have been found by P. B. Moon,[8] and these may produce some photo-neutrons in assemblies *I* and *II*, which would contribute to our short period.

The initial intensity of the short period after an infinitely short irradiation is about 10 times that of the other periods together. If irradiated to equilibrium however, it amounts to only 2 percent of all delayed neutrons, or about 0.01 percent of all the neutrons.

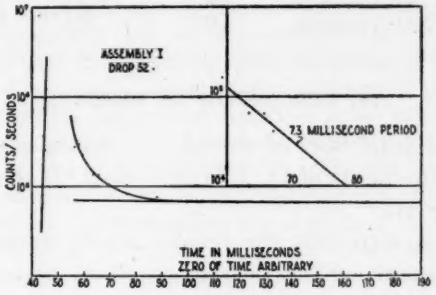

FIG. 12.

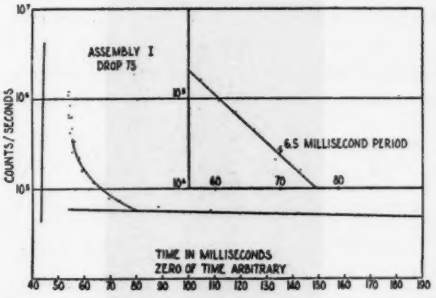

FIG. 13.

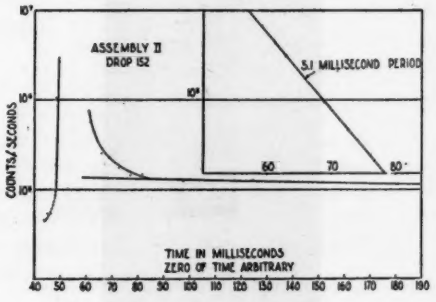

FIG. 14.

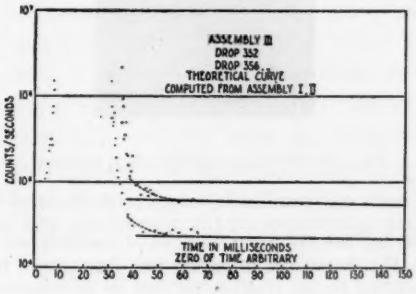

FIG. 15.

[7] This follows from theory and is borne out by the measurements on the dragon; O. R. Frisch, private communication.

[8] Private communication.

UNIVERSITY OF MICHIGAN LIBRARIES

TABLE II. Results of analysis into periods.

τ_i	A_{0i}	$A_{0i}\tau_i$	r_i
79.9 ±1.0 seconds	2.99	239	0.054
32.4 ±0.6 seconds	40.0	1296	0.294
7.9 ±0.5 seconds	165	1308	0.297
2.5 ±0.3 seconds	490	1225	0.279
0.52±0.1 seconds	640	333	0.076

TABLE III. Comparison of results with those of Hughes.*

This paper		Hughes	
τ_i	r_i	τ_i	r_i
79.9	0.054	80.2	0.035
32.4	0.294	31.7	0.227
7.9	0.297	6.51	0.292
2.5	0.279	2.19	0.330
0.52	0.076	0.62	0.116

* See reference 1.

IV. DISCUSSION OF RESULTS

A comparison of the above results with the measurements of D. J. Hughes *et al.*[1] is shown in Table III.[9]

It is seen that the results are in substantial agreement in the delayed neutron periods reported. However, the discrepancies in the values of r_i are greater than the experimental errors of these measurements would seem to warrant. Only part of this discrepancy can be attributed to the inherent inaccuracies of the "peeling" technique. The explanation for the divergence in the reported r_i's probably lies in the fact that the energies of the delayed neutrons emitted in the different periods vary over a rather wide range.[10] Hence, for an absolute evaluation of the strengths of the various periods, account must be taken of the varying efficiency of the neutron detectors used with the energies of the different delayed neutron periods. Such corrections have not been applied to our measurements, while the values of Hughes *et al.* are corrected for the energies of the delayed neutrons.

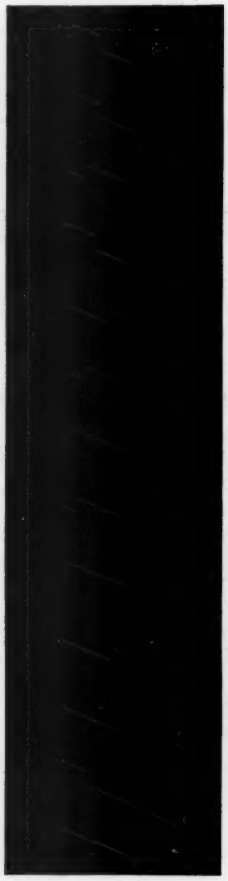

FIG. 16. Typical oscilloscope pattern.

Although the evidence for the 6.3-millisecond delay period seems rather strong, the fact that the effect measured is a very small tail on the exceedingly strong primary neutron pulse makes the interpretation of the results rather uncertain. We cannot, therefore, claim great accuracy for either the value of the period or for its relative intensity. Certainly we cannot exclude the possibility that the period observed is really a super position of many short periods.

Our experiments show no evidence for a 50-millisecond delayed neutron period, as reported by Hughes *et al.* While the accuracy of our measurements of the 6.3-millisecond group is not very great, and it would have been quite difficult for the above-mentioned authors to have observed such a short period, it seems unlikely that we would have missed a 50-millisecond period of the intensity reported by them.

We would like to thank Professor O. R. Frisch for helpful advice during the course of this experiment.

This paper is based on work performed at the

[9] We have compared our values with those of Hughes, since his measurements are the most recent, and have been corrected for the different energies of the delayed neutron periods. We have not included the very short 6.3-millisecond period in our results, nor the 50-millisecond period reported by Hughes, in computing the r_i's.

[10] See the paper by D. J. Hughes of reference 1 for values.

Los Alamos Scientific Laboratory of the University of California under Government Contract No. W-7405-eng-36, and the information contained therein will appear in Division V of the National Nuclear Energy Series (Manhattan Project Technical Section) as part of the contribution of the Los Alamos Laboratory.

APPENDIX

Figure 2 shows that the plate of the 5th "Higginbotham" Scaler was tapped and the signal fed to the vertical sweep plates of a blue-screen 5-inch DuMont oscillograph, Model 247. On the horizontal plates a specially built linear sweep was imposed and adjusted to a frequency of 1000 cycles/second. The screen was photographed by means of a continuously moving film, with the film moving vertically. The camera used was a General Radio Company oscillograph camera. The developed films showed a pattern like the sample shown in Fig. 16.

This pattern can be interpreted easily, since the first stage of the scaler contains a "flip-flop" circuit, and consequently its output changes from a maximum to a minimum and back to a maximum with successive pulses. Thus a shift of the height of the line on the scope (or film) will indicate that a pulse has registered. It should be clearly understood that with the use of this scheme the length of time between "breaks" (i.e., shifts in line-height) is the time elapsed between the appearance of two consecutive pulses and not the duration of a single pulse.

It is important that the sweep return be very fast in order that pulses may not be lost between the end of one and the beginning of another sweep. Since a signal pulse in between two sweeps is easily detected because of the shift in line-height, and, further, since two pulses within that time are rather unlikely because of the limitations in the resolving time of the amplifier, this sweep was found entirely adequate. Both the sweep and incoming signal were put directly on the respective sets of plates of the oscilloscope in order to by-pass the comparatively long time constants of the internal scope amplifiers. The incoming pulse height was regulated by means of a volume control between scaler and oscilloscope. It was so adjusted as to make the pulse height about a quarter of the distance between consecutive sweeps on the film, as can be seen in Fig. 16. This volume control had to be varied, of course, when a different film speed was used. The developed film is easily read on a Recordak Microfilm Reader.

PHYSICAL REVIEW VOLUME 74, NUMBER 10 NOVEMBER 15, 1948

The Capture Probability of Negative Mesotrons*

HAROLD K. TICHO
Department of Physics, University of Chicago, Chicago, Illinois

(Received August 5, 1948)

Disintegration curves of positive and negative mesotrons stopping in H_2O, NaF, Mg, Al, and S have been determined. The relative counting rates of positive and negative disintegration electrons support the view that the change of the mean life of negative mesotrons can be interpreted as due to a competition between the processes of spontaneous disintegration and nuclear capture. The mean-life values of positive mesotrons in the various materials are in agreement and yield a mean of $\tau_+ = 2.11 \pm 0.10$ μsec. From the mean life values of negative mesotrons the capture probabilities of mesotrons in the neighborhood of the absorber nuclei are calculated and shown to obey an empirical law of the form kZ^a with $a = 3.7 \pm 0.85$.

INTRODUCTION

TWO years ago, the author carried out a determination of the mean life of cosmic-ray mesotrons at an altitude of 11,500 feet[1] to investigate whether there might exist a variation of the mean life with altitude. The experimental method was similar to that used by Nereson and Rossi.[2] The absorber stopping the mesotrons was aluminum, and the mean life obtained was 1.78 ± 0.10 μsec. However, since a sea level check of the apparatus also yielded a value slightly lower than 2.15 ± 0.07 μsec., the best sea level value of Nereson and Rossi, an altitude variation of the mean life could not be considered as established. When the results of the experiment of Conversi, Pancini, and Piccioni on the disintegration of negative mesotrons in light materials became known,** it seemed more reasonable to

* Assisted by the joint program of the Office of Naval Research and Atomic Energy Commission.

[1] H. Ticho, Phys. Rev. 72, 255 (1947).

[2] N. Nereson and B. Rossi, Phys. Rev. 64, 199 (1943).

** Private communication by Prof. Amaldi.

UNIVERSITY OF MICHIGAN LIBRARIES

attribute the reduced values of the mean life *both* at sea level and at the high altitude to a contribution to the disintegration curve of *negative* mesotrons with an *apparently* shorter mean life.[3] Ticho and Schein[4] calculated that such a shortened mean life of negative mesotrons would result if the probabilities for capture and spontaneous disintegration were comparable and if the two processes proceeded independent of each other.

In 1940, Tomonaga and Araki[5] calculated on the basis of meson theory that mesotrons stopping in a solid absorber should be captured by the nuclei within 10^{-12} second. This time interval is small compared to the mean life of mesotrons; hence, they concluded that *all negative* mesotrons stopping in a solid absorber should be captured. Positive mesotrons are repelled by the Coulomb field of the absorber nuclei; consequently they should disintegrate. Experiments by Rasetti,[6] Nereson and Rossi,[2] and Ticho[1] seemed to confirm this prediction. These authors found that the counting rate of observed disintegration electrons was roughly one-half of the counting rate of mesotrons stopping in the absorber. This was interpreted as being due to the fact that while in the cosmic radiation near sea level positive and negative mesotrons are about equally abundant, only the positive mesotrons give rise to disintegration electrons. For this determination, the authors mentioned above used aluminum absorbers; but because of the uncertainty in the range of the disintegration electrons, the results merely indicated a trend.

This qualitative agreement with theory disappeared when Conversi, Pancini, and Piccioni[7] actually separated positive and negative mesotrons by means of magnetized iron bars and showed that while in iron, as predicted, only positive mesotrons disintegrated, in carbon disintegrations of both positive and negative mesotrons occurred in about equal numbers. This result was later confirmed by Sigurgeirsson and Yamakawa,[8] and Valley.[9] These authors also proved the existence of this effect in other light materials.

Such a result could be interpreted in two ways. The interval between the time when the negative mesotron enters the absorber and the time when it stops close to the nucleus may be comparable to the natural mean life; or, the probability for capture of a negative mesotron within the range of nuclear forces may be comparable to the probability for spontaneous disintegration.

The processes, by which a heavy charged particle continues to lose energy when it does not have sufficient energy to cause ionization or excitation of the absorber nuclei, were investigated by Wheeler,[10] Fermi, Teller, and Weisskopf,[11] and discussed in detail by Fermi and Teller.[12] Fermi and Teller[12] showed that both in conductors and insulators a mesotron of 2000 ev loses the remainder of its kinetic energy and drops into a mesotronic K-shell within 10^{-12} second. This time interval is negligible compared to the mean life and hence the first interpretation above must be abandoned. It was shown,[11] however, that the second interpretation implies disagreement with meson theories by a factor of 10^{12}.

The present experiments were carried out to investigate the disintegration of negative mesotrons in more detail—to establish conclusively the existence of a change in their mean life and to examine the dependence of this change of the mean life upon the atomic number Z of the absorber.

ANALYSIS OF THE MEAN-LIFE CHANGE

Let N_0^- be the number of negative mesotrons stopping in an absorber. Within 10^{-12} second they lose the remainder of their energy and fall into K-orbits of the absorber nuclei. They may disappear from this orbit in two ways: they may disintegrate spontaneously and eject disintegration electrons or they may be captured by the nucleus. According to Ticho and Schein,[4] the number dN^-, disappearing in a time interval dt is proportional to the sum of the probabilities per unit time for disintegration λ and for capture Λ,

$$-dN^- = (\lambda+\Lambda)N^- dt. \qquad (1)$$

[3] H. Ticho, Phys. Rev. **71**, 463 (1947).
[4] H. Ticho and Marcel Schein, Phys. Rev. **72**, 248 (1947).
[5] S. Tomonaga and G. Araki, Phys. Rev. **58**, 90 (1940).
[6] F. Rasetti, Phys. Rev. **60**, 198 (1941).
[7] M. Conversi, E. Pancini, and O. Piccioni, Phys. Rev. **71**, 209 (1947).
[8] T. Sigurgeirsson and A. Yamakawa, Phys. Rev. **71**, 319 (1947).
[9] G. Valley, Phys. Rev. **72**, 772 (1947).
[10] J. A. Wheeler, Phys. Rev. **71**, 320 (1947).
[11] E. Fermi, E. Teller, and V. Weisskopf, Phys. Rev. **71**, 314 (1947).
[12] E. Fermi and E. Teller, Phys. Rev. **72**, 399 (1947).

If $a(Z)$ is the probability of *observing* a disintegration electron emitted in the absorber and $b(Z)$ the probability of *observing* the particles, if any, emitted immediately after capture,

$$N_{\text{obs}}^-(t)=N_0^-[(\lambda a(Z)+\Lambda b(Z))/(\lambda+\Lambda)] \times\exp[-(\lambda+\Lambda)t]. \quad (2)$$

Thus *both processes* proceed with a *changed mean life* $1/(\lambda+\Lambda)$. For positive mesotrons, which presumably disintegrate with the same constant λ as the negative ones and yield disintegration electrons of the same energy, the corresponding equation reads

$$N_{\text{obs}}^+(t)=N_0^+a(Z)\exp(-\lambda t). \quad (3)$$

From these two equations, at $t=0$,

$$N_{\text{obs}}^+/N_{\text{obs}}^-=[1/\epsilon][(\lambda+\Lambda)/(\lambda+c(Z)\Lambda)]: \quad (4)$$

Here $\epsilon=N_0^-/N_0^+=0.82$ is the ratio of the intensities of mesotrons of opposite polarities in the cosmic radiation at sea level, and $c(Z)=b(Z)/a(Z)$. Ordinarily, it is assumed that in an apparatus of the type to be described no observable particles result from capture. Hence, $b(Z)=c(Z)=0$.

$$\epsilon(N_{\text{obs}}^+/N_{\text{obs}}^-)=(\lambda+\Lambda)/\lambda=\tau_+/\tau_-. \quad (5)$$

In the last equation $\tau_+=1/\lambda=2.15$ μsec.,

$$\tau_-=1/(\lambda+\Lambda).$$

According to Wheeler,[10] the capture probability should increase approximately with the fourth power of the atomic number Z of the absorber. The probability for capture per unit time is given by the product of the probabilities Λ_n, that a mesotron which is the K-orbit is in the nucleus, and Λ_c, that a mesotron within the nucleus is captured

$$\Lambda=\Lambda_c\Lambda_n=\Lambda_c\int_0^{r_0}\psi_0^*\psi_0 d\tau\simeq 4r_0^3\Lambda_c/3a_0^3. \quad (6)$$

In the equation above, r_0 is the radius of the absorber nucleus, ψ_0 is the wave function of the mesotron in the K shell, and a_0 the Bohr radius of the orbit. Substituting appropriate numbers

$$\Lambda=4.6\times10^{-7}\Lambda_cZ^4. \quad (7)$$

DISCUSSION OF THE INSTRUMENT

A cross-sectional view of the counter tube assembly is shown in Fig. 1. The apparatus was

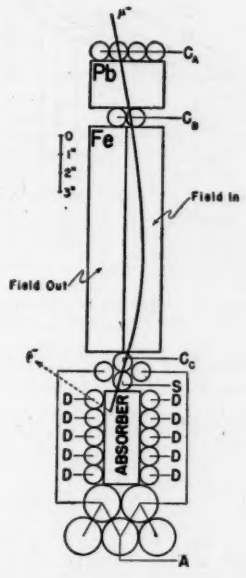

FIG. 1. Cross-sectional view of the magnetic lens, absorber, and counter tube assembly.

designed to concentrate either positive or negative mesotrons by means of a magnetized-iron lens and to record the individual lifetimes of those mesotrons which stop in the absorber. The measurement was performed by determining the time interval between the firing of counter tube S and any one of the counter tubes D, provided the pulse from counter tube S was in coincidence with an anticoincidence (C_A, C_B, C_C, $-A$). The anticoincidence counter tubes A did not cover the solid angle subtended by C_A, C_B, and C_C completely in the axial direction. They served mainly to reduce the counting rate, caused by single particles passing through the entire apparatus. The counter tubes D were situated just outside the solid angle defined by the counter tubes C_B and S. It appeared preferable to have the beginning of the time interval measurement started by the pulse from a single counter tube S, rather than by the anticoincidence pulse (C_A, C_B, C_C, $-A$). Any counter tube exhibits *random* natural time lags between the time when the ionizing particle passes through it and the time when the pulse is registered. A coincidence circuit can operate only after it receives the last pulse from its associated counter tubes; the *spread* of time intervals at which this *last* pulse occurs is therefore neces-

UNIVERSITY OF MICHIGAN LIBRARIES

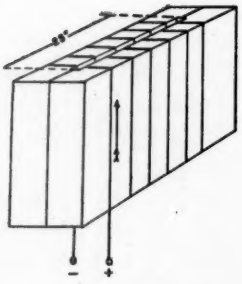

FIG. 2. Schematic diagram of the magnetic lens.

sarily larger than the *spread* of delays of a single counter tube.

The Geiger-Mueller counter tubes were of the all-metal type and were filled with a 90 percent argon, 10 percent alcohol mixture to a total pressure of 12.6 cm Hg. The 1-in. counter tubes in Fig. 1 had an active length of 24 in.; the 2-in. anticoincidence counter tubes had an active length of 36 in. The center wire was made of 5-mil Kovar metal. The D counter tubes had a 0.38-mm brass cylinder cathode. All the counter tubes were operated close to the upper ends of their plateaus.

Mesotrons of one polarity were selected by means of a magnetic lens, similar to the one used by the Rome group.[13] This lens, shown schematically in Fig. 2, consisted of two Armco magnetic iron bars which were placed side by side to form a complete magnetic circuit and hollowed out on the inside faces to accommodate the coil windings. With the magnetic field as indicated in Fig. 1, low energy negative mesotrons are concentrated on the absorber below; by reversing the exciting current in the coils the magnetic field could be reversed so that positive mesotrons were collected and negative ones dispersed. The magnetic field in the bars was 14,700 gauss, close to saturation for Armco iron. A representative trajectory for a field of 14,700 gauss is shown in Fig. 1. Obviously, high energy (>1 Bev) mesotrons pass through the lens whatever their polarity; however, such high energy particles cannot stop in the absorber below. In fact, when the lens concentrates mesotrons of *one* polarity, mesotrons of the *opposite* polarity can establish a coincidence (C_A, C_B, C_C, S) only if, upon *emerging* from the lens, their residual energy is *larger than* 160 Mev. Mesotrons of such large energies could not stop in any one of the absorbers which were employed in this series of experiments. The H_2O, NaF, Mg, Al, and S absorbers all had a thickness of 12.5 cm; the mesotron energies, corresponding to a range of 12.5 cm in the absorbers are listed in column 4 of Table I. The conclusions regarding the exclusion of mesotrons of the undesired polarity are rendered less definite by the scatterings which the mesotron may undergo during its passage through the iron. It has been shown[14] that in a

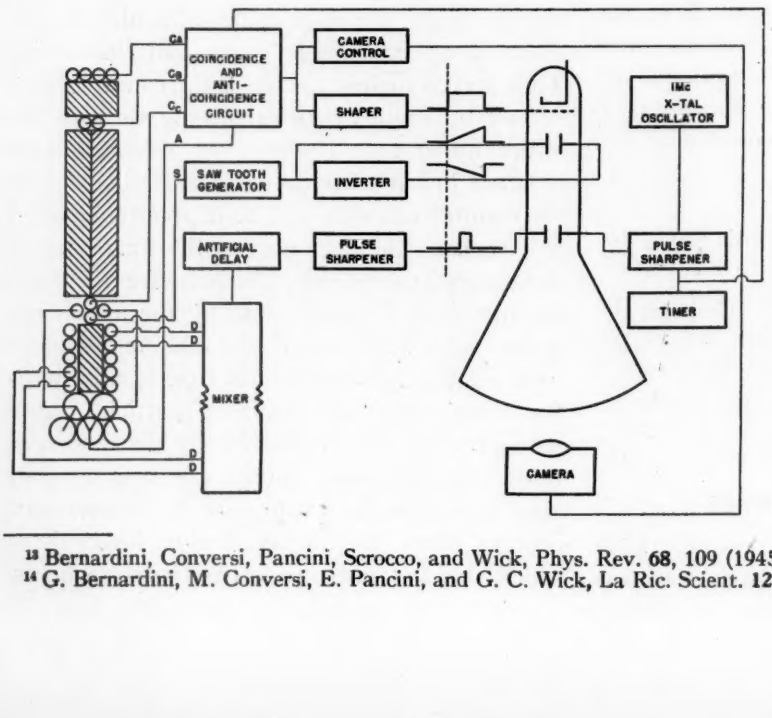

FIG. 3. Block diagram of the timing circuit.

[13] Bernardini, Conversi, Pancini, Scrocco, and Wick, Phys. Rev. 68, 109 (1945).
[14] G. Bernardini, M. Conversi, E. Pancini, and G. C. Wick, La Ric. Scient. 12, 1227 (1941).

lens of this sort the mean angle of scattering is about 0.4 of the angle of magnetic deflection. The effectiveness of the lens in barring mesotrons of the "wrong" polarity will be discussed further as the results of the measurements are presented.

A block diagram of the timing circuit is shown in Fig. 3. The pulses from the counter tubes C_A connected in parallel, counter tubes C_B, counter tube C_C, and counter tubes A are applied to an anticoincidence circuit which then "turns on" the electron beam of a 5CP11A cathode-ray tube and also actuates the camera rewinding circuit. The beam remains turned on for 7 μsec. The pulse from counter tube S actuates a sawtooth generator which produces a balanced linear sweep which lasts 8 μsec. The pulses from the ten counter tubes D are combined in a cathode-follower mixing circuit to avoid the reduction in pulse rise speed due to increased shunt capacity which results when many counter tubes are operated in parallel. The pulse from the mixer is applied to a delay circuit of the type discussed by Chance.[15] This circuit delays the pulse for a fixed time interval before it is applied to one of the vertical deflecting plates of the oscillograph tube. This delay circuit permits the zero point of the time scale to be set so that the pulse of a counter tube D always appears on the sweep *after* the anticoincidence pulse had turned on the electron beam. The zero was normally set to about 1 μsec. from the starting point of the sweep. Thus by means of this circuit *all* delays between 0 and 6 μsec. could be recorded. The traces were photographed on Super XX film by means of a special camera which employed a coated Ektar f:2 lens.

Since in this apparatus the anticoincidence monitor circuit and the circuits starting and terminating the time interval measurement were electrically independent, the calibration consisted of two entirely separate steps: (a) the calibration of the writing speed of the sweep and (b) the determination of the zero point of the time scale. The sweep was calibrated automatically every hour, when for one minute the timer in Fig. 3 opened a gate such that marker pips derived from a 1-megacycle crystal oscillator were applied to the one remaining deflection plate of the cathode-ray tube. During this one-minute period the timer also disconnected the anticoincidence tubes A to increase the counting rate. Figure 4 shows a sample of the photographic record of the timing circuit; sweep calibration traces appear at the bottom. In the six months, during which the measurements were carried out, the writing speed of the sweep never varied by more than two percent over the 24-hour periods during which the apparatus ran unattended.

TABLE I.

1 Material	2 Density	3 Range	4 Energy
H_2O	1.00 g/cm³	12.5 cm	52 Mev
NaF	1.30 g/cm³	12.5 cm	56 Mev
Mg	1.74 g/cm³	12.5 cm	68 Mev
S	2.07 g/cm³	12.5 cm	75 Mev
Al	2.70 g/cm³	12.5 cm	99 Mev

The zero point of the time scale was determined at the beginning and at the end of each 24-hour period by disconnecting the counter tubes A, removing the absorber from its place, and transferring one of the counter tubes D into the solid angle defined by the telescope C_A, C_B,

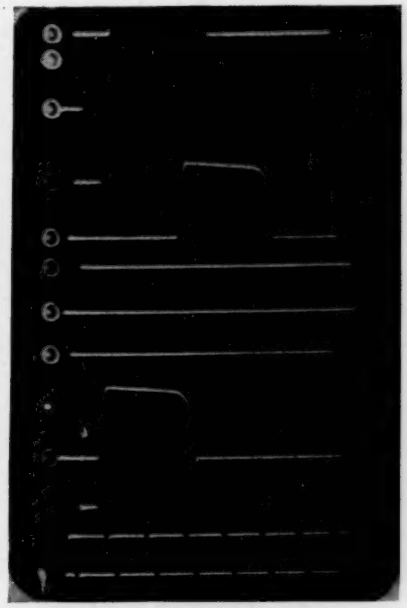

FIG. 4. Sample photographic record obtained from the timing circuit. Traces a are produced by anticoincidences (C_A, C_B, C_C, S, $-A$); trace b is due to an anticoincidence (C_A, C_B, C_C, S, D, $-A$); trace c is caused by an anticoincidence (C_A, C_B, C_C, S, $-A$) and a disintegration electron ejected with a delay of 1.75 μsec.; traces d are sweeps with 1-μsec. marker pips.

[15] Britton Chance, Rev. Sci. Inst. 17, 396 (1946).

UNIVERSITY OF MICHIGAN LIBRARIES

C_C, and S; then counter tubes S and D should be tripped simultaneously by single particles passing through the entire apparatus, and zero time intervals should be recorded. However, due to the random delays in the counter tubes themselves, there results, instead of a single value, a distribution of readings. The average of this distribution was defined as the "true zero." Data were rejected if the averages obtained at the beginning and at the end of a 24-hour run differed by more than 0.05 μsec.; in general, the averages agreed within 0.03 μsec. The delays due to the lags in the counter tubes are, of course, independent of the time when the two counter tubes are tripped. Therefore, it is proper to consider the delay distribution curve obtained with a true delay of zero as the error curve which applies to any time interval reading. Such a delay distribution curve, with the data of all the counter tubes D added, is shown in Fig. 5; the probable error is 0.05 μsec.

Aside from indicating the error in each lifetime measurement, the delay distribution curve puts a limit on the *smallest* time intervals for which a disintegration curve obtained by this apparatus remains valid. First of all, an observed delay between 0 and 0.25 μsec. can be produced by a lag in one of the counters D associated with a simultaneous event such as a shower. Furthermore, Rossi and Nereson[16] have shown that if the delay distribution curve is represented by $f(t')$, a function which is zero for $t_1<t'$, and for $t_2>t'$, then the decay curve is given by

$$N(t)=N_0\exp(-\lambda t)\int_{-\infty}^{+\infty} f(t')\exp(\lambda t')dt',$$

provided $t>t_1$. In the region $t>t_1$ the counter lags affect the decay curve only in changing its amplitude; in the region $t<t_1$, the integral becomes a function of t_1. In the experiments to be described, only time interval measurements larger than 0.35 μsec. were accepted as due to disintegrations.

The multiplicative constant

$$F(\lambda)=\int_{-\infty}^{+\infty} f(t')\exp(\lambda t')dt'$$

must be considered if counting rates of disintegration electrons resulting from decay processes with *different* life times are to be compared. If the delay distribution curve in Fig. 5 is represented by a Gaussian error curve with a precision modulus $h=10^7$ sec.$^{-1}$, then $F(\lambda)=\exp(\lambda^2/4h^2)\simeq 1+\frac{1}{4}(\lambda/h)^2$. The smallest mean life obtained in this series of measurements is about 0.5 μsec., hence $F(\lambda)\simeq 1.010$. This correction is small compared to other errors and will be neglected.

On the average, 22 anticoincidences (C_A, C_B, C_C, $S-A$) were registered per hour. Of those, 15 were not accompanied by any pulse from the counter tubes D, in six cases one of the counter tubes D was discharged simultaneously, and one anticoincidence was accompanied by a delayed firing of a counter tube D due to a disintegration. From the 15 simple anticoincidences per hour and the counting rate of 60 pulses per second of all the counter tubes D in parallel one deduces that the rate of spurious delays, caused by an anticoincidence (C_A, C_B, C_C, $S-A$) and a

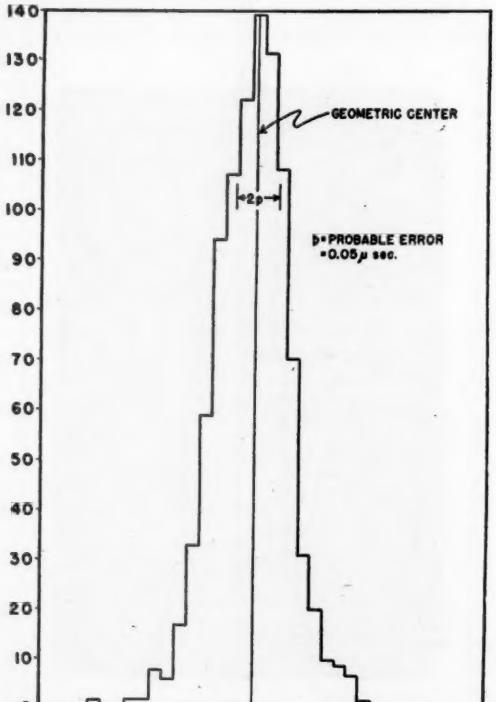

FIG. 5. Frequency distribution of observed time intervals between the firing of two G-M counters when they are actuated simultaneously.

[16] B. Rossi and N. Nereson, Phys. Rev. **62**, 417 (1942).

TABLE II.

1 Material	2 Atomic number	3 Charge	4 Time of observation in hours	5 Total number of decay electrons observed	6 Correction factors*	7 Counting rate per hour ϵN_+, N_-	8 Mean life τ in microseconds	9 Capture probability $\times 10^{-6}$ sec.**	10 τ_+/τ_-**	11 $\epsilon N_+/N_-$
H_2O	8***	+	77.5	135±12	0.82/0.75	1.90±0.16	2.19±0.30			
		−	277.8	333±18	1.00/0.76	1.58±0.09	1.89±0.15	0.65±0.4	1.14±0.09	1.20±0.12
NaF	10.1†	+	102.0	174±14	0.82/0.72	1.93±0.14	2.14±0.27			
		−	201.3	171±13	1.00/0.73	1.16±0.09	1.28±0.12	3.2 ±0.6	1.68±0.17	1.66±0.17
Mg	12	+	158.3	307±18	0.82/0.75	2.11±0.12	2.14±0.21			
		−	445.5	330±18††	1.00/0.63	1.18±0.06	0.96±0.06	5.8 ±0.6	2.24±0.16	1.79±0.14
Al	13	+	137.4	339±18	0.82/0.73	2.75±0.15	2.04±0.18			
		−	397.1	256±16††	1.00/0.59	1.10±0.07	0.75±0.07	8.7 ±1.1	2.9 ±0.3	2.5 ±0.2
S	16	+	105.5	202±14	0.82/0.79	2.00±0.14	2.13±0.25			
		−	473.9	167±13††	1.00/0.63	0.57±0.06	0.54±0.12	13.9±3.3	4.0 ±0.7	3.5 ±0.4

* Numerator corrects positive excess, denominator corrects for decay times beyond the limits of the time interval under observation.
** $\tau_+ = 2.15 \pm 0.07$ μsec. used throughout.
*** Only oxygen is effective. See text.
† Average Z according to Fermi and Teller (reference 12).
†† Corrected for an inefficiency of the magnetic lens of four percent.

subsequent, unrelated firing of a counter tube D, was 4.5×10^{-3} per hour.

EXPERIMENTAL RESULTS

In the course of this series of experiments the mean life of positive and negative mesotrons was investigated in water, sodium fluoride, magnesium, aluminum, and sulfur. The counting rates of positive and negative disintegration electrons were determined at the same time. Table II summarizes the results obtained. All the mean-life values and their errors, listed in column 8, except those given for negative mesotrons stopping in aluminum and in sulfur, were computed by means of the statistical method of Peierls.[17] The mean-life data of positive mesotrons from all the materials investigated combined yield $\tau_+ = 2.11 \pm 0.10$ μsec., in good agreement with the best value reported by Nereson and Rossi,[2] namely 2.15 ± 0.07 μsec.

The total numbers of positive and negative disintegration electrons observed in each material are listed in column 5. In order to make the counting rates of positive and negative disintegration electrons coming from each material comparable, they had to be corrected so that they referred to equal numbers of mesotrons stopping in the material. The correction factor, in column 6, shows how this correction was applied; the numerator normalizes the counting rate with respect to the excess of 20 percent of positive mesotrons present in the hard component at sea level—the denominator corrects for

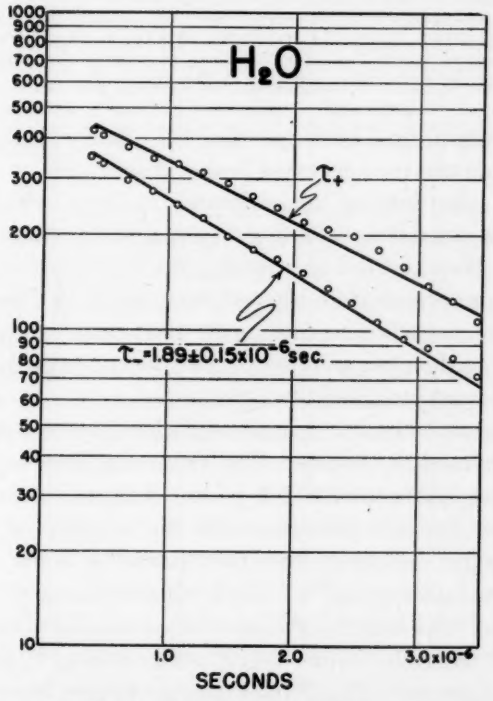

FIG. 6. Disintegration curves of positive and negative mesotrons stopping in water. The disintegration curve of negative mesotrons is plotted accurately; the disintegration curve of positive mesotrons is plotted normalized, such that both curves represent the same numbers of mesotrons stopping in the absorber.

[17] R. Peierls, Proc. Roy. Soc. 149, 467 (1935).

UNIVERSITY OF MICHIGAN LIBRARIES

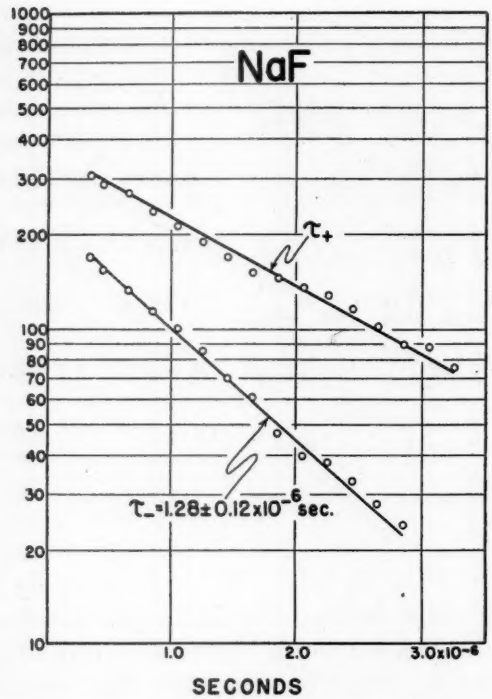

FIG. 7. Disintegration curves of positive and negative mesotrons stopping in sodium fluoride. The disintegration curve of negative mesotrons is plotted accurately; the disintegration curve of positive mesotrons is plotted normalized, such that both curves represent the same numbers of mesotrons stopping in the absorber.

disintegrations corresponding to decay times outside the time interval under observation.

In the *integral* disintegration curves which follow the data pertaining to negative mesotrons have been plotted accurately; the data for positive mesotrons were plotted normalized to those of the negative mesotrons so that both curves refer to the same number of positive and negative mesotrons stopping in the absorber.

Figure 6 shows the disintegration curves with water used as absorber. The water was kept in a copper container of 0.5 g/cm² wall thickness. When the mesotron stops in the vicinity of a hydrogen nucleus, the two particles form a neutral system and it is easily shown that within 2 μsec. this neutral system makes several thousand collisions with oxygen nuclei in which the mesotron may attach itself to the oxygen. Hence it may be safely assumed that all the disintegration electrons observed are due to mesotrons which disintegrated in the neighborhood of oxygen nuclei.[9] The mean life $\tau_-=1.89\pm0.15$ μsec. therefore corresponds to the mean life of negative mesotrons stopping in oxygen.

The sodium fluoride absorber used to obtain the decay curves of Fig. 7 consisted of NaF powder pressed to a density of 1.3 g/cm³ in a Bakelite container of 0.25 g/cm² wall thickness. Fermi and Teller[12] have shown that the probability that a mesotron stops in the neighborhood of any atom of a chemical compound is directly proportional to the atomic number of this atom. The mean life $\tau_-=1.28\pm0.12$ μsec. may therefore be regarded as resulting when negative mesotrons are stopped in an absorber consisting of an element with $Z=10.1$.

Figure 8 shows the disintegration curves of positive and negative mesotrons stopping in magnesium. From the disintegration curve of negative mesotrons one obtains $\tau_-=0.96\pm0.06$ μsec.

When the mean life of negative mesotrons was measured in aluminum and in sulfur, the inefficiency of the magnetic lens in barring mesotrons of the opposite polarity became noticeable. This can be seen by examining the upper sets of

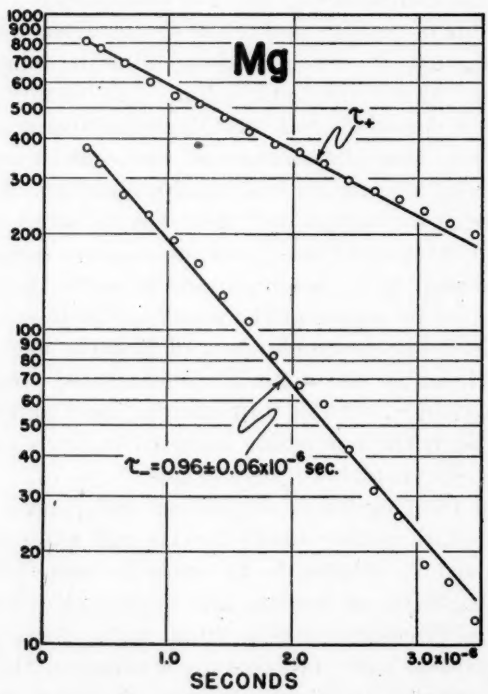

FIG. 8. Disintegration curves of positive and negative mesotrons stopping in magnesium. The disintegration curve of negative mesotrons is plotted accurately; the disintegration curve of positive mesotrons is plotted normalized, such that both curves represent the same numbers of mesotrons stopping in the absorber.

points on the decay curves of negative mesotrons in Figs. 9 and 10; in both cases after a time interval of about 1.5 μsec. more mesotrons seem to remain than the original slope of the disintegration curve would require. In either case the departure from linearity is only slightly outside the statistical error; but the fact that this deviation is observed *only* in the two cases when the negative mesotrons disappear most rapidly strongly suggests a slight admixture of positive mesotrons as the cause. Consequently, from the decay curves observed a decay curve was subtracted whose slope corresponded to 2.15 μsec. and whose amplitude was adjusted such as to make the difference curve linear. The lower sets of points in Figs. 9 and 10 were obtained by such a subtraction and they yield $\tau_-=0.75\pm0.07$ μsec. for aluminum, and $\tau_-=0.54\pm0.12$ μsec. for sulfur. This procedure appears less arbitrary in the light of the facts (a) that for *both* aluminum and sulfur it was necessary to assume an inefficiency of four percent to make the difference curves linear, and (b) that a short measurement in which the aluminum was replaced by an equivalent amount of lead, in which no negative mesotrons should disintegrate also yielded an inefficiency of the magnetic lens of four percent. Finally, in these two cases, the errors of the mean-life values have been increased beyond those given by Peierls' statistics such that they include the mean lives exhibited by the disintegration curves before the correction was applied. The mean life of negative mesotrons in aluminum is in good agreement with the result of Valley and Rossi,[18] 0.74 ± 0.17 μsec. The disintegration curve of negative mesotrons in magnesium has not been corrected for the inefficiency of the magnetic lens since here this correction is smaller than the statistical error; the correction *was applied* to the counting rate of disintegration electrons.

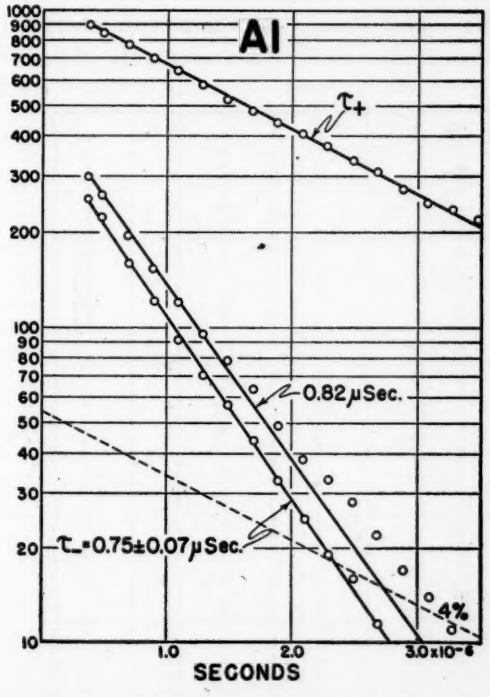

FIG. 9. Decay curves of positive and negative mesotrons stopping in aluminum. The curve whose slope corresponds to a mean life of 0.82 μsec. was obtained for negative mesotrons. The curve below is the same curve corrected for an admixture of four percent of positive mesotrons. The disintegration curve of negative mesotrons is plotted accurately; the disintegration curve of positive mesotrons is plotted normalized, such that both curves represent the same numbers of mesotrons stopping in the absorber.

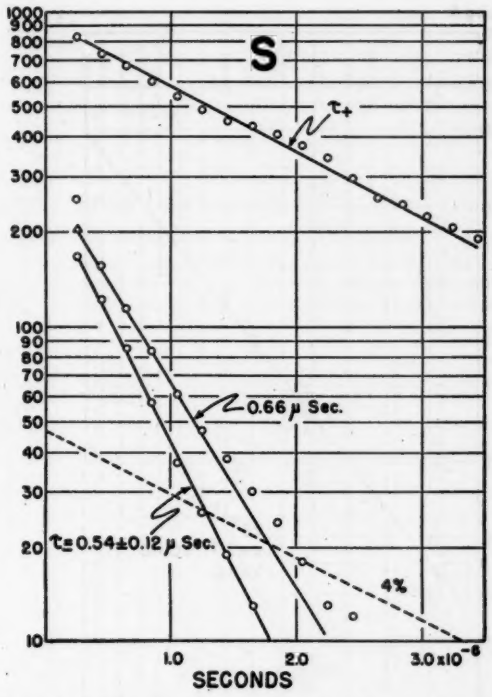

FIG. 10. Disintegration curves of positive and negative mesotrons stopping in sulfur. The curve whose slope corresponds to a mean life of 0.66 μsec. was obtained for negative mesotrons. The curve below is the same curve corrected for an admixture of four percent of positive mesotrons. The disintegration curve of negative mesotrons is plotted accurately; the disintegration curve of positive mesotrons is plotted normalized, such that both curves represent the same numbers of mesotrons stopping in the absorber.

[18] G. E. Valley and B. Rossi, Phys. Rev. **73**, 177 (1948).

UNIVERSITY OF MICHIGAN LIBRARIES

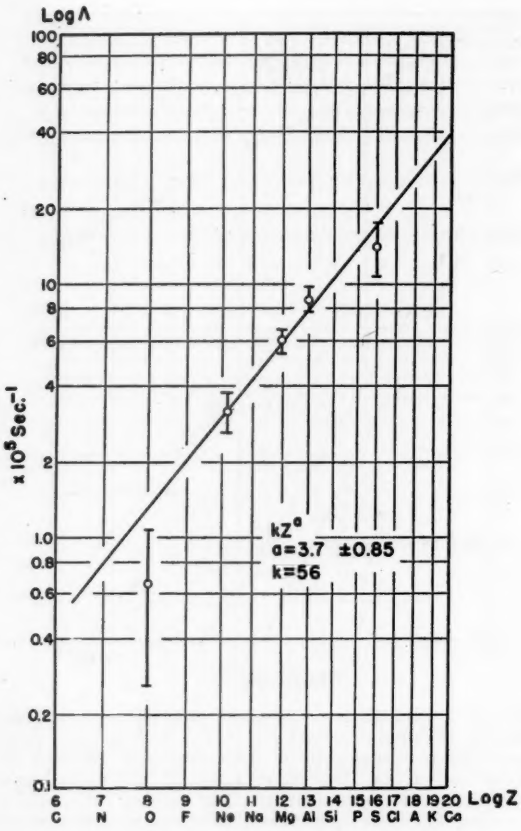

FIG. 11. The measured probabilities for nuclear capture per unit time plotted as a function of the atomic number, and a least squares curve of the form kZ^a fitted through the points.

For the mean-life measurements the sulfur was cast in a copper vessel of 0.5 g/cm² wall thickness. In this case it seemed very desirable to extend the time interval under observation into the region which was previously excluded because of the presence of natural counter tube lags. Hence the apparatus was operated without any absorber and the delays thus observed were subtracted from the disintegration curve *before* the correction for the inefficiency of the magnetic lens was applied. The triangular point at 0.25 μsec. represents the result of this subtraction.

In the course of these measurements the equipment was moved from one laboratory to another; furthermore, the sulfur measurement was performed with nine D counter tubes only. For these reasons the absolute counting rates in the various materials investigated cannot be compared.

CONCLUSIONS

From the mean-life values of negative mesotrons the capture probabilities Λ, mentioned earlier, were calculated for the materials investigated using $\tau_+ = 2.15 \pm 0.07$ μsec. They are tabulated in column 9 of Table II and plotted in Fig. 11. The points have been fitted using the method of least squares to a curve of the form kZ^a and the resultant constants are $a = 3.7 \pm 0.85$, and $k = 56$. In this fit the error in k is very large due to the power law character of the relationship. The result for a is in rough agreement with the prediction of Wheeler[10] that a should be approximately equal to 4.

The ratios of the mean lives τ_+/τ_- and the ratios of the corrected counting rates $\epsilon N_+/N_-$ are listed, respectively, in columns 10 and 11 of Table II and plotted in Fig. 12. In all cases, except in that of magnesium, the two ratios are the same within experimental error, in agreement with Eq. (5) given earlier. The large difference between the two ratios in aluminum, reported by Valley and Rossi,[18] has not been observed. This result also makes a completely different

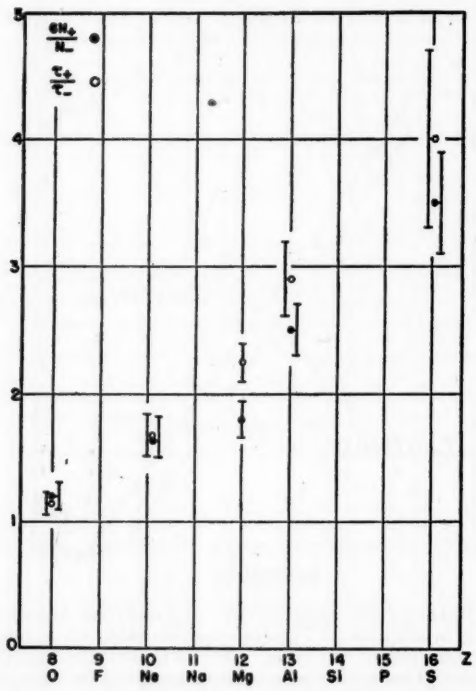

FIG. 12. The ratios of the mean lives τ_+/τ_- (empty points) and the ratios of the corrected counting rates $\epsilon N_+/N_-$ (solid points) plotted *vs.* the atomic number of the absorber.

interpretation of the decay of negative mesotrons in the neighborhood of an atomic nucleus which was suggested by Epstein, Finkelstein, and Oppenheimer[19] seem rather improbable. These authors have suggested that the change of the mean life may be due to an *acceleration* of the decay process by the intense electrostatic field of the nucleus. This hypothesis has two consequences of interest here: it follows that the counting rates of positive and negative disintegration electrons should be equal, and that the capture probability should increase with the *fifth* power of the atomic number. Neither of these two consequences was verified here.

Although the ratios τ_+/τ_- and the ratios $\epsilon N_+/N_-$ are generally within statistical error, there seems to be a trend for $\epsilon N_+/N_-$ to be somewhat smaller than τ_+/τ_-. Such a discrepancy would result if the nucleus, *immediately* after it captures a mesontron, could emit a particle which could discharge a counter tube. In such a case, of the equations discussed previously (4) instead of (5) would apply. Figure 13 shows curves for the ratio $\epsilon N_+/N_-$ for various values of $c(Z)$ with c assumed constant for simplicity. The experimental results are not inconsistent with the possibility that a particle is emitted after capture. However, because of the errors involved here further experiments will be required to decide this question.

The writer wishes to express his gratitude to Professor Marcel Schein for his continuing interest and guidance throughout the course of these experiments. It is also a pleasure to acknowledge the assistance of Mr. Ivar Kalberg, who designed the automatic camera, and of Mr. David M. Haskin, who built the G-M counters used in this experiment.

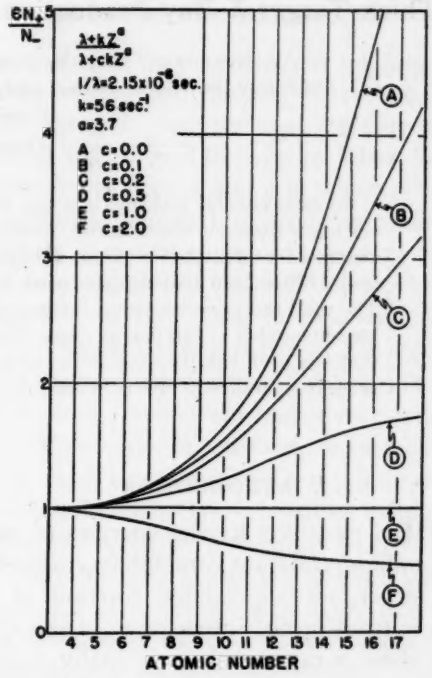

FIG. 13. Ratio of the counting rates of positive and negative disintegration electrons as a function of the atomic number of the absorber with the ratio of observabilities of particles emitted by the nuclear upon mesotron capture, and disintegration electrons as a parameter.

[19] S. T. Epstein, R. J. Finkelstein, and J. R. Oppenheimer, Phys. Rev. **73**, 1140 (1948).

UNIVERSITY OF MICHIGAN LIBRARIES

PHYSICAL REVIEW VOLUME 74, NUMBER 10 NOVEMBER 15, 1948

Thick-Target X-Ray Production in the Range from 1250 to 2350 Kilovolts*

W. W. Buechner, R. J. Van de Graaff, E. A. Burrill,** and A. Sperduto
Laboratory for Nuclear Science and Engineering, Massachusetts Institute of Technology
Cambridge, Massachusetts

(Received July 29, 1948)

An experimental investigation has been made of the thick-target production of x-rays by electrons from an electrostatic accelerator. Measurements were made with an ionization chamber for targets of beryllium, aluminum, copper, silver, tungsten, and gold. Various voltages from 1250 to 2350 kilovolts were used, and the angular range covered was from 0 to 140 degrees. The total radiation intensity, integrated over all angles, is found to be accurately linear with atomic number in this energy range. From these measurements, the efficiency of x-ray production has been calculated. For the case of 2.35-million-volt electrons on gold, a value of 7.4 percent is obtained. This is in adequate agreement with theoretical predictions.

I. INTRODUCTION

When electrons having energies of several million volts are completely stopped in a thick target, an appreciable fraction of their energy is transformed into x-rays. In this energy range, these x-rays result principally from the deflection of the electrons in the electrostatic field of the nucleus, and the basic theory of the process has been developed by Bethe and Heitler.[1] The intensity of these x-rays is a function of the electron energy, the atomic number of the target, and the angle between the direction of observation and the incident electron beam. Knowledge of the manner in which the intensity depends upon these variables is useful, both because of its utility in the design of apparatus in which electrons are to be accelerated, or in which high-speed electrons may be produced as a result of other processes, and because it affords an experimental test of the theory developed for the process.

II. APPARATUS

Certain essential features of the experimental arrangement are shown schematically in Fig. 1. A beam of electrons from an electrostatic accelerator was further focused by a magnetic lens so as to impinge cleanly upon a target placed in the center of the vacuum chamber. This vacuum chamber is a steel cylinder 12 inches in diameter and 8 inches deep. The targets were mounted around the rim of an insulated aluminum wheel which could be rotated so as to place any one of six different targets at the center of the chamber, and which could be tipped at an angle about a horizontal axis passing through this center. This was accomplished by an arrangement of concentric shafts passing through one of the flat lids of the vacuum chamber. Both motions were controlled independently by Selsyn motors.

The targets used were slightly thicker than the maximum range of the electrons in the particular material. In order to avoid overheating of the targets, the electron-beam currents were in general less than 20 microamperes. These currents were measured by a meter connected directly to the insulated target holder. In order to check the diameter and position of the electron beam when it struck the target, one of the target positions on the wheel was left open. Thus, the wheel could be rotated at any time to allow the beam to pass through and into a long extension, at the bottom of which was an insulated gold target. As shown in Fig. 1, an insulated diaphragm was placed at the entrance to this extension, and the absence of current to this diaphragm when the beam was passing through was a check on both its diameter and its position. The water-cooled gold target at the bottom of this extension provided a convenient source of intense x-rays for calibrating the generating voltmeter employed for energy measurements against the

* An account of these measurements was presented at the New York Meeting of the Physical Society, January 31, 1947, Phys. Rev. 71, 470 (1947).
** Now at the High Voltage Engineering Corporation, Cambridge 38, Massachusetts.
[1] W. Heitler, *Quantum Theory of Radiation* (University Press, Oxford, England, 1936).

threshold voltages for the photodisintegration of deuterium and beryllium.

X-ray intensities were measured with an ionization chamber of cylindrical geometry that was locally shielded with lead except in the direction of the target. The use of this type of thimble chamber for intensity measurements has been discussed by Petrauskas, Van Atta, and Myers[2] and has been found satisfactory in this energy range.

The ionization chamber currents were measured with a Lindemann electrometer used with calibrated high resistors. The chamber was calibrated to read in roentgens by comparison with a Victoreen r-meter used under identical conditions, and by measurements made on a standard radium source placed at the target position.

The chamber assembly was mounted on a disk attached to a shaft passing out through one of the chamber lids. The ionization chamber was filled with air at atmospheric pressure, and for this purpose a small tube was brought out through the center of this shaft, together with the necessary electrical leads. The angle between the axis of the ionization-chamber assembly and the incident electron beam was also controlled by means of a Selsyn motor placed outside the vacuum region. In general, the angles θ and φ, shown in Fig. 1, were kept equal so that the target thickness as seen by the ionization chamber was constant. Sufficient absorber was placed in front of the chamber to filter out soft components and to insure that substantially only the equilibrium distribution[2] was being measured. The final results were corrected for the effect of this filter as well as for absorption by the target material.

Selsyns for the control of the targets and angles were located at the remote control desk, together with those for controlling the generator voltage and beam current. The continuous control of the main experimental variables that these arrangements provided made it possible not only to take the measurements very rapidly and conveniently, but also to keep a continuous check on the experimental conditions and on possible sources of error, such as background radiation.

[2] Petrauskas, Van Atta, and Myers, Phys. Rev. 63, 390 (1943).

III. EXPERIMENTAL RESULTS

Measurements were carried out on targets of beryllium, aluminum, copper, silver, tungsten, and gold. In each case, the angle of observation was varied from 0 to 140 degrees. These results are presented in Figs. 2 and 3 in which the radiation intensity, reduced to units of roentgens per minute per milliampere at one meter, is plotted as a function of the angle of observation for various voltages and for various target materials. For each target material, the intensity scale has been adjusted to make the curves comparable in area. It is evident that, for a particular target, an increase in electron energy results primarily in an increase of the x-ray intensity in the forward direction The intensities, as plotted, have been corrected for absorption in the target and in the filter used at the ionization chamber. The variation of intensity with angle is similar to that previously found by Petrauskas, Van Atta, and Myers[2] for the case of gold.

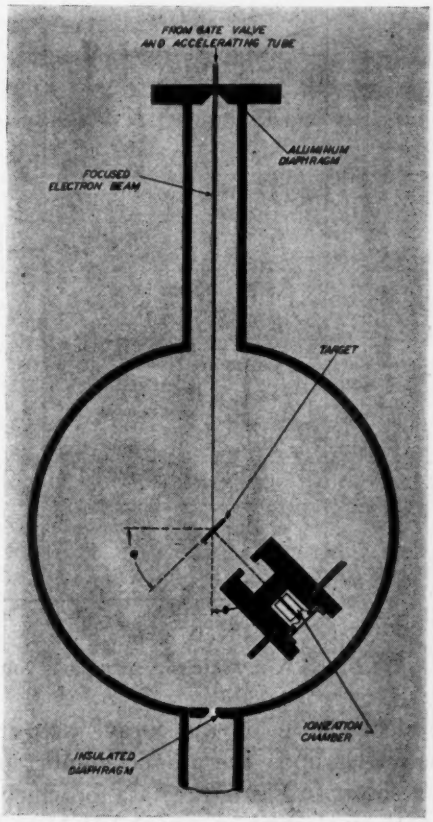

FIG. 1. Schematic diagram of apparatus.

UNIVERSITY OF MICHIGAN LIBRARIES

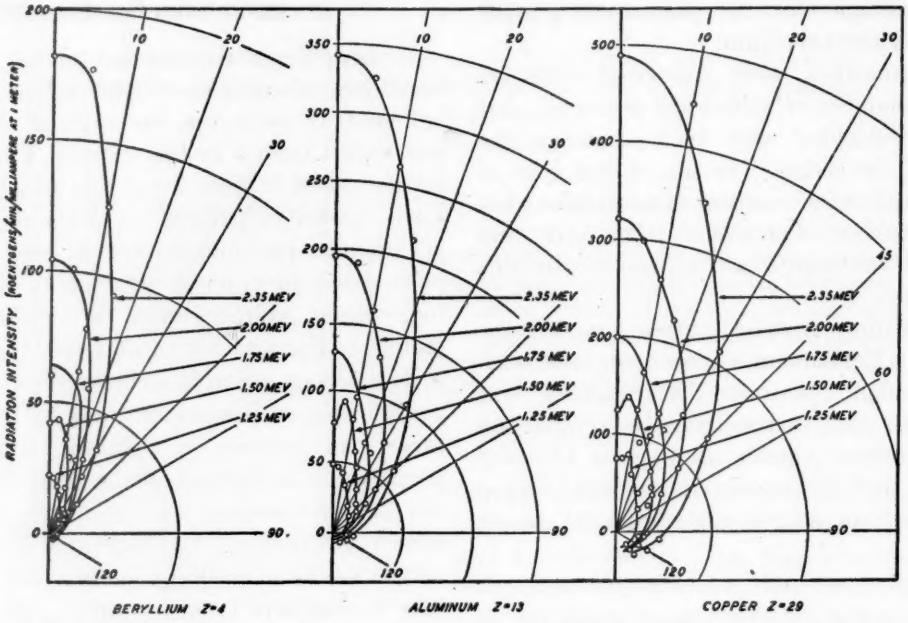

FIG. 2. X-ray intensity at various voltages as a function of angle for Be, Al, and Cu targets.

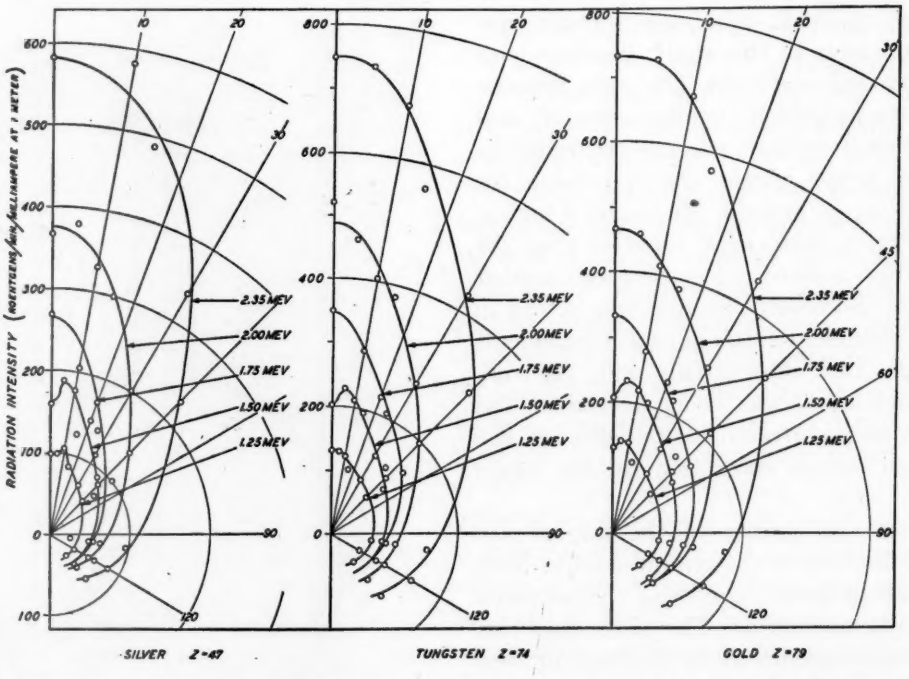

FIG. 3. X-ray intensity at various voltages as a function of angle for Ag, W, and Au targets.

The dependence of the x-ray intensity at various angles upon the atomic number of the target is shown in Fig. 4, the data for which were taken with an electron energy of 2.35 Mev. From this figure it appears that the variation of intensity with atomic number is more rapid at 90 degrees than at 0 degrees. In fact, in the forward direction the intensity from a tungsten target ($Z=74$) is somewhat higher than for one of gold ($Z=79$). At about 45 degrees the de-

pendence of intensity for atomic number is approximately linear.

IV. DISCUSSION

These measurements indicate that there is no simple dependence of the x-ray intensity in a given direction upon either the atomic number of the target or upon the bombarding electron voltage. The formula derived by Bethe and Heitler for the radiative losses for fast electrons applies only to a single collision. In a target thick enough so that the electrons are completely stopped, the situation is very much complicated by the various scattering processes, both elastic and inelastic. The effect of these processes tends to increase the radiation intensity at the larger angles and is most important for the targets of higher atomic number. This can be noticed in the curves in Figs. 2 and 3. Hence, the theory cannot be compared with the results of these measurements directly. It is, however, possible to integrate over the total range of the electrons in the target to obtain an approximate expression for the total quantity of x-radiation produced in this case. The result of such a calculation indicates that the total energy radiated should vary linearly with the atomic number.[3,4] In order to compare these results with this prediction of theory, we have integrated over the total solid angle surrounding the target the intensities found for each target at each voltage. The results of these calculations are presented in Fig. 5. It is evident that for a given voltage the total radiation flux is quite linear with atomic number. To this extent, the measurements may be interpreted as an experimental confirmation of the Bethe-Heitler theory; this confirmation being more rigorous than that provided by previous observers,[3,4] whose measurements appear to have been limited in angle.

The theory in its integrated form also provides a prediction of the fraction of the incident electron energy that is radiated. This figure may be arrived at experimentally if the ionization chamber readings are converted into units of radiation energy. The incident energy per unit time is determined from the electron voltages and

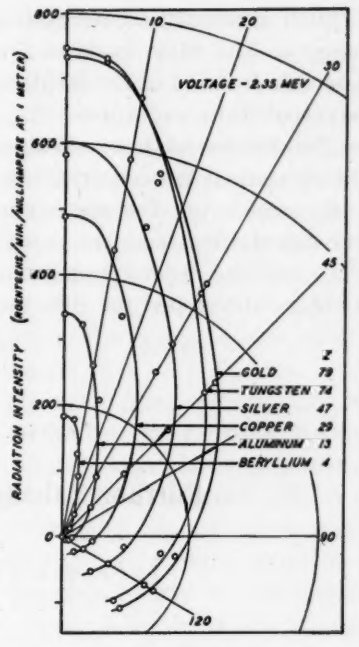

FIG. 4. Variation of x-ray intensity with angle. Voltage = 2.35 Mev.

the beam current. Using the figure of 33-electron volts as the energy required to produce an ion pair in air, we have followed the procedure of Petrauskas, Van Atta, and Myers[2] in making this

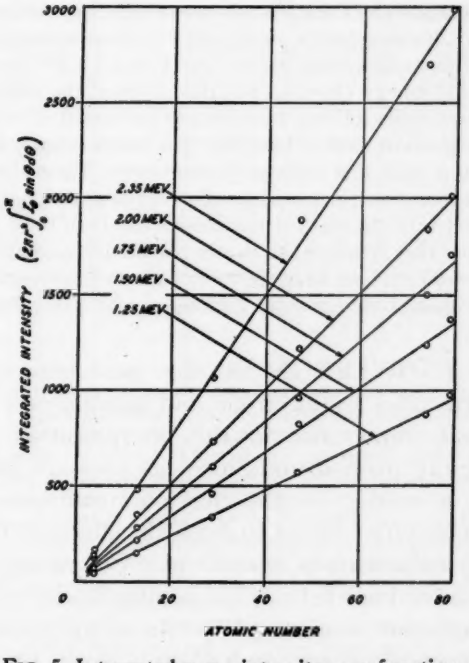

FIG. 5. Integrated x-ray intensity as a function of atomic number of target.

[3] L. A. Arcimovic and V. A. Chramov, Comptes Rendus Acad. Sci., U.S.S.R. 18, 415 (1938).
[4] Chien-Shiung Wu, Phys. Rev. 59, 481 (1941).

UNIVERSITY OF MICHIGAN LIBRARIES

conversion. Such a calculation for gold, and an electron energy of 2.35 Mev, leads to a value of 7.4 percent for the fraction of the incident power that is converted into radiation. The theory under these conditions predicts a value of 8.3 percent. The agreement between the two figures is quite good, considering the uncertainties involved in the calculations from the experimental measurements and the approximations made in applying a theory developed for thin targets to those in which the electrons are completely stopped. A similar agreement between experiment and theory has been found by other observers in the case of copper,[3] lead,[5] and gold.[2]

We are happy to acknowledge the support of the Research Corporation, the Carnegie Corporation of New York, and the Office of Naval Research.

[5] Ivanov, Walter, Sinelnikov, Taranov, and Abramovich, J. Phys. U.S.S.R. 4, 319 (1941).

PHYSICAL REVIEW VOLUME 74, NUMBER 10 NOVEMBER 15, 1948

Further Calculations on the Cascade Theory

H. J. BHABHA
Tata Institute of Fundamental Research, Bombay, India

AND

S. K. CHAKRABARTY
Colaba Observatory, Bombay, India

(Received July 1, 1948)

The paper summarizes the previous work, and briefly gives the steps by which the mathematical solution of the cascade equations given in our previous papers can be established rigorously.

This solution has been used to calculate the number of shower particles for thicknesses between 0.25 characteristic unit and 20 characteristic units, and for primary energies from 2.7 times the critical energy ($y_0=1$) to 2.7×10^{10} times the critical energy ($y_0=24$). For this purpose, the second term of our series solution has also been calculated. The results are given in Table III and Fig. 3 in a form suitable for comparison with, and analysis of, experiment. These show that the second and higher terms of our series are negligible compared with the first for thicknesses less than three to four times that at which the shower reaches its maximum.

A method has been developed which allows the integrals to be evaluated at very small thicknesses where transition effects are still of importance, so that it is now possible to trace a shower from its very beginning to large depths. It is shown that for very small showers started by particles of two to three times the critical energy the shower must penetrate to depths which are three times the maximum depth to which a single particle could penetrate as a result of collision loss alone. This is possible because part of the path of the shower is covered by photons alone which then materialize at a subsequent depth.

A simple formula has been given (37) which enables one to calculate with considerable accuracy the spectrum of shower electrons of energy much below the critical energy. It is proved that this spectrum increases monotonically with decreasing energy at all thicknesses. Its form is approximately that of a modified inverse square law at the maximum of the shower, the power of the law becoming higher with increasing depth.

A KNOWLEDGE of the generation of cascades by electrons and gamma-rays is of great importance in the interpretation of cosmic-ray phenomena. Since cascades are produced so readily by the electronic component, they have often served to mask the effects of the other components of cosmic rays. For example, an accurate knowledge of the number of electrons to be expected in a cascade produced by an electron of known energy in a plate of given thickness, of the fluctuations in this number, and of the energy spectrum of the electrons in the cascade, would enable one to decide by experiment whether the cascades in cosmic radiation conform entirely to the theoretical pattern, or if not, to unravel other effects which may be mixed up with them, such as, for example, the creation of mesons, or of particles having masses a few times that of the electron, as has been suggested by Auger and his co-workers.[1] Knowledge of the

[1] Auger, Daudin, Fréon, and Maze, Comptes Rendus 226, 169, 569 (1948).

spread of electrons in a cascade and of the fluctuations in the lateral density distribution of electrons would enable one to decide by an analysis of experiment whether intervening links other than electrons and gamma-rays play any part in the generation of large air showers. Perhaps the accurate numerical answers to some of these problems, particularly those connected with the lateral spread of showers, will be given only with the help of the new types of calculating machines which are now being developed in different parts of the world. Nevertheless, a good deal can be done by analytical methods, and in some problems answers can be given which are at least as accurate as the experimental data available at present. For this reason we have though it desirable to push the analytical solutions as far as possible, and we believe that the results given in this paper are more accurate than any that have been given till now.

There is one approximation which underlies all the treatments that have been given hitherto, namely, neglect of the lateral spread of a shower and its treatment as a one-dimensional phenomenon. Only very qualitative estimates of the lateral spread of showers have been made in some cases. With this universal underlying simplification, the only complete and rigorous solution of the cascade problem has been given by K. S. K. Iyengar.[2] He has treated the collision loss of electrons as a constant independent of the energy, but he has taken the exact cross sections for radiation loss and pair creation as given by Bethe and Heitler for all energies and not only their asymptotic form for high energies. However, it is not easy to derive numerical values from Iyengar's solution, and it has therefore not been of use in interpreting and analyzing experimental data. Taking only the asymptotic forms of the cross sections for radiation and pair creation at very high energies, Snyder,[3] and later Serber,[4] have given solutions which if correct* would enable one to calculate the total number of particles in a shower with fair accuracy provided the depth of material is not too small. Their solutions, however, do not allow the number of electrons to be calculated for small thicknesses because of the circumstance that their boundary condition corresponds to a spectrum of lower energy electrons incident on the material in addition to the high energy electron whose effect we are investigating. They are also not suitable for calculating the energy spectrum of electrons in a cascade.

With the same basic assumptions we gave a solution of the cascade problem in two previous papers[5,6] which allowed the spectrum of electrons in a shower to be calculated with considerable accuracy. Although our solution was valid for all thicknesses, numerical data could be extracted from it previously only for thicknesses which were not too small. We have now found a method of overcoming this limitation, so that figures are given in this paper for the growth of a shower in thin layers of material. We can now trace with considerable confidence the course of a shower from its very beginning to thicknesses three to four times that at which it reaches its maximum, and calculate the energy spectrum throughout this range. Secondly, our solution was in the form of an infinite series and it was shown that for most of the energies and thicknesses concerned, the first term alone gave almost the entire contribution. We have now extended these figures to higher energies and greater thicknesses, and, in addition, evaluated the next term of the series. This has thrown further light on the regions in which the first term is insufficient and increased our confidence in the figures which have been given in the rest of the range. For

[2] K. S. K. Iyengar, Proc. Ind. Acad. Sci. **A15**, 195 (1942).
[3] H. Snyder, Phys. Rev. **53**, 960 (1938).
[4] R. Serber, Phys. Rev. **54**, 317 (1938).
* The difficulty is essentially the following. The solution depends on finding the value at the point $r=-s$ of a function $k(s,r)$ which satisfies a difference equation (see, for example, Rossi and Greisen, Rev. Mod. Phys. **13**, 240 (1941), Eq. (A12)). The values of the function $k(s,r)$ can be given explicitly as functions of s at all positive and negative integral values of r, and from this the value of $k(s,-s)$ is arrived at by graphical interpolation on the assumption that $k(s,r)$ is a smooth function of r. However, it can be shown from the difference equation that provided $k(s,-s)\neq 0$ then $k(s,-s-1)$ must be infinite although $k(s,r)$ is finite for the integral values of r on each side of the point $r=-s-1$. This alone casts some doubt on the validity of the assumption that $k(s,r)$ is a smooth function of r in a finite range round the point $r=-s$. In any case, this assumption remains to be justified mathematically, and an estimate of the error in arriving at the value of $k(s,-s)$ by the empirical method used needs to be given. Till this is done, one does not know what faith to place in the numerical figures obtained.
[5] H. J. Bhabha and S. K. Chakrabarty, Proc. Roy. Soc. **A181**, 267 (1943), referred to in this paper as A.
[6] H. J. Bhabha and S. K. Chakrabarty, Proc. Ind. Acad. Sci. **A15**, 464 (1942).

UNIVERSITY OF MICHIGAN LIBRARIES

example, if the total number of particles is considered, the second term of our series only becomes comparable with the first at depths which are three to four times that at which the cascade reaches its maximum.

It is shown that the third and higher terms of our series are of importance only at large thicknesses where the shower is being absorbed, and then too their contribution is mainly to the number of electrons whose energy is much smaller than the critical energy. But this is precisely the range where radiation loss and pair creation are badly represented by their asymptotic forms for high energies. Thus it is a satisfactory feature of our solution that the neglect of the higher terms becomes serious precisely in the conditions in which the basic physical assumptions are no longer sufficiently accurate.

We have given a formula (37) which, with the help of the table we have given, allows one to calculate the low energy spectrum of electrons with considerable accuracy. As far as possible we have given our numerical results in the form of tables and graphs which would make them easily accessible for the experimenter who wishes to compare theory and experiment, or to use theory for an analysis of his experiments.

It must be emphasized that there is a considerable range of the energy spectrum below the critical energy for which the use of the radiation and pair-creation cross sections for complete screening is fully justified, especially in substances of low atomic number like air or water where the critical energy is of the order of a hundred million volts. In this range full confidence can be placed in our figures. Even in this range our figures differ considerably from those given by Arley,[7] which must now be regarded as definitely erroneous.

II. THE MATHEMATICAL SOLUTION

In our original paper we gave only a formal proof of the correctness of our solution, and its convergence was not demonstrated. This lacuna was filled by Iyengar, who established the convergence of our solution rigorously in the paper already quoted. Since Iyengar's paper does not appear to be as well known as it deserves and some misapprehension exists about the rigorousness of our solution, we think it desirable to take this opportunity to sketch the steps by which it can be rigorously established.

Denoting by $P(E, t)dE$ the mean number of electrons, positive and negative, in the energy range E, $E+dE$ to be found in a cascade at a depth t, and by $Q(E, t)$ the corresponding expression for the number of quanta, the fundamental equations of the cascade theory are[5]

$$\frac{\partial P(E,t)}{\partial t}-\beta\frac{\partial P(E,t)}{\partial E}=\int_E^\infty P(E',t)R(E',E'-E)\frac{E'-E}{E'^2}dE'-P(E,t)\int_0^E R(E,E')\frac{E'dE'}{E^2}+2\int_E^\infty Q(E',t)R(E,E')\frac{dE'}{E'}, \quad (1a)$$

$$\frac{\partial Q(E,t)}{\partial t}=\int_E^\infty P(E',t)R(E',E)\frac{EdE'}{E'^2}-Q(E,t)\int_0^E R(E',E)\frac{dE'}{E}. \quad (1b)$$

The thickness of the substance t is measured in radiation units of length, namely,

$$\left[4\frac{Z^2N}{137}\left(\frac{e^2}{mc^2}\right)^2\log 183Z^{-\frac{1}{3}}\right]^{-1},$$

Z being the atomic number of the substance, N the number of atoms per cubic centimeter, and the other symbols having their usual meaning. The collision loss per radiation unit is denoted by β. The probabilities for radiation loss and pair creation are expressed in terms of the function $R(E, U)$ defined by

$$R(E,U)=\left(1-\frac{4}{3}\frac{E}{U}+\frac{4}{3}\frac{E^2}{U^2}\right)(x_1+x_2)-x_2, \quad (2)$$

x_1 and x_2 being functions of a variable

$$\zeta=100\frac{mc^2}{Z^{\frac{1}{3}}}\frac{U}{E|U-E|}. \quad (3)$$

[7] N. Arley, Proc. Roy. Soc. **A168**, 519 (1938).

Integrating (1b), remembering that $Q(E,t)=0$ at $t=0$ is the required boundary condition, and substituting the resulting expression for Q in (1a), we get

$$\frac{\partial P}{\partial t}-\beta\frac{\partial P}{\partial E}=\left[\int_E^\infty R(U,U-E)\frac{U-E}{U^2}P(U,t)dU - P(E,t)\int_0^E R(E,U)\frac{U}{E^2}dE\right] +2\int_0^t\int_E^\infty\int_E^U R(E,V)R(U,V) \times\exp(D(V)(t'-t))dV\cdot\frac{1}{U^2}P(U,t')dUdt', \quad (4)$$

where

$$D(E)=\int_0^E\frac{R(U,E)}{E}dU.$$

In the limit of very high energies $\zeta\to 0$ and then

$$x_1\to 1, \quad x_2\to\tfrac{3}{4}\alpha=(12\log 183Z^{-\frac{1}{3}})^{-1}. \quad (5)$$

(5) is the approximation which underlies most of the treatments. In the limit (5)

$$D=(7/9)-(1/6)\alpha.$$

Let A_s, B_s, and C_s be those functions of the complex variable s defined by

$$A_s=\left(\frac{4}{3}+\alpha\right)\left\{\frac{d}{ds}\log\Gamma(s)+\gamma-1+\frac{1}{s}\right\} +\frac{1}{2}-\frac{1}{s(s+1)}, \quad (6a)$$

$$B_s=2\left\{\frac{1}{s}-\left(\frac{4}{3}+\alpha\right)\frac{1}{(s+1)(s+2)}\right\}, \quad (6b)$$

$$C_s=\frac{1}{s+1}+\left(\frac{4}{3}+\alpha\right)\frac{1}{s(s-1)}. \quad (6c)$$

γ is the Euler-Mascheroni constant. Then the differential equation

$$\left\{\frac{\partial^2}{\partial t^2}+(A_s+D)\frac{\partial}{\partial t}+(A_sD-B_sC_s)\right\}\psi_0(s,t)=0 \quad (7)$$

has the solution

$$\psi_0(s,t)=\frac{D-\lambda_s}{\mu_s-\lambda_s}e^{-\lambda_s t}+\frac{\mu_s-D}{\mu_s-\lambda_s}e^{-\mu_s t}, \quad (8)$$

$$\lambda_s=\tfrac{1}{2}(A_s+D)-\tfrac{1}{2}\{(A_s-D)^2+4B_sC_s\}^{\frac{1}{2}}, \quad (9a)$$

$$\mu_s=\tfrac{1}{2}(A_s+D)+\tfrac{1}{2}\{(A_s-D)^2+4B_sC_s\}^{\frac{1}{2}} \quad (9b)$$

for any fixed value of s. The solution (8) satisfies the boundary conditions

$$\psi(s,0)=1, \quad \left(\frac{\partial\psi(s,t)}{\partial t}\right)_{t=0}=-A_s \text{ at } t=0. \quad (10)$$

Let $\psi_1(s,t)$, $\psi_2(s,t)$, $\cdots\psi_n(s,t)$, $\cdots$ be a set of functions defined by the recurrence formula

$$\psi_n(s,t)=\int_0^t\psi_0(s+n,t-t')\psi_{n-1}(s,t')dt'. \quad (11)$$

Then it can be shown without difficulty, as has already been done in the appendix of our previous paper A, that ψ_n and ψ_{n-1} satisfy the equation

$$\left\{\frac{\partial^2}{\partial t^2}+(A_{s+n}+D)\frac{\partial}{\partial t} +(A_{s+n}D-B_{s+n}C_{s+n})\right\}\psi_n(s,t) =\left(\frac{\partial}{\partial t}+D\right)\psi_{n-1}(s,t). \quad (12)$$

This follows simply by substituting (11) in (12) and using (10). We now prove by induction that (11) is equivalent to a formula evolved by Iyengar, namely,

$$\psi_n(s,t)=\int_0^t\psi_0(s,t_1)\psi_{n-1}(s+1,t-t_1)dt_1. \quad (13)$$

Let (13) hold for all integral n from 1 to $n-1$. Then submitting for ψ_{n-1} by (13) in (11) we get

$$\psi_n(s,t)=\int_0^t\psi_0(s+n,t')\psi_{n-1}(s,t-t')dt' =\int_0^t\psi_0(s+n,t')\left\{\int_0^{t-t'}\psi_0(s,t_1) \times\psi_{n-2}(s+1,t-t'-t_1)dt_1\right\}dt',$$

UNIVERSITY OF MICHIGAN LIBRARIES

and on changing the order of the t' and t_1 integrations

$$=\int_0^t \psi_0(s,t_1)\left\{\int_0^{t-t_1}\psi_0(s+n,t') \times\psi_{n-2}(s+1,t-t_1-t')dt'\right\}dt_1$$

$$=\int_0^t \psi_0(s,t_1)\psi_{n-1}(s+1,t-t_1)dt_1$$

by (11).

Now consider the expression

$$P(E,t)=\frac{1}{2\pi iE_0}\int_C\left(\frac{E_0}{E}\right)^s \times\left\{\sum_{n=0}^{\infty}\left(-\frac{\beta}{E}\right)^n\frac{\Gamma(s+n)}{\Gamma(s)}\psi_n(s,t)\right\}ds \quad (14)$$

for $E\leqslant E_0$, where the contour C of integration in the complex plane runs along the straight lines from $-\infty-i\tau$ to $\sigma-i\tau$, then to $\sigma+i\tau$ and then to $-\infty+i\tau$, τ being a large real number and $\sigma>1$. It has been proved by Iyengar that

$$\psi_n(s,t)<(1+\epsilon)^{n+1}\frac{t^n}{n!} \quad (15)$$

for every value of s on C. Indeed (15) is simply a consequence of (13) and the inequality $|\psi_0(s,t)|<1+\epsilon$. It follows that the series in curly brackets in (14) is uniformly and absolutely convergent if $E>\beta t$. Moreover, it follows from the inequalities for $\psi_n(s,t)$ given by Iyengar that the integral on the contour C is convergent. $P(E,t)$ is therefore a well defined function of E and t, and the absolute and uniform convergence of the series in curly brackets allows one to interchange the orders of summation and integration. We introduce (14) into the right-hand side of (4), interchange the orders of the E and s integrations, and carry out the E integration first. Using the approximation for complete screening, namely, (5), and remembering the definitions (6), we find that it is equal to the left-hand side of (4) provided $\psi_n(s,t)$ and $\psi_{n-1}(s,t)$ satisfy Eq. (12) for all integral $n\geqslant 0$. It follows that (14) must be an exact solution of (4) for $E>\beta t$. This restriction does not interfere with the proof since in (4) $P(E,t)$ on the left is connected only through the integral on the right with value of $P(E',t)$ for which $E'\geqslant E$.

Now introduce the functions

$$g(s,t)=\frac{\psi_1(s,t)}{\psi_0(s,t)}, \quad (16)$$

$$f_n(s,t)=\left\{\psi_0(s,t)\frac{g^n}{n!}-\psi_1(s,t)\frac{g^{n-1}}{(n-1)!}+\cdots\right\}. \quad (17)$$

Write the integrand of (14) in the form

$$E_0{}^s\sum_{n=0}^{\infty}(-\beta)^n\frac{\Gamma(s+n)}{\Gamma(s)}\frac{\psi_n(s,t)}{\{(E+\beta g)-\beta g\}^{n+s}}$$

$$=E_0{}^s\sum_{n=0}^{\infty}(-\beta)^n\frac{\Gamma(s+n)}{\Gamma(s)}\psi_n(s,t)\frac{1}{(E+\beta g)^{n+s}} \times\sum_{m=0}^{\infty}\frac{\Gamma(n+s+m)}{\Gamma(m+1)\Gamma(n+s)}\left(\frac{\beta g}{E+\beta g}\right)^m \quad (18)$$

by expanding $\{(E+\beta g)-\beta g\}^{n+s}$ in powers of $\beta g/(E+\beta g)$.

The double series is absolutely convergent because of (15) and its terms can therefore be rearranged. We therefore get

$$P(E,t)=\frac{1}{2\pi iE_0}\int_C\left(\frac{E_0}{E+\beta g}\right)^s \times\left\{\sum_{n=0}^{\infty}\left(\frac{\beta}{E+\beta g}\right)^n\frac{\Gamma(s+n)}{\Gamma(s)}f_n(s,t)\right\}ds. \quad (19)$$

The restriction $E>\beta t$ can be dropped now, since (19) exists for $E\geqslant 0$. It follows from the principle of analytic continuation that (19) is the exact solution of (4) for all $E\geqslant 0$. It can be shown that the contribution to (19) from the parts of the contour C from $-\infty-i\tau$ to $\sigma-i\tau$ and from $\sigma+i\tau$ to $-\infty+i\tau$ tends to zero as $\tau\to\infty$. The contour C can therefore be replaced by a line running from $\sigma-i\infty$ to $\sigma+i\infty$ with $\sigma>1$.

To get the total number of particles whose energy is greater than E we integrate (19) from E to E_0 and get

$$N(E,t)=\frac{1}{2\pi i}\int_{\sigma-i\infty}^{\sigma+i\infty}\frac{1}{s-1}\left(\frac{E_0}{E+\beta g}\right)^{s-1} \times\left\{\sum_{n=0}^{\infty}\left(\frac{\beta}{E+\beta g}\right)^n\frac{\Gamma(s+n)}{\Gamma(s)}f_n(s,t)\right\}ds, \quad (20)$$

TABLE I. Values of $g(s, t)$ as function of s and t.

t \ s	1.2	1.3	1.4	1.5	1.8	2.0	2.3	2.5	2.8	3.0	3.5	4.0	4.5	5.0	5.5	6.0
0.25		0.2095		0.2205	0.2280	0.2312	0.2338	0.2352	0.2367	0.2376	0.2391					
0.5		0.3195		0.3673	0.4027	0.4168	0.4301	0.4365	0.4441	0.4481	0.4555					
1.0	0.3100	0.3790	0.4392	0.4892	0.5965	0.6309	0.6985	0.7264	0.7565	0.7738	0.8054	0.8317	0.8475	0.8630	0.8712	0.8846
2.0	0.3099	0.3904	0.4622	0.5269	0.6868	0.7705	0.8765	0.9339	1.006	1.048	1.129	1.189	1.239	1.287	1.313	1.347
4.0	0.3099	0.3921	0.4667	0.5353	0.7086	0.8009	0.9048	0.9564	1.010	1.037	1.066	1.064	1.047	1.027	1.000	0.9693
6.0		0.3922		0.5360	0.7149	0.8119	0.9259	0.9735	1.023	1.041	1.047	1.029	0.9978	0.9621		
8.0		0.3922		0.5361	0.7166	0.8164	0.9331	0.9891	1.043	1.063	1.069	1.048	1.020	0.9803		
10.0	0.3099	0.3922	0.4673	0.5364	0.7167	0.8186	0.9387	0.9993	1.059	1.083	1.094	1.067	1.027	0.9876	0.9526	0.9156
15.0			0.4673	0.5364	0.7167	0.8186		1.009		1.112	1.136	1.120	1.080	1.036		
20.0								1.011		1.126	1.164	1.158	1.120	1.074		
∞	0.3099	0.3922	0.4673	0.5364	0.7167	0.8186	0.9450	1.013	1.095	1.141	1.226	1.292	1.350	1.386		

the expression obtained by putting $E=E_0$, which has to be subtracted from (20), being exactly zero, as can be seen by deforming the contour C into an infinite semicircle to the right of the imaginary axis.

It remains to determine the boundary conditions satisfied by $P(E, t)$ at $t=0$. For this purpose it is more convenient to consider $N(E, t)$. It follows from (10) that for small t

$$\psi_0(s, t)=1-A_s t+\cdots, \tag{21}$$

and from (13) that

$$\psi_n(s, t)=\frac{t^n}{n!}+0(t^{n+1}). \tag{22}$$

Hence, for small t,

$$g(s, t)=t+0(t^2) \tag{23}$$

as already proved in our previous paper.[5] Thus,

$$N(E, 0)=\frac{1}{2\pi i}\int_{\sigma-i\infty}^{\sigma+i\infty}\frac{1}{s-1}\left(\frac{E_0}{E}\right)^{s-1}ds=1$$

for all $E\leqslant E_0$. Since we are then left with only the residue of the integrand at the point $s=1$. Our solution therefore corresponds to exactly one electron of energy E_0 incident on the surface $t=0$. It similarly corresponds to no quanta incident on the surface $t=0$. This is automatically ensured by the substitution we made for $Q(E, t)$ in deriving (4) from (1a) and (1b).

Expression (20) can be written

$$N(E, t)=\sum_{n=0}^{\infty}N_n(E, t), \tag{25a}$$

where

$$N_n(E, t)=\frac{1}{2\pi i}\int\frac{1}{s+n-1}\left(\frac{E_0}{\beta}\right)^{s-1}\times\left(\frac{\beta}{E+\beta g}\right)^{s+n-1}\frac{\Gamma(s+n)}{\Gamma(s)}f_n(s, t)ds. \tag{25b}$$

It should be noted that by definition $f_0=\psi_0$ and $f_1(s, t)=0$, so that $N_1(E, t)=0$ always. The second term of the series (25) is $N_2(E, t)$, and it is already proportional to β^2.

Multiplying Eqs. (1a) and (1b) by E, integrating with respect to E from 0 to ∞, and adding the two equations, we get

$$\frac{\partial}{\partial t}\left\{\int_0^{\infty}EP(E, t)dE+\int_0^{\infty}EQ(E, t)dE\right\}=-\beta\int_0^{\infty}P(E, t)dE=-\beta N(0, t), \tag{26}$$

which simply states that the change in the total energy of the shower is entirely due to collision loss. Integrating (26), with respect to t, from 0 to ∞ we get, for a shower initiated by an electron of energy E_0

$$\int_0^{t}N(0, t)dt=E_0/\beta. \tag{27}$$

Since the solution (25) satisfies Eqs. (1) exactly, it must satisfy (27). This need not, of course, be true of the first term alone. Some misapprehension appears to have existed on this point.[8] We shall return to this point in the next section, where we show that N_0+N_2 together contribute between 70 and 85 percent of the whole primary energy. From the physical point of view, however, Eq. (27) must be taken with caution, especially in substances of high atomic number where the critical energy is low. It is not true that all the energy of a cascade is dissipated by the collision loss of *cascade* electrons alone. A good deal of energy is lost in the form of quanta of energy less than $2mc^2$ which are incapable of further pair creation. Thus the complete series

[8] I. E. Tamm and S. Belenky, Phys. Rev. 70, 660 (1946).

UNIVERSITY OF MICHIGAN LIBRARIES

(25a) for $N(0, t)$ must give too many cascade electrons of low energy at large thicknesses, and the first two or three terms of the series may well give a truer picture of the physical process in substances of high atomic number.

III. NUMERICAL RESULTS; ENERGY SPECTRUM OF SHOWER ELECTRONS

It is next necessary to evaluate the first term of the series (25a), namely, $N_0(E, t)$. Now $f_0(s, t)$, which occurs in the integrand, is given by (8) and consists of a sum of two parts. As is well known, the coefficient λ_S is much smaller than μ_S for real values of s, so that for all but small t the second part containing $\exp(-\mu_S t)$ makes a negligible contribution compared with the first. The first part can be evaluated with considerable accuracy by the saddle point method. The second part expressed the result of transition effects, and it is therefore necessary to evaluate it if one wishes to know what happens at small thicknesses. However, it cannot be evaluated in the same way as the first part since the integrand has no saddle point. We have now found a method of overcoming this difficulty. Our method is equally applicable to the higher terms $N_n(E, t)$, so that it will be developed in general. Let

$$\phi_n(s, r)=\int_0^\infty e^{-rt} f_n(s, t)dt. \qquad (28a)$$

Then

$$f_n(s, t)=\frac{1}{2\pi i}\int_{\rho-i\infty}^{\rho+i\infty} e^{rt}\phi_n(s, r)dr, \qquad (28b)$$

where ρ is a large real number such that all the singularities of ϕ_n lie to the left of the path of integration. Introducing this expression into (25b) we get

$$N_n(E, t)=\frac{1}{(2\pi i)^2}\int_{\sigma-i\infty}^{\sigma+i\infty} ds\int_{\rho-i\infty}^{\rho+i\infty} dr\frac{1}{s+n-1}$$
$$\times\left(\frac{E_0}{\beta}\right)^{s-1}\left(\frac{\beta}{E+\beta g}\right)^{s+n-1}\frac{\Gamma(s+n)}{\Gamma(s)}$$
$$\times\exp(rt)\phi_n(s, r). \qquad (29)$$

(29) is an exact expression and it has the advantage that the double integral can be evaluated by the saddle point method. Writing the integral in the form $\exp\omega_n(s, r)$, so that

$$\omega_n(s, r)=(s-1)y_0+(s+n-1)\log\frac{\beta}{E+\beta g}$$
$$+rt-\log(s+n-1)+\log\Gamma(s+n)$$
$$-\log\Gamma(s)+\log\phi_n(s, r), \qquad (30)$$

where $y_0=\log E_0/\beta$. We determine the double

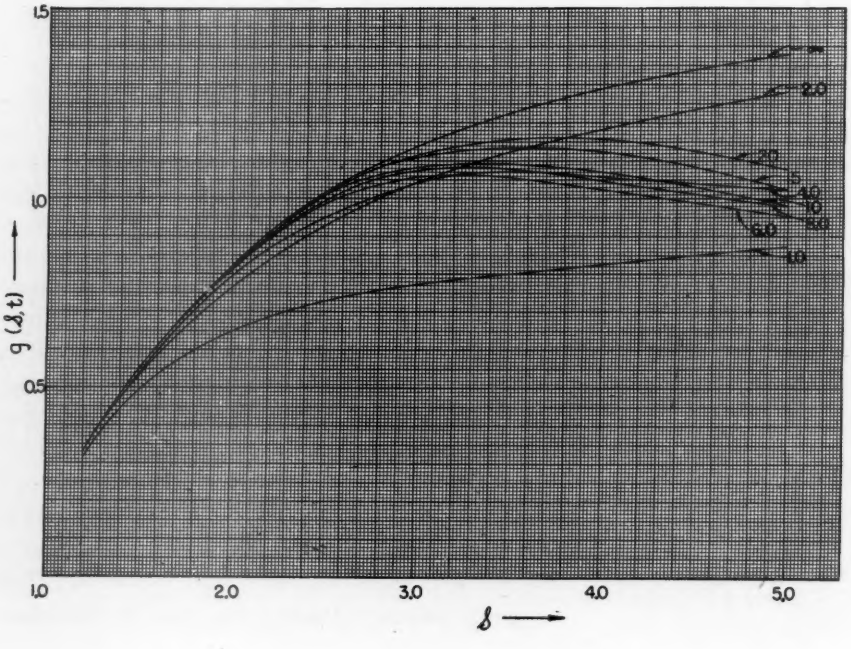

FIG. 1. $g(s, t)$ as a function of s.

TABLE II. y_0 as a function of t and s as determined by Eq. (31a). The figures in line with each t give the values of y_0 for the principal term $n=0$. Those below give y_0 for the next term $n=2$.

$t \backslash s$	1.2	1.3	1.4	1.5	1.6	1.7	1.8	1.9	2.0	2.2	2.3	2.4	2.5	2.6	3.0	3.5
0.25		2.54		0.877												
0.5		5.77		3.23			1.93		1.53							
1.0	14.13	8.56	6.05	4.64					2.11				1.36		1.01	
2.0	23.69	14.06	9.79	7.42		4.93			3.22				1.99		1.40	1.05
	18.02	10.12	6.74	4.94			2.64		2.03				1.39		1.13	
4.0		24.95	17.16	12.88	10.20		7.07		5.31				3.09		2.04	1.45
		20.83	14.04	10.32	8.03		5.42		4.01		2.83		2.35		1.63	
6.0			24.50	18.29		11.78	9.88		7.34		5.10		4.13		2.62	
			20.82	15.70	11.17		8.20		5.99				3.32		2.13	
8.0				23.69	18.62		12.69		9.35		6.41		5.14		3.18	2.12
				21.08	15.36		10.97		7.97	6.08			4.28		2.63	
10.0				29.08	22.81		15.48		11.35		7.70		6.14		3.71	2.42
					20.58		13.75		9.95				5.25		3.13	
12.0					27.00	21.93	18.27		13.35		9.00				4.24	
					24.76		16.52		11.93				6.21		3.63	
15.0						26.99	22.44	19.01	16.33		10.92				5.02	
						25.02	20.69		14.91				7.66		4.38	
20.0								24.85	21.30	16.09		12.46		9.81	6.31	
							27.63	23.26	19.86		13.00		10.07		5.63	

saddle point s_n, r_n through the equations

$$\frac{\partial \omega_n}{\partial r}=0, \quad \frac{\partial \omega_n}{\partial s}=0,$$

namely,

$$t+\frac{\partial}{\partial r}\log\phi_n(s,r)=0, \tag{31a}$$

$$y_0+\left[\log\frac{\beta}{E+\beta g}-(s+n-1)\frac{\beta}{E+\beta g}\frac{\partial g}{\partial s}\right] -\frac{1}{s+n-1}+\frac{\partial}{\partial s}\{\log\Gamma(s+n)-\log\Gamma(s)\} +\frac{\partial}{\partial s}\log\phi_n(s,r)=0. \tag{31b}$$

We then get as usual

$$N_n(E,t)=\frac{\exp(\omega_n(s_n,r_n))}{2\pi\left\{\frac{\partial^2\omega_n}{\partial r_n^2}\frac{\partial^2\omega_n}{\partial s_n^2}-\left(\frac{\partial^2\omega_n}{\partial r_n\partial s_n}\right)^2\right\}^{\frac{1}{2}}}. \tag{32}$$

The values of $g(s,t)$ for different values of s and t are given in Table I. For this purpose we have used the exact expression for $g(s,t)$ as defined by (16) and given explicitly by formula (57) of our previous paper A, and not the approximate expression $A(58)$. Table I is, in fact, an extension of Table 4B of A to cover a much greater range of values of t and a larger number of values of s. We note that $g(s,t)$ is a fairly slowly varying function of s of the order 1. For $E\gg\beta$ the second term in square brackets in (31b) is negligible compared with the first. Its neglect means that the variation of $g(s,t)$ with s plays no part in determing the saddle point. (See Fig. 1.) Thus as far as the high energy part of the spectrum, $E\gg\beta$, is concerned, the effect of collision loss is simply to shift it to lower energies by a constant amount $\beta g(s_n,t)$. The spectrum is, however, not represented by a simple power law for high energies, since the value of s_n changes with the value of E for a given E_0. Only if s_n were fixed, would the spectrum be of the form $\{E_0/E+\beta g\}^{s_n}$, and this is not so. Indeed, for fixed E_0 and t the saddle point s_n shifts to large values as E increases, so

UNIVERSITY OF MICHIGAN LIBRARIES

that the number of shower particles of high energy is greater than would be obtained by a simple power law.

For low energies E less than or of the order β, the second term in square brackets cannot be neglected. However, the saddle point s_n changes very slowly with E, and one can therefore take for s_n the value obtained by putting $E=0$. For small E (32) can therefore be written approximately in the form

$$N_n(E,t)=\frac{\exp(\omega_n'(s_n,r_n))}{2\pi\left\{\frac{\partial^2\omega_n'}{\partial r_n^2}\frac{\partial^2\omega_n'}{\partial s_n^2}-\left(\frac{\partial^2\omega_n'}{\partial r_n\partial s_n}\right)^2\right\}^{\frac{1}{2}}}\times\left(\frac{\beta}{E+\beta g(s_n,t)}\right)^{s_n+n-1}, \quad (33)$$

where ω_n' differs from ω_n defined by (30) only by the omission of the second term. This approximation is not permissible for primary energies E_0 of the order β, and then we have to turn to the more exact expression (32).

The contribution to the total number of electrons is obtained by putting $E=0$. We write $N_n(t)=N_n(0,t)$ for brevity. (33) shows that for electrons below the critical energy

$$N_n(E,t)\approx\left\{\frac{\beta g(s_n,t)}{E+\beta g(s_n,t)}\right\}^{s_n+n-1}N_n(t), \quad (34)$$

and the contribution of the corresponding term to the low energy spectrum is

$$P_n(E,t)=-\frac{\partial N_n(E,t)}{\partial E}\approx\frac{s_n+n-1}{\beta g(s_n,t)}\times\left\{\frac{\beta g(s_n,t)}{E+\beta g(s_n,t)}\right\}^{s_n+n}N_n(t), \quad (35a)$$

the total energy spectrum being

$$P(E,t)=\sum_{n=0}^{\infty}P_n(E,t). \quad (35b)$$

This double saddle point method is particularly easy to apply to the main term $N_0(E,t)$. Inserting f_0, given by (8) (28a) yields

$$\phi_0(s,r)=\frac{D+r}{(r+\lambda_S)(r+\mu_S)}. \quad (36)$$

An insertion of (36) into the right-hand side of (28b) obviously leads to (28a), since we are left

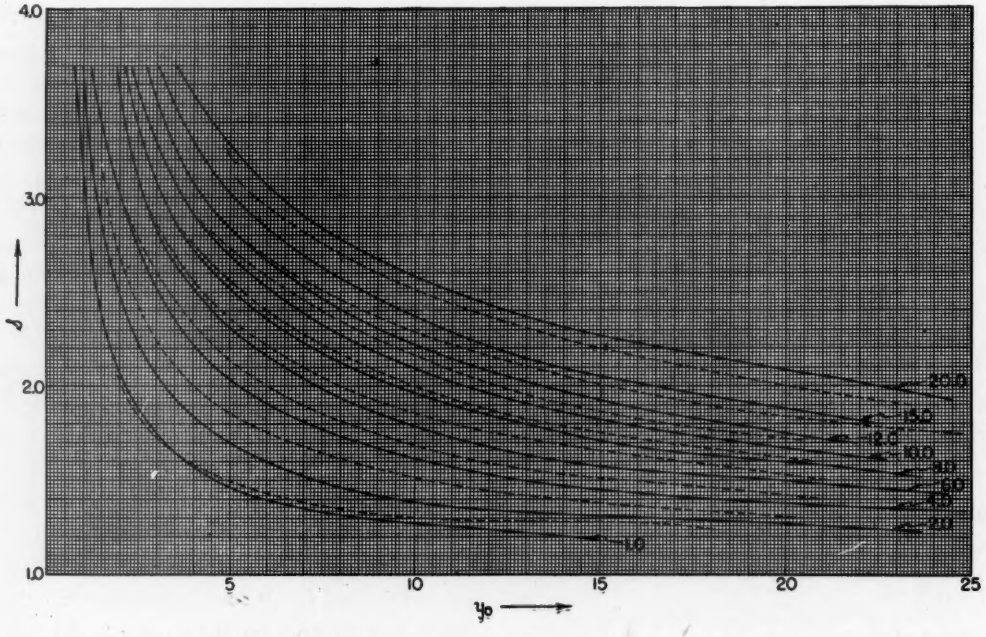

FIG. 2. s as a function of y_0 for different values of t. Numbers indicate values of t. ———relation between s and y_0 for the first term $N_0(t)$; ---- relation between s and y_0 for the second term $N_2(t)$.

with only the residues of the integrand at the points $r=-\lambda_S$ and $r=-\mu_S$.

From the point of view of numerical calculation it is easiest to proceed as follows. We assume a value of t and s_n. We then determine r_n by Eq. (31a), and y_0 by Eq. (31b). One can then determine $N_n(t)$ by (32). In this way we obtain y_0 and $N_n(t)$ as functions of s_n for different values of t. From these figures it is easy to obtain $N_n(t)$ as a function of y_0. The upper figures of Table II give y_0 for different values of t and s_0, that is, the corresponding value of y_0 for the principal term. The lower figures give y_0 as determined by (31b) for the second term N_2, of the series (25). The values of s at the head of the table are then to be understood to denote s_2. The same results have been given graphically in Fig. 2. Here s_0 and s_2 have been plotted as functions of y_0 for different values of t.

The values of N_0 and N_2 calculated from (25) are given in Table III for different values of y_0 and t, the upper figure in each space giving N_0 and the lower figure N_2. The space for N_2 has been left a blank, whenever the number is quite negligible compared with N_0. In Fig. 3 both N_0 and N_2 are plotted logarithmically as functions of t for four typical values of y_0. Table III as well as Fig. 3 show that N_2 becomes equal to N_0 only at thicknesses which are three to four times those at which the maximum number of particles occurs in the shower. One may be sure that as long as N_2 is less than N_0, N_3 and the higher terms will be still smaller. Their contribution is significant only at the tail end of a shower, and that only to electrons of very low energy.

The spectrum of electrons whose energy is of the order of the critical energy β, or less, is given by (35). Whenever $N_2 \ll N_0$ the spectrum is determined almost entirely by the first term of (35b) and is of the form of a modified power law $\{\beta g/(E+\beta g)\}^{s_0}$. Here g is a quantity approximately equal to 1, the exact value of which can be read from Table I, for any given value of t and s_0. The value of s_0 can be obtained from Fig. 2 for any t and y_0. At the maximum of the shower $s_0 \approx 2$, while before the maximum s_0 moves from about 1.3 to 2 with increasing t. This means that the power of the modified power law gradually increases with thickness, corresponding to an increasing concentration of

TABLE III. The total number of particles $N=N_0+N_1+\cdots$ as a function of thickness t and primary energy, $y_0=\log E_0/\beta$. The figures in line with each t give N_0, the figures below give N_2.

t \ y_0	1.0	2.0	3.0	4.0	5.0	6.0	7.0	8.0	9.0	10.0	12.0	14.0	16.0	18.0	20.0	22.0	24.0
0.25	1.140	1.231	1.310	1.390	1.472	1.561	1.650	1.720									
0.5	1.151	1.501	1.838	2.184	2.510	2.851	3.195	3.520									
1.0	0.8730	1.897	2.824	3.788	5.449	7.002	8.698	10.57	12.64	14.86	19.95	26.54					
2.0	0.1272	0.9734	2.809	5.957	11.33	18.10	26.93	36.34	54.03	75.35	130.5	210.6	318.6	463.0	661.8	951.0	
	0.09660	0.1765	0.2025	0.2439	0.3066	0.3818	0.4666	0.5651	0.6643	0.7507	0.9660	1.236	1.605	2.180			
4.0		0.2596	1.384	5.006	13.88	33.90	72.23	142.1	261.7	452.8	1211	2792	5991	1.223×10⁴	2.322×10⁴	4.201×10⁴	7.323×10⁴
		0.2565	0.5293	0.9906	1.729	2.904	4.678	6.486	10.95	15.47	29.38	56.92	102.3	173.7	278.4		
6.0			0.4762	2.382	8.923	28.86	82.64	209.4	485.0	1062	4152	1.337×10⁴	3.751×10⁴	9.690×10⁴	2.279×10⁵	5.076×10⁵	1.114×10⁶
			0.4496	1.159	2.742	6.005	12.30	23.61	43.06	75.12	205.2	511.3	1223	2677	5283		
8.0			0.1448	0.9031	4.433	17.88	61.50	187.2	525.4	1365	7364	3.106×10⁴	1.133×10⁵	3.826×10⁵	1.162×10⁶	3.197×10⁶	
			0.1490	0.6546	2.164	6.084	14.95	34.83	74.93	155.7	615.6	2038	6000	1.597×10⁴	3.962×10⁴		
10.0			0.04263	0.3076	1.764	8.538	35.62	130.8	435.2	1311	8950	5.051×10⁴	2.452×10⁵	1.054×10⁶	4.004×10⁶	1.293×10⁷	3.810×10⁷
			0.07312	0.3222	1.191	3.913	11.80	33.11	87.55	214.7	1079	4.599×10³	1.685×10⁴	5.631×10⁴	1.799×10⁵		
12.0					0.2563	3.763	11.61	60.38	268.0	935.2	8925	6.412×10⁴	3.664×10⁵	1.936×10⁶	7.920×10⁶	3.209×10⁷	1.166×10⁸
					0.6014	2.349	8.110	25.86	77.19	216.5	1434	7.574×10³	3.520×10⁴	1.429×10⁵	5.158×10⁵	1.733×10⁶	5.596×10⁶
15.0					0.1261	0.8107	4.625	23.27	104.6	425.9	5399	5.285×10⁴	4.215×10⁵	2.787×10⁶	1.613×10⁷	8.163×10⁷	3.711×10⁸
					0.1716	0.7862	3.295	12.47	42.76	138.7	1269	9.591×10³	5.939×10⁴	3.136×10⁵	1.511×10⁶	6.405×10⁶	2.356×10⁷
20.0						0.05720	0.3970	2.484	13.87	69.97	1376	2.034×10⁴	2.427×10⁵	1.859×10⁶	1.998×10⁷	1.434×10⁸	9.209×10⁸
						0.09140	0.5148	2.475	10.37	38.65	381.8	3.492×10³	2.813×10⁴	2.528×10⁵	2.855×10⁶	1.856×10⁷	8.270×10⁷

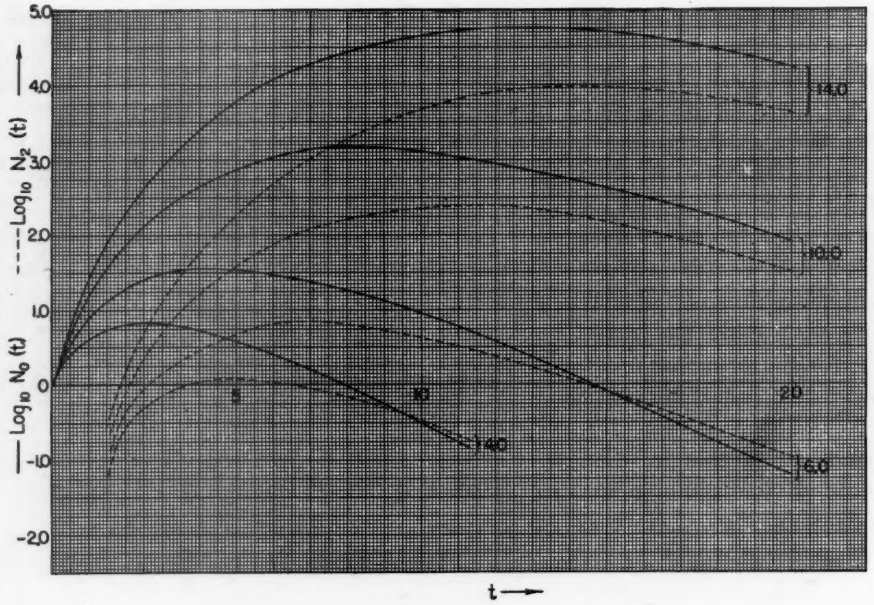

FIG. 3. N_0 and N_2 as functions of t. Numbers on the curves indicate the value of y_0.

electrons at the low energy end. The spectrum is nearly a modified inverse square law at the maximum of the shower. The effect of N_2 and the higher terms is to still further accentuate this tendency. For as shown by Fig. 2, s_0 and s_2 do not differ very much in the region where N_2 is comparable with N_0. Hence according to (35), N_2 makes a contribution to the spectrum of the form of a modified power law with a power 2 higher than N_0. Indeed, keeping only the first two terms of (35), we get roughly

$$P(E,t)\approx\text{const.}\left\{(s_0-1)\left(\frac{\beta g}{E+\beta g}\right)^{s_0}N_0 + (s_0+1)\left(\frac{\beta g}{E+\beta g}\right)^{s_0+2}N_2\right\}. \quad (37)$$

Thus, even if N_2 is a little less than N_0 the effect of the factors s_0-1 and s_0+1 is to make the contribution of the second term greater than the first for energies lower than those determined by

$$\left(\frac{E+\beta g}{\beta g}\right)^2\sim\frac{s_0+1}{s_0-1}\frac{N_2}{N_0}.$$

As a concrete example, take $t=20$, $y=10$. Then $s_0=2.58$, $s_2=2.50$, $N_0=70.0$, $N_2=38.7$, $g=1.01$. Hence

$$\frac{s_0+1}{s_0-1}\frac{N_2}{N_0}=1.25.$$

We therefore see that N_2 makes a larger contribution than N_0 to the spectrum of electrons of energy *less than a tenth* of the critical energy. For any given thickness and primary energy, the contribution of the first two terms to the low energy spectrum can be calculated easily by using the tables and figures of this paper. As we have already stated, the contribution of the higher terms is negligible, except for the very tail end of a shower and low energies.

Electrons below the critical energy arise by electrons of high energy emitting large quanta, and by pair creation, and not only by electrons of energy above the critical energy coming into regions of lower energy by collision loss, as has been assumed by Arley. Indeed, for any thickness before the shower reaches its maximum the former processes certainly predominate. Iyengar has proved that for thickness $t<1/((4/3)+\alpha)\approx\frac{3}{4}$ there is still a trace left of the delta-function representing the original electron, but for $t>1/((4/3)+\alpha)$ this completely disappears. For $t\ll1$ the form of the spectrum was given by us in *A*. For $t>1/((4/3)+\alpha)$ formula (37) shows that the spectrum increases monotonically as E decreases, contrary to the results of Arley.

Iyengar has shown that this result remains true even if the variation of the radiation and pair creation cross sections with energy is taken into account.

Table III brings out an interesting feature of cascades started by low energy electrons corresponding to, say, $y_0 \lesssim 2$. Take, for example, $y_0=1$, that is, $E_0=2.7\beta$. The first column of Table III shows that N_2 becomes comparable with N_0 only when $t \gtrsim 2$, and here N_0 has already fallen to about one-tenth of its value at the maximum. Thus the contribution of N_0 to the left-hand side of (27) can hardly be greater than 1.5. In order that (27) should be satisfied the cascade must have a long tail of height <0.2, say, extending to $t \sim 6$. Now it has already been remarked that the critical energy is in fact the collision loss in characteristic units, so that *because of collision loss alone* a particle of energy $E_0=2.7\beta$ cannot travel more than a distance 2.7. The mean number of particles can therefore be other than zero at a distance greater than 2.7 only if no energy has been lost by collision loss for part of the distance. This is possible only if no particles have traveled along some of this distance. Thus, for showers produced by low energy primaries, at certain thicknesses there may only be quanta but no electrons present in the shower, and at a greater distance quanta may materialize into a pair of particles. For small showers, the whole path of the shower is not covered by ionizing particles, as is the case for larger showers. This result is simply a rather interesting case of the fluctuation phenomenon which may be of considerable importance in interpreting the experiment.

UNIVERSITY OF MICHIGAN LIBRARIES

A Search for Delayed Photons from Stopped Sea Level Cosmic-Ray Mesons*

R. D. SARD AND E. J. ALTHAUS
Department of Physics, Washington University, St. Louis, Missouri

(Received July 19, 1948)

If the meson disintegrates into a photon and an electron, the stopping of a meson and its subsequent decay should give rise to a delayed 50-Mev photon. Delayed coincidences were sought between the stopped meson and the photon, detected by its materialization in a Pb sheet (calculations are presented of the photon detection efficiency for various lead thicknesses and photon energies of 20, 40, and 60 Mev; the electron range-energy curves used in the calculation are also shown). In 477.4 hours, nine apparent delayed photon coincidences were found. The measured inefficiency of the anticoincidence arrangement leads us to expect five spurious delayed photon coincidences in this time, so we conclude that the number of true delayed photon coincidences is small, if not zero. If the hypothesis under test is correct, the expected number of true delayed photon coincidences, computed from the rate of delayed electron coincidences (as measured with the same geometry) and the calculated photon detecting efficiency, is of the order of 100. The negative result of this test argues not only against decay into a photon and an electron, but also shows that if meson decay leads to a neutral meson which then decays into two photons, the mean life against the latter process must be greater than about 10^{-10} sec.

I. INTRODUCTION

WHILE it is well established that the sea level cosmic-ray meson disintegrates spontaneously with a mean life of about 2.2 microseconds,[1] one of the decay products having, very approximately, the mass and charge of an electron,[2] the exact nature of the disintegration process has not yet been determined. One possibility is that the meson disintegrates into a photon and an electron. There is some indirect evidence against it;[3] but in view of the current uncertainties in the physics of elementary particles, it seemed worth while to make a more direct test.[4]

If the meson does disintegrate in this fashion, the photon and the electron have equal and opposite momenta of about 50 Mev/c in the rest system of the meson,[5] which practically coincides with the laboratory system in the case of mesons slowed down in a dense absorber. A 50 Mev photon has a relatively high probability, in passing through an appropriate thickness of material, of being converted into an electron pair of which at least one electron has sufficient range to emerge from the material (see Section III below). We have made use of this property to detect the hypothetical photon. Our apparatus was designed to detect delayed coincidences between the arrival of a meson that gets stopped in a brass plate and the subsequent emission of a high energy photon detected by its materialization in a lead sheet. In order to permit comparison of the time distribution of the delayed photons with the known time distribution of decay electrons,

* This experiment was reported at the New York meeting of the American Physical Society, Jan. 29, 1948 (R. D. Sard and E. J. Althaus, Bull. Am. Phys. Soc. **23**, 2, 20 (1948); (Phys. Rev. **73**, 1251 (1948)). The present paper gives a more detailed account and includes additional data obtained since Dec. 8, 1947, confirming the result already published.

[1] B. Rossi and N. Nereson, Phys. Rev. **64**, 199 (1943); M. Conversi and O. Piccioni, Phys. Rev. **70**, 859 (1946); R. Maze, R. Chaminade, and A. Fréon, J. de Phys. et Rad. **7**, 202 (1945). These papers give references to earlier work.

[2] E. J. Williams and G. E. Roberts, Nature **145**, 102 (1940); R. P. Shutt, S. De Benedetti, and T. H. Johnson, Phys. Rev. **62**, 552 (1942). See also the work of Anderson and his collaborators [Phys. Rev. **72**, 724 (1947)].

[3] L. Nordheim, Phys. Rev. **59**, 554 (1941); G. Bernardini, *Colloque sur les Rayons Cosmiques* (Union Internationale de Physique Pure et Appliquée, Paris, 1947), p. 43 *et seq.* of Document R.C. 48–1.

[4] E. P. Hincks and B. Pontecorvo, Phys. Rev. **73**, 257 (1948) have independently performed an experiment very similar to our own, with the same negative result. The two experiments complement each other, as the meson absorbers are different (graphite as against brass), the lead materialization sheets are of different thickness (0.21 as against 0.86 cm), and the circuits are different.

[5] W. B. Fretter, Phys. Rev. **70**, 625 (1946). Anderson and his collaborators have recently obtained two cloud-chamber pictures at 9200 meters altitude [Anderson, Adams, Lloyd and Rau, Phys. Rev. **72**, 724 (1947); Adams, Anderson, Lloyd, Rau, and Saxena, Rev. Mod. Phys. **20**, 334 (1948)] that can be interpreted most directly as showing the disintegration of a meson with emission of a 25-Mev electron. This result is incompatible with the photon-electron hypothesis if the rest mass of the disintegrating meson is 100 Mev/c^2. In view of the evidence now available for the existence of different types of mesons, it is not certain that the two mesons observed by Anderson *et al.* at high altitudes are of the same kind as those which form the bulk of the hard component of the cosmic radiation at sea-level. The negative result of the present experiment is, however, perfectly consistent with Anderson's suggestion that his mesons do have mass 100 Mev/c^2, disintegrating into an electron and a neutral particle of mass 70 Mev/c^2.

the delayed coincidences were measured in four adjacent time intervals covering in total the range from 1.2 to 8.0 microseconds after arrival of the meson.

II. EXPERIMENTAL ARRANGEMENT

The experiment was carried out in the sub-basement of the Physics Building, at an elevation of about 30 meters above sea level. The floors and roof overhead amounted to approximately one-half meter of reenforced concrete, and there was some earth outside the walls of the sub-basement that was in the solid angle of the meson-selecting telescope. Figure 1 shows the arrangement of Geiger-Mueller tubes and absorbers in the two configurations used.

The G-M tubes were of 2.4 cm inside diameter and 25 cm (A, B, D, E) and 50 cm (C) effective length. They were filled with a 9:1 mixture of argon and ethyl alcohol to a pressure of 10 cm Hg, and were operated at 950 volts, 80–100 volts above threshold. They were grouped in parallel as shown. The walls of the tubes of groups A and B were of 0.8 mm brass; those of the tubes of C, D, and E were of 0.4 mm brass. The individual counter groups were enclosed in boxes made of 1.6 mm aluminum; the boxes for D and E were, however, open over the effective areas so that an electron moving downward from the lead sheet had only to penetrate the 0.8 mm steel plate

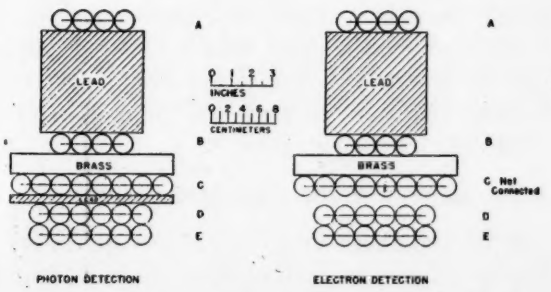

FIG. 1. The two experimental configurations. In both we are interested in mesons that pass through A and B and stop in the brass plate. The photon detection arrangement is designed to detect downgoing photons resulting from the decay of the stopped mesons. C is in anticoincidence with (AB). The lead slab serves to materialize the photons; one or both of the pair of electrons may pass through D and E, giving rise to a delayed coincidence of (DE) with respect to (AB). The electron detection arrangement is designed to detect downgoing decay electrons. There is no high-voltage on C and the lead slab is absent. Delayed coincidences of (DE) with respect to (AB) result from these decay electrons.

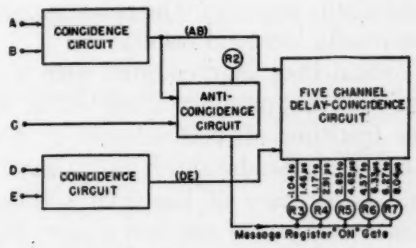

FIG. 2. Block diagram of the circuit.

supporting the lead, and the brass counter walls of D and E, in order to be counted.

Referring to the "photon detection" arrangement, shown in Fig. 1, trays A and B, separated by 12.7 cm Pb, defined a cone of incident mesons, some of which stopped in the 21.6 g/cm² brass absorber. Tray C more than covered the incident cone, and was connected in anticoincidence with the coincidences of A and B. To detect photons produced in meson disintegrations, a 9.75 g/cm² Pb sheet was placed beneath C. Its function was to produce electrons from high energy photons (mainly by pair production), the electrons being detected by coincidences between D and E. The lead sheet was supported by an 0.8 mm steel plate.

In order to determine how many delayed photon coincidences were to be expected, we took data with the "electron detection" arrangement also shown in Fig. 1. This differed from the photon detection arrangement only in that the lead sheet was removed and the high voltage was not applied to the G-M tubes C. In this case, decay electrons emerging downward from the brass were detected. Since the decay of stopped mesons is isotropic, and the angular divergence in pair-production by a 50-Mev photon is small, the geometrical factors in the photon detection, and electron detection arrangements were essentially the same. If the hypothesis being tested is correct, the ratio of delayed photon coincidences to delayed electron coincidences should be equal to the chance that an incident photon produces in the Pb sheet at least one electron capable of actuating D and E (as shown in Section III, the chance of the decay photon emerging from the brass is very nearly equal to that for the decay electron). An alternative electron detection arrangement was also used, different only in that

UNIVERSITY OF MICHIGAN LIBRARIES

C was physically removed. The two arrangements gave essentially identical results.

The coincidences were counted with a circuit identical with that used previously at the Massachusetts Institute of Technology.[6] It was designed by M. L. Sands, and built by the M.I.T. Research Laboratory of Electronics. The anticoincidence unit was of our own design. Figure 2 shows schematically the mode of operation of the circuits. The pulses from A and B went into a coincidence circuit, giving an output whenever the two input pulses were within 1.3 microseconds of each other. The circuit was designed so that the output pulse occurred at a fixed interval of time (1.3 μsec.) after whichever of the two input pulses was the earlier. The purpose of this was to reduce the effect of spontaneous lags in the G-M tubes, as it is very unlikely that both tubes will have large delays when actuated by the same particle. Trays D and E fed an identical circuit, producing a pulse 1.3 μsec. after the earlier of D and E provided that they discharged within 1.3 μsec. of each other. The two output pulses (AB) and (DE) went to a five channel double-coincidence circuit. The first channel, actuating the electromechanical counter $R3$, measured prompt coincidences in which (DE) occurred between 1.0 μsec. before and 1.5 μsec. after (AB). The remaining four channels, actuating $R4$, $R5$, $R6$, and $R7$ respectively, measured delayed coincidences of (DE) with respect to (AB) in successive time channels, the first covering delays from 1.2 to 2.9 μsec., the second 2.9 to 4.6 μsec., the third 4.6 to 6.3 μsec., and the fourth 6.3 to 8.0 μsec. The distribution of counts between these four channels indicated whether or not the delayed coincidences were due to the 2.2 μsec. decay process. Our anticoincidence circuit passed (AB) whenever tray C did not discharge between 1.0 μsec. before and 10.0 μsec. after the time of occurrence of (AB). Its output turned on the recorders $R3$, $R4$, $R5$, $R6$, and $R7$. Thus the delay discriminator proper recorded counts if and only if C were not discharged. In the photon detection arrangement, this prevented counting of charged particles emerging downward from the brass, as these could not reach D and E without tripping C. It did not do so in the electron detecting arrangement, because there was then no high voltage on C.

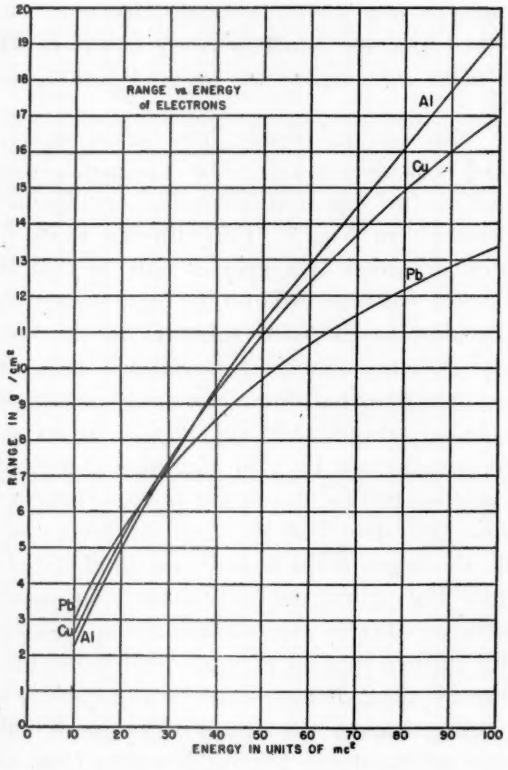

FIG. 3. Calculated range-energy curves for electrons.

The M.I.T. unit contained a monitoring circuit, which could be switched to record any one of the following: (AB), $A+B$, $D+E$, (DE). $A+B$ means the sum of the A and B counts as passed through a mixer insensitive for about 15 μsec. after each pulse that reached it; similarly for $D+E$. The monitoring circuit was continually switched between the four positions while data was being taken.

III. THEORY OF THE EXPERIMENT

If the hypothesis under test is correct, an electron and a photon, each of about 50 Mev, fly off in opposite directions from the point at which the stopped meson disintegrates. Our test of the hypothesis was based on the assumption that the formulas of Bethe and Heitler for pair creation by photons and energy loss by electrons are at least approximately correct for energies up to 50 Mev. This assumption can be considered to be well verified experimentally.

It was necessary to know first of all the relation

[6] B. Rossi, M. Sands, and R. D. Sard, Phys. Rev. 72, 120 (1947).

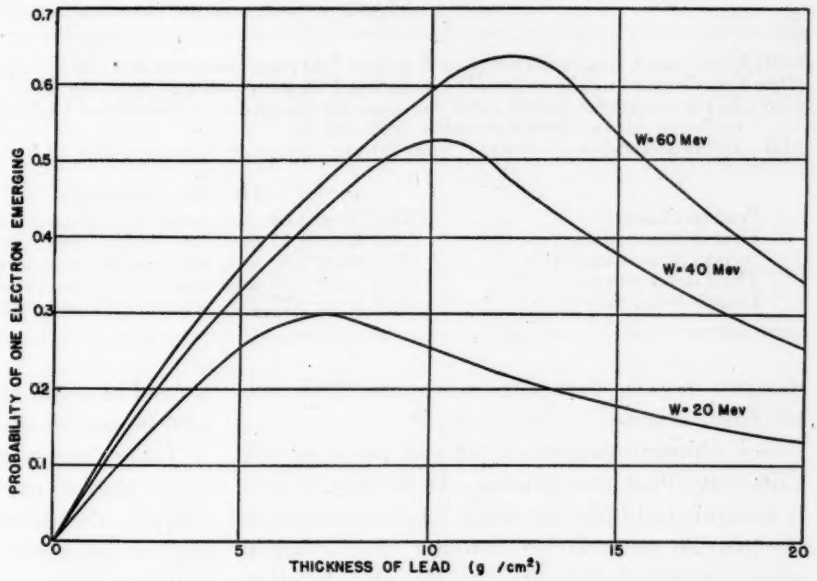

FIG. 4. Calculated probability that at least one electron (+ or −) emerges downward per vertically incident photon of energy W.

between energy and mean range for electrons. One of us (R.D.S.) has computed it for a number of materials; the results for Al, Cu, and Pb are plotted in Fig. 3. For total energies above 10 mc^2, the theoretical expressions for the mean radiative loss[7] and the loss by non-radiative collisions[8] were used; the reciprocal of the rate of energy loss so computed was integrated numerically to give the range down to a total energy of 10 mc^2. As scattering was neglected, the range obtained was actual path length rather than thickness of material. The result for 100 mc^2 electrons agrees to within one percent with the result of Bethe and Heitler[7] for Cu and of Heitler[9] for Pb. At energy 10 mc^2, the curves were joined to the theoretical points calculated by Widdowson,[10] diminished by 0.4 g/cm² to bring them into closer agreement with experimental data on β-ray ranges.

The efficiency of the lead slab in making photons detectable depends on the probabilities of pair production for various partitions of the energy in the pair and on the range-energy relation for the electrons. In our calculation we used the Bethe-Heitler formulas[7] for pair creation and the range-energy curve for Pb of Fig. 3. The major approximations were neglect of electron scattering and neglect of fluctuations in the rate of radiation by electrons. The same range-energy relation was applied to negatrons and positrons, and their angular divergence was taken to be zero.

The results are shown in Fig. 4. For small thicknesses, the calculation is elementary. In effect, one of the pair electrons is bound to emerge so long as the thickness of the Pb is less than the range of an electron of half the photon's energy, $R(W/2)$. The required probability is therefore simply the probability of pair production:

$$1-\exp(-\sigma_p(W)T),$$

where $\sigma_p(W)$ is the probability of pair production per unit thickness and T is the thickness. At large thicknesses ($T>R(W)$) the dependence on thickness is again simple, as

$$\exp(-\sigma_t(W)(T-R(W)),$$

where $\sigma_t(W)$ is the sum of the probabilities of pair production and Compton scattering. This dependence expresses the fact that only the lower part of the slab is effective. At intermediate thicknesses, $R(W/2)<T<R(W)$, the emergence or not of at least one electron depends on the particular mode of division of energy in the pair, and a numerical integration over the various partitions was carried out. It is in this inter-

[7] H. A. Bethe and W. Heitler, Proc. Roy. Soc. **A146**, 83 (1934). Radiation probabilities for materials other than Pb, Cu, and H_2O were obtained by interpolation in Fig. 3 of this reference.

[8] B. Rossi and K. Greisen, Rev. Mod. Phys. **13**, 240 (1941); formula (1.12) with $I=11.5Z$ ev.

[9] W. Heitler, *Quantum Theory of Radiation*, first edition (Oxford University Press, London, 1936), p. 223.

[10] E. E. Widdowson, Proc. Phys. Soc. **51**, 19 (1939).

UNIVERSITY OF MICHIGAN LIBRARIES

TABLE I. Calibration of the circuits.

(AB) Coincidence circuit: either A or B within 1.30 μsec. before or after the other.
(DE) Coincidence circuit: either D or E within 1.28 μsec. before or after the other.
Note: In the remainder of this Table we mean by the time of occurrence of (AB) or (DE) the time of occurrence of the earlier of the two pulses A and B or D and E.
($AB-C$) Anticoincidence circuit: C from 1.0 μsec. before to 10.0 μsec. after (AB).

	(AB:DE) coincidences	Width
Prompt channel	(DE) from 1.04 μsec. before to 1.46 μsec. after (AB)	2.50 μsec.
First delay channel	(DE) from 1.17 μsec. after to 2.91 μsec. after (AB)	1.74 μsec.
Second delay channel	(DE) from 2.85 μsec. after to 4.62 μsec. after (AB)	1.77 μsec.
Third delay channel	(DE) from 4.57 μsec. after to 6.33 μsec. after (AB)	1.76 μsec.
Fourth delay channel	(DE) from 6.27 μsec. after to 8.04 μsec. after (AB)	1.77 μsec.

mediate region that the maximum detection efficiency is found.

For photon energies of 40 and 60 Mev, the Compton effect was ignored. At 20 Mev, where it amounts to 12 percent of the total cross section, the photon attenuation through the Compton effect was taken into account, but the contribution of the Compton electrons to the photon-detection efficiency was neglected. This underestimation is no doubt more than compensated by our neglect of scattering.

For the 9.75 g/cm² thickness used in the experiment, the calculated probability is 52 percent for a 40 Mev photon and 58 percent for a 60 Mev photon. Interpolation gives 56 percent for a 50 Mev photon. It is to be noted that for a photon energy as low as 20 Mev, the calculated probability is as high as 26 percent; of course, the neglect of scattering makes our calculation less reliable the lower the energy.

It was also necessary to know the relative probabilities of a decay electron and a decay photon emerging from the brass meson stopper. We calculated each probability only for 50 Mev energy, but for various thicknesses of brass. The chance of an isotropically emitted photon's emerging unconverted and unscattered from the bottom of the brass plate involves only σ_t and μ, the meson absorption coefficient. The chance of an isotropically emitted electron's emerging involves μ and the mean range, for which the value for Cu of Fig. 3 was used. Both integrals could be evaluated in closed form. At no thickness do the two probabilities differ by more than 25 percent; at the thickness of 21.6 g/cm² used in the experiment, the photon probability is 1.04 times the electron probability. The ratio of the two is essentially independent of μ; the error involved in assuming the brass slab infinite should also be practically cancelled out in the ratio.

Taking our numerical results literally, we conclude that if the photon-electron hypothesis is correct, the delayed coincidence rate with the photon detection arrangement ought to be $1.04 \times 0.56 = 58$ percent of the delayed coincidence rate with the electron detection arrangement. This number is, as already remarked, somewhat of an overestimate, but it is difficult to believe that it is wrong as to order of magnitude.

IV. RESULTS

The apparatus was used between the end of August 1947 and March 1, 1948. Data obtained during periods of known or suspected malfunctioning of the equipment were discarded, leaving data from about 1475 hours in the period October 2, 1947 to March 1, 1948. All the G-M tubes were checked at least once every two weeks. Complete calibrations of the circuits were made three times, near the beginning, middle, and the end of the October to March period. In these calibrations we employed artificial pulses having the same general shape as the G-M tube pulses and adjusted in amplitude to match the G-M tube tray being simulated; their relative times of occurrence were continuously adjustable by means of helical wire-wound potentiometers.[11] The dials of the potentiometers were calibrated in 0.4 μsec. steps by means of marker pips derived, like the artificial pulses, from a 2.5 Mc crystal-controlled oscillator; one scale division on the dial corresponded to 0.01 μsec. The calibrations never differed by more than a few hundredths of a microsecond. The average of the first and third

[11] 'Helipots,' obtained from The Helipot Corporation, South Pasadena, California.

TABLE II. Raw data on electron and photon delayed coincidences.

	Counts in					Duration	Rate
	First delay channel	Second delay channel	Third delay channel	Fourth delay channel	Sum of delay channels	Hours	Counts per hour
Photons $(AB:DE)-C$	5	2	2	0	9	477.4	0.019 ± 0.006
Electrons $(AB:DE)$							
C in place	112	43	28	16	199	341.5	0.58 ± 0.04
C removed	87	57	30	12	186	330.1	0.56 ± 0.04
Combined	199	100	58	28	385	671.6	0.57 ± 0.03

calibrations, which we considered the most reliable, were used in analyzing the data. The numbers are given in Table I. The regions of uncertainty at the channel edges never exceeded 0.03 μsec.; the numbers given are the half-way points between the fully off and fully on settings.

Table II gives the accepted delayed coincidence data. As already remarked, two alternative arrangements were used for decay electron detection. In one, C was disconnected; in the other, physically removed. It is thought that the former is perhaps slightly better suited for comparison with the photon detection arrangement, but since the two gave the same rates within statistical uncertainties the results were combined. The uncertainties assigned to the rates are estimated standard deviations.

Certain corrections had to be made to the raw data. The data needed in making these corrections are given in Table III. For the photon detection configuration, the most important correction was that for the inefficiency of the anticoincidence arrangement. This inefficiency appeared to be due mainly to the non-zero thickness of the counter walls; for vertically incident particles the walls filled 3 percent of the area of C. Our data gave us a measured value of the inefficiency. In effect, decay products made a negligible contribution ($<5\times10^{-4}$) to the prompt coincidence rates, so that the ratio of the prompt coincidences $(AB:DE)-C$ obtained with the photon arrangement to the prompt coincidences $(AB:DE)$ obtained with the Pb in place but no high voltage on C was the anticoincidence inefficiency. From the first two rows of Table III we found this ratio to be 2.66 ± 0.02 percent. This is perhaps a slight underestimate, as it refers mainly to the central portion of C; a rough check, involving comparison of $(AB)-C$ with (AB) and (ABC) gave a value of about 3 percent. Because of the inefficiency, mesons could occasionally slip through tray C without discharging it, stop in the lead sheet, and produce decay electrons actuating D and E. Also, a few decay electrons from the brass could slip through C, penetrate the lead sheet, and actuate D and E. Both these effects are comprised in the delayed coincidence rate obtained with the Pb in place but C not sensitive, given in the third row. Multiplying this rate by 2.7 percent we obtained 0.010 ± 0.001 per hour as the expected spurious delayed photon rate. For the 477.4 hours of delayed photon recording, the expected number of spurious delayed coincidences is therefore five. Actually, nine counts were obtained; the chance is not too small (~4 percent) that all nine were of spurious origin. It is seen that the number of delayed photons detected is essentially zero.

We had also to consider the effect of accidental delayed coincidences. As the anticoincidence "gate" extended beyond the end of the last delay channel, the expected accidental rate was $[(AB)-C][(DE)-C]\tau$, where τ is the channel width. Using the rates of the fourth and fifth rows of Table III and the value 7.04 μsec. for the sum of the delay channel widths, we obtained for the expected accidental rate $(1.167\pm0.008)\times10^{-4}$ per hour, or 0.0557 ± 0.0004 in 477.4 hours. This correction could therefore be neglected.

For the delayed electron coincidences, the only correction applied was for accidentals. These occurred when one event triggered A and B but neither D nor E, and a subsequent unrelated event triggered D and E.[6] The expected acci-

TABLE III. Data used for corrections.

	Number of counts		Duration	Rate
1. Prompt $(AB:DE)-C$ (Photon arrangement)		17,762	28,644 min.	0.620±0.005 per min.
2. Prompt $(AB:DE)$ (Pb in, no H.V. on C)		334,669	14,368 min.	23.29 ±0.04 per min.
3. Delayed $(AB:DE)$ (Pb in, no H.V. on C)	first channel	50	239.6 hr.	0.36 ±0.04 per hr.
	second channel	20		
	third channel	10		
	fourth channel	7		
	sum	87		
4. $(AB)-C$ (Photon arrangement)		43,549	28,644 min.	1.520±0.007 per min.
5. $(DE)-C$ (Photon arrangement with D and E leads connected to circuit inputs normally used for A and B.)		28,868	2,646 min.	10.91 ±0.06 per min.
6. $(AB:D$ or $E)$ (Electron arrangements using $D+E$ instead of (DE))		74,176	2,533 min.	29.28 ±0.11 per min.
7. (AB) (Electron arrangements using $D+E$ instead of (DE))		50,240	1,172 min.	42.87 ±0.19 per min.
8. (AB) (Electron arrangements)		781,824	18,375 min.	42.55 ±0.05 per min.
9. (DE) (Electron arrangements)		2,983,456	16,639 min.	179.3 ±0.1 per min

dental rate was, therefore, $\{(AB)-(AB:D$ or $E)\}(DE)\tau$, where $(AB:D$ or $E)$ was the prompt coincidence rate between (AB) and D or E, measured by throwing a switch so as to feed the $(AB:DE)$ coincidence circuit with $D+E$ rather than (DE). The expression in curly brackets is the rate at which A and B but neither D nor E were triggered; the data of lines 6 and 7 of Table III give the value 13.59±0.22 per min., or a fraction 0.317±0.004 of the (AB) rate. Applying this factor to the (AB) rate of row 8, multiplying by the (DE) rate of row 9, and finally multiplying by the sum of the delay channel widths (7.04 μsec.), we obtain 0.0170±0.0002 per hour for the accidental delayed coincidence rate. This gives an expectation of 11.4 accidental delayed coincidences in 671.6 hours, or about 3 per delay channel. Row 1 of Table IV gives the (combined) results of the last row of Table II, with 3 counts subtracted in each channel. The corrected decay electron rate is seen to be 0.55±0.03 per hour. For an over-all photon detecting efficiency of 58 percent, there should have been 152 delayed photon coincidences in 477.4 hours. Only an overestimate of the photon detecting efficiency by a factor of the order of 40 could bring our result into agreement with the photon-decay hypothesis. Another way of describing the result is to say that less than 5 percent or so of the mesons decaying in the brass could give rise to a high energy photon.

The second line of Table IV shows the expected distribution of 373 counts, calculated for a meson mean life of 2.2 μsec. The observed distribution (first line) is seen to agree with it within the statistical uncertainty. This agreement is an added indication that the observed delayed electron coincidences are not of spurious origin.

TABLE IV. Delayed electron coincidences.

	Counts in					Duration	Rate
	First delay channel	Second delay channel	Third delay channel	Fourth delay channel	Sum of delay channels	Hours	Counts per hour
Corrected data on delayed coincidences caused by electrons	196	97	55	25	373	671.6	0.55±0.03
Expected decay electron distribution for 2.2 μsec. mean life	211	97	44	21	373		

V. CONCLUSIONS

Our results indicate that the bulk of the sea level cosmic-ray mesons which disintegrate after stopping in brass do not have a photon of energy above about 15 Mev as a disintegration product. This seems to be clear-cut evidence against the hypothesis that the μ-meson splits into an electron and a photon. It is also evidence against the suggestion[12] that the μ-meson disintegrates into an electron and a neutral meson, the latter immediately ($\sim 10^{-15}$ sec.) disintegrating into two photons of about 35 Mev. One can conclude[13] from our result that the neutral meson's mean life against this process would have to be greater than about 10^{-10} sec.; in fact, ascribing to the neutral meson a mass of 70 Mev/c^2 and a kinetic energy of 4 Mev,[14] the lower limit on the lifetime is about 3×10^{-10} sec.

Since very few negative mesons disintegrate in brass,[15] our results refer primarily to positive μ mesons. The independent experiment of Hincks and Pontecorvo,[4] in which graphite was used as the meson stopper, leads to the same negative result, for mesons of both signs.

Piccioni[16] has recently reported an experiment designed to detect photons resulting from meson capture. His experimental arrangement was such as to detect decay photons as well. Here also, a negative result was obtained.

VI. ACKNOWLEDGMENTS

We are indebted to the Office of Naval Research for support extended through Research Contract N6onr-202, T.O. III.

We should like to thank M. L. Sands, B. Rossi, and M. M. Hubbard for providing the delay discriminator used in this experiment. There have been stimulating discussions with H. A. Primakoff.

[12] For example, R. E. Marshak, Bull. Am. Phys. Soc. **22**, 6, 14 (1947) (Phys. Rev. **73**, 1226 (1948)).
[13] The same conclusion has been drawn by E. P. Hincks and B. Pontecorvo, Phys. Rev. **73**, 1122 (1948).
[14] C. D. Anderson *et al.*, reference 5.
[15] G. E. Valley, Phys. Rev. **72**, 772 (1947).
[16] O. Piccioni, Bull. Am. Phys. Soc. **23**, 3, 42 (1948).

UNIVERSITY OF MICHIGAN LIBRARIES

On the Configurations d^2sp, d^3p, and d^7p

F. ROHRLICH*
Department of Physics, The Hebrew University, Jerusalem, Palestine
(Received June 22, 1948)

The energy matrices of the configurations d^2sp, d^3p and d^7p are calculated in terms of Slater's F^k and G^k integrals for Russell-Saunders coupling. The calculations are based on Racah's method of tensor operators.

INTRODUCTION

THE analysis of complex spectra meets with difficulties if the spectrum is due to more than two or three electrons outside closed shells. In these cases intensities and selection rules seldom provide satisfactory evidence for a complete classification of the observed levels. For this reason it seems desirable to obtain the energy levels on theoretical grounds.

However, only the simplest configurations have been calculated thus far. Slater's method of diagonal sums[1] which forms the basis of most of these calculations does not permit a separation of multiply-occurring terms. This difficulty was finally removed in a satisfactory way by the method of tensor operators proposed by Racah[2] and based to a certain extent on earlier work by Condon, Shortley, and others.[3]

In this paper we shall apply Racah's method to the configurations d^2sp, d^3p and d^7p occurring in Ti *I*, Fe *I* and their isoelectronic sequences. In the succeeding paper we shall use the results obtained here for the spectrum of Ti *I*. This will then enable us to confirm and partly correct the existing configuration assignments in this spectrum.

d^2sp

The calculation of this configuration can be simplified significantly by the following procedure. Starting from the known[4] configuration d^2p we use Dirac's vector model[5] and add an s electron. The result will be the energy matrices of d^2ps labeled by the terms of its parent configuration d^2p. A unitary transformation will then lead to the scheme of d^2sp where the terms of d^2s label the matrices. Both schemes have of course the same energy terms, but since the s electron is in general more strongly bound to d^2 than is the p electron, the matrices of d^2sp will be "more diagonal" than those of d^2ps. This is of importance in numerical applications. Also, the series limits are the terms of d^2s rather than of d^2p.

The energy of d^2ps is

$$W(d^2ps)=W(d^2p)+2F_0(d,s)+F_0(p,s)+g_dG_d+g_pG_p,$$

where

$$F_0(d,s)=F^0(d,s),\quad F_0(p,s)=F^0(p,s),$$
$$G_d=(1/5)G^2(d,s),\quad G_p=(1/3)G^1(p,s).$$

As in reference 3, the F^k and G^k are defined 8[6]. By g_d and g_p we mean the matrices of the operators

$$\mathbf{g}_d=-(1+2\mathbf{S}_d\cdot\mathbf{s}_s),\quad \mathbf{g}_p=-(\tfrac{1}{2}+2\mathbf{s}_p\cdot\mathbf{s}_s),$$

where $\mathbf{S}_d$ is the resultant spin of d^2, i.e., either 0 or 1. In the first case $g_d=-1$, the spin of d^2p is $\frac{1}{2}$, and the matrix of $\mathbf{g}_p$ is simply 1 or -1, according to whether S, the total spin of d^2ps, is 0 or 1. In the second case we find from an easy calculation that $(S'\ s_s\ S|\mathbf{g}_d|S''\ s_s\ S)$ has the following values:

$$(\tfrac{1}{2}\ \tfrac{1}{2}\ 0|\mathbf{g}_d|\tfrac{1}{2}\ \tfrac{1}{2}\ 0)=1,$$
$$(\tfrac{3}{2}\ \tfrac{1}{2}\ 2|\mathbf{g}_d|\tfrac{3}{2}\ \tfrac{1}{2}\ 2)=-2,$$

* Now at Harvard University, Cambridge, Massachusetts.

[1] J. C. Slater, Phys. Rev. **34**, 1293 (1929).

[2] G. Racah, Phys. Rev. **61**, 186 (1942); **62**, 438 (1942); **63**, 367 (1943). These papers will be referred to in the following as I, II and III.

[3] See: E. U. Condon and G. H. Shortley, *The Theory of Atomic Spectra* (Cambridge University Press, Teddington, 1935), where also further references are given.

[4] See reference 2, II, p. 457.

[5] P. A. M. Dirac, *The Principles of Quantum Mechanics*, third edition (Oxford University Press, London, 1947), Chap. IX. J. H. Van Vleck, Phys. Rev. **45**, 412 (1934).

$$(S'\ \tfrac{1}{2}\ 1|\mathbf{g}_d|S''\ \tfrac{1}{2}\ 1)=\begin{matrix}\tfrac{1}{2}\\ \tfrac{3}{2}\end{matrix}\left\|\begin{matrix}-5/2 & -(2/3)2^{\frac{1}{2}}\\ -(2/3)2^{\frac{1}{2}} & 2/3\end{matrix}\right\|.$$

Here S' and S'' denote the resulting spin of d^2p.

Similarly one obtains for g_p

$$(\tfrac{1}{2}\ \tfrac{1}{2}\ 0|\mathbf{g}_p|\tfrac{1}{2}\ \tfrac{1}{2}\ 0)=-1,$$
$$(\tfrac{3}{2}\ \tfrac{1}{2}\ 2|\mathbf{g}_p|\tfrac{3}{2}\ \tfrac{1}{2}\ 2)=-1,$$
$$(S'\ \tfrac{1}{2}\ 1|\mathbf{g}_p|S''\ \tfrac{1}{2}\ 1)=\begin{matrix}\tfrac{1}{2}\\ \tfrac{3}{2}\end{matrix}\left\|\begin{matrix}-1/3 & (2/3)2^{\frac{1}{2}}\\ (2/3)2^{\frac{1}{2}} & 1/3\end{matrix}\right\|.$$

These results enable one to write down the complete energy matrix of d^2ps. Since d^2p involves the terms ${}^{2,4}SPDFG$, ${}^2H$, the configuration d^2ps will consist of the terms ${}^{1,3,5}SPDFG$ and ${}^{1,3}H$.

It is not necessary to give these matrices here. We shall rather proceed and carry out the similarity transformation leading to d^2sp. This transformation will diagonalize the matrix g_d. Obviously, the transformation is non-trivial only for the case $S=1$. In this case, however, the resulting diagonal matrix g_d is

$$(S'\ s_p\ 1|\mathbf{g}_d|S''\ s_p\ 1)=\begin{matrix}\tfrac{1}{2}\\ \tfrac{3}{2}\end{matrix}\left\|\begin{matrix}1 & 0\\ 0 & -2\end{matrix}\right\|,$$

as can be seen from the known[6] energy terms of d^2s. The quantum numbers S' and S'' refer here to the total spin of d^2s. The required transformation matrix for $S=1$ which brings g_d into the above diagonal form is now uniquely determined. Numerically it is identical with the matrix g_p above and it will therefore leave g_p invariant. The same result could have been obtained from the general formula for the elements of this transformation matrix.[7]

When we carry out the transformation of the matrices of d^2ps we obtain finally for the energy terms of d^2sp the matrices in Table I.

The parameters G_d and G_p have been defined above. The others were given by Racah (see reference 2, II), but will be repeated here for completeness.

$$A(d^2sp)=F^0(d,d)+2F^0(d,p)+2F^0(d,s)+F^0(p,s)-(1/9)F^4(d,d),$$
$$B=(1/441)(9F^2(d,d)-5F^4(d,d)),$$
$$C=(5/63)F^4(d,d),$$
$$F_2=(1/35)F^2(d,p),$$
$$G_1=(1/15)G^1(d,p),$$
$$G_3=(3/245)G^3(d,p).$$

[6] See reference 3, p. 203.

[7] See reference 2, III, p. 368.

d^3p and d^7p

These configurations have to be calculated by Racah's method.[3] With the above definitions each matrix element will be given by[4]

$$W(d^3p)=W(d^3)+3F_0(d,p)+f_2F_2+g_1G_1+g_3G_3.$$

The coefficients f_2, g_1 and g_3 are the matrix elements of sums of scalar products of tensor operators.

$$\mathbf{f}_2=10(21)^{\frac{1}{2}}\mathbf{U}^{(2)}\cdot\mathbf{u}_p^{(2)},$$

$$\mathbf{g}_1=-(3+4\mathbf{S}\cdot\mathbf{s}_p+(9/2)5^{\frac{1}{2}}\mathbf{U}^{(1)}\cdot\mathbf{u}_p^{(1)}+(5/2)(21)^{\frac{1}{2}}\mathbf{U}^{(2)}\cdot\mathbf{u}_p^{(2)}+18(5)^{\frac{1}{2}}\mathbf{V}^{(11)}\cdot\mathbf{v}^{(11)}+10(21)^{\frac{1}{2}}\mathbf{V}^{(12)}\cdot\mathbf{v}^{(12)}),$$

$$\mathbf{g}_3=-((21/2)+14\mathbf{S}\cdot\mathbf{s}_p-(21/2)5^{\frac{1}{2}}\mathbf{U}^{(1)}\cdot\mathbf{u}_p^{(1)}+(5/2)(21)^{\frac{1}{2}}\mathbf{U}^{(2)}\cdot\mathbf{u}_p^{(2)}-42(5)^{\frac{1}{2}}\mathbf{V}^{(11)}\cdot\mathbf{v}^{(11)}+10(21)^{\frac{1}{2}}\mathbf{V}^{(12)}\cdot\mathbf{v}^{(12)}).$$

The operator $\mathbf{S}$ refers to the resultant spin of d^3. The other operators are

$$\mathbf{U}^{(k)}=\sum_i\mathbf{u}_i^{(k)},\quad \mathbf{V}^{(1k)}=\sum_i\mathbf{s}_i\mathbf{u}_i^{(k)},\quad \mathbf{v}^{(1k)}=\mathbf{s}_p\mathbf{u}_p^{(k)},$$

where the summation is extended over the three equivalent d electrons. The tensor $\mathbf{u}^{(k)}$ is defined by

$$(l\|\mathbf{u}^{(k)}\|l')=\delta_{ll'}.$$

In the same notation

$$(l\|1\|l')=[l(l+1)(2l+1)]^{\frac{1}{2}}\delta_{ll'},$$

and we conclude, therefore, that the matrix of $\mathbf{U}^{(1)}$ will be diagonal. One finds in general

$$(l^nSL\|\mathbf{U}^{(1)}\|l^nSL)=(l^nSL\|\mathbf{u}^{(1)}\|l^nSL)\times\frac{(l^nSL\|\mathbf{L}\|l^nSL)}{(l^nSL\|\mathbf{1}\|l^nSL)}=\left(\frac{L(L+1)(2L+1)}{l(l+1)(2l+1)}\right)^{\frac{1}{2}}$$

independent of S. The matrices of $\mathbf{U}^{(2)}$, $\mathbf{V}^{(11)}$ and $\mathbf{V}^{(12)}$ are calculated in reference 2, III. The scalar product is defined in reference 2, II. The calculation is therefore perfectly straightforward and one finds for the matrices of d^3p those in Table II[8].

[8] Note that the parameter A differs of course for all three configurations. It gives the energy of the "center" of each configuration.

TABLE I. The Energy Matrices of the Configuration d^3sp.

$$
\begin{aligned}
{}^1S &= A+7B-14F_2-3G_1+7G_3+G_d-G_p\\
{}^5S &= A+7B-14F_2+6G_1-14G_3-2G_d-G_p\\
{}^5P &= A+7B+7F_2-6G_1-21G_3-2G_d-G_p\\
{}^5F &= A-8B-3F_2-G_1-16G_3-2G_d-G_p\\
{}^5G &= A-8B+F_2-9G_1-4G_3-2G_d-G_p\\
{}^1H &= A+4B+2C+4F_2-6G_1-G_3-G_d+G_p\\
{}^3H &= A+4B+2C+4F_2-6G_1-G_3-G_d-G_p
\end{aligned}
$$

$$
{}^3S = \begin{matrix} {}^3P \\ {}^4P \end{matrix}\left\|\begin{matrix} A+7B+G_d-14F_2+5G_1-(35/3)G_3-(1/3)G_p & (2/3)2^{\frac{1}{2}}(3G_1-7G_3+G_p) \\ (2/3)2^{\frac{1}{2}}(3G_1-7G_3+G_p) & A+7B-2G_d-14F_2-2G_1+(1/3)(14G_3+G_p) \end{matrix}\right\|
$$

$$
{}^5D = \begin{matrix} {}^4P \\ {}^4F \end{matrix}\left\|\begin{matrix} A+7B-2G_d-(1/5)(7F_2+24G_1+49G_3)-G_p & (6/5)(14)^{\frac{1}{2}}(2F_2-G_1-G_3) \\ (6/5)(14)^{\frac{1}{2}}(2F_2-G_1-G_3) & A-8B-2G_d+(1/5)(12F_2+4G_1-146G_3)-G_p \end{matrix}\right\|
$$

$$
{}^1G = \begin{matrix} {}^2F \\ {}^2G \end{matrix}\left\|\begin{matrix} A-8B+G_d+F_2+(9/2)G_1+2G_3-G_p & -(1/2)(15)^{\frac{1}{2}}(3G_1-2G_3) \\ -(1/2)(15)^{\frac{1}{2}}(3G_1-2G_3) & A+4B+2C-G_d-11F_2+(3/2)G_1-6G_3+G_p \end{matrix}\right\|
$$

$$
{}^1P = \begin{matrix} {}^2S \\ {}^2P \\ {}^2D \end{matrix}\left\|\begin{matrix} A+14B+7C-G_d-2G_1-7G_3+G_p & -3^{\frac{1}{2}}(3G_1-7G_3) & 7^{\frac{1}{2}}(4F_2-G_1-G_3) \\ -3^{\frac{1}{2}}(3G_1-7G_3) & A+7B+G_d+7F_2+3G_1+(21/2)G_3-G_p & (5/2)(21)^{\frac{1}{2}}G_3 \\ 7^{\frac{1}{2}}(4F_2-G_1-G_3) & (5/2)(21)^{\frac{1}{2}}G_3 & A-3B+2C-G_d-3F_2+G_1-(23/2)G_3+G_p \end{matrix}\right\|
$$

$$
{}^1D = \begin{matrix} {}^2P \\ {}^2D \\ {}^2F \end{matrix}\left\|\begin{matrix} A+7B+G_d+(1/5)(-7F_2+12G_1+(49/2)G_3)-G_p & -(3/2)(21/5)^{\frac{1}{2}}(2G_1-3G_3) & (3/5)(14)^{\frac{1}{2}}(4F_2+G_1+G_3) \\ -(3/2)(21/5)^{\frac{1}{2}}(2G_1-3G_3) & A-3B+2C-G_d+3F_2-2G_1-(19/2)G_3+G_p & (6/5)^{\frac{1}{2}}(G_1+11G_3) \\ (3/5)(14)^{\frac{1}{2}}(4F_2+G_1+G_3) & (6/5)^{\frac{1}{2}}(G_1+11G_3) & A-8B+G_d+(1/5)(12F_2-2G_1+73G_3)-G_p \end{matrix}\right\|
$$

$$
{}^1F = \begin{matrix} {}^2D \\ {}^2F \\ {}^2G \end{matrix}\left\|\begin{matrix} A-3B+2C-G_d-(1/7)(6F_2+23G_1+23G_3)+G_p & -10(3/7)^{\frac{1}{2}}(G_1-G_3) & (6/7)3^{\frac{1}{2}}(4F_2-G_1-G_3) \\ -10(3/7)^{\frac{1}{2}}(G_1-G_3) & A-8B+G_d-3F_2+(1/2)G_1+8G_3-G_p & (9/2)7^{-\frac{1}{2}}(G_1+6G_3) \\ (6/7)3^{\frac{1}{2}}(4F_2-G_1-G_3) & (9/2)7^{-\frac{1}{2}}(G_1+6G_3) & A+4B+2C-G_d+(1/7)(55F_2-(3/2)G_1-124G_3)+G_p \end{matrix}\right\|
$$

TABLE I. The Energy Matrices of the Configuration d^2sp.—*Continued.*

$$
{}^3P = \begin{array}{c|cccc}
 & {}^2S & {}^2P & {}^4P & {}^2D \\ \hline
{}^2S & A+14B+7C-G_d-2G_1-7G_2-G_p & 7(3)^{-\frac{1}{2}}(3G_1-7G_2) & -2(2/3)^{\frac{1}{2}}(3G_1-7G_2) & 7^{\frac{1}{2}}(4F_2-G_1-G_2) \\
{}^2P & 7(3)^{-\frac{1}{2}}(3G_1-7G_2) & A+7B+G_d+7F_2-5G_1-(35/2)G_2-(1/3)G_p & -(2^{\frac{1}{2}}/3)(6G_1+21G_2-2G_p) & -(5/6)(21)^{\frac{1}{2}}G_2 \\
{}^4P & -2(2/3)^{\frac{1}{2}}(3G_1-7G_2) & -(2^{\frac{1}{2}}/3)(6G_1+21G_2-2G_p) & A+7B-2G_d+7F_2+2G_1+7G_2+(1/3)G_p & 5(14/3)^{\frac{1}{2}}G_2 \\
{}^2D & 7^{\frac{1}{2}}(4F_2-G_1-G_2) & -(5/6)(21)^{\frac{1}{2}}G_2 & 5(14/3)^{\frac{1}{2}}G_2 & A-3B+2C-G_d-3F_2+G_1-(23/2)G_2-G_p
\end{array}
$$

$$
{}^3F = \begin{array}{c|cccc}
 & {}^2D & {}^2F & {}^4F & {}^2G \\ \hline
{}^2D & A-3B+2C-G_d-G_p-(1/7)(6F_2+23G_1+23G_2) & 10(21)^{-\frac{1}{2}}(G_1-G_2) & -20(2/21)^{\frac{1}{2}}(G_1-G_2) & (6/7)3^{\frac{1}{2}}(4F_2-G_1-G_2) \\
{}^2F & 10(21)^{-\frac{1}{2}}(G_1-G_2) & A-8B+G_d-3F_2-(5/6)(G_1+16G_2)-(1/3)G_p & -(2^{\frac{1}{2}}/3)(G_1+16G_2-2G_p) & -(3/2)7^{-\frac{1}{2}}(G_1+6G_2) \\
{}^4F & 20(2/21)^{\frac{1}{2}}(G_1-G_2) & -(2^{\frac{1}{2}}/3)(G_1+16G_2-2G_p) & A-8B-2G_d-3F_2+(1/3)(G_1+16G_2+G_p) & 6(14)^{-\frac{1}{2}}(G_1+6G_2) \\
{}^2G & (6/7)3^{\frac{1}{2}}(4F_2-G_1-G_2) & -(3/2)7^{-\frac{1}{2}}(G_1+6G_2) & 6(14)^{-\frac{1}{2}}(G_1+6G_2) & A+4B+2C-G_d-G_p+(1/7)(55F_2-(3/2)G_1-124G_2)
\end{array}
$$

$$
{}^3G = {}^4F = \begin{array}{c|ccc}
 & {}^2F & {}^4F & {}^2G \\ \hline
{}^2F & A-8B+G_d+F_2-(15/2)G_1-(1/3)(10G_2+G_p) & -(2^{\frac{1}{2}}/3)(9G_1+4G_2-2G_p) & (1/6)(15)^{\frac{1}{2}}(3G_1-2G_2) \\
{}^4F & -(2^{\frac{1}{2}}/3)(9G_1+4G_2-2G_p) & A-8B-2G_d+F_2+3G_1+(1/3)(4G_2+G_p) & -(1/3)(30)^{\frac{1}{2}}(3G_1-2G_2) \\
{}^2G & (1/6)(15)^{\frac{1}{2}}(3G_1-2G_2) & -(1/3)(30)^{\frac{1}{2}}(3G_1-2G_2) & A+4B+2C-G_d-11F_2+(3/2)G_1-6G_2-G_p
\end{array}
$$

$$
{}^3D = {}^2D = \begin{array}{c|ccccc}
 & {}^2P & {}^4P & {}^2D & {}^2F & {}^4F \\ \hline
{}^2P & A+7B+G_d-(7/5)F_2-4G_1-(1/6)(49G_2+2G_p) & -(2^{\frac{1}{2}}/15)(24G_1+49G_2-10G_p) & (21/20)^{\frac{1}{2}}(2G_1-3G_2) & (14^{\frac{1}{2}}/5)(12F_2-5G_1-5G_2) & -(4/5)7^{\frac{1}{2}}(G_1+G_2) \\
{}^4P & -(2^{\frac{1}{2}}/15)(24G_1+49G_2-10G_p) & A+7B-2G_d+(1/3)G_p-(1/5)(7F_2-8G_1-(49/3)G_2) & -(42/5)^{\frac{1}{2}}(2G_1-3G_2) & -(4/5)7^{\frac{1}{2}}(G_1+G_2) & (2/5)(14)^{\frac{1}{2}}(6F_2+G_1+G_2) \\
{}^2D & (21/20)^{\frac{1}{2}}(2G_1-3G_2) & -(42/5)^{\frac{1}{2}}(2G_1-3G_2) & A-3B+2C-G_d+3F_2-2G_1-(19/2)G_2-G_p & -(2/15)^{\frac{1}{2}}(G_1+11G_2) & (4/15^{\frac{1}{2}})(G_1+11G_2) \\
{}^2F & (14^{\frac{1}{2}}/5)(12F_2-5G_1-5G_2) & -(4/5)7^{\frac{1}{2}}(G_1+G_2) & -(2/15)^{\frac{1}{2}}(G_1+11G_2) & A-8B+G_d+(12/5)F_2+(1/3)(2G_1-73G_2-G_p) & (2/15)2^{\frac{1}{2}}(2G_1-73G_2+5G_p) \\
{}^4F & -(4/5)7^{\frac{1}{2}}(G_1+G_2) & (2/5)(14)^{\frac{1}{2}}(6F_2+G_1+G_2) & (4/15^{\frac{1}{2}})(G_1+11G_2) & (2/15)2^{\frac{1}{2}}(2G_1-73G_2+5G_p) & A-8B-2G_d+(12/5)F_2-(1/15)(4G_1-146G_2-5G_p)
\end{array}
$$

UNIVERSITY OF MICHIGAN LIBRARIES

TABLE II. The Energy Matrices of the Configuration d^3p

$$
\begin{aligned}
{}^1S &= A - 6B + 3C - 4F_2 - 10G_1 - 5G_3 \\
{}^5S &= A + 14F_2 - 10G_1 - 35G_3 \\
{}^5P &= A - 7F_2 - G_1 - 21G_3 \\
{}^5F &= A - 15B + 3F_2 - 6G_1 - 26G_3 \\
{}^5G &= A - 15B - F_2 - 10G_1 - 10G_3 \\
{}^1I &= A - 6B + 3C + 3F_2 - 3G_1 + 2G_3 \\
{}^3I &= A - 6B + 3C + 3F_2 - 9G_1 - 4G_3
\end{aligned}
$$

$$
{}^3S = \begin{matrix} {}^2P \\ {}^4P \end{matrix} \left\| \begin{matrix} A - 6B + 3C - 4F_2 + (1/3)(8G_1 - 47G_3) & -(4/3)(14)^{\frac{1}{2}}(G_1 - 4G_3) \\ -(4/3)(14)^{\frac{1}{2}}(G_1 - 4G_3) & A + 14F_2 + (5/3)(2G_1 + 7G_3) \end{matrix} \right\|
$$

$$
{}^5D = \begin{matrix} {}^4P \\ {}^4F \end{matrix} \left\| \begin{matrix} A + (1/5)(7F_2 - 41G_1 - 91G_3) & -(6/5)(14)^{\frac{1}{2}}(2F_2 - G_1 - G_3) \\ -(6/5)(14)^{\frac{1}{2}}(2F_2 - G_1 - G_3) & A - 15B - (1/5)(12F_2 - 6G_1 + 169G_3) \end{matrix} \right\|
$$

$$
{}^1H = \begin{matrix} {}^2G \\ {}^2H \end{matrix} \left\| \begin{matrix} A - 11B + 3C + (1/5)(4F_2 - G_1 + 4G_3) & -(6/5)(2F_2 - 8G_1 + 7G_3) \\ -(6/15)(2F_2 - 8G_1 + 7G_3) & A - 6B + 3C - (1/5)(39F_2 - 21G_1 - 16G_3) \end{matrix} \right\|
$$

$$
{}^3H = \begin{matrix} {}^2G \\ {}^2H \end{matrix} \left\| \begin{matrix} A - 11B + 3C + (1/5)(4F_2 - 41G_1 - 26G_3) & -(6/5)(2F_2 + 2G_1 - 3G_3) \\ -(6/5)(2F_2 + 2G_1 - 3G_3) & A - 6B + 3C - (1/5)(39F_2 + 9G_1 + 74G_3) \end{matrix} \right\|
$$

$$
{}^1P = \begin{matrix} {}^2P \\ {}^2{}_1D \\ {}^2{}_3D \end{matrix} \left\| \begin{matrix} A - 6B + 3C - 2F_2 + (7/2)G_1 + 6G_3 & (1/2)(21/2)^{\frac{1}{2}}(6F_2 - 3G_1 + 2G_3) & -(3/2)2^{-\frac{1}{2}}(2F_2 - G_1 + 14G_3) \\ -(1/2)(21/2)^{\frac{1}{2}}(6F_2 - 3G_1 + 2G_3) & A + 7B + 7C + (1/4)(14F_2 + 13G_1) + 7G_3 & (3/4)(21)^{\frac{1}{2}}(4B + 2F_2 + G_1 - 4G_3) \\ -(3/2)2^{-\frac{1}{2}}(2F_2 - G_1 + 14G_3) & (3/4)(21)^{\frac{1}{2}}(4B + 2F_2 + G_1 - 4G_3) & A + 3B + 3C + (3/4)(2F_2 + 3G_1) - 9G_3 \end{matrix} \right\|
$$

$$
{}^1G = \begin{matrix} {}^2F \\ {}^2G \\ {}^2H \end{matrix} \left\| \begin{matrix} A + 9B + 3C + F_2 - 5G_1 + (25/4)G_3 & (3^{\frac{1}{2}}/4)(8F_2 - 8G_1 + 17G_3) & -(11/2)^{\frac{1}{2}}(4F_2 + G_1 + G_3) \\ (3^{\frac{1}{2}}/4)(8F_2 - 8G_1 + 17G_3) & A - 11B + 3C - (11/5)F_2 - (1/20)(4G_1 + 9G_3) & (1/5)(33/2)^{\frac{1}{2}}(4F_2 - G_1 - 21G_3) \\ -(11/2)^{\frac{1}{2}}(4F_2 + G_1 + G_3) & (1^{0}/5)(33/2)^{\frac{1}{2}}(4F_2 - G_1 - 21G_3) & A - 6B + 3C + (2/5)(13F_2 - 2G_1 - 17G_3) \end{matrix} \right\|
$$

$$
{}^3P = \begin{matrix} {}^2P \\ {}^4P \\ {}^2{}_1D \\ {}^2{}_3D \end{matrix} \left\| \begin{matrix} A - 6B + 3C + 2F_2 - (29/6)G_1 - 19G_3 & -(2/3)(14)^{\frac{1}{2}}(2G_1 - 3G_3) & (1/2)(7/6)^{\frac{1}{2}}(18F_2 - 3G_1 - 8G_3) & -(1/2)2^{-\frac{1}{2}}(6F_2 - G_1 - 16G_3) \\ -(2/3)(14)^{\frac{1}{2}}(2G_1 - 3G_3) & A - 7F_2 + (1/3)G_1 + 7G_3 & -(2/3^{\frac{1}{2}})(3G_1 - 7G_3) & 2(7)^{\frac{1}{2}}(G_1 + G_3) \\ (1/2)(7/6)^{\frac{1}{2}}(18F_2 - 3G_1 - 8G_3) & -(2/3^{\frac{1}{2}})(3G_1 - 7G_3) & A + 7B + 7C + (1/4)(14F_2 - 13G_1 - 98G_3) & (1/4)(21)^{\frac{1}{2}}(12B + 6F_2 - 3G_1 + 2G_3) \\ -(1/2)2^{-\frac{1}{2}}(6F_2 - G_1 - 16G_3) & 2(7)^{\frac{1}{2}}(G_1 + G_3) & (1/4)(21)^{\frac{1}{2}}(12B + 6F_2 - 3G_1 + 2G_3) & A + 3B + 3C + (1/4)(6F_2 - 9G_1 - 74G_3) \end{matrix} \right\|
$$

$$
{}^1D = \begin{matrix} {}^2P \\ {}^2{}_1D \\ {}^2{}_3D \\ {}^2F \end{matrix} \left\| \begin{matrix} A - 6B + 3C - (1/10)(4F_2 + G_1 + 26G_3) & -(3/2)(21/10)^{\frac{1}{2}}(2F_2 + G_1 - 4G_3) & (3/2)(10)^{-\frac{1}{2}}(2F_2 + 17G_1 - 28G_3) & -(6/5)(4F_2 + G_1 + G_3) \\ -(3/2)(21/10)^{\frac{1}{2}}(2F_2 + G_1 - 4G_3) & A + 7B + 7C - (1/4)(14F_2 + 19G_1 + 14G_3) & (1/4)(21)^{\frac{1}{2}}(12B - 6F_2 + 3G_1 - 2G_3) & (42/5)^{\frac{1}{2}}(2F_2 + G_1 - 4G_3) \\ (3/2)(10)^{-\frac{1}{2}}(2F_2 + 17G_1 - 28G_3) & (1/4)(21)^{\frac{1}{2}}(12B - 6F_2 + 3G_1 - 2G_3) & A + 3B + 3C - (3/4)(2F_2 - 3G_1 + 2G_3) & (2/5)^{\frac{1}{2}}(18F_2 + 3G_1 - 2G_3) \\ -(6/5)(4F_2 + G_1 + G_3) & (42/5)^{\frac{1}{2}}(2F_2 + G_1 - 4G_3) & (2/5)^{\frac{1}{2}}(18F_2 + 3G_1 - 2G_3) & A + 9B + 3C + (3/5)(4F_2 + G_1 - 24G_3) \end{matrix} \right\|
$$

TABLE II. The Energy Matrices of the Configuration d^3p.—*Continued.*

$^2F = {}^2F$

	$^2{}_1D$	$^2{}_2D$	^2F	^4F	^2G
$^2{}_1D$	$A+7B+7C+F_2-7G_1-(19/2)G_3$	$(1/2)(21)^{-\frac{1}{2}}(126B+18F_2+6G_1-29G_3)$	$-(1/2)3^{-\frac{1}{2}}(12F_2+3G_1-17G_3)$	$(2/3^{\frac{1}{2}})(3G_1-7G_3)$	$-(3/2)(15/7)^{\frac{1}{2}}\times(4F_2-G_1-G_3)$
$^2{}_2D$	$(1/2)(21)^{-\frac{1}{2}}(126B+18F_2+6G_1-29G_3)$	$A+3B+3C+(1/7)(3F_2-37G_1)-(467/42)G_3$	$-(1/6)7^{-\frac{1}{2}}(108F_2-33G_1-53G_3)$	$-(2/3)7^{-\frac{1}{2}}(21G_1-29G_3)$	$-(3/14)5^{\frac{1}{2}}(4F_2-5G_1-5G_3)$
^2F	$-(1/2)3^{-\frac{1}{2}}(12F_2+3G_1-17G_3)$	$-(1/6)7^{-\frac{1}{2}}(108F_2-33G_1-53G_3)$	$A+9B+3C-3F_2-4G_1-(193/12)G_3$	$-4G_1-(7/3)G_3$	$-(3/4)(5/7)^{\frac{1}{2}}\times(8F_2-4G_1+G_3)$
^4F	$(2/3^{\frac{1}{2}})(3G_1-7G_3)$	$-(2/3)7^{-\frac{1}{2}}(21G_1-29G_3)$	$-4G_1-(7/3)G_3$	$A-15B+3F_2+2G_1+(26/3)G_3$	$15(5/7)^{\frac{1}{2}}G_3$
^2G	$-(3/2)(15/7)^{\frac{1}{2}}\times(4F_2-G_1-G_3)$	$-(3/14)5^{\frac{1}{2}}(4F_2-5G_1-5G_3)$	$-(3/4)(5/7)^{\frac{1}{2}}(8F_2-4G_1+G_3)$	$15(5/7)^{\frac{1}{2}}G_3$	$A-11B+3C+(1/7)(11F_2+2G_1)-(727/28)G_3$

$^1F =$

	$^2{}_1D$	$^2{}_2D$	^2F	^2G
$^2{}_1D$	$A+7B+7C+2G_1-(1/2)G_3+F_2$	$(1/2)(3/7)^{\frac{1}{2}}(42B+6F_2-12G_1+23G_3)$	$-(3^{\frac{1}{2}}/2)(4F_2-7G_1+13G_3)$	$-(3/2)(15/7)^{\frac{1}{2}}(4F_2-G_1-G_3)$
$^2{}_2D$	$(1/2)(3/7)^{\frac{1}{2}}(42B+6F_2-12G_1+23G_3)$	$A+3B+3C+(3/14)(2F_2-12G_1+23G_3)$	$-(1/2)7^{-\frac{1}{2}}(36F_2-3G_1+17G_3)$	$-(3/14)5^{\frac{1}{2}}(4F_2+11G_1+11G_3)$
^2F	$-(3^{\frac{1}{2}}/2)(4F_2-7G_1+13G_3)$	$-(1/2)7^{-\frac{1}{2}}(36F_2-3G_1+17G_3)$	$A+9B+3C-3F_2+6G_1+(9/4)G_3$	$-(3/4)(5/7)^{\frac{1}{2}}(8F_2+4G_1-11G_3)$
^2G	$-(3/2)(15/7)^{\frac{1}{2}}(4F_2-G_1-G_3)$	$-(3/14)5^{\frac{1}{2}}(4F_2+11G_1+11G_3)$	$-(3/4)(5/7)^{\frac{1}{2}}(8F_2+4G_1-11G_3)$	$A-11B+3C+(1/28)(44F_2+16G_1-19G_3)$

$^2G =$

	^2F	^4F	^2G	^2H
^2F	$A+9B+3C+F_2-(1/3)(17G_1+(113/4)G_3)$	$(1/3)(8G_1-7G_3)$	$(1/4)3^{-\frac{1}{2}}(24F_2-25G_1)$	$-(1/3)(11/2)^{\frac{1}{2}}(12F_2-5G_1-5G_3)$
^4F	$(1/3)(8G_1-7G_3)$	$A-15B-F_2+(10/3)(G_1+G_3)$	$-(1/3^{\frac{1}{2}})(12G_1-13G_3)$	$(2/3)(22)^{\frac{1}{2}}(G_1+G_3)$
^2G	$(1/4)3^{-\frac{1}{2}}(24F_2-25G_1)$	$-(1/3^{\frac{1}{2}})(12G_1-13G_3)$	$A-11B+3C-(11/5)(F_2+G_1)-(309/20)G_3$	$(1/5)(11/6)^{\frac{1}{2}}(12F_2-3G_1+17G_3)$
^2H	$-(1/3)(11/2)^{\frac{1}{2}}(12F_2-5G_1-5G_3)$	$(2/3)(22^{\frac{1}{2}})(G_1+G_3)$	$(1/5)(11/6)^{\frac{1}{2}}(12F_2-3G_1+17G_3)$	$A-6B+3C+(2/15)\times(39F_2+4G_1-206G_3)$

$^1D =$

	^2P	^4P	$^2{}_1D$	$^2{}_2D$	^2F	^4F
^2P	$A-6B+3C-(2/5)F_2-(1/6)(29G_1+64G_3)$	$(2/15)(14)^{\frac{1}{2}}(8G_1-17G_3)$	$-(1/2)(21/10)^{\frac{1}{2}}(6F_2-3G_1+2G_3)$	$(1/2)(10^{-\frac{1}{2}}(6F_2-19G_1+26G_3)$	$-(24/5)F_2+2(G_1+G_3)$	$(22/5)(G_1+G_3)$
^4P	$(2/15)(14)^{\frac{1}{2}}(8G_1-17G_3)$	$A+(1/15)(21F_2+41G_1+91G_3$	$-2(3/5)^{\frac{1}{2}}(3G_1-7G_3)$	$-2(7/5)^{\frac{1}{2}}(G_1+G_3)$	$(4/5)(14)^{\frac{1}{2}}(G_1+G_3)$	$-(2/5)(14)^{\frac{1}{2}}(6F_2+G_1+G_3)$
$^2{}_1D$	$-(1/2)(21/10)^{\frac{1}{2}}\times(6F_2-3G_1+2G_3)$	$-2(3/5)^{\frac{1}{2}}(3G_1-7G_3)$	$A+7B+7C-14G_3-(1/4)(14F_2+G_1)$	$(1/12)(21)^{\frac{1}{2}}(36B-18F_2+3G_1+8G_3)$	$(1/3)(21/10)^{\frac{1}{2}}(3F_2-6G_1+4G_3)$	$(1/3)(42/5)^{\frac{1}{2}}(3G_1-7G_3)$
$^2{}_2D$	$(1/2)(10)^{-\frac{1}{2}}(6F_2-19G_1+26G_3)$	$-2(7/5)^{\frac{1}{2}}(G_1+G_3)$	$(1/12)(21)^{\frac{1}{2}}(36B-18F_2+3G_1+8G_3)$	$A+3B+3C-(46/3)G_3-(1/4)(6F_2+13G_1)$	$(3/2)(10)^{-\frac{1}{2}}(54F_2-21G_1-16G_3)$	$-(1/15)(10)^{\frac{1}{2}}(3G_1-47G_3)$
^2F	$-(24/5)F_2+2(G_1+G_3)$	$(4/5)(14)^{\frac{1}{2}}(G_1+G_3)$	$(1/3)(21/10)^{\frac{1}{2}}\times(3F_2-6G_1+4G_3)$	$(2/3)(10)^{-\frac{1}{2}}(54F_2-21G_1-16G_3)$	$A+9B+3C-G_1+(12/5)F_2-(58/3)G_3$	$(4/15)(3G_1+28G_3)$
^4F	$(22/5)(G_1+G_3)$	$-(2/5)(14)^{\frac{1}{2}}(6F_2+G_1+G_3)$	$(1/3)(42/5)^{\frac{1}{2}}(3G_1-7G_3)$	$-(1/15)(10)^{\frac{1}{2}}\times(3G_1-47G_3)$	$(4/15)(3G_1+28G_3)$	$A-15B+(169/15)G_3-(1/5)(12F_2+2G_1)$

UNIVERSITY OF MICHIGAN LIBRARIES

TABLE III. The Energy Matrices of the Configuration d^7p.

$$
\begin{aligned}
{}^1S &= A - 6B + 3C + 4F_2 \\
{}^5S &= A - 14F_2 \\
{}^5P &= A + 7F_2 \\
{}^5F &= A - 15B - 3F_2 \\
{}^5G &= A - 15B + F_2 \\
{}^1I &= A - 6B + 3C - 3F_2 + 35G_3 \\
{}^3I &= A - 6B + 3C - 3F_2 + 15G_3
\end{aligned}
$$

$$
{}^3S = \begin{matrix} {}^2P \\ {}^4P \end{matrix} \left\| \begin{matrix} A - 6B + 3C + 4F_2 + (14/3)G_1 + 8G_3 & (4/3)(14)^{\frac{1}{2}}(2G_1 - 3G_3) \\ (4/3)(14)^{\frac{1}{2}}(2G_1 - 3G_3) & A - 14F_2 + (4/3)(16G_1 + 21G_3) \end{matrix} \right\|
$$

$$
{}^5D = \begin{matrix} {}^4P \\ {}^4F \end{matrix} \left\| \begin{matrix} A - (7/5)F_2 & (12/5)(14)^{\frac{1}{2}}F_2 \\ (12/5)(14)^{\frac{1}{2}}F_2 & A - 15B + (12/5)F_2 \end{matrix} \right\|
$$

$$
{}^1H = \begin{matrix} {}^2G \\ {}^2H \end{matrix} \left\| \begin{matrix} A - 11B + 3C - (2/5)(2F_2 - 2G_1 - 87G_3) & (6/5)(2F_2 - 2G_1 + 13G_3) \\ (6/5)(2F_2 - 2G_1 + 13G_3) & A - 6B + 3C + (1/5)(39F_2 + 36G_1 + 91G_3) \end{matrix} \right\|
$$

$$
{}^3H = \begin{matrix} {}^2G \\ {}^2H \end{matrix} \left\| \begin{matrix} A - 11B + 3C - (4/5)F_2 + 12G_3 & (12/5)F_2 - 6G_3 \\ (12/5)F_2 - 6G_3 & A - 6B + 3C + (39/5)F_2 + 3G_3 \end{matrix} \right\|
$$

$$
{}^1P = \begin{matrix} {}^2P \\ {}^2D \\ {}^2D \end{matrix} \left\| \begin{matrix} A - 6B + 3C - 2F_2 + (27/2)G_1 + 21G_3 & -(1/2)(21/2)^{\frac{1}{2}}(6F_2 - 3G_1 + 2G_3) & (3/2)2^{-\frac{1}{2}}(2F_2 - 9G_1 + 6G_3) \\ -(1/2)(21/2)^{\frac{1}{2}}(6F_2 - 3G_1 + 2G_3) & A + 7B + 7C - (1/4)(14F_2 - 71G_1) + 14G_3 & (3/4)(21)^{\frac{1}{2}}(4B - 2F_2 - G_1 + 4G_3) \\ (3/2)2^{-\frac{1}{2}}(2F_2 - 9G_1 + 6G_3) & (3/4)(21)^{\frac{1}{2}}(4B - 2F_2 - G_1 + 4G_3) & A + 3B + 3C - (3/4)(2F_2 - 9G_1) + 18G_3 \end{matrix} \right\|
$$

$$
{}^1G = \begin{matrix} {}^2F \\ {}^2G \\ {}^2H \end{matrix} \left\| \begin{matrix} A + 9B + 3C - F_2 + (15/4)(G_1 + 6G_3) & -(3^{\frac{1}{2}}/4)(8F_2 - 11G_1 + 14G_3) & (11/2)^{\frac{1}{2}}(4F_2 - 3G_1 - 3G_3) \\ -(3^{\frac{1}{2}}/4)(8F_2 - 11G_1 + 14G_3) & A - 11B + 3C + (1/20)(44F_2 + 121G_1 + 326G_3) & -(1/5)(33/2)^{\frac{1}{2}}(4F_2 + 11G_1 - 9G_3) \\ (11/2)^{\frac{1}{2}}(4F_2 - 3G_1 - 3G_3) & -(1/5)(33/2)^{\frac{1}{2}}(4F_2 + 11G_1 - 9G_3) & A - 6B + 3C - (1/5)(26F_2 - 66G_1 - 21G_3) \end{matrix} \right\|
$$

$$
{}^3P = \begin{matrix} {}^2P \\ {}^4P \\ {}^2D \\ {}^2D \end{matrix} \left\| \begin{matrix} A - 6B + 3C - 2F_2 + (1/6)(7G_1 + 32G_3) & (2/3)(14)^{\frac{1}{2}}(G_1 - 4G_3) & -(1/6)(21/2)^{\frac{1}{2}}(18F_2 - 3G_1 - 8G_3) & (1/2)2^{-\frac{1}{2}}(6F_2 + 7G_1 - 8G_3) \\ (2/3)(14)^{\frac{1}{2}}(G_1 - 4G_3) & A + 7F_2 + (4/3)(4G_1 + 14G_3) & (2/3^{\frac{1}{2}})(3G_1 - 7G_3) & 2(7)^{\frac{1}{2}}(G_1 + G_3) \\ -(1/6)(21/2)^{\frac{1}{2}}(18F_2 - 3G_1 - 8G_3) & (2/3^{\frac{1}{2}})(3G_1 - 7G_3) & A + 7B + 7C - (1/4)(14F_2 - 9G_1 - 14G_3) & (1/4)(21)^{\frac{1}{2}}(12B - 6F_2 + 3G_1 - 2G_3) \\ (1/2)2^{-\frac{1}{2}}(6F_2 + 7G_1 - 8G_3) & (2)7^{\frac{1}{2}}(G_1 + G_3) & (1/4)(21)^{\frac{1}{2}}(12B - 6F_2 + 3G_1 - 2G_3) & A + 3B + 3C - (3/4)(2F_2 - 7G_1 - 2G_3) \end{matrix} \right\|
$$

$$
{}^1D = \begin{matrix} {}^2P \\ {}^2D \\ {}^2D \\ {}^2F \end{matrix} \left\| \begin{matrix} A - 6B + 3C + (1/10)(4F_2 + 27G_1 + 252G_3) & (3/2)(21/10)^{\frac{1}{2}}(2F_2 + G_1 - 4G_3) & -(3/2)(10)^{-\frac{1}{2}}(2F_2 + 9G_1 - 36G_3) & (6/5)(4F_2 - 3G_1 - 3G_3) \\ (3/2)(21/10)^{\frac{1}{2}}(2F_2 + G_1 - 4G_3) & A + 7B + 7C + (7/4)(2F_2 + G_1 + 6G_3) & (1/4)(21)^{\frac{1}{2}}(12B + 6F_2 - 3G_1 + 2G_3) & -(42/5)^{\frac{1}{2}}(2F_2 + G_1 - 4G_3) \\ -(3/2)(10)^{-\frac{1}{2}}(2F_2 + 9G_1 - 36G_3) & (1/4)(21)^{\frac{1}{2}}(12B + 6F_2 - 3G_1 + 2G_3) & A + 3B + 3C + (1/4)(6F_2 + 27G_1 + 82G_3) & -(2/5)^{\frac{1}{2}}(18F_2 - 9G_1 - 14G_3) \\ (6/5)(4F_2 - 3G_1 - 3G_3) & -(42/5)^{\frac{1}{2}}(2F_2 + G_1 - 4G_3) & -(2/5)^{\frac{1}{2}}(18F_2 - 9G_1 - 14G_3) & A + 9B + 3C - (2/5)(6F_2 - 12G_1 - 37G_3) \end{matrix} \right\|
$$

TABLE III. The Energy Matrices of the Configuration d^7p.—*Continued.*

$^3F =$

	$^2{}_1D$	$^2{}_3D$	^3F	^4F	^2G
$^2{}_1D$	$A+7B+7C-F_2+G_1+(17/2)G_3$	$(1/2)(21)^{-\frac{1}{2}}(126B-18F_2-6G_1+29G_3)$	$(1/2)3^{-\frac{1}{2}}(12F_2+3G_1-17G_3)$	$-(2/3^{\frac{1}{2}})(3G_1-7G_3)$	$(3/2)(15/7)^{\frac{1}{2}}(4F_2-G_1-G_3)$
$^2{}_3D$	$(1/2)(21)^{-\frac{1}{2}}(126B-18F_2-6G_1+29G_3)$	$A+3B+3C-(3/7)(F_2-G_1)+(473/42)G_3$	$(1/6)7^{-\frac{1}{2}}(108F_2-9G_1-29G_3)$	$(2/3)7^{-\frac{1}{2}}(9G_1-41G_3)$	$(3/14)5^{\frac{1}{2}}(4F_2+3G_1+3G_3)$
^3F	$(1/2)3^{-\frac{1}{2}}(12F_2+3G_1-17G_3)$	$(1/6)7^{-\frac{1}{2}}(108F_2-9G_1-29G_3)$	$A+9B+3C+3F_2+(1/12)(9G_1+34G_3)$	$-3G_1-(14/3)G_3$	$(3/4)(5/7)^{\frac{1}{2}}(8F_2-3G_1+2G_3)$
^4F	$-(2/3^{\frac{1}{2}})(3G_1-7G_3)$	$(2/3)7^{-\frac{1}{2}}(9G_1-41G_3)$	$-3G_1-(14/3)G_3$	$A-15B-3F_2+12G_1+(76/3)G_3$	$3(5/7)^{\frac{1}{2}}(3G_1-2G_3)$
^2G	$(3/2)(15/7)^{\frac{1}{2}}(4F_2-G_1-G_3)$	$(3/14)5^{\frac{1}{2}}(4F_2+3G_1+3G_3)$	$(3/4)(5/7)^{\frac{1}{2}}(8F_2-3G_1+2G_3)$	$3(5/7)^{\frac{1}{2}}(3G_1-2G_3)$	$A-11B+3C-(1/28)(44F_2-135G_1-30G_3)$

$^1F =$

	$^2{}_1D$	$^2{}_3D$	^2F	^2G
$^2{}_1D$	$A+7B+7C-F_2+4G_1+(63/2)G_3$	$(1/2)(3/7)^{\frac{1}{2}}(42B-6F_2+12G_1-23G_3)$	$(3^{\frac{1}{2}}/2)(4F_2-7G_1+13G_3)$	$(3/2)(15/7)^{\frac{1}{2}}(4F_2-G_1-G_3)$
$^2{}_3D$	$(1/2)(3/7)^{\frac{1}{2}}(42B-6F_2+12G_1-23G_3)$	$A+3B+3C-(1/14)(6F_2-72G_1-317G_3)$	$(1/2)7^{-\frac{1}{2}}(36F_2-27G_1-7G_3)$	$(3/14)5^{\frac{1}{2}}(4F_2-13G_1-13G_3)$
^2F	$(3^{\frac{1}{2}}/2)(4F_2-7G_1+13G_3)$	$(1/2)7^{-\frac{1}{2}}(36F_2-27G_1-7G_3)$	$A+9B+3C+3F_2+(1/4)(39G_1+94G_3)$	$(3/4)(5/7)^{\frac{1}{2}}(8F_2+G_1-14G_3)$
^2G	$(3/2)(15/7)^{\frac{1}{2}}(4F_2-G_1-G_3)$	$(3/14)5^{\frac{1}{2}}(4F_2-13G_1-13G_3)$	$(3/4)(5/7)^{\frac{1}{2}}(8F_2+G_1-14G_3)$	$A-11B+3C-(1/28)(44F_2-395G_1-150G_3)$

$^3G =$

	^2F	^4F	^2G	^2H
^2F	$A+9B+3C-F_2+(1/12)(G_1+166G_3)$	$-(1/3)(G_1-14G_3)$	$-(1/4)3^{-\frac{1}{2}}(24F_2+3G-22G_3)$	$(1/3)(11/2)^{\frac{1}{2}}(12F_2-G_1-G_3)$
^4F	$-(1/3)(G_1-14G_3)$	$A-15B+F_2+(4/3)(G_1+31G_3)$	$(1/3^{\frac{1}{2}})(3G_1+22G_3)$	$(1/3^{\frac{1}{2}})(3G_1+22G_3)$
^2G	$-(1/4)3^{-\frac{1}{2}}(24F_2+3G_1-22G_3)$	$(1/3^{\frac{1}{2}})(3G_1+22G_3)$	$A-11B+3C+(11/5)F_2+(1/4)(9G_1+22G_3)$	$-(1/5)(11/6)^{\frac{1}{2}}(12F_2-15G_1+5G_3)$
^2H	$(1/3)(11/2)^{\frac{1}{2}}(12F_2-G_1-G_3)$	$(2/3)(22)^{\frac{1}{2}}(G_1+G_3)$	$-(1/5)(11/6)^{\frac{1}{2}}(12F_2-15G_1+5G_3)$	$A-6B+3C-(26/5)F_2+(1/3)(22G_1+G_3)$

$^3D =$

	^2P	^4P	$^2{}_1D$	$^2{}_3D$	^2F	^4F
^2P	$A-6B+3C+(2/5)F_2+(59/30)G_1+(39/5)G_3$	$-(2/15)(14)^{\frac{1}{2}}\times(7G_1-18G_3)$	$(1/2)(21/10)^{\frac{1}{2}}(6F_2-3G_1+2G_3)$	$-(1/2)(10)^{-\frac{1}{2}}(6F_2-11G_1+34G_3)$	$(2/5)(12F_2-G_1-G_3)$	$(22/5)(G_1+G_3)$
^4P	$-(2/15)(14)^{\frac{1}{2}}(7G_1-18G_3)$	$A+(104/15)G_1-(7/5)F_2+(168/5)G_3$	$2(3/5)^{\frac{1}{2}}(3G_1-7G_3)$	$-2(7/5)^{\frac{1}{2}}(G_1+G_3)$	$(4/5)(14)^{\frac{1}{2}}(G_1+G_3)$	$(1/5)(14)^{\frac{1}{2}}(12F_2-8G_1-8G_3)$
$^2{}_1D$	$(1/2)(21/10)^{\frac{1}{2}}(6F_2-3G_1+2G_3)$	$2(3/5)^{\frac{1}{2}}(3G_1-7G_3)$	$A+7(B+C+G_3)+(1/4)(14F_2+13G_1)$	$(1/12)(21)^{\frac{1}{2}}(36B+18F_2-3G_1-8G_3)$	$-(1/3)(21/10)^{\frac{1}{2}}\times(3F_2-6G_1+4G_3)$	$-(14/15)^{\frac{1}{2}}(3G_1-7G_3)$
$^2{}_3D$	$-(1/2)(10)^{-\frac{1}{2}}(6F_2-11G_1+34G_3)$	$-2(7/5)^{\frac{1}{2}}(G_1+G_3)$	$(1/12)(21)^{\frac{1}{2}}(36B+18F_2-3G_1-8G_3)$	$A+3B+3C+(3/4)\times(2F_2+3G_1)+(13/3)G_3$	$-(2/3)(10)^{-\frac{1}{2}}\times(54F_2-9G_1-4G_3)$	$(1/15)(10)^{\frac{1}{2}}(27G_1-23G_3)$
^2F	$(2/5)(12F_2-G_1-G_3)$	$(4/5)(14)^{\frac{1}{2}}(G_1+G_3)$	$-(1/3)(21/10)^{\frac{1}{2}}\times(3F_2-6G_1+4G_3)$	$-(2/3)(10)^{-\frac{1}{2}}\times(54F_2-9G_1-4G_3)$	$A+9B+3C-(12/5)\times(F_2-3G_1)+(8/15)G_3$	$(4/15)(18G_1-7G_3)$
^4F	$(22/5)(G_1+G_3)$	$(1/5)(14)^{\frac{1}{2}}(12F_2-8G_1-8G_3)$	$-(14/15)^{\frac{1}{2}}(3G_1-7G_3)$	$(1/15)(10)^{\frac{1}{2}}(27G_1-23G_3)$	$(4/15)(18G_1-7G_3)$	$A-15B+(12/5)F_2+(4/5)(18G_1+(29/3)G_3)$

UNIVERSITY OF MICHIGAN LIBRARIES

The two ^2D terms of d^3 are distinguished by their seniority numbers which indicate in which configuration of the chain d, d^2, $\cdots d^n$ the term occurred first. This distinction is made possible by the operator Q, defined in reference 2, III, which is diagonal simultaneously with S and L, and which gives a unique relation between terms of equal S and L belonging to configurations l^n and l^{n-2}, respectively. Such a relationship, however, exists only for non-vanishing Q. One can show that the lower of the two ^2D terms of d^3 gives $Q=0$ and has therefore seniority number 3, whereas the higher one is related to the ^2D of d and has seniority number 1. We thus write $^2{}_1D$ and $^2{}_3D$ instead of $^2D^+$ and $^2D^-$, or a^2D and b^2D as is sometimes used in the literature.

It is clear that the general formula for d^3p given above can be used to calculate d^7p, since d^3 and d^7 are conjugate configurations, the maximum number of equivalent d electrons being ten. In order to obtain the energy of the conjugate configuration we simply have to change the sign of all the tensors of even degree (reference 2, II, Eq. (74)), i.e., of the constant matrix, $\mathbf{U}^{(2)}$ and $\mathbf{V}^{(11)}$. With this recipe one finds for d^7p the matrices given in Table III.

In conclusion, I wish to thank Professor G. Racah for suggesting this problem to me and for many helpful discussions.

PHYSICAL REVIEW VOLUME 74, NUMBER 10 NOVEMBER 15, 1948

The Classification of the Odd Terms of Ti *I*

F. ROHRLICH
Lyman Laboratory of Physics, Harvard University, Cambridge, Massachusetts
(Received June 22, 1948)

The odd configurations $3d^24s4p$, $3d^34p$ and $3d4s^24p$ of Ti *I* are calculated using the results of the preceding paper. Numerical values for the F^k and G^k integrals are found by comparison with the observed levels in a method of successive approximation. A correction is applied for configuration interaction which improves the general agreement.

Explicit formulae are given for the multiplet strengths of transition arrays involving equivalent electrons. They are applied to the transitions d^2sp-d^3s and $d^2sp-d^2s^2$ of Ti *I*. Tables of multiplet strengths are calculated corresponding to interaction energies diagonal in first-order and second-order eigenfunctions, respectively.

On the basis of these calculations and known measurements of line intensities and gf values, a new classification of the odd terms of Ti *I* is proposed. Of the 83 observed odd terms, 76 were classified. In 74 cases the calculated terms fit with a mean deviation of ± 1023 cm^{-1} on a range of about 30,000 cm^{-1}. Although the experimental data on multiplet strengths are rather scarce, they seem to be in better agreement with theory when based on the new classification.

I. INTRODUCTION

THE spectra of Ti *I* and Ti *II* were analyzed in 1927 by Henry Norris Russell.[1] His classification is based to a large extent on the intensity estimates by A. S. King.[2] He was able to identify 142 terms in Ti *I* and 50 terms in Ti *II*, and thus accounted for 1394 and 529 lines, respectively.

However, whereas the spin, orbital, and total angular momenta of a level can be identified experimentally in a rather reliable manner, it is sometimes very difficult to specify the configuration and the series limit. A number of terms, therefore, were classified on admittedly doubtful arguments, especially in the spectrum of Ti *I*.

The classification of the even terms of Ti *I* was shown by Many[3] to be in satisfactory agreement with theory. The odd terms will be considered in this paper. Most of the odd terms arise from the configurations $3d^24s4p$, $3d^34p$, and $3d4s^24p$. In these configurations the p electron is bound more weakly than the s electron, so that the excited configurations are of the form $3d^24smp$, $3d^3mp$, and $3d4s^2mp$ ($m=5, 6, \cdots$) and have as their series limit the even configurations of Ti *II*. These latter configurations, $3d^24s$, $3d^3$, and $3d4s^2$, were also found to be in agreement with theory.[3] The only doubtful point in the Ti *II* spectrum was the assignment of the two lowest terms, a^4F and b^4F, which Many assigned to $3d^3$ and $3d^24s$, respectively, contrary to Russell's original assignment. This question remained open until recently when Russell showed conclusively[4] that the lowest term of Ti *II* has the configuration d^2s, in agreement with his original assignment.

Since the calculated energy terms are not always conclusive for the purpose of configuration assignments, we had to make use of the experimental data on intensities and line strengths.[5] It was necessary, therefore, to calculate the multiplet strengths of the most important transition arrays.

The next section will give a brief outline of the numerical methods adopted to find the values of the F^k and G^k integrals which are here simply regarded as parameters. Section III will deal with the resulting term energies and the correction for configuration interaction. Intensities and line strengths are discussed in Section IV, and tables of multiplet strengths are given which are calculated by means of the general formulae derived in the appendix. The last section is devoted to a discussion of the most important aspects of the proposed new classification.

[1] H. N. Russell, Astrophys. J. **66**, 347 and 283 (1927).
[2] A. S. King, Astrophys. J. **39**, 139 (1914) and **59**, 155 (1924).
[3] A. Many, Phys. Rev. **70**, 511 (1946).
[4] H. N. Russell, Phys. Rev. **74**, 689 (1948). Kindly communicated by letter before publication.
[5] A. S. King and R. B. King, Astrophys. J. **87**, 24 (1938).

TABLE I. List of parameters for Ti *I*. Columns 1 and 2 give the parameters as calculated on the basis of the current assignment for d^3p and d^2sp, respectively. Column 3 gives the results under the assumption that some configuration assignments have to be interchanged. Column 4 gives an estimate; columns 5, 6, and 7 list the parameters as found in steps by the method of successive approximation.

	1	2	3	4	5	6	7
$A(d^3p)$	39,240	——	36,732	38,000	38,410	38,290	37,972
$A(d^2sp)$	——	28,291	29,456	29,800	30,651	30,729	30,491
$A(ds^2p)$	——	——	——	45,000	——	——	45,241
B	578	522	577	600	570	573	563
C	1,641	4,259	2,555	2,400	2,193	2,108	2,122
F_2	239	106	40	300	295	293	281
G_1	305	96	256	280	332	315	306
G_3	37	−81	17	20	9	2	0
G_d	——	740	0	1,300	938	1,344	1,381
G_p	——	5,499	4,624	4,000	5,628	5,145	4,834

II. CALCULATION OF THE PARAMETERS F^k AND G^k

The matrices for the term energies of the configurations d^2sp and d^3p were calculated in the preceding paper.[6] The terms of ds^2p follow immediately from the well-known[7] terms of dp, since these two configurations differ only by a constant.

In the Ti *I* spectrum the spin-orbit interaction is small compared to the electrostatic interaction, and the decomposition of each term into the multiplet levels is in general well represented by Lande's interval rule. We expect, therefore, that Russell-Saunders coupling is a good approximation and that the above mentioned theoretical term energies should fit the experimental values.

We can further assume that the integrals B, C, F_2, G_1 and G_3 occurring in the matrices of the three odd configurations are the same for all cases where the principal quantum number is the same. The configurations $3d^24s4p$, $3d^34p$ and $3d4s^24p$ are therefore determined by the ten parameters

$$A(d^2sp),\ A(d^3p),\ A(ds^2p),$$
$$B,\ C,\ F_2,\ G_1,\ G_3,\ G_d,\ G_p.$$

Under these conditions one can easily show that the current assignment of the odd Ti *I* terms cannot be completely correct. For this purpose we equated the traces of the matrices of d^3p to the corresponding sums of observed terms, leaving out those traces which involve unobserved terms. The resulting set of ten weighted linear equations for the six parameters involved in d^3p were then solved by the method of least squares.[8] The same was done for d^2sp. The results are listed respectively in Table I, columns 1 and 2. We see that the parameters do not at all agree in the two configurations. Also, from considerations of related spectra like Ti *II*, V *II*, etc., one can estimate the values of the parameters of Ti *I*. These estimates are given in the same table in column 4. A comparison with the parameters listed in columns 1 and 2 shows rather poor agreement. A negative value like that of G_3 of d^2sp (column 2) is of course already excluded by virtue of the postiveness of Slater's integrals.

The odd terms $^{1,3}SPDFGH$ occur in both configurations, d^3p and d^2sp. It seems, therefore, possible that some of these terms have a wrong configuration assignment and that they should be interchanged. We recalculated, therefore, the parameters, this time by equating the sum of the traces of d^3p and d^2sp to the observed values for each of the above terms. The result is given in column 3 and is seen to be in much better agreement with the estimates (column 4). The persisting disagreement of F_2 and of G_d, however, indicates that further corrections will be necessary in addition to interchanges of configuration assignments. On solving the secular equations with the parameters of column 3 we did not obtain satisfactory agreement with the experiments. However, when these secular equations were solved with the parameters of column 4 the agreement was much improved.

We used, therefore, the estimated parameters as a first approximation and tried to improve these values by a method of successive approximation. This method is essentially a repeated application of Schrödinger's first-order perturbation theory. One finds the transformation matrix (or eigenvectors) which diagonalizes the energy matrix when the estimated set of parameters is used. This transformation matrix is then used to diagonalize the energy matrix with unspecified parameters. The diagonal elements of the resulting "nearly diagonal" matrix are then equated to the corresponding observed

[6] F. Rohrlich, Phys. Rev. **74**, 1372 (1948).
[7] E. U. Condon and G. H. Shortley, *The Theory of Atomic Spectra* (Cambridge 1935), p. 200.
[8] For the standard procedures employed see, e.g., *Handbuch der Physik* (Julius Springer, Berlin, 1928), Vol. III, Chap. 13.

terms, and the obtained set of n linear equations for m ($m<n$) parameters is solved by the method of least squares.[8] One finds an improved set of parameters with which the whole procedure may be repeated. In our case this process yielded the set of parameters listed in Table I, columns, 5 6 and 7. For column 5 only those terms were taken into account which involve matrices of order one or two in d^3p and d^2sp. In the calculation of the parameters of column 6 all terms of d^3p and d^2sp were used[9] and finally the configuration ds^2p was included and the resulting parameters (column 7) were regarded as final. A further improvement of the parameters A, as a result of the interaction of the parent configurations, will be discussed in Section III.

From Table I we see that the convergence of the method of successive approximation seems satisfactory and that the final set of parameters is not too far off the estimated values. We think that the improvement caused by one further iteration will hardly justify the great amount of work involved.

The least square method involved the solution of 25, 32, and 41 simultaneous weighted linear equations for 9, 9, and 10 unknowns, respectively.[8] This could easily be done on an ordinary calculating machine. For the diagonalization of the matrices of order 4, 5, and 6, and for the evaluation of the eigenvectors, however, we used the Electric Network for the Solution of Secular Equations of R. H. Hughes and E. B. Wilson.[10] With its aid symmetrical secular equations up to order six can be solved and the eigenvectors can be measured. For our purpose the accuracy of the instrument had to be improved from 1 percent to about 0.1 percent for the roots. More precisely, the final accuracy obtained was an average error of 0.1 for all roots up to about 250, on an arbitrary scale. Proper scaling enabled us to have most of our roots lying between 100 and 200 or more. The improvement in accuracy was achieved by better calibration of coils and condensors, and by exact determination of corrections for stray capacities. The latter was done by solving quite a number of test problems.

[9] Single terms with doubtful assignment were omitted. For closely spaced terms whose assignment may have to be interchanged, the weighted average was used.

[10] R. H. Hughes and E. B. Wilson, Rev. Sci. Inst. 18, 103 (1947).

TABLE II. Odd quintet terms of Ti *I*. All energy values are in units of cm^{-1}. Columns *A* and *B* refer to calculations without and with configuration interaction, respectively.

Observed term		Limit $3d^24s$	Limit $3d^3$	Calc. *A* Term	Calc. *A* Δ_i	Calc. *B* Term	Calc. *B* Δ_i
z^5G°	16202	a^4F		15918	−284	16072	−130
z^5F°	17046	a^4F		17242	196	17396	350
z^5D°	18598	a^4F		19085	487	19239	641
z^5S°	25103	b^4P		24738	−365	24892	−211
y^5D°	25797	b^4P		25199	−598	25353	−444
y^5G°	26726		b^4F	26186	−540	26092	−634
z^5P°	27794	b^4P		26967	−827	27121	−673
y^5F°	28767		b^4F	28534	−233	28440	−327
x^5D°	29975		b^4F	29027	−948	28933	−1042
w^5D°	35654		a^4P	36049	395	35955	301
y^5P°	36367		a^4P	35699	−668	35605	−762
y^5S°	37359		a^4P	38846	1487	38752	1393
				$\Delta=\pm682$		$\Delta=\pm674$	
				$\mu=\pm1365$		$\mu=\pm1651$	

Also, the routine calibration of the small coils which changed their inductance by about 0.1 percent per week was vital to this accuracy. The eigenvectors were measured with an electronic voltmeter which limited the accuracy to a maximum error of 2 percent. Actually, however, the accuracy of the eigenvectors was about 1 percent in most cases as could easily be checked by their orthogonality relations.

III. TERM ENERGIES AND CONFIGURATION INTERACTION

The term energies calculated with the final set of parameters are listed in Tables II, III, and IV (column *A*) for the quintet, singlet and triplet system, respectively. The corresponding terms and their limits are shown in the first two sections of Table II for the quintet system, and in the first and third sections of Tables III and IV (assignment *II*) for the singlet and triplet systems, respectively. Russell's assignment[1] of limits is given in the second section of each table (assignment *I*). For the quintet system assignment *I* and assignment *II* are identical, i.e., Russell's assignment is completely confirmed by the above calculations. In the other two systems quite a number of terms show differences in the two assignments, some in the parent term, some in the parent configuration, and some in both.

We define, as usual, the mean deviation and the mean error in terms of the deviation Δ_i of each term

$$\Delta^2=\sum\Delta_i^2/n, \quad \mu^2=\sum\Delta_i^2/(n-m),$$

where n is the number of terms and m is the number of parameters which were used to fit these terms.

TABLE III. Odd singlet terms of Ti *I*. The current assignment (due to Russell) is given as *I*, the proposed assignment as *II*. The deviations Δ_i are calculated with respect to assignment *II*. Columns *A* and *B* refer to calculations without and with configuration interaction, respectively. All energy values are in units of cm^{-1}.

Obs. term		Assignment I			Assignment II			Calc. *A*		Calc. *B*	
		$3d^24s$	$3d^3$	$3d4s^2$	$3d^24s$	$3d^3$	$3d4s^2$	Term	Δ_i	Term	Δ_i
z^1D°	22081	a^2F			a^2F			21919	−162	21972	−109
z^1F°	22405	a^2F			a^2F			21523	−882	21621	−784
z^1G°	24695	a^2F			a^2F			23964	−731	24054	−641
$^1S^\circ$	——		——		b^2P			26127	——	25771	——
y^1D°	27907	a^2D			b^2P			31861	(3954)	31293	(3386)
y^1F°	32858		a^2G		a^2D			35385	2527	35211	2353
z^1P°	33661	a^2D			b^2P?			33753	92	33329	−332
z^1H°	34700		a^2G			a^2G		36756	2056	36490	1790
y^1P°	34947	b^2P			a^2D?			35749	802	35477	530
x^1D°	35035	b^2P			a^2D			37356	2321	36827	1792
y^1G°	36000		a^2G			a^2G		37350	1350	36817	817
x^1F°	37623	a^2D				a^2G		37533	−90	37289	−334
z^1S°	38201		a^2P			a^2P		36776	−1425	37192	−1009
x^1G°	38960	b^2G			b^2G			38036	−924	38629	−331
x^1P°	39078		b^2D			$b^2{}_3D$		40400	1322	40477	1399
$w^1P^{\circ *}$	39266		a^2P			a^2P		37610	−1656	38387	−879
w^1F°	40303		b^2D			$b^2{}_3D$		42323	2020	42260	1957
z^1I°	40320		a^2H			a^2H		40885	565	40791	471
w^1G°	40883		?			a^2H		40763	−120	40669	−214
y^1H°	41040		a^2H		b^2G			39728	−1312	39859	−1181
v^1F°	41585	b^2G			b^2G			42771	1186	43075	1490
v^1P°	42928	a^2S?				a^2P		42929	1	43413	485
v^1G°	43674		a^2H			——		——	——	——	——
w^1D°	43710		a^2P				c^2D	42356	−1354	42305	−1405
v^1D°	43800		b^2D			$b^2{}_3D$		44912	1112	44236	436
x^1H°	44163	b^2G				a^2H		41606	−2557	41707	−2456
u^1G°	46258		b^2F?			——		——	——	——	——
$^1P^\circ$	——		——				c^2D	47514	——	47499	——
u^1F°	48365		b^2F?				c^2D	47639	−726	47613	−752
$^1D^\circ$	——		——			b^2F		49139	——	49624	——
$^1G^\circ$	——		——			b^2F		49685	——	49655	——
$^1F^\circ$	——		——			b^2F		51143	——	51105	——
$^1P^\circ$	——		——		a^2S			56392	——	56546	——
$^1D^\circ$	——		——			$^2{}_1D$		60043	——	60527	——
$^1F^\circ$	——		——			$^2{}_1D$		61181	——	61299	——
$^1P^\circ$	——		——			$^2{}_1D$		65146	——	65211	——
								$\Delta=\pm1358$		$\Delta=\pm1195$	
								$\mu=\pm1846$		$\mu=\pm1624$	

* This term is believed to be $^1D^\circ$.

If we take assignment *II* as a basis, we obtain the differences between observed and calculated term energies as stated in the above-mentioned three tables. We then find for the mean deviations ±682, ±1358 and ±1033 cm^{-1}, and for the mean errors ±1365, ±1846 and ±1225 cm^{-1}, corresponding to the quintet, singlet, and triplet system. All three systems together fit with a total mean deviation of ±1105 cm^{-1} and with a total mean error of ±1189 cm^{-1}. In these calculations only 74 of the 76 classified terms have been taken into account. The two terms y^1D° and v^3F° show much larger deviations than any of the other terms and were therefore omitted in the least-square calculation.

When we consider the interaction between the parent configurations d^3, d^2s and ds^2 which we have neglected so far, we may expect improved agreement. The corresponding matrix elements were calculated by Ufford.[11] He found that the interaction integral

$$H_2=(1/35)R^2(dd, ds)$$

is 192 cm^{-1} for Ti *II* whereas Many[3] found by the least square method 172 cm^{-1} for Ti *II* and 153 cm^{-1} for V *II*. Since Ti *I* and V *II* have the same electron configurations, but the latter has a higher nuclear charge, we expect a still smaller configuration interaction in Ti *I*. A rough estimate of $H_2=100$ cm^{-1} turned out to be not much too small.

With this value for the interaction parameter

[11] C. W. Ufford, Phys. Rev. **44**, 732 (1933).

TABLE IV. Odd triplet terms of Ti *I*. For explanation see Table III.

Obs. term		Assignment I			Assignment II			Calc. *A*		Calc. *B*	
		$3d^24s$	$3d^3$	$3d4s^2$	$3d^24s$	$3d^3$	$3d4s^2$	Term	Δ_i	Term	Δ_i
$z^3F°$	19463	a^2F			a^2F			19364	−99	19473	10
$z^3D°$	20048	a^2F			a^2F			20279	231	20368	320
$z^3G°$	21619	a^2F			a^2F			21115	−504	21208	−411
$z^3S°$	24921	b^2P			b^4P			24632	−289	24672	−249
$y^3F°$	25268	a^4F			a^2D			25761	493	25734	466
$z^3F°$	25510_{13}	b^2P			a^2D			26039	529	26009	499
$y^3D°$	25510_{34}	a^4F			a^2D			26478	968	26452	942
$x^3F°$	26929		b^4F		a^4F			29029	2100	29137	2208
$x^3D°$	27434	b^2P				b^4F		27635	201	27527	93
$y^3G°$	27640		b^4F		a^4F			27370	−270	27524	−116
$w^3D°$	29814		b^4F		a^4F			30067	253	30137	323
$x^3G°$	29984	a^4F			b^2G			29433	−551	29470	−514
$v^3D°$	31197	a^2D			b^2P			30861	−336	30391	−806
$w^3G°$	31516	b^2G				b^4F		29473	−2043	29379	−2137
$y^3P°$	31766	a^2D			b^2P			30638	−1128	30407	−1359
$z^3H°$	31930	b^2G			b^2G			30060	−1870	30052	−1878
$x^3P°$	33103	b^4P				a^4P		35219	2116	34997	1894
$w^3F°$	33683	a^2D				b^4F		30470	(−3213)	30376	(−3307)
$v^3F°$	34109	b^2G			b^2G			33099	−1010	33069	−1040
$y^3S°$	35439	b^4P			b^2P			35901	462	35428	−11
$y^3H°$	35580		a^2G			a^2G		35202	−378	35253	−327
$w^3P°$	37249		a^4P		b^4P			38849	1600	38466	1219
$v^3G°$	37631		a^2G			a^2G		37421	−210	37444	−187
$u^3F°$	37769		b^2D					—	—	—	—
$u^3D°$	38037	b^4P			b^4P			37403	−634	37557	−480
$t^3F°$	38576		a^2G			a^2G?		38024	−552	38118	−458
$z^3I°$	38685		a^2H			a^2H		39049	364	38955	270
$t^3D°$	38721		b^2F					—	—	—	—
$x^3H°$	39161		a^2H			a^2H		38876	−285	38799	−362
$s^3D°$	39695		a^4P			a^4P		38774	−921	38872	823
$v^3P°$	40429		b^2D			a^2P		38843	−1583	39529	−900
$r^3D°$	40729		a^2P			a^2P		40436	−293	40856	127
$x^3S°$	40844		a^4P			a^2P		39885	−959	40404	−440
$u^3G°$	41268		a^2H			a^2H		42391	1123	42297	1029
$s^3F°$	41500		b^2F			$b^2{}_3D$		40670	−830	40423	−1077
$u^3P°$	41936		a^2P			$b^2{}_3D$		42971	1035	43051	1115
$q^3D°$	42244		b^2D			b^2D		41582	−662	41229	−1015
$r^3F°$	43625			c^2D			c^2D	43967	342	44012	387
$o^3D°$	44130			c^2D			c^2D	44192	62	44322	192
$w^3S°$	44858		a^2P			a^4P		43693	−1165	43727	−1131
$t^3P°$	45134			c^2D			c^2D	46902	1768	46804	1670
$^3F°$	—		—			b^2F		47333	—	47329	—
$^3P°$	—		—		a^2S			47669	—	47893	—
$^3G°$	—		—			b^2F		48371	—	48338	—
$^3D°$	—		—			b^2F		50303	—	50291	—
$^3D°$	—		—			$^2{}_1D$		58662	—	58765	—
$^3F°$	—		—			$^2{}_1D$		59933	—	60014	—
$^3P°$	—		—			$^2{}_1D$		61634	—	61735	—
								$\Delta=\pm1033$		$\Delta=\pm\ 996$	
								$\mu=\pm1225$		$\mu=\pm1182$	

the corrections to the previously calculated term values were found approximately. The corrections are larger for S and P terms. The $^3P°(^2P)$ term of d^3p has the largest correction, viz., 686 cm^{-1}. It is clear that configuration interaction causes in general a shift of the centers of the configurations. These shifts are found by correcting the parameters A so that the sum of the deviations vanishes for each configuration. In the previous calculation the vanishing of this sum was guaranteed by the method of least squares. The new values for the A's are

$$A(d^3p) \quad 37{,}878\ cm^{-1},$$
$$A(d^2sp) \quad 30{,}645\ cm^{-1},$$
$$A(ds^2p) \quad 45{,}130\ cm^{-1}.$$

Using these values instead of those of Table I, column 7, and adding the corrections resulting from configuration interaction to the terms listed in the Tables II, III and IV, column A, one obtains the improved term energies listed in column B of the same three tables. We see that

TABLE V. Observed intensities and multiplet strengths of Ti *I* (quintet system). The columns *M* and *KK* list intensities (strongest line of each multiplet) and multiplet strengths, respectively. Estimated values are in brackets. The symbols *i*, *m*, *n*, *tr*, *r*, and *R* indicate infra-red, masked, fuzzy lines, trace, narrow, and wide self-reversal, respectively . (See Tables VI and VII.)

			$3d^34s$			
	Limit / Term		a^4P a^6P		b^4F a^6F	
Limit	Term		*M*	*KK*	*M*	*KK*
$3d^34s4p$						
	z^6S^0		25			
b^4P	z^6P°		(1)			
	y^6D°		40		6	(5)
	z^6D^0				300	
a^4F	z^6F°				100	
	z^6G°				30	
$3d^34p$						
	y^6S°		15			
a^4P	y^6P°		30	(440)		
	w^6D°		30	(450)	4	
	x^6D°		(2)		60	637
b^4F	y^6F°				80	802
	y^6G°				60	(910)

the improvement is considerable. The quintet system is affected only indirectly (by the change of the *A*'s), since there is no interaction between the ^4F terms of the parent configurations.[11] The mean deviations are now reduced to ±674, ±1195 and ±996 cm^{-1}, and the mean errors to ±1651, ±1624 and ±1182 cm^{-1} for the quintet, singlet, and triplet systems, respectively. The total mean deviation is ±1023 cm^{-1}, and the total mean error is ±1109 cm^{-1}.

IV. INTENSITIES AND LINE STRENGTHS

It is well known that the theoretical formulae for the multiplet and super-multiplet analysis are based on relative line strengths whereas the experimenter measures in general intensities. The two differ by the fourth power of the frequency and the Boltzmann factor, which corresponds to a correction to infinite temperature. For multiplet analysis these two corrections can be neglected and one can work with intensities as well as with line strengths. For super-multiplet analysis this is generally not the case, since the separation of the terms which have the same limit is not necessarily negligible with respect to the lines of the transition array, and these lines are not always excited at the same temperature.

However, it seems difficult to find the appropriate corrections for A. S. King's original intensity measurements.[2] On the other hand, more recent experiments by A. S. King and R. B. King[5] are much more reliable, both as to homogeneity and to accuracy. Unfortunately, they measured only the strongest multiplets. Their list of *gf* values has to be multiplied by the wave-lengths to obtain line strengths.

In Russell's intensity tables[1] the strongest line (principal line) of each multiplet is given as an indication of the intensity of the total multiplet. In many cases this gives a good relative estimate, but it is not always reliable, and in some cases it seems to distort the picture considerably. In the following, we used, therefore, the sum of the strengths of all the lines of a multiplet to calculate its multiplet strength. If some weak components were not known experimentally, they could easily be estimated from theoretical intensity tables.[12] Usually, this amounted to a correction of not more than 10 percent. In a few cases, however, most of the multiplet strength is due to estimates. These values are given in brackets in Tables V–VII. The columns *M* of these tables list the multiplet intensities, as in Russell's paper, in terms of their principal lines. They include some intensity measurements which were not known to Russell at that time, and some values which are corrected measurements. All these are taken from the Multiplet Tables compiled by Moore,[13] and are due to various investigators. The multiplet strengths as calculated from the measured *gf* values[5] are given in the columns *KK* of the same tables. The main differences between the columns *M* and *KK* have to be attributed, therefore—apart from a scale factor—to frequency and temperature corrections. The tables are arranged according to the new assignment.

These Tables (V–VII) of observed multiplet strengths must be compared with Tables VIII–XIII which give the calculated multiplet strengths. The latter are obtained by the following procedure.

The calculation is carried out in two steps. Firstly, we regard the quantum numbers of the

[12] See reference 7, p. 241.
[13] C. E. Moore, *A Multiplet Table of Astrophysical Interest* (Princeton University Press, Princeton, 1945).

TABLE VI. Observed intensities and multiplet strengths of Ti *I* (singlet system). In this table the proposed classification is adopted. The meaning of the various symbols is indicated in Table V.

			$3d^24s^2$					$3d^24s$				
	Limit / Term	a^2S a^1S	a^2D a^1D		b^2G a^1G		a^2P a^1P		b^2D b^1D	b^2F a^1F	a^2G b^1G		a^2H a^1H
Limit	Term	*M*	*M*	*KK*	*M*	*KK*	*M*	*KK*	*M*	*M*	*M*	*KK*	*M*
$3d^24s4p$													
b^2P	z^1P°		20	55			(1)						
	y^1D°		25	22			*i*						
	y^1P°	3	12	31			(1)						
a^2D	x^1D°		15				(0)						
	y^1F°		40*n*	90	20				(2)	*i*	6		
	z^1D°		10	3			*i*						
a^2F	z^1F°		12	1	25					*i*	*i*		
	z^1G°				(3)					*i*	*i*		*i*
	v^1F°		40	10					1	(1)	*m*		
b^2G	x^1G°				20	127				*i*	6		8
	y^1H°				6						8		8
$3d^34p$													
	z^1S°						2						
a^2P	v^1P°	1	15				3		(2)				
	w^1P°*	(1)	15	18			5	859	2				
	x^1P°	(3)	15	14			(1)		4				
b^2D	v^1D°		6				4		7				
	w^1F°		2		15				10	*i*	(1)		
	x^1F°		20	35	5				1	*i*	(0)		
a^2G	y^1G°				25					*i*	18	186	3
	z^1H°				40						20		2
	w^1G°				*m*						2		1
a^2H	x^1H°				15								7
	z^1I°												12
$3d4s^24p$													
c^2D	w^1D°		15				5						
	u^1F°		(1)		20					(2)	4		
Unclassified													
	v^1G°				2*n*					(0)	2*n*		5*n*
	u^1G°				30					(1)	8		10

* This term is believed to be a $^1D^\circ$ term.

parent configurations as "good quantum numbers," and neglect, therefore, the interaction between multiply-occurring terms in each configuration. This amounts to neglecting the off-diagonal elements in the energy matrices calculated in the preceding paper.[6] The matrices are then diagonal in "first-order eigenfunctions" as defined by Ufford.[11] The multiplet strengths can then be calculated with the well-known formulae of Kronig.[14] These formulae are not sufficient, however, in case the jumping electron belongs to a group of equivalent electrons in one of the configurations. For those cases general formulae are derived in the appendix. With their aid the multiplet strengths of transitions involving equivalent electrons can be calculated from the Kronig strength for transitions not involving equivalent electrons and the coefficients of fractional parentage.[15,16] The results for the important transition arrays of Ti *I* are listed in the columns 1 of Tables VIII–XIII.

[14] Kronig, Zeits. f. Physik **33**, 261 (1925).

[15] R. F. Bacher and S. Goudsmit, Phys. Rev. **46**, 948 (1934).

[16] G. Racah, Phys. Rev. **63**, 367 (1943).

TABLE VII. Observed intensities and multiplet strengths of Ti *I* (triplet system). In this table the proposed classification is adopted. The meaning of the various symbols is indicated in Table V.

			$3d^24s^2$								$3d^24s$					
		Limit / Term	b^3P, b^1P a^1P		a^3F, a^1F a^1F		a^1P c^1P	b^1F b^1F		a^3P b^1P	b^3D a^1D	a^3G a^1G		a^3H a^1H	
Limit	Term		M	KK	M	KK	M	M	KK	M	M	M	KK	M	KK
$3d^24s4p$															
	$z^3S°$		20	10	(3)		i			i					
b^4P	$w^3P°$		12	46			6				8				
	$u^3D°$		15	52	40			8		1	8				
	$w^3D°$		20	24	40r	75	2	25	136	60					
a^4F	$x^3F°$				80r	143		25	28		i	100			
	$y^3G°$				100r	229		50	145			(4)		10	
	$y^3S°$		20	68						2					
b^2P	$y^3P°$		2		tr					(2)	(1)				
	$v^3D°$		10		5	1	(1)	12	78	(2)	(1)				
	$z^3P°$		10	8	40	8	i	5		i	i				
a^2D	$y^3D°$		35	36	80	104	i	20		i	i				
	$y^3F°$				100R	163		4			(1)	25			
	$z^3D°$		150		25	22	i	6		i	i				
a^2F	$z^3F°$				40	31		i			25	i			
	$z^3G°$				30	14		15				i		i	
	$v^3F°$				70R	(125)		40			4n	10	158		
b^2G	$x^3G°$		3		80R	168		6	(19)		i	(1)		75	
	$z^3H°$				3							30	180	(1)	
$3d^24p$															
	$w^3S°$		6												
a^4P	$x^3P°$		30	105			(1)				(2)				
	$s^3D°$		6	(36)	20		12	3			(2)				
	$x^3D°$		4	9	15	12	2	8		3	(1)				
b^4F	$w^3F°$				20			8			3	6			
	$w^3G°$				100R	177		25	315			4		(3)	
	$x^3S°$		8							3					
a^2P	$v^3P°$		1				8				4				
	$r^3D°$		12		(3)		2	8		6	3				
	$u^3P°$		tr							8	8				
b^2D	$q^3D°$		15		4			(5)			10				
	$s^3F°$				10						10	4			
	$t^3F°$		2		25			1			9	15			
a^2G	$v^3G°$				20			2				30		(1)	
	$y^3H°$											20	429	9	
	$u^3G°$				10			2						10n	
a^3H	$x^3H°$											7		25	(156)
	$z^3I°$													20	(334)
$3d4s^24p$															
	$t^3P°$		30				1			3	1				
c^3D	$o^3D°$		6		12			1							
	$r^3F°$				12			2				3			
Unclassified															
	t^3D		15	166	5			15		2	4				
	$u^3F°$		1		5			3			12	15			

In the second step we do take into account the off-diagonal matrix elements of the multiply-occurring terms of each configuration, but we still neglect configuration interaction. The energy matrices are now diagonal in "second-order eigenfunctions." The latter are linear combina-

TABLE VIII. Calculated multiplet strengths d^3sp-d^3s, (quintets).

d^2s	d^3 / d^3sp	^4P ^5P 1	^4P ^5P 2	^4F ^5F 1	^4F ^5F 2
	$^5S°$	80	80		
^4P	$^5P°$	60	60		
	$^5D°$	4	8	126	127
	$^5D°$	126	122	144	143
^4F	$^5F°$			315	315
	$^5G°$			45	45
		3×90		7×90	

TABLE IX. Calculated multiplet strengths d^3p-d^3s, (quintents).

d^3	d^3 / d^3ps	^4P ^5P 1	^4P ^5P 2	^4F ^5F 1	^4F ^5F 2
	$^5S°$	5	5		
^4P	$^5P°$	15	15		
	$^5D°$	25	24		1
	$^5D°$		1	25	24
^4F	$^5F°$			35	35
	$^5G°$			45	45
		3×15		7×15	

tions of the first-order eigenfunctions; the corresponding coefficients are the eigenvectors which were measured on the secular equation solver described in Section II. Unfortunately, we do not have these eigenvectors for the even configurations. We have to assume that the first-order eigenfunctions are good enough for them. Under these conditions we obtain the results given in Tables VIII–XIII, column 2. It is important to note that these values are only very rough approximations, since the interactions between the multiply-occurring terms of d^3s are certainly not all negligible (especially in the ^3P and ^3F terms). Also, we had available only the eigenvectors corresponding to the parameters of Table I, column 6, rather than to the final set of parameters.

Configuration interaction was taken into account only as a correction to the energy terms (cf. Section 3). Therefore, no third-order eigenfunctions are available which would diagonalize all electrostatic interactions, including configuration interaction. It is for this reason that no calculations of apparent two-electron jumps could be made. This affects the transitions $d^3p-d^2s^2$ and ds^2p-d^3s.

V. THE NEW CLASSIFICATION

On the basis of energy terms and multiplet strengths it should be possible to classify all the observed terms of the three deep odd configurations of Ti *I*. It is mainly due to the relatively small number of measurements of *gf* values that several assignments remain still uncertain.

The bulk of the classification is based on the calculated terms (Tables II–IV, column *B*). Although these terms do not always fit the experimental data very closely, the deviations in most cases are small enough for the identification of the experimental terms, which alone is the final aim of this investigation. On the other hand, there are quite a number of cases where even better agreement would not help very much, because the terms are so closely spaced that the possibility of an interchange of the assignment is not outside the error of the calculation. In these cases one has to rely upon the tables of multiplet strength. For many multiplets, however, only the intensities are measured (columns *M* of Tables V–VII), whereas no data on multiplet strengths are available. When we compare the intensities (principal lines) with the calculated multiplet strengths we cannot expect more than a rough qualitative agreement in many cases. Only within the theoretical approximations dis-

TABLE Xa. Calculated multiplet strengths $d^2sp-d^2s^2$ (singlets).

d^2s	d^2s / d^2s^2 / d^2sp	^2S ^1S 1	^2S ^1S 2	^2D ^1D 1	^2D ^1D 2	^2G ^1G 1	^2G ^1G 2
^2S	$^1P°$	6	5.9	—	0.1		
	$^1S°$						
^2P	$^1P°$	—	0.0	—	0.0		
	$^1D°$			—	0.5		
	$^1P°$	—	0.1	6	5.9		
^2D	$^1D°$			10	9.4		
	$^1F°$			14	13.4	—	0.3
	$^1D°$			—	0.1		
^2F	$^1F°$			—	0.3	—	0.0
	$^1G°$					—	0.2
	$^1F°$			—	0.3	14	13.7
^2G	$^1G°$					18	17.8
	$^1H°$					22	22.0
		1×6		5×6		9×6	

TABLE Xb. Calculated multiplet strengths d^2sp-d^2s (singlets).

d^2s	d^2sp \ d^2s	^2P ^1P		$^2{}_1D$ ^1D		$^2{}_2D$ ^1D		^2F ^1F		^2G ^1G		^2H ^1H	
		1	2	1	2	1	2	1	2	1	2	1	2
^2S	$^1P°$	——	0	24.000	24	——	0						
	$^1S°$	7.00	7.0										
^2P	$^1P°$	5.25	5.5	10.125	10	23.625	24						
	$^1D°$	0.35	2.5	3.375	6	7.875	8	50.400	43				
	$^1P°$	20.35	20	2.625	3	10.125	10						
^2D	$^1D°$	6.75	6	4.375	4	16.875	16	12.000	14				
	$^1F°$			0.500	1	1.929	2	6.000	6	38.571	38		
	$^1D°$	14.40	13	21.000	19	9.000	9	3.600	9				
^2F	$^1F°$			10.500	10	4.500	5	7.875	8	50.625	51		
	$^1G°$							1.125	1	30.375	30	99.00	99
	$^1F°$			13.500	13	16.071	16	28.125	28	10.804	12		
^2G	$^1G°$							16.875	17	27.225	27	59.40	60
	$^1H°$									4.400	4	39.60	39
		3×18		5×18		5×18		7×18		9×18		11×18	

cussed in the last section can we expect quantitative agreement, when the measured line strengths are compared. It should be noted that the theoretical and experimental multiplet strengths are in general related by different scale factors for different transition arrays, as is explained in the Appendix.

In order to facilitate the comparision between the observed and the calculated terms, the energies are plotted in Figs. 1–3, for the quintet, singlet, and triplet system, respectively. All terms which have the same S and L value are plotted in the same column, so that one can easily interchange the configuration assignments. Each column shows the observed terms together with Russell's limit assignment to the left, and the calculated terms with their limits to the right. The limit assignment gives the term of the parent configuration in brackets, and bears

TABLE XI. Calculated multiplet strengths, d^2p-d^2s (singlets).

d^2	d^2p \ d^2s	^2P ^1P		$^2{}_1D$ ^1D		$^2{}_2D$ ^1D		^2F ^1F		^2G ^1G		^2H ^1H	
		1	2	1	2	1	2	1	2	1	2	1	2
	$^1S°$	1	1.0										
^2P	$^1P°$	3	2.5	−	0.1	−	0.4						
	$^1D°$	5	3.0	−	0.4	−	1.4	−	0.2				
	$^1P°$	−	0.0	3	2.3	−	0.7						
$^2{}_1D$	$^1D°$	−	0.0	5	3.1	−	1.2	−	0.8				
	$^1F°$			7	5.7	−	1.2	−	0.0	−	0.1		
	$^1P°$	−	0.5	−	0.6	3	1.9						
$^2{}_2D$	$^1D°$	−	2.0	−	0.5	5	2.4	−	0.1				
	$^1F°$			−	1.3	7	4.7	−	0.1	−	1.0		
	$^1D°$	−	0.0	−	1.0	−	0.0	5	3.9				
^2F	$^1F°$			−	0.0	−	0.3	7	6.6	−	0.1		
	$^1G°$							9	7.4	−	0.0	−	1.5
	$^1F°$			−	0.0	−	0.8	−	0.3	7	5.8		
^2G	$^1G°$							−	0.0	9	8.8	−	0.2
	$^1H°$									11	7.4	−	3.6
	$^1G°$							−	1.6	−	0.2	9	7.3
^2H	$^1H°$									−	3.6	11	7.4
	$^1I°$									−	3.6	13	13.0
		3×3		5×3		5×3		7×3		9×3		11×3	

TABLE XIIa. Calculated multiplet strengths, $d^2sp-d^2s^2$ (triplets).

d^2s	d^2sp \ d^2s^2	$(2/3)^4P+(1/3)^2P$ ^3P		$(2/3)^4F+(1/3)^2F$ ^3F	
		1	2	1	2
^2S	$^3P°$	—	0.4		
	$^3S°$	2	2.9		
^2P	$^3P°$	6	7.2		
	$^3D°$	10	9.1	—	1.3
	$^3S°$	4	3.1		
^4P	$^3P°$	12	10.3		
	$^3D°$	20	16.0	—	1.1
	$^3P°$	—	0.1		
^2D	$^3D°$	—	1.8	—	0.9
	$^3F°$			—	2.1
	$^3D°$	—	1.7	10	12.8
^2F	$^3F°$			14	18.3
	$^3G°$			18	22.0
	$^3D°$	—	1.4	20	13.9
^4F	$^3F°$			28	21.5
	$^3G°$			36	25.2
	$^3F°$			—	0.1
^2G	$^3G°$			—	6.8
	$^3H°$				
		3×18		7×18	

TABLE XIIb. Calculated multiplet strengths, d^3sp-d^3s (triplets).

d^3 / d^3s		^2P ^3P		^4P ^3P		^2_1D ^3D		^2_3D ^3D		^2F ^3F		^4F ^3F		^2G ^3G		^2H ^3H	
d^3s	d^2sp	1	2	1	2	1	2	1	2	1	2	1	2	1	2	1	2
^2S	$^3P^\circ$	——	1	——	2	72.000	67	——	1								
	$^1S^\circ$	2.333	10	42.667	26												
^2P	$^1P^\circ$	1.750	6	32.000	23	3.375	13	7.875	22								
	$^3D^\circ$	0.117	4	2.133	9	1.125	6	2.625	15	16.800	42	67.200	45				
	$^1S^\circ$	18.667	11	5.333	22												
^4P	$^1P^\circ$	14.000	11	4.000	11	27.000	21	63.000	48								
	$^3D^\circ$	0.933	3	0.267	2	9.000	9	21.000	16	134.400	95	8.400	24				
	$^3P^\circ$	60.750	59	——	0	7.875	9	30.375	30								
^2D	$^3D^\circ$	20.250	17	——	5	13.125	12	50.625	43	36.000	39	——	10				
	$^3F^\circ$					1.500	3	5.786	6	18.000	17	——	25	115.714	99		
	$^3D^\circ$	4.800	18	67.200	35	7.000	27	3.000	14	1.200	14	76.800	43				
^2F	$^3F^\circ$					3.500	13	1.500	6	2.625	12	168.000	94	16.875	72		
	$^3G^\circ$									0.375	3	24.000	18	10.125	31	33.000	98
	$^3D^\circ$	38.400	22	8.400	27	56.000	32	24.000	14	9.600	8	9.600	40				
^4F	$^3F^\circ$					28.000	18	12.000	8	21.000	14	21.000	70	135.000	93		
	$^3G^\circ$									3.000	14	3.000	5	81.000	72	264.000	213
	$^3F^\circ$					40.500	40	48.214	47	84.375	83	——	0	32.411	36		
^2G	$^3G^\circ$									50.625	37	——	4	81.675	70	178.200	164
	$^3H^\circ$													13.200	13	118.800	119
		3×54		3×54		5×54		5×54		7×54		7×54		9×54		11×54	

a subscript 1, 2, or 3, which indicates the configurations of the parent ion, $3d^24s$, $3d^3$, and $3d4s^2$, respectively. In all those cases where Russell's assignment and the proposed assignment are identical, the limit is written in the middle between the observed and the calculated term.

As an example, we see from Fig. 3 that the two $^3P^\circ$ terms based on ^4P of d^3 and d^2s, respectively, have to be interchanged in their configuration assignment. Although the calculated terms do not fit very accurately, this identification seems fairly certain. Similarly, the two $^3S^\circ$ terms of d^2sp have to be interchanged in their assignment of the parent terms ^2P and ^4P, respectively. The same is true for the two $^3S^\circ$ terms of d^3p. Here the calculated terms alone permit a unique assignment. When we now look for these terms in the tables of multiplet strength, we find these assignments completely confirmed (see especially the super-multiplet $d^2s(^4P)p\,^3SPD^\circ - d^2s^2\,^3P$, Tables VII and XIIa). In many cases the assignment is not so obvious as in the examples given above, but finally only a few doubtful assignments remain. After long and careful consideration the assignments indicated in Figs. 1–3 were adopted. It should be noted that the off-diagonal matrix elements of the configurations d^2sp and d^3p (see reference 6) are sometimes so large that a unique assignment of limits becomes rather meaningless. This is the case in most of the multiply-occurring terms based on ^2P and ^4P, or ^2F and ^4F, respectively. If the line strength tables give no indication for the identification of these terms with one or the other limit, we assign them so as to conform with Russell's classification as closely as possible. In the following we give some of the important points in which the proposed assignment differs from the current one. The details are seen from the figures and tables.

The current assignment of the quintet system is completely confirmed. Both energy terms and multiplet strengths are in satisfactory agreement (Fig. 1 and Tables V, VIII, and IX).

In the singlet system the most important

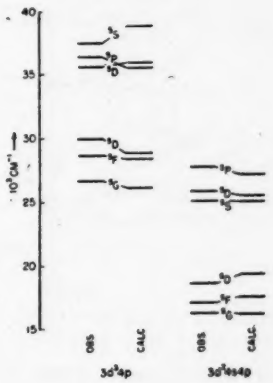

FIG. 1. The deep odd quintet terms of Ti *I*.

TABLE XIII. Calculated multiplet strengths, d^3p-d^3s (triplets).

d^3	d^3p \ d^3s	^2P ^3P 1	2	^4P ^3P 1	2	$^2{}_1D$ ^3D 1	2	$^2{}_3D$ ^3D 1	2	^2F ^3F 1	2	^4F ^3F 1	2	^2G ^3G 1	2	^3H ^3H 1	2
	$^3S°$	3	2.5	—	0.5												
^2P	$^3P°$	9	6.0	—	0.0	—	1.0	—	1.9								
	$^3D°$	15	9.9	—	4.0	—	0.0	—	0.1	—	0.1	—	1.0				
	$^3S°$	—	0.5	3	2.5												
^4P	$^3P°$	—	0.5	9	7.9	—	0.1	—	0.6								
	$^3D°$	—	4.1	15	8.9	—	0.0	—	1.4	—	0.1	—	0.3				
	$^3P°$	—	0.1	—	0.0	9	7.0	—	1.9								
$^2{}_1D$	$^3D°$	—	0.0	—	0.1	15	12.5	—	2.3	—	0.0	—	0.0				
	$^3F°$					21	15.8	—	4.7	—	0.4	—	0.0	—	0.1		
	$^3P°$	—	2.4	—	1.1	—	0.9	9	4.6								
$^2{}_3D$	$^3D°$	—	0.6	—	0.8	—	2.3	15	10.7	—	0.6	—	0.0				
	$^3F°$					—	3.3	21	13.5	—	0.1	—	0.7	—	3.4		
	$^3D°$	—	0.1	—	0.1	—	0.2	—	0.5	15	14.2	—	0.0				
^2F	$^3F°$					—	0.4	—	0.0	21	20.3	—	0.1	—	0.2		
	$^3G°$									27	25.6	—	0.0	—	0.1	—	1.4
	$^3D°$	—	0.3	—	1.1	—	0.0	—	0.0	—	0.0	15	13.7				
^4F	$^3F°$					—	0.2	—	0.8	—	0.1	21	19.9	—	0.0		
	$^3G°$									—	0.1	27	24.1	—	2.5	—	0.3
	$^3F°$					—	1.3	—	2.0	—	0.1	—	0.3	21	17.3		
^2G	$^3G°$									—	0.1	—	2.7	27	23.9	—	0.2
	$^3H°$													33	27.1	—	5.9
	$^3G°$									—	1.2	—	0.2	—	0.5	27	25.1
^3H	$^3H°$													—	5.9	33	27.1
	$^3I°$															39	39.0
		3×9		3×9		5×9		5×9		7×9		7×9		9×9		11×9	

change seems to be the reassignment of the $w^1P°$ term as $^1D°$. The limit assignment, ^2P and d^3, remains unchanged. There is a very weak line (intensity (1)) which seems to be due to a transition to a^1S of d^2s^2, and which would contradict this assignment; but this line is not listed in the new tables,[13] and the a^1S term is probably spurious.[4]

At this point one should remark on the huge multiplet strength (859) observed for the transition $a^1P-w^1P°$, in the notation of the current assignment (Table VI). Theoretically, this line

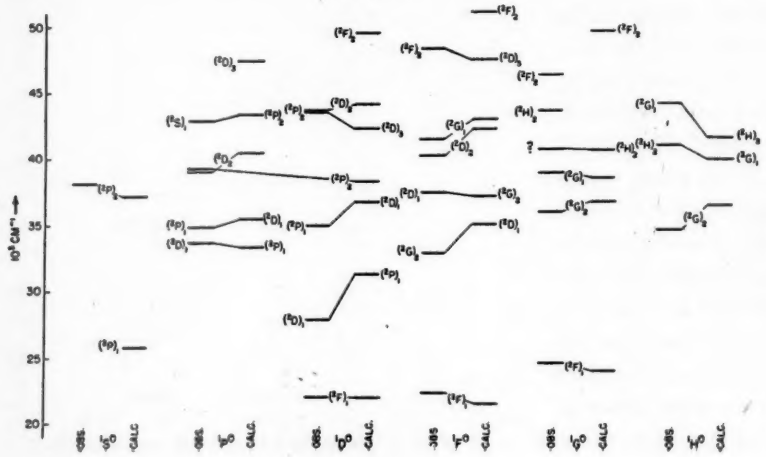

FIG. 2. The deep odd singlet terms of Ti *I*. The $^1I°$ term and the calculated terms above the ionization limit (55,138 cm^{-1}) are omitted to save space.

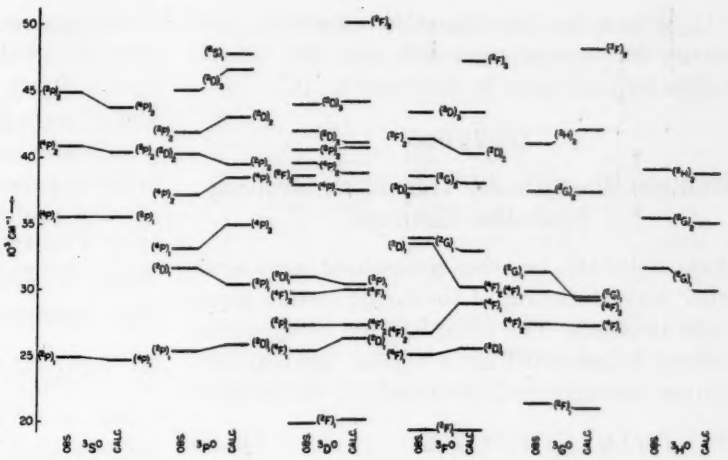

FIG. 3. The deep odd triplet terms of Ti *I*. The $^3I^\circ$ term and the calculated terms above the ionization limit (55,138 cm^{-1}) are omitted to save space.

should be weak, in agreement with the measured intensity of 5. Closer inspection shows that this line overlaps with a very strong line of Cr *I* and is no doubt mainly due to the presence of a small amount of this element.* One cannot exclude the possibility, therefore, that other abnormally strong lines which do not compare with theory might be caused by similar experimental errors.

The assignments of z and y^1P° are somewhat doubtful and may have to be interchanged restoring the original assignment. The prediction of the $^1S^\circ$ term of $3d^24s4p$ seems to be of interest.

In both the singlet and the triplet system, the terms based on ^2F of d^3 are calculated to lie much higher than was assumed by Russell, and have not been found experimentally, as far as is known to the writer. The inclusion of these terms in the traces for the calculation of the parameters of Table I, columns 1–3, seems to have been the main reason for the large discrepancies.

For the triplet system some reassignments were discussed above. In addition to this, one should note the interchange of the ^2P and ^2D limits of the $^3P^\circ$ and $^3D^\circ$ terms, and especially the reassignment of all the terms based on ^4F of d^3 and d^2s. The latter assignment seems somewhat doubtful in view of the bad fit of some of the terms and multiplet strengths with ^4F limits. A check from an other source seems, therefore, desirable. It is found in the lines connecting related terms in the Fe group. Such lines were first given by Russell.[17] He showed that one obtains smooth curves if one plots the differences between the lowest terms of $d^{n-2}sp$ and $d^{n-2}s^2$, and $d^{n-1}p$ and $d^{n-1}s$, respectively, against n. This is done in Fig. 4, which is taken from Russell's paper with the substitution of the new assignment for Ti *I*. Russell's assignment is also indicated. The new assignment is seen to give smoother curves. In addition, these curves indicate that some of the lowest terms of the configurations d^4p and d^3sp of V *I* have wrong assignments.

ACKNOWLEDGMENTS

My thanks are due first of all to Professor Henry Norris Russell for two very interesting and stimulating discussions. I would also like to thank Professor J. H. Van Vleck for helpful suggestions, and Professor G. Racah of the Hebrew University in Jerusalem for his continued interest in this work. Finally, I wish to thank Professor

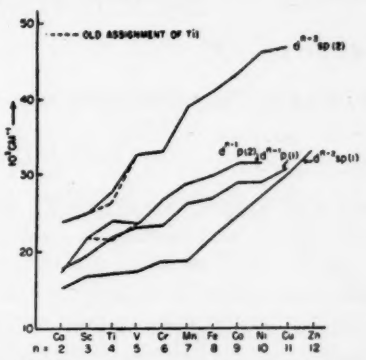

FIG. 4. Related terms in the iron group. The lowest terms of $d^{n-2}sp$ and $d^{n-1}p$ are drawn relative to the lowest terms of $d^{n-2}s^2$ and $d^{n-1}s$, respectively.

* I am indebted to Prof. D. H. Menzel for pointing this out.

[17] H. N. Russell, Astrophys. J. 66, 184 (1927).

E. B. Wilson for permission to use his electric network for secular equations, and Mr. R. H. Hughes for assistance in the work on it.

APPENDIX

Multiplet Strengths for Transitions Involving Equivalent Electrons

Let $\Psi(l^nJM)$ be the normalized anti-symmetric wave function of the configuration given in the brackets. The complete set of quantum numbers is indicated by a typical angular momentum characterized by J and M. We write

$$\psi(l^{n-1}(J')lJM)\sum_{mM'}\Psi(l^{n-1}J'M')\times\Psi(ljm)(J'jM'm|J'jJM),$$

$$\Psi(l^nJM)=\sum_{j'}\psi(l^{n-1}(J')lJM)(l^{n-1}(J')lJ\|l^nJ).$$

Here ψ is anti-symmetric only in the group of equivalent electrons.

The above equations define $\Psi(l^n)$ in terms of $\Psi(l^{n-1})$ and the coefficients of fractional parentage $(l^{n-1}l\|l^n)$. Tables of these coefficients for p^n and d^n were given by Racah.[16]

Consider now the transition $l^{n-1}l'\cdot l''-l^n\cdot l'$. In order to express its multiplet strengths in terms of the multiplet strengths of the transition $l^{n-1}l'\cdot l''-l^{n-1}l'\cdot l$ which can be calculated by means of Kronig's formulae,[14] we need the unitary transformation[16]

$$(l^{n-1}l(J_1)\cdot l'J|l^{n-1}l'(J_2)\cdot lJ)=[(2J_1+1)(2J_2+1)]^{\frac{1}{2}}W(J_1j'jJ_2;JJ').$$

This transformation changes the order in which the last two electrons are coupled to the rest. The dot separates the groups of electrons which are coupled last. The letters j, j', and J' denote the typical angular momenta of l, l', and l^{n-1}. The function W is defined as follows:[18]

$$W(abcd;ef)=\left[\frac{(a+b-e)!(b+e-a)!(e+a-b)!(c+d-e)!(d+e-c)!(e+c-d)!(a+c-f)!\times(c+f-a)!(f+a-c)!(b+d-f)!(d+f-b)!(f+b-c)!}{(a+b+e+1)!(c+d+e+1)!(a+c+f+1)!(b+d+f+1)!}\right]^{\frac{1}{2}}$$

$$\times\sum_z(-1)^z\frac{(a+b+c+d+1-z)!}{(a+b-e-z)!(c+d-e-z)!(a+c-f-z)!(b+d-f-z)!z!(e+f-a-d+z)!(e+f-b-c+z)!}.$$

Combining this transformation with the coefficient of fractional parentage we obtain

$$\Psi(l^n(J_1)\cdot l'JM)=(n+1)^{-\frac{1}{2}}\sum_P(-1)^P\psi(l^n(J_1)\cdot l_p'JM)$$

$$=(n+1)^{-\frac{1}{2}}\sum_P(-1)^{P+1}\sum_{J_2}\psi(l^{n-1}l_p'(J_2)\cdot lJM)\times(l^{n-1}l'(J_2)\cdot lJ\|l^n(J_1)\cdot l'J),$$

$$(l^nl'(J_2)\cdot lJ\|l^n(J_1)\cdot l'J)=\sum_{J'}(l^{n-1}l'(J_2)\cdot lJ|l^{n-1}l(J_1)\cdot l'J)\times(l^{n-1}(J')lJ_1\|l^nJ_1).$$

TABLE XIV. $3(d^3s(S_2L_2)\cdot d2L\|d^3(S_1L_1)\cdot s2L)^2$.

d^3s / d^3 / d^2s	^5P / ^4P	^5F / ^4F
^4P	8/5	3/5
^4F	7/5	12/5

[18] G. Racah, Phys. Rev. 62, 438 (1942).

The groups l^n and $l^{n-1}l$ consist of the electrons $1, 2\cdots p-1, p+1, \cdots n+1$, and P is the parity which exchanges p with $n+1$.

A typical matrix element of the electric dipole moment,

$$\mathbf{P}=\sum_{i=1}^{n+1}\mathbf{p}_i,$$

is therefore

$$\int\Psi^*(l^{n-1}l'(J_2)\cdot l''J'')\mathbf{P}\Psi(l^n(J_1)\cdot l'J)d\tau$$

$$=(n+1)\int\Psi^*(l^{n-1}l'(J_2)\cdot l''J'')\mathbf{p}_i\times\Psi(l^n(J_1)\cdot l'J)d\tau$$

$$=n^{-\frac{1}{2}}\sum_{P,Q,R}(-1)^{P+Q+R+1}\sum_{J_2'}\int\psi^*(l^{n-1}l_q'\times(J_2),l_r''J'')\mathbf{p}_i\psi(l^{n-1}l_p'(J_2')\cdot lJ)d\tau\cdot(l^{n-1}l'(J_2')lJ\|l^n(J_1)l'J).$$

TABLE XV. $3(d^2s(S_2L_2)\cdot d0L\,]d^3(S_1L_1)\cdot s0L)^2$.

d^2s \ d^3 \ d^3s	^1P ^2P	^1D $^2{}_1D$	^1D $^2{}_2D$	^1F ^2F	^1G ^2G	^1H ^2H
^2S		4/5				
^2P	7/10	9/20	21/20	6/5		
^2D	3/2	1/4	27/28	3/7	5/7	
^2F	4/5	21/20	9/20	3/10	3/2	3/2
^2G		9/20	15/28	15/14	11/14	3/2

TABLE XVI. $3(d^2s(S_2L_2)\cdot d1L\,]d^3(S_1L_1)\cdot s1L)^2$.

d^2s \ d^3 \ d^3s	^3P ^2P	^3P ^4P	^3D $^2{}_1D$	^3D $^2{}_2D$	^3F ^2F	^3F ^4F	^3G ^2G	^3H ^2H
^2S	——	——	4/5	——				
^2P	7/90	64/45	1/20	7/60	2/15	8/15		
^4P	28/45	8/45	2/5	14/15	16/15	1/15		
^2D	3/2	——	1/4	27/28	3/7	——	5/7	
^2F	4/45	56/45	7/60	1/20	1/30	32/15	1/6	1/6
^4F	32/45	7/45	14/15	2/5	4/15	4/15	4/3	4/3
^2G			9/20	15/28	15/14	——	11/14	3/2

The wave function ψ^* is anti-symmetrical in the group l^{n-1} consisting of the electrons $1, 2, \cdots q-1$, $q+1, \cdots r-1, r+1 \cdots n+1$. The parities of the permutations which exchange q with n, and r with $n+1$ are denoted by Q and R, respectively. The matrix element vanishes unless the two configurations differ by one electron only, and unless all corresponding electrons have the same parity. It follows, therefore, that

$$P=Q+1, \quad J_2'=J_2, \quad i=r=n+1.$$

Since there are n ways of realizing this, we obtain

$$(l^{n-1}l'(J_2)\cdot l''J''|\mathbf{P}|l^n(J_1)\cdot l'J)$$
$$=n^{\frac{1}{2}}(l^{n-1}l'(J_2)\cdot l_{n+1}''J''|\mathbf{p}_{n+1}|l^{n-1}l'(J_2)\cdot l_{n+1}J)$$
$$\times(l^{n-1}l'(J_2)lJ\,]l^n(J_1)l'J).$$

The multiplet strength now becomes

$$S(l^{n-1}l'(J_2)\cdot l''J'';\, l^n(J_1)\cdot l'J)$$
$$=nS(l^{n-1}l'(J_2)\cdot l''J'';\, l^{n-1}l'(J_2)\cdot lJ)$$
$$\times(l^{n-1}l'(J_2)\cdot lJ\,]l^n(J_1)\cdot l'J)^2.$$

The multiplet strength on the right hand side is for a transition which does not involve an equivalent electron, and can be calculated, therefore, from Kronig's formulae. The transition $l^{n-1}l'\cdot l''-l^n\cdot l'$ occurs in the Fe group as $d^{n-1}sp-d^ns$.

Similarly, one finds easily for the transition array $l^n-l^{n-1}\cdot l'$

$$S(l^nJ'(J_1);\, l^{n-1}(J_1)l'J)$$
$$=nS(l^{n-1}(J_1)lJ';\, l^{n-1}(J_1)l'J)(l^{n-1}(J_1)lJ'\,]l^nJ')^2,$$

and for $l^nl'\cdot l''-l^n\cdot l'^2$

$$S(l^nl'(J_1)\cdot l''J';\, l^n(J_1')\cdot l'^2(J_2)J)$$
$$=2S(l^nl'(J_1)\cdot l''J';\, l^nl'(J_1)\cdot l'J)$$
$$\times(l^nl'(J_1)\cdot l'J|l^n(J_1')\cdot l'l'(J_2)J)^2.$$

The unitary transformation occurring in the last equation can again be expressed in terms of the function W; one obtains[16]

$$(j_1j_2(J')\cdot j_3J|j_1\cdot j_2j_3(J'')J)$$
$$=[(2J'+1)(2J''+1)]^{\frac{1}{2}}W(j_1j_2Jj_3;\, J'J'').$$

From these formulae one can readily calculate the multiplet strengths of the transition arrays $d^n-d^{n-1}p$ and $d^nsp-d^ns^2$ occurring in the Fe group.

It is convenient to measure the absolute multiplet strength in units of the square of the radial integral over the electric dipole moment

$$\sigma=-|e|[(2l+1)(2l'+1)]^{-\frac{1}{2}}\int_0^\infty rR(nl)R(n'l')dr$$

where $R(nl)$ and $R(n'l')$ are r times the normalized radial parts of the one-electron wave functions of the initial and final state of the jumping electron. Since these functions differ for different configurations, the values of S are not comparable between different transition arrays. With this normalization

$$\sum_{s_2L_2L''} S(l^{n-1}l'(S_2L_2)\cdot l''SL'';\, l^n(S_1L_1)\cdot l'SL)$$
$$=(n/2)(2S+1)(2L+1)(l+l''+1)(2l''+1).$$

These sums are indicated in Tables VIII–XIII.

As a numerical example we may calculate the array d^2sp-d^3s of Ti *I*. The parentage coefficients of multiplet strength $3(d^2s(S_2L_2)\cdot dSL\,]d^3(S_1L_1)\cdot sSL)^2$, which result from the above equations that are listed in Tables XIV–XVI for the quintet, singlet, and triplet system, respectively. They agree with those calculated by Menzel and Goldberg.[19] However, these authors

[19] D. H. Menzel and L. Goldberg, Astrophys. J. **84**, 1 (1936)

were not able to separate the parentages of multiply occurring terms. The formulae derived above overcome this difficulty.

Kronig strengths for a great number of transitions were calculated by Goldberg.[20] His tables have to be multiplied by suitable factors to comply with the normalization adopted above.[21] From the Kronig strengths for $d^2s \cdot p - d^2s \cdot d$ and the parentages of Tables XIV–XVI we then obtain the multiplet strengths for $d^2s \cdot p - d^3 \cdot s$ as listed in Tables VIII, X, and XII, column 1. When these values are summed over the multiply-occurring terms of both configurations one obtains the multiplet strengths listed by Goldberg.[20]

In the same fashion other tables of multiplet strength relevant to Ti *I* are calculated and are given in Tables IX–XIII, column 1.

[20] L. Goldberg, Astrophys. J. **82**, 1 (1935).
[21] L. Goldberg, Astrophys. J. **84**, 11 (1936).

PHYSICAL REVIEW VOLUME 74, NUMBER 10 NOVEMBER 15, 1948

The Zeeman Effect in Microwave Molecular Spectra*

C. K. JEN
Cruft Laboratory, Harvard University, Cambridge, Massachusetts

(Received July 26, 1948)

A microwave cavity spectroscope is described, which possesses a high sensitivity and resolution for the observation of the Zeeman effect of molecular absorption lines in the microwave frequency range. The theory of operation for this spectroscope and the criteria for sensitivity are formulated.

The Zeeman effect of a number of microwave spectral lines has been measured for the gas molecules $N^{14}H_3$, $N^{15}H_3$, and CH_3Cl^{35} and observed for CH_3Cl^{37} and SO_2. All the experimental results obtained so far can be satisfactorily explained by the combined magnetic contribution due to nuclear and molecular g factors, if there exists a spin-rotation coupling, or solely by the magnetic contribution due to molecular rotation, if there is no such coupling. Thus, further knowledge of the nuclear and molecular magnetic properties of molecules can be obtained through the examination of the Zeeman effect in microwave absorption spectra.

I. INTRODUCTION

THROUGHOUT the history of atomic spectra, the study of the Zeeman effect has provided an exceedingly powerful tool in elucidating the mechanism of the emission and absorption of radiation energy. It gave a great impetus to the early electron theory by emphasizing the important role of the electron in the radiation process. It laid a physical basis for the theory of space quantization, which is an important feature of the quantum theory. Then, the unassailable evidence of the "anomalous" Zeeman effect which had puzzled physicists for a quarter of a century finally led, together with the phenomenon of multiplet structure, to the introduction of the electron spin hypothesis. It soon became clear that an analogous situation existed in the atomic hyperfine structure, where the nuclear spin played a role similar to that of the electron spin in the atomic fine structure. The Zeeman effect became again instrumental in clarifying the situation through the effect of the magnetic moment, associated with the nuclear spin, in an external magnetic field.

The advent of microwave techniques in recent years has given rise to a new branch of spectroscopy. It has been found that a microwave system used as a spectroscopic instrument is capable of a very high resolving power, essentially because the frequency is directly measurable. Such a property can be used to great advantage for investigating the Zeeman effect, since measurements are possible with hyperfine line splittings in a fairly weak magnetic field,

* The research reported in this document was made possible through support extended Cruft Laboratory, Harvard University, jointly by the Navy Department (Office of Naval Research) and the Signal Corps, U. S. Army, under Contract N5ori-76, T. O. 1.

whereas similar measurements in optical atomic spectra would require enormously high fields. Moreover, the fact that microwave frequencies fall mostly in the range of molecular rotational frequencies means that some of the molecular properties can also be studied through the Zeeman effect.

II. A MICROWAVE CAVITY SPECTROSCOPE

There are essentially two requirements that must be satisfied for a microwave spectroscope to be used in connection with experiments on the Zeeman effect. First, the spectroscope must fulfill the usual function of exhibiting the intensity of a spectral line as a function of frequency. In so doing, it must possess the desired degree of sensitivity and resolving power. Second, a magnetic field of sufficient strength and uniformity must be applied to the absorbing specimen. A consideration of these requirements has led to the adoption of a resonant cavity as the absorption cell in the present experiment.

A. Theory of a Gas-Filled Resonant Cavity

The resonant property of a cavity may be characterized by a loss factor δ, which is the ratio of the energy lost per radian to the stored energy, and a resonant frequency ν_0. If there is only one coupling hole between the cavity and a wave guide as in the case of a reflection cavity, then the reflection factor Γ_0 of an empty cavity,[1] defined as the ratio of the complex amplitude of the reflected wave to that of the incident wave, is, for the case $\nu \doteq \nu_0$,

$$\Gamma_0 = \frac{2\delta_1}{\delta_1+\delta_0+i2[(\nu-\nu_0)/\nu_0]} - 1, \qquad (1)$$

where $\delta_0 = \delta$-factor due to energy loss in the cavity wall, $\delta_1 = \delta$-factor due to energy loss through the window, $\nu =$ frequency of the incident wave, $\nu_0 =$ resonant frequency of the empty cavity, and $i = (-1)^{\frac{1}{2}}$. If the cavity is now filled with a low pressure gas, then the reflection factor Γ_g would be the same as in Eq. (1), except that ν_0 should now be replaced by $\nu_0/(\epsilon)^{\frac{1}{2}}$, where $\epsilon = \epsilon' - i\epsilon''$, the complex dielectric constant of the gas. In the case of resonance absorption, the real and imaginary parts of ϵ are given as follows[2] ($\nu \doteq \nu_g$):

$$\epsilon' = 1 + (A\nu_g/2)[(\nu_g-\nu)/((\Delta\nu)^2+(\nu-\nu_g)^2)], \qquad (2)$$

$$\epsilon'' = (A\nu_g/2)[\Delta\nu/((\Delta\nu)^2+(\nu-\nu_g)^2)], \qquad (3)$$

where $\nu_g =$ resonant frequency of a gas molecule, $\Delta\nu =$ "half-breadth" of a spectral line, $A =$ dimensionless constant dependent on the nature of gas, pressure, temperature, etc. We can assume for most gases at a low pressure $\epsilon'' \ll \epsilon' \doteq 1$. Hence, the reflection factor Γ_g for a gas-filled cavity is

$$\Gamma_g = \frac{2\delta_1}{\delta_1+\delta_0+\epsilon''+i2[((\epsilon')^{\frac{1}{2}}\nu-\nu_0)/\nu_0]} - 1. \qquad (4)$$

It may be seen from Eq. (1) that $|1+\Gamma_0|^2$ as a function of ν is representable by a simple resonance curve, while Eq. (4) indicates that $|1+\Gamma_g|^2$ is representable by a "double-hump" resonance curve with a dip in the middle, if $\nu_g = \nu_0$ and $\Delta\nu/\nu_g \ll (\delta_1+\delta_0)/2$ (i.e., the spectral line breadth is much narrower than the breadth of the cavity response curve). A spectral line can thus be shown in the midst of a cavity resonance curve, as illustrated in Fig. 1.

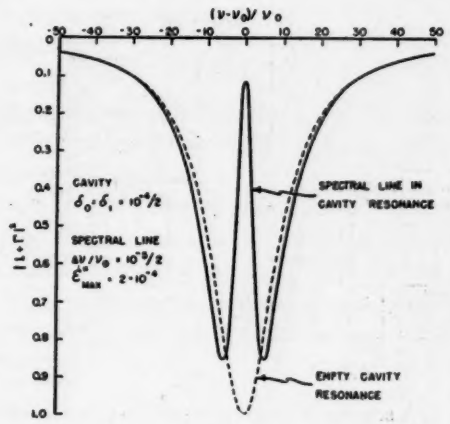

FIG. 1. Theoretical curve of a spectral line in cavity resonance.

B. Spectroscopic Sensitivity

As a measure of the spectroscopic sensitivity, the minimum detectable absorption coefficient will now be derived. The largest change of the reflection factor resulting from the introduction

[1] C. K. Jen. J. App. Phys. **19**, 649 (1948).

[2] P. Debye, *Polar Molecules* (Reinhold Publishing Corporation, New York, 1929), Chap. V.

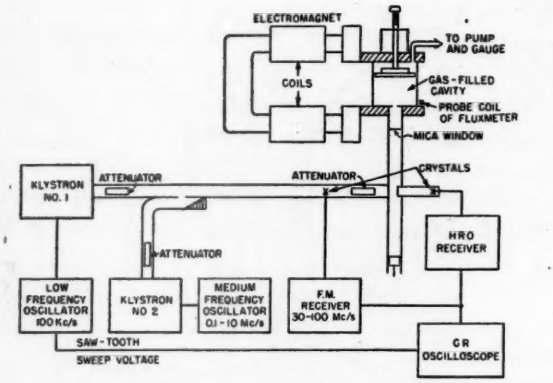

FIG. 2. A schematic diagram of the complete system for measurements of microwave Zeeman spectra.

of the absorbing gas occurs at $\nu=\nu_0=\nu_g$. Let V_0 represent the voltage amplitude of the incident wave, then the change in voltage caused by resonance absorption is, according to Eqs. (1) and (4), with $\epsilon''\ll\delta_1+\delta_0$,

$$\Delta V=V_0(\Gamma_0-\Gamma_g)_{\nu=\nu_0=\nu_g}=[2\delta_1/(\delta_1+\delta_0)^2]\epsilon''V_0. \quad (5)$$

Maximizing ΔV relative to the parameter δ_1 leads to the condition $\delta_1=\delta_0$. Let $\delta_1+\delta_0=\delta=1/Q$, where Q is the "loaded" Q factor of the cavity, then the maximum value of ΔV is

$$(\Delta V)_{\max}=Q\epsilon''V_0. \quad (6)$$

For minimum detectability, this voltage should be equated[3] to the r.m.s. voltage associated with thermal noise $(\overline{V_n^2})^{\frac{1}{2}}=(4kTN\Delta fZ_0)^{\frac{1}{2}}$, where k=Boltzmann's constant, T=absolute temperature, N="noise figure," Δf=band width of the receiver, and Z_0=characteristic impedance of the wave guide. Using the usual relation $\alpha=(2\pi/\lambda)(\epsilon''/(\epsilon')^{\frac{1}{2}})\doteq(2\pi/\lambda)\epsilon''$, where α=absorpsion coefficient due to gas and λ=free space wave-length, we have for the minimum detectable α

$$(\alpha)_{\min}=(4kTN\Delta f/P_0)^{\frac{1}{2}}(2\pi/Q\lambda), \quad (7)$$

in which $P_0=V_0^2/Z_0$, the incident power. It is well known that the factor $Q\lambda/2\pi$ in Eq. (7) is the cavity equivalent of the absorption path length in free space. Thus a high Q cavity is required for high spectroscopic sensitivity.

As a numerical example, assume $T=293°$K, $Q=10^4$, $\lambda=1.25$ cm, and the following two cases: (a) $N=100$, $\Delta f=3000$ c.p.s., $P_3=10^{-4}$w, then $(\alpha)_{\min}=0.35\times10^{-8}$ cm^{-1}; (b) $N=31.6$, $\Delta f=30$ c.p.s., $P_0=10^{-3}$w, then $(\alpha)_{\min}=0.62\times10^{-10}$ cm^{-1}. Case (a) represents very nearly the condition of the present experiment, while case (b) may perhaps be achievable with further improvement of technique.

[3] R. V. Pound, Proc. I.R.E. **35**, 1414 (1947).

C. Cavity Design

It was shown in Eq. (7) that for use in a sensitive spectroscope, a cavity must possess a high Q-factor, while maintaining the condition of "match," $\delta_1=\delta_0$. Yet, this Q-factor should be smaller (e.g., ten times) than what might be described as the Q-factor of a spectral line, $\nu/2\Delta\nu$. This latter condition is to allow almost the whole of a spectral line to be well within the most sensitive portion of the cavity resonance.[4] Thus, for a microwave frequency ν of about 24,000 Mc/sec. in the K-band, and a spectral line breadth $\Delta\nu$ of about 0.12 Mc/sec., then the cavity Q-factor should be of the order of 10^4. A cavity with this Q would be equivalent to about 20 meters of absorption path and would have the sensitivity mentioned in the preceding section. However, it has been found difficult to attain such a Q-factor, with the linear dimensions of the cavity comparable to one-half of the wave-length in the cavity. One should therefore use the resonances occurring at higher modes in a larger cavity, since the Q-value of such a cavity would increase almost in proportion with the linear dimensions. A larger cavity is also more favorable from the standpoint of "intensity saturation" of spectral lines (cf. the following section).

In view of the above discussion, we have adopted for use in our K-band spectroscope a cylindrical cavity of the size ordinarily used as an X-band wave meter. This cavity has an inner diameter of 4.952 cm and a tunable length roughly 2.1 to 3.4 cm. At any particular frequency, the cavity can be tuned to any one of approximately twenty modes which have Q-values varying from twice 10^4 to many times less. This situation is conveniently adaptable to meeting various requirements of observation.

[4] The other alternative is to make $Q\gg\nu/2\Delta\nu$ and thus "trace out" a spectral line with the cavity resonance. This will call for exceedingly high cavity Q-factors for narrow spectral lines.

For the study of the Zeeman effect, the end plates of the cylindrical cavity serve as pole pieces for the electromagnet. They are made of magnetic steel, silver-plated on the inside to maintain high conductivity. In terms of the classical Zeeman effect, one observes the π-components, when the microwave electric field is parallel to the steady (axial, in this case) magnetic field, or the σ-components when the two fields are perpendicular.

D. Microwave Circuit

The choice of the microwave circuit, together with the methods of modulation, detection, and amplification, should be consistent with the implications contained in Eq. (7). The objective is obviously to keep the factor $N\Delta f/P_0$ as low as possible for high sensitivity. There is, however, an upper limit for the incident power on account of the effect of "intensity saturation." This means that the gas absorption coefficient will drop and the spectral line will broaden, if P_0 exceeds a limiting value, which is essentially a direct function of the total number of absorbing gas molecules. With a given cavity size and an operating pressure, which determines a desired line breadth, the limiting incident power is a well defined quantity. The noise figure is a result of random disturbances from many sources: klystron, crystal detector, amplifier, etc. It is currently believed that a major portion of this noise, particularly that arising from the crystal detector, is an inverse function of frequency. This suggests the desirability of using a modulation technique so that the signal can be detected and amplified at an intermediate frequency. The band width Δf should be narrow to minimize noise, but, if we are going to use a frequency modulation such as that produced by a saw-tooth voltage on the repeller plate of the klystron, Δf has to be wide enough to secure a complete representation of a spectral line. Let D = maximum microwave frequency displacement caused by a modulation voltage, f_s = repetition or sweep rate of the frequency modulation, n = a number large enough to include many Fourier harmonic terms for accurate representation of the spectral line, and $\Delta\nu$ = half-breadth of the spectral line; then we can derive the following expression

$$f_s = \Delta f \Delta\nu / nD. \tag{8}$$

Eq. (8) shows that, for a given $\Delta\nu$, the quantity f_sD must be kept low enough as to achieve a satisfactorily small Δf.

Figure 2 gives a complete schematic diagram of the microwave circuit adopted for the present experiment, including arrangements for the magnetic field and measurement of frequency differences to be discussed later. Klystron No. 1 (a 2K33 tube) sends a radiation along a K-band wave guide through two attenuators. The wave splits into two components at the "magic tee," one going toward the resonant cavity and the other toward the tuning plunger. The vector difference of the two reflected waves will go through the E-plane arm of the magic tee and finally to the crystal. If the two wave guide arms are exactly equal, the amplitude of the voltage received at the output crystal, V_R, is then

$$V_R = (|1+\Gamma|/2)V_0, \tag{9}$$

which shows that we now have an experimental representation of the factor $|1+\Gamma|$, already theoretically discussed in Eqs. (1) and (4).

Since it has been shown above that crystal detection is more favorable at an intermediate frequency from the point of view of low noise figure, we have adopted a frequency-modulation scheme first suggested by Hershberger.[5] The repeller plate of the Klystron is modulated by a sinusoidal voltage with a frequency around 100 kc, in addition to the saw-tooth voltage sweep. Reception at this frequency or a higher harmonic is, in this instance, accomplished by an HRO

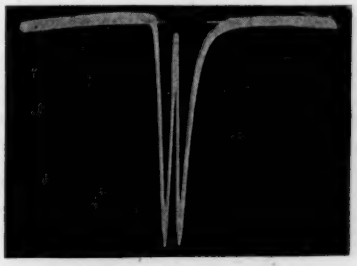

FIG. 3. Oscilloscopic pattern for a spectral line in cavity resonance.

[5] At the Symposium on Molecular Structure and Spectroscopy, Ohio State University, Columbus, Ohio (June 9–14, 1947).

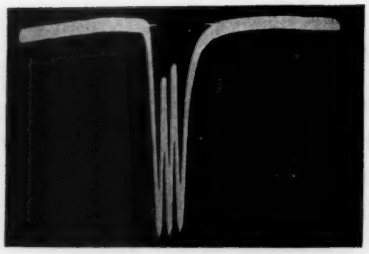

FIG. 4. Zeeman splitting of a spectral line in cavity resonance at $H=700$ oersteds.

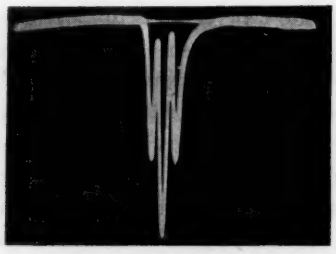

FIG. 5. Zeeman splitting of a spectral line in cavity resonance at $H=1200$ oersteds.

receiver, and the output is applied to the vertical plates of an oscilloscope. The horizontal plates of the oscilloscope are driven by the same saw-tooth voltage that sweeps the klystron at a rate of about 20 c.p.s. Some characteristics of this system are typified by the numerical example in case (a) in Section B of Part II.

Figure 3 is an experimental curve for a spectral line ($N^{14}H_3$)($JK=88$) in the middle of a cavity resonance curve (at a pressure of about 10^{-2} mm Hg), a verification of the theory illustrated in Fig. 1.

E. Zeeman Splitting and Frequency Measurement

The Zeeman effect of the microwave spectral lines can now be very readily studied by applying an axial magnetic field as shown in Fig. 2. Only a weak field, continuously variable from 0 up to 1670 oersteds, has been used thus far in this experiment. The field strength is measured by means of a small search coil connected in series with a Rawson fluxmeter, and the mean field inside the cavity is estimated from the results of probing another similar but cut-away cavity. The maximum non-uniformity of field has been found to be about four percent from the mean value.

Figure 4 shows a typical Zeeman doublet pattern for the $N^{14}H_3$ $JK=88$ line in a field of about 700 oersteds, and Fig. 5 shows the splitting at about 1200 oersteds. The spectral resolution is partly limited by the natural breadth of the spectral line and partly by the non-uniformity of the magnetic field. The limit of resolution for the present apparatus is roughly of the order of 250 kc.

The method of measuring frequency differences for the Zeeman splitting is also shown in Fig. 2. The radiation from Klystron No. 2 forms a variable beat frequency with that of Klystron No. 1, which is being linearly swept, as a result of the mixer action of the crystal situated just before the second attenuator. The f-m receiver selects a beat frequency that is coincident with its own tuning and presents a pip on the scope. If frequency modulation is applied to Klystron No. 2, then there is an evenly spaced line spectrum on each side of the pip, with the spacing between any two adjacent lines equal to the modulation frequency itself. Thus the difference frequency between any two Zeeman components can be measured by matching the variable measuring pips to the Zeeman components. This procedure is shown in Fig. 6.[6]

III. ZEEMAN SPECTRA AND INTERPRETATION

The Zeeman effect in the microwave region was first observed by Coles and Good[7] in the inversion spectrum of ammonia. They applied a magnetic field of 6600 oersteds to a coil of wave guide containing the absorbing gas and found a doublet splitting when the magnetic field was perpendicular to the microwave electric field. No interpretation of the effect was given in their paper.

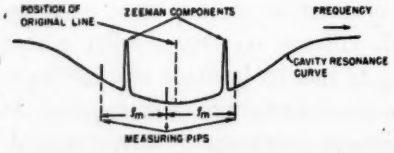

FIG. 6. Measurement of frequency difference for Zeeman splitting.

[6] The use of this modulation spectrum as a frequency-difference indicator instead of the single pip movable with the tuning of the f-m receiver is to obviate any difficulties arising from the inherent instability of the Klystron No. 2.

[7] D. K. Coles and W. E. Good, Phys. Rev. **70**, 979 (1946).

In this paper, the Zeeman effect for the microwave spectra of several gases,[8,9] including $N^{14}H_3$, $N^{15}H_3$, CH_3Cl^{35}, CH_3Cl^{37}, and SO_2 has been investigated, using a resonant cavity as the absorption cell and a weak but perhaps more uniform magnetic field. On the basis of quantitative data obtained for the first three of these gases, satisfactory interpretations of the phenomena can be made in terms of nuclear and molecular magnetic moments, which will be explained in the following sections.

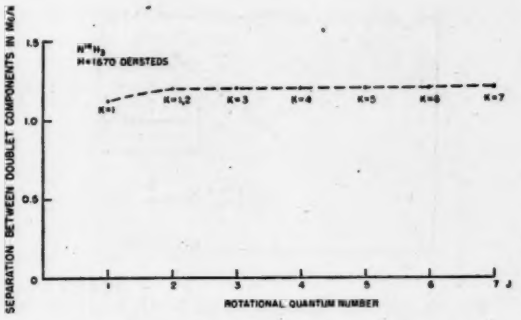

FIG. 8. Zeeman splitting of $N^{14}H_3$ inversion lines.

A. Zeeman Spectra of $N^{14}H_3$ Inversion Spectrum

The inversion spectrum of $N^{14}H_3$ has the distinction of being historically the first and so far the most attractive subject of investigation in microwave spectroscopy. In particular, it was in this spectrum that the hyperfine structure of a microwave spectral line was first discovered by Good[10] and later successfully explained by Van Vleck and his collaborators[11] and by Coles and Good[7] in terms of the nuclear quadrupole moment coupling. More recently, Hendersen and Van Vleck[12] have introduced an additional coupling term due to the nuclear magnetic moment interacting with the magnetic field set up by the molecular rotation. This term, though smaller than that of the nuclear quadrupole coupling, appears to be a necessary inclusion for closer agreement with experiment.

To study the Zeeman effect of this spectrum, we have here applied a magnetic field perpendicular to the microwave electric field for a TE-mode in the cavity. It was found that each line in the hyperfine structure was split in the manner shown in Fig. 4 or 5. Figure 7 shows the Zeeman pattern for each group of such lines characterized by the same JK value (J=quantum number of the total angular momentum, and K=quantum number of the component of the angular momentum about the figure axis). It is seen that each line is split into a doublet. Measurements have further shown that the doublet separation is essentially the same for the central line as for any one of the satellite lines.

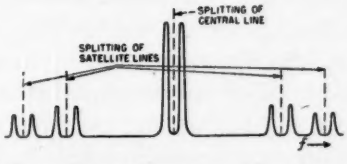

FIG. 7. Zeeman splitting of an $N^{14}H_3$ line and its satellite lines.

When the Zeeman effect of the central line is studied at a constant magnetic field from one JK line to another, it was found that the doublet separation is approximately independent of the quantum numbers (see Fig. 8).

The variation in the doublet separation as a function of the magnetic field follows very nearly a linear relationship. A typical curve is shown in Fig. 9 for the $JK=33$ line, with the result $2\Delta\nu/\Delta H=0.718$ Mc/sec. per 1000 oersteds. It is evident, therefore, that we are dealing with a first-order Zeeman effect.

B. Discussion of the $N^{14}H_3$ Zeeman Spectrum

The standard interpretation of the Zeeman effect is based upon the existence of a permanent magnetic moment along the direction of the magnetic field. For the first-order Zeeman effect, the frequency separation between the Zeeman components is proportional to the magnetic field and another factor which is related to the permanent magnetic moment. Thus we may have

$$\Delta\nu=g(\mu_0/h)H, \tag{10}$$

where $\Delta\nu$=difference between the frequency of a Zeeman component and that of the undisplaced line ($\frac{1}{2}$ of the frequency separation between

[8] C. K. Jen, Phys. Rev. **72**, 956 (1947).
[9] C. K. Jen, Bull. Am. Phys. Soc. **23**, May; No. 3 (April, 1948); Phys. Rev. **73**, 1237 (1948).
[10] W. E. Good, Phys. Rev. **70**, 213 (1946).
[11] B. P. Dailey, R. L. Kyhl, M. W. P. Strandberg, J. H. Van Vleck, and E. B. Wilson, Jr., Phys. Rev. **70**, 984 (1946).
[12] R. S. Hendersen and J. H. Vleck, Phys. Rev. **74**, 106–107 (1948).

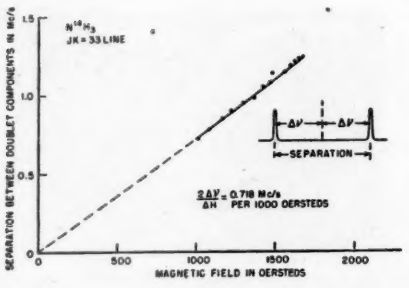

FIG. 9. Zeeman splitting of an $N^{14}H_3$ line as a function of the magnetic field.

two symmetric doublet components), μ_0 = nuclear magneton $= eh/4\pi Mc$, M = proton mass, h = Planck's constant, and g = gyromagnetic ratio or the g-factor. We see from Eq. (10) that the experimental result for a given Zeeman splitting may be concisely stated in terms of the corresponding g-factor. Referring to Figs. 8 and 9, the g-factor for most of the $N^{14}H_3$ lines is of the order of 0.47. It follows that any plausible interpretation of the Zeeman spectra for $N^{14}H_3$ must be able to account for the correct magnitude of the g-factor, the doublet structure of the Zeeman pattern and also the approximate independence of this g-factor as a function of the quantum numbers.

There are at least three possible sources of permanent magnetic moments for an $N^{14}H_3$ molecule: the N^{14} nuclear nuclear magnetic moment, the nuclear magnetic moments due to the three H nuclei and the molecular moment due to rotation. The last one is understood here to include all the magnetic contributions due to orbital motion of all nuclei and electrons in the molecule. The contribution due to the three H nuclei may be ruled out, because the g-factor for a proton, about 5.6, is much to high for any agreement with the experimental g-factor, which is approximately ten times smaller.

It is only necessary now to deal with the interactions between the external magnetic field and the two remaining magnetic moments, one due to N^{14} nuclear spin and the other due to molecular rotation. In the absence of an external field, there exists a spin-rotation coupling, as mentioned above, which gives rise to the hyperfine structure. If, in the presence of the field, the Zeeman splitting is less than the hyperfine structure spacing, the spin-rotation coupling is still in effect. Such a field is usually described by the term "weak," a common restriction in the study of the Zeeman effect. However, as the field is raised beyond this range, the spin-rotation coupling begins to break down gradually, until the field is strong enough to break up the coupling completely (Paschen-Back effect). In the following, a general theory of the Zeeman effect will be developed for the coupling between the spin of a single nucleus and molecular rotation.

C. Theory of Zeeman Splitting for Spin-Rotation Coupling

When the Zeeman effect is smaller than the spin-rotation interaction, we can start with the unperturbed Hamiltonian $\mathcal{H}_0$ describable by a diagonal matrix in the system of representation labeled by $JIFM$, where J = angular momentum quantum number of the molecule, I = nuclear spin quantum number, $F = J+I, J+I-1, ---, J-I+1, J-I$, and $M = F, F-1, ---, -F+1, -F$. The eigenvalues of $\mathcal{H}_0$, W_0, are the energy levels of the unperturbed states labeled in the same way, except that the energy is now independent of M (i.e., each JIF state has a $(2F+1)$-fold degeneracy). The total Hamiltonian $\mathcal{H}$, including the interactions of the external field with the nuclear and molecular magnetic moments, is

$$\mathcal{H} = \mathcal{H}_0 - g_{\text{mole}}\mu_0 \mathbf{J}\cdot\mathbf{H} - g_N\mu_0 \mathbf{I}\cdot\mathbf{H}, \qquad (11)$$

where g_{mole} = g-factor of the molecule along J, g_N = g-factor of the nucleus coupled with the molecule, μ_0 = nuclear magneton, $\mathbf{J},\mathbf{I}$ = vector operators of J, I, and H = external magnetic field. The solution for Eq. (11), with the aim of finding its eigenvalues, is almost exactly the same as the case of the Russell-Saunders coupling in atomic spectra. The only essential difference is that while the g-factors for electron spin and orbital motion are definitely related (ratio = 2:1), the g-factors here, g_{mole} and g_N, are not related at all. We can therefore follow the same procedure of solution,[13] while preserving the identities of the g-factors, and arrive at the following results, which can also be obtained from vector

[13] E. U. Condon and G. H. Shortley, *The Theory of Atomic Spectra* (Cambridge University Press, 1935) Chapter XVI.

model considerations.[14]

$$W=W_0(JIF)-M\mu_0H\{\alpha_J g_{\text{mole}}+\alpha_I g_N\}, \quad (12)$$

where

$$\alpha_J=[F(F+1)+J(J+1)-I(I+1)]/2F(F+1)$$

and

$$\alpha_I=[F(F+1)+I(I+1)-J(J+1)]/2F(F+1).$$

It is worth noting that in Eq. (12), if we let $g_t=\alpha_J g_{\text{mole}}+\alpha_I g_N$ we may say g_t is a total g-factor, which is a linear combination of g_{mole} and g_N with the combination coefficients α_J and α_I as functions of the quantum numbers.

The frequency displacement of any Zeeman component relative to the zero-field position of a hyperfine line can be readily calculated from the following

$$\Delta\nu(J_1F_1M_1\rightarrow J_2F_2M_2)=(\mu_0H/h)\{(Mg_t)_2-(Mg_t)_1\}, \quad (13)$$

where the change of quantum numbers has to obey the usual selection rules: $\Delta J=0, \pm1$; $\Delta F=0, \pm1$; $\Delta M=0, \pm1$. It is understood that the nuclear spin remains constant ($\Delta I=0$), and the axial quantum number K suffers no change ($\Delta K=0$) for transitions in linear and symmetric molecules.

The intensity of any Zeeman component can be calculated from the standard formulas used in atomic Zeeman spectra with only slight changes in notation.[13]

D. Interpretation of the $N^{14}H_3$ Zeeman Spectra

For the Zeeman splitting of the $N^{14}H_3$ inversion spectrum, Eq. (13) takes the following form for $\Delta J=0$ and $\Delta M=\pm1$ (σ components, normally observed in this experiment).

(a) Central line Zeeman components ($\Delta F=0$):

$$\Delta\nu_0=\pm\frac{\mu_0H}{h}\left\{\frac{g_{\text{mole}}+g_N}{2}+\frac{J(J+1)-I(I+1)}{F(F+1)}\frac{(g_{\text{mole}}-g_N)}{2}\right\}. \quad (14)$$

(b) Satellite line Zeeman components ($\Delta F=\pm1$) for satellites closer to central line:

$$\Delta\nu_s=\Delta\nu_0+\frac{M\mu_0H}{h}\left(\frac{1}{J+2}-\frac{1}{J}\right)\times\frac{J(J+1)-I(I+1)}{J+1}\frac{(g_{\text{mole}}-g_N)}{2} \quad (15)$$

where, $-J\leq M\leq J$, for satellites further from central line:

$$\Delta\nu_s'=\Delta\nu_0+\frac{M\mu_0H}{h}\left(\frac{1}{J+1}-\frac{1}{J-1}\right)\times\frac{J(J+1)-I(I+1)}{J}\frac{(g_{\text{mole}}-g_N)}{2} \quad (16)$$

where $-(J-1)\leq M\leq J-1$. It is commonly accepted that $I(N^{14})=1$, and it follows that $F=J+1, J, J-1$. We note that the theoretical Zeeman pattern may generally be quite complicated and much dependent on the quantum numbers. There is, however, one important special case, namely $J=I$, for which the equations reduce simply to

$$\Delta\nu_0=\Delta\nu_s=\Delta\nu_s'=\pm\frac{\mu_0H}{h}\frac{g_{\text{mole}}+g_N}{2}. \quad (17)$$

This means, for the $JK=11$ line of $N^{14}H_3$, the Zeeman splitting is strictly a doublet and has the same doublet separation for the satellite lines as for the central line. We can thus determine a value for g_{mole} from the expression $(g_{\text{mole}}+g_N)/2=g_{11}$, where g_{11} is the experimental g-value for the $JK=11$ line. Using $g_N(N^{14})=0.403$ from published nuclear resonance data and $g_{11}=0.44$ from the present experiment, we arrive at the result $g_{\text{mole}}(N^{14}H_3)=0.48\pm0.03$,

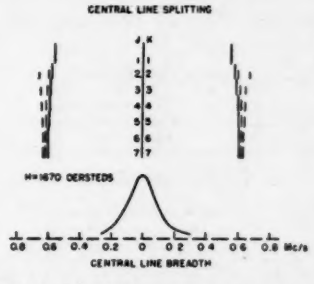

FIG. 10. Calculated Zeeman spectrum for $N^{14}H_3$ lines with $g_N=0.403$ $g_{\text{mole}}=0.48$.

[14] S. Goudsmit and R. F. Bacher, Zeits. f. Physik **66**, 13 (1930).

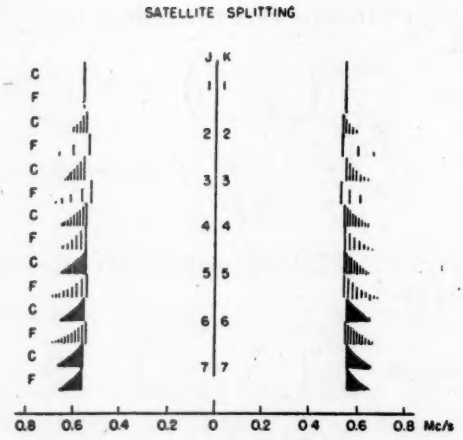

FIG. 11. Calculated Zeeman spectrum for the satellite lines of $N^{14}H_3$ lines with $g_N=0.403$ and $g_{mole}=0.48$ and $H=1670$ oersteds, (C) that satellite close to central line, (F) that satellite further from central line.

taking into account the inhomogeneity of the magnetic field and other experimental errors.

While g_{mole} may itself depend upon the values of J and K, we can at least temporarily assume that the same g-value holds true for higher JK values and examine the theoretical results from Eqs. (14), (15), and (16). It is clear from these equations that the departure from the strict doublet relationship is proportional to $g_{mole}-g_N$, with the coefficient of proportionality a function of the quantum numbers. However, the fact that g_{mole}, in the case of $N^{14}H_3$, is so close to g_N makes the contribution from the $g_{mole}-g_N$ term sufficiently small so that the experimental Zeeman pattern appears to be a doublet within the limits of resolution and the frequency separation is sensibly independent of the quantum numbers. This statement is well supported by the theoretical results calculated from Eqs. (14), (15), and (16). Figure 10 shows the calculated splittings for the central line bearing various $J=K$ designations and Fig. 11 the same for the satellite lines. It can thus be concluded that within the limits of resolution, the calculated patterns are in good agreement with experiment and that g_{mole} does not depend strongly on the J and K values.

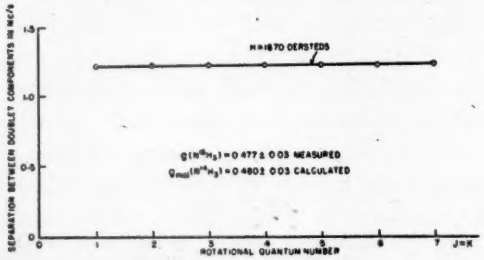

FIG. 12. Zeeman splitting of $N^{15}H_3$ inversion lines.

E. Experimental Results and Interpretation for $N^{15}H_3$ Zeeman Spectra

Since it is known that $I(N^{15})=\frac{1}{2}$, there cannot be any nuclear quadrupole coupling by theory and no trace of hyperfine structure has been found in experiment.[11] The Zeeman splitting in this case should therefore depend exclusively on the molecular g-factor,

$$\Delta\nu=\pm g'_{mole}(\mu_0 H/h), \tag{18}$$

where $g'_{mole}=g_{mole}(N^{15}H_3)$. Now, $g(N^{15}H_3)$ should be slightly less than $g(N^{14}H_3)$ because of the somewhat larger reduced mass resulting from the heavier isotope. A calculation shows, however, that this difference is quite negligible relative to the accuracy of the present experiment. Thus we may take $g(N^{15}H_3)\doteq g(N^{14}H_3)$. This indicates the prospect of verifying the calculated result for $N^{14}H_3$ by the experimental result for $N^{15}H_3$.

Experiments have been performed on the Zeeman splitting of the $N^{15}H_3$ inversion spectrum, following published frequencies.[15] A doublet splitting has been found for all the lines observed in this experiment and the separation is indeed sensibly independent of the quantum numbers for the case $J=K$. Figure 12 shows a plot of these results and also a comparison of the experimental $g(N^{15}H_3)$ with the calculated g_{mole} ($N^{14}H_3$). The agreement between the two is seen to be quite satisfactory, thus furnishing a further evidence for the interpretation of the $N^{14}H_3$ Zeeman spectra.

F. Zeeman Effect of the Rotational Spectra of CH_3Cl

The Zeeman effect of methyl chloride has been studied because this molecule combines the desirable features of a very strong nuclear quadrupole coupling with the simple structure of a symmetric top. Moreover, its first rotational lines corresponding to $J=0\rightarrow1$ for both CH_3Cl^{35} and

[15] W. E. Good and D. K. Coles, Phys. Rev. **71**, 383 (1947).

CH_3Cl^{37} occur very conveniently near the upper end of the K-band.[16] These lines have been found here in a resonant cavity and their positions determined. Figure 13 shows an energy level diagram including the effects of the nuclear quadrupole coupling and the three possible transitions in zero-field. The nuclear spin I for either Cl^{35} or Cl^{37} has to be 3/2 to get very close agreement with the hyperfine structure. This confirms Townes' assignment for $I(Cl)$ in ClCN.[17] Also, it seems that the nuclear electric quadrupole coupling accounts very accurately for the separation of the energy levels. The theoretical ratio between the frequency difference $\nu(F=3/2\rightarrow 5/2)-\nu(F=3/2\rightarrow 3/2)$ and the frequency difference $\nu(F=3/2\rightarrow 1/2)-\nu(F=3/2\rightarrow 5/2)$ is 1.250, whereas that determined experimentally is 1.252. If there is some other kind of coupling present (e.g., the magnetic dipole interaction), it will have to bear the same ratio (which is not probable), or else it must be negligibly small.

Figure 14 shows a comparison between the calculated and experimental spectra for the $J=0\rightarrow 1(K=0)$ transition of CH_3Cl^{35} before and after Zeeman splitting. Calculations were performed by putting the known quantities $I(Cl^{35})=3/2$, $g(Cl^{35})=0.547$ and $H=1670$ oersteds (experimental) into Eq. (13) to see what value of g_{mole} will best fit the experimental pattern. This amounts to an experimental determination of $g_{mole}(CH_3Cl^{35})$, which is the only unknown factor. It turns out that the best fit occurs when we assume $g_{mole}\ll g_N(Cl^{35})$. While it is not possible to observe experimentally all the theoretical Zeeman components because of insufficient resolution and sensitivity, the general agreement seems to be good. This may be taken as further evidence supporting the general theory developed in Section C of Part III.

G. Zeeman Effect of SO_2

Since SO_2 has no known nuclear magnetic moment, the only contribution toward the Zeeman effect should come from its molecular moment. This molecule is different from $N^{15}H_3$ in that it is an asymmetric top and it has a larger reduced mass. The Zeeman effect of such a molecule has been investigated at the known frequencies published by Dailey and others.[18] It turned out, at $H=1670$ oersteds, that all the lines tested showed an incipient Zeeman effect in the form of a very marked reduction of the line intensity and accompanying broadening of the line. The splitting is, however, in no case resolvable in this weak field. It is hoped that complete resolution can be achieved with a stronger field. These results will be interesting from the standpoint of the size of the molecular g-factor and also as an aid to the assignment of quantum numbers to the spectral lines through the individual characteristics of the Zeeman patterns.

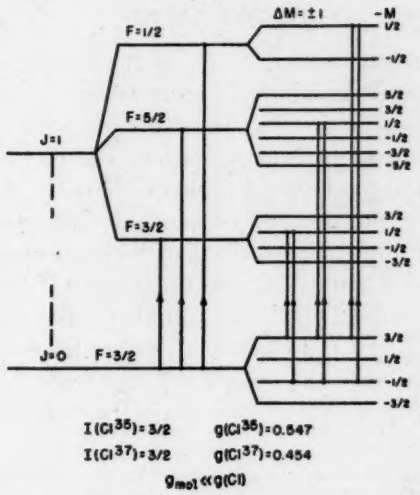

FIG. 13. Energy level diagram and Zeeman splitting for CH_3Cl.

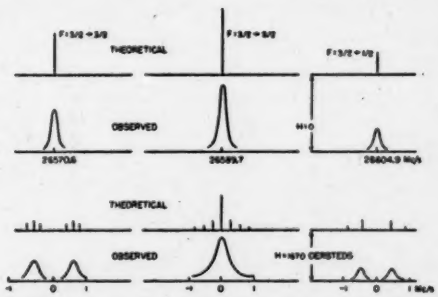

FIG. 14. The $J=0\rightarrow 1$ lines of CH_3Cl^{35} with and without magnetic field, $I(Cl^{35})=\frac{3}{2}$, $g(Cl^{35})=0.547$, $g_{mole}\ll g_N(Cl^{35})$.

[16] W. Gordy, J. W. Simmons, and A. G. Smith, Phys. Rev. 72, 344 (1947).
[17] C. H. Townes, A. N. Holden, J. Bardeen, and F. R. Merritt, Phys. Rev. 71, 644 (1947).
[18] B. P. Dailey, S. Golden and E. B. Wilson, Jr., Phys. Rev. 72, 871 (1947).

IV. CONCLUSION

From the above preliminary studies on the Zeeman effect in the absorption spectra of gas molecules, it is seen that a knowledge of the nuclear and molecular g-factors can be obtained from the analysis of Zeeman splitting, if there exists a spin-rotation coupling. If one g-factor is known, the other g-factor can be determined from the experimental data, on the basis of known spin and rotational quantum numbers. By studying the Paschen-Back effect at strong fields in conjunction with the analysis of the Zeeman effect, it will be possible to evaluate the two g-factors separately.

If the spin-rotation coupling is absent, the Zeeman splitting of the spectral lines of a molecule will yield direct information on the molecular g-factor. This information bears a close relationship to the charge distribution in a molecule and may throw some light on the nature of molecular bonds. The same knowledge should be particularly useful for the study of the interaction between the nuclear magnetic moment and the magnetic moment resulting from molecular rotation. Also, if the spectral lines of a molecule differ among themselves in their characteristic Zeeman patterns, the Zeeman studies can lend much help to the identification and assignment of molecular lines.

A new magnet-cavity assembly has now been built which is capable of yielding a magnetic field of the order of 10,000 oersteds. It is planned that more intensive investigations will be carried out for a large class of molecules in both the Zeeman and Paschen-Back spectra.

ACKNOWLEDGMENTS

I am deeply indebted in this work to Professor E. L. Chaffee for much encouragement, Mr. S. P. Cooke for technical advice, and Professors J. H. Van Vleck and E. B. Wilson, Jr. for very valuable suggestions.

PHYSICAL REVIEW VOLUME 74, NUMBER 10 NOVEMBER 15, 1948

Relation between Apparent Shapes of Monoenergetic Conversion Lines and of Continuous β-Spectra in a Magnetic Spectrometer*

G. E. OWEN AND H. PRIMAKOFF
Department of Physics, Washington University, St. Louis, Missouri

(Received August 2, 1948)

A method has been worked out for correcting distortions which affect the apparent shape of a continuous β-ray spectrum. Internal conversion lines are studied in the β-spectrometer and found to have a finite width and in the case of 180° focusing an unsymmetrical shape.

On the assumption that these conversion lines are actually monoenergetic, it is possible to calculate the distortion produced by the spectrometer and source, and thus to determine the approximate true shape of the continuous β-ray spectrum from the experimental data.

The Kurie plots for a continuous β-ray spectrum corrected in this way are, in general, straight over a greater range than the plots of the uncorrected data. The correction has been applied to the ratio of the number of positrons to the number of negatrons in Cu^{64} and gives results in better agreement with the Fermi theory than if there has been no correction.

1. INTRODUCTION

IN recent years one of the most important problems in the investigation of the shapes of the continuous β-spectra has been the study of their low energy regions. In the course of such study, discrepancies have been reported between experiment and the Fermi theory,[1] in particular, for the supposedly allowed β^+- and β^--spectra from Cu^{64}.[1] In the present note a systematic method is described for correcting

* Assisted by the joint program of the Office of Naval Research and Atomic Energy Commission.

[1] C. S. Cook and L. M. Langer, Phys. Rev. **73**, 601 (1948); J. Backus, Phys. Rev. **68**, 59 (1945).

the directly observed shapes of the continuous spectra for distortions of various kinds that occur in a given spectrometer with a given source. These distortions, arise from various factors, e.g., the finite width of an actually monoenergetic line due to the focussing properties of the spectrometer, the elastic and inelastic scattering of beta-particles in the source and its backing, by the slits, chamber walls, and residual gases, etc.

The nature of the corrections is based upon a study of the apparent shapes of monoenergetic internal conversion lines taken with the same spectrometer and with sources of the same thickness as used in the continuous spectrum work.[2] The magnitude of the corrections is in general not negligible, and is in a direction tending to decrease the above mentioned (low energy) discrepancies.

II. METHOD OF CORRECTION

Let $\mathfrak{N}(H)$ be the number of electrons recorded by the detector (counter) of the spectrometer[4] from some continuous β-spectrum at a magnetic field setting H, The maximum electron path radius of curvature and the counter slit width are $\bar{\rho}$ and $\Delta\rho$, respectively.[5] Then, if $N(p')dp'$ is the number of electrons emitted by the nuclei of the source with magnetic rigidity between p' and $p'+dp'$,[6] and if $P(p', p)dp$ is the probability that, because of the various distortions, an electron emitted with magnetic rigidity p' appears at the counter slit at a field H appropriate to a magnetic rigidity between p and $p+dp$, one has,

$$\frac{\mathfrak{N}(H)}{H\Delta\rho}=\frac{\mathfrak{N}(p/\bar{\rho})}{p\Delta\rho/\bar{\rho}}=\frac{1}{\Delta\rho}\int_{\bar{\rho}-\Delta\rho}^{\bar{\rho}}d\rho\left\{\int_0^\infty N(p')P(p', p'')dp'\right\},$$
$$\frac{\mathfrak{N}(p/\bar{\rho})}{p\Delta\rho/\bar{\rho}}=\int_0^\infty dp'N(p')\left\{\frac{1}{H\Delta\rho}\int_{H\bar{\rho}-H\Delta\rho}^{H\bar{\rho}}P(p', p'')dp''\right\}, \tag{1}$$

where $H\bar{\rho}=p$, $H\rho=p''$.

Thus, it is seen that the directly observed $\mathfrak{N}(H)/H\Delta\rho$, the quantity usually considered to give the electron momentum distribution and so compared with theory by means of the Kurie plot, is not equal to the true momentum distribution $N(H\bar{\rho})$ unless $P(p', p'')=\delta(p'-p'')$[3] and $\Delta\rho/\bar{\rho}\approx 0$, i.e., unless the scattering and focusing distortions are absent and the counter slit is very narrow. In the presence of such distortions, one is first confronted with the physical problem of discovering the probability function $P(p', p'')$ or rather the integral

$$\int_{H\bar{\rho}-H\Delta\rho}^{H\bar{\rho}}P(p', p'')dp'',$$

and then with the mathematical problem of deducing

$$N(H\bar{\rho})=N(p),$$

with

$$\int_{H\bar{\rho}-H\Delta\rho}^{H\bar{\rho}}P(p', p'')dp''$$

and $\mathfrak{N}(H)$ being considered known. Now

$$\int_{H\bar{\rho}-H\Delta\rho}^{H\bar{\rho}}P(p', p'')dp''$$

may, for a given spectrometer and source geometry and thickness, be found by studying the observed shapes of monoenergetic lines (with sources of the same geometry and thickness as used in the continuous spectrum work); thus for a monoenergetic line with momentum p_0, one has $N_{p_0}(p)=C(p_0)\delta(p-p_0)$,[7] whence, from Eq. (1),

[2] Corrections to the apparent shapes of β-spectra deduced from the theoretical focusing properties of 180° spectrometers have been discussed by W. H. Henderson, Camb. Phil. Soc. **31**, 285 (1935) and by J. L. Lawson and A. W. Tyler, Rev. Sci. Inst. 11, 7 (1940).

[3] δ is the usual Dirac delta-function.

[4] To fix ideas, a 180° focusing spectrometer, provided with a fixed source and counter, is envisaged. It will be clear from the ensuing discussion in this and the following sections that the considerations developed apply, with obvious changes, to other types of spectrometers as well.

[5] $\bar{\rho}$ is the distance from the center of the source to the far edge of the counter.

[6] $N(p')dp'$ is the *true* magnetic rigidity or momentum distribution of the continuous β-spectrum.

[7] N_{p_0} is the true momentum distribution of the monoenergetic line; one has $C(p_0)=\int_0^\infty N_{p_0}(p)dp=$ total number of electrons emitted in the conversion.

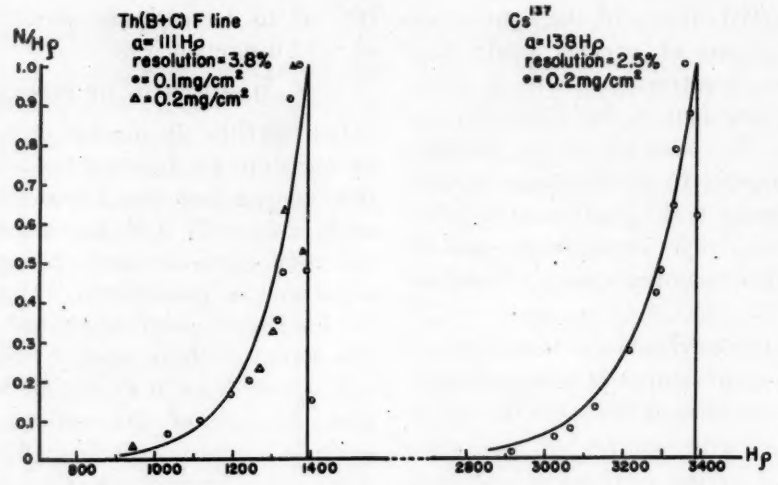

FIG. 1.

$$\frac{\mathfrak{N}_{p0}(H)}{H\Delta\rho}=\frac{\mathfrak{N}_{p0}(p/\bar{\rho})}{p\Delta\rho/\bar{\rho}}$$

$$=\frac{C(p_0)}{H\Delta\rho}\int_{H\bar{\rho}-H\Delta\rho}^{H\bar{\rho}}P(p_0,p'')dp''. \quad (2)$$

Combining Eqs. (2) and (1), one has,

$$\frac{\mathfrak{N}(p/\bar{\rho})}{p\Delta\rho/\bar{\rho}}=\int_0^\infty dp'N(p')\left\{\frac{\mathfrak{N}_{p'}(p/\bar{\rho})}{C(p')p\Delta\rho/\bar{\rho}}\right\}, \quad (3)$$

so that if the shapes of a sufficient number of monoenergetic lines are observed, one needs only to solve the integral equation,

$$M(p)=\int_0^\infty dp'N(p')K(p',p),$$
$$M(p)=\frac{\mathfrak{N}(p/\bar{\rho})}{p\Delta\rho/\bar{\rho}};\quad K(p',p)=\frac{\mathfrak{N}_{p'}(p/\bar{\rho})}{C(p')p\Delta\rho/\bar{\rho}}, \quad (4)$$

in order to find the true momentum distribution $N(p)$. This last can always be done, at least formally, by writing,

$$N(p)=\int_0^\infty dp'M(p')L(p',p), \quad (5)$$

with, L, the "kernel" reciprocal to the "kernel" P, satisfying,

$$\int_0^\infty dpK(p',p)L(p,p'')=\delta(p'-p'')$$
$$=\int_0^\infty dpL(p',p)K(p,p''). \quad (6)$$

Thus in principle, and in simple cases in practice (see below) the true momentum distribution of the continuous spectrum, $N(p)$, may be found from the observed number of counts (as a function of $H\bar{\rho}$) divided by $H\Delta\rho$, and from the observed shapes of a sufficient number of monoenergetic lines. An example of the procedure is given in the next section.

III. APPLICATION TO A SMALL 180° FOCUSING SPECTROMETER[8]

In this instrument the monoenergetic internal conversion lines of Cs^{137} (3380 gauss cm) and Th B+C (1385 gauss cm) were studied. The sources were mounted upon a Formvar backing of 0.03 mg/cm² and covered with a Formvar film of 0.005 mg/cm². The total source thickness was 0.2 mg/cm². It was found that the apparent shape of the Thorium line was independent of the thickness below 0.2 mg/cm² by comparing the line shapes for sources of 0.1 mg/cm² and 0.2 mg/cm² thickness. Comparable backing and source thickness were used in a companion study of the β^+- and β^--spectra of Cu^{64}, the Cu^{64} being prepared by an (n,p) reaction on Zn^{64}.[9] The Cu was separated chemically and was found to have a very high specific activity.

The observed shapes of the monoenergetic lines could be reasonably well fitted by a con-

[8] This instrument was constructed in the Washington University Physics Department under the direction of F. N. D. Kurie and F. Rasetti. It has $\bar{\rho}=5.72$ cm and $\Delta\rho=0.2$ cm.

[9] Suggested by F. N. D. Kurie.

venient empirical formula,

$$\frac{\mathfrak{N}_{p0}(H)}{C(p_0)H\Delta\rho}=\frac{1}{a}\exp\left\{-\frac{(p_0-p)}{a}\right\}, \quad (7)$$

where a is the average spread in $H\bar{\rho}=p$. In Fig. 1 the experimental points of the Cs^{137} line and the Th F line are given with the exponential fit:

Thorium $a=111$ gauss cm,
Cs^{137} $a=138$ gauss cm.

As a very rough approximation, one may then consider three limiting forms for $K(p', p)$.

$$K(p', p)=\frac{1}{a}\exp\left\{-\frac{(p'-p)}{a}\right\}, \quad \text{if} \quad p'\geqslant p,$$
$$K(p', p)=0, \quad \text{if} \quad p'<p, \quad (8)$$

for all p' and p, and with

I: $a(p')=$const.,
II: $a(p')=$(const.)$p'+$const.,
III: $a(p')=$(const.)p'.

Using Eq. (8) for $K(p', p)$ and I for $a(p')$ the integral Eq. (4) for $N(p)$ can be solved easily by Fourier analysis. Writing

$$M(p)=\int_{-\infty}^{+\infty}\mu(q)\exp(2\pi ipq)dq,$$

$$N(p)=\int_{-\infty}^{+\infty}\nu(q)\exp(2\pi ipq)dq,$$

and substituting into Eq. (4), one gets

$$\mu(q)=\nu(q)[1-2\pi iaq]^{-1}$$

so that,

$$N(p)=M(p)-a(dM(p)/dp). \quad (9)$$

The form of Eq. (9) maintains equal areas under the $N(p)$ and the $M(p)$ momentum distribution curves.

Using II and III for $a(p')$, Eq. (9) (with $a=$(const.)$p+$const., or $a=$(const.)p) is still a valid approximation provided that

$$da(p')/dp'\ll 1.$$

The true momentum distribution $N(p)$, given by Eq. (9), may now be compared with experiment. Calculations have been made for all three cases of $a(p')$. The corrections for cases I, II, and III are based on the following $a(p')$:

I: $a(p')=(111+138)/2$ gauss cm
$=125$ gauss cm,
II: $a(p')=[0.0135p'+92]$ gauss cm,
III: $a(p')=0.05p'$ gauss cm.

Corrections based on I, II, and III give essentially the same results down to the low energy region below 200 kev. Since the experimental measurement of the internal conversion lines gives $a(p')=[0.0135p'+92]$ gauss cm as a rough approximation, this $a(p')$ of case II is used for the graphical presentation of the correction.[10]

We use first in Eq. (9) the directly observed

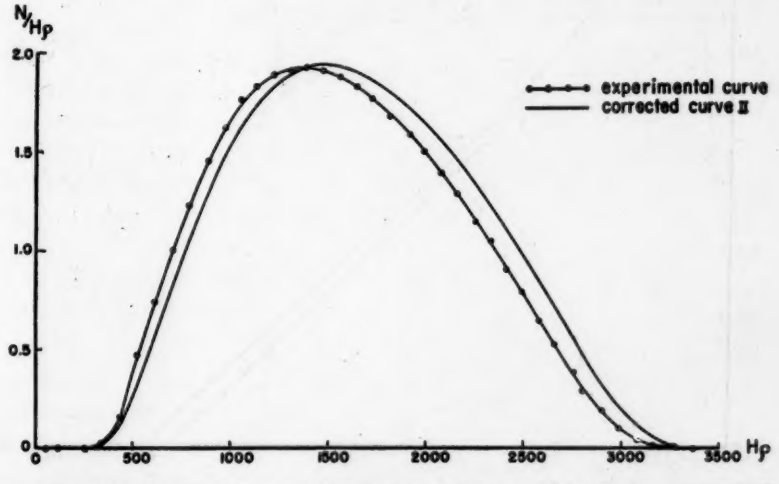

FIG. 2. Momentum distribution of the negatrons from Cu^{64}.

[10] One might expect the $a(p')$ to be of case II for 180° instruments since the apparent width of a monoenergetic line is the sum of a contribution arising from the focusing which is proportional to p', and a contribution arising from the scattering which may be roughly independent of p'.

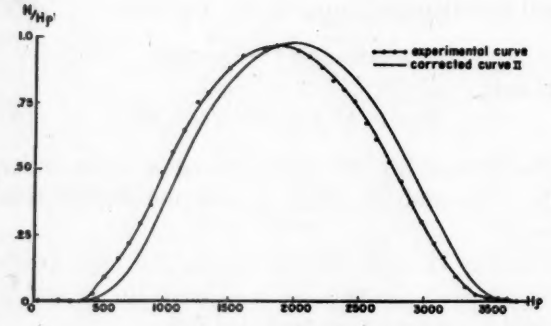

FIG. 3. Momentum distribution of the positrons from Cu^{64}.

$\mathfrak{N}(H)/H\Delta\rho = M(p)$ and then take the correction:

$$a(p')_{II}\frac{dM(p)}{dp}.$$

Figures 2 and 3 show that the experimental momentum distribution is shifted in the direction of the higher momenta after this correction is applied.

Figures 4 and 5 then show the Kurie plots for the β^+- and β^--spectra of Cu^{64}. An apparent decrease in the number of particles in the low energy region as a result of the correction is observed in both cases. In Figs. 6 and 7 the logarithm of the ratio of the number of positrons to the number of negatrons is given for the experimental data ($M(p)$) and the corrected data ($N(p)$).[11] The superior agreement of the latter with the theory is apparent. The limiting cases I and III are shown in Fig. 8 and it is noted that for $a(p') = \text{const.} = 125$ gauss cm, the best agreement with theory is obtained.

A shift in the end point of about 5 percent to a higher energy is noted on the corrected Kurie plots. In principle this corrected end point is no more dubious than the uncorrected one since both involve theoretical extrapolations of experimental data.

From the present discussion it is evident that these corrections have no meaning in the region where Geiger window distortions are present. A study of window transmission characteristics is planned in order that corrections for the entire spectrum can be applied.

IV. DISCUSSION

It is clear that while the corrections to the observed momentum distribution discussed in

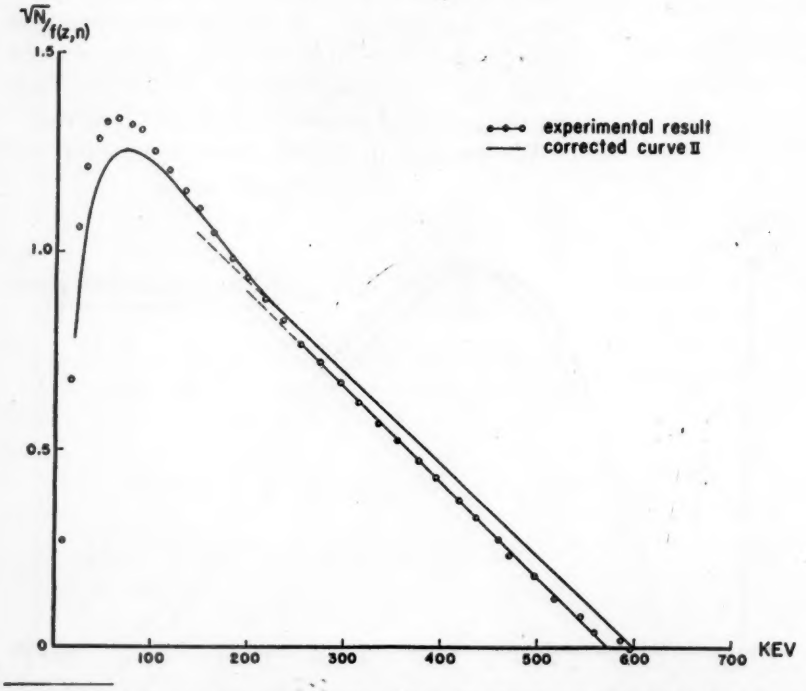

FIG. 4. Kurie plot of the negatrons from Cu^{64}.

[11] Qualitatively, our uncorrected β^+- and β^--distributions agree with those of Cook and Langer, reference 1, though the deviations from the Fermi theory in our original experimental data are greater than in theirs. This is no doubt due to the poorer resolution and greater scattering of our instrument.

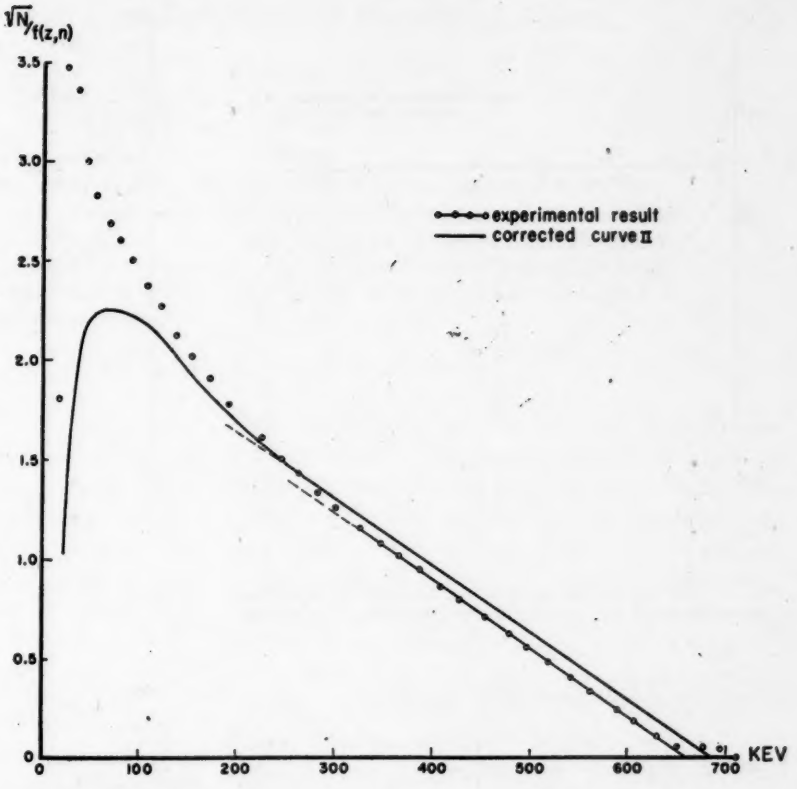

FIG. 5. Kurie plot of the positrons from Cu^{64}.

the present note always exist, it is possible that with low scattering and high resolution instruments they may be quite negligible. For example, if in Eq. (9), $a(p')=0.005p'$, the Kurie plots constructed from the $M(p)$ and the $N(p)$ distributions are very similar. On the other hand, considerable caution must always be exercised in ensuring that the difference between the directly observed $M(p)$ and the corrected $N(p)$ distribution is indeed small with a particular instrument and source; this should be done by an investigation of the apparent shapes of a sufficient number of strategically situated monoenergetic lines[12] and by the subsequent application of Eqs. (4) and (5).

One remark should be added in conclusion. It may be expected (and has indeed been observed in this laboratory)[13] that a thin magnetic lens β-spectrometer gives monoenergetic line shapes which are much more symmetrical in $p'-p$ than those given by a 180° focusing spectrometer. The line shapes given by the thin magnetic lens spectrometer are roughly repre-

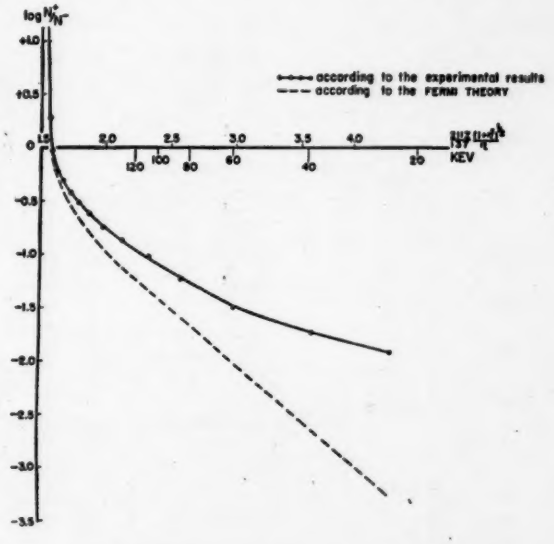

FIG. 6. The log of the ratio of the number of positrons to the number of negatrons in the low energy region for Cu^{64}.

[12] Using sources of the same geometry and stopping power as in the continuous spectrum work.

[13] J. Townsend, Washington University, St. Louis, Missouri.

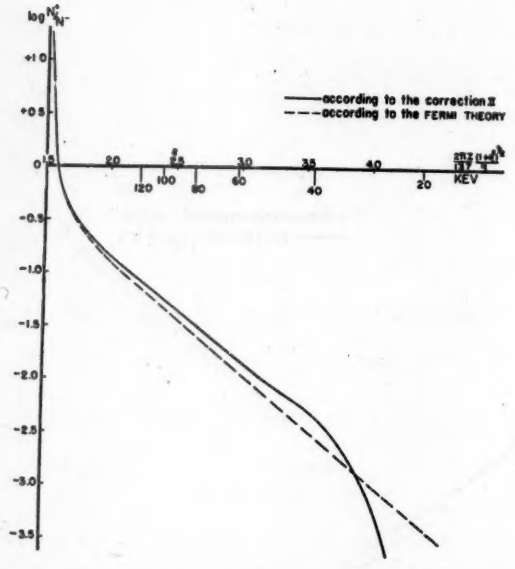

FIG. 7. The log of the ratio of the number of positrons to the number of negatrons in the low energy region for Cu^{64}.

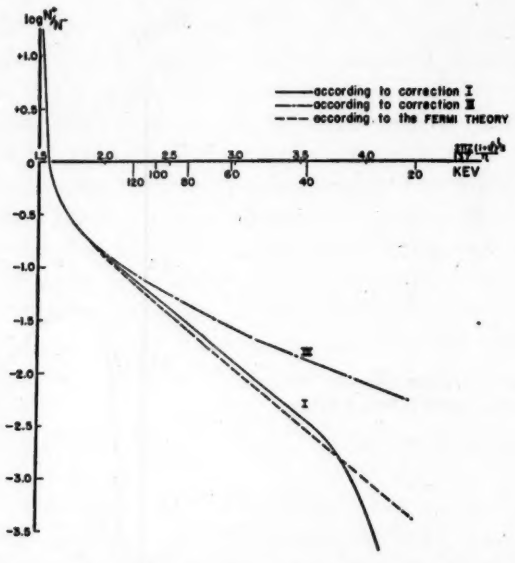

FIG. 8. The log of the ration of the number of positrons to the number of negatrons in the low energy region for Cu^{64}.

sentable by a Gaussian error function:

$$K(p', p) = \frac{1}{a(\pi)^{\frac{1}{2}}} \exp\left\{-\frac{(p'-p)^2}{a^2}\right\}. \quad (10)$$

In such instruments, using Eq. (4),

$$M(p) = \int_{-p/a}^{\infty} dx N(p+ax) \frac{e^{-x^2}}{(\pi)^{\frac{1}{2}}} \approx N(p) + \frac{a^2}{4} \frac{d^2N(p)}{dp^2},$$

whence

$$N(p) \approx M(p) - \frac{a^2}{4} \frac{d^2M(p)}{dp^2}, \quad (11)$$

so that, in general, a much smaller difference between N and M (for a given a) is to be expected for a thin magnetic lens spectrometer than for a 180° spectrometer. It would therefore be highly interesting to carry out a study of the Cu^{64} spectra with a thin magnetic lens spectrometer. Experiments along these lines are to be undertaken in this laboratory.

We are grateful to Professor F. N. D. Kurie and Professor A. L. Hughes for their stimulating comments and discussion; we also wish to thank Mr. David Moe for his aid in obtaining experimental data.

The Emissivity of Iron-Tungsten and Iron-Cobalt Alloys

HARRY W. KNOP, JR.
Department of Physics, University of Wisconsin, Madison, Wisconsin
(Received August 3, 1948)

The spectral emissivity at $\lambda=0.667\mu$ has been determined for an 18 percent W–Fe alloy and a 40 percent Fe–Co alloy. Changes have been detected at the peritectoid and peritectic reaction temperatures for W–Fe and at the A_3 point for Fe–Co. Emissivity changes found at 1044°K and 1292°K in Fe–Co are attributed to the order-disorder transition and the ferro to paramagnetic transformation, respectively. The resistivity of 40 percent Fe–Co has been determined as a function of temperature.

INTRODUCTION

CHANGES in spectral emissivity at phase changes in iron and cobalt have been reported by Wahlin and Wright[1] and by Wahlin and Knop.[2] This is a report on the extension of these investigations to alloys.

APPARATUS AND PROCEDURE

The spectral emissivity at $\lambda=0.667\mu$ of an 18 percent W-Fe alloy and a 40 percent Fe-Co alloy was determined in the following manner. From a flat strip of the alloy 12 cm long, 1 cm wide, and 0.009 cm thick a hollow cylinder was formed, the overlapping edges being spot-welded in several places. A hole 0.5 mm in diameter was drilled through the side of the cylinder equidistant from the ends. The radiation from this hole was taken as blackbody radiation. The cylinder was mounted in a glass tube which was sealed to a vacuum system capable of evacuating the tube to a pressure of 3×10^{-8} mm of mercury. The cylinder was heated by an alternating conduction current of from 50 to 100 amperes taken from the secondary of a 110-volt primary 5-volt secondary transformer.

The glass tube was equipped with a flat glass window through which temperatures could be determined pyrometrically. A disappearing filament optical pyrometer equipped with a lamp having a 1.5-mil filament, and calibrated by sectoring up and down from the gold point, was used in the measurements.

The procedure in taking data was to match the pyrometer with radiation from the hole and from the metal above and below the hole. The pyrometer currents were determined from the voltage drop produced by them across a standard ohm. A sufficient number of pyrometer settings was taken at each temperature so that a reliable mean could be found. A confusion resistance, which was adjusted unknown to the observer after each reading, was placed in series with the pyrometer lamp. The spread in current readings obtained corresponded to less than a degree. From the pyrometer currents the true and apparent temperatures were determined. The spectral emissivity was calculated using the formula

$$\log \exp(E_\lambda = C_2/\lambda(1/T_1 - 1/T_2)),$$

where T_1 is the true temperature corresponding to radiation from the hole, T_2 is the apparent temperature corresponding to radiation from the surface of the cylinder, and $C_2/\lambda=21{,}500$°K. All of the data was taken with hydrogen at a pressure of about 5 cm in the system.

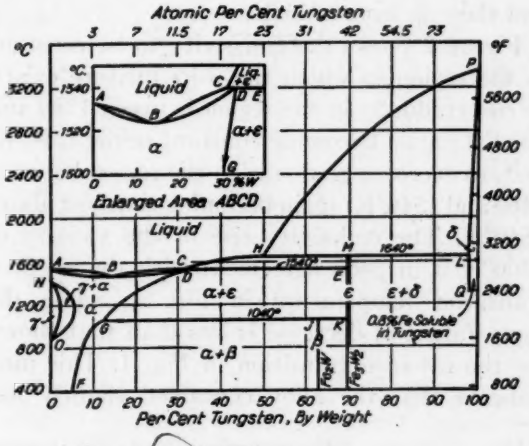

FIG. 1.

[1] H. B. Wahlin and Rufus Wright, "The spectral emissivity of the iron group," J. App. Phys. 13, 40 (1942).
[2] H. B. Wahlin and H. W. Knop, Jr., "Spectral emissivity of iron and cobalt," Phys. Rev. 74, 687 (1948).

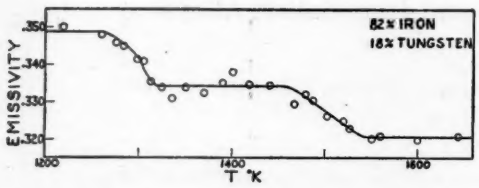

FIG. 2.

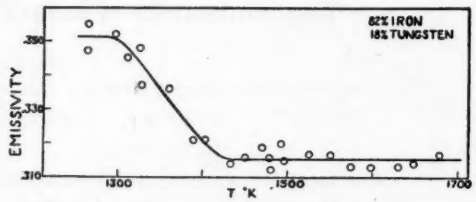

FIG. 3.

RESULTS

18 Percent Tungsten–82 Percent Iron Alloy

The constitution diagram of the binary iron-tungsten system shown in Fig. 1 is taken from a report of W. P. Sykes.[3] It shows the following forms of the 18 percent W-Fe alloy to be stable at various temperatures. Below 1313°K a mixture of α-solid solution of tungsten in iron and an intermetallic β-phase corresponding to the formula Fe_2W exists. Above 1313°K the β-intermetallic compound is no longer stable and a second intermetallic phase ϵ, corresponding to the formula Fe_3W_2, is formed by a peritectoid reaction. Thus, from 1313°K to approximately 1573°K a mixture of $\alpha+\epsilon$ exists. Above 1573°K the ϵ-phase is unstable and α-solid solution alone exists up to the melting point.

Figure 2 is a plot of emissivity against true temperature for an 18 percent W-Fe alloy. The results shown represent the average of two complete runs taken two weeks apart. For one week prior to each of these runs the specimen was maintained at a temperature of 1375°K. Therefore, it is assumed that the alloy was in the form of the $\alpha+\epsilon$ mixture stable at that temperature. The runs averaged were taken going first down and then up from 1375°K.

Figure 2 shows the emissivity to be constant in the region in which the $\alpha+\epsilon$ mixture exists, to rise gradually in the region between 1280 and 1320°K, again becoming constant below 1280°K, and, to decrease gradually in the region between 1460 and 1540°K, again becoming constant above 1540°K. The emissivity rise in the vicinity of 1300°K is in good agreement with the $\alpha+\beta\rightleftarrows\epsilon$ transition temperature in Fig. 1, while the temperature of decrease is less than that shown for the $\alpha+\epsilon\rightleftarrows\alpha$ transition in Fig. 1. This may indicate that the alloy contained slightly less than 18 percent tungsten. The reproducibility of this curve after two weeks of heat treatment shows that no selective diffusion of one of the metals in the alloy to the surface takes place.

Figure 3 shows the results of a run starting from a temperature of 1680°K and proceeding downward. These data were taken in between the runs averaged in Fig. 2. At 1680°K it is assumed that the alloy existed in the form of an α-solid solution. The emissivity remained constant with decreasing temperature down to approximately 1400°K. Decreasing the temperature of the cylinder below 1400°K the emissivity continued to rise, apparently reaching a constant value, in good agreement with that for the $\alpha+\beta$ mixture obtained in Fig. 2, at a temperature around 1280°K. It appears as though upon reaching a temperature low enough for some of the ϵ-phase to form, the remaining α-solid solution contains less tungsten, and hence no more ϵ is formed until a lower temperature is reached. This process of the gradual formation of ϵ-phase then continues until the peritectoid reaction temperature is reached at which the β-intermediate phase is formed. The fact that a constant emissivity is obtained below 1280°K seems to indicate that the $\alpha+\epsilon\rightarrow\beta$ transition has gone to completion or that the amount of β formed from the α-solid solution between G and F in Fig. 1 is to small to effect the observations.

40 Percent Iron–60 Percent Cobalt Alloy

Figure 4 is a plot of emissivity against true temperature for a 40 percent iron–60 percent cobalt alloy. The alloy was prepared electrolytically, making use of a report by Glasstone and Speakman.[4] These authors studied the composition of iron-cobalt alloys deposited from well buffered solutions, of definite hydrogen ion

[3] W. P. Sykes, "The constitution of iron-tungsten alloys," *Metals Handbook* (1939), edition p. 401.

[4] S. Glasstone and J. C. Speakman, "Electrodeposition of iron-cobalt alloys," Trans. Faraday Soc. **28**, 733 (1932), and **29**, 426 (1933).

concentrations, containing various proportions of ferrous and cobaltous sulfates, over a range of current densities. They found that the composition of the alloys tends toward a constant value as the current density is increased and that this value appears to be independent of the hydrogen ion concentration of the solution. In order to obtain a ductile deposit it was necessary to modify their procedure. An unbuffered solution of ferrous and cobaltous chlorides of reagent quality was used. The total concentration of iron plus cobalt in the solution was 2 gram equivalents per liter, and the amount of iron was 40 percent of the total atomic percent of iron plus cobalt. This composition is an interpolation between two sulfate solutions reported by Glasstone and Speakman to yield alloys of 60 atomic percent iron and 40 atomic percent iron. Thus, a composition of 50 atomic percent iron was expected. The solution was made slightly acidic with HCl and was kept at a temperature of 80°C during the deposition. The deposit was made on a stainless steel cathode from which it was readily removed. The graphite anode was separated from the main body of the solution by a porous cup. This separation was to prevent oxidation of the ferrous ions at the anode. A current density of 5 amperes/decimeter^2 was used. The time of deposit was seven hours.

Quantitative analysis revealed the composition of the deposit to be 40 percent iron–60 percent cobalt by weight. The deviation from the expected amount is attributed to the fact that no allowance was made for the depletion of the ferrous ion concentration during the deposition. Also, the appearance of a slight amount of flocculent ferric precipate indicated the oxidation of some of the ferrous ions in spite of the porous cup.

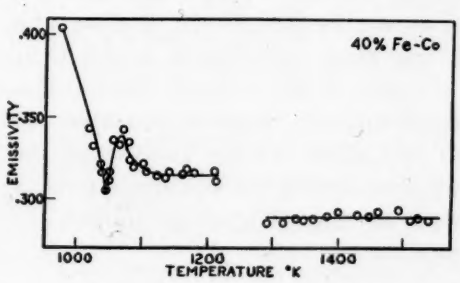

FIG. 4.

The rise in emissivity at the low temperature end in Fig. 4 is attributed to the deviation from blackbody conditions. The length of the cylinder radiating visible energy at these low temperatures is too short to insure blackbody radiation from the hole. The dip at 1044°K may correspond to the critical temperature of the order-disorder transition reported for iron-cobalt alloys in the middle of the system. The reported critical temperature for a 40 percent iron–60 percent cobalt alloy is 951°K.[5]

The missing portion of the Fe-Co emissivity curve corresponds to a temperature region in which thermal equilibrium of the cylinder could not be obtained. Raising the true temperature of the cylinder above 1213°K by decreasing the resistance in the primary of the heating current circuit, the true temperature continued to rise; and, for the same rheostat setting, thermal equilibrium was reached at a temperature above 1300°K. Approaching this unstable region from the high temperature side, it was found that thermal equilibrium could be obtained down to a true temperature of 1292°K. Lowering the true temperature below 1292°K, it fell rapidly, and thermal equilibrium was reached slightly below 1200°K. It was impossible to obtain thermal equilibrium at any point in between 1213°K and 1292°K. 1213°K is in fair agreement with the 1223°K reported as the temperature of the body-centered cubic to face centered cubic transition of this alloy.[5] 1292°K may represent the Curie temperature for this alloy. No experimentally obtained values of the Curie temperature for the purpose of comparison have been found in the literature. A very noticeable change

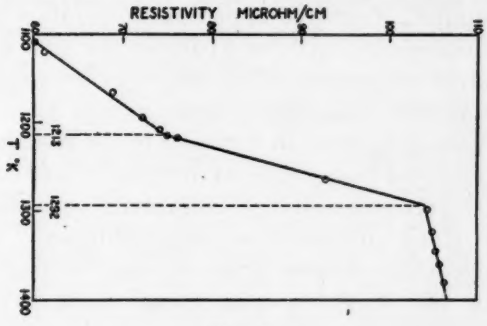

FIG. 5.

[5] W. C. Ellis and E. S. Greiner, "Equilibrium relations in the solid state in the iron-cobalt system," Am. Soc. Metals 21, 415 (1941).

in heating current was observed as the true temperature traversed this unstable region, indicating a very marked change in the resistivity of the alloy.

Resistivity of a 40 Percent Iron–60 Percent Cobalt Alloy

In the hope of finding an explanation for the missing portion of the iron-cobalt emissivity curve a determination of the resistivity of this alloy as a function of temperature was made. A flat strip of the alloy 13 cm long, 0.3958 cm wide, and 0.0085 cm thick was mounted vertically in a glass tube which was connected to a vacuum system. Two iron wires 0.002 cm in diameter were spot-welded to the strip 0.6839 cm apart in the region of the center of the strip. These wires were in turn spot-welded to tungsten wires sealed into the side of the glass tube. This tube was equipped with a flat glass window through which the temperature of the strip could be determined pyrometrically.

After baking and evacuating the system, 5 cm of hydrogen was introduced. The strip was heated by passing a direct current through it. The magnitude of this current was determined by measuring the voltage drop produced by it across a standard resistance. At each current setting the voltage drop across the known length of the strip between the fine iron wires was also determined. Finally, at each current setting the apparent temperature of the portion of the strip between the iron wires was ascertained using an optical pyrometer.

From the current and voltage values, and the dimensions of the strip, the resistivity was computed. From the apparent temperature and the emissivity curve in hydrogen for this alloy the true temperature of the strip was determined. The results obtained are shown in Fig. 5.

A sharp increase in the slope of the resistivity curve at the body-centered to face-centered cubic crystal structure change and a sharp decrease at the Curie temperature were obtained. The temperature of these phase changes as obtained from the resistivity-temperature curve are in exact agreement with the temperatures obtained from the emissivity-temperature curve.

In determining the emissivity of this alloy the geometry of the hollow cylinder with plugged ends apparently prevented the conduction of heat away from the cylinder from occurring fast enough in the region 1213°K to 1292°K to allow equilibrium to be reached. Thus, since a constant voltage source was not used, in the region between the A_3 and the Curie temperatures where the resistivity increases so rapidly with temperature, the temperature and resistance continued to rise until a temperature above the Curie temperature was reached.

CONCLUSIONS

The change in roughness of the surface of the cylinder as a phase change is undergone has been suggested as a possible explanation of the emissivity changes observed. However, the fact that the results are reproducible, even after going back and forth through a phase change several times, probably rules out this possibility.

A correspondence exists between the number density of electrons and the emissivity changes noted at the A_3 and A_4 points in iron and at the Curie temperature in cobalt. A decrease in electron density causes a decrease in reflectivity and hence an increase in emissivity. Similarly, an increase in electron density results in a decrease in emissivity.

In order to arrive at definite conclusions concerning phase changes in metals from observed changes in emissivity, certainly, one must first prove that spectral emissivity is a function of the phase in which a metal exists. It is hoped that the results reported here may form a part of that proof.

ACKNOWLEDGMENTS

I deeply appreciate the guidance and assistance given to me by Dr. H. B. Wahlin while this work was being carried out. I also thank Mr. L. G. Cover of the General Electric Company for furnishing the tungsten-iron alloy and Mr. Keith McCallum for his analysis of the iron-cobalt alloy. This work was made possible by a grant from the Wisconsin Alumni Research Foundation.

The Geiger Discharge

D. H. WILKINSON
Cavendish Laboratory, Cambridge, England
(Received March 17, 1948)

It is pointed out that those phenomena concerned with Geiger counter operation which are well understood are those associated with the motion of the positive ion sheath while those awaiting explanation are associated with its development. A theory of this development is presented and used to calculate the following phenomena:

(i) The relation between starting potential and counter variables.
(ii) The amount of charge generated in the discharge.
(iii) The shape of the plateau curve.
(iv) The velocity of propagation of the discharge down the wire.

Good agreement is obtained at all points.

The curve connecting the charge generated and the overvolts is shown to consist of two parts, each a straight line, their slopes bearing a ratio of 2:1. The plateau curve is shown to climb more steeply to its constant value, the greater the number of electrons liberated in the counter by the ionizing particle, and the effect is confirmed experimentally. The velocity of propagation is shown to vary roughly linearly with overvolts but to tend to a finite value at zero overvolts. All forms of counter behavior are shown to depend strongly on the ratio of charge generated in the counter to that originally on the wire.

INTRODUCTION

BROADLY speaking, those aspects of Geiger counter behavior which are well understood are those which are concerned with the radial motion across the counter of the positive ion sheath formed in intimate contact with the wire by the discharge. Of these, the most important are:

(i) The form of the voltage pulse as a function of time.
(ii) The dead-time phenomena.

The first has been elucidated by the work of Ramsey[1] and Montgomery and Montgomery,[2] and in more detail by van Gemert, den Hartog, and Muller,[3] and by Alder, Baldinger, Huber, and Metzger.[4] The second has been treated by van Gemert, den Hartog, and Muller,[5] and by Stever.[6]

These phenomena, however, occur after the end of the discharge proper, which has been quenched by the action of the positive ion sheath—all avalanche activity has ceased and the starting point of the discussion is the "burnt out" positive ion space charge sheath which remains. There are several important phenomena, however, which depend on the growth of the discharge itself, and to explain which, one has to enquire more closely into the actual mechanism of formation of the space charge sheath. The most important are:

(i) The relation between the counter starting potential (V_s) and the counter variables.
(ii) The quantity of charge generated in the discharge (q) and its dependence on counter overvolts ($V-V_s$), filling gas pressure (p), and counter geometry.
(iii) The shape of the plateau curve.
(iv) The velocity of propagation of the discharge down the counter wire (v) and its dependence on counter variables.

It is the object of this paper to discuss these four phenomena, and to attempt to explain the facts concerned with them.

THE DEVELOPMENT OF THE DISCHARGE

The characteristic feature of the Geiger discharge is that it spreads the whole length of the counter wire, and so there must exist some mechanism which enables the first electron avalanche to breed others and so on. This mechanism, in the case of the "self-quenching" counters at any rate, is the emission of photoelectrons from molecules of the gas under the action of photons proceeding from excited mole-

[1] W. E. Ramsey, Phys. Rev. **57**, 1022 (1940).
[2] C. G. Montgomery and D. D. Montgomery, Phys. Rev. **57**, 1030 (1940).
[3] A. G. M. Van Gemert, H. Den Hartog, and F. A. Muller, Physica **9**, 556 (1942).
[4] Alder, Baldinger, Huber, and Metzger, Hel. Phys. Acta **20**, 73 (1947).
[5] A. G. M. Van Gemert, H. Den Hartog, and F. A. Muller, Physica **9**, 658 (1942).
[6] H. G. Stever, Phys. Rev. **61**, 38 (1942).

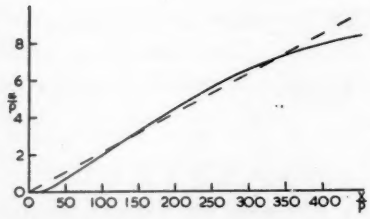

FIG. 1. α/p *versus* X/p for pure argon (after Kruithof and Penning). Solid line: experimental values; dotted line: linear approximation.

cules or ions formed in the first avalanche. This is shown by the beaded wire experiments of Stever[6,7] and others. It is the self-quenching counters which are considered here. We may assume a constant probability ϵ per ion of an avalanche that a further avalanche should arise by this mechanism. Then, if the first avalanche contains $N(1)$ ions, the condition for the Geiger discharge is

$$N(1)\epsilon > 1$$

the threshold V_s being given by

$$N(1)\epsilon = 1. \tag{1}$$

(Straggling effects in $N(1)$ are neglected, and will not influence much the greater part of the calculation.) $N(1)\epsilon$ has a Poisson distribution since $\epsilon \ll 1$. The value of ϵ is uncertain, but nearly all the results to follow depend only logarithmically on it. $N(1)$ is the gas amplification which would have obtained at V had not the divergent chain Geiger action set in. This is usually about 10^5 at V_s, so we will set $\epsilon = 10^{-5}$.

Thus, for the calculation of problem (i) all that is required is $N(1)$ as a function of the counter variables.

THE FORM OF THE FIRST AVALANCHE

An electron, born inside the counter, will drift towards the wire under the influence of a field

$$X = \frac{V}{r \log b/a} \tag{2}$$

at a distance r from the axis. V is the applied counter voltage, b and a the cathode and anode radii. At some distance r_c ionization by collision begins, r_c being determined by some critical value of X/p, p being the pressure in the counter

[7] H. G. Stever, Phys. Rev. **59**, 765 (1941).

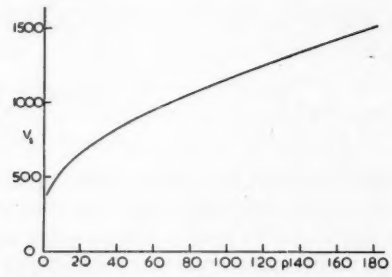

FIG. 2. Relation between V_s and p for the typical counter.

(in the following, X will be measured in volts/cm and p in mm Hg). Thus

$$\frac{r_c}{a} = \frac{V_s}{V_p}$$

where V_p is the starting potential for proportional counter action. So

$$N(1) = \exp\left(\int_a^{r_c} \alpha \cdot dr\right), \tag{3}$$

α being the first Townsend coefficient effective under the counter conditions. We now make the assumption on which the whole treatment is based, namely:

$$\alpha = \text{constant} \times X. \tag{4}$$

Generally α/p will be some function of X/p for electrons remaining in equilibrium with the field, and over the range of X/p of interest (about 60–300 for the average counter) this approximation is reasonable, as may be seen from Fig. 1 representing the results of Kruithof and Penning[8] for pure argon. Other gases behave similarly. Relations (23), (3) and (4) give together

$$N(1) = \left(\frac{r_c}{a}\right)^{Q_0 c}, \tag{5}$$

where Q_0 is the charge per unit length of the counter wire, given by

$$\frac{Q_0}{V} = \frac{1}{2 \log b/a},$$

and c is a constant related to that in (4).

If now by $N(1, r)$ we mean the number of ions

[8] A. A. Kruithof and F. M. Penning, Physica **3**, 515 (1936).

produced by the avalanche between r_c and r

$$N(1, r) = \left(\frac{r_c}{r}\right)^{Q_{0c}}.* \quad (6)$$

DEPENDENCE OF V_s ON THE COUNTER VARIABLES

We may now at once give an answer to problem (i) using relations (1) and (5) and find, for the dependence of V_s on p

$$V_s \log\frac{k_1 V_s}{p} = \text{constant}, \quad (7)$$

where k_1 is a constant given by

$$\frac{k_1 V_s}{p} = \frac{r_c}{a}.$$

If we now consider a typical counter which we shall discuss throughout this paper where a numerical value is to be derived, having $b=1.0$ cm, $a=0.01$ cm, $V_s=1000$ volts, $V_p=200$ volts, $p=70$ mm Hg, we have $k_1=0.35$ mm Hg/volt and a relation between V_s and p given in Fig. 2.

The dependence of V_s on b and a may similarly be found to be given by, at a fixed p,

$$\frac{V_s}{\log b/a} \log\left(\frac{V_s}{k_2 a \log b/a}\right) = \text{constant},$$

k_2 being another constant of value 4.35×10^3 volts/cm for our typical counter considered above. V_s is shown in Fig. 3 as a function of a for several b values.

These relations are subject to two limitations. The first concerns r_c which should be considerably smaller than b, or the whole avalanche may not be formed. Thus the results may not be used at very low counter pressures or small b/a values. The second concerns the constancy of composition of the gas. This has been implicitly assumed as ϵ has been held constant. The fact that, for example, in argon-alcohol counters, V_s depends more rapidly on the partial pressure of the alcohol than on that of the argon, is interpreted simply as a decrease of ϵ with increasing alcohol pressure, which may be understood from many points of view.

These relations are in good accord with experience, and, rather than being a product of the theory, should be regarded as confirmation of the basic assumptions.

THE BUILDING-UP OF THE SPACE-CHARGE SHEATH

For the attacking of the main problems we must consider the way in which the space charge of positive ions is developed, and its manner of quenching the discharge. Before this can be done, we must establish three important characteristics of the sheath.

(i) It is uniform in structure and does not preserve any of the granular nature which might be expected of it, having been built up from discrete avalanches.

(ii) It is effectively stationary until the discharge has terminated in its immediate neighborhood.

(iii) It holds on to the wire by induction all the electrons formed in the avalanches.

These three characteristics will be discussed in turn:

(i) Although the avalanches building up the sheath are quite discrete, each one undergoes

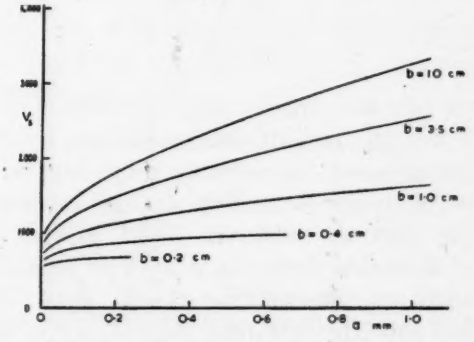

FIG. 3. Relation between V_s, a, and b for $p=7$ cm Hg.

* It is not suggested that this is a complete account of the first avalanche. It is merely desired to have some simple analytic expression for its form which is in adequate accord with the facts and on which the formal treatment of the space-charge build-up may be based. A detailed account of the first avalanche has been given by S. C. Brown [Phys. Rev. 62, 244 (1942)] for a helium-filled counter. Such an account should be given in a complete study, but would complicate enormously its development. Brown considers the space-charge effect of a single avalanche on itself. It is well known that this effect is all-important in cases of small b/a ratio—as Brown's results reveal—but in the specifically Geiger-counter geometry considered here it is relatively small. The diffusion results of the next section but one may be used to estimate the effect, which amounts to a few percent at the wire.

considerable diffusion in the course of its formation, and the positive ions from neighboring ones completely overlap. This diffusion effect may be roughly estimated by calculating that obtaining in a parallel plate chamber of electrode spacing $\delta=r_c-a$ across which is applied the potential difference V' between r_c and the wire.

$$V'=V\frac{\log r_c/a}{\log b/a}$$

$\sim$300 volts for our typical counter. Remembering that

$$\frac{v_e'}{D}=\frac{LeX}{\eta P},$$

where v_e' is the electron drift velocity, D the coefficient of diffusion, L Loschmidt's number, P 760 mm Hg expressed in dynes/cm^2, and η the Townsend coefficient giving the ratio between the mean electron agitation energy and $\frac{3}{2}kT$, we have: the probability of finding our electron between x and $x+dx$ from the plane of the center of gravity of the distribution at time t is

$$\frac{\exp\left(-\frac{x^2}{4Dt}\right)}{(4\pi Dt)^{\frac{1}{2}}}\cdot dx,$$

and the mean electron displacement, which may be taken as a measure of the spread of the avalanche, is

$$d=\left(\frac{4Dt}{\pi}\right)^{\frac{1}{2}}.$$

This gives a fractional displacement $f=d/\delta$ of

$$f=0.178\left(\frac{\eta}{V'}\right)^{\frac{1}{2}}$$

$$\sim 0.01(\eta)^{\frac{1}{2}}.$$

Now η for pure argon is already 310 for $X/p=5$ and, though considerably reduced by the quenching agent, is probably quite big in the $X/p\sim 100$ region in which we are interested. Letting then $\eta=100$ gives $f=0.1$ so that the lateral extension down the wire of an individual avalanche is about $2f(r_c-a)\sim 0.1$ mm. This, coupled with the fact that the number of avalanches per cm of counter wire is usually of the thousands order, as will be seen, shows that the positive ions are in fact quite mixed up, and we may assume the desired uniform space-charge sheath.

(ii) The assumption of the locally stationary positive ion sheath is based on the enormously greater mobility of the electrons than positive ions (the ratio is about 10^3:1). As we shall see, the local discharge lasts a few times 10^{-8} sec. in which time the positive ions formed in the beginning at the wire surface will have moved a few times 0.001 cm—a few tenths of a wire radius. Those at r_c will have moved about a fifth as much, and, as most of the avalanches are formed quite late on in the discharge, because of its exponential nature, these movements may be neglected.

(iii) The assumption that all the electrons formed are held on to the wire by induction of the positive ions may be justified by calculation. Applying Green's Theorem in electrostatics, we find that the fraction q_- of electrons which can escape from the wire is given by, using (6)

$$q_-=\frac{Q_0c\int_a^{r_c}\frac{1}{r}\cdot\left(\frac{r_c}{r}\right)^{Q_0c}\log\frac{r}{a}dr}{\log b/a\left(\frac{r_c}{a}\right)^{Q_0c}}$$

$$\sim\frac{1}{Q_0c}\cdot\frac{1}{\log b/a}.$$

Now, as seen, $r_c/a\sim 5$ and $\epsilon\sim 10^{-5}$ so $Q_0c\sim 7$ and $q_-\sim 0.03$. Thus all but about 3 percent are retained by induction.

THE CHARGE DEVELOPED IN THE COUNTER

To find the charge developed in the discharge we must examine the action of the space charge sheath. We assume that all the photoelectrons are born outside r_c. (This will be discussed later.) Thus, until a new photo-electron reaches r_c it will experience the same field (2) as if no space charge were present, since the positive ions retain an equal number of electrons on the wire. If we now imagine all the avalanches to fall in a length x of counter wire, and if we number them successively, $N(n, r)$ being the ionization produced by the nth avalanche between r_c and r,

we have a field at r for the $(n+1)$th avalanche of

$$\frac{2}{r}\left\{Q_0-\frac{e}{x}\sum_1^n N(n,r)\right\}, \tag{8}$$

(implicitly assuming $x\gg r_c$ which we shall see is true). Thus, to calculate $N(n+1)$ the total number of electrons in the $(n+1)$th avalanche, we have

$$\frac{1}{c}\cdot\frac{dN(n+1,r)}{N(n+1,r)}=\frac{dr}{r}\left\{Q_0-\frac{e}{x}\sum_1^n N(n,r)\right\}, \tag{9}$$

and so $N(n+1)<N(n)$.

The direct solution for the form of $N(n,r)$ is very difficult, but two approximations suggest themselves:

$$\text{(i)}\qquad N(n,r)=\left(\frac{r_c}{r}\right)^{Q(n)e}, \tag{10}$$

$$\text{(ii)}\qquad N(n,r)=A(n)\left(\frac{r_c}{r}\right)^{Q_0e}. \tag{11}$$

The first allows the form of successive avalanches to change, as it must, and so is more realistic. As both give the same results, the calculation will be described in terms of the first. The second will be used later. The calculation is easy and proceeds as follows. The sum in (8) is replaced by an integral since dN/dn is small and the final value of n is large. (10) is substituted in (9) and the integration over r performed, giving, since $N(n+1)\sim N(n)$,

$$\frac{1}{c}\log N(n)=Q_0\log\frac{r_c}{a}-\frac{e}{x}\int_a^{r_c}\left(\int_1^n\left(\frac{r_c}{r}\right)^{Q(n)e}dn\right)\frac{1}{r}dr. \tag{12}$$

Differentiating (12) with respect to n, and performing the integration over r gives an expression for $Q(n)$, which, combined with (10) and solved, gives

$$\frac{e}{x}(n-1)=\left(\frac{r_c}{a}\right)^{-Q(n)e}\left\{Q(n)+\frac{1}{c\log r_c/a}\right\}-\left(\frac{r_c}{a}\right)^{-Q_0e}\left\{Q_0+\frac{1}{c\log r_c/a}\right\}.$$

Neglecting small terms and retaining only the more powerful $Q(n)$ in the power term, setting the other equal to Q_0, gives

$$N(n)=\frac{1}{\frac{en}{Q_0x}+\theta}, \tag{13}$$

$$\left(\theta=\left(\frac{r_c}{a}\right)^{-Q_0e}=N(1)^{-1}\right),$$

showing an inverse linear dependence of $N(n)$ on n.

At some avalanche n_f we shall have

$$N(n_f)\epsilon=1,$$

and the discharge will converge. Thus the total charge qx generated in the length x of counter is given by

$$qx=e\int_1^{n_f}N(n)dn,$$

giving the simple result

$$q=Q_0\log\frac{\epsilon}{\theta}.$$

This may be expressed in terms of the very important ratio

$$m=\frac{q}{Q_0}$$

which is found to govern almost all aspects of counter behavior

$$m=\log\frac{\epsilon}{\theta}. \tag{14}$$

Now the chief experimental facts concerning the dependence of q on the counter variables are the following:

(i) q depends almost linearly on $V-V_s$ to begin with, most authors agreeing that the increase is a little more rapid than linear.[5, 6, 9–11]

[9] A. Nawijn, *Het Gasontladings Mechanisme van den Geiger-Müller Teller* (Drukkerij Hoogland-Delft, 1943).
[10] S. H. Liebson, Phys. Rev. **72**, 602 (1947).
[11] J. D. Craggs and A. A. Jaffe, Phys. Rev. **72**, 784 (1947).

(ii) At a well-defined overvoltage $(V_B - V_s)$ corresponding approximately to $m=1$, a sharp break occurs in the curve, the slope $dq/d(V-V_s)$ falling to about half its previous value, the dependence now being quite linear.[5, 9, 11]

(iii) For a given overvoltage $V-V_s$, q is practically independent of p and depends only slowly on b/a.[6, 9]

(iv) If the results for the pulse size q be expressed in terms of m, we have the relation, for the first part of the curve

$$m=\frac{V-V_s}{100}\times C, \tag{15}$$

C being a constant depending on the counter, its value ranging from about 0.4 to about 2 (see Stever,[6] and Nawijn[9] for extreme values).

We must now see whether relation (14) can explain all these facts. Using relation (5) and remembering that $r_c \propto V$ we find

$$m=\text{constant}\times\left\{(V-V_s)\log\frac{V_s}{V_p}+V\log\frac{V}{V_s}\right\} \tag{16}$$

for a given counter and pressure.

Now generally $(V-V_s)/V_s$ is small, and we write

$$\log\frac{V}{V_s}=\frac{V-V_s}{V_s},$$

giving

$$m=\text{constant}\times(V-V_s)\times\left\{1+\log\frac{V_s}{V_p}+\frac{V-V_s}{V_s}\right\}, \tag{17}$$

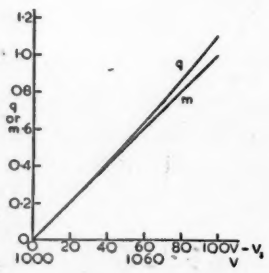

FIG. 4. Relation between q or m and $V-V_s$ or V up to $m=1$.

or

$$q=\text{constant}\times V(V-V_s)\left\{1+\log\frac{V_s}{V_p}+\frac{V-V_s}{V_s}\right\},$$

showing the desired sensibly linear dependence of m on $V-V_s$, with the almost linear dependence of q, the extra V term serving to give the noted slight departure from linearity. m and q are shown in Fig. 4 for our typical counter detailed above (which we now assume, in addition, has $C=1$) up to $m=1$, q being simply plotted as $V/V_s\times m$.

The dependence of q on p may be derived by eliminating the pressure from the constant in (16) and when this is done we find, neglecting the $(V-V_s)/V_s$ term in the curly bracket of (17)

$$q=\text{constant}\times(V-V_s)\frac{V}{V_s}\left(1+\left(\log\frac{V_s}{V_p}\right)^{-1}\right),$$

showing the almost complete lack of dependence of q on p, V_s as we have seen in relation (7), changing only slowly with p.

The dependence on b/a is similarly found, giving, with a "geometry-free" constant

$$q=\text{constant}\times\frac{V}{V_s}(V-V_s)\frac{1}{\log b/a},$$

giving the slow change of q with counter geometry.

To find the predicted value of the constant C we must have an equation free from undetermined constants. This may be found, with the help of ϵ to be

$$m=\frac{V-V_s}{V_s}\left\{1+\left(\log\frac{V_s}{V_p}\right)^{-1}\right\}\log\frac{1}{\epsilon} \tag{18}$$

giving, for the counter considering above, $C=1.86$. This C value lies in the range 0.4–2 noted in (iv) above, though it is a little on the high side. It is quite satisfactory in view of the nature of the calculation.

The theory has thus accounted quantitatively for facts (i), (iii), and (iv) above, and only (ii), the sharp break at $m=1$ awaits explanation. Expression (14) is clearly incapable of accounting for the phenomenon, giving a smooth indefinite increase of m with $V-V_s$. However, something is going to happen at $m=1$ since at this point the

field at the wire has been reduced to zero, and further avalanches cannot multiply all the way to the wire. (Actually they must stop a little way from the wire even at $m=1$, and V_B will not occur quite at $m=1$ but at $(1-a/r_c)\sim 0.8$ as indeed is found by some experimenters, but we neglect this.)

For the calculation of this effect it is more convenient to use the simpler expression (11) for $N(n, r)$ which, we have noted above, gives the same answer for m in the $0<m<1$ range. We then have, treating unit length of counter wire, x having no effect on m as we have seen above,

$$A(n)=\frac{1}{(en/Q_0\theta)+1},$$

so if $m=1$ occurs when $n=n_m$ we have

$$\log\left(\frac{en_m}{Q_0\theta}+1\right)=1.$$

So for $n>n_m$ multiplication will proceed only as far as $a(n)$ and the total number of electrons generated so far in the discharge is

$$\Phi(n)=\frac{Q_0}{e}+\int_{nm}^{n} A(n)\left(\frac{r_c}{a(n)}\right)^{Q_0c}dn, \quad (19)$$

$a(n)$ being the r value, for the nth avalanche, for which the positive ion space charge outside $a(n)$ is Q_0. So for $r>a(n)$ we always have

$$\Phi(n, r)=\frac{Q_0}{e}\log\left(\frac{en}{Q_0\theta}+1\right)\left(\frac{r_c}{r}\right)^{Q_0c}\theta.$$

Thus, if $a(n)$ increases by $da(n)$ from the nth to the $(n+1)$th avalanche $(n>n_m)$, the charge brought down by the $(n+1)$th avalanche must equal the positive ion charge between $a(n)$ and $a(n)+da(n)$. Thus, writing $a(n)-a=\Delta(n)$,

$$\frac{1}{(en/Q_0\theta)+1}\left(\frac{r_c}{a(n)}\right)^{Q_0c}=-\frac{d\Phi}{dr}\cdot\frac{d\Delta(n)}{dn},$$

$d\Phi/dr$ being evaluated at $r=a(n)$. Solution yields, noting that $\Delta/a\ll 1$

$$Q_0c\frac{\Delta(n)}{a}=\log\log\left(\frac{en}{Q_0\theta}+1\right). \quad (20)$$

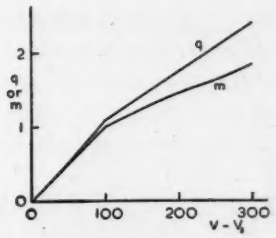

FIG. 5. Complete relation between q or m and $V-V_s$.

We now have an expression for $a(n)$ which may be inserted in (19). The solution is, under the fair approximation

$$\left(\frac{a(n)}{a}\right)^{Q_0c}=1+\frac{Q_0c\Delta(n)}{a},$$

$$\Phi=\frac{Q_0}{e}\left\{1+\frac{\bar{E}_i[1+\log\log((en_f/Q_0\theta)+1)]-\bar{E}_i(1)}{e}\right\}.$$

The e in the denominator of the expression in brackets is the base of the Napierian logarithms, and

$$\bar{E}_i(x)=-\int_{-\infty}^{x}\frac{e^x}{x}\cdot dx.$$

Equation (20) may also be used to find n_f, giving

$$\left(\frac{en_f}{Q_0\theta}+1\right)\log\left(\frac{en_f}{Q_0\theta}+1\right)=\frac{\epsilon}{\theta}.$$

If now $m=1$ occurs at V_B we may rewrite (18) for $V<V_B$ as

$$m=\frac{V-V_s}{V_B-V_s},$$

or, for any V, using (14)

$$\frac{V-V_s}{V_B-V_s}=R=\log\frac{\epsilon}{\theta}.$$

We may thus express the behavior of m above $m=1$ in terms of the ratio R of the overvolts to the overvolts required to give the break in the q curve since,

for $R<1$ $\quad m=R,$

for $R>1$

$$m=1+\frac{\bar{E}_i(1+\log\log\xi)-\bar{E}_i(1)}{e}, \quad (21)$$

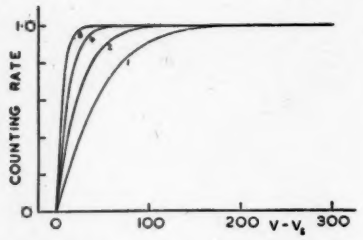

FIG. 6. Calculated plateau curves for the liberation of 1, 2, 4 or 8 initial electrons.

where

$$\xi \log \xi = e^R. \tag{22}$$

This gives

R	m
0	0
0.5	0.5
1.0	1.0
1.5	1.23
2.0	1.45
2.5	1.63
3.0	1.85

This should be the same for all internally quenched counters. The relation between m and R is almost linear above $m=1$, but that between q and R is more so. In Fig. 5 are plotted q and m as functions of V for our typical counter, in the same way as in Fig. 4.

The ratio of the slopes above and below $m=1$ is given by differentiation of (21) with respect to R, when, using (22) one finds a ratio of exactly $\frac{1}{2}$.

A. G. Fenton working in Birmingham has made 20 independent determinations of this slope ratio for counters with values of p from 80 to 180 mm Hg and a values of 0.005, 0.007 and 0.01 cm. The ratio ranged from 0.4 to 0.67 with an average value of 0.50. There was no significant difference in the ratio for various pressures and wires.**

(A rather simpler expression for m may be obtained by a slight further approximation. It is, for $m>1$

$$m = 1 + \log \log \xi$$

giving results almost identical with those tabulated above, and the same slope-ratio.)

It thus seems that all points concerned with pulse size are satisfactorily dealt with by the theory.

One point has been overlooked. The above calculation refers only to the total ionization generated. Since this is greater than Q_0 the question arises, how can all the positive ions traverse the counter, since reverse fields seem to be present? This is not so, however, since the electrons cannot all attain the wire either, and remain trapped in the space-charge sheath, the separation occurring gradually as the more remote positive ions begin to move across the counter, reducing the induction on the wire.

THE SHAPE OF THE PLATEAU CURVE

When the threshold V_s is passed, the counting rate in a Geiger counter climbs rapidly to a constant value at which it remains until multiple discharges and so on mark the end of the plateau. It is the purpose of this section to inquire into the nature of the initial rapid climb and to see whether it depends on any variable.

At some $V > V_s$ we have an average of

$$Z = N(1)\epsilon = \frac{\epsilon}{\theta}$$

avalanches breeding from the first. Now $Z>1$ is the condition for a divergent chain of avalanches, that is, a count, but statistical fluctuations in the number of daughter avalanches may extinguish the discharge by breaking off the chain before enough charge has been generated to give a count. Thus, the probability that there should be not even one daughter avalanche is, for one initial electron in the counter,

$$p(1) = e^{-Z}$$

assuming a Poisson distribution.

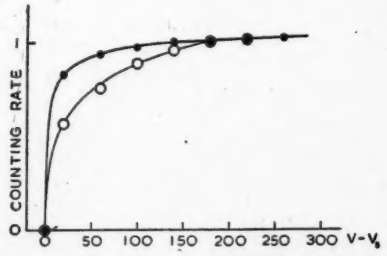

FIG. 7. Experimental plateaus for CuO cathode counter. Open circles: ultraviolet irradiation; solid circles: γ-ray irradiation.

** I am grateful to Mr. Fenton for permission to make use of these results prior to their publication.

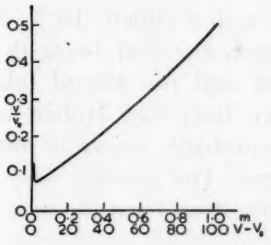

FIG. 8. Relation between v and m or $V-V_s$.

If now $p(w)$ represents the probability of the discharge converging at or before the wth stage of multiplication, it is easy to show that

$$p(w+1)=\exp(-Z(1-p(w))). \qquad (23)$$

The probability of a convergent chain $p(\infty)$ is thus given by

$$p(\infty)=\exp(-Z(1-p(\infty)))$$

or

$$\log p(\infty)=Zp(\infty)-Z \qquad (24)^{***}$$

assuming Z to be constant, which is reasonable since we are effectively interested only in the first few multiplication stages.

Now the plateau curve is given simply by $1-p(\infty)$ and so may be calculated as a function of Z or $V-V_s$. If there are n intial electrons liberated by the ionizing particle, the probability of a convergent discharge is $p(\infty)^n$ and the plateau curve is given by $1-p(\infty)^n$. The plateau curve has been calculated for our typical counter for $n=1$, 2, 4 and 8 and is shown in Fig. 6.

It is seen from Fig. 6 that the plateau curve, for the release of single electrons should be detectably worse than for the release of four or five. To check this, the inside of the cathode of a copper counter was irradiated with ultra-violet light, liberating single electrons, and then with γ-rays, giving a few electrons at a time. The results are given in Fig. 7 where it is seen that the plateau is indeed much worse for the single electrons.

It seems probable that 100 percent counting is being approached for an overvoltage of about 180 (the plateaus have been normalized over their upper regions). Thus when Geiger counters are used to monitor ultra-violet radiation, or in, say, specific ionization studies where the liberation of a single electron is generally considered enough to initiate the discharge, the overvoltage should always be as high as possible.

*** Since this work was completed I have seen a copy of Nawijn's book (see reference 9), in which this problem is discussed, and Eq. (24) derived in a simple way. For this reason I have thought it worth while to give the intermediate probabilities expressed in (23).

THE PROPAGATION OF THE DISCHARGE DOWN THE COUNTER WIRE

The last important problem to be tackled with the aid of our theory is that of the velocity of propagation of the discharge down the wire (v). The theory presented here is based on the remark that if at any instant a length x of counter wire is "burning" in the sense that dense avalanche activity is taking place in it, and if it "burns" for a time T, then

$$v=\frac{x}{T}. \qquad (25)$$

We thus require to calculate x and T. Matters are simplified by the observation that the number of stages w_f of multiplication of avalanches required to burn out the length x of counter wire (achieving the n_f avalanches) does not depend much on x—logarithmically, as will be seen.

x is now the distance which the region of intense avalanche activity propagates in both directions combined along the wire during the w_f stages of multiplication. If now we represent by t_0 the average distance, measured along the wire, which an ultra-violet photon moves before being absorbed and giving its daughter avalanche, we can find x in terms of it. If $Z=1$, the problem is

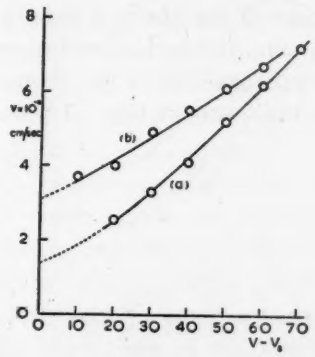

FIG. 9. Miss Freeman's results for the relation between v and $V-V_s$ for the counter fillings of (a) 9.5 cm Hg argon plus 0.5 cm Hg alcohol, (b) 9.5 cm Hg argon plus 2.8 cm Hg alcohol.

that of the random walk with w_f steps. The solution is that the probability of a final displacement ψ (measured in units of the step length) is proportional to

$$\exp\left(-\frac{\psi^2}{2w_f}\right)$$

a Gaussian distribution of width $2(w_f)^{\frac{1}{2}}$. The region of intense avalanche concentration would thus have a length $x=2(w_f)^{\frac{1}{2}}\times t_0$, being quite well defined because of the rapid fall of the Gaussian distribution. For $Z>1$ the problem is more complicated, but one may approximate by increasing the step length proportionally with the probability $(1-(\frac{1}{2})^Z)$ that a step will be taken in a given direction in any single multiplying event. t_0 may be calculated from ν, the mean free path for photon absorption, and is

$$t_0=\frac{\nu}{2}. \tag{26}$$

Thus

$$x=2(w_f)^{\frac{1}{2}}\times 2(1-(\tfrac{1}{2})^Z)\frac{\nu}{2}. \tag{27}$$

We have now limited x by the Gaussian distribution, and imagine the new length of wire to start burning at the end of the first, the peaks of the Gaussians being placed one half-width apart. Thus the time of burning on any one spot on the wire is

$$T=2w_f\tau \tag{28}$$

where τ is the time for a single stage of multiplication. τ depends on various factors—the migration time of the electron from its point of birth to the wire, the excitation time of the (say argon) atoms responsible for the photon emission, and the photon's transit time. These times are, respectively, a few times 10^{-9}, 2×10^{-10} and 3×10^{-12} second, the first being derived as explained below and the second taken from the paper of Alder, Baldinger, Huber, and Metzger.[4] We thus may probably ignore all but the electron migration time. The average distance of birth of the photoelectrons from the wire is

$$r_e=\frac{\pi\nu}{4} \tag{29}$$

((26) and (29) are calculated on the assumption that $\nu\gg a$).

Thus, if the mean electron velocity in the immediate vicinity of the wire is v_e, we have

$$\tau=\frac{\pi\nu}{4v_e}. \tag{30}$$

Thus the problem is reduced to the calculation of w_f.

Considering the length x of counter wire, suppose that at stage w of multiplication there are j photoelectrons present, n avalanches having already taken place, then

$$j(w+1)=j(w)N(n)\epsilon,$$

and

$$\frac{dn}{dw}=j(w);$$

using (13) we obtain the relation between n and w

$$\frac{d^2n}{dw^2}=\frac{dn}{dw}\left(\frac{\epsilon}{(en/Q_0x)+\theta}-1\right),$$

so

$$\frac{dn}{dw}=\frac{Q_0x\epsilon}{e}\log\left(\frac{en}{Q_0x\theta}+1\right)-n+1. \tag{31}$$

Noting that the greater part of the build-up process is spent at $n\ll n_f$ we write the log term as $en/Q_0x\theta$, integration yielding

$$w_f=\frac{\log\left(\frac{xQ_0}{e}\frac{(\epsilon-\theta)^2}{\epsilon}\right)}{\frac{\epsilon}{\theta}-1}. \tag{32}$$

(A numerical integration of (31) shows the approximation leading to (32) to be accurate to

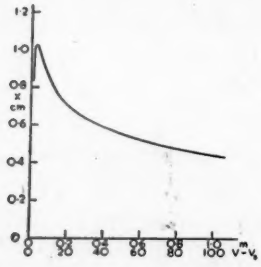

FIG. 10. Relation between x and m or $V-V_s$ ($p=1$ mm).

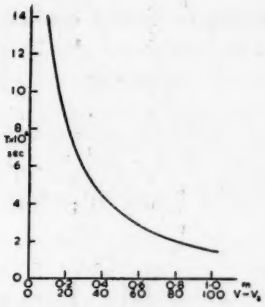

FIG. 11. Relation between T and m or $V-V_s$ ($p=1$ mm).

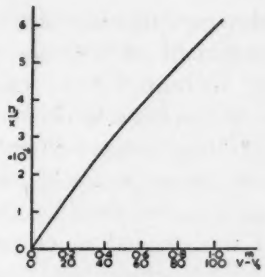

FIG. 12. The number of avalanches per cm of counter wire (n_f/x) as a function of overvoltage.

about 20 percent over the interesting range of m.)

w_f is seen to depend only logarithmically on x and, as $x\sim 0.5-1.0$ cm, it is set $=1$ and effectively omitted from (32). Thus, combining (25), (27), (28), (30) and (32) we have

$$v=\frac{4}{\pi}(1-(\tfrac{1}{2})^{e^m})\left(\frac{e^m-1}{\log((Q_0\epsilon/e)(1-e^{-m})^2)}\right)^{\frac{1}{2}}\times v_s. \quad (33)$$

Having now obtained our expression for v, we may examine the facts which it has to explain. These are derived chiefly from the work of Alder, Baldinger, Huber, and Metzger,[4] of Hill and Dunworth,[12] and from the unpublished results of Miss Freeman obtained in this laboratory.†

(i) The relation between v and $V-V_s$ is roughly linear, the curve being slightly concave towards the v axis.

(ii) A lowering of noble gas pressure, keeping the quenching gas pressure constant, results in a roughly inverse increase of v for a given value of $V-V_s$.

(iii) v depends on the nature of the noble gas, all other factors being constant.

(iv) The v *versus* $V-V_s$ curve does not pass through the origin, but may be extrapolated to a finite positive value of v at $V-V_s=0$.

(v) v does not depend very strongly on quenching agent pressure for a given value of $V-V_s$, though at low $V-V_s$ a higher quenching gas pressure gives a higher value of v.

Alder, Baldinger, Huber, and Metzger[4] have put forward a theory of v, but it is unsatisfactory because it requires the fixing of three constants, is not in very good accord with the facts, and makes no mention of any role of the space charge sheath. It also does not allow for the fact that before a pulse can be observed the local discharge is extinguished.

Figure 8 shows v plotted as a function of $V-V_s$ or m, being taken from (33) appropriately for our typical counter. v is plotted only as far as $m=1$ where a break must occur. It is seen that the result satisfies fact (i) above.

The second and third facts are explained with reference to the v_s of expression (33). A decrease of p will produce a roughly inverse increase of v_s, hence of v, and v_s will obviously depend on the nature of the noble gas. (Hill and Dunworth[12] find v values in the ratio of about 3:1 for helium and argon counters. This is just the ratio if the v_s's in the pure gases for measured values of X/p, though this is probably coincidental, considering the profound effect on v_s of admixed gases.) The fourth fact is seen to be correctly explained, the curve of Fig. 8 giving a finite intercept at $V-V_s=0$. For our typical counter, the ratio of v at $V-V_s=50$ to that at $V-V_s=0$ (extrapolated value) is 0.3. Experimental values range from 0.2 to 0.5. It is seen that the theoretical curve goes off to infinity for very small $V-V_s$ values of the order of one volt. This divergence is probably mathematical, and, in any case, at such tiny overvoltages the assumption of a uniform space charge sheath can no longer hold. Examination of fact (v) brings to us the necessity of deciding in which constituent of the filling mixture the absorption of the photons to give the secondary avalanches takes place. It has generally been assumed that the absorption is in the quenching agent, and Alder, Baldinger,

[12] J. M. Hill and J. V. Dunworth, Nature **158**, 833 (1946).

† I am very grateful to Miss Freeman for her kind permission to quote and discuss her results prior to their publication.

Huber, and Metzger,[4] for example, have found an absorption coefficient of 640 cm^{-1} for normal alcohol vapor. Liebson,[10] however, claims that the noble gas is responsible for the absorption. It is almost certainly a mixed effect, but we shall make the more plausible assumption—that the quenching agent is responsible. One thus sees that v should not depend much on the partial pressure of the quenching agent, since there is no ν in the expression (33) for v. However, v_e will depend somewhat on ν, a bigger ν giving a smaller v_e since the mean X for the electron path will be smaller. Thus increasing the quenching gas pressure should increase v. One thing tends to hold v_e constant however, and that is the space charge, whose effect is to tend to equalize the fields near the wire in the manner calculated above. Thus, the bigger m, the less should v depend on ν. This is shown in Fig. 9, where Miss Freeman's results are displayed.

It is seen that at low overvoltages, the bigger alcohol pressure does indeed give the bigger v, but that the curves approach for higher overvoltages.

It may be remarked that if the assumption of a negligible excitation time for the argon atom is incorrect, we must write

$$\tau=\frac{\pi\nu}{4v_e}+\phi,$$

ϕ being the mean excitation time. The v_e in expression (33) then becomes

$$\frac{v_e}{1+(4\phi v_e/\pi\nu)},$$

and v does not change so rapidly with ν, both numerator and denominator increasing with decreasing ν.

All five facts having been adequately explained, it remains to compare the absolute values of v predicted by expression (33) with those experimentally determined. This comparison is rendered difficult by our lack of knowledge of electron mobilities in very high fields. Den Hartog, Muller, and Verster[13] have measured electron mobilities in a counter gas (9 cm Hg of argon plus 1 cm Hg of alcohol), finding

$$v_e'=k_3X,$$

k_3 being a true mobility constant of value 15,600 cm/sec./volt/cm at $p=100$ mm Hg. Sherwin[14] has found a conflicting result, namely a parabolic relation

$$v_e'=k_4\left(\frac{X}{p}\right)^{\frac{1}{2}},$$

k_4 equalling 4.5×10^6 for a 92 percent argon 8 percent amyl acetate mixture. If these results could be extrapolated down to the X/p values of interest in the present problem, they would yield, for an alcohol pressure of 0.5 cm Hg and an argon pressure of 6.5 cm Hg, using Alder, Baldinger, Huber, and Metzger's[4] value for the effective absorption coefficient, τ values of 4×10^{-9} and 8×10^{-9} sec., respectively. This corresponds to effective v_e's of 4×10^7 and 2×10^7 cm/sec. These values are not widely different, and are of the order to be expected from cloud-chamber photographs of electron avalanches at high X/p values such as those taken by Raether,[15] and Kerr cell studies such as those of White.[16] We thus average, and take $v_e=3\times10^7$ cm/sec. This yields, for our typical counter, a value of v at $V-V_s=50$ of 8×10^6 cm/sec. The alcohol pressure used by Hill and Dunworth[12] was also 0.5 cm Hg and they found, for a counter containing 4.5 cm Hg of argon and $V-V_s=50$ a value of v of 7×10^6 cm/sec. The uncertainties in v_e and the C value of the counter used make wider comparisons unprofitable, but it is seen that the predicted value of v is at any rate roughly correct.

THE MEAN FREE PATH OF THE PHOTONS

We may remark here on the assumption made above that all photoelectrons are born outside r_c. Under the alcohol absorption hypothesis, the value of ν would be a little over 1 mm for 1 cm Hg pressure of alcohol. As noted, $r_c/a\sim5$, hence for $a=0.01$ cm, as large a wire as normally used, $r_c-a=0.04$ cm, and the majority of the photoelectrons will indeed be born outside r_c. The

[13] H. Den Hartog, F. A. Muller, and N. F. Verster, Physica 13, 251 (1947).

[14] C. W. Sherwin, Phys. Rev. 71, 479 (A) (1947).
[15] H. Raether, Zeits. f. Physik 107, 91 (1937).
[16] H. J. White, Phys. Rev. 46, 99 (1934).

smaller a and the alcohol pressure the better is the assumption. On Liebson's picture of argon absorption, almost the same ν would result for a 10-cm Hg argon pressure, so the two views should give roughly the same result for the majority of the effects calculated above. If the absorption is in the argon, the small effect of alcohol pressure on v is more readily understood, but greater difficulty would be encountered in explaining the dependence of v on total pressure p. In any case, the photons mainly responsible for spreading the discharge may have a very small ν and not be observed in the experiments of Liebson and Alder, Baldinger, Huber, and Metzger. The agreement of observed and calculated v however, seems to tell against this. If ν were less than r_c one effect would be to impose another straggling on that of numbers of ions in individual avalanches. In the present state of uncertainty it is not profitable to modify the calculations for the $\nu<r_c$ case.

SOME MAGNITUDES OF THE DISCHARGE

It is of interest to evaluate x, the "burning length" of the wire, T the time of "burning" at any one spot on the wire, and n_f, the number of avalanches taking place per cm of the wire. These are obtained from the appropriate relations above.

x is shown in Fig. 10 for our typical counter (setting $\nu=1$ mm).

It is seen to vary but slowly with $V-V_s$, being 0.5–1.0 cm in the usual range of counter operation.

T is shown in Fig. 11, being of the order of a few times 10^{-8} sec. n_f is shown in Fig. 12.

This is the only quantity which depends much on ϵ (being proportional to it) and so is liable to considerable error. Only its order is of any interest fortunately. All other quantities are of the $\log\epsilon$ type.

It has not been thought worth while to calculate the behavior above $m=1$, since these quantities are more interesting for their rough magnitude than for their exact dependence on $V-V_s$.

DISCUSSION

It is seen that all features of the Geiger discharge considered here depend strongly on m, which should therefore be measured when counter behavior of any kind is being studied. It may be enough simply to find V_B, and hence the C value (relation (15)), but a direct measurement would always be preferable. The C value of a counter is of great importance in determining other aspects of counter behavior—the dead time, for example, which drops sharply above V_B.

Note added June 26, 1948: Sherwin[17] has recently published experimental results which may be interpreted as evidence in favor of the dependence on overvolts and absolute magnitude of T as calculated above and shown in Fig. 11 He finds in Geiger counters a delay between the entry of the ionizing particle and the manifestation of the pulse which can be only partially interpreted in terms of the time of drift of the initial electrons to the wire. There remains a residual delay of the form and magnitude shown in Fig. 11. It is clear that a delay of order T must occur after the initial electrons have arrived at the wire, as sufficient charge must be generated to manifest the pulse. Because of the exponential growth of n with w the delay will certainly be of order T.

[17] C. W. Sherwin, Rev. Sci. Inst. 19, 111 (1948).

Relativistic Cut-Off for Quantum Electrodynamics

RICHARD P. FEYNMAN
Cornell University, Ithaca, New York

(Received July 12, 1948)

A relativistic cut-off of high frequency quanta, similar to that suggested by Bopp, is shown to produce a finite invariant self-energy for a free electron. The electromagnetic line shift for a bound electron comes out as given by Bethe and Weisskopf's wave packet prescription. The scattering of an electron in a potential, without radiation, is discussed. The cross section remains finite. The problem of polarization of the vacuum is not solved. Otherwise, the results will in general agree essentially with those calculated by the prescription of Schwinger. An alternative cut-off procedure analogous to one proposed by Wataghin, which eliminates high frequency intermediate states, is shown to do the same things but to offer to solve vacuum polarization problems as well.

THE main problems of quantum electrodynamics have been essentially solved by the observations of Bethe[1] and of Weisskopf[2] that the divergent terms in the line shift problem can be thought to be contained in a renormalization of the mass of a free electron. That this principle applies as well to other problems was demonstrated by Lewis[3] in analyzing the radiationless scattering of an electron in a potential. Ambiguities which remained in the subtraction procedures are removed by Schwinger.[2,4] He formulated, in a general way, which terms are to be identified in a future correct theory with rest mass, and hence should be omitted from a calculation which does not renormalize the mass. These results are remarkable because they solve the problem without the addition of any new fundamental lengths or dimensions.

The solution given by Schwinger does, however, assume that in some future theory the divergent self-energy terms will be finite. Therefore, it is of interest to point out that there is a model, a modification of ordinary electrodynamics, for which all quantities automatically do come out finite. With this model the ideas of Bethe, Oppenheimer, and Lewis and Schwinger can be directly confirmed.

The model results from the quantization of a classical theory described in a previous paper.[5] In this paper we describe only the results for processes in which only virtual quanta are emitted and absorbed. The problems of permanent emission and the position of positron theory must be more completely studied. It is hoped that a complete physical theory may be published in the near future. Lacking such a complete picture, the present paper may be looked upon merely as presenting an arbitrary rule to cut off at high frequencies in a relativistically invariant manner, the otherwise divergent integrals appearing in quantum field theories. For electrodynamics the rule is to consider the (positive) frequency ω and wave number $\mathbf{k}$ of the field oscillators as independent and to integrate them over the density function $g(\omega^2-k^2)d\omega d\mathbf{k}$ where

$$g(\omega^2-k^2)=\int_0^\infty[\delta(\omega^2-k^2)-\delta(\omega^2-k^2-\lambda^2)]G(\lambda)d\lambda. \quad (1)$$

Here $\delta(x)$ is Dirac's delta function and $G(\lambda)$ is some smooth function such that $\int_0^\infty G(\lambda)d\lambda=1$ and for which the mean values of λ which are important are of order of the frequency 137 $mc^2/\hbar$, or higher. Ordinary quantum electrodynamics replaces the function $g(\omega^2-k^2)$ by $\delta(\omega^2-k^2)$. According to (1), the density g is not everywhere positive.[5] Therefore, the model is essentially that due to Bopp.[6]

The model therefore contains an arbitrary function and the numerical results depend on the

[1] H. A. Bethe, Phys. Rev. **72**, 339 (1947); **73**, 1271A (1948).
[2] J. Schwinger and V. Weisskopf, Phys. Rev. **73**, 1272A (1948).
[3] H. W. Lewis, Phys. Rev. **73**, 173 (1948).
[4] J. Schwinger, Phys. Rev. **73**, 415A (1948).
[5] R. P. Feynman, Phys. Rev. **74**, 939 (1948).
[6] F. Bopp, Ann. d. Physik **42**, 573 (1942).

form of $G(\lambda)$. However, the only term that depends seriously (logarithmically) on the cut-off frequency is the self-energy, which can be used to renormalize the electron mass. After this is done, the remaining terms are nearly independent of the function $G(\lambda)$.

We shall illustrate these points by studying the particular examples of self-energy and radiationless scattering. We shall then discuss an alternative cut-off procedure in which the density of electron states is cut off rather than that of the quanta. This promises to solve problems of vacuum polarization which are not touched by the former procedure.

SELF-ENERGY

The transverse self-energy of a free electron, of mechanical mass μ, in state of momentum $\mathbf{P}_0$ energy $E_0=(\mu^2+P_0^2)^{\frac{1}{2}}$ is given to the first order in e^2 by the second-order perturbation theory, using the one-electron theory of Dirac, by

$$\Delta E=-\frac{e^2}{4\pi^2}\sum_i\int\frac{d\mathbf{k}}{k}\Big\{\sum_+\frac{(0|\alpha_i|f)(f|\alpha_i|0)}{E_f-E_0+k}+\sum_-\frac{(0|\alpha_i|f)(f|\alpha_i|0)}{-E_f-E_0+k}\Big\}. \quad (2)$$

Here the intermediate state f arises from the initial state through emission of a quantum of momentum $\mathbf{k}$ and of energy $k=|\mathbf{k}|$ (the velocity of light is taken as unity, as is Planck's constant). Thus in the intermediate state the electron has momentum $\mathbf{P}_f=\mathbf{P}_0-\mathbf{k}$ and an energy of magnitude $E_f=+(\mu^2+P_f^2)^{\frac{1}{2}}$ but which may be either plus or minus in sign. The sums indicate the sum over all such intermediate states (actually just two) for each sign of the energy. The terms for positive and negative energy have been separated and the sums are written $\sum_+$ and $\sum_-$ for these two cases. The $(f|\alpha_i|0)$ are the matrix elements of Dirac's α-matrices, the sum on i being over the two directions of polarization of the quanta. We shall henceforth write the integral $d\mathbf{k}/k$ over $\mathbf{k}$ space by its equivalent $2\int d\omega d\mathbf{k}\delta(\omega^2-k^2)$, the integral being over all *positive* ω, and all wave numbers $\mathbf{k}$. We shall also write ω for k in the energy denominators as we shall later wish to distinguish the energy of a quantum and the magnitude of the momentum change that its recoil represents. We may further simplify the expression by the use of the well-known projection operators:

$$\Lambda_f^{\pm}=(E_f\pm H_f)/2E_f=(E_f\pm\boldsymbol{\alpha}\cdot\mathbf{P}_f\pm\beta\mu)/2E_f.$$

According to the theory of holes, the last term, the transition to negative energy states, is to be left out; such transitions are prevented because the negative levels are already occupied. On the other hand, in the vacuum, electrons in state of energy $-E_f$ could make virtual transitions to positive energy state E_0. This is now prevented by the presence of an electron in the state E_0, so that, relative to the vacuum, the transverse self-energy is

$$\Delta E=-\frac{e^2}{2\pi^2}\sum_i\int d\omega d\mathbf{k}\delta(\omega^2-k^2)\times\Big\{\frac{(0|\alpha_i\Lambda_f^+\alpha_i|0)}{E_f-E_0+\omega}-\frac{(0|\alpha_i\Lambda_f^-\alpha_i|0)}{E_f+E_0+\omega}\Big\}. \quad (3)$$

The treatment of the longitudinal self-energy is usually different, for the longitudinal oscillators are first eliminated from the Hamiltonian, their effect being the term e^2/r_{00} where r_{00} is the meaningless distance of the electron from itself. These terms must be expressed as integrals over oscillators and combined with (3) before the change suggested by (1) is to be performed. An additional point of confusion is that the longitudinal elimination assumes the intermediate states to form a complete set as they do in (2), but the situation in (3) is not so clear. Fortunately, all these points may be most easily circumvented by simply not eliminating the longitudinal oscillators from the field Hamiltonian at all. One need simply to specify that the sum on i in (3) now be interpreted to mean the sum over each of three perpendicular space directions minus a term for the time direction. We may write $\sum_i\alpha_i\Lambda\alpha_i=\boldsymbol{\alpha}\cdot\Lambda\boldsymbol{\alpha}-\Lambda$, which is a relativistic combination since $\alpha_4=1$. One does not need to be concerned about the gauge condition in a problem in which all quanta are virtual, for the quanta are created by a charge which is conserved. This solution automatically insures the gauge condition just as the Lienard Wiechert classical solution of the Maxwell equations will automatically satisfy the gauge

condition if the charge which produces the potential is conserved.

With this convention for $\sum_i$, Eq. (3) represents the total self-energy. It is easily calculated. The numerator of first term may be written as $1/2E_f$ times $\sum_i(0|\alpha_i(H_f+E_f)\alpha_i|0)$ where H_f is $\boldsymbol{\alpha}\cdot\mathbf{P}_f+\beta\mu$. Now since $\sum_i \alpha_i\alpha_i=+2$, $\sum_i \alpha_i\beta\alpha_i=-4\beta$, and $\sum_i \alpha_i\alpha\alpha_i=-2\boldsymbol{\alpha}$, this becomes

$$-2(0|-E_f+2\beta\mu+\boldsymbol{\alpha}\cdot\mathbf{P}_f|0).$$

The diagonal elements of β and $\boldsymbol{\alpha}$ for the state 0 are μ/E_0 and $\mathbf{P}_0/E_0$, respectively.

The change in energy ΔE_0 can, since the momentum is given, be represented as a change $\Delta\mu$ in rest mass of the electron. In virtue of the general relation $E^2=\mu^2+P^2$, the relation between these quantities is $\mu\Delta\mu=E_0\Delta E_0$. Thus we find, treating the sum of negative energies in a similar manner,

$$\Delta\mu_0=\frac{e^2}{2\pi^2\mu}\int d\omega d\mathbf{k}\,\delta(\omega^2-k^2)\left\{\frac{2\mu^2-E_0E_f+\mathbf{P}_0\cdot\mathbf{P}_f}{E_f(E_f-E_0+\omega)}+\frac{2\mu^2+E_0E_f+\mathbf{P}_0\cdot\mathbf{P}_f}{E_f(E_f+E_0+\omega)}\right\}. \quad (4)$$

The integral diverges logarithmically and $\Delta\mu_0$ defined here is meaningless. If the $\delta(\omega^2-k^2)$ is replaced by $g(\omega^2-k^2)$ defined in (1), the result is finite and invariant (i.e., does not depend on the momentum $\mathbf{P}_0$ of the electron).

How this comes about may be seen by calculating the integral in (4) for

$$g(\omega^2-k^2)=\delta(\omega^2-k^2)-\delta(\omega^2-k^2-\lambda^2)$$

and reserving an integration on λ until later. The integral (4) will converge with this $g(\omega^2-k^2)$, but it is convenient to divide it for purposes of calculation into the difference of two diverging ones.

This is legitimate providing the divergent integrals are first both computed over the same finite region of $\mathbf{k}$ space, the difference taken, and then the region allowed to pass to infinity. Therefore, we shall define $\Delta\mu_0$ by (4), in which we choose the region arbitrarily to be first over all (positive) ω and then over a sphere in $\mathbf{k}$ space of very large radius K. Likewise $\Delta\mu_\lambda$ is defined as expression (4) with $\delta(\omega^2-k^2-\lambda^2)$ replacing $\delta(\omega^2-k^2)$, and the integration taken over the same region.

The true self-mass is therefore

$$\Delta\mu=\int_0^\infty[\operatorname*{Lim}_{K\to\infty}(\Delta\mu_0-\Delta\mu_\lambda)]G(\lambda)d\lambda. \quad (5)$$

We may now calculate these integrals, starting with $\Delta\mu_\lambda$. Since $\mathbf{P}_0\cdot\mathbf{P}_f=\mathbf{P}_0\cdot(\mathbf{P}_0-\mathbf{k})=E_0^2-\mu^2-\mathbf{P}_0\cdot\mathbf{k}$ and $E_f^2=E_0^2+k^2-2\mathbf{P}_0\cdot\mathbf{P}_f$, the $\mathbf{P}_0\cdot\mathbf{P}_f$ term in the numerator of the first term may be eliminated, the numerator becoming

$$\tfrac{1}{2}(E_f^2+E_0^2-k^2)-E_0E_f+\mu^2=\mu^2+\tfrac{1}{2}(\omega^2-k^2)+\tfrac{1}{2}(E_f-E_0-\omega)(E_f-E_0+\omega).$$

Thus the first term in $\Delta\mu_\lambda$ becomes

$$\int\frac{\mu^2+\frac{1}{2}(\omega^2-k^2)}{E_f(E_f-E_0+\omega)}\delta(\omega^2-k^2-\lambda^2)d\omega d\mathbf{k}+\tfrac{1}{2}\int\delta(\omega^2-k^2-\lambda^2)d\omega d\mathbf{k}(E_f-E_0-\omega)/E_f. \quad (6)$$

Adding the corresponding second term which differs from the first only in the sign of E_0, and performing the integral on ω (which requires simply division by 2ω), we find

$$(2\pi^2/e^2)\mu\Delta\mu_\lambda=(\mu^2+\tfrac{1}{2}\lambda^2)\int\frac{1}{(E_f+\omega)^2-E_0^2}\cdot\frac{E_f+\omega}{E_f}\frac{d\mathbf{k}}{\omega}+\frac{1}{2}\int\frac{d\mathbf{k}}{\omega}-\frac{1}{2}\int\frac{d\mathbf{k}}{E_f}, \quad (7)$$

where $\omega=(k^2+\lambda^2)^{\frac{1}{2}}$ and the integration is to be taken over a sphere of radius K in $\mathbf{k}$ space. The first and, obviously, the second integrals turn out to be invariant; the third is not, but its contribution will cancel out on taking $\Delta\mu_0-\Delta\mu_\lambda$ as it does not depend on λ.[7] The result of the integrations[8] is, dropping terms of order $1/K$ and

[7] Pais has suggested that one subtract from $\Delta\mu_0$ the $-\Delta\mu_\lambda$ that one gets not from electrodynamics but from the scalar f field (for which $\beta\cdots\beta$ replaces $\Sigma_i\,\alpha_i\cdots\alpha_i$). Proceeding in this way the integrals $\int d\mathbf{k}/E_f$ do not appear with the same coefficient. Therefore, although this procedure leads to a finite rest mass it is not invariant in the sense here, that the limits of $\mathbf{k}$ space integration can be taken to be independent of the momentum of the electron. A. Pais, Kon. Ned. Akad. v. Wet. Verh. D1, 19, 1 (1947).

[8] The first integral may be performed in the following manner: First integrate over the directions in $\mathbf{k}$ space at constant magnitude k. Only E_f depends on the direction of k and one may therefore replace the solid angle integral by one on E_f. The limits of E_f are $E_+=(\mu^2+(P_0+k)^2)^{\frac{1}{2}}$ and $E_-=(\mu^2+(P_0-k)^2)^{\frac{1}{2}}$ but both terms may be considered together as one if the integral on k be extended from $-K$ to K instead of 0 to K. To integrate this on k, substitute the variable $x=E_++\omega-E_0$ and (the algebra is long) integrate by parts to reduce it to elementary integrals.

smaller:

$$(\pi/e^2)\mu\Delta\mu_\lambda=(\mu^2+\tfrac{1}{2}\lambda^2)[N_\lambda+\mu^2X_\lambda(\mu,\mu)]$$
$$+\tfrac{1}{2}[K^2-\lambda^2(\ln(2K/\lambda)-\tfrac{1}{2})]$$
$$-\tfrac{1}{2}[K^2-\tfrac{1}{3}P_0^2-\mu^2(\ln(2K/\mu)-\tfrac{1}{2})],$$

where

$$N_\lambda=N_0-[\lambda^2/(\lambda^2-\mu^2)]\ln(\lambda/\mu), \quad (7a)$$

with $N_0=\ln(2K/\mu)-\frac{1}{2}$, and the quantity $X_\lambda(\mu,\mu)$ is finite as $K\to\infty$. It is given by setting $\mu_0=\mu$ in the complicated expression

$$2\mu_0{}^4X_\lambda(\mu,\mu_0)=((\lambda^2-\mu^2-\mu_0{}^2)^2-4\mu^2\mu_0{}^2)^{\frac{1}{2}}$$
$$\times\ln\frac{\lambda^2+\mu^2-\mu_0{}^2+((\lambda^2-\mu^2-\mu_0{}^2)^2-4\mu^2\mu_0{}^2)^{\frac{1}{2}}}{2\lambda\mu}$$
$$+\left(\lambda^2-\mu^2+\mu_0{}^2-\frac{2\lambda^2\mu_0{}^2}{\lambda^2-\mu^2}\right)\ln\frac{\mu}{\lambda}+\mu_0{}^2. \quad (7b)$$

Thus $X_0(\mu,\mu)=1/2\mu^2$ and for λ large compared to μ, $X_\lambda(\mu,\mu)=1/4\lambda^2$. Hence

$$(\pi/e^2)(\Delta\mu_0-\Delta\mu_\lambda)=\frac{3\mu}{2}\cdot\frac{\lambda^2}{\lambda^2-\mu^2}\cdot\ln\frac{\lambda}{\mu}+\frac{\mu}{2}$$
$$-(\mu^2+\tfrac{1}{2}\lambda^2)\mu X_\lambda(\mu,\mu), \quad (8)$$

which is independent of K (in the limit $K\to\infty$). If the important values of λ are much greater than μ, we find approximately (to terms of order $(\mu/\lambda)^2$)

$$\Delta\mu=\mu(e^2/\pi)[\tfrac{3}{2}\ln(\lambda_0/\mu)+\tfrac{3}{8}], \quad (9)$$

where

$$\ln\lambda_0=\int_0^\infty\ln\lambda G(\lambda)d\lambda.$$

Judging from the classical case we would have expected to take λ_0 of order 137μ, for then all mass would be electromagnetic. But $\Delta\mu$ here is too small for this to represent a real possibility. The experimental electron mass m is of course $\mu+\Delta\mu$.

The value of λ would have to be of phenomenal size ($\sim e^{137}\mu$) before $\Delta\mu$ can represent a sizeable fraction of the experimental mass. However, to go to the limit of the conventional electrodynamics, λ_0 should be taken as infinite. Then the self-energy diverges logarithmically in the manner found by Weisskopf.[9]

[9] V. Weisskopf, Phys. Rev. 56, 72 (1939).

The emission and subsequent absorption of a quantum acts similarly to the effect of a change in mass not only on the diagonal matrix element which we have just calculated, but on non-diagonal elements as well. Consider that the state appearing on the left of all the matrices in (3) were arbitrary, say x. Then the numerator of the first term can be expressed, as we have seen, by $(-1/E_f)(x|-E_f+2\beta\mu+\boldsymbol{\alpha}\cdot\mathbf{P}_f|0)$. The second term can be expressed similarly. The two terms can be combined so that the whole expression in brackets in (3) can be written

$$2\left\{\frac{(x|-E_fE_0+(E_f+\omega)(2\beta\mu+\boldsymbol{\alpha}\cdot\mathbf{P}_0-\boldsymbol{\alpha}\cdot\mathbf{k})|0)}{E_f((E_f+\omega)^2-E_0^2)}\right\}. \quad (10)$$

This expression may be multiplied by

$$\delta(\omega^2-k^2-\lambda^2)$$

and integrated with respect to ω and over a sphere of radius K in $\mathbf{k}$ space. We make use of the following integrals which can be directly verified:

$$\int\frac{1}{(E_f+\omega)^2-E_0^2}\cdot\frac{E_f+\omega}{E_f}\delta(\omega^2-k^2-\lambda^2)d\omega d\mathbf{k}/\pi$$
$$=N_\lambda+\mu_0{}^2X_\lambda(\mu,\mu_0),$$

$$\int\frac{1}{(E_f+\omega)^2-E_0^2}\delta(\omega^2-k^2-\lambda^2)d\omega d\mathbf{k}/\pi$$
$$=\tfrac{1}{2}N_\lambda+\tfrac{1}{2}(\mu^2+\mu_0{}^2-\lambda^2)X_\lambda(\mu,\mu)_0, \quad (11)$$

$$\int\frac{\mathbf{k}}{(E_f+\omega)^2-E_0^2}\cdot\frac{E_f+\omega}{E_f}\delta(\omega^2-k^2-\lambda^2)d\omega d\mathbf{k}/\pi$$
$$=\tfrac{1}{2}\mathbf{P}_0[\tfrac{1}{3}+N_\lambda+(\lambda^2+\mu_0{}^2-\mu^2)X_\lambda(u,\mu_0)].$$

The integrals have been calculated under the assumption that $E_0{}^2=\mu_0{}^2+P_0{}^2$. In our application we should take $\mu_0=\mu$. The quantities N_λ and $X_\lambda(\mu,\mu_0)$ are given by (7a), (7b). (The extra parameter μ_0 is helpful in obtaining other integrals, useful in the radiationless scattering problem, by differentiations with respect to the various parameters under the integral sign.)

The result of integration (10) with the density $\delta(\omega^2-k^2)-\delta(\omega^2-k^2-\lambda^2)$ is therefore

$$(e^2/\pi)(x|-E_0(\tfrac{1}{2}(N_0-N_\lambda)+\tfrac{1}{2}-(\mu^2-\tfrac{1}{2}\lambda^2)X_\lambda)$$
$$+(2\beta\mu+\boldsymbol{\alpha}\cdot\mathbf{P}_0)(N_0-N_\lambda+\tfrac{1}{2}-\mu^2X_\lambda)$$
$$-\tfrac{1}{2}\boldsymbol{\alpha}\cdot\mathbf{P}_0(N_0-N_\lambda-\lambda^2X_\lambda)|0).$$

Now the energy of state 0 is E_0 so that $\alpha \cdot \mathbf{P}_0 = H_0 - \beta\mu$ is equivalent to $E_0 - \beta\mu$, since it operates on state 0 (no implication about state x is involved). Making this replacement, all the terms in E_0 are seen to cancel and the result is simply

$$(x|\beta|0)\cdot(\Delta\mu_0 - \Delta\mu_\lambda), \tag{12}$$

where $\Delta\mu_0 - \Delta\mu_\lambda$ is given in (8). On integrating over $G(\lambda)d\lambda$ then we find $(x|\beta\Delta\mu|0)$. But this is just the perturbation element which would result from a change of mass by $\Delta\mu$ in the Dirac equation.

We may use this result to show that the level shift for an electron in a bound state given in the present theory will be essentially that given by Weisskopf and Bethe according to their so-called wave-packet method. The change in energy of our electron in a bound state may be calculated in a straightforward manner according to the present formulation. One would simply start with Eq. (2) but with the wave functions and energies for states 0 and f being appropriate for the potential by which the electron is bound. Then one would integrate over $g(\omega^2 - k^2)$ rather than $\delta(\omega^2 - k^2)$ and obtain a definite finite result. The result would show a fairly large change in E_0 depending logarithmically on λ.

A good part of this change could be accounted for as simply due to the change in E_0 that would occur if the mass of the electron were altered from μ to $m = \mu + \Delta\mu$. We can define the true term shift, then, as the complete change in E_0, less $\Delta\mu(\partial E_0/\partial\mu)$, the change due to using μ instead of m in computing the energy with radiation absent. But $\partial E_0/\partial\mu$ is by perturbation theory the expected value $(\psi_0^*|\beta|\psi_0)$ of β for the state ψ_0 in question. From the result (12), however, this is also equivalent to computing the self-energy of a wave packet ψ_0, assuming the electron as free. But Bethe[1] and Weisskopf[2] compute their term shift by just this prescription: the total effect less the self-energy of the free packet. The only difference here is that we would compute the term shift integral on $g(\omega^2 - k^2)$ rather than $\delta(\omega^2 - k^2)$. But since the integral converges either way, the difference between the two results is very small, being of order of (μ^2/λ_0^2) times smaller than the result.

RADIATIONLESS SCATTERING

We can study the radiationless scattering problem in a similar manner. This problem is the correction to the scattering by a first-order potential due to the possibility of emission and absorption of a virtual quantum. For example, this emission and absorption can occur at any time previous to the scattering. (It would, in this case, be nearly equivalent to a change in mass in the wave function of the electron arriving at the scatterer.) There will be a large change in cross section, which would be expected as the result of a change in mass of the electron plus a smaller change caused essentially by emissions previous to and absorptions subsequent to the scattering. As in the case of the self-energy in a field and, in fact, in all such problems, we will really be interested in those effects of radiation over and above that resulting from the change in mass. It is, therefore, simpler to compute the difference between the desired quantity calculated with no radiation and electrons of mass m, and the same quantity computed with the possibility of a virtual quantum emission and absorption with an electron of mass μ. This difference, which we shall call the radiative correction, can be looked upon as the result of perturbation due to the addition to the Hamiltonian of both the radiative interaction terms and a term $-\beta\Delta\mu$. The latter term can, as we have shown, be represented by the integral over oscillators of

$$-\sum_i \left(\frac{\alpha_i \Lambda_f^+ \alpha_i}{E_f - E_0 + \omega} - \frac{\alpha_i \Lambda_f^- \alpha_i}{E_f + E_0 + \omega} \right) \tag{13}$$

when acting on a free electron state of positive energy E_0 and momentum $\mathbf{P}_0$. When acting on a state of negative energy $-E_0$, the term can be shown in a similar manner to be the expression (13) with the sign of E_0 changed in the denominator.

Terms like these are just the ones that Schwinger[4] thought should be omitted from the Hamiltonian if one wishes to get meaningful results, so that the present model agrees with Schwinger's prescription.

When this proces is applied to the scattering problem to obtain the radiative correction to the matrix elements, we are left with several

residual terms. First, the emissions and absorptions previous to scattering are not exactly equivalent to a change in mass. If the emission occurs too close (in time) to the scattering, the absorption must occur in a restricted time, rather than at leisure as for a free electron forming $\beta\Delta\mu$. The correction to the matrix element (in the theory of holes) for this is proportional to

$$-\tfrac{1}{2}\sum_i \frac{(2|\,V\Lambda_1{}^+\alpha_i\Lambda_f{}^+\alpha_i|\,1)}{(E_f+\omega-E_1)^2} \qquad -\tfrac{1}{2}\sum_i \frac{(2|\,V\Lambda_1{}^+\alpha_i\Lambda_f{}^-\alpha_i|\,1)}{(E_f+\omega+E_1)^2}. \quad (14)$$

We assume the potential V (vector or scalar) depending on position like $e^{i\mathbf{q}\cdot\mathbf{R}}$ and time like e^{-iQt} induces transitions from a state 1 of momentum $\mathbf{P}_1$, energy E_1, to the state 2 of momentum $\mathbf{P}_2=\mathbf{P}_1+\mathbf{q}$, energy $E_2=E_1+Q=(\mu^2+P_2^2)^{\frac{1}{2}}$. The operator V is just 1 for scalar potential, α_x for vector potential in x direction, etc. The term (14) represents only that contribution due to a quantum of momentum $\mathbf{k}$, frequency ω. We expect later to integrate over ω and $\mathbf{k}$, times $g(\omega^2-k^2)$. We put $\mathbf{P}_f=\mathbf{P}_1-\mathbf{k}$, $E_f=(\mu^2+P_f^2)^{\frac{1}{2}}$. This term can also be regarded as due to the second-order normalization correction in the ordinary perturbation theory on the incoming wave function. There is a corresponding correction for the final wave function resulting from virtual quanta emitted and absorbed after the scattering: ($\mathbf{P}_g=\mathbf{P}_2-\mathbf{k}$, $E_g=(\mu^2+P_g^2)^{\frac{1}{2}}$).

$$-\tfrac{1}{2}\sum_i \frac{(2|\,\alpha_i\Lambda_g{}^+\alpha_i\Lambda_2{}^+V|\,1)}{(E_g+\omega-E_2)^2} \qquad -\tfrac{1}{2}\sum_i \frac{(2|\,\alpha_i\Lambda_g{}^-\alpha_i\Lambda_2{}^+V|\,1)}{(E_g+\omega+E_2)^2}. \quad (15)$$

All the effects of $\beta\Delta\mu$ are now included. The remaining terms are those for which the potential scattering occurs between the emission and absorption. They may be worked out as by Dancoff[10] (except that we include the longitudinal waves by summing i from 1 to 4). They are

$$+\sum_i \frac{(2|\,\alpha_i\Lambda_g{}^+V\Lambda_f{}^+\alpha_i|\,1)}{(E_f+\omega-E_1)(E_g+\omega-E_2)} + \sum_i \frac{(2|\,\alpha_i\Lambda_g{}^-V\Lambda_f{}^-\alpha_i|\,1)}{(E_f+\omega+E_1)(E_g+\omega+E_2)} \quad (16)$$

and

$$-\sum_i \frac{(2|\,\alpha_i\Lambda_g{}^+V\Lambda_f{}^-\alpha_i|\,1)}{(E_g+\omega-E_2)(E_f+\omega+E_1)} \times\left[1+\frac{2\omega}{E_f+E_g-E_2+E_1}\right] - \sum_i \frac{(2|\,\alpha_i\Lambda_g{}^-V\Lambda_f{}^+\alpha_i|\,1)}{(E_f+\omega-E_1)(E_g+\omega+E_2)} \times\left[1+\frac{2\omega}{E_f+E_g+E_2-E_1}\right]. \quad (17)$$

Although each separate term diverges, the sum of (14), (15), (16), (17) will lead to an integral convergent for large $\mathbf{k}$ even if integrated in the conventional manner on $\delta(\omega^2-k^2)$. This is the result of Lewis. Integration on $g(\omega^2-k^2)$ will make each term converge for large $\mathbf{k}$, but will then only make correction to the sum of order $(\mu/\lambda)^2$ smaller. These we shall neglect.

The integrals do, however, diverge logarithmically at the lower limit of small momentum transfer. This infra-red catastrophe has been completely cleared up by Bloch and Nordsieck.[11] They show that for very long wave-length quanta the amplitude for emission and reabsorption of more than one quantum is not negligible. Inclusion of these higher order terms, which is necessary only in the non-relativistic region, solves the problem. To keep the results given here in a simple form, we can imagine the integrals to be performed down to some minimum momentum $k_{\min}$, small compared to μ. What is effectively the same thing but which is easier (because relativistic invariance is maintained) for practical purposes, is to imagine that the quanta have a very small rest mass $\lambda_{\min}$. Thus we integrate the density

$$\delta(\omega^2-k^2-\lambda_{\min}{}^2)d\omega d\mathbf{k}$$

[10] S. M. Dancoff, Phys. Rev. **55**, 959 (1939).

[11] F. Bloch and A. Nordsieck, Phys. Rev. **52**, 54 (1937).

and assume $\lambda_{\min} \ll \mu$. The two methods are equivalent if one replaces $\ln\lambda_{\min}$ by $\ln(2k_{\min})-1$.

The integrals may be expanded in powers of $\mathbf{q}$ and Q, say up to the second.[12] The constant term vanishes on integration. The integrals appearing may all be expressed in terms of various parametric derivatives of the integrals already given in (11). The result may be expressed in terms of a general potential in a very simple way. A term linear in $\mathbf{q}$, such as proportional to q_x say, is equivalent to taking the matrix element $(2|q_x \exp(i\mathbf{q}\cdot\mathbf{R})|1)$ directly between the two states 2, 1. But this is also equivalent to the matrix element of $-i(\partial/\partial x)\exp(i\mathbf{q}\cdot\mathbf{R})$. Thus if the potential varied in any other manner in space, one sees by superposition that the matrix element is the same as that of $-i\partial V/\partial x$. Thus the terms up to second order can be represented by matrix elements of first and second space and time derivatives of the potential. That is, the radiative correction to the scattering in any potential is equivalent to the first order in e^2 and in the potential, to the scattering produced by a perturbation ΔH to the Dirac Hamiltonian. The perturbation up to terms of first and second derivatives of the vector potential $\mathbf{A}$ and the scalar potential φ is calculated in this manner to be

$$\Delta H=\frac{e^2}{2\pi\hbar c}\left\{-\frac{\hbar e}{2\mu c}(\beta(\sigma\cdot\mathbf{B})-i\beta\alpha\cdot\mathbf{E})\right.$$
$$\left.+\frac{2\hbar^2 e}{3\mu^2c^2}(\Box^2\varphi-\alpha\cdot\Box^2\mathbf{A})\left(\ln\frac{\mu}{\lambda_{\min}}-\frac{3}{8}\right)\right\}. \quad (18)$$

The first term, where $\mathbf{B}=\nabla\times\mathbf{A}$ and $\mathbf{E}=-\nabla\varphi-(1/c)\partial\mathbf{A}/\partial t$, has the same effect as an alteration in the electron magnetic moment[13] by a fraction $e^2/2\pi\hbar c$. This effect was first discovered by Schwinger.[4]

LINE SHIFT

The perturbation to H given here is useful not only for scattering problems but also for the line-shift problem. The actual motion of an electron in a binding potential can be visualized as simply a continued sequence of scatterings in this potential. For each scattering we can calculate the effect of virtual quanta in the way outlined above. However, it is possible, if the potential is strong, that *two* scatterings occur between the emission and reabsorption of the quantum, in which case the above formula for ΔH is incorrect. In hydrogen the potential over most of the atom is sufficiently weak that this does not occur with effective probability. The very long wave-length quanta do have a tendency to exist in the virtual state for long periods, but they have been eliminated by the cut-off $\lambda_{\min}$ at low frequencies.

In hydrogen, then, the line shift due to quanta above minimum wave number $k_{\min}$ is the expected value, for the state in question, of

$$\Delta H=\frac{e^2}{2\pi\hbar c}\left\{-\frac{\hbar ei}{2\mu c}\beta\alpha\cdot\nabla\varphi+\frac{2\hbar^2 e}{3\mu^2c^2}(\nabla^2\varphi)\right.$$
$$\left.\times\left(\ln\frac{\mu c}{2\hbar k_{\min}}+\frac{5}{8}\right)\right\}, \quad (19)$$

where $\varphi=e/r$, r being the distance to the proton, and we have used the relation

$$\ln\lambda_{\min}=\ln(2k_{\min})-1.$$

The first term insures that the fine structure separation correction will be that expected from the change in the electron's magnetic moment. The second may be combined with Bethe's nonrelativistic calculation for quanta below $k_{\min}$.[14]

APPLICATION TO OTHER PROCESSES

The important problem of verifying that the self-energy will not diverge in higher-order approximations has not been carried to completion. It appears unlikely that trouble will arise here. If that is true the model probably gives sensible answers to all problems of quantum electrodynamics other than those involving Uehling polarization effects, discussed below. It has been found to give finite self-mass if we have, instead of a vector field, a scalar field or a pseudoscalar field, coupled to the electron in the simplest way possible without gradient operators. If the field

[12] The integrals have also been worked out, by other methods, for arbitrarily large $\mathbf{q}$ and Q. These will appear in a future publication.

[13] W. Pauli, *Handbuch der Physik* (1933), Vol. 24/1, p. 233.

[14] Using Eq. (18), Professor Bethe finds 1050 megacycles for the separation between $2p_{1/2}$ and $2s_{1/2}$ in hydrogen. (Solvay Report.)

quanta have mass M, $g(\omega^2-k^2)$ is replaced by $g(\omega^2-k^2-M^2)$, and the values of λ of importance are chosen to be large compared to M.

The results for electrodynamics, then, after mass renormalization, depend only slightly on the form of $G(\lambda)$ and the size of λ_0. Since λ_0 may be taken to be extremely large without spoiling the smallness of $\Delta\mu$, there would appear to be good reason to drop the dependence on λ altogether. Thus the $G(\lambda)$ appears only as a complicated scaffold which is removed after the calculation is done.

On the other hand, electrodynamics probably does break down somewhere and it is interesting to keep the terms in λ for various phenomena to see if one might be selected which is particularly sensitive to λ. This phenomena would then be a promising one to study experimentally. The Møller interaction between two electrons is modified by the present theory. There is, of course, the radiative correction, but in addition to that there is simply a change due to the change in the density function for the quanta which can be exchanged. The Møller interaction ordinarily is proportional to $1/q^2$, where q is the magnitude of the momentum transferred from one electron to the other in the center of gravity system. The modification is only that this factor is changed to $\int_0^\infty(1/q^2-1/(q^2+\lambda^2))G(\lambda)d_\lambda$. This represents a decrease in cross section for hard collisions. If λ is of order 137 μc^2, we would need electrons in the center of gravity system of roughly 30 Mev to find a strong effect. This corresponds, however, to bombardment of stationary electrons by electrons of $3\frac{1}{2}$ Bev.[15]

It is interesting to note that the Møller interaction can be viewed as simply a correction to self-energy due to the exclusion principle. The self-energy of two electrons, 1 and 2, is not the sum of the self-energy of each, for one of the virtual states that 2 could ordinarily enter by emission of a quantum is now occupied by 1. The difference between the self-energy of two electrons and the sum of the self-energy of each separately comes out to be just their interaction energy.

[15] A more promising way to obtain processes with high momentum transfer would be wide-angle scattering of electrons from nuclei. But here deviations from expectations might be associated with uncertainties in the nuclear charge distributions rather than electrodynamics. Very wide angle pair production is a phenomena which does occur for high energy incident γ-rays with large momentum transfer in a region not too close to the nucleus.

VACUUM POLARIZATION. ALTERNATIVE CUT-OFF PROCEDURES

In the above calculation, terms of the type discussed by Uehling[16] have been omitted. These terms represent processes involving a pair production followed by annihilation of the *same* pair. For example, a pair produced by the potential may annihilate again emitting a quantum. This quantum is then absorbed by the electron in state 1 transferring it to state 2. These terms are infinite and are not made convergent by the present scheme. There is some point, nevertheless, to solving problems at first without taking them into account. This is because their net effect is only to alter the effective potential in which the electron finds itself, for it may be scattered either directly or by the quantum produced by the Uehling terms. That is, if this problem of polarization of the vacuum is solved it will mean, if there is any effect, simply that the potential A, φ appearing in the Dirac equation and (to high order) in such terms as (18) should be replaced by new "polarized" potentials A', φ'.

These polarization terms can be characterized in a relativistically invariant manner. All the terms which have been calculated above contain matrix elements of operators between states in a sequence such as 1 to f, f to g, g to 2. The omitted polarization terms contain transitions like f to g, g to f, 1 to 2. For higher order processes the polarization terms are those which do not contain a continued sequence of transitions from the initial to the final state.

The polarization terms are not affected in any helpful way by the changes in the density of quanta. It is likely that this problem will have its answer in a changed physical viewpoint. However, there is a simple alternative procedure to produce finite self-energies which also makes convergent the integrals appearing in Serber's[17] treatment of the polarization problem. (Since, however, this treatment of Serber already presupposes a partial subtraction procedure of Heisenberg and Dirac, the situation is not so clear here as in the self-energy problem.)

[16] E. A. Uehling, Phys. Rev. **48**, 55 (1935).
[17] R. Serber, Phys. Rev. **48**, 49 (1935).

From the point of view of coordinate space, the reason that the electronic self-energy diverges appears to be this. A virtual light quantum emitted at one point spreads out as $\delta(t^2-r^2)$ from the origin. The wave packet of the electron spreading out after the emission of the quantum has, as a consequence of Dirac's equation, a similar discontinuous value along the light cone. It is the continued coincidence of these singularities which makes the matrix element for the subsequent absorption of the quantum infinite. The method outlined above of changing $\delta(\omega^2-k^2)$ to $g(\omega^2-k^2)$ has the effect of changing $\delta(t^2-r^2)$ to $f(t^2-r^2)$ where $f(s^2)$ is everywhere finite and goes to zero rapidly for $|s^2|>1/\lambda_0^2$. The quanta have been moved away from the electrons so that overlap on the light cone is reduced.

An obvious alternative procedure is to move the electron wave function away from the quanta. This is easily done in a very similar manner. We assume the density of electron states of energy E, momentum $\mathbf{P}$ to be $g(E^2-P^2-\mu^2)$ rather than $\delta(E^2-P^2-\mu^2)$.[18] The quanta are conventional, $\omega=k$, density $d\mathbf{k}/k$. The self-energy integrals (2) can, of course, be expressed as an integral over the intermediate state momentum $\mathbf{P}_f$ rather than $\mathbf{k}$. Replacing $d\mathbf{P}_f/E_f$ by $g(E_f^2-P_f^2-\mu^2)dE_f d\mathbf{P}_f$, we find

$$\Delta E_0' = -\frac{e^2}{2\pi^2}\int g(E_f^2-P_f^2-\mu^2)dE_f d\mathbf{P}_f \cdot\frac{E_f}{k}\sum_i\left\{\frac{(0|\alpha_i\Lambda_f^+\alpha_i|0)}{E_f+k-E_0}-\frac{(0|\alpha_i\Lambda_f^-\alpha_i|0)}{E_f+k+E_0}\right\},$$

where $k=|\mathbf{P}_f-\mathbf{P}_0|$, $E_0=(\mu^2+P_0^2)^{\frac{1}{2}}$. The projection operators are unchanged since it is only the density of states which we wish to alter. They are still $\Lambda_f^{\pm}=(E_f\pm\alpha\cdot\mathbf{P}_f\pm\beta\mu)/2E_f$. The result of this calculation is to verify that $\Delta E_0'$ is finite, (depending logarithmically on λ_0). The other problems can be analyzed in the same way.

In the problem of polarization of the vacuum, the wave functions of both electron and positron ordinarily spread with a singularity on the light core. The matrix element for their subsequent annihilation is therefore infinite. With the modification here described these wave functions are made less singular and their overlap integral is finite. The polarization integrals in Serber's article[17] may now be integrated to yield finite results.

Other than terms which might be removed by a small renormalization of charge (depending logarithmically on λ_0), the net effect in (17) would be to change the $-(\frac{3}{8})$ in the last term of (17) to $-(\frac{3}{8})-(\frac{1}{5})$. However, the real existence of such polarization corrections is, in the author's view, uncertain. These matters will be discussed in much more detail in future publications. Also reserved for future publication is a more complete physical theory from which the results reported here may be directly deduced. It yields much more powerful techniques for setting up problems and performing the required integrations.

The author would like to express his gratitude to Mr. P. V. C. Hough for assistance in the calculations and to Professor H. A. Bethe and Dr. F. Dyson and many others for useful discussions.

[18] This is seen to be essentially the method proposed by Wataghin. G. Wataghin, Zeits. f. Physik 88, 92 (1934).

PHYSICAL REVIEW VOLUME 74, NUMBER 10 NOVEMBER 15, 1948

Quantum Electrodynamics. I. A Covariant Formulation

JULIAN SCHWINGER
Harvard University, Cambridge, Massachusetts

(Received July 29, 1948)

Attempts to avoid the divergence difficulties of quantum electrodynamics by mutilation of the theory have been uniformly unsuccessful. The lack of convergence does indicate that a revision of electrodynamic concepts at ultra-relativistic energies is indeed necessary, but no appreciable alteration of the theory for moderate relativistic energies can be tolerated. The elementary phenomena in which divergences occur, in consequence of virtual transitions involving particles with unlimited energy, are the polarization of the vacuum and the self-energy of the electron, effects which essentially express the interaction of the electromagnetic and matter fields with their own vacuum fluctuations. The basic result of these fluctuation interactions is to alter the constants characterizing the properties of the individual fields, and their mutual coupling, albeit by infinite factors. The question is naturally posed whether all divergences can be isolated in such unobservable renormalization factors; more specifically, we inquire whether quantum electrodynamics can account unambiguously for the recently observed deviations from the Dirac electron theory, without the introduction of fundamentally new concepts. This paper, the first in a series devoted to the above question, is occupied with the formulation of a completely covariant electrodynamics. Manifest covariance with respect to Lorentz and gauge transformations is essential in a divergent theory since the use of a particular reference system or gauge in the course of calculation can result in a loss of covariance in view of the ambiguities that may be the concomitant of infinities. It is remarked, in the first section, that the customary canonical commutation relations, which fail to exhibit the desired covariance since they refer to field variables at equal times and different points of space, can be put in covariant form by replacing the four-dimensional surface t=const. by a space-like surface. The latter is such that light signals cannot be propagated between any two points on the surface. In this manner, a formulation of quantum electrodynamics is constructed in the Heisenberg representation, which is obviously covariant in all its aspects. It is not entirely suitable, however, as a practical means of treating electrodynamic questions, since commutators of field quantities at points separated by a time-like interval can be constructed only by solving the equations of motion. This situation is to be contrasted with that of the Schrödinger representation, in which all operators refer to the same time, thus providing a distinct separation between kinematical and dynamical aspects. A formulation that retains the evident covariance of the Heisenberg representation, and yet offers something akin to the advantage of the Schrödinger representation can be based on the distinction between the properties of non-interacting fields, and the effects of coupling between fields. In the second section, we construct a canonical transformation that changes the field equations in the Heisenberg representation into those of non-interacting fields, and therefore describes the coupling between fields in terms of a varying state vector. It is then a simple matter to evaluate commutators of field quantities at arbitrary space-time points. One thus obtains an obviously covariant and practical form of quantum electrodynamics, expressed in a mixed Heisenberg-Schrödinger representation, which is called the interaction representation. The third section is devoted to a discussion of the covariant elimination of the longitudinal field, in which the customary distinction between longitudinal and transverse fields is replaced by a suitable covariant definition. The fourth section is concerned with the description of collision processes in terms of an invariant collision operator, which is the unitary operator that determines the over-all change in state of a system as the result of interaction. It is shown that the collision operator is simply related to the Hermitian reaction operator, for which a variational principle is constructed.

INTRODUCTION

THE predictions of quantum electrodynamics concerning higher order perturbation effects have long been discredited in view of the divergent nature of the results. Several attempts[1] have been made to arbitrarily remove supposedly objectionable features of the theory—the so-called "subtraction physics." All such efforts have been fruitless; either failing in their avowed purpose, or lacking internal consistency. The unqualified success of quantum electrodynamics in applications involving the lowest order of perturbation theory indicates its essential validity for moderately relativistic particle energies. The objectionable aspects of quantum electrodynamics are encountered in virtual processes involving particles with ultra-relativistic energies. The two basic phenomena of this type

[1] P. A. M. Dirac, Proc. Camb. Phil. Soc. **30**, 150 (1934); W. Heisenberg, Zeits. f. Physik **90**, 209 (1934); W. Heitler and H. W. Peng, Proc. Camb. Phil. Soc. **38**, 296 (1942).

[2] R. Serber, Phys. Rev. **49**, 545 (1936); H. A. Bethe and J. R. Oppenheimer, Phys. Rev. **70**, 451 (1946).

are the polarization of the vacuum and the self-energy of the electron.

The phrase "polarization of the vacuum" describes the modification of the properties of an electromagnetic field produced by its interaction with the charge fluctuations of the vacuum. In the language of perturbation theory, the phenomenon considered is the generation of charge and current in the vacuum through the virtual creation and annihilation of electron-positron pairs by the electromagnetic field. If the electromagnetic field is that of a light quantum, the vacuum polarization effects are equivalent to ascribing a proper mass to the photon. Previous calculations have yielded non-vanishing, divergent expressions for the light quantum proper mass. However, the latter quantity must be zero in a proper gauge invariant theory. The failure to obtain this result from a gauge invariant formulation can be ascribed only to a faulty application of the theory, rather than to an essential deficiency thereof. When the electromagnetic field is that of a given current distribution, one obtains a logarithmically divergent contribution to the vacuum polarization current which is everywhere proportional to the given distribution. This divergent result expresses the possibility, according to present theory, of creating electron-positron pairs with unlimited energy, a situation that presumably will be corrected in a more satisfactory theory. Thus the physically significant divergence arising from the vacuum polarization phenomenon occurs in a factor that alters the strength of all charges, a uniform renormalization that has no observable consequences other than the conflict with the empirical finiteness of charge.

The interaction between the electromagnetic field vacuum fluctuations and an electron, or more exactly, the electron-positron matter field, modifies the properties of the matter field and produces the self-energy of an electron. The mechanism here under discussion is commonly described as the virtual emission and absorption of a light quantum by an otherwise free electron, although an equally important effect is the partial suppression, via the exclusion principle, of the coupled vacuum fluctuations of the electromagnetic and matter fields. In a Lorentz invariant theory, self-energy effects for a free electron can only result in the addition of an electromagnetic proper mass to the electron's mechanical proper mass. Calculations performed for a stationary electron[3] have yielded a logarithmically divergent electromagnetic proper mass, a divergence that results from the possibility of emitting light quanta with unlimited energy. It is here, as in the vacuum polarization problem, that modifications will be introduced in a more satisfactory theory. However, the electromagnetic proper mass merely produces a renormalization of the electron mass that has no observable consequences, other than the conflict with the empirical finiteness of mass.

It is evident that these two phenomena are quite analogous and essentially describe the interaction of each field with the vacuum fluctuations of the other field. The effect of these fluctuation interactions is simply to alter the fundamental constants e and m, although by logarithmically divergent factors. However, it may be argued that a future modification of the theory, inhibiting the virtual creation of particles that possess energies many orders of magnitude in excess of mc^2, will ascribe a value to these logarithmic factors not vastly different from unity. The charge and mass renormalization factors will then differ only slightly from unity, as befits a perturbation theory, in consequence of the small coupling constant for the matter and electromagnetic fields,

$$e^2/4\pi\hbar c = 1/137.$$

We may now ask the fundamental question: Are all the physically significant divergences of the present theory contained in the charge and mass renormalization factors? Will the consideration of interactions more complicated than these simple vacuum fluctuation effects introduce new divergences; or will all further phenomena involve only moderate relativistic energies, and thus be comparatively insensitive to the high energy modifications that are presumably to be introduced in a more satisfactory theory? This series of papers represents an attempt to supply at least a partial answer to the question, which has acquired an immediate importance in view of recent conclusive evidence

[3] V. Weisskopf, Phys. Rev. **56**, 72 (1939).

that the electromagnetic properties of the electron are not fully described by the Dirac wave equation. Fine structure measurements on hydrogen, deuterium,[4] and ionized helium[5] have revealed energy level displacements that imply the existence of a weak, short range repulsive interaction between electron and proton. Experiments on the hyperfine structure of hydrogen and deuterium,[6] together with electron g value determinations for several states of gallium and sodium,[7] prove that the electron possesses a small additional spin magnetic moment.

Immediately upon completion of the Lamb-Retherford experiment, it was generally recognized[8] that the most probable explanation was to be found in higher order electrodynamic effects; the radiative corrections to the properties of a bound electron other than mass and charge renormalization. A provisional non-relativistic calculation[9] lent support to this view. However, it required a completely relativistic treatment[10] to demonstrate that radiative corrections could account simultaneously for the two apparently unrelated deviations from the Dirac electron theory. It is our major task to enlarge on this development.

In order to isolate the divergent aspects of quantum electrodynamics in a manner that is Lorentz and gauge invariant, it is necessary to employ a formulation of the theory that preserves these covariant features at all stages. The use of a particular reference system or gauge in the course of calculation can result in a loss of covariance in view of the ambiguities that may arise in a divergent theory. The first paper is occupied with the development of a suitable covariant formulation. In the second paper we treat the problems of electron and photon self-energy, together with the polarization of the vacuum. The third paper is concerned with the major topic, the determination of the radiative corrections to the properties of an electron, and the comparison with experiment. Scalar and vector matter fields will be discussed in a fourth paper. It is hoped that successive papers of this series will deal with such subjects as the corrections to the Klein-Nishina formula, the scattering of light by light, and by a Coulomb field.

[4] W. E. Lamb, Jr., and R. C. Retherford, Phys. Rev. **72**, 241 (1947).
[5] J. E. Mack and N. Austern, Phys. Rev. **72**, 972 (1947).
[6] J. E. Nafe, E. B. Nelson, and I. I. Rabi, Phys. Rev. **71**, 914 (1947); D. E. Nagle, R. S. Julian, and J. R. Zacharias, Phys. Rev. **72**, 971 (1947).
[7] P. Kusch and H. M. Foley, Phys. Rev. **72**, 1256 (1947); H. M. Foley and P. Kusch, Phys. Rev. **73**, 412 (1948).
[8] Discussion at the Shelter Island Conference on the Foundations of Quantum Mechanics, June 1947.
[9] H. A. Bethe, Phys. Rev. **72**, 339 (1947).
[10] J. Schwinger, Phys. Rev. **73**, 415 (1948).

1. COVARIANCE IN THE HEISENBERG REPRESENTATION

In this section, we employ the following notation: Greek subscripts assume values ranging from 1 to 4, and a repeated index is to be so summed. The coordinate vector of a four dimensional point x is denoted by $x_\mu=(\mathbf{r},ict)$. The real time coordinate $x_0=(1/i)x_4=ct$ is also used. In particular, the four dimensional element of volume is defined as $d\omega=dx_0dx_1dx_2dx_3$. The four-vector potential of the electromagnetic field is $A_\mu(x)=(\mathbf{A}(\mathbf{r},t),i\phi(\mathbf{r},t))$, while $\psi_\alpha(x)$ designates the four-component Dirac spinor. The spinor index will often be suppressed; thus, if A and A^T designate a four-rowed matrix and its transposed matrix, $A\psi=\psi A^T$ is a four component spinor of which the α component is $A_{\alpha\beta}\psi_\beta=\psi_\beta A_{\beta\alpha}{}^T$. Similarly, the scalar product of two spinors, χ and ψ, is denoted by $\chi\psi=\chi_\alpha\psi_\alpha$. The notation γ_μ is used for the four Hermitian matrices that obey the anticommutation relations

$$\gamma_\mu\gamma_\nu+\gamma_\nu\gamma_\mu=2\delta_{\mu\nu}. \tag{1.1}$$

The adjoint spinor $\bar{\psi}_\alpha(x)$ is defined by

$$\bar{\psi}(x)=\psi^+(x)\gamma_4=\gamma_4{}^T\psi^+(x), \tag{1.2}$$

where $\psi_\alpha{}^+(x)$ is the Hermitian conjugate of $\psi_\alpha(x)$. The so-called charge conjugate spinor $\psi_\alpha{}'(x)$ and its adjoint $\bar{\psi}_\alpha{}'(x)$ are represented by

$$\psi'(x)=C\bar{\psi}(x),\quad \bar{\psi}'(x)=C^{-1}\psi(x). \tag{1.3}$$

Here C is a matrix such that

$$\gamma_\mu{}^T=\gamma_\mu{}^*=-C^{-1}\gamma_\mu C, \tag{1.4}$$

which has the property of being skew-symmetric:

$$C^T=-C, \tag{1.5}$$

and unitary:

$$C^+C=1. \tag{1.6}$$

In the latter equation, $C^+=C^{T*}$ is the Hermitian

conjugate matrix. For the particular representation in which all elements of γ_4 are imaginary, while all elements of the other matrices are real, the conditions on C are satisfied with $C=-\gamma_4$. With this choice, $\psi'(x)=\psi^+(x)$; charge and Hermitian conjugation are equivalent. Finally,

$$\kappa_0=m_0c/\hbar, \tag{1.7}$$

where m_0 is the mechanical proper mass of the electron.

The equations of motion of the coupled electromagnetic and electron-positron matter fields can be derived from the variational principle:

$$\delta\int \mathfrak{L}d\omega=0, \tag{1.8}$$

where the Lagrangian density $\mathfrak{L}$ is

$$\mathfrak{L}=-\frac{1}{2}\frac{\partial A_\mu(x)}{\partial x_\nu}\frac{\partial A_\mu(x)}{\partial x_\nu}$$
$$-\frac{\hbar c}{2}\bar\psi(x)\left[\gamma_\mu\left(\frac{\partial}{\partial x_\mu}-\frac{ie}{\hbar c}A_\mu(x)\right)+\kappa_0\right]\psi(x)$$
$$-\frac{\hbar c}{2}\bar\psi'(x)\left[\gamma_\mu\left(\frac{\partial}{\partial x_\mu}+\frac{ie}{\hbar c}A_\mu(x)\right)+\kappa_0\right]\psi'(x), \tag{1.9}$$

and is so constructed that it is invariant with respect to Lorentz transformations, gauge transformations and charge conjugation. The proof of Lorentz invariance follows the conventional treatment and need not be repeated. Gauge invariance, that is, invariance under the combined transformations

$$A_\mu(x)\rightarrow A_\mu(x)-\frac{\partial\Lambda(x)}{\partial x_\mu}$$
$$\psi(x)\rightarrow\exp\left[-\frac{ie}{\hbar c}\Lambda(x)\right]\psi(x) \tag{1.10}$$
$$\psi'(x)\rightarrow\exp\left[\frac{ie}{\hbar c}\Lambda(x)\right]\psi'(x)$$

induced by a scalar function of position, $\Lambda(x)$, would be generally valid were it not for the term in the Lagrangian density that refers to the electromagnetic field alone. The addition to $\mathfrak{L}$ arising therefrom is

$$-\frac{\partial}{\partial x_\mu}\left[\left(A_\nu+\frac{1}{2}\frac{\partial\Lambda}{\partial x_\nu}\right)\frac{\partial^2\Lambda}{\partial x_\mu\partial x_\nu}\right]$$
$$+\left(A_\nu+\frac{1}{2}\frac{\partial\Lambda}{\partial x_\nu}\right)\frac{\partial}{\partial x_\nu}\frac{\partial^2\Lambda}{\partial x_\mu{}^2},$$

of which the first term has no effect on the equations of motion. Hence gauge invariance is restricted to the group of generating functions that obey

$$\frac{\partial^2\Lambda(x)}{\partial x_\mu{}^2}=\Box^2\Lambda(x)=0. \tag{1.11}$$

Invariance under charge conjugation expresses the complete symmetry between positive and negative charge. The interchange of $\psi(x)$ and $\psi'(x)$, together with $+e$ and $-e$, evidently leaves the Lagrangian density unaltered.

In order to obtain the equations of motion for the matter field, it is necessary to express the Lagrangian density entirely in terms of $\psi(x)$ and $\bar\psi(x)$, or alternatively, $\psi'(x)$ and $\bar\psi'(x)$. By virtue of Eqs. (1.3), (1.4), and (1.5), the following relations hold

$$\begin{aligned}\bar\psi'\gamma_\mu\psi'&=\psi C^{-1T}\gamma_\mu C\bar\psi=\psi\gamma_\mu{}^T\bar\psi\\ \bar\psi'\psi'&=\psi C^{-1T}C\bar\psi=-\psi\bar\psi,\end{aligned} \tag{1.12}$$

and therefore the third term of (1.9) can be written

$$-\frac{\hbar c}{2}\psi(x)\left[\gamma_\mu{}^T\left(\frac{\partial}{\partial x_\mu}+\frac{ie}{\hbar c}A_\mu(x)\right)-\kappa_0\right]\bar\psi(x).$$

We find, as the result of variation, apart from discarded divergences,

$$\delta\mathfrak{L}=-\frac{1}{2}\delta A_\mu\left[\Box^2A_\mu+\frac{1}{c}j_\mu\right]+\frac{1}{2}\left[\Box^2A_\mu+\frac{1}{c}j_\mu\right]\delta A_\mu$$
$$-\frac{\hbar c}{2}\delta\bar\psi\left[\gamma_\mu\left(\frac{\partial}{\partial x_\mu}-\frac{ie}{\hbar c}A_\mu\right)+\kappa_0\right]\psi$$
$$+\frac{\hbar c}{2}\left[\gamma_\mu\left(\frac{\partial}{\partial x_\mu}-\frac{ie}{\hbar c}A_\mu\right)+\kappa_0\right]\psi\delta\bar\psi$$
$$-\frac{\hbar c}{2}\delta\psi\left[\gamma_\mu{}^T\left(\frac{\partial}{\partial x_\mu}+\frac{ie}{\hbar c}A_\mu\right)-\kappa_0\right]\bar\psi$$
$$+\frac{\hbar c}{2}\left[\gamma_\mu{}^T\left(\frac{\partial}{\partial x_\mu}+\frac{ie}{\hbar c}A_\mu\right)-\kappa_0\right]\bar\psi\delta\psi=0, \tag{1.13}$$

where

$$j_\mu(x)=\frac{iec}{2}[\bar\psi(x)\gamma_\mu\psi(x)-\bar\psi'(x)\gamma_\mu\psi'(x)] \quad (1.14)$$

represents the four-vector of charge and current; $j_\mu=(\mathbf{j},ic\rho)$. It is consistent with the form of the commutation relations imposed on the field quantities to infer that

$$\Box^2 A_\mu(x)=-\frac{1}{c}j_\mu(x), \quad (1.15)$$

and

$$\left[\gamma_\mu\left(\frac{\partial}{\partial x_\mu}-\frac{ie}{\hbar c}A_\mu(x)\right)+\kappa_0\right]\psi(x)=0$$
$$\left[\gamma_\mu^T\left(\frac{\partial}{\partial x_\mu}+\frac{ie}{\hbar c}A_\mu(x)\right)-\kappa_0\right]\bar\psi(x)=0. \quad (1.16)$$

The Dirac equations for the matter field can also be cast in the charge conjugate form

$$\left[\gamma_\mu\left(\frac{\partial}{\partial x_\mu}+\frac{ie}{\hbar c}A_\mu(x)\right)+\kappa_0\right]\psi'(x)=0$$
$$\left[\gamma_\mu^T\left(\frac{\partial}{\partial x_\mu}-\frac{ie}{\hbar c}A_\mu(x)\right)-\kappa_0\right]\bar\psi'(x)=0. \quad (1.17)$$

To the equations of motion must be added a supplementary condition, and the commutation relations. The supplementary condition

$$\frac{\partial A_\mu(x)}{\partial x_\mu}\Phi=0 \quad (1.18)$$

restricts the admissible states of the system, as characterized by the constant vector Φ of our Heisenberg representation. The compatability of (1.18) with the equations of motion is a consequence of the charge conservation equation

$$\frac{\partial j_\mu(x)}{\partial x_\mu}=0. \quad (1.19)$$

The customary Maxwell equations, involving the field strengths

$$F_{\mu\nu}=\frac{\partial A_\nu}{\partial x_\mu}-\frac{\partial A_\mu}{\partial x_\nu}, \quad (1.20)$$

rather than the potentials, appear as derived supplementary conditions:

$$\left[\frac{\partial F_{\mu\nu}(x)}{\partial x_\mu}+\frac{1}{c}j_\nu(x)\right]\Phi=0. \quad (1.21)$$

The commutation relations, in their conventional canonical form, read

$$\left[A_\mu(\mathbf{r},t),\frac{1}{c}\frac{\partial}{\partial t}A_\nu(\mathbf{r}',t)\right]=i\hbar c\delta_{\mu\nu}\delta(\mathbf{r}-\mathbf{r}') \quad (1.22a)$$

$$\{\psi_\alpha(\mathbf{r},t),(\bar\psi(\mathbf{r}',t)\gamma_4)_\beta\}=\delta_{\alpha\beta}\delta(\mathbf{r}-\mathbf{r}'), \quad (1.22b)$$

where the bracket symbols signify the commutator and anticommutator, respectively:

$$[A,B]=AB-BA,\quad \{A,B\}=AB+BA. \quad (1.23)$$

We have written the non-vanishing brackets; the bracket symbols whose values are zero are:

$$[A_\mu(\mathbf{r},t),A_\nu(\mathbf{r}',t)],\quad \left[\frac{\partial}{\partial t}A_\mu(\mathbf{r},t),\frac{\partial}{\partial t}A_\nu(\mathbf{r}',t)\right],$$
$$\{\psi_\alpha(\mathbf{r},t),\psi_\beta(\mathbf{r}',t)\},\quad \{\bar\psi_\alpha(\mathbf{r},t),\bar\psi_\beta(\mathbf{r}',t)\},$$

and, of course

$$[A_\mu(\mathbf{r},t),\psi_\alpha(\mathbf{r}',t)],\ \text{etc.}$$

It should be noted that the particle field commutation relations are invariant with regard to charge conjugation. Thus,

$$\begin{aligned}&\{\psi_\alpha'(\mathbf{r},t),(\bar\psi'(\mathbf{r}',t)\gamma_4)_\beta\}\\&=-\{(C\gamma_4{}^T\bar\psi(\mathbf{r},t)\gamma_4)_\alpha,(\psi(\mathbf{r}',t)C^{-1}\gamma_4)_\beta\}\\&=(\gamma_4C)_{\alpha\gamma}\{(\bar\psi(\mathbf{r},t)\gamma_4)_\gamma,\psi_\delta(\mathbf{r}',t)\}(C^{-1}\gamma_4)_{\delta\beta}\\&=\delta_{\alpha\beta}\delta(\mathbf{r}-\mathbf{r}'). \quad (1.24)\end{aligned}$$

A further remark concerns the consistency of the supplementary condition and the commutation relations. Since (1.18) contains the arbitrary point x, one will obtain additional supplementary conditions by commutation, unless

$$\left[\frac{\partial A_\mu(x)}{\partial x_\mu},\frac{\partial A_\nu(x')}{\partial x_\nu'}\right]=0 \quad (1.25)$$

for arbitrary x and x'. In actuality, the canonical commutation relations are such as to yield (1.25). It must be realized that the commutator, considered as a function of x, obeys the wave equation, whence the validity of (1.25) is assured provided the commutator and its time derivative vanish for $t=t'$. This is easily verified.

The physical quantities characterizing the distribution of energy and momentum in the field are combined in the canonical energy-momentum tensor

$$T_{\mu\nu}=-\frac{1}{2}\left[\frac{\partial A_\lambda}{\partial x_\mu}\frac{\partial A_\lambda}{\partial x_\nu}+\frac{\partial A_\lambda}{\partial x_\nu}\frac{\partial A_\lambda}{\partial x_\mu}-\delta_{\mu\nu}\left(\frac{\partial A_\lambda}{\partial x_\sigma}\right)^2\right]+\frac{\hbar c}{2}\bar{\psi}\gamma_\mu\frac{\partial\psi}{\partial x_\nu}+\frac{\hbar c}{2}\bar{\psi}'\gamma_\mu\frac{\partial\psi'}{\partial x_\nu} \quad (1.26)$$

which satisfies the conservation equation

$$\frac{\partial}{\partial x_\mu}T_{\mu\nu}=0 \quad (1.27)$$

since

$$\frac{\partial}{\partial x_\mu}T_{\mu\nu}=-\frac{1}{c}j_\mu\frac{\partial A_\mu}{\partial x_\nu}+\frac{ie}{2}[\bar{\psi}\gamma_\mu\psi-\bar{\psi}'\gamma_\mu\psi']\frac{\partial A_\mu}{\partial x_\nu}=0. \quad (1.28)$$

The canonical tensor can be replaced by a symmetrical energy-momentum tensor

$$\Theta_{\mu\nu}=\tfrac{1}{2}[F_{\mu\lambda}F_{\nu\lambda}+F_{\nu\lambda}F_{\mu\lambda}-\delta_{\mu\nu}\tfrac{1}{2}F_{\lambda\sigma}{}^2]+\frac{\hbar c}{2}\left[\bar{\psi}\gamma_\mu\left(\frac{\partial}{\partial x_\nu}-\frac{ie}{\hbar c}A_\nu\right)\psi+\bar{\psi}\gamma_\nu\left(\frac{\partial}{\partial x_\mu}-\frac{ie}{\hbar c}A_\mu\right)\psi+\bar{\psi}'\gamma_\mu\left(\frac{\partial}{\partial x_\nu}+\frac{ie}{\hbar c}A_\nu\right)\psi'+\bar{\psi}'\gamma_\nu\left(\frac{\partial}{\partial x_\mu}+\frac{ie}{\hbar c}A_\mu\right)\psi'\right]. \quad (1.29)$$

However, it is only the expectation value of $\Theta_{\mu\nu}$,

$$\langle\Theta_{\mu\nu}\rangle=(\Phi,\Theta_{\mu\nu}\Phi), \quad (1.30)$$

that satisfies the conservation equation

$$\frac{\partial}{\partial x_\mu}\langle\Theta_{\mu\nu}\rangle=0 \quad (1.31)$$

as a consequence of the identity

$$\langle\Theta_{\mu\nu}-T_{\mu\nu}\rangle=\left\langle\frac{\partial}{\partial x_\lambda}\tfrac{1}{2}[A_\nu F_{\lambda\mu}+F_{\lambda\mu}A_\nu]-\frac{1}{2}\left[\frac{\partial A_\mu}{\partial x_\lambda}\frac{\partial A_\lambda}{\partial x_\nu}+\frac{\partial A_\lambda}{\partial x_\nu}\frac{\partial A_\mu}{\partial x_\lambda}-\delta_{\mu\nu}\frac{\partial A_\lambda}{\partial x_\sigma}\frac{\partial A_\sigma}{\partial x_\lambda}\right]-\frac{i\hbar c}{4}\frac{\partial}{\partial x_\lambda}\tfrac{1}{2}[\bar{\psi}\sigma_{\mu\lambda}\gamma_\nu\psi+\bar{\psi}'\sigma_{\mu\lambda}\gamma_\nu\psi']\right\rangle, \quad (1.32)$$

since the supplementary condition is required in the derivation and use of this identity. In Eq. (1.32), $\sigma_{\mu\lambda}$ represents the Dirac matrix spin tensor:

$$\sigma_{\mu\lambda}=(\gamma_\mu\gamma_\lambda-\gamma_\lambda\gamma_\mu)/2i. \quad (1.33)$$

The symmetrical energy-momentum tensor is evidently invariant with respect to gauge transformations and charge conjugation. The simple formula

$$\Theta_{\mu\mu}=-m_0c^2\tfrac{1}{2}(\bar{\psi}\psi+\bar{\psi}'\psi') \quad (1.34)$$

should also be noted.

The spatial volume integrals

$$P_\mu=-\frac{i}{c}\int T_{4\mu}dv \quad (1.35)$$

form a time independent four-vector that unites the momentum and energy integrals of the equations of motion; $P_\mu=(\mathbf{P},iW/c)$. It is a simple consequence of the relation (1.32) that the expectation value of P_μ can be calculated from either stress tensor. Thus

$$\langle P_\mu\rangle=-\frac{i}{c}\int\langle\Theta_{4\mu}\rangle dv. \quad (1.36)$$

The operators P_μ form the infinitesimal generators of the coordinate translation group. It is a consequence of the commutation relations that, for example,

$$\frac{i}{\hbar}[A_\mu(x),P_\nu]=\frac{\partial A_\mu(x)}{\partial x_\nu},$$

$$\frac{i}{\hbar}[\psi_\alpha(x),P_\nu]=\frac{\partial\psi_\alpha(x)}{\partial x_\nu}. \quad (1.37)$$

More generally, if $F(x)$ is an arbitrary function of the field variables at the point x, but does not explicitly involve position coordinates,

$$\frac{i}{\hbar}[F(x),P_\nu]=\frac{\partial F(x)}{\partial x_\nu}. \quad (1.38)$$

One can exploit this aspect of the operators P_μ to prove anew that they constitute constants of the motion, and to demonstrate that the canonical commutation relations are consistent with the equations of motion. In a similar way, one can

introduce other operator constants of the motion which compose the angular momentum tensor. These quantities form the infinitesimal generators of the Lorentz group, and with their aid the covariance of the canonical quantization scheme can be demonstrated. However, it is at this point that we must deviate from the conventional development that here has so briefly been outlined.

The equations of motion and the supplementary condition are manifestly covariant; the canonical commutation relations lack this essential characteristic since a special Lorentz reference system is employed. The commutation relations involve field variables at two points of a four dimensional surface characterized by $t=$const. We shall achieve the desired covariance by replacing such surfaces with the invariant concept of a space-like surface. The latter is such that light signals cannot be propagated between any two points on the surface. In terms of the position vectors of two points, x_μ and x_μ', it is required that

$$(x_\mu-x_\mu')^2=(\mathbf{r}-\mathbf{r}')^2-c^2(t-t')^2>0, \quad (1.39)$$

which clearly involves no special reference system. Surfaces of the type $t=$const. form a special non-covariant class of plane space-like surfaces. The customary commutation relations are essentially an expression of the kinematical independence of field quantities at different points of space for a given time. It is evident that the proper covariant description of this general property should involve field quantities at two space-time points that cannot be connected by light signals, that is, two points on a space-like surface. Accordingly, we endeavor thus to generalize the commutation relations into a manifestly covariant form.

The simplest basis for a generalization of (1.22a) is provided by the two statements that express the properties of $\delta(\mathbf{r}-\mathbf{r}')$:

$$\left[A_\mu(\mathbf{r},t),\frac{1}{c}\frac{\partial}{\partial t}A_\nu(\mathbf{r}',t)\right]=0, \quad \mathbf{r}\neq\mathbf{r}' \quad (1.40a)$$

$$\int\left[A_\mu(\mathbf{r},t),\frac{1}{c}\frac{\partial}{\partial t}A_\nu(\mathbf{r}',t)\right]dv'=i\hbar c\delta_{\mu\nu} \quad (1.40b)$$

in which the spatial volume integration is extended over an arbitrary region that includes the point $\mathbf{r}$. The proper generalization of (1.40a), together with the other vanishing electromagnetic field commutators, is simply

$$[A_\mu(x),A_\nu(x')]=0, \quad (x_\mu-x_\mu')^2>0; \quad (1.41)$$

that is, the field quantities associated with two distinct points on a space-like surface commute. In order to generalize (1.40b), it will prove convenient to define a four-vector differential surface area:

$$d\sigma_\mu=(dx_2dx_3dx_0,dx_1dx_3dx_0, dx_1dx_2dx_0,dx_1dx_2dx_3/i). \quad (1.42)$$

Considered as defining the direction of the normal to a space-like surface, $d\sigma_\mu$ must be a time-like vector, that is, $d\sigma_\mu^2<0$. It should be noted that our definitions of surface area and volume are such that the volume generated by the displacement δx_μ imparted to the surface area $d\sigma_\mu$ is $\delta\omega=d\sigma_\mu\delta x_\mu$. It is evident from the notation $dv'=id\sigma_4'$, $\partial A_\nu(\mathbf{r}',t)/\partial ct=i\partial A_\nu(x')/\partial x_4'$, that the proper covariant generalization of (1.40b) is

$$\int_\sigma\left[A_\mu(x),\frac{\partial}{\partial x_\lambda'}A_\nu(x')\right]d\sigma_\lambda'=\frac{\hbar c}{i}\delta_{\mu\nu} \quad (1.43)$$

in which the x' integration is extended over an arbitrary portion of a space-like surface σ that includes the point x.

In order to demonstrate the self-consistency of these and further covariant commutation relations, we must show that the values attributed to such surface integrals are unaltered as the space-like surface σ passing through the point x is varied; and, for a fixed surface relative to the point x, that the commutation relations are compatible with an arbitrary displacement of x. The latter requirement involves a detailed consideration of the equations of motion and will be discussed at an appropriate place. The verification of the first requirement is facilitated by introducing the notion of the functional derivative. The quantity occurring on the left side of (1.43) involves the field variables at all points of the surface σ and is thus a functional of the space-like surface σ, say $F[\sigma]$. We may compare this with the functional of a neighboring space-like surface σ', $F[\sigma']$, which surface is such that it deviates from σ only in a neighborhood of the

point x. If the volume enclosed between the surfaces, $\delta\omega$, is allowed to approach zero, we obtain a definition of the functional derivative of $F[\sigma]$ at the point x:

$$\frac{\delta F[\sigma]}{\delta\sigma(x)}=\operatorname*{Lim}_{\delta\omega\to 0}\frac{F[\sigma']-F[\sigma]}{\delta\omega}, \tag{1.44}$$

in which the notation emphasises that we are considering the variation in F produced by a deformation of the surface σ at the point x. A special class of functional, as exemplified by (1.43), is of the form

$$F[\sigma]=\int_\sigma F_\lambda(x')d\sigma_\lambda', \tag{1.45}$$

that is, a surface integral of a point function. The functional derivative has a particularly simple aspect with this type of functional for, according to Gauss' theorem,

$$\frac{\delta F[\sigma]}{\delta\sigma(x)}=\operatorname*{Lim}_{\delta\omega\to 0}\left(\int_{\sigma'}-\int_\sigma\right)F_\lambda(x')d\sigma_\lambda'$$

$$=\frac{\partial F_\lambda(x)}{\partial x_\lambda}. \tag{1.46}$$

We are now prepared to ascertain the change in (1.43) produced by a deformation of the surface σ at the point $x'\neq x$:

$$\frac{\delta}{\delta\sigma(x')}\int_\sigma\left[A_\mu(x),\frac{\partial}{\partial x_\lambda''}A_\nu(x'')\right]d\sigma_\lambda''$$

$$=[A_\mu(x),\Box'^2A_\nu(x')]$$

$$=-\frac{1}{c}[A_\mu(x),j_\nu(x')]=0, \tag{1.47}$$

in which the latter statement is a consequence of the covariant expression of the kinematical independence of the quantities associated with the two fields:

$$[A_\mu(x),\psi_\alpha(x')]=[A_\mu(x),\bar\psi_\alpha(x')]=0,$$
$$(x_\mu-x_\mu')^2>0. \tag{1.48}$$

The corresponding generalizations of the matter field commutation relations are:

$$\{\psi_\alpha(x),\psi_\beta(x')\}=\{\bar\psi_\alpha(x),\bar\psi_\beta(x')\}$$
$$=\{\psi_\alpha(x),\bar\psi_\beta(x')\}=0,\quad (x_\mu-x_\mu')^2>0, \tag{1.49}$$

and

$$i\int_\sigma\{\psi_\alpha(x),(\bar\psi(x')\gamma_\lambda)_\beta\}d\sigma_\lambda'=\delta_{\alpha\beta}. \tag{1.50}$$

Another version of the last relation, namely

$$i\int_\sigma\{(\gamma_\lambda\psi(x'))_\alpha,\bar\psi_\beta(x)\}d\sigma_\lambda'=\delta_{\alpha\beta} \tag{1.51}$$

can be obtained by taking the Hermitian conjugate of (1.50). To verify that the values given to the surface integrals (1.50) and (1.51) are independent of the particular surface passing through the point x, we examine for example,

$$\frac{\delta}{\delta\sigma(x')}\int_\sigma\{(\gamma_\lambda\psi(x''))_\alpha,\bar\psi_\beta(x)\}d\sigma_\lambda''$$

$$=\left\{\left(\gamma_\lambda\frac{\partial}{\partial x_\lambda'}\psi(x')\right)_\alpha,\bar\psi_\beta(x)\right\}$$

$$=\frac{ie}{\hbar c}\{(\gamma_\lambda A_\lambda(x')\psi(x'))_\alpha,\bar\psi_\beta(x)\}$$

$$-\kappa_0\{\psi_\alpha(x'),\bar\psi_\beta(x)\}=0, \tag{1.52}$$

in view of the vanishing of all such anti-commutators for distinct points of a space-like surface. It can be shown, as before, that the commutation relations are also valid for the charge conjugate matter fields. Thus

$$i\int_\sigma\{(\gamma_\lambda\psi'(x'))_\alpha,\bar\psi_\beta'(x)\}d\sigma_\lambda'$$

$$=i\int_\sigma\{(\bar\psi(x')\gamma_\lambda C)_\alpha,(C^{-1}\psi(x))_\beta\}d\sigma_\lambda'$$

$$=C_{\beta\gamma}{}^{-1}i\int_\sigma\{\psi_\gamma(x),(\bar\psi(x')\gamma_\lambda)_\delta\}d\sigma_\lambda'C_{\delta\alpha}$$

$$=(C^{-1}C)_{\beta\alpha}=\delta_{\alpha\beta}, \tag{1.53}$$

in virtue of (1.50). In the course of these rearrangements, the following relation has also been employed

$$(\gamma_\lambda C)^T=\gamma_\lambda C, \tag{1.54}$$

which is an immediate consequence of the properties of the matrix C.

An obviously covariant definition of the energy-momentum four-vector, replacing Eq. (1.35),

is

$$P_\mu=-\frac{1}{c}\int_\sigma d\sigma_\lambda T_{\lambda\mu}(x), \tag{1.55}$$

in which the integration is extended over an entire space-like surface. The conservation laws now have their covariant expression in the statement that P_μ is independent of the surface σ. Thus

$$\frac{\delta}{\delta\sigma(x)}P_\mu c=\frac{\partial}{\partial x_\lambda}T_{\lambda\mu}(x)=0. \tag{1.56}$$

The conservation law for the total charge

$$Q=-\frac{1}{c}\int_\sigma d\sigma_\mu j_\mu(x)$$

has an analogous expression:

$$\frac{\delta}{\delta\sigma(x)}Qc=\frac{\partial}{\partial x_\mu}j_\mu(x)=0. \tag{1.57}$$

It may be instructive to verify that the commutation relations expressing the displacement operator interpretation of the P_μ emerge from the covariant commutation rules that have been developed. For this purpose, the following lemma is useful:

$$\int_\sigma\left[d\sigma_\mu\frac{\partial}{\partial x_\nu}F(x)-d\sigma_\nu\frac{\partial}{\partial x_\mu}F(x)\right]=0. \tag{1.58}$$

The proof of the lemma is given by remarking that the surface integral is independent of σ:

$$\frac{\delta}{\delta\sigma(x)}\int_\sigma\left[d\sigma_\mu'\frac{\partial}{\partial x_\nu'}F(x')-d\sigma_\nu'\frac{\partial}{\partial x_\mu'}F(x')\right]$$
$$=\frac{\partial}{\partial x_\mu}\frac{\partial}{\partial x_\nu}F(x)-\frac{\partial}{\partial x_\nu}\frac{\partial}{\partial x_\mu}F(x)=0, \tag{1.59}$$

and that, for the particular surface $t=$const., the only components of (1.58) that are not identically zero are $\mu=4$, $\nu=k=1, 2, 3$, say. But

$$i\int d\sigma_4\frac{\partial}{\partial x_k}F(x)=\int dv\frac{\partial}{\partial x_k}F(x)=0 \tag{1.60}$$

for a closed system.

In order to express the operator P_ν in terms of ψ and $\bar\psi$ alone, we note that, according to (1.12),

$$\bar\psi'\gamma_\mu\frac{\partial\psi'}{\partial x_\nu}=\psi\gamma_\mu{}^T\frac{\partial\bar\psi}{\partial x_\nu}=\psi\frac{\partial\bar\psi}{\partial x_\nu}\gamma_\mu, \tag{1.61}$$

whence

$$\int_\sigma d\sigma_\mu\bar\psi'\gamma_\mu\frac{\partial\psi'}{\partial x_\nu}=-\int_\sigma d\sigma_\mu\frac{\partial\psi}{\partial x_\nu}\bar\psi\gamma_\mu$$
$$+\int_\sigma d\sigma_\mu\frac{\partial}{\partial x_\nu}(\psi\bar\psi\gamma_\mu). \tag{1.62}$$

The lemma (1.58) now assures us that

$$\int_\sigma d\sigma_\mu\frac{\partial}{\partial x_\nu}(\psi\bar\psi\gamma_\mu)=\int_\sigma d\sigma_\nu\frac{\partial}{\partial x_\mu}(\psi\bar\psi\gamma_\mu)=0, \tag{1.63}$$

in which the latter statement involves the charge conservation equation. Therefore, P_ν can be written

$$P_\nu=\frac{1}{2c}\int_\sigma d\sigma_\mu\left[\frac{\partial A_\lambda}{\partial x_\mu}\frac{\partial A_\lambda}{\partial x_\nu}+\frac{\partial A_\lambda}{\partial x_\nu}\frac{\partial A_\lambda}{\partial x_\mu}-\delta_{\mu\nu}\left(\frac{\partial A_\lambda}{\partial x_\sigma}\right)^2\right]$$
$$+\frac{\hbar}{2}\int_\sigma d\sigma_\mu\left[\bar\psi\gamma_\mu\frac{\partial\psi}{\partial x_\nu}-\frac{\partial\psi}{\partial x_\nu}\bar\psi\gamma_\mu\right], \tag{1.64}$$

whence

$$\frac{i}{\hbar}[\psi_\alpha(x),P_\nu]=i\int_\sigma d\sigma_\mu'\{\psi_\alpha(x),(\bar\psi(x')\gamma_\mu)_\beta\}$$
$$\times\frac{\partial\psi_\beta(x')}{\partial x_\nu'}=\frac{\partial\psi_\alpha(x)}{\partial x_\nu}, \tag{1.65}$$

and

$$\frac{i}{\hbar}[A_\mu(x),P_\nu]=\frac{i}{\hbar c}\int_\sigma d\sigma_\lambda'\left[A_\mu(x),\frac{\partial A_\sigma(x')}{\partial x_\lambda'}\right]$$
$$\times\frac{\partial A_\sigma(x')}{\partial x_\nu'}+\frac{i}{\hbar c}\int_\sigma\left(d\sigma_\lambda'\left[A_\mu(x),\frac{\partial A_\sigma(x')}{\partial x_\nu'}\right]\right.$$
$$\left.-d\sigma_\nu'\left[A_\mu(x),\frac{\partial A_\sigma(x')}{\partial x_\lambda'}\right]\right)\frac{\partial A_\sigma(x')}{\partial x_\lambda'}$$
$$=\frac{\partial A_\mu(x)}{\partial x_\nu}. \tag{1.66}$$

In the latter proof, the lemma (1.58) has been used, in addition to the properties of commutators.

It can now be shown that the covariant com-

mutation relations are consistent with the equations of motion. We examine the change in the commutator or anticommutator of two field variables associated with two points on a space-like surface, produced by a rigid displacement of the surface. In other words, we seek to evaluate

$$\frac{\partial}{\partial x_\nu}[F(x),G(x-\xi)] \quad \text{or} \quad \frac{\partial}{\partial x_\nu}\{F(x),G(x-\xi)\},$$

where ξ_μ is a space-like vector and F, G are any two field variables. It is a consequence of elementary identities that if F and G obey the equations of motion (1.38), so also do the brackets

$$[F(x),G(x-\xi)] \quad \text{and} \quad \{F(x),G(x-\xi)\}.$$

Therefore, the specification of such brackets as ξ-dependent multiples of the unit operator is self-consistent, since both the derivative with respect to x_ν, and the commutator with P_ν, vanish.

The formulation of quantum mechanics that has now been developed is obviously covariant in all its aspects. However, it is not entirely suitable as a practical means of treating electrodynamic questions. In the course of application, it is often necessary to evaluate commutators of field quantities at points separated by a time-like interval. Such commutators are to be constructed by solving the equations of motion subject to boundary conditions on a space-like surface. This jumbling of the kinematical and dynamical aspects of the situation is a detriment in the systematic discussion of electrodynamic problems. At the opposite extreme is the Schrödinger picture, in which all operators are time independent, and the time development of the system is represented by a varying state vector; a procedure that is non-covariant in its aspect. We now seek a formulation that enables us to retain the evident covariance of the Heisenberg representation, and yet offers something akin to the advantage of the Schrödinger representation, a distinct separation between kinematical and dynamical aspects. The desired separation is to be found in that between the elementary properties of non-interacting fields, and the modification of these properties by the coupling between fields. For non-interacting fields, it is a simple matter to carry out the program previously mentioned, and construct commutation relations for field quantities at arbitrary space-time points. In order to exploit this advantage, it is necessary to find a canonical transformation that changes the equations of motion for field quantities in the Heisenberg representation into those of non-interacting fields, and therefore describes the coupling between fields in terms of a varying state vector. We shall perform this transformation in the next section, and thus obtain an obviously covariant and practical form of quantum electrodynamics, expressed in a mixed Heisenberg-Schrödinger representation, which may be called the interaction representation.[11]

2. THE INTERACTION REPRESENTATION

To alter the equations of motion in the above outlined manner, we introduce a unitary operator $U[\sigma]$, defined for a space-like surface σ, and construct the state vector of the interaction representation

$$\Psi[\sigma]=U[\sigma]\Phi, \qquad (2.1)$$

which depends upon the surface σ, in contrast with the constant vector Φ of the Heisenberg representation. The expectation value of some field variable $\mathbf{F}(x)$ becomes (in this section, the operators of the Heisenberg representation will be denoted by bold face letters)

$$\begin{aligned}(\Phi,\mathbf{F}(x)\Phi)&=(\Psi[\sigma],U[\sigma]\mathbf{F}(x)U^{-1}[\sigma]\Psi[\sigma])\\&=(\Psi[\sigma],F(x)\Psi[\sigma]),\end{aligned} \qquad (2.2)$$

which defines the operators of the interaction representation in terms of those of the Heisenberg representation:

$$F(x)=U[\sigma]\mathbf{F}(x)U^{-1}[\sigma]. \qquad (2.3)$$

It is understood that σ is a space-like surface passing through the point x. In order, however, that $F(x)$ depend only on the point x and not on the particular surface σ, the form of $U[\sigma]$ must be restricted, as indicated by the following

[11] The interaction representation can be regarded as a field generalization of the many-time formalism, from which point of view it has already been considered by S. Tomonaga, Prog. Theor. Phys. 1, 27 (1946). Relativistic quantum theories have also been discussed recently by P. A. M. Dirac, Phys. Rev. 73, 1092 (1948).

requirement:

$$\frac{\delta}{\delta\sigma(x')}F(x)=\frac{\delta U[\sigma]}{\delta\sigma(x')}\mathbf{F}(x)U^{-1}[\sigma]$$
$$-U[\sigma]\mathbf{F}(x)U^{-1}[\sigma]\frac{\delta U[\sigma]}{\delta\sigma(x')}U^{-1}[\sigma]$$
$$=\left[\frac{\delta U[\sigma]}{\delta\sigma(x')}U^{-1}[\sigma],F(x)\right]=0,$$
$$(x_\mu-x_\mu')^2>0. \quad (2.4)$$

This will be satisfied if

$$\frac{\delta U[\sigma]}{\delta\sigma(x')}U^{-1}[\sigma]$$

is an invariant function of the field operators at the point x', since the commutation properties on the surface σ are unaffected by the unitary transformation. If, further, the unitary character of $U[\sigma]$ is to be preserved by its equation of motion, it is necessary that

$$i\frac{\delta U[\sigma]}{\delta\sigma(x)}U^{-1}[\sigma]$$

be a Hermitian operator. Therefore, on writing

$$i\hbar c\frac{\delta U[\sigma]}{\delta\sigma(x)}=\mathcal{H}(x)U[\sigma], \quad (2.5)$$

we obtain a covariant equation of motion for $U[\sigma]$, in which $\mathcal{H}(x)$ is a Hermitian operator, an invariant function of the field quantities at the point x, and has the dimensions of an energy density. The equation of motion for $\Psi[\sigma]$ is, correspondingly,

$$i\hbar c\frac{\delta\Psi[\sigma]}{\delta\sigma(x)}=\mathcal{H}(x)\Psi[\sigma]. \quad (2.6)$$

We have obtained the conditions that must be satisfied by any canonical transformation. It will now be shown that the special transformation desired is attained with $\mathcal{H}(x)$ chosen as the negative of the coupling term in the Lagrangian density, that is,

$$\mathcal{H}(x)=-(1/c)j_\mu(x)A_\mu(x). \quad (2.7)$$

To construct the equations of motion in the interaction representation, we first note that the gradient of any field quantity can be exhibited as a functional derivative, through an obvious generalization of Gauss' theorem:

$$\frac{\partial F(x)}{\partial x_\nu}=\frac{\delta}{\delta\sigma(x)}\int_\sigma F(x')d\sigma_\nu'$$
$$=\frac{\delta}{\delta\sigma(x)}U[\sigma]\int_\sigma\mathbf{F}(x')d\sigma_\nu'U^{-1}[\sigma]. \quad (2.8)$$

The functional derivative in the latter form affects both the surface of integration and the operator $U[\sigma]$, whence

$$\frac{\partial F(x)}{\partial x_\nu}=U[\sigma]\frac{\partial\mathbf{F}(x)}{\partial x_\nu}U^{-1}[\sigma]$$
$$+\int_\sigma\left[\frac{\delta U[\sigma]}{\delta\sigma(x)}U^{-1}[\sigma],F(x')\right]d\sigma_\nu'$$
$$=U[\sigma]\frac{\partial\mathbf{F}(x)}{\partial x_\nu}U^{-1}[\sigma]$$
$$-\frac{i}{\hbar c}\int_\sigma[\mathcal{H}(x),F(x')]d\sigma_\nu'. \quad (2.9)$$

If we first place $F(x)=A_\mu(x)$, it is immediately found from the covariant commutation relations on the space-like surface σ, that

$$\frac{\partial A_\mu(x)}{\partial x_\nu}=U[\sigma]\frac{\partial\mathbf{A}_\mu(x)}{\partial x_\nu}U^{-1}[\sigma], \quad (2.10)$$

which, indeed, is necessary, in order that the electromagnetic field commutation relations retain their form under this canonical transformation. However, with $F(x)=\partial A_\mu(x)/\partial x_\nu$, one obtains

$$\Box^2A_\mu(x)=U[\sigma]\Box^2\mathbf{A}_\mu(x)U^{-1}[\sigma]$$
$$+\frac{1}{c}j_\lambda(x)\frac{i}{\hbar c}\int_\sigma\left[A_\lambda(x),\frac{\partial A_\mu(x')}{\partial x_\nu'}\right]d\sigma_\nu'$$
$$=-\frac{1}{c}U[\sigma]\mathbf{j}_\mu(x)U^{-1}[\sigma]+\frac{1}{c}j_\mu(x)$$
$$=0; \quad (2.11)$$

the equations of motion for the electromagnetic field in the interaction representation are those of an isolated field. In addition, the supple-

mentary condition is unchanged in form:

$$\frac{\partial A_\mu(x)}{\partial x_\mu}\Psi[\sigma]=0 \tag{2.12}$$

provided the point x lies on the surface σ. Finally, if $F(x)=\gamma_\nu\psi(x)$,

$$\left(\gamma_\nu\frac{\partial}{\partial x_\nu}+\kappa_0\right)\psi(x)$$

$$=U[\sigma]\left(\gamma_\nu\frac{\partial}{\partial x_\nu}+\kappa_0\right)\psi(x)U^{-1}[\sigma]$$

$$+\frac{1}{c}A_\mu(x)\frac{i}{\hbar c}\int_\sigma[j_\mu(x),\gamma_\nu\psi(x')]d\sigma_\nu'. \tag{2.13}$$

But, according to (1.12) and (1.14)

$$j_\mu(x)=\frac{iec}{2}[\bar\psi(x)\gamma_\mu\psi(x)-\psi(x)\bar\psi(x)\gamma_\mu], \tag{2.14}$$

and

$$[j_\mu(x),\gamma_\nu\psi(x')]$$

$$=-iec\{\gamma_\nu\psi(x'),\bar\psi_\alpha(x)\}(\gamma_\mu\psi(x))_\alpha, \tag{2.15}$$

so that

$$\left(\gamma_\nu\frac{\partial}{\partial x_\nu}+\kappa_0\right)\psi(x)$$

$$=\frac{ie}{\hbar c}\gamma_\mu A_\mu(x)\psi(x)-i\int_\sigma\{\gamma_\nu\psi(x'),\bar\psi_\alpha(x)\}$$

$$\times d\sigma_\nu'\left(\frac{ie}{\hbar c}\gamma_\mu A_\mu(x)\psi(x)\right)_\alpha$$

$$=0; \tag{2.16}$$

the equations of motion for the matter field in the interaction representation are those of an isolated field. This completely proves the correctness of the choice (2.7) for $\mathcal{K}(x)$.

We may now proceed to construct the general commutation laws for the field quantities in the new representation, by employing their elementary equations of motion. This process will be facilitated by introducing two invariant functions of position, $D(x)$ and $\Delta(x)$, which are associated with the electromagnetic and matter fields, respectively, and have the following covariant definitions:

$$\Box^2D(x)=0;\quad D(x)=0,\quad x_\mu^2>0$$

$$\int_\sigma\frac{\partial D(x)}{\partial x_\mu}d\sigma_\mu=1, \tag{2.17}$$

$$(\Box^2-\kappa_0^2)\Delta(x)=0;\quad \Delta(x)=0,\quad x_\mu^2>0$$

$$\int_\sigma\frac{\partial\Delta(x)}{\partial x_\mu}d\sigma_\mu=1. \tag{2.18}$$

In these definitions, the surface integrations are to be extended over a space-like surface that includes the origin. It is easily verified that the constant value attributed to the surface integrals for arbitrary σ is consistent with the other equations. The detailed construction of these and related functions will be postponed to the second paper of this series; the properties contained in the equations of definition will suffice for our present purposes. It is easily deduced for example, that D and Δ are odd functions of the coordinates:

$$D(-x)=-D(x),\quad \Delta(-x)=-\Delta(x). \tag{2.19}$$

We note that

$$\frac{\delta}{\delta\sigma(x)}\int_\sigma\Big[\Delta(x-x')\frac{\partial}{\partial x_\mu}\Delta(x-x'')$$

$$-\Delta(x-x'')\frac{\partial}{\partial x_\mu}\Delta(x-x')\Big]d\sigma_\mu$$

$$=\Delta(x-x')(\Box^2-\kappa_0^2)\Delta(x-x'')$$

$$-\Delta(x-x'')(\Box^2-\kappa_0^2)\Delta(x-x')$$

$$=0, \tag{2.20}$$

which implies that the surface integral is independent of the particular surface σ. By choosing σ to be, successively, a space-like surface through the points x' and x'', it is inferred that

$$\Delta(x''-x')=-\Delta(x'-x'') \tag{2.21}$$

which proves the second statement of (2.19). The proof for $D(x)$ is identical.

The importance of these invariant functions stems from their utility in expressing the solutions of the equations of motion in terms of boundary values prescribed on some space-like surface. The electromagnetic potentials are uniquely determined if $A_\mu(x)$ and its normal

derivative are specified on a surface σ. The explicit realization of this relation is provided by

$$A_\mu(x)=\int_\sigma\left[D(x-x')\frac{\partial}{\partial x_\nu'}A_\mu(x')-A_\mu(x')\frac{\partial}{\partial x_\nu'}D(x-x')\right]d\sigma_\nu'. \quad (2.22)$$

To verify this statement, it is sufficient to observe that, analogously to Eq. (2.20), the right side of (2.22) is independent of σ, which can be specially chosen as a space-like surface through the point x, yielding

$$\int_\sigma A_\mu(x')\frac{\partial}{\partial x_\nu'}D(x'-x)d\sigma_\nu'=A_\mu(x)$$

as the value of the surface integral. The corresponding solution of the boundary value problem for the first order Dirac equation is provided by

$$\psi(x)=\int_\sigma S(x-x')\gamma_\mu\psi(x')d\sigma_\mu', \quad (2.23)$$

where

$$S(x)=\left(\gamma_\nu\frac{\partial}{\partial x_\nu}-\kappa_0\right)\Delta(x). \quad (2.24)$$

Following the general pattern, we remark that the right side of (2.23) is independent of σ:

$$\begin{aligned}\frac{\delta}{\delta\sigma(x')}\int_\sigma S(x-x')\gamma_\mu\psi(x')d\sigma_\mu'&=\frac{\partial}{\partial x_\mu'}(S(x-x')\gamma_\mu\psi(x'))\\&=S(x-x')\left(\gamma_\mu\frac{\partial}{\partial x_\mu'}+\kappa_0\right)\psi(x')\\&\quad-\left(\frac{\partial}{\partial x_\mu}S(x-x')\gamma_\mu+\kappa_0S(x-x')\right)\psi(x')\\&=0,\end{aligned} \quad (2.25)$$

since

$$\begin{aligned}\left(\gamma_\mu\frac{\partial}{\partial x_\mu}+\kappa_0\right)S(x)&=\frac{\partial}{\partial x_\mu}S(x)\gamma_\mu+\kappa_0S(x)\\&=(\Box^2-\kappa_0^2)\Delta(x)=0;\end{aligned} \quad (2.26)$$

and that an evaluation with a surface through the point x, gives

$$\begin{aligned}&\int_\sigma\gamma_\nu\gamma_\mu\frac{\partial}{\partial x_\nu}\Delta(x-x')\psi(x')d\sigma_\mu'\\&=\int_\sigma\frac{\partial}{\partial x_\mu'}\Delta(x'-x)\psi(x')d\sigma_\mu'\\&\quad+\frac{i}{2}\sigma_{\nu\mu}\int_\sigma\left[\frac{\partial}{\partial x_\nu'}\Delta(x'-x)d\sigma_\mu'-\frac{\partial}{\partial x_\mu'}\Delta(x'-x)d\sigma_\nu'\right]\psi(x')=\psi(x)\end{aligned}$$

with the aid of the lemma (1.58). The adjoint equation

$$\bar\psi(x)=\int_\sigma d\sigma_\mu'\bar\psi(x')\gamma_\mu S(x'-x) \quad (2.27)$$

can be proved directly, or inferred from (2.23).

The construction of the general commutation relations is now trivial. To evaluate $[A_\mu(x), A_\nu(x')]$, for example, it is merely necessary to express $A_\mu(x)$ in terms of the field variables on a space-like surface that includes the point x', and employ the commutation relations for such surfaces. Thus

$$[A_\mu(x),A_\nu(x')]=-\int_\sigma D(x-x'')\times\left[A_\nu(x'),\frac{\partial}{\partial x_\lambda''}A_\mu(x'')\right]d\sigma_\lambda'',$$

whence

$$[A_\mu(x),A_\nu(x')]=i\hbar c\delta_{\mu\nu}D(x-x'). \quad (2.28)$$

In a similar way,

$$\{\psi_\alpha(x),\bar\psi_\beta(x')\}=\int_\sigma S_{\alpha\gamma}(x-x'')\times\{(\gamma_\mu\psi(x''))_\gamma,\bar\psi_\beta(x')\}d\sigma_\mu''$$

so that

$$\begin{aligned}\{\psi_\alpha(x),\bar\psi_\beta(x')\}&=\frac{1}{i}S_{\alpha\beta}(x-x')\\&=\frac{1}{i}\left(\gamma_\mu\frac{\partial}{\partial x_\mu}-\kappa_0\right)_{\alpha\beta}\Delta(x-x').\end{aligned} \quad (2.29)$$

All other matter field anti-commutators vanish. Of course, the matter field commutation relations are invariant with respect to charge conjugation.

Finally, we turn to the generalization of the supplementary condition (2.12), which consists of removing the restriction that x be situated on the surface σ. It follows from (2.22) that, for an arbitrary point x,

$$\frac{\partial A_\mu(x)}{\partial x_\mu}\Psi[\sigma]=\int_\sigma D(x-x'')\times\frac{\partial}{\partial x_\nu''}\left(\frac{\partial A_\mu(x'')}{\partial x_\mu''}\right)d\sigma_\nu''\Psi[\sigma]. \quad (2.30)$$

However, according to (2.9), with $F=\partial A_\mu(x'')/\partial x_\mu''$,

$$\begin{aligned}&\frac{\partial}{\partial x_\nu''}\left(\frac{\partial A_\mu(x'')}{\partial x_\mu''}\right)\Psi[\sigma]\\&=U[\sigma]\frac{\partial}{\partial x_\nu''}\left(\frac{\partial A_\mu(x'')}{\partial x_\mu''}\right)\Phi\\&\quad-\frac{i}{\hbar c}\int_\sigma\left[\mathcal{H}(x''),\frac{\partial A_\mu(x')}{\partial x_\mu'}\right]d\sigma_\nu'\Psi[\sigma]\\&=\frac{i}{\hbar c}\int_\sigma\left[A_\lambda(x''),\frac{\partial A_\mu(x')}{\partial x_\mu'}\right]\times d\sigma_\nu'\frac{1}{c}j_\lambda(x'')\Psi[\sigma]\\&=\frac{i}{\hbar c}\int_\sigma\left[A_\mu(x'),\frac{\partial A_\lambda(x'')}{\partial x_\nu''}\right]\times d\sigma_\mu'\frac{1}{c}j_\lambda(x'')\Psi[\sigma]. \quad (2.31)\end{aligned}$$

In the last transformation, we have used the lemma (1.58) and the fact that the electromagnetic field commutators contain only the difference in coordinates of the two points involved. On introducing (2.31) into (2.30) and performing the x'' integration, we find without further difficulty that

$$\left[\frac{\partial A_\mu(x)}{\partial x_\mu}-\int_\sigma D(x-x')\frac{1}{c}j_\mu(x')d\sigma_\mu'\right]\Psi[\sigma]=0, \quad (2.32)$$

which is the supplementary condition for the interaction representation. Although the consistency of the supplementary condition is guaranteed by the corresponding property in the Heisenberg representation, it is well to verify it directly. However, since the proof involves the commutation properties of the current four-vector, we digress briefly to derive the necessary theorems.

It is easy to deduce from the expression (2.14) for $j_\mu(x)$, and the anti-commutator (2.29), that

$$\begin{aligned}&[j_\mu(x),j_\nu(x')]\\&\quad=ie^2c^2[\bar\psi(x)\gamma_\mu S(x-x')\gamma_\nu\psi(x')\\&\qquad-\bar\psi(x')\gamma_\nu S(x'-x)\gamma_\mu\psi(x)]. \quad (2.33)\end{aligned}$$

Of course, all components of j_μ commute at two distinct points on a space-like surface. However, the important statement is that a time-like component of j_μ commutes with all components of the current at the same point. We prove this by demonstrating that

$$\int_\sigma[j_\mu(x),j_\nu(x')]d\sigma_\nu'=\frac{1}{c}[j_\mu(x),Q]=0 \quad (2.34)$$

where σ is any space-like surface, which, in particular, can include the point x. The validity of this statement follows immediately from (2.23) and (2.27), since

$$\begin{aligned}&\int_\sigma[j_\mu(x),j_\nu(x')]d\sigma_\nu'\\&\quad=ie^2c^2[\bar\psi(x)\gamma_\mu\psi(x)-\bar\psi(x)\gamma_\mu\psi(x)]\\&\quad=0. \quad (2.35)\end{aligned}$$

Indeed, Eq. (2.34) is an expression of charge conservation, for, according to (2.9), with $F=j_\nu(x)$:

$$\begin{aligned}\frac{\partial j_\nu(x)}{\partial x_\nu}&=\frac{i}{\hbar c}\frac{1}{c}\int_\sigma[j_\mu(x),j_\nu(x')]d\sigma_\nu'A_\mu(x)\\&=\frac{i}{\hbar c}[j_\mu(x),Q]A_\mu(x). \quad (2.36)\end{aligned}$$

To prove the suitability of (2.32) as a supplementary condition, we must show that it is consistent with the field equations of motion, the equation of motion for $\Psi[\sigma]$, and the commutation relations. In terms of the operator

$$\Omega[x,\sigma]=\frac{\partial A_\mu(x)}{\partial x_\mu}-\int_\sigma D(x-x')\frac{1}{c}j_\mu(x')d\sigma_\mu', \quad (2.37)$$

we must verify that

$$\Box^2\Omega[x,\sigma]=0, \tag{2.38a}$$

$$i\hbar c\frac{\delta\Omega[x,\sigma]}{\delta\sigma(x')}+[\Omega[x,\sigma],\mathfrak{IC}(x')]=0, \tag{2.38b}$$

$$[\Omega[x,\sigma],\Omega[x',\sigma]]=0. \tag{2.38c}$$

The first statement is trivial. As to (2.38b), note that

$$i\hbar c\frac{\delta\Omega[x,\sigma]}{\delta\sigma(x')}=i\hbar\frac{\partial D(x-x')}{\partial x_\mu}j_\mu(x')$$

while

$$[\Omega[x,\sigma],\mathfrak{IC}(x')]=-\frac{1}{c}\left[\frac{\partial A_\mu(x)}{\partial x_\mu},A_\nu(x')\right]j_\nu(x')$$
$$=-i\hbar\frac{\partial D(x-x')}{\partial x_\mu}j_\mu(x')$$

in view of the property of $j_\mu(x)$ just established. Finally, the same property implies that

$$[\Omega[x,\sigma],\Omega[x',\sigma]]=\left[\frac{\partial A_\mu(x)}{\partial x_\mu},\frac{\partial A_\nu(x')}{\partial x_\nu'}\right]$$
$$=-i\hbar c\Box^2D(x-x')=0.$$

Gauge invariance has a different aspect in the new representation from that of the Heisenberg representation, since the matter field equations do not involve the electromagnetic field. On introducing a change in gauge

$$A_\mu(x)\rightarrow A_\mu(x)-\frac{\partial\Lambda(x)}{\partial x_\mu},$$

where $\Lambda(x)$ is a scalar function of position such that

$$\Box^2\Lambda(x)=0,$$

the supplementary condition, commutation relations and field equations of motion are unaffected, but the equation of motion for $\Psi[\sigma]$ becomes

$$i\hbar c\frac{\delta\Psi[\sigma]}{\delta\sigma(x)}$$
$$=\left\{\mathfrak{IC}(x)+\frac{\partial}{\partial x_\mu}\left(\frac{1}{c}j_\mu(x)\Lambda(x)\right)\right\}\Psi[\sigma], \tag{2.39}$$

in which the charge conservation equation has been used. We shall show that it is possible to restore this equation to its original form, and thus prove gauge invariance, by a canonical transformation on $\Psi[\sigma]$. Indeed, the proper transformation is

$$\Psi[\sigma]\rightarrow e^{-iG[\sigma]}\Psi[\sigma] \tag{2.40}$$

where

$$G[\sigma]=\frac{1}{\hbar c}\int_\sigma^1 j_\mu(x)\Lambda(x)d\sigma_\mu. \tag{2.41}$$

The equation of motion for the new state vector is

$$i\hbar c\frac{\delta\Psi[\sigma]}{\delta\sigma(x)}+i\hbar ce^{iG[\sigma]}\frac{\delta e^{-iG[\sigma]}}{\delta\sigma(x)}\Psi[\sigma]$$
$$=\left\{\mathfrak{IC}(x)+\frac{\partial}{\partial x_\mu}\left(\frac{1}{c}j_\mu(x)\Lambda(x)\right)\right\}\Psi[\sigma], \tag{2.42}$$

as a consequence of the commutation properties of j_μ on a space-like surface. We may now employ the simple expansion theorem

$$e^{iG}\frac{\delta e^{-iG}}{\delta\sigma(x)}=-i\frac{\delta G}{\delta\sigma(x)}+\frac{1}{2!}\left[G,\frac{\delta G}{\delta\sigma(x)}\right]$$
$$+\frac{i}{3!}\left[G,\left[G,\frac{\delta G}{\delta\sigma(x)}\right]\right]+\cdots \tag{2.43}$$

to deduce that

$$i\hbar ce^{iG}\frac{\delta e^{-iG}}{\delta\sigma(x)}=\frac{\partial}{\partial x_\mu}\left(\frac{1}{c}j_\mu(x)\Lambda(x)\right)$$
$$+\frac{i}{2c}[G,j_\mu(x)]\frac{\partial\Lambda(x)}{\partial x_\mu}+\cdots=\frac{\partial}{\partial x_\mu}\left(\frac{1}{c}j_\mu(x)\Lambda(x)\right),$$

in which the commutability of j_μ with a time-like component of j_μ on the surface σ ensures that only the first term of the series survives. We have thereby demonstrated the correctness of the transformation (2.40).

The form of the energy-momentum quantities, as well as their significance as displacement operators, is altered by the canonical transformation that generates the interaction representation. In the Heisenberg representation, the functional derivative of an operator is of immediate significance in computing the functional

derivative of the expectation value of that operator:

$$\frac{\delta}{\delta\sigma(x)}(\Phi,\mathbf{F}[\sigma]\Phi)=\left(\Phi,\frac{\delta\mathbf{F}[\sigma]}{\delta\sigma(x)}\Phi\right). \quad (2.44)$$

In the interaction representation, however, part of the change in the expectation value is accounted for by the variation in $\Psi[\sigma]$:

$$\frac{\delta}{\delta\sigma(x)}(\Psi[\sigma],F[\sigma]\Psi[\sigma])=\left(\Psi[\sigma],\frac{\delta F[\sigma]}{\delta\sigma(x)}\Psi[\sigma]\right)+\frac{i}{\hbar c}(\Psi[\sigma],[\mathcal{H}(x),F[\sigma]]\Psi[\sigma]). \quad (2.45)$$

Accordingly, it is natural to define the total functional derivative of an operator,

$$\frac{\Delta F[\sigma]}{\Delta\sigma(x)}=\frac{\delta F[\sigma]}{\delta\sigma(x)}+\frac{i}{\hbar c}[\mathcal{H}(x),F[\sigma]]=U[\sigma]\frac{\delta\mathbf{F}[\sigma]}{\delta\sigma(x)}U^{-1}[\sigma] \quad (2.46)$$

which is composed of the partial functional derivatives, expressing the explicit coordinate variation and the implicit dynamical variation. With this definition,

$$\frac{\delta}{\delta\sigma(x)}(\Psi[\sigma],F[\sigma]\Psi[\sigma])=\left(\Psi[\sigma],\frac{\Delta F[\sigma]}{\Delta\sigma(x)}\Psi[\sigma]\right). \quad (2.47)$$

If the functional is of the form

$$F_\mu[\sigma]=\int_\sigma F(x)d\sigma_\mu,$$

we are led to write

$$\frac{\Delta F_\mu[\sigma]}{\Delta\sigma(x)}=\frac{dF(x)}{dx_\mu},$$

where

$$\frac{dF(x)}{dx_\mu}=\frac{\partial F(x)}{\partial x_\mu}+\frac{i}{\hbar c}\left[\mathcal{H}(x),\int_\sigma F(x')d\sigma_\mu'\right]$$

defines the total coordinate derivative. It should be clear that the conservation theorem (1.56) and the equation of motion (1.38), in the interaction representation are to be written

$$\frac{\Delta P_\mu[\sigma]}{\Delta\sigma(x)}=\frac{\delta P_\mu[\sigma]}{\delta\sigma(x)}+\frac{i}{\hbar c}[\mathcal{H}(x),P_\mu[\sigma]]=0, \quad (2.48)$$

and

$$\frac{i}{\hbar}[F(x),P_\mu[\sigma]]=\frac{dF(x)}{dx_\mu}=\frac{\partial F(x)}{\partial x_\mu}+\frac{i}{\hbar c}\left[\mathcal{H}(x),\int_\sigma F(x')d\sigma_\mu'\right]. \quad (2.49)$$

Now the partial coordinate derivative $\partial F(x)/\partial x_\mu$ is that to be associated with the behavior of noninteracting fields, and can therefore be calculated from the energy-momentum four-vector of the isolated fields, $P_\mu^{(0)}$, according to

$$\frac{i}{\hbar}[F(x),P_\mu^{(0)}]=\frac{\partial F(x)}{\partial x_\mu}. \quad (2.50)$$

Therefore,

$$[F(x),P_\mu[\sigma]-P_\mu^{(0)}]=\frac{1}{c}\int_\sigma[\mathcal{H}(x),F(x')]d\sigma_\mu'=-\frac{1}{c}\int_\sigma[F(x),\mathcal{H}(x')]d\sigma_\mu' \quad (2.51)$$

in which we have used the fact that only the point $x'=x$ will contribute to the surface integral. One may infer that

$$P_\mu[\sigma]=P_\mu^{(0)}-\frac{1}{c}\int_\sigma\mathcal{H}(x)d\sigma_\mu, \quad (2.52)$$

which, indeed, is compatible with the conservation theorem (2.48), since

$$\frac{\Delta P_\mu[\sigma]}{\Delta\sigma(x)}=\frac{\delta P_\mu^{(0)}}{\delta\sigma(x)}-\frac{1}{c}\left(\frac{\partial\mathcal{H}(x)}{\partial x_\mu}-\frac{i}{\hbar}[\mathcal{H}(x),P_\mu^{(0)}]\right)=0. \quad (2.53)$$

The statement (2.52) can be confirmed by direct calculation. The appropriate transcription of the Heisenberg operator (1.64) involves the introduction of the total derivatives dA_λ/dx_ν and $d\psi/dx_\nu$. Only the latter differs from the explicit coordinate derivative. Now the operator $P_\nu^{(0)}$ is formally identical with (1.64), but expressed in terms of the interaction representation operators and their explicit coordinate derivatives. Therefore,

$$P_\nu[\sigma]=P_\nu^{(0)}+\frac{i}{2c}\int_\sigma d\sigma_\mu \times[\bar\psi(x),[\mathfrak{H}(x),\gamma_\mu\psi(x')]]d\sigma_\nu'. \quad (2.54)$$

However,

$$[\mathfrak{H}(x),\gamma_\mu\psi(x')]=-\frac{1}{c}[j_\lambda(x),\gamma_\mu\psi(x')]A_\lambda(x)$$
$$=ie\{\gamma_\mu\psi(x'),\bar\psi_\alpha(x)\}(\gamma_\lambda\psi(x))_\alpha A_\lambda(x), \quad (2.55)$$

whence

$$P_\nu[\sigma]-P_\nu^{(0)}$$
$$=\frac{ie}{2c}\int_\sigma d\sigma_\mu i\{\gamma_\mu\psi(x'),\bar\psi_\alpha(x)\}[\bar\psi(x),(\gamma_\lambda\psi(x))_\alpha]A_\lambda(x)d\sigma_\nu'$$
$$=\frac{ie}{2c}\int_\sigma[\bar\psi(x)\gamma_\lambda\psi(x)-\gamma_\lambda\psi(x)\bar\psi(x)]A_\lambda(x)d\sigma_\nu$$
$$=\frac{1}{c^2}\int_\sigma j_\lambda(x)A_\lambda(x)d\sigma_\nu, \quad (2.56)$$

which is the content of Eq. (2.52).

3. COVARIANT ELIMINATION OF THE LONGITUDINAL FIELD

It is the function of the supplementary condition to ensure that the electromagnetic field contains no spin-less light quanta, which have various unphysical properties. It is possible, indeed to eliminate the scalar potential and the longitudinal part of the vector potential, leaving only the transverse vector potential as the quantity truly descriptive of light waves. Such conventional procedures suffer from a lack of covariance which will be remedied in this section.

We shall show that one can replace the electromagnetic field vector, $A_\mu(x)$, by two scalar fields, $\Lambda(x)$ and $\Lambda'(x)$, together with a restricted vector field $\mathfrak{A}_\mu(x)$, in such a way that the supplementary condition involves only the scalar fields, while the equation of motion for $\Psi[\sigma]$ contains only $\mathfrak{A}_\mu(x)$, the sole physically significant part of the field. The decomposition will be conveniently expressed with the aid of an arbitrary time-like unit vector n_μ; $n_\mu^2=-1$. The procedure of the customary theory corresponds to the special choice: $n_\mu=(0,0,0,i)$.

We decompose $A_\mu(x)$ into the gradient in the time-like direction specified by n_μ of a scalar operator $\Lambda(x)$, the gradient in the space-like direction orthogonal to n_μ of a scalar operator $\Lambda'(x)$ and the vector $\mathfrak{A}_\mu(x)$ which has no component in the direction n_μ, and is divergence-less. Symbolically

$$A_\mu(x)=n_\mu n_\nu\frac{\partial}{\partial x_\nu}\Lambda(x)-\left(\frac{\partial}{\partial x_\mu}+n_\mu n_\nu\frac{\partial}{\partial x_\nu}\right)\Lambda'(x)+\mathfrak{A}_\mu(x), \quad (3.1)$$

where

$$n_\mu\mathfrak{A}_\mu(x)=0,\quad \frac{\partial}{\partial x_\mu}\mathfrak{A}_\mu(x)=0. \quad (3.2)$$

It is our first task to construct the commutation relations of the three fields thus defined, and in particular, to prove that they are kinematically independent. It follows from the definitions that

$$n_\mu A_\mu(x)=-n_\mu\frac{\partial}{\partial x_\mu}\Lambda(x) \quad (3.3)$$

and

$$\left(\frac{\partial}{\partial x_\mu}+n_\mu n_\nu\frac{\partial}{\partial x_\nu}\right)A_\mu(x)=-\left(n_\mu\frac{\partial}{\partial x_\mu}\right)^2\Lambda'(x), \quad (3.4)$$

in which the latter statement also involves the field equations

$$\Box^2\Lambda=\Box^2\Lambda'=\Box^2\mathfrak{A}_\mu=0. \quad (3.5)$$

The commutation laws for $A_\mu(x)$ imply that

$$\left[n_\mu\frac{\partial}{\partial x_\mu}\Lambda(x),n_\nu\frac{\partial}{\partial x_\nu'}\Lambda(x')\right]=-ihcD(x-x') \quad (3.6)$$

and

$$\left[\left(n_\mu\frac{\partial}{\partial x_\mu}\right)^2\Lambda'(x),\left(n_\nu\frac{\partial}{\partial x_\nu'}\right)^2\Lambda'(x')\right]$$
$$=-i\hbar c\left(n_\mu\frac{\partial}{\partial x_\mu}\right)^2 D(x-x'). \quad (3.7)$$

These can be simplified by the introduction of an odd function of the coordinates, $\mathfrak{D}(x)$, defined by

$$\left(n_\mu\frac{\partial}{\partial x_\mu}\right)^2\mathfrak{D}(x)=D(x)$$
$$\Box^2\mathfrak{D}(x)=0. \quad (3.8)$$

The relations (3.6) and (3.7) are satisfied if

$$[\Lambda(x),\Lambda(x')]=i\hbar c\mathfrak{D}(x-x')$$
$$[\Lambda'(x),\Lambda'(x')]=-i\hbar c\mathfrak{D}(x-x'). \quad (3.9)$$

The further commutation relation

$$[\Lambda(x),\Lambda'(x')]=0 \quad (3.10)$$

is consistent with the result deduced from (3.3) and (3.4), namely

$$\left[n_\mu\frac{\partial}{\partial x_\mu}\Lambda(x),\left(n_\nu\frac{\partial}{\partial x_\nu'}\right)^2\Lambda'(x')\right]$$
$$=i\hbar c n_\mu\left(\frac{\partial}{\partial x_\mu'}+n_\mu n_\nu\frac{\partial}{\partial x_\nu'}\right)D(x-x')=0. \quad (3.11)$$

The commutation properties

$$[A_\mu(x)+n_\mu n_\nu A_\nu(x),n_\lambda A_\lambda(x')]=0,$$
$$\left[A_\mu(x)+\left(\frac{\partial}{\partial x_\mu}+n_\mu n_\lambda\frac{\partial}{\partial x_\lambda}\right)\Lambda'(x),\right.$$
$$\left.\left(\frac{\partial}{\partial x_\nu'}+n_\nu n_\sigma\frac{\partial}{\partial x_\sigma'}\right)A_\nu(x')\right]=0, \quad (3.12)$$

when combined with the commutativity of Λ and Λ', imply that

$$[\Lambda(x),\mathfrak{A}_\mu(x')]=[\Lambda'(x),\mathfrak{A}_\mu(x')]=0. \quad (3.13)$$

Finally, we deduce from (3.1) that

$$[\mathfrak{A}_\mu(x),\mathfrak{A}_\nu(x')]=i\hbar c\delta_{\mu\nu}D(x-x')$$
$$+i\hbar c n_\mu n_\nu\left(n_\lambda\frac{\partial}{\partial x_\lambda}\right)^2\mathfrak{D}(x-x')$$
$$-i\hbar c\left(\frac{\partial}{\partial x_\mu}+n_\mu n_\lambda\frac{\partial}{\partial x_\lambda}\right)$$
$$\times\left(\frac{\partial}{\partial x_\nu}+n_\nu n_\sigma\frac{\partial}{\partial x_\sigma}\right)\mathfrak{D}(x-x') \quad (3.14)$$

or

$$[\mathfrak{A}_\mu(x),\mathfrak{A}_\nu(x')]=i\hbar c\delta_{\mu\nu}D(x-x')$$
$$-i\hbar c\left(\frac{\partial}{\partial x_\mu}\frac{\partial}{\partial x_\nu}+\left(n_\mu\frac{\partial}{\partial x_\nu}\right.\right.$$
$$\left.\left.+n_\nu\frac{\partial}{\partial x_\mu}\right)n_\lambda\frac{\partial}{\partial x_\lambda}\right)\mathfrak{D}(x-x'). \quad (3.15)$$

It will be noted that this commutation rule is compatible with the restrictions (3.2) imposed on $\mathfrak{A}_\mu(x)$.

The supplementary condition involves only the scalar fields and, indeed, only the combination $\Lambda(x)-\Lambda'(x)$, since

$$\frac{\partial}{\partial x_\mu}A_\mu(x)=\left(n_\mu\frac{\partial}{\partial x_\mu}\right)^2(\Lambda(x)-\Lambda'(x)). \quad (3.16)$$

Equation (2.32) will now be satisfied if

$$\left(\Lambda(x)-\Lambda'(x)-\int_\sigma\mathfrak{D}(x-x')\right.$$
$$\left.\times\frac{1}{c}j_\mu(x')d\sigma_\mu'\right)\Psi[\sigma]=0. \quad (3.17)$$

The equation of motion for $\Psi[\sigma]$ becomes

$$i\hbar c\frac{\delta\Psi[\sigma]}{\delta\sigma(x)}$$
$$=\left\{-\frac{1}{c}j_\mu(x)\mathfrak{A}_\mu(x)+\frac{\partial}{\partial x_\mu}\left(\frac{1}{c}j_\mu(x)\Lambda'(x)\right)\right.$$
$$\left.-\frac{1}{c}n_\mu j_\mu(x)n_\nu\frac{\partial}{\partial x_\nu}(\Lambda(x)-\Lambda'(x))\right\}\Psi[\sigma]. \quad (3.18)$$

It may be expected that, by a suitable gauge

transformation, $\Lambda'(x)$ can be eliminated, leaving $\Lambda(x)-\Lambda'(x)$ and $\mathfrak{A}_\mu(x)$ as the fundamental variables of the electromagnetic field. Accordingly, we introduce the transformation (Cf. (2.40) and (2.41)).

$$\Psi[\sigma]\rightarrow e^{-iG'[\sigma]}\Psi[\sigma], \tag{3.19}$$

where

$$G'[\sigma]=\frac{1}{\hbar c}\int_\sigma \frac{1}{c}j_\mu(x)\Lambda'(x)d\sigma_\mu. \tag{3.20}$$

The new equations of motion and supplementary condition are:

$$ihc\frac{\delta\Psi[\sigma]}{\delta\sigma(x)}+ihce^{iG'[\sigma]}\frac{\delta e^{-iG'[\sigma]}}{\delta\sigma(x)}\Psi[\sigma]$$
$$=e^{iG'[\sigma]}\left\{-\frac{1}{c}j_\mu(x)\,\mathfrak{A}_\mu(x)+\frac{\partial}{\partial x_\mu}\left(\frac{1}{c}j_\mu(x)\Lambda'(x)\right)\right.$$
$$\left.-\frac{1}{c}n_\mu j_\mu(x)n_\nu\frac{\partial}{\partial x_\nu}(\Lambda(x)-\Lambda'(x))\right\}$$
$$\times e^{-iG'[\sigma]}\Psi[\sigma] \tag{3.21}$$

and

$$\left(\Lambda(x)-e^{iG'[\sigma]}\Lambda'(x)e^{-iG'[\sigma]}\right.$$
$$\left.-\int_\sigma \mathfrak{D}(x-x')\frac{1}{c}j_\mu(x')d\sigma_\mu'\right)\Psi[\sigma]=0. \tag{3.22}$$

The transformation now under discussion differs from the previous gauge transformation in that $\Lambda'(x)$ is an operator, subject to the commutation relation (3.9). To indicate the modifications thereby introduced, we first evaluate

$$e^{iG'[\sigma]}\Lambda'(x)e^{-iG'[\sigma]}=\Lambda'(x)+i[G'[\sigma],\Lambda'(x)]$$
$$-\frac{1}{2!}[G'[\sigma],[G'[\sigma],\Lambda'(x)]]+\cdots. \tag{3.23}$$

Now

$$i[G'[\sigma],\Lambda'(x)]$$
$$=-\frac{i}{\hbar c}\int_\sigma[\Lambda'(x),\Lambda'(x')]\frac{1}{c}j_\mu(x')d\sigma_\mu'$$
$$=-\int_\sigma \mathfrak{D}(x-x')\frac{1}{c}j_\mu(x')d\sigma_\mu', \tag{3.24}$$

and therefore, only the first two terms of the series (3.23) survive:

$$e^{iG'[\sigma]}\Lambda'(x)e^{-iG'[\sigma]}$$
$$=\Lambda'(x)-\int_\sigma \mathfrak{D}(x-x')\frac{1}{c}j_\mu(x')d\sigma_\mu'. \tag{3.25}$$

Hence, the supplementary condition becomes, simply,

$$(\Lambda(x)-\Lambda'(x))\Psi[\sigma]=0. \tag{3.26}$$

In a similar way

$$e^{iG'[\sigma]}\left(\frac{\partial\Lambda'(x)}{\partial x_\mu}+n_\mu n_\nu\frac{\partial\Lambda'(x)}{\partial x_\nu}\right)e^{-iG'[\sigma]}=\frac{\partial\Lambda'(x)}{\partial x_\mu}$$
$$+n_\mu n_\nu\frac{\partial\Lambda'(x)}{\partial x_\nu}-\int_\sigma\left(\frac{\partial}{\partial x_\mu}+n_\mu n_\nu\frac{\partial}{\partial x_\nu}\right)$$
$$\times\mathfrak{D}(x-x')\frac{1}{c}j_\lambda(x'')d\sigma_\lambda', \tag{3.27}$$

and

$$ihce^{iG'[\sigma]}\frac{\delta e^{-iG'[\sigma]}}{\delta\sigma(x)}=\frac{\partial}{\partial x_\mu}\left(\frac{1}{c}j_\mu(x)\Lambda'(x)\right)$$
$$-\frac{1}{2}\int_\sigma\frac{\partial\mathfrak{D}(x-x')}{\partial x_\mu}\frac{1}{c}j_\mu(x)\frac{1}{c}j_\nu(x')d\sigma_\nu'. \tag{3.28}$$

The equation of motion for $\Psi[\sigma]$ now reads

$$ihc\frac{\delta\Psi[\sigma]}{\delta\sigma(x)}=\left\{-\frac{1}{c}j_\mu(x)\,\mathfrak{A}_\mu(x)-\int_\sigma\left(\frac{1}{2}\frac{\partial\mathfrak{D}(x-x')}{\partial x_\mu}\right.\right.$$
$$\left.+n_\mu n_\nu\frac{\partial\mathfrak{D}(x-x')}{\partial x_\nu}\right)\frac{1}{c}j_\mu(x)\frac{1}{c}j_\lambda(x')d\sigma_\lambda'$$
$$\left.-\frac{1}{c}n_\mu j_\mu(x)n_\nu\frac{\partial}{\partial x_\nu}(\Lambda(x)-\Lambda'(x))\right\}\Psi[\sigma] \tag{3.29}$$

which, in view of the supplementary condition (3.26), reduces to

$$ihc\frac{\delta\Psi[\sigma]}{\delta\sigma(x)}=\left\{-\frac{1}{c}j_\mu(x)\,\mathfrak{A}_\mu(x)\right.$$
$$-\int_\sigma\left(\frac{1}{2}\frac{\partial\mathfrak{D}(x-x')}{\partial x_\mu}+n_\mu n_\nu\frac{\partial\mathfrak{D}(x-x')}{\partial x_\nu}\right)$$
$$\left.\times\frac{1}{c}j_\mu(x)\frac{1}{c}j_\lambda(x')d\sigma_\lambda'\right\}\Psi[\sigma]. \tag{3.30}$$

We have thereby succeeded in constructing an equation of motion for $\Psi[\sigma]$ which no longer contains the electromagnetic field variables involved in the supplementary condition. The additional term thus introduced is evidently the covariant generalization of the Coulomb interaction between charges.

To exhibit the latter property somewhat more clearly, we must restrict the arbitrary space-like surface σ to a plane surface with the normal n_μ. The advantage thereby acquired is the possibility of asserting that

$$\left(\frac{\partial}{\partial x_\mu}+n_\mu n_\nu\frac{\partial}{\partial x_\nu}\right)\mathfrak{D}(x-x')=0,$$

$$n_\mu(x_\mu-x_\mu')=0 \quad (3.31)$$

which enables (3.30) to be simplified, yielding:

$$i\hbar c\frac{\delta\Psi[\sigma]}{\delta\sigma(x)}=\left\{-\frac{1}{c}j_\mu(x)\mathfrak{A}_\mu(x)-\frac{1}{2}\int_\sigma n_\nu\frac{\partial\mathfrak{D}(x-x')}{\partial x_\nu}\times\frac{1}{c}n_\mu j_\mu(x)\frac{1}{c}j_\lambda(x')d\sigma_\lambda'\right\}\Psi[\sigma]. \quad (3.32)$$

To prove (3.31), it is sufficient to verify it in a particular coordinate system. It is always possible to construct a reference system for which the normal to a plane space-like surface is directed along the time axis; in other words, in this reference system, $n_\mu=(0,0,0,i)$. Equation (3.31) then states that the spatial derivatives of $\mathfrak{D}(\mathbf{r}-\mathbf{r}',t-t')$ vanish for $t=t'$. This will be true if $\mathfrak{D}(\mathbf{r},0)=0$ for all $\mathbf{r}$, that is, if $\mathfrak{D}(\mathbf{r},t)$ is an odd function of t. Now, in this special coordinate system, (3.8) becomes

$$\left(\frac{1}{c}\frac{\partial}{\partial t}\right)^2\mathfrak{D}(\mathbf{r},t)=\nabla^2\mathfrak{D}(\mathbf{r},t)=D(\mathbf{r},t) \quad (3.33)$$

and, since (2.17) assures us that $D(\mathbf{r},t)$ is an odd function of the time, the necessary property of $\mathfrak{D}(\mathbf{r},t)$ is established. As a final step, we note that, in this special coordinate system,

$$n_\nu\frac{\partial}{\partial x_\nu}\mathfrak{D}(x-x')=\frac{1}{c}\frac{\partial}{\partial t}\mathfrak{D}(\mathbf{r}-\mathbf{r}',0),$$

$$n_\mu(x_\mu-x_\mu')=0 \quad (3.34)$$

and

$$\nabla^2\frac{1}{c}\frac{\partial}{\partial t}\mathfrak{D}(\mathbf{r},0)=\frac{1}{c}\frac{\partial}{\partial t}D(\mathbf{r},0)=-\delta(\mathbf{r}), \quad (3.35)$$

in which the latter statement involves the content of the equations of definition (2.17) as adapted to the special coordinate system. It follows from (3.35) that

$$\frac{1}{c}\frac{\partial}{\partial t}\mathfrak{D}(\mathbf{r},0)=\frac{1}{4\pi r}, \quad (3.36)$$

of which the covariant expression is

$$n_\nu\frac{\partial}{\partial x_\nu}\mathfrak{D}(x-x')=\frac{1}{4\pi}\frac{1}{[(x_\mu-x_\mu')^2]^{\frac{1}{2}}},$$

$$n_\mu(x_\mu-x_\mu')=0. \quad (3.37)$$

The energy-momentum four-vector is modified by the unitary transformation (3.19), according to

$$P_\nu[\sigma]\rightarrow e^{iG'[\sigma]}P_\nu[\sigma]e^{-iG'[\sigma]}. \quad (3.38)$$

The evaluation of the new operator $P_\nu[\sigma]$ involves the following transformations, which we note without proof:

$$e^{iG'[\sigma]}A_\mu(x)e^{-iG'[\sigma]}=\overset{\circ}{A}_\mu(x)+\int_\sigma\left(\frac{\partial}{\partial x_\mu}+n_\mu n_\nu\frac{\partial}{\partial x_\nu}\right)\mathfrak{D}(x-x')\frac{1}{c}j_\lambda(x')d\sigma_\lambda',$$

$$e^{iG'[\sigma]}\frac{1}{2}\int_\sigma d\sigma_\mu\left[\bar\psi\gamma_\mu\frac{\partial\psi}{\partial x_\nu}-\frac{\partial\psi}{\partial x_\nu}\bar\psi\gamma_\mu\right]e^{-iG'[\sigma]}$$

$$=\frac{1}{2}\int_\sigma d\sigma_\mu\left[\bar\psi\gamma_\mu\frac{\partial\psi}{\partial x_\nu}-\frac{\partial\psi}{\partial x_\nu}\bar\psi\gamma_\mu\right]+\frac{1}{\hbar c}\int_\sigma\left[d\sigma_\nu\frac{1}{c}j_\lambda\frac{\partial\Lambda'}{\partial x_\lambda}-d\sigma_\lambda\frac{1}{c}j_\lambda\frac{\partial\Lambda'}{\partial x_\nu}\right]. \quad (3.39)$$

In virtue of the supplementary condition (3.26), we may write

$$A_\mu(x)\Psi[\sigma]=\left(\mathfrak{A}_\mu(x)-\frac{\partial\Lambda'(x)}{\partial x_\mu}\right)\Psi[\sigma]. \quad (3.40)$$

It follows, as a result of straightforward simpli-

fication, that

$$P_\nu[\sigma]=\frac{1}{2c}\int_\sigma d\sigma_\mu\Big[\frac{\partial \mathfrak{A}_\lambda}{\partial x_\mu}\frac{\partial \mathfrak{A}_\lambda}{\partial x_\nu}+\frac{\partial \mathfrak{A}_\lambda}{\partial x_\nu}\frac{\partial \mathfrak{A}_\lambda}{\partial x_\mu}-\delta_{\mu\nu}\Big(\frac{\partial \mathfrak{A}_\lambda}{\partial x_\sigma}\Big)^2\Big]$$
$$+\frac{\hbar}{2}\int_\sigma d\sigma_\mu\Big[\bar\psi\gamma_\mu\frac{\partial\psi}{\partial x_\nu}-\frac{\partial\bar\psi}{\partial x_\nu}\gamma_\mu\Big]$$
$$+\frac{1}{c}\int_\sigma d\sigma_\nu\Big[\frac{1}{c}j_\mu(x)\,\mathfrak{A}_\mu(x)+\frac{1}{2}\int_\sigma n_\xi\frac{\partial\mathfrak{D}(x-x')}{\partial x_\xi}\times\frac{1}{c}n_\mu j_\mu(x)\frac{1}{c}j_\lambda(x')d\sigma_\lambda'\Big],\quad(3.41)$$

which has been stated as an operator equation, rather than a derived supplementary condition, with the understanding that the operator $\Lambda-\Lambda'$ shall no longer appear in the theory.

As the final comment of this section, we remark that the derivatives of $\mathfrak{A}_\lambda$, occurring in (3.41), can be combined into the field strengths

$$\mathfrak{F}_{\mu\nu}=\frac{\partial}{\partial x_\mu}\mathfrak{A}_\nu-\frac{\partial}{\partial x_\nu}\mathfrak{A}_\mu\quad(3.42)$$

with the result that

$$P_\nu[\sigma]=\frac{1}{2c}\int_\sigma d\sigma_\mu[\mathfrak{F}_{\mu\lambda}\mathfrak{F}_{\nu\lambda}+\mathfrak{F}_{\nu\lambda}\mathfrak{F}_{\mu\lambda}-\tfrac{1}{2}\delta_{\mu\nu}\mathfrak{F}_{\lambda\sigma}{}^2]$$
$$=\frac{\hbar}{2}\int_\sigma d\sigma_\mu\Big[\bar\psi\gamma_\mu\frac{\partial\psi}{\partial x_\nu}-\frac{\partial\bar\psi}{\partial x_\nu}\gamma_\mu\Big]$$
$$+\frac{1}{c}\int_\sigma d\sigma_\nu\Big[\frac{1}{c}j_\mu(x)\,\mathfrak{A}_\mu(x)+\frac{1}{2}\int_\sigma n_\xi\frac{\partial\mathfrak{D}(x-x')}{\partial x_\xi}\times\frac{1}{c}n_\mu j_\mu(x)\frac{1}{c}j_\lambda(x')d\sigma_\lambda'\Big].\quad(3.43)$$

We need only notice that (Cf. (1.32))

$$\frac{\partial \mathfrak{A}_\lambda}{\partial x_\mu}\frac{\partial \mathfrak{A}_\lambda}{\partial x_\nu}+\frac{\partial \mathfrak{A}_\lambda}{\partial x_\nu}\frac{\partial \mathfrak{A}_\lambda}{\partial x_\mu}-\delta_{\mu\nu}\Big(\frac{\partial \mathfrak{A}_\lambda}{\partial x_\sigma}\Big)^2$$
$$=\mathfrak{F}_{\mu\lambda}\mathfrak{F}_{\nu\lambda}+\mathfrak{F}_{\nu\lambda}\mathfrak{F}_{\mu\lambda}-\tfrac{1}{2}\delta_{\mu\nu}\mathfrak{F}_{\lambda\sigma}{}^2$$
$$+\frac{\partial}{\partial x_\lambda}(\mathfrak{A}_\nu\mathfrak{F}_{\mu\lambda}+\mathfrak{F}_{\mu\lambda}\mathfrak{A}_\nu)+\frac{\partial \mathfrak{A}_\mu}{\partial x_\lambda}\frac{\partial \mathfrak{A}_\lambda}{\partial x_\nu}+\frac{\partial \mathfrak{A}_\lambda}{\partial x_\nu}\frac{\partial \mathfrak{A}_\mu}{\partial x_\lambda}-\delta_{\mu\nu}\frac{\partial \mathfrak{A}_\lambda}{\partial x_\sigma}\frac{\partial \mathfrak{A}_\sigma}{\partial x_\lambda}.\quad(3.44)$$

The lemma (1.58), together with the antisymmetry of $\mathfrak{F}_{\mu\lambda}$, then informs us that

$$\int_\sigma d\sigma_\mu\frac{\partial}{\partial x_\lambda}(\mathfrak{A}_\nu\mathfrak{F}_{\mu\lambda}+\mathfrak{F}_{\mu\lambda}\mathfrak{A}_\nu)=0,$$

while the divergence-less nature of $\mathfrak{A}_\mu$ is combined with (1.58) in the following proof:

$$\int_\sigma d\sigma_\mu\Big[\frac{\partial \mathfrak{A}_\mu}{\partial x_\lambda}\frac{\partial \mathfrak{A}_\lambda}{\partial x_\nu}+\frac{\partial \mathfrak{A}_\lambda}{\partial x_\nu}\frac{\partial \mathfrak{A}_\mu}{\partial x_\lambda}-\delta_{\mu\nu}\frac{\partial \mathfrak{A}_\lambda}{\partial x_\sigma}\frac{\partial \mathfrak{A}_\sigma}{\partial x_\lambda}\Big]$$
$$=\frac{1}{2}\int_\lambda d\sigma_\mu\frac{\partial}{\partial x_\lambda}\Big[\mathfrak{A}_\mu\frac{\partial \mathfrak{A}_\lambda}{\partial x_\nu}+\frac{\partial \mathfrak{A}_\lambda}{\partial x_\nu}\mathfrak{A}_\mu+\mathfrak{A}_\lambda\frac{\partial \mathfrak{A}_\mu}{\partial x_\nu}+\frac{\partial \mathfrak{A}_\mu}{\partial x_\nu}\mathfrak{A}_\lambda\Big]-\int_\sigma d\sigma_\nu\frac{\partial}{\partial x_\lambda}\frac{\partial}{\partial x_\sigma}(\mathfrak{A}_\lambda\mathfrak{A}_\sigma)$$
$$=\frac{1}{2}\int_\sigma d\sigma_\mu\frac{\partial}{\partial x_\nu}\frac{\partial}{\partial x_\lambda}(\mathfrak{A}_\mu\mathfrak{A}_\lambda+\mathfrak{A}_\lambda\mathfrak{A}_\mu)-\int_\sigma d\sigma_\nu\frac{\partial}{\partial x_\lambda}\frac{\partial}{\partial x_\sigma}(\mathfrak{A}_\lambda\mathfrak{A}_\sigma)=0.\quad(3.45)$$

4. THE INVARIANT COLLISION OPERATOR

While the interactions between fields and their vacuum fluctuations are conveniently regarded as modifying the properties of the non-interacting fields, other types of interactions are often best viewed as producing transitions among the states of the individual fields. We shall conclude this paper with a brief discussion of a covariant manner of describing such transitions. The change in state of several fields arising from their mutual interaction is described by the equation of motion (2.6) for the state vector $\Psi[\sigma]$. The question that must be answered in order to describe collisions between the particles associated with the quantized fields is: given the state vector on a surface σ_1, what is the state vector on the surface σ_2, in the limit as σ_1 and σ_2 recede into the remote and past and future, respectively? In this limit, no precise characterization of the surfaces is required and we shall accordingly denote them by the symbols $-\infty$ and $+\infty$, respectively. It will be useful to derive the state vector on an arbitrary surface σ from that for the initial surface σ_1 by a unitary operator:

$$\Psi[\sigma]=U[\sigma,\sigma_1]\Psi[\sigma_1]\quad(4.1)$$

which is to be determined by an equation of motion

$$i\hbar c\frac{\delta}{\delta\sigma(x)}U[\sigma,\sigma_1]=\mathcal{H}(x)\,U[\sigma,\sigma_1], \quad (4.2)$$

and an initial condition

$$U[\sigma_1,\sigma_1]=1. \quad (4.3)$$

The functional differential equation (4.2) is conveniently replaced by a functional integral equation, which incorporates the initial condition (4.3):

$$U[\sigma,\sigma_1]=1-\frac{i}{\hbar c}\int_{\sigma_1}^{\sigma}\mathcal{H}(x')\,U[\sigma',\sigma_1]d\omega'. \quad (4.4)$$

The volume integral in this equation is extended between the surfaces σ_1 and σ. In particular,

$$U[\sigma_2,\sigma_1]=1-\frac{i}{\hbar c}\int_{\sigma_1}^{\sigma_2}\mathcal{H}(x)\,U[\sigma,\sigma_1]d\omega. \quad (4.5)$$

In terms of the limiting surfaces $\pm\infty$, the integral equation becomes

$$U[\sigma,-\infty]=1-\frac{i}{\hbar c}\int_{-\infty}^{\sigma}\mathcal{H}(x')\,U[\sigma',-\infty]d\omega', \quad (4.6)$$

while

$$S=1-\frac{i}{\hbar c}\int_{-\infty}^{\infty}\mathcal{H}(x)\,U[\sigma,-\infty]d\omega. \quad (4.7)$$

Here

$$S=U[\infty,-\infty], \quad (4.8)$$

which we call the collision operator, determines the over-all change in state of the system as the result of interaction:

$$\Psi[\infty]=S\Psi[-\infty]. \quad (4.9)$$

The expectation value of some physical quantity F can then be calculated in the final state, for a prescribed initial state:

$$(\Psi[\infty],F\Psi[\infty])=(\Psi[-\infty],S^{-1}FS\Psi[-\infty]) \quad (4.10)$$

from which the probabilities of various transitions can be inferred.

The problem of determining the unitary collision operator S can be replaced by that of determining a Hermitian operator K, which we may call the reaction operator. Our procedure will be precisely analogous to the use, in classical electrodynamics, of the sum and difference of advanced and retarded potentials rather than the latter alone. The integral equation (4.6) can be rewritten as

$$U[\sigma,-\infty]+\frac{i}{2\hbar c}\left[\int_{-\infty}^{\sigma}\mathcal{H}(x')\,U[\sigma',-\infty]d\omega'-\int_{\sigma}^{\infty}\mathcal{H}(x')\,U[\sigma',-\infty]d\omega'\right]$$
$$=1-\frac{i}{2\hbar c}\left[\int_{-\infty}^{\sigma}\mathcal{H}(x')\,U[\sigma',-\infty]d\omega'+\int_{\sigma}^{\infty}\mathcal{H}(x')\,U[\sigma',-\infty]d\omega'\right], \quad (4.11)$$

or

$$U[\sigma,-\infty]+\frac{i}{2\hbar c}\int_{-\infty}^{\infty}\epsilon[\sigma,\sigma']\mathcal{H}(x')\,U[\sigma',-\infty]d\omega'=1-\frac{i}{2\hbar c}\int_{-\infty}^{\infty}\mathcal{H}(x')\,U[\sigma',-\infty]d\omega', \quad (4.12)$$

where $\epsilon[\sigma,\sigma']=1$ if σ' antedates the surface σ while $\epsilon[\sigma,\sigma']=-1$ if σ' succeeds the surface σ. It is useful to introduce the functional $V[\sigma]$ according to the definition

$$U[\sigma,-\infty]=V[\sigma]\left(1-\frac{i}{2\hbar c}\int_{-\infty}^{\infty}\mathcal{H}(x')\,U[\sigma',-\infty]d\omega'\right)$$
$$=V[\sigma]\tfrac{1}{2}(1+S) \quad (4.13)$$

so that

$$V[\sigma]+\frac{i}{2\hbar c}\int_{-\infty}^{\infty}\epsilon[\sigma,\sigma']\mathcal{H}(x')\,V[\sigma']d\omega'=1. \quad (4.14)$$

On computing S from (4.7) and (4.13), we learn that

$$i\frac{S-1}{S+1}=\frac{1}{2\hbar c}\int_{-\infty}^{\infty}\mathcal{H}(x)\,V[\sigma]d\omega=K, \quad (4.15)$$

or

$$S=\frac{1-iK}{1+iK}. \quad (4.16)$$

While the Hermitian character of K is an immediate consequence of the unitary nature of S, it is instructive to give a direct proof. Associated

with the integral equation for $V[\sigma]$ is the Hermitian conjugate equation

$$V^+[\sigma]+\frac{i}{2\hbar c}\int_{-\infty}^{\infty}d\omega' V^+[\sigma']\mathfrak{K}(x')\epsilon[\sigma',\sigma]=1, \quad (4.17)$$

in which we have used the evident relation

$$\epsilon[\sigma,\sigma']=-\epsilon[\sigma',\sigma] \quad (4.18)$$

and the Hermiticity of $\mathfrak{K}(x)$. We may now multiply (4.14) to the left with $V^+[\sigma]\mathfrak{K}(x)$, multiply (4.17) to the right with $\mathfrak{K}(x)V[\sigma]$, and integrate with respect to x over all space-time. A comparison of the resultant formulae yields:

$$\int_{-\infty}^{\infty}V^+[\sigma]\mathfrak{K}(x)V[\sigma]d\omega+\frac{i}{2\hbar c}\times\int_{-\infty}^{\infty}V^+[\sigma]\mathfrak{K}(x)\epsilon[\sigma,\sigma']\mathfrak{K}(x')V[\sigma']d\omega d\omega'=\int_{-\infty}^{\infty}\mathfrak{K}(x)V[\sigma]d\omega=\int_{-\infty}^{\infty}V^+[\sigma]\mathfrak{K}(x)d\omega \quad (4.19)$$

or

$$K=K^+. \quad (4.20)$$

An important stationary property of the reaction operator K should be noted. On writing (4.19) as

$$2\hbar c\int_{-\infty}^{\infty}V^+[\sigma]\mathfrak{K}(x)V[\sigma]d\omega+i\int_{-\infty}^{\infty}V^+[\sigma]\mathfrak{K}(x)\epsilon[\sigma,\sigma']\mathfrak{K}(x')V[\sigma']d\omega d\omega'=\int_{-\infty}^{\infty}V^+[\sigma]\mathfrak{K}(x)d\omega K^{-1}\times\int_{-\infty}^{\infty}\mathfrak{K}(x')V[\sigma']d\omega', \quad (4.21)$$

we obtain a formula for K which is homogeneous in $V[\sigma]$ and $V^+[\sigma]$ and stationary with respect to small variations of $V[\sigma]$ and $V^+[\sigma]$. On performing such a variation, we obtain

$$-\int_{-\infty}^{\infty}V^+[\sigma]\mathfrak{K}(x)d\omega K^{-1}\delta K K^{-1}\int_{-\infty}^{\infty}\mathfrak{K}(x)V[\sigma]d\omega=2\hbar c\int_{-\infty}^{\infty}d\omega\,\delta V^+[\sigma]\mathfrak{K}(x)\Big[V^+[\sigma]+\frac{i}{2\hbar c}\int_{-\infty}^{\infty}\epsilon[\sigma,\sigma']\mathfrak{K}(x')V[\sigma']d\omega'-\frac{1}{2\hbar c}K^{-1}\int_{-\infty}^{\infty}\mathfrak{K}(x')V[\sigma']d\omega'\Big]+2\hbar c\int_{-\infty}^{\infty}\Big[V^+[\sigma]+\frac{i}{2\hbar c}\times\int_{-\infty}^{\infty}V^+[\sigma']\mathfrak{K}(x')\epsilon[\sigma',\sigma]d\omega'-\frac{1}{2\hbar c}\int_{-\infty}^{\infty}V^+[\sigma']\mathfrak{K}(x')d\omega' K^{-1}\Big]\mathfrak{K}(x)\delta V[\sigma]d\omega. \quad (4.22)$$

Evidently, if $V[\sigma]$ satisfies (4.14) and (4.15), together with the Hermitian adjoint equations for $V^+[\sigma]$, $\delta K=0$. Conversely, if K is stationary for arbitrary variations, the quantities within brackets on the right side of (4.22) must vanish. It is easily seen that the functional

$$V'[\sigma]=V[\sigma]\left(\int_{-\infty}^{\infty}\mathfrak{K}(x')V[\sigma']d\omega'\right)^{-1}2\hbar cK \quad (4.23)$$

obeys Eqs. (4.14) and (4.15), while $V'^+[\sigma]$ obey the corresponding Hermitian adjoint equations. This type of variational principle has been extensively applied in the treatment of scattering problems,[12] and will be discussed in detail elsewhere.

As a final remark, we observe that the representation of S as an integral extended over all space-time indicates that it is unaffected by a translation of the coordinate system, and therefore commutes with the operator $P_\mu^{(0)}$ (cf. Eq. (2.50)):

$$[S,P_\mu^{(0)}]=0. \quad (4.24)$$

This is the energy-momentum conservation law for collision processes, since, according to (4.10), the expectation value of $P_\mu^{(0)}$ is unchanged by the course of interaction, for an arbitrary initial state.

[12] J. Schwinger, Phys. Rev. 72, 742 (1947) and unpublished lecture notes.

Photoelectric Emission and Contact Potentials of Semiconductors*

L. APKER, E. TAFT, AND J. DICKEY
General Electric Research Laboratory, Schenectady, New York

(Received June 21, 1948)

In spherical photo-tubes with interchangeable emitters, energy distributions of external photoelectrons from the semiconductors, Te, Ge, and B, were compared with those of several metals. Contact potentials were determined from the saturation points of current-voltage characteristics. For the semiconductors, as contrasted with metals of the same work function, there was a pronounced sparsity of electrons with energies near the Einstein maximum. In general form, the distributions could be described by the expression,

$$N(\nu, E)dE \propto q(\nu)E(h\nu-\varphi-\delta-E)^m dE,$$

based on simplified assumptions analogous to those previously applied in the case of metals. Here φ is the work function; δ is the energy difference between the Fermi level and the top of the occupied band of energy states; m is a parameter depending both on the form of this band and on the energy dependence of the photoelectric excitation probability; q is a slowly varying function of ν. The photoelectric properties of the semiconductors could also be specified conveniently by plotting measured values of $N(\nu, E)/E$ as functions of $h\nu-\varphi-E$. Spectral distributions of the photoelectric yields varied more rapidly with ν than those for metals and were not measurable unless $h\nu$ exceeded φ by several tenths of an electron volt.

Near the Einstein maximum, energy distributions deviated from the simple relation given above. The experiments failed to disclose sharply defined stopping potentials corresponding to upper edges of occupied bands of energy states in the semiconductors. Thus m and δ were not defined uniquely. Typical values of m obtained both from energy and spectral measurements were $\frac{1}{2}$ and 2; illustrative values of δ were 0.10 to 0.18 ev for evaporated Te($\varphi\sim$4.76 ev), 0.2 to 0.3 for evaporated Ge($\varphi\sim$4.8), and 0.3 to 0.5 for pyrolytic films of B($\varphi\sim$4.6). Thermoelectric measurements showed that all samples were P type. For Te the results were in agreement with available data on electrical properties.

Using the above values of δ, upper limits were found for photo-currents originating in the "forbidden" zones (as defined by $E>h\nu-\varphi-\delta$). For the surface states that were assumed as possible sources of these currents, estimated densities were of the order of magnitude, 10^{12} cm^{-2}.

I. INTRODUCTION

THEORETICAL considerations indicate that the external photoelectric effect is valuable for investigating semiconductor surfaces. The work of Wilson,[1] as extended by Fowler,[2] has shown that a material of this type may exhibit a photoelectric threshold energy that exceeds its thermionic work function by as much as 1 or 2 ev. Condon[3] has pointed out that this effect may explain the anomalous contact-potential differences[4] observed by Millikan[5] in his experiments verifying Einstein's photoelectric equation. Since the photoelectrons from a simple semiconductor originate in levels near the top of a filled band of energy states,[2,3] their velocity distribution and the spectral distribution of the yield should differ markedly from those for metals.[6] Detectable emission may conceivably be associated with surface states of the type recently discussed by Bardeen,[7] Brattain and Shockley,[8,9] and Meyerhof.[10]

This paper describes an attempt to measure these various effects. The work is essentially a repetition of Millikan's experiment, with the emphasis shifted to questions like those discussed by Condon. The main purpose is to determine the position of the Fermi level in the energy spectrum for electrons at the surface of a semiconductor. To make results more amenable to interpretation, a spherical geometry was adopted. For the same reason, effort was concentrated on the elementary semiconductors, Te and Ge, many

* Presented in part at the meetings of the Amerianc Physical Society, Washington, D. C., May, 1947, and New York, New York, January, 1948.

[1] A. H. Wilson, Proc. Roy. Soc. **A133**, 458 (1931); **A134**, 277 (1931).

[2] R. H. Fowler, *Statistical Mechanics* (Cambridge University Press, Teddington, England, 1936).

[3] E. U. Condon, Phys. Rev. **54**, 1089 (1938).

[4] Hereafter this term is abbreviated to c.p.d.

[5] R. A. Millikan, Phys. Rev. **7**, 18 (1916); **18**, 236 (1921).

[6] V. F. Weisskopf and L. Apker, Phys. Rev. **60**, 170(A) (1941). The exponent 2 should be deleted from the formula in this abstract.

[7] J. Bardeen, Phys. Rev. **71**, 717 (1947), and references cited there; H. M. James, Bull. Am. Phys. Soc. **23**, 22(A) (1948); P. H. Miller, Jr., and J. J. Markham, Bull. Am. Phys. Soc. **23**, 21(A) (1948).

[8] W. H. Brattain and W. Shockley, Phys. Rev. **72**, 345 (1947).

[9] W. H. Brattain, Phys. Rev. **72**, 345 (1947).

[10] Walter E. Meyerhof, Phys. Rev. **71**, 727 (1947).

properties of which have been examined in considerable detail.[11–15]

It is highly desirable, of course, that work of this kind be done on single crystals. The emitting surfaces should be clean and smooth—preferably simple crystal planes. In a survey of the kind reported here, however, the difficulties of producing such emitters become prohibitive. Hence polycrystalline samples were used almost exclusively. The surfaces were undoubtedly nonuniform, and there is no proof that they were free of adsorbed gases. We have proceeded in these circumstances, nevertheless, by restricting our attention almost entirely to reproducible first-order effects that are relatively insensitive to contamination or to patch fields.

In all cases, semiconductors exhibited a behavior strikingly different from that of metals investigated under the same conditions.

A satisfactory interpretation of the results would require quantitative knowledge, as yet unavailable, of the transition probabilities involved. Simplifying assumptions compatible with present theory have been used, therefore, to analyze the data. In some cases, analytical expressions are applicable. The procedure then leads to graphical techniques similar to those developed for metals by Fowler[2] and DuBridge.[16,17] Lest features of unrealized importance be obscured, typical data are given in original form.

II. THEORY OF RETARDING POTENTIAL MEASUREMENTS

We shall first review, in slightly modified fashion, the theory[2,3,5] of the measurements described in later sections of this paper.

Figure 1 shows the density n of electron energy states as a function of energy ϵ for the following materials: (1) an ideal metal with a comparatively high work function φ_c; (2) a metal with a lower work function φ; (3) an ideal intrinsic semiconductor also having a work function φ. To aid in comparing these diagrams with current-voltage curves, they are drawn with ϵ increasing from right to left. Metal (1) will be of interest primarily as an electron collector in a photo-tube, although it will be considered also as an emitter. Materials (2) and (3) will be used as typical examples of metallic and semiconducting emitters, respectively.

When these three substances are in thermal equilibrium, their Fermi levels μ assume the same energy.[2] Accordingly, the diagrams in Fig. 1 are

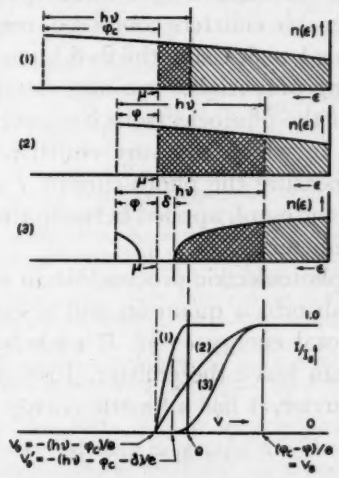

FIG. 1. Schematic diagram showing the density of electron energy states $n(\epsilon)$ as a function of energy ϵ for: (1) an ideal metal with a comparatively high work function φ_c; (2) a metal with a lower work function φ; (3) an ideal intrinsic semiconductor also with a work function φ. Note that ϵ increases from right to left. Occupied states from which external photoelectrons can be excited by radiation of frequency ν are crosshatched; other occupied states are shaded. Below the energy diagrams are theoretical current-voltage characteristics derived for a spherical photo-tube. The number next to each curve designates the emitter material; the collector is assumed to be made of metal 1. The saturation line, shown as $I/I_s=1.0$, has a small but measurable slope due to the Schottky effect, which is neglected in this figure.

---

[11] C. H. Cartwright and M. Haberfeld-Schwarz, Proc. Roy. Soc. **A148**, 648 (1935).

[12] V. A. Johnson, Bull. Am. Phys. Soc. **22**, 20(A) (1947); **23**, 5(A) (1948); Wayne Scanlon and K. Lark-Horovitz, Phys. Rev. **72**, 530(A) (1947); Bull. Am. Phys. Soc. **23**, 26(A) (1948); A. von Hippel, Bull. Am. Phys. Soc. **23**, 26(A) (1948).

[13] W. H. Brattain and H. B. Briggs, Phys. Rev. **72**, 174(A) (1947).

[14] Georg Hass, Phys. Rev. **72**, 174(A) (1947).

[15] K. Lark-Horovitz and V. A. Johnson, Phys. Rev. **69**, 259(A) (1946); K. Lark-Horovitz, A. E. Middleton, E. P. Miller, and I. Walerstein, *ibid.*, 258(A) (1946); K. Lark-Horovitz, A. E. Middleton, E. P. Miller, W. W. Scanlon, and I. Walerstein, *ibid.*, 259(A) (1946); V. A. Johnson and K. Lark-Horovitz, *ibid.*, 259(A) (1946); *ibid.* **71**, 483(A) (1947); *ibid.*, 374; *ibid.*, 909 (1947); Bull. Am. Phys. Soc. **23**, 26(A) (1948); E. Conwell and V. F. Weisskopf, Phys. Rev. **69**, 258(A) (1946); G. L. Pearson and W. Shockley, *ibid.* **71**, 142(A) (1947); I. Estermann, A. Foner, and J. A. Randall, *ibid.*, 484(A) (1947); *ibid.*, 530(A) (1947); W. Crawford Dunlap, Jr., *ibid.* **71**, 471(A) (1947); S. Benzer, *ibid.*, 141(A) (1947); Bull. Am. Phys. Soc. **23**, 25(A) (1948); V. E. Bottom, Bull. Am. Phys. Soc. **23**, 21(A) (1948).

[16] A. L. Hughes and L. A. DuBridge, *Photoelectric Phenomena* (McGraw-Hill Book Company, Inc., New York, 1932).

[17] L. A. DuBridge, Phys. Rev. **39**, 108 (1932); **43**, 727 (1933); *Actualites Scientifiques et Industrielles* (Hermann and Cie, Paris, 1935), No. 268.

adjusted to make these levels coincide. States with the same total energy thus lie on the same vertical line. The potential energy of an electron just outside the surface barrier exceeds μ by an amount equal to the work function. This is indicated by the dashed line at the left-hand side of each energy diagram. The displacement $\varphi_c-\varphi$ between the lines for metals (1) and (2) corresponds to the c.p.d. between these conductors.

In this paper we shall be concerned mainly with temperatures of 300°K. Thermal excitation of electrons to levels as much as 0.20 ev above μ is measurable in precise photoelectric work on metals at this temperature. This effect is not indicated in Fig. 1, however, and states above μ are shown unoccupied. For the semiconductor 3, μ exceeds the highest energy in the occupied band by an amount δ. Except for quantities of the order of kT, δ is equal to one-half the width of the forbidden zone. The discussion that follows may be extended to impurity semiconductors by assigning other well-known values to δ.[1,2,7]

Let us consider a photo-tube with a large spherical collector made of metal 1 in Fig. 1. In this tube we arrange to have three small, central, interchangeable emitters composed, respectively, of materials 1 to 3. Using the well-known method of retarding potentials,[16] we may determine the energies of the photoelectrons irrespective of the directions in which they are emitted. In doing this, we measure the photo-current I as a function of V, the e.m.f. applied between the collector and the emitters.

In the photoelectric process,[17,18] an electron of energy ϵ absorbs a quantum and is excited to a state of total energy $\epsilon+h\nu$. If $\epsilon+h\nu>\mu+\varphi$, the electron can leave the emitter. Just outside the surface barrier, it has a kinetic energy

$$E=\epsilon+h\nu-(\mu+\varphi). \tag{1}$$

Occupied states for which this emission process is possible are crosshatched in Fig. 1.

An important feature of this experiment is that the total energy, not the kinetic, determines whether or not the electron can reach the collector. If we take the coincident Fermi levels of the emitters as our reference energy, an accelerating e.m.f. lowers the potential of an electron just outside the collector by an amount eV. A photoelectron originating in the state ϵ will just be collected, therefore, when

$$\mu+\varphi_c-eV=\epsilon+h\nu. \tag{2}$$

The scales in Fig. 1 are adjusted to make corresponding values of V and ϵ in Eq. (2) fall on the same vertical line. In particular, electrons originating at the level μ are collected at a voltage V_0 given by

$$eV_0=\varphi_c-h\nu. \tag{3}$$

At 0°K, levels above μ are unpopulated in a metal, of course, and $I=0$ when $V<V_0$. DuBridge[17] has shown that the initial increase of I is linear at this temperature; hence V_0 is an easily determined stopping potential, and by using Eq. (3) one may find φ_c. At higher temperatures, V_0 may be located by DuBridge's graphical technique if the c.p.d. is known.

For the semiconductor (3), we neglect the electrons in the conduction band. This is justifiable in photoelectric work at 300°K if the forbidden zone is more than 0.3 or 0.4 ev wide. Then $I=0$ if $V<V_0'$, where

$$eV_0'=\varphi_c+\delta-h\nu=eV_0+\delta. \tag{4}$$

Because of the shape of the occupied band near its upper limit, one expects the current from a semiconductor to exhibit a tangential rather than a linear approach to the voltage axis.[6] Results to be presented in Section VI show that this is the case. If electrons in the conduction band are detectable, the current-voltage curve should exhibit a plateau in the region directly below the forbidden zone in Fig. 1. If there is a continuous distribution of surface states in this zone,[7] the characteristic for the semiconductor should be more nearly like that for a metal.

A convenient property of retarding-potential methods that has long been recognized is that Eqs. (2) to (4) are independent of the emitter work function. In a photo-tube of the type we are discussing, several metallic emitters may be used for making independent determinations of V_0. Substitution of a semiconductor then allows one to investigate the points discussed in the preceding paragraph. Stray fields in the photo-tube are serious only when comparable with the

[18] For a discussion of work on metals, see E. Rudberg, Phys. Rev. 48, 811 (1935). The treatment above is not applicable to bound states (see reference 27).

field produced by the collector voltage V_0 (or V_0'). Variations in φ that produce a 30 percent uncertainty in $h\nu-\varphi$ (or in $h\nu-\varphi-\delta$) for a non-uniform surface do not disturb the results measurably near V_0 (or V_0'). Variations in δ associated with patch structures, or with different crystal directions, may produce superposed characteristics with various values of V_0', but a minimum value of δ should nevertheless be evident. The most serious difficulty met in practice is distortion of current-voltage curves because of non-uniformity of the collector.

In order to determine the kinetic energies of the photoelectrons, one must know the c.p.d. From (1) and (2) we obtain the well-known relation,

$$E=\varphi_c-\varphi-eV. \tag{5}$$

Setting $E=0$, we find the saturation point, V_s, of the current-voltage characteristic:

$$eV_s=\varphi_c-\varphi. \tag{6}$$

For $V>V_s$, I is constant and equal to I_s if the Schottky effect is neglected. The Einstein relations are obtained by setting ϵ equal to μ or to $\mu-\delta$ in (1):

$$\begin{aligned} E_m&=h\nu-\varphi=e(V_s-V_0),\\ E_m'&=h\nu-\varphi-\delta=h\nu-\varphi'=e(V_s-V_0'). \end{aligned} \tag{7}$$

Here E_m and E_m' are the maximum energies of the photoelectrons from a metal at 0°K and from an ideal semiconductor, respectively; φ' is the photoelectric threshold energy of the semiconductor. It is evident that phenomena dependent on Eqs. (5) to (7) will be sensitive to non-uniformity of the emitter surface and to stray fields in the photo-tube.

III. FORM OF ENERGY AND SPECTRAL DISTRIBUTIONS

The probability that an incident quantum will eject an electron having a kinetic energy E in the range dE is given by

$$N(\nu, E)dE=p(\nu, \epsilon)f(\epsilon)n(\epsilon)d\epsilon. \tag{8}$$

Here N is the energy distribution function, p is the transition probability, and f is the Fermi factor, $[1+\exp((\epsilon-\mu)/kT)]^{-1}$; as before, n is the density of states and E is related to ϵ through (1).

Now p can be calculated only if one knows the wave functions for the states involved in the transitions. Work of this sort has been done for simple metals,[19,20] but semiconductors have not been treated. In the absence of such information, we shall attempt to get a rough idea of the form of N by writing p as the product

$$p(\nu, \epsilon)=s(\nu, \epsilon)t(\epsilon+h\nu). \tag{9}$$

Here s is the probability of excitation from the state ϵ to the state $\epsilon+h\nu$, and t is the probability that an electron reaching the state $\epsilon+h\nu$ will appear outside the surface barrier. It is evident that t must be zero for $E=0$ and must increase at higher values of E. To a first approximation we set

$$t(\epsilon+h\nu)\propto E. \tag{10}$$

This assumption is closely related to those used by Fowler and DuBridge in their work on the photoelectric emission of a Sommerfeld metal.[2,17] It is in good agreement with detailed calculations made on sodium by A. G. Hill.[20,21]

A special case of particular interest is that for which

$$s(\nu, \epsilon)n(\epsilon)\propto q(\nu)(\mu-\delta-\epsilon)^m=q(\nu)(E_m'-E)^m. \tag{11}$$

---

[19] For references and discussion, see F. Seitz, *The Modern Theory of Solids* (McGraw-Hill Book Company, Inc., New York, 1940); A. H. Wilson, *The Theory of Metals* (The Cambridge University Press, New York, 1936); L. B. Linford, Rev. Mod. Phys. **5**, 34 (1933).

[20] A. G. Hill, Phys. Rev. **53**, 184 (1938).

[21] In treating a Sommerfeld metal, Fowler and DuBridge considered in detail the velocities of the electrons before and after excitation. Anisotropies in s due to the one-dimensional character of the ideal surface barrier were introduced in some cases and neglected in others. In the final approximations, the results reduce to the equivalent, in our symbols, of $stn\propto E$ (with the variation being due almost entirely to t). Hill's more rigorous computations for sodium gave very closely the same result, except that s contained a factor lying between ν^{-3} and ν^{-4} (Hill, reference 20, Fig. 1). As a consequence, the spectral distribution calculated from Hill's data would drop noticeably below the Fowler curve when $h\nu-\varphi>0.5$ ev. Nevertheless, the energy distributions fit DuBridge plots even when $h\nu-\varphi=1.2$ ev. A similar result has been found experimentally for tungsten (see reference 24). The optical constants of the emitter may also have an important influence on this problem (see R. J. Maurer, Phys. Rev. **57**, 653 (1940), and the papers cited there). A more complete form of (10) may be derived for ideal metals by considering electrons isotropically distributed in velocity space and incident on a one-dimensional barrier. Then, $2t=1-[(\mu+\varphi)/W]^{\frac{1}{2}}\sim E/2W$. Here W, the energy relative to the bottom of the conduction band, is assumed large compared to E. This naive argument may fail entirely for semiconductors (one objection, for example, is that the bottom of the conduction band may approach or exceed $\mu+\varphi$; another is that the effects of crystal anisotropy may be much more pronounced for semiconductors than for metals).

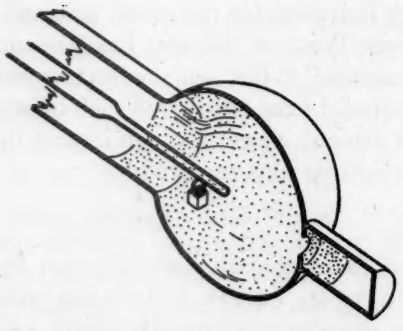

FIG. 2. Schematic diagram of photo-tube showing the hairpin-shaped emitter support with one of the interchangeable emitters hanging on it. During measurements, the bucket-shaped emitter is placed over the end of the hairpin. The quartz window that admits the radiation is at the lower right. The inside of the glass sphere is coated with a conducting layer which serves as the collector.

Here $s(\nu, \epsilon)$ is separable into a frequency-dependent part $q(\nu)$ and an energy-dependent part. The latter combines with $n(\epsilon)$ to make up the second factor on the right. Using (8) to (11) we get the following energy distribution:

$$N(\nu, E) \propto q(\nu)E(E_m'-E)^m. \tag{12}$$

The current-voltage characteristic at 0°K is given by

$$(I/I_s)Y=\int_E^{E_m'} N(\nu, E)dE \propto q(\nu)(h\nu-\varphi')^{m+2}$$

$$\times[(m+2)(1-v')^{m+1}-(m+1)(1-v')^{m+2}], \tag{13}$$

where $v'=(V_s-V)/(V_s-V_0')$, and where the photoelectric yield Y is expressed in electrons/quantum. The lower limit of the integral is to be regarded as a function of v'. At a given frequency, energy data are normally obtained by measuring only V and the ratio I/I_s.

Setting $m=\delta=0$ in (13), we obtain DuBridge's equation for an ideal metal at 0°K.[17] If, in addition, q is constant and $v'=0$, the result is identical with Fowler's equation for 0°K.[2] By taking account of the Fermi factor for $T>0$, one may derive the complete forms of these equations for metals.

If n has the familiar form[19]

$$n \propto (\mu-\delta-\epsilon)^{\frac{1}{2}}, \tag{14}$$

at the high energy end of the filled band in a semiconductor, and if s is independent of ϵ, then $m=\frac{1}{2}$; if s is proportional to the velocity of the "hole" formed in the filled band by the transition,[6] $m=1$. This value is used in Fig. 1; however, the energy dependence of s will be treated as an open question in this paper.

The study of soft x-ray emission spectra[22] has shown that (14) is sometimes valid over such a limited range that it is not very useful. In certain cases (Skinner, reference 22, Fig. 3; O'Bryan and Skinner, reference 22, p. 261) the results can be described within experimental accuracy by a relation in which the exponent $\frac{1}{2}$ is replaced by a larger number. For this reason we maintain an interest in values of m greater than 1 in (13).

This relation may be compared with experiment by methods similar to those of Fowler and DuBridge. V_s can be determined with sufficient precision by parabolic extrapolation of I to the saturation line.[23,24] Then I/I_s and its logarithm may be plotted as functions of $\log E=\log e(V_s-V)$. The logarithmic curve is sensitive to the form of the results near V_0, as is the linear one near V_s. The value of m can be found from the plots which best fit the data. (An independent value may be obtained from the spectral distribution.) V_0 is determined from the horizontal displacement required to superpose the experimental and theoretical curves.

A preferable method of analyzing data involves only expression (10). The quantity sn may be found by differentiating the current-voltage curves and by evaluating the ratio $N(\nu, E)/E \propto s(\nu, \epsilon)n(\epsilon)$. Using several values of ν, one may determine the frequency dependence of s.

IV. SURFACE STATES AND IMPURITY LEVELS

We shall assume that surface states and impurity levels may be treated on the same basis. The probability that a quantum will be absorbed by an electron in a bound level may be estimated from the formula[25-27]

$$\sigma=(\pi h/mc)(e^2/h\Delta\nu)F. \tag{15}$$

---

[22] H. W. B. Skinner, Phil. Trans. **A239**, 95 (1940); H. M. O'Bryan and H. W. B. Skinner, Proc. Roy. Soc. **176**, 229 (1940); D. H. Tomboulian, Phys. Rev. **60**, 551 (1941).

[23] S. S. Prilezaev, J. Tech. Phys. U.S.S.R. **9**, 1439 (1939).

[24] L. Apker, E. Taft, and J. Dickey, Phys. Rev. **73**, 46 (1948).

[25] H. Bethe, *Handbuch der Physik* (1933), Vol. 24, p. 1. We are indebted to Dr. Bethe for discussions of this subject.

[26] H. Frohlich and R. A. Sack, Proc. Phys. Soc. **59**, 30 (1946).

[27] The influence of the Franck-Condon principle on the problem of emission from impurity levels has been treated

Here σ is the cross section for absorption in the range $\Delta\nu$, and F is the oscillator strength for this range. Estimating that $F=0.2$ and $h\Delta\nu=1$ ev, we get $\sigma=2\times10^{-17}$ cm². For a density of surface states equal to the density of surface atoms, 10^{15} cm^{-2}, the absorption is 0.02. If 10 percent of the excited electrons escape ($E/W=0.4$),[21] the yield is 0.002 electron/quantum. This is more than twice as large as the total photoelectric yield given for Te or for Ge in Section VI ($h\nu=5.80$ ev). A more reasonable value for the density of surface states, however, is 10^{13} cm^{-2}.[7-9] In this case, the emission from these states amounts to a few percent of that mentioned for Te and Ge above. This would be enough to obscure the point V_0' on the current-voltage characteristic.

Bardeen[7] has shown that a surface state density of 10^{12} cm^{-2} is sufficient to set up a space-charge layer at the free surface of a typical semiconductor containing 10^{17} impurities/cm³. Consequently, at the surface δ approaches half the band separation, although it differs from this value in the interior. This effect would show up in a shift of V_0', even though the emission from the surface states themselves might not be measurable.[28]

V. EXPERIMENTAL METHOD

A schematic diagram of the type of photo-tube used in this work is shown in Fig. 2. The collectors were glass spheres 15 cm in diameter. Each was coated on the inside with a conducting layer of Aquadag, coarse graphite, Ni, W, or Pt. From 5 to 8 bucket-shaped emitters were hung on a Ta wire bent in the shape of a hairpin. These buckets could be moved about by tilting the sealed-off photo-tube. During measurements, the emitter in question was slipped over the end of the hairpin. Retainers (in the part of the tube not shown in Fig. 2) held the other buckets in fixed positions during this operation.

Between the retainers and the collector, an evaporation chamber was mounted in a side tube. Graphite crucibles heated by induction, or Ta boats heated by the passage of current, served to evaporate Ge in four tubes used to investigate this element. A Ta boat was used for Te in one tube; in two others the element was distilled through 8-section hard-glass trains. After the metal buckets (Pt, Ni, W, Mo, Ta, or Cb) had been investigated, some of them were moved over the evaporation bulb and were covered with a layer of semiconductor. In the course of the measurements, many of the emitters were subjected to heat treatment (with induction heaters or with 1-kw tungsten lamps having wide-aperture elliptic reflectors). At least one metal

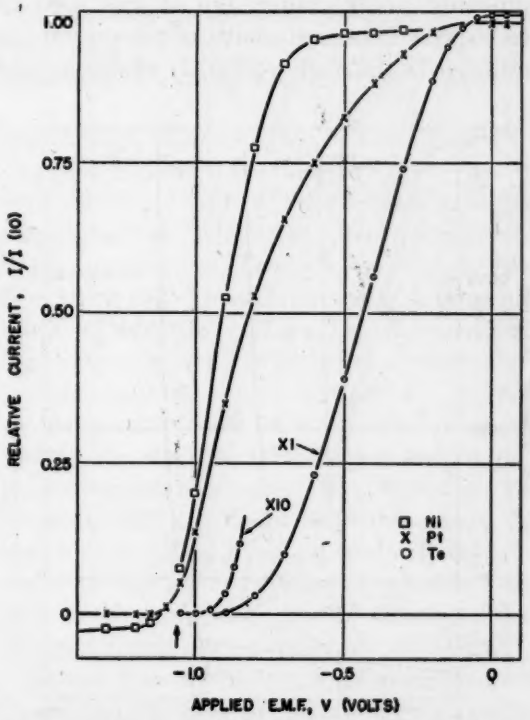

FIG. 3. Typical set of current-voltage characteristics for Te, Ni, and Pt; $h\nu=5.80$ ev and $T=300°$K. The upper curve for Te has been expanded vertically by a factor of 10. To avoid confusion, only a few of the experimental points are given. The curve for Ni shows very poor saturation and large reverse currents. V_0 is marked by the arrow below the abscissa axis. Currents were normalized with $I_{10}=1.0$ at $V=+10.0$ volts. Complete curves extended from -10 to $+1000$ volts. Note the similarity between these characteristics and those in Fig. 1.

recently by C. Herring in theoretical work on oxide cathodes, Bull. Am. Phys. Soc. **23**, 27(T) (1948). We wish to thank Dr. Herring for discussions of his results.

[28] Dr. Bardeen has kindly pointed out to us that if detectable emission originates at the top of the filled band in the space-charge layer of a P-type semiconductor, the decrease of δ with increasing depth must be considered. On the characteristic analogous to (3) in Fig. 1, a tail extends from V_0' toward V_0 to a voltage determined by the maximum depth at which external photoelectrons originate. It will be recalled that photoelectric processes occurring at appreciable depths are due ordinarily to a volume effect for which selection rules increase the threshold energy. Electron collisions, lattice distortions, or impurity levels, however, may permit otherwise forbidden transitions. See H. Y. Fan, Phys. Rev. **68**, 44 (1945), and the references cited there.

was kept in its original condition for use as a reference surface.

A fused-quartz bucket with Pt contacts was coated with Ge in one tube. Three Ge single crystals with exposed (111) faces were fastened to buckets in this same tube.

Ta buckets that had been coated with B by pyrolysis of B_2H_6 were investigated in 5 tubes. In three other cases, W ribbons in tubes previously described[24] were coated by the same method.

The ends of the buckets were 8 mm square. The area irradiated during photoelectric measurements was smaller than 3 mm×1 mm. This spot could be moved over the surface to investigate the uniformity of emission. By means of an auxiliary optical system, visible or infra-red radiation from a projection lamp could be focused on the emitting area. This radiation did not excite photo-emission, of course, but it was used to detect surface non-uniformity of Ge crystals as mentioned in the next section. It could be used also to test for changes in work function resulting from illumination, as reported recently by Brattain.[9]

Other experimental details are given in a previous paper.[24]

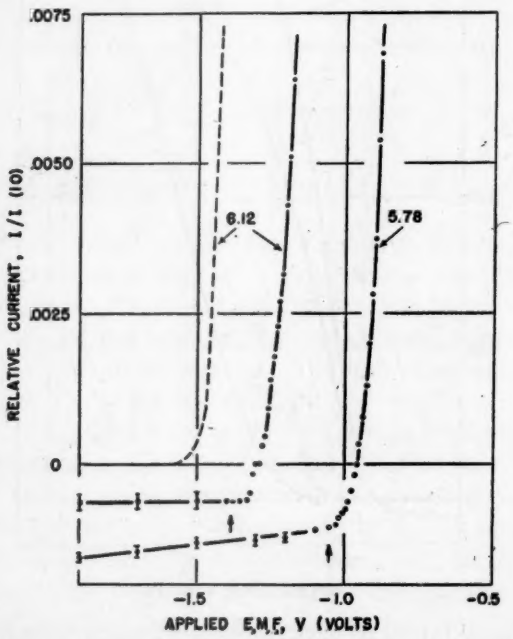

FIG. 4. Lower portions of curves like those in Fig. 3. The ordinate scale is expanded by a factor of 100 relative to that in the previous figure. Numbers next to the curves give values of $h\nu$. At these levels, 5.78 ev is preferable to 5.80 ev (used in Fig. 3), since its source emits no radiation of higher frequency. Note sudden departure of the curves from the reverse-current line. The dashed curve for 6.12 ev applies to a metal with the same work function as Te and with $T=300°K$. Values of V_0 are marked with arrows.

VI. DISCUSSION OF RESULTS

(a) Tellurium

Figure 3 shows typical current-voltage characteristics for evaporated Te, sheet Ni, and sheet Pt. The similarity between these curves and those in Fig. 1 is immediately evident. Values of V_0 determined by DuBridge's method from measurements on Ni, Pt, Mo, and Ta in this tube lay in the range -1.06 ± 0.01 volt for $h\nu=5.80$ ev, corresponding to a collector (Aquadag) work function, $\varphi_c=4.74$ ev; other values of $h\nu$ gave this same result for φ_c.[29] Curves for Te ($h\nu=6.12$, 5.80, and 5.42) had a common saturation point, $V_s=-0.02$ volt, as determined by parabolic extrapolation techniques.[23,24] The work function thus found for Te was 4.76 ev.

Figure 4 shows the lower portions of characteristics analogous to those in Fig. 3, except that the ordinate scale is expanded by a factor of 100. At these levels a measurable fraction of the observed photo-current may be due to stray radiation scattered from the emitter to the collector and then to the hairpin.[30] Hence the curves (after correction for reverse currents[16,23]) represent upper limits to the current from the Te. The dashed curve in Fig. 4 applies to an ideal metal with the same work function as the Te. Data for the Pt emitter in Fig. 3 fit this characteristic after correction for a relative reverse current of 0.003.

If the simple arguments of Section II are adequate, it is evident that photo-current originating in states above the Fermi level in Te amounts to

[29] The Ni and Pt had contaminated surfaces, since the degassing temperature after the last exposure to active gas was only 500°C. The curves therefore show peculiarities such as poor saturation and, in the case of Pt, a bulge at $V\sim-0.8$ volt. These effects have no important influence on the determination of V_0, however. Aquadag on glass, baked at 500°C, practically always has a work function within 0.1 ev of the value given above.

[30] An estimate based on the relative yields of the surfaces involved indicates that spurious current from this source amounts to less than $10^{-3}I_{10}$ for $V<-0.9$ volt and $h\nu=5.78$ ev. In a more refined experiment, such current may be isolated by covering the hairpin with sleeves held at an independent potential (see reference 24).

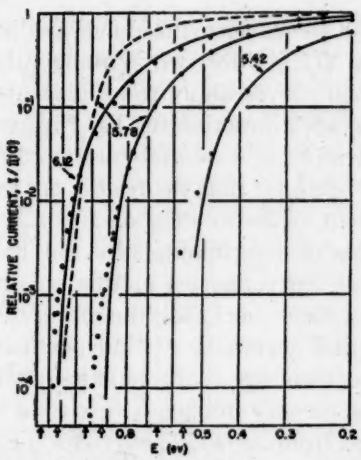

FIG. 5. Logarithmic plots of current *vs.* kinetic energy for Te. The solid curves are calculated from Eq. (13) with $m=\frac{3}{2}$ and are identical except for appropriate horizontal displacements. Solid arrows mark values of E_m, open arrows E_m'. Values of δ are 0.12, 0.10, and 0.10 ev for decreasing values of $h\nu$; corresponding values of E_m are 1.36, 1.02, and 0.66. The dashed curve is for the Pt in Fig. 3 with $T=300°K$ and with $h\nu=5.78$. Note that principal departures from the solid lines occur below $I/I_{10}=10^{-2}$ and that the curves for Te and Pt are roughly parallel in this region. The curve labeled 5.42 has a 3 percent contribution due to $h\nu=5.47$.

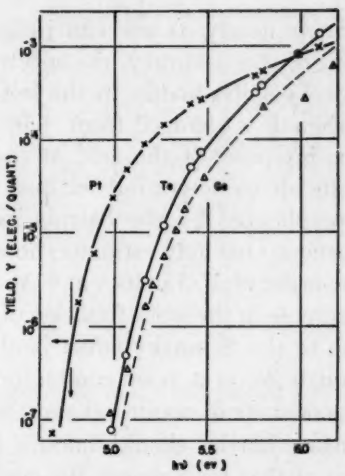

FIG. 6. Spectral distribution of the yield from the Te and Pt emitters of Fig. 3. The solid line through the points for Pt is computed from Fowler's equation. For $h\nu>5.0$ ev, it is closely approximated by $Y=5\times10^{-4}(h\nu-4.76)^2$ electrons/quantum. The line through the points for Te is calculated from the relation $Y=6\times10^{-4}(h\nu-4.89)^4$. Data for the Ge emitter of curve 7 in Fig. 10 are also shown. This sample has the same work function as the Te and the Pt. A measured point on the Ge curve at ($h\nu=4.89$, $Y\sim4\times10^{-8}$) is not shown. The dashed line through the points for Ge is given by $Y=4\times10^{-4}(h\nu-4.94)^4$.

less than $10^{-4}I_{10}$ at either $h\nu=5.78$ or 6.12 ev. This is shown more clearly in the plot of Fig. 5. The solid arrows indicate values of E_m (corresponding to V_0 in Fig. 4; see Eq. (7)). The open arrows indicate values of E_m' for the solid curves, which are calculated from Eq. (13) with $m=\frac{3}{2}$. Corrections were made for the reverse currents shown in Fig. 4. Within 0.02 ev, the intervals between arrows (both open and closed) agree with known differences in $h\nu$. Although the last 1 percent of the current deviates markedly from the curves, the agreement is reasonably good above $I/I_{10}=10^{-2}$. As shown by the dashed curve, a metal with the same work function as Te emits at least 350 times as much relative photo-current capable of overcoming the retarding potential V_0 when $h\nu=5.78$ ev.

Figure 6 shows the spectral distribution of the photoelectric yield Y for the Te and Pt emitters of Fig. 3. At $h\nu=5.78$ ev, yields varied by less than 2 percent from point to point on these surfaces. The Pt sample is interesting because it has the same work function as the Te and because it has almost the same yield for $h\nu=5.78$ ev. For this reason, the curves in Fig. 6 and those for 5.78 ev in Fig. 5 show similar behaviors. The solid line through the points for Pt is computed from Fowler's equation; in this particular case it is given by $Y=7\times10^{-7}\Phi[(h\nu-4.76)/0.0258]$ electrons/quantum, where the quantity in brackets is the argument of Fowler's function Φ. Above $h\nu=5.0$ ev, this expression is closely approximated by $Y=5\times10^{-4}(h\nu-4.76)^2$. The distribution for Te, in contrast, is given within experimental error by the equation $Y=6\times10^{-4}(h\nu-4.89)^4$. It falls to unmeasurable values when $h\nu<5.0$ ev, even though the work function is 4.76 ev. As determined from these spectral data, m in Eq. (13) is 2 instead of $\frac{3}{2}$, as found from the energy data; the value of δ is 0.13 as compared with 0.12, 0.10, and 0.10 in Fig. 5. Because of possible inaccuracy of these measurements,[31] discrepancies of this magnitude are probably not significant.

Figure 7 shows high voltage portions of two Te characteristics with current plotted as a function of $V^{\frac{1}{2}}$. In this range, the data fit two straight lines having slopes with a ratio of roughly 1.7. For these same two values of $h\nu$, the slopes of the spectral distribution in Fig. 6 have a ratio of

[31] No corrections were made for losses in the fused quartz photo-tube windows, in the crystalline quartz thermocouple window, or at the thermocouple receivers.

about 1.5. As nearly as one can judge from an experiment of this accuracy, the spectral characteristic for Te shifts bodily to the left by about 0.01 ev when V is changed from +10 to +1000 volts. The intensity of the field at the emitting area is difficult to determine because the geometry is complicated by the hairpin and by the bucket corners. One may estimate, however, that it is of the order of $V/3$ volts/cm.[32] At 330 volts/cm the decrease in the work function of a uniform metal due to the Schottky effect is about 0.007 ev. Although Te is a poor conductor, it has a dielectric constant of about 5,[12] and the lowering of the surface barrier should amount to at least 70 percent of that for a metal. We conclude that the variation of photo-current with change in the applied field is of the same order of magnitude as that computed for a uniform surface.[33] Such behavior is rare at these comparatively low fields.

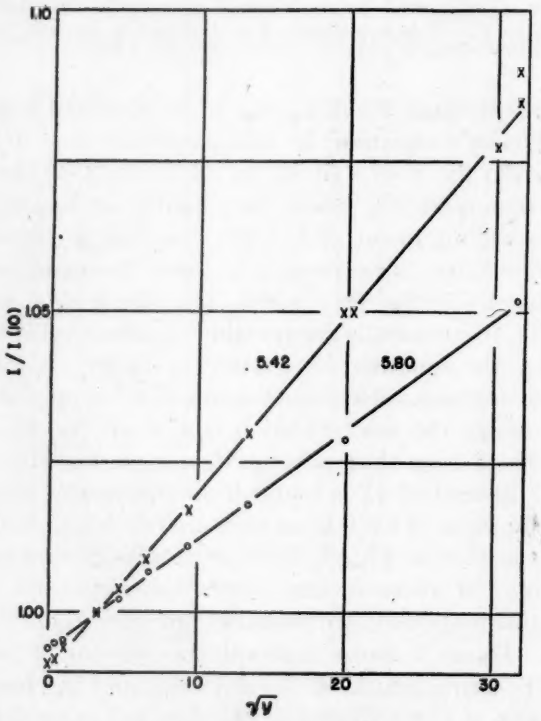

FIG. 7. Relative photo-current from Te as a function of $V^{\frac{1}{2}}$.

[32] R. N. Hall, private communication.

[33] More accurately stated, the results agree with those expected for a surface with patches smaller than about 10^{-4} cm and with a value of δ independent of V. See N. Morgulis, J. Phys. U.S.S.R. 11, 67 (1947); L. B. Linford, reference 19.

Figure 8 shows normalized energy distribution functions $N(E)/Y$ for two extreme values of $h\nu$. The dashed curves apply to an ideal metal with the same work function as Te. Figure 9 shows values of $N(E)/E \propto s(\epsilon)n(\epsilon)$ computed from Fig. 8. It will be noted that the results are practically independent of $h\nu$ as long as $E>0.2$ ev. Since the process of determining sn is unreliable when E is small, discrepancies in this region are not significant. One concludes, therefore, that within experimental accuracy, s is independent of ν for Te. Current-voltage characteristics or energy distributions for any frequency discussed here may be derived from the single curve for Te in Fig. 9.

Data presented thus far apply to a Te layer deposited on a degassed Ni bucket near 300°K. Similar results were obtained for 8 other surfaces evaporated on to Pt and Ni substrates in two photo-tubes.[34] Film thicknesses range from 10^{-5} to 10^{-2} cm, and pressures during deposition ranged from less than 10^{-7} mm Hg (for evaporation from Ta) to 5×10^{-6} (for evaporation from glass). Some surfaces consisted of highly oriented crystallites, while others had random structure.[35] Values of φ ranged from 4.76 to 4.83 ev. Other deviations from the results already given were found only for two layers deposited on a Mo bucket; current-voltage characteristics were like that in Fig. 3 but were shifted bodily toward V_0 by 0.04 volt (as though δ were slightly smaller than for the other samples).

To obtain different types of surfaces, evaporated Te was heated to the melting point.[36] Visual inspection showed that the optical properties of the layers changed radically. Reverse currents indicated that the reflection factors for $h\nu=5.80$ ev increased from two to eight times (this prevented measurements as precise as those in Fig. 4). The photoelectric yields at $h\nu=5.80$ ev increased by about 10 percent, and the saturation points shifted toward positive voltages by about 0.1 volt, indicating a slight decrease in the aver-

[34] Non-uniformity of the collector in another tube rendered φ_c uncertain by 0.1 volt; within this limit the results agreed with those above.

[35] Miss Eileen Alessandrini kindly took electron diffraction data on all samples discussed in this paper.

[36] In one case, a thick layer was partially re-evaporated. The resulting sample consisted of crystallites with [00·1] axes oriented perpendicular to the surface and with (00·1) planes exposed by thermal etching. We are grateful to Dr. David Harker and to Mrs. B. Decker for making x-ray diffraction measurements on this sample.

age work function. On the scale of Fig. 3, the changes were hardly evident.

On the basis of these measurements, we have concluded that the general behavior displayed in Figs. 3 to 9 is characteristic of crystalline Te and is not fundamentally affected by the procedures used in preparing particular samples. Admittedly, the methods of interpreting the data are crude. Without more complete knowledge of transition probabilities and energy structures, we are hardly justified in ascribing more than empirical significance to the values $\frac{3}{2}$ and 2 used for m in Figs. 5 and 6. These numbers are higher, however, than would be expected from relation (14), and we have found no experimental indication of a definite edge for the occupied band in Te. Values of δ derived from the data depend, therefore, on arbitrary extrapolation processes such as those used in the figures above. Three considerations of particular interest have already been mentioned in Sections II and III. They are the following: The experimental curves may be made up of superposed characteristics having a smaller value of m than the composite curves and having various values of δ.[37] Emission from surface states or similar levels may conceal the point V_0' and give misleading values of m. The density of states itself may have a form like that in Fig. 9.

In any event, though δ cannot be determined uniquely, it can be correlated with estimated densities of surface levels. Thus, if $\delta=0.10$ ev, as found for $m=\frac{3}{2}$ in Fig. 5, an upper limit[30] to the current originating in the "forbidden" zone ($\epsilon>\mu-\delta$) is about 4×10^{-7} electrons/quantum at $h\nu=5.78$ ev. As estimated in Section IV, this corresponds to a density of occupied surface states, 10^{11} cm^{-2}. For $h\nu=5.42$ and 6.12 ev, the results of similar estimates are 2×10^{11} in each case (taking account of the change in t with E as given by (10)).

On the other hand, if the lower portions of the current-voltage curves are extrapolated to zero parabolically (as when $m=1$ in (13)), or if linear extrapolation is used in Figs. 8 and 9, then $\delta\sim0.18$ ev. The corresponding density of occupied surface levels is about 10^{12} cm^{-2}. Fewer than 1 percent of these lie above the Fermi level at 300°K.

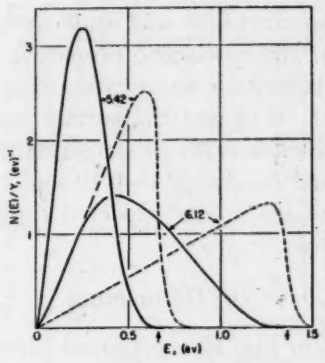

FIG. 8. Normalized energy distribution functions for Te. The curve for $h\nu=5.42$ ev has a contribution due to 5.47 ev. The dashed curves are for an ideal metal with the same work function as Te and with $T=300$°K. Arrows mark values of E_m.

Lark-Horovitz and his collaborators[12,15] have found that evaporated Te is a P-type semiconductor (i.e., with hole conduction predominating). The activation energy for electrical conductivity is about 0.36 ev in the intrinsic range and 0.04 ev at low temperatures. The impurity concentration in typical samples was 10^{17} cm^{-3}.

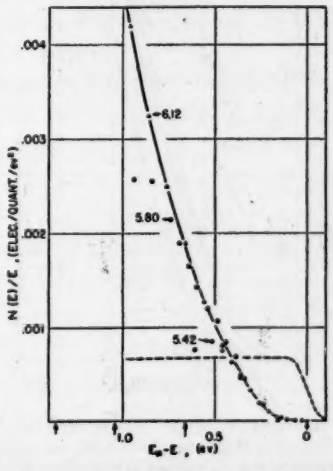

FIG. 9. Values of $N(\nu, E)/E \propto s(\nu, \epsilon)n(\epsilon)$ for Te. The abscissa scale is reversed relative to those in Fig. 1. The arrow at the right marks E_m; the others mark the points at which $E=0$ for the three values of $h\nu$. The dashed curve is for an ideal metal having the same yield as Te at $h\nu=5.80$ ev. If $s(\nu, \epsilon)$ for Te is independent of ϵ, as for the metal, the solid curve gives the density of occupied states in the vicinity of the Fermi level. In the ranges where E is small, deviations from this curve are not significant; they may arise from the extrapolation process used in locating V_0. Distributions derived from the solid curve represent the original data within experimental error.

[37] We are indebted to Dr. W. Shockley for discussions of this subject. A family of curves with the parameter m and with values of δ uniformly distributed in a given interval forms a composite characteristic (in the given range) for which the parameter is $m+1$.

The Te described here was similarly treated and had similar thermoelectric properties. Assuming that the impurity concentration was the same, the value $\delta \sim 0.18$ and the surface state density 10^{12} cm^{-2} are not in disagreement with Bardeen's conclusions;[7] the value $\delta \sim 0.10$ and the density 2×10^{11} deviate in the expected direction from these figures.

(b) Germanium

Curve 7 in Fig. 10 is a typical current-voltage characteristic for evaporated Ge. This particular sample was deposited on a Mo bucket. Approximately 50 similar surfaces (most of them more than 10^{-4} cm thick) were investigated in 4 phototubes. Pressures during evaporation ranged from values which were not measurable with an ionization gauge ($<3\times10^{-8}$ mm Hg) when a graphite crucible was used, to values as high as 5×10^{-7}. Substrates of degassed Ni, Ta, Mo, Pt, crystalline Ge, and fused quartz were unavoidably heated by radiation from the evaporation chamber but were probably below 650°K during deposition of the Ge (the Ni buckets did not reach the Curie point). For some layers, electron diffraction photographs exhibited diffuse rings, but for others the patterns were sharp.[14,35]

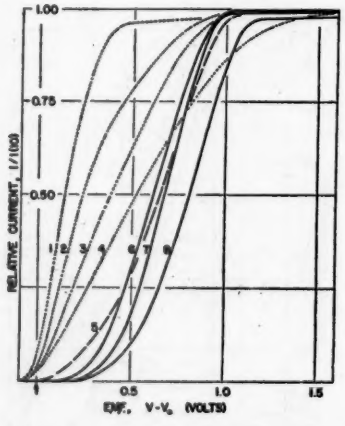

FIG. 10. Current-voltage characteristics for several metals and semiconductors; $h\nu = 5.80$ ev and $T = 300$°K. Note that abscissa scales are set coincident at $V = V_0$. Work functions are given below in electron volts, yields in electrons/quantum:

1. Ni (sheet) *;	$\varphi \sim 5.3$;	$Y = 5\times10^{-3}$.
2. Pt (sheet) *;	$\varphi = 4.76$;	$Y = 5\times10^{-4}$.
3. Ni (sheet) *;	$\varphi = 4.74$;	$Y = 1\times10^{-4}$.
4. Ta (ribbon);	$\varphi = 4.15$;	$Y = 3\times10^{-4}$.
5. Ge (7 after heating to 800°K);	$\varphi \sim 4.6$;	$Y = 1\times10^{-4}$.
6. Te (evaporated);	$\varphi = 4.76$;	$Y = 4\times10^{-4}$.
7. Ge (evaporated);	$\varphi = 4.76$;	$Y = 2\times10^{-4}$.
8. B (pyrolytic);	$\varphi \sim 4.6$;	$Y = 7\times10^{-5}$.

Those marked * were degassed at only 500°C after the last exposure to air.

Work functions ranged from 4.66 to 4.80 ev. For more than 80 percent of the surfaces, φ lay within a few hundredths of an electron volt of the latter figure. For the curve in Fig. 10, $\varphi = 4.76$ ev, the same as was found for Te. This curve may be fitted approximately by Eq. (13) if $m \sim 2$ and if $\delta \sim 0.18$ ev.

A typical spectral distribution for Ge is given in Fig. 6. It is compared with the relation $Y = 4\times10^{-4}(h\nu - 4.94)^4$ electrons/quantum; here $\delta = 0.18$ ev, the value derived from the energy data. The experiments were not as precise as those for Te, and the comparatively high reflection factor of Ge renders the points near $h\nu = 5$ ev valid only as upper limits, since currents this small could be due to scattered radiation. At $h\nu = 5.80$ ev, yields varied by less than 2 percent when different points on the surfaces were irradiated. The slopes of the saturation lines were about twice as large as those shown for Te in Fig. 7.

For $h\nu = 5.80$ ev and $\delta = 0.18$ ev, the upper limit to current originating in the forbidden zone of Ge is about 10^{-6} electron/quantum, corresponding to a surface level density, 5×10^{11} cm^{-2}.

As in the case of Te, a different value of δ was obtained by linear extrapolation of $N(E)/E$ (see Fig. 11). The result was 0.33 ev, and the corresponding density of occupied surface states was 4×10^{12} cm^{-2}.

Thermoelectric measurements made on two of these evaporated samples showed that the conduction was P type. The values of δ given above may be compared with the total width, about 0.75 ev, of the forbidden zone in crystalline Ge.[12,13,15]

When the Ge layers just described were heated to 800°K,[38] the current-voltage characteristics changed radically. The saturation points shifted in the positive direction by about 0.1 volt, and the lower portions of the characteristics shifted toward V_0, as shown by curve 5 in Fig. 10. Analogous changes occurred in the spectral distributions; although the yields at $h\nu = 5.80$ ev

[38] Ni is not a suitable substrate for this experiment, since the Ge apparently forms a metallic substance when heated in contact with it. Dr. W. H. Brattain has informed us that he has noticed a similar effect.

decreased by a factor of 2, they increased by a factor of 40 at 4.89 ev. One concludes either that δ decreased practically to zero or that the density of surface states increased by at least an order of magnitude. Thermoelectric measurements made after the tube was dismantled showed that the samples were P type, a result consistent with a small value of δ.

Data on (111) planes of degassed Ge single crystals[39] were like those for the heated layers. These samples were also P type after removal from the tube.

(c) Boron

Curve 8 in Fig. 10 is typical of B layers (about 0.005 cm thick) deposited by pyrolysis of B_2H_6 on Ta at 1000°K.[40] The samples were degassed in vacuum at 1600°K. If Eq. (13) is used to describe this characteristic, $m\sim 2$ and $\delta\sim 0.25$ ev. The spectral distribution was given roughly by $Y=10^{-4}(h\nu-4.9)^4$ electrons/quantum. The deviations from these simple expressions were greater for B than for Ge and Te. The saturation lines had slopes about 4 times greater than those in Fig. 7.

Work functions for various samples ranged from 4.4 to 4.6 ev. When surfaces were allowed to stand at 300°K, φ increased by about 0.3 ev in the course of 20 hours. This effect was similar to that shown by degassed W in tubes with comparable vacuum treatment.[24] The results for the contaminated surfaces of B having work functions as high as 4.9 ev were no different in character from those for degassed samples and gave approximately the same values of δ.

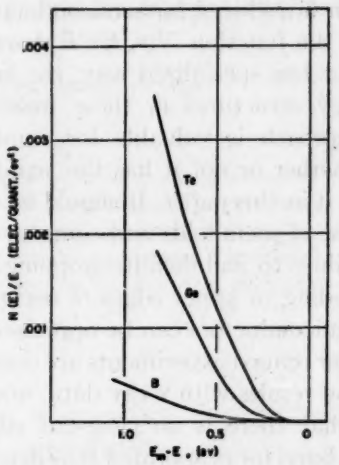

FIG. 11. Curves showing $N(\nu, E)/E \propto s(\nu, \epsilon)n(\epsilon)$ for Te, Ge, and B with $h\nu=5.80$ ev. The results for Te are independent of ν, as shown in Fig. 9. For Ge, results for $h\nu=5.42$ fit the curve shown. No data were taken at 6.12. For B, the results for $h\nu=5.42$ fit the curve shown if multiplied by 0.4.

Taking $\delta=0.25$ ev, one obtains an upper limit of 6×10^{-7} electron/quantum for photo-current originating in the forbidden zone when $h\nu=5.80$ ev. The corresponding density of occupied surface levels is 3×10^{11} cm^{-2}. Linear extrapolation of $N(E)/E$ in Fig. 11 gives $\delta\sim 0.5$ ev and a density 3×10^{12} cm^{-2}.

In the range from 300 to 900°K, the electrical conductivity of samples produced in the same way as those on the buckets was given by $\sigma=a\exp(-b/kT)$, where a varied from 1000 to 5000 ohm^{-1} cm^{-1}, and where b ranged from 0.4 to 0.5 ev. Photo-conduction occurred in the near infra-red. Thermoelectric measurements showed that the material was P type at 300°K. Electron diffraction photographs showed no sharp patterns, so the samples were presumably amorphous.

VII. SUMMARIZING REMARKS

The results in the preceding section indicate that the expressions of Section III give the general form of the spectral and energy distributions for Te, Ge, and B. While the work function φ and the value of the yield Y (at a single frequency) specify the emission near the threshold of a simple metal, the additional parameters m and δ

[39] Before these crystals were degassed, illumination of the emitting area with infra-red radiation shifted the saturation points of current-voltage curves by several tenths of a volt in the positive direction. The photoelectric yield, however, did not change by as much as 0.3 percent. The sample behaved as though a fraction of the emitting surface were charged positively with respect to the rest during illumination. The effect disappeared after the crystal was heated to 1000°K for ten minutes. It may be related to the photovoltaic effects found in non-uniform samples by Benzer (see reference 15). Since the current-voltage curves did not undergo a simple translation, and since the effect occurred at 300°K, it was assumed that the phenomenon was not the one reported by Brattain (reference 9). The crystals were N type when they were put into the tube, and they had a resistivity of about 2 ohm cm at 300°K. The surfaces were formed when the Ge solidified slowly. We are indebted to Mr. E. F. Hennelly for furnishing these samples and to Dr. W. C. Dunlap for the results of Hall effect measurements.

[40] A. W. Laubengayer, D. T. Hurd, A. E. Newkirk, and J. L. Hoard, J. Am. Chem. Soc. 65, 1924 (1943). We are indebted to Dr. Hurd and to Dr. L. V. McCarty for samples of pure B_2H_6.

have been introduced for semiconductors. Alternatively, the function $N(\nu, E)/E$ describes, in a simple but less specialized way, the influence of the energy structures in these materials. The latter approach is valuable for empirical purposes, whether or not it has the significance assigned to it in this paper. It should be useful also in the case of metalloids and complex metals.

Our failure to find definite stopping potentials corresponding to upper edges of occupied bands in the semiconductors can be appraised more reliably after refined experiments are done. In comparing the results with x-ray data, however, one notices that there is no clear-cut edge on the occupied band for evaporated B as determined by Skinner.[22] Si shows a similar effect; we have found no information for Te or Ge. If the high energy electrons observed in our tubes arise entirely in surface states, the elementary interpretations in this report indicate that the levels are not uniformly distributed in energy. It would be desirable to examine this point more closely in the light of Herring's recent work.[27]

For Te, at least, the photo-current approaches zero as rapidly as that from a metal at 300°K. There is an effect like that discussed by Condon,[3] and its magnitude agrees roughly with that expected from conductivity data. In agreement with Millikan's early observations on CuO,[5] there are large discrepancies between work functions and "photoelectric thresholds" for semiconductors.

Our emitters were all P-type materials. Similar experiments on reproducible N-type samples would be more interesting. In such cases, the currents presented here as upper limits to emission from surface states could be differentiated more clearly from photoelectrons arising in the occupied band. Conversion of N-type materials to P type should produce easily measurable effects even more pronounced than those associated here with the heating of evaporated Ge. Interpretation of results would be aided greatly by theoretical investigations comparable with those available for metals.

Prilezaev[23] has made extensive photoelectric measurements on Sb-Cs alloys. The yields from these interesting emitters are several hundred times larger than those for the elements described here.[41] The distributions, however, and the function $N(\nu, E)/E$ (determined roughly from data in Prilezaev's Fig. 12) are similar in form to those for Te. If interpreted in the same way, they indicate that the emitters were semiconductors with a small value of δ. There was no sharp stopping potential and measurable currents originated even at the Fermi level.

For helpful discussions and criticism, we wish to thank Professor V. F. Weisskopf, Dr. Harvey Brooks, and Dr. A. W. Hull, as well as those already mentioned.

[41] More complete spectral data and optical properties have been given by J. A. Burton, Phys. Rev. **72**, 531(A) (1947). We are indebted to Dr. Burton for calling Prilezaev's work to our attention.

A Theory of the Production of Electrode Vapor Jets by Sparks and Arcs

WOLFGANG FINKELNBURG
Engineer Research and Development Laboratories, Fort Belvoir, Virginia

(Received July 14, 1948)

A thermal theory of the production of electrode vapor jets by arcs and sparks is presented which accounts satisfactorily for all known experimental results on vapor jets. The computed vapor jet velocities are in excellent agreement with those measured for mercury sparks by Haynes and for the high current carbon arc by the author and his co-workers. Theoretical predictions concerning the dependence of vapor jet production on the electrode materials provide a possibility for further checks of the theory.

THE ejection of electrode vapor, frequently in the form of vapor jets, is a phenomenon well known for many arc and spark discharges. Detailed studies of such vapor jets have been made by the author and his collaborators[1] (cf., also, Rohloff[2]) for the anode vapor jet of the high current carbon arc, and recently by J. R. Haynes[3] for certain mercury sparks. It is the purpose of this paper to show that the mercury vapor jets, discussed by Haynes, which are emitted from the positively and negatively charged mercury surfaces by his spark discharge, can be explained satisfactorily by a thermal theory developed earlier by the author for the explanation of jet phenomena in the high current carbon arc. The basic concepts of this theory are as follows:

Vapor jets are ejected from the electrodes of any discharge if sufficient energy for vapor production is transferred to the surface of either electrode by the incident electrons or positive ions accelerated by the anode or cathode fall, respectively. As a consequence of the continuous production of new vapor, the vapor produced in the time element just before is pushed away perpendicularly from the electrode surface by the vapor being formed, as if ejected from a nozzle in the electrode surface. The jet velocity then is uniquely determined by the vapor production per unit surface and the temperature-dependent vapor density.

We begin by computing the energy released per unit surface of an electrode. Now a liquid mercury electrode, because of its limited temperature, cannot emit an appreciable quantity of electrons or ions, so that the current immediately in front of it must consist exclusively of the charge carriers arriving at it, i.e., electrons at the anode, positive ions at the anode. We designate by j_a and j_c the current density at the anode and cathode, respectively, by ϕ the work function of the material for electron emission, and by V_a and V_c the respective anode and cathode fall by which the charge carriers are accelerated. An electron incident on the anode surface then releases here

$$W_a = j(V_a + \phi) \text{ watts/cm}^2. \quad (1)$$

At the cathode, also assumed not to emit electrons, a positive ion, incident with the kinetic energy eV_c, can spend the energy $e\phi$ in removing an electron from the metal and then returning neutralized into the vapor, thus releasing at the cathode the energy $e(V_c - \phi)$. It can, on the other hand, become bound to the metal and thus release its entire kinetic energy eV_c plus its binding energy. We shall not make a very large error in assuming that on the average the energy loss $e\phi$ of each neutralized ion will be compensated by the binding energy of other ions which become bound to the cathode, so that the energy released at the cathode will be

$$W_c = jV_c \text{ watts/cm}^2. \quad (2)$$

We designate furthermore by Q the energy necessary to evaporize one gram of electrode

[1] W. Finkelnburg, Zeits. f. Physik 114, 714 (1939); 116, 214 (1940); H. Schluge and W. Finkelnburg, *ibid.* 122, 714 (1944); W. Finkelnburg and G. Heinzmann, *ibid.* 1948 (in press). Monograph: W. Finkelnburg, *Der Hochstromkohlebogen* (Verlag Julius Springer, Berlin, 1948); *The High Current Carbon Arc*, FIAT Final Report 1052, 1947 (PB-81644, Office of Technical Services, Department of Commerce, Washington, D. C.).

[2] E. Rohloff, Reichsberichte f. Physik 1, 47 (1944).

[3] J. R. Haynes, Phys. Rev. 73, 891 (1948).

material and heat it to the jet temperature (watt sec./g), and by δ the vapor density in grams per cm³. W/Q is then the quantity of vapor produced per second and per cm² at the electrode surface, and

$$u=(W/Q\delta)\ \text{cm/sec.} \qquad (3)$$

is the initial velocity of the electrode vapor jet ejected perpendicularly from the electrode surface as a result of the vaporization.

We now show that the values of the vapor jet velocity following from our theory are in agreement with the experiment for the mercury sparks of Haynes' as well as for our high current carbon arc, and that the theory furthermore accounts for the fact that, contrary to the mercury spark, a negative vapor jet is not observed in the high current carbon arc at currents below 400 amperes.

Data for the discharges under consideration and their electrode materials are presented in Table I.

The current density at the electrodes of the mercury spark was computed from dimensions taken from the published photographs and the current intensity; for the carbon arc it was known from our earlier work.[1] The same applies for the anode and cathode fall of the arc (the last one being not too accurate), while for the spark only the sum of both figures has been published to be 40 ± 5 volts, the distribution having been made by the author as plausible and in agreement with our general knowledge on mercury arcs. The vapor jet temperature near the electrodes has been measured by the author for the carbon arc, while it could be only estimated for the mercury arc; it is not too important, however, for the final result. The vapor density can be easily computed for the carbon arc (taking into account that according to spectroscopic evidence a large fraction of the vapor consists of diatomic molecules and some percent of the particles are rare earth atoms), while for the spark the accuracy of our knowledge of the vapor density is limited by the uncertainty of the extent to which the pressure in the vapor jet is equal to the gas pressure in the spark chamber (900 mm Hg). The vapor production energy, necessary for the production of one gram of vapor at jet temperature from the solid (or liquid) state, is well known from several independent measurements for the carbon arc and agrees satisfactorily with the theoretical estimates (vaporization energy 4.6×10^4 watt-sec./gram, heating energy 20 to $30RT$ per mole $=1.0$ to 1.7×10^5 watt-sec./gram).[1] For mercury the vaporization energy of only 300 watt-sec./gram is negligible, while the heating energy to 10,000°K, according to Rompe and Steenbeck,[4] is $40RT$/mole $=1.6\times10^4$ watt-sec./gram. For carbon arc electrode material, Q is thus about one order of magnitude larger than for mercury.

TABLE I. Data on the discharges and electrode materials.

			Mercury spark	Carbon arc
Anodic current density	j_a	amp./cm²	20,000	300
Cathodic current density	j_c	amp./cm²	100,000	5,000
Anode drop	V_a	volts	30	30
Cathode drop	V_c	volts	10	10
Work function	ϕ	electron volts	4.5	4.5
Vapor temperature	T	°K	10,000	7,000
Vapor density	δ	g/cm³	3×10^{-4}	5×10^{-3}
Specific vapor Production energy	Q	watt sec./g	1.6×10^4	1.3×10^5

The second essential difference between carbon and mercury electrodes (we consider the difference between arc and spark, in agreement with Haynes, as rather unimportant) follows from the energy balance at the electrodes. From Eq. (1) and the data of Table I we get for the energy released per second per unit anode surface:

$$W_a(\text{Hg spark})=7\times10^5\ \text{watt/cm}^2,$$
$$W_a(\text{carbon arc})=1\times10^4\ \text{watts/cm}^2.$$

The surface energy density at the anode thus is 70 times larger for the spark than for the high current carbon arc. At the cathode the difference is still more pronounced. As the mercury cathode cannot emit an appreciable quantity of electrons, the current at the cathode consists wholly of positive ions which here release, according to (2) and Table I, the energy

$$W_c=1\times10^6\ \text{watt-sec./cm}^2.$$

The carbon cathode, on the other hand, with its temperature of approximately 4000°K emits thermally an appreciable electron current, each electron carrying away from the cathode the energy $e\phi$. According to v. Engel and Steenbeck,[5] in this case the ion and electron currents in

[4] R. Rompe and M. Steenbeck, Ergeb. d. exakt. Naturwiss. **18**, 335 (1939).

[5] A. v. Engel and M. Steenbeck, *Elektrische Gasentladungen* (Verlag Julius Springer, Berlin, 1934).

front of a thermally emitting cathode adjust themselves so that the energy released at the cathode by the arriving positive ions is equal to that required for the release of the electrons:

$$j_c^-\phi = j_c^+(V_c-\phi), \tag{4}$$

if we designate by j_c^- and j_c^+ the electron and ion current densities at the cathode, respectively. In contrast to the mercury cathode, there is no energy available for vapor production at the carbon cathode. In agreement with the few reported experimental results, a vaporization of the carbon cathode can occur only if its current density is so large that the thermal electron emission can account for only a small fraction of the cathodic current, i.e., for

$$W_c = j_c^+(V_c-\phi) - j_c^-\phi \gg 0. \tag{5}$$

This discussion has thus revealed why the high current carbon arc usually does not show a negative vapor jet, while Haynes with his mercury sparks finds two seemingly identical positive and negative vapor jets. The quantitative check of the initial vapor jet velocities u from formula (3) and the figures of Table I leads to the results which are listed and compared with the experimental values in Table II.

In the calculation neither the radiation of electrodes and vapors nor the heat conduction in the electrodes have been taken into account. The last contribution can be proved to be negligible, while the energy loss of the electrodes resulting from radiation is approximately compensated by an energy gain due to absorption of energy from the luminous vapor.[6] The accuracy of our results thus is limited mainly by that of the figures of Table I.

Considering these uncertainties, the agreement of our theoretical and experimental vapor jet velocities, according to Table II, is even better than we should expect. Our theory thus not only explains why the positive vapor jet velocities of mercury spark and high current carbon arc differ by two orders of magnitude and why a negative vapor jet usually is not ejected by the high current carbon arc, but accounts also, with a surprising accuracy, for the absolute values of vapor jet velocities. We take this agreement as evidence for the correctness of our basic theoretical ideas on the mechanism of vapor jet production.

[6] Cf. W. Finkelnburg, *Der Hochstromkohlebogen* (Verlag Julius Springer, 1948). p. 172 and 173.

TABLE II. Theoretical and experimental vapor jet velocities for mercury spark and high current carbon arc.

	Hg spark	Carbon arc
Computed velocity of positive jet (cm/sec.)	1.5×10^5	1.4×10^5
Observed velocity of positive jet (cm/sec.)	1.55×10^5	$1.5-4 \times 10^5$
Computed velocity of negative jet (cm/sec.)	2.1×10^5	0
Observed velocity of negative jet (cm/sec.)	1.9×10^5	0

Quite generally, we conclude from our theory that positive vapor jets ought to be observed in all discharges having a sufficient anodic current density. The initial jet velocity ought to be the larger, the higher the current density and anode drop, and the smaller the vapor production energy of the electrode material in question is. Negative vapor jets, on the other hand, according to our theory, should be ejected at the same current density only from cathodes of comparatively low temperature which cannot emit an appreciable amount of electrons, or at so high a current density that the thermal electron emission accounts for only a small fraction of the cathodic current. There is a relation, however, between current density and electrode material. High current density is not possible for a pure electron or ion current because of its high space charge; it requires a compensation of the space charge by charge carriers of the opposite sign. These can be formed, even in the last mean free paths in front of an electrode, by ionization of an evaporating metal, while there are not enough ionizable atoms (and of much higher ionization potential) near an electrode of sufficiently low vapor pressure. Any evaporation of an electrode thus, resulting from increased ionization, tends to increase the current density by contraction of the discharge and thus increases in turn the vapor production. Vapor jet production, requiring high current densities, therefore is much more probable when easily evaporated electrodes are used instead of metals like molybdenum or tungsten. Investigations with different electrode materials and current densities would permit a check of these predictions and thus of the correctness of our theory of vapor jet production which seems to describe satisfactorily the experimental results known at the present time.

Magnetic Resonance Absorption in the Chrome Alums

C. A. WHITMER, R. T. WEIDNER, J. S. HSIANG, AND P. R. WEISS
Department of Physics, Rutgers University, New Brunswick, New Jersey
(Received August 2, 1948)

Measurements of paramagnetic resonance absorption at room temperature in single crystals of potassium chrome alum and ammonium chrome alum made at a frequency of 9375 mc/sec. are described. The method makes use of a magic-T bridge with a low level crystal detector which essentially measures the magnetic susceptibility. Data are given for three orientations of the crystals for both the diluted and undiluted salts. The Stark splitting and the g factor of the ground state are evaluated from the positions of the absorption peaks. The theory which is used for the computation of the Stark splitting is extended to include the (110) orientation.

I. INTRODUCTION

THE magnetic resonance absorption of microwaves by paramagnetic salts first reported by Zavoisky[1] provides a direct and powerful method for investigating the lowest quantum states of the paramagnetic ion of the salt. The method as usually applied[2–4] consists in subjecting the salt to a fixed frequency microwave magnetic field and a d.c. magnetic field perpendicular to the r-f field. When the intensity of the d.c. field is adjusted to the resonant value an absorption of r-f power occurs, corresponding to induced transitions between the lowest energy states of the paramagnetic ion. The magnetic absorption as a function of the d.c. field shows one or more absorption peaks having line widths of the order of several hundred oersteds.

The condition for resonant absorption is given by the well-known relation,

$$h\nu = g\beta H, \tag{1}$$

where ν is the frequency of the r-f field, g is the gyromagnetic ratio, β is the Bohr magneton, and H is the intensity of the d.c. field. For a free electron spin ($g=2$) and a frequency of 9375 mc/sec. the resonant value of the d.c. field is 3340 oersteds.

In the hydrated salts of the iron group, measurements at low temperatures of the paramagnetic susceptibility and the specific heat indicate that the orbital angular momentum of the paramagnetic ion is quenched by the cubic electric fields of the neighboring atoms and molecules. There is, in addition, a fine splitting of the ground state of the order of 0.1 cm^{-1}. In magnetic resonance absorption experiments, the d.c. field produces a Zeeman splitting of these levels. Consequently, different pairs of levels are brought into the resonance condition by different values of the applied field. From these values of the d.c. field it is possible to deduce the magnitude of the zero-field splitting.

In the case of chrome alum the zero-field fine splitting can be explained by the presence of a small cylindrically symmetric electric field. In the unit cell there are four paramagnetic ions, and the axes of the cylindrical fields are arranged along the body diagonals of the cube. The level separations depend on the orientation of the axes of the cylindrical electric field with respect to the d.c. magnetic field. The energy level separations have been computed by one of us[5] as a function of d.c. field strength and zero-field splitting. There, computations were made for two orientations of the d.c. field, namely, perpendicular (a) to a (111) face, and (b) to a (100) face. The alums belong to the cubic system so that in orientation (a) the d.c. field is parallel to one of the body diagonals of the unit cell. In the present paper computations are included in Section V for the case in which the d.c. field is perpendicular to the (110) face. Similar computations have been made independently by Kittel and Luttinger[6] for chrome alum for the (100) orientation.

For a given value of δ, the zero-field splitting,

[1] E. Zavoisky, J. Phys. U.S.S.R. **10**, 170, 197 (1946).
[2] R. L. Cummerow, D. Halliday, and G. E. Moore, Phys. Rev. **72**, 1233 (1947).
[3] D. M. S. Bagguley and J. H. E. Griffiths, Nature **160**, 532 (1947).
[4] P. R. Weiss, C. A. Whitmer, H. C. Torrey, and Jen-Sen Hsiang, Phys. Rev. **72**, 975 (1947).
[5] P. R. Weiss, Phys. Rev. **73**, 470 (1948).
[6] C. Kittel and J. M. Luttinger, Phys. Rev. **73**, 162 (1948).

the theory predicts a set of values of the d.c. field at which resonance peaks may be expected. Conversely, if the peak fields are known, a value of δ can be chosen which gives best agreement between computed and experimentally determined positions of the peaks for each of the three crystal orientations.

We have previously reported in Letters to the Editor of this journal[4,7] preliminary results of our measurements at room temperature of the resonance absorption in single crystals of ammonium chrome alum and potassium chrome alum, and in diluted crystals of these salts in which some of the chromium ions are replaced by aluminum ions. It is the purpose of this paper to give a more complete and detailed account of the experimental methods and results.

Independent experiments similar to ours on undiluted chrome alum have been reported by Bagguley and Griffiths[3] and by Halliday and Wheatley.[8] A comparison of results is given in Section VI of this paper.

Accurate determinations of the zero-field splitting are necessary to establish a theoretical relationship between the absolute temperature scale and the Curie scale used at very low temperatures. Measurements of the resonance absorption of microwaves therefore afford a very convenient tool for the accurate determination of this quantity. Recent experiments by Bleaney and Penrose,[9] who determined the zero-field splitting in ammonium chrome alum as a function of temperature down to 20°K, show that the splitting decreases down to about 80°K, at which temperature an abrupt increase occurs. It is necessary therefore to make these measurements at very low temperatures for the purpose mentioned.

II. EXPERIMENTAL METHOD

The resonance absorption was obtained by observing the decrease in the Q of a resonant cavity containing the salt, through the measurement of the reflected power in a magic-T bridge.

The equivalent admittance of a resonant cavity is given by

$$Y=G+j\omega C+1/j\omega L. \tag{2}$$

The magnetic absorption from a paramagnetic salt in the cavity may be regarded as a change in the complex permeability, $1+4\pi(\chi'-j\chi'')$, of the salt, where $\chi'-j\chi''$ is the complex susceptibility of the salt. The total inductance, L, of the cavity and salt is given by

$$L=L_c+L_s(1+4\pi\chi'-4\pi j\chi''), \tag{3}$$

where L_c is the contribution of the inductance of the cavity alone and $L_s(1+4\pi\chi'-4\pi j\chi'')$ is the contribution of the salt.

With zero magnetic absorption

$$L=L_0=L_c+L_s. \tag{4}$$

This condition is realized experimentally by tuning the cavity to resonance for a value of the d.c. magnetic field large compared to that for which resonance absorption occurs.

The reflection coefficient, γ, for a cavity terminating a transmission line of characteristic conductance G_0 is given by

$$\gamma=|(Y-G_0)/(Y+G_0)|. \tag{5}$$

Equations (2), (3), and (5) combine to give

$$\gamma=\left|\frac{G-G_0+j\omega C+\{j\omega[L_c+L_s(1+4\pi\chi'-4\pi j\chi'')]\}^{-1}}{G+G_0+j\omega C+\{j\omega[L_c+L_s(1+4\pi\chi'-4\pi j\chi'')]\}^{-1}}\right|. \tag{6}$$

Since the cavity is matched to the transmission line and tuned to resonance for zero magnetic absorption,

$$G=G_0 \quad \text{and} \quad j\omega C+1/j\omega L=0.$$

Since χ' and χ'' are small compared to unity, Eq. (6) reduces to

$$\gamma=\left|\frac{-(4\pi/j\omega L_0)(L_s/L_0)(\chi'-j\chi'')}{2G_0-(4\pi/j\omega L_0)(L_s/L_0)(\chi'-j\chi'')}\right|. \tag{7}$$

The small term in the denominator can be neglected and

$$\gamma^2=4\pi^2Q_0^2(L_s/L_0)^2(\chi'^2+\chi''^2), \tag{8}$$

[7] C. A. Whitmer, R. T. Weidner, and P. R. Weiss, Phys. Rev. **73**, 1468 (1948).
[8] D. Halliday and J. Wheatley, Bull. Am. Phys. Soc. **23**, No. 3, 13 (1948).
[9] B. Bleaney and R. P. Penrose, Proc. Phys. Soc. **60** 395 (1948).

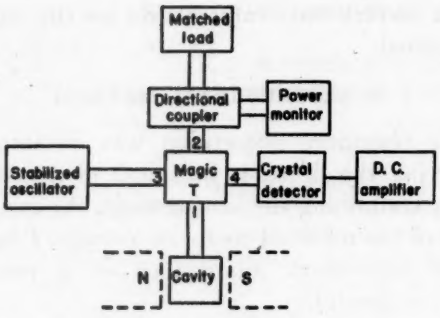

FIG. 1. Block diagram of the apparatus.

where

$$Q_0 = 1/\omega L_0 G_0.$$

Thus Eq. (8) shows that the measured power is proportional to $\chi'^2+\chi''^2$, the absolute value squared of the complex susceptibility of the salt. If a single resonance alone is involved and if the absorption follows a dispersion law (which is highly unlikely in these measurements), it follows that $\chi'^2+\chi''^2$ is proportional to the imaginary part of the susceptibility. That is,

$$\chi'^2+\chi''^2 = \nu_0\chi_0\chi''/\Delta\nu,$$

where ν_0 is the resonance frequency, $\Delta\nu$ the width of the absorption peak, and χ_0 the d.c. susceptibility.

If overlapping absorption lines occur, an interference between the lines is present in the method used here. This affects the shape of the curve in a manner different from that which occurs in a method which measures χ'' alone for multiple resonances. Consequently, the locations of the absorption peaks are somewhat different in the two cases. In the present method the reflected waves tend to cancel in the region between the peaks and therefore tend to increase the observed peak separation. In a method which measures χ'' alone, the addition of the absorption from adjacent peaks tends to decrease the observed peak separation. The correction for these effects requires a knowledge of the shape of an absorption line. In the absence of these corrections it seems probable that the true peak separations lie between those determined by the two methods. It should be pointed out that the present method is advantageous in resolving lines which are close together, but it suffers from the fact that the quantity measured is not strictly the power absorbed.

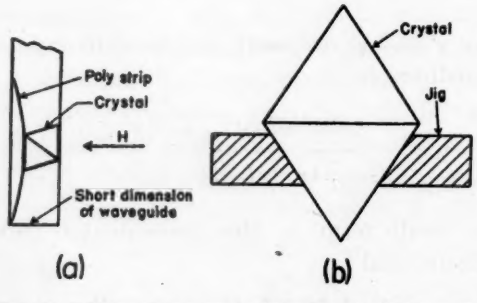

FIG. 2. (a) Crystal mount, (b) crystal grinding jig.

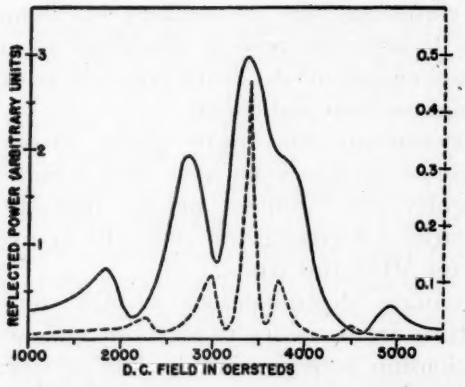

FIG. 3. Reflected power as a function of d.c. field for ammonium chrome alum with the d.c. field perpendicular to a (111) face. The full line curve refers to the undiluted, the dashed curve to the diluted salt. The scales for the undilute (left) and the dilute (right) salts refer to the same input power.

The power reflected from the cavity is measured by the apparatus shown in the block diagram of Fig. 1. Microwave power from the frequency-stabilized oscillator divides at the magic-T into arms 1 and 2, which are terminated, respectively, by the cavity and a matched load. The power is monitored by a crystal detector which is connected through a directional coupler to arm 2. The power incident upon the cavity was about one milliwatt. The cavity which contains the paramagnetic crystal is a shorted waveguide section which is tuned to resonance and matched by the use of a sliding micrometer tuning screw. The loaded Q of the empty cavity was 1700. A dielectric absorption Q of 500 was found for both undilute and dilute crystals. A paramagnetic absorption Q of 1400 was found for the undilute crystals; the corresponding value of χ'' is of the order of 0.3×10^{-25} cm^3/ion.

When the cavity is tuned to the matched condition no power reaches the low level square-law crystal detector terminating arm 4. When the magnetic field is adjusted for resonance absorption the detector current is accurately proportional to the power reflected from the cavity and hence proportional to γ^2.

The d.c. magnetic field was calibrated by means of a ballistic galvanometer and search coil with an accuracy of 0.2 percent. The calibration was checked against the proton magnetic resonance absorption using the accepted value of the proton moment.

III. PREPARATION OF THE SPECIMENS

The single crystals used in this investigation were grown from the saturated solution by evaporation at room temperature. Since the alums have a face-centered cubic lattice, the interatomic distance is least in the (111) plane and the crystals grow along the (111) face in the form of octahedra. The samples were grown to a

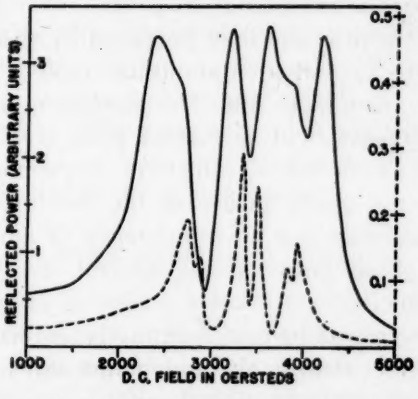

FIG. 4. Reflected power as a function of d.c. field for ammonium chrome alum with the d.c. field perpendicular to a (110) face. The remarks in the title of Fig. 3 apply here.

thickness of about 1 cm between opposite (111) faces, corresponding to a mass of about 2 grams.

The diluted crystals were grown from a solution made up of 5 parts by weight of aluminum alum to one part chrome alum. A quantitative analysis showed the ratio of aluminum to chrome atoms to be 8.5 to 1.

The samples were mounted on curved strips of polystyrene which fitted into the wave-guide as shown in Fig. 2a. A crystal is mounted so that its center is about one-half wave-guide wavelength from the shorted end.

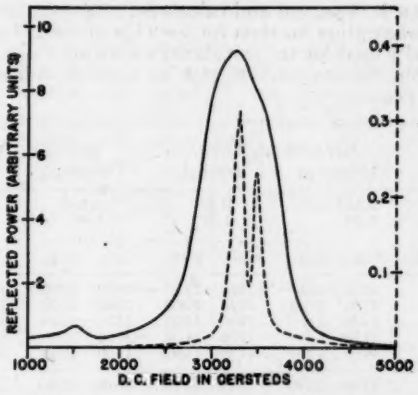

FIG. 5. Reflected power as a function of d.c. field for ammonium chrome alum with the d.c. field perpendicular to a (100) face. The remarks in the title of Fig. 3 apply here.

Three orientations of the crystal with respect to the d.c. field were used, namely, with the d.c. field perpendicular (a) to the (111) face, (b) to the (110) face, and (c) to the (100) face. For orientations (b) and (c) surfaces were ground along the appropriate crystal faces by mounting the crystal in a jig and grinding the surfaces with dry emery paper. The jig consists of a V-shaped slot in a metal plate which holds the crystal as shown in Fig. 2b. The part of the crystal projecting through the slot is ground off flush with the surface of the plate. The angle between the faces of the slot is 70° 32′ for the (100) orientation and 109° 28′ for the (110) orientation.

The curved strip of polystyrene (Fig. 2a) presses the appropriate face of the crystal against the broad face of the wave-guide, perpendicular to the d.c. magnetic field, thereby fulfilling the condition of perpendicularity of the

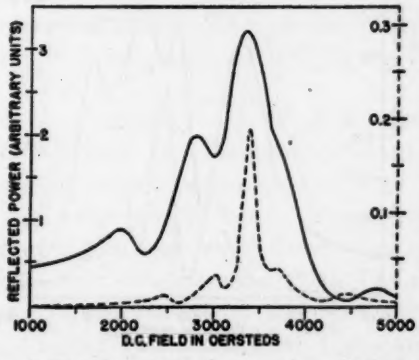

FIG. 6. Reflected power as a function of d.c. field for potassium chrome alum with the d.c. field perpendicular to a (111) face. The remarks in the title of Fig. 3 apply here.

TABLE I. Observed and calculated magnetic field values of the absorption maxima for $\nu = 9375$ mc/sec. The values of δ and g used for the calculated values are those listed in the table. Spaces marked with an asterisk indicate unresolved peaks.

	$NH_4Cr(SO_4)_2 \cdot 12H_2O$				$KCr(SO_4)_2 \cdot 12H_2O$			
	Undiluted		Diluted		Undiluted		Diluted	
δ	0.143 cm^{-1}		0.100		0.130		0.91	
g	1.99		1.97		1.99		1.98	
H (oersteds)	Calc.	Exp.	Calc.	Exp.	Calc.	Exp.	Calc.	Exp.
(111)	1830	1830	2310	2270	1990	1990	2390	2450
	2780	2720	2970	2980	2840	2800	3020	3020
	3370	3370	3400	3400	3370	3340	3390	3380
	3770	*	3720	3710	3750	*	3670	3670
	4910	4920	4490	4480	4760	4760	4380	4450
(110)	2390	2380	2740	2740	2500	2530	2790	2850
	2630	*	2860	2880	2730	*	2890	
	3240	3220	3330	3330	3280	3240	3330	3340
	3580	3600	3500	3500	3550	3600	3480	3460
	3910	*	3830	3820	3850	*	3790	3850
	4130	4190	3910	3920	4070	4130	3880	
(100)	3120		3280	3300	3170		3280	3300
		3250				3260		
	3540		3480	3480	3520		3450	*

r-f and d.c. magnetic fields. The error in the orientation of the crystals is estimated to be no more than one degree.

IV. RESULTS

Figures 3–5 show the absorption at a frequency of 9375 mc/sec. of undiluted and dilute single crystals of ammonium chrome alum ($NH_4Cr(SO_4)_2 \cdot 12H_2O$) for the three orientations, and Figs. 6, 7, and 8 are corresponding absorption curves for undiluted and diluted single crystals of potassium chrome alum ($KCr(SO_4)_2 \cdot 12H_2O$). All experimental points fell accurately on the curves shown, and all curves were checked by measurements on at least two crystals. The positions of the sharp peaks could be determined to within ± 10 oersteds. The scale of the reflected power has been adjusted for the same input power in all the curves.

It is seen that the dilution improves the resolution of the peaks by decreasing the widths of the lines; also it is to be noted that the resolution is more pronounced for both the undilute and dilute crystals of the ammonium salt than for those of the potassium salt. Furthermore the dilution decreases the crystalline field splitting for both salts, as shown in Table I.

Table I shows the magnetic field strengths for the peaks, taken from the absorption curves, and as calculated from the theory using the g-values and zero-field splittings, δ, shown there. The g-values are calculated from the principle absorption peak in the (111) orientation, as described by one of us in an earlier paper.[5] It is clear that there is some uncertainty in the g-value because of the effect on the position of this peak of the interference from adjacent peaks.

All the principal lines predicted by theory for the three crystal orientations are resolved for the dilute ammonium salt. The agreement between the observed and calculated peak positions is better for the diluted salts than for the undiluted salts; the discrepancies for the undiluted salts are probably due to interference in amplitude and phase between the several overlapping resonances.

The crystalline field splitting is smaller in the potassium than in the ammonium salt for both the undiluted and diluted salts.

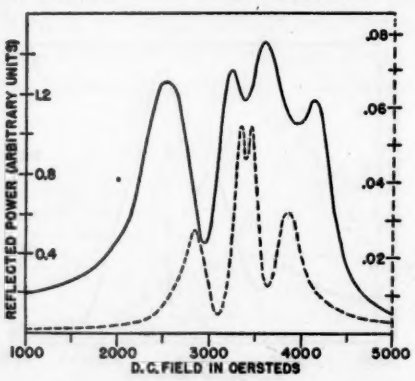

FIG. 7. Reflected power as a function of d.c. field for potassium chrome alum with the d.c. field perpendicular to a (110) face. The remarks in the title of Fig. 3 apply here.

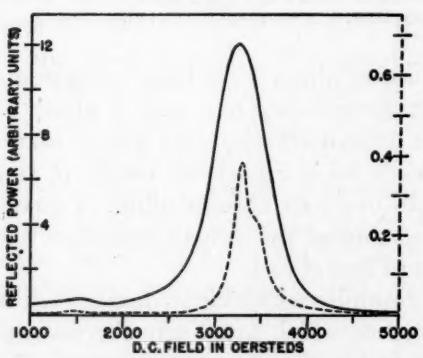

FIG. 8. Reflected power as a function of d.c. field for potassium chrome alum with the d.c. field perpendicular to a (100) face. The remarks in the title of Fig. 3 apply here.

Since the absorbed power was found to be proportional to the incident power, no saturation effects occur at the power level used. The dielectric losses were found to be closely the same for all diluted and undiluted crystals used, whose volumes differed by no more than a factor of 1.5. Nevertheless, the measurements show a marked diminution in the peak absorption with dilution.

A simple computation based on the supposition that the width of the line is due to spin-spin interaction shows that the peak intensity is independent of the density of the absorbing spins. Actually this involves the tacit assumption* that the change in density is brought about by a change in lattice size but no change in the regularity of the positions of the spins. When, however, the change in density is achieved by the substitution of non-absorbing atoms in the lattice, the absorbing spins may occupy random positions in the lattice. In case the positions are completely random, the width of the line is affected by space fluctuations in the positions of the absorbing spins. In this case the width of the line is proportional to the square root of the density of the absorbing spins rather than to the density. In this event the peak absorption is proportional to the square root of the density. Further experiments are in progress to study the effect of dilution on peak absorption.

V. SOME ADDITIONAL THEORY

Detailed computations of the magnitudes of the d.c. field at which resonance absorption occurs in chrome alums have been recorded for the (111) and (100) orientations of the d.c. field. In this section the corresponding results are presented when the d.c. field is perpendicular to a (110) plane. In this orientation, the axes of the cylindrical electric fields at two of the four chrome ions of the unit cell are perpendicular to the magnetic field; the axes of the electric fields at the other two chrome ions make an angle of 35° 16′ ($\sin^{-1}1/\sqrt{3}$) with the magnetic field. The Hamiltonian of the ion in the case of perpendicularity can be solved in closed form. The levels are:

$$E=\pm\tfrac{1}{2}\xi+(\xi^2\mp\xi+1)^{\frac{1}{2}}$$

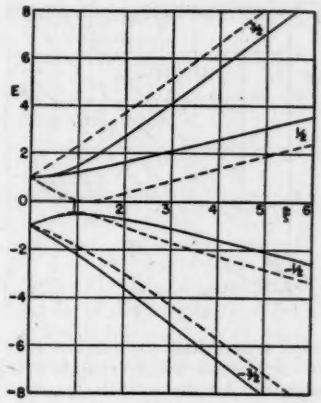

FIG. 9. Energy levels (in units of $\delta/2$) as a function of $\xi=2g\beta H/\delta$ for chrome alum crystals oriented with the d.c. field perpendicular to a (110) plane. The full line curves belong to atoms for which the axis of the cylindrical electric field makes a polar angle of $\theta=90°$ with the magnetic field; the dashed curves belong to atoms for which $\theta=35°\ 16'$.

and

$$E=\pm\tfrac{1}{2}\xi-(\xi^2\mp\xi+1)^{\frac{1}{2}}.$$

The notation is the same as in reference 5, namely, δ is the energy separation of the levels in the absence of a d.c. field; g, the effective g-value of the spin; β, the Bohr magneton; H, the magnitude of the d.c. field; $\xi=2g\beta H/\delta$ and $E=2W/\delta$. A plot of these energy levels in units of $\delta/2$ as a function of the magnetic energy in the same units is shown by the full line curves in Fig. 9. In the case where the angle between the d.c. field and the axis of the electric field is $\theta=35°\ 16'$, the secular equation expressing the energy levels is the quartic

$$E^4-E^2(2+(5/2)\xi^2)-2\xi^2E+(1-\tfrac{3}{4}\xi^2)^2=0.$$

For each value of ξ this can be solved by successive approximation. The results, the energy levels as functions of ξ, are shown by the dashed curves in Fig. 9.

When the frequency of the r-f field is large compared to δ/h (h=Planck's constant), the resonance absorption occurs only at large values of the d.c. field; that is, large values of ξ. For this region, the only allowed transitions are those of a "free" spin in a magnetic field. The energy levels can be designated by the usual m-values and the selection rule is $\Delta m=\pm1$. Consequently, six absorption peaks appear in this region as shown in Fig. 10, where the energy differences

* This was pointed out to us in a private communication from Dr. E. M. Purcell.

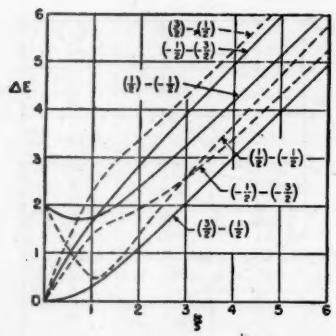

FIG. 10. Level separations (in units of $\delta/2$) as a function of $\xi=2g\beta H/\delta$ for chrome alum crystals oriented with the d.c. field perpendicular to a (110) plane. The full line curves belong to atoms for which the axis of the cylindrical electric field makes a polar angle $\theta=90°$ with the magnetic field; the dashed curves belong to atoms for which $\theta=35°\,16'$.

between levels involved in the absorption are plotted as a function of ξ. The width in field strength of the entire pattern is less in the (110) orientation than in the (111) orientation. For very large frequencies of the r-f field this width is roughly δ as measured in oersteds for the (110) orientation compared to 2δ for the (111) orientation. The resolution of the lines in the (111) orientation is better than in the (110) orientation. The lines occur in closely neighboring pairs. The width of the lines causes overlapping of these lines and therefore obscures the fundamental pattern more so in this than in the (111) orientation. When the frequency of the r-f field is not large compared to δ/h, the selection rules stated above do not apply and the intensities of other transitions become significant. The pattern then can contain more than six absorption lines. For purposes of computation in the region of large field strengths it is convenient to use series expressions for the positions in field strength of the six lines. These are, to terms in ξ^{-3},

$$\theta=\sin^{-1}1/\sqrt{3}=35°\,16'$$

$$\begin{aligned}
(\tfrac{3}{2}\leftrightarrow\tfrac{1}{2}):&\quad \xi-1 && +\tfrac{3}{8}\xi^{-2}\\
(\tfrac{1}{2}\leftrightarrow\tfrac{1}{2}):&\quad \xi && +\tfrac{3}{4}\xi^{-1}\\
(-\tfrac{1}{2}\leftrightarrow\tfrac{3}{2}):&\quad \xi+1 && -\tfrac{3}{8}\xi^{-2}
\end{aligned}$$

$$\theta=90°$$

$$\begin{aligned}
(\tfrac{3}{2}\leftrightarrow\tfrac{1}{2}):&\quad \xi+1 && +(4/3)\xi^{-1} && -(11/8)\xi^{-2}\\
(\tfrac{1}{2}\leftrightarrow-\tfrac{1}{2}):&\quad \xi && -(5/8)\xi^{-1}\\
(-\tfrac{1}{2}\leftrightarrow-\tfrac{3}{2}):&\quad \xi-1 && +(4/3)\xi^{-1} && +(11/8)\xi^{-2}.
\end{aligned}$$

VI. CONCLUSION

Our values of the zero-field splitting for undiluted single crystals of ammonium chrome alum and potassium chrome alum are compared with the published results of others in Table II. All of the values listed in this table were computed from data taken at room temperature. The first, second, and third columns in the table list,

TABLE II. Published values of the zero-field splitting, δ, of the undiluted chrome alums.

Salt \ Reference	7	3	8
$NH_4Cr(SO_4)_2\cdot 12H_2O$	0.143 cm^{-1}	0.135 cm^{-1}	0.13 cm^{-1}
$KCr(SO_4)_2\cdot 12H_2O$	0.130	0.12	0.12

respectively, the values obtained by the authors, by Bagguley and Griffiths,[3,**] and by Halliday and Wheatley.[8] It can be seen that the results obtained by the authors are larger than the other reported values; this discrepancy is considerably larger than can be accounted for by the experimental error in fitting the computed peaks to the experimental values. The interference effects discussed earlier in this paper may account for the discrepancy in the values of the splitting computed from the absorption peaks. A comparison of our curves with those of Bagguley and Griffiths shows that our method yields a better resolution of the lines.

The results of experiments described here show excellent agreement with the theory and substantiate the following conclusions:

1. The Stark splitting of the ground state of the chrome ion can be explained by the presence of a cylindrical electric field.
2. The splitting is larger for ammonium than for potassium chrome alum.
3. The effect of dilution is to narrow the line widths and decrease the zero-field splitting for both ammonium and potassium chrome alum. The peak intensities are markedly diminished by dilution.

In conclusion we should like to acknowledge the support of the Rutgers University Research Fund, the Research Corporation, and the Office Naval Research. We are indebted to Dr. H. C. Torrey, who suggested the use of a magic-T bridge for this work.

** The value of 0.135 cm^{-1} for ammonium chrome alum is quoted by Bleaney and Penrose (reference 9) from unpublished results of Bagguley and Griffiths.

PHYSICAL REVIEW VOLUME 74, NUMBER 10 NOVEMBER 15, 1948

Phenomenological Quantum Electrodynamics. Part II. Interaction of the Field with Charges

J. M. JAUCH AND K. M. WATSON
Department of Physics, State University of Iowa, Iowa City, Iowa
and
Institute for Advanced Study, Princeton, New Jersey
(Received July 12, 1948)

The quantization of the phenomenological field is carried through with the presence of charged particles described by a Dirac Hamiltonian. The elimination of the longitudinal field presents some features which are qualitatively different from the vacuum case. In the first place the Coulomb energy has an angular dependent term. Further the elimination procedure introduces an additional term in the interaction Hamiltonian which is proportional to the medium velocity. The physical significance of this term is clarified in the discussion of the Čerenkov radiation which is carried through in the two coordinate systems: medium at rest, particle moving and particle at rest, medium moving. The result for the total radiation emitted is in agreement with the corresponding classical calculation.

A. CLASSICAL FIELD WITH CHARGES

IN the first part we have developed the classical and quantum theory of the pure radiation field in a refractive medium. In this part we shall study the interaction of charges with the field. In classical field theory the charges and current density together form a four-vector density which we may call j^μ. Here $j^0=\rho$ is the charge density and $j^k=s^k$ $(k=1, 2, 3)$ is the current density. Maxwell's field equations are now in rationalized units of the charge (such that $e^2=4\pi/137$)

$$\nabla\times\mathbf{E}=-\dot{\mathbf{B}}, \quad \nabla\times\mathbf{H}=\dot{\mathbf{D}}+\mathbf{s}, \tag{1}$$

$$\nabla\cdot\mathbf{B}=0, \quad \nabla\cdot\mathbf{D}=\rho, \tag{2}$$

$$\mathbf{D}=\epsilon\mathbf{E}, \quad \mathbf{B}=\mu\mathbf{H}. \tag{3}$$

Charges and currents are connected by the continuity equation

$$\dot{\rho}+\nabla\cdot\mathbf{j}=0. \tag{4}$$

Introducing the tensors $F^{\lambda\mu}$ and $G^{\lambda\mu}$ of Part I (Eqs. (4) and (5), Part I) we may write Eqs. (1), (2), and (3) in the form

$$\partial_\lambda F_{\mu\nu}+\partial_\mu F_{\nu\lambda}+\partial_\nu F_{\lambda\mu}=0, \tag{5}$$

$$\partial_\mu G^{\lambda\mu}=\mu j^\lambda, \tag{6}$$

$$G_{\lambda\mu}=F_{\lambda\mu}+\kappa(F_{\mu\sigma}v_\lambda-F_{\lambda\sigma}v_\mu)v^\sigma. \tag{7}$$

It is seen that in Eq. (6) the constant μ enters explicitly in contradistinction to the radiation field where ϵ and μ entered only in the combination $n^2=\epsilon\mu$. In order to have the radiation field only dependent on n^2 we have defined the tensor $G_{\lambda\mu}$ different from the usual way[1] by multiplying it with μ. For the radiation field the equations for $G_{\lambda\mu}$ are thereby not changed since they are homogeneous. However, when sources are present the μ shows up explicitly either in the definition of the $G_{\lambda\mu}$ or on the right-hand side of (6). We have maintained here the definition of the $G_{\lambda\mu}$ for the pure radiation field and correspondingly find the inhomogeneous field equations in the form (6) and therefore in the following all the expressions for the energy will occur multiplied with μ. The continuity equation for charge and current density is then

$$\partial_\lambda j^\lambda=0.$$

Equation (5) is the same as for the radiation field and permits the introduction of the vector potential ϕ_λ

$$F_{\lambda\mu}=\partial_\lambda\phi_\mu-\partial\phi_\lambda. \tag{9}$$

The field equations for the potentials are then from (6):

$$(-\partial^\mu\partial_\mu+\partial_\mu v^\mu\partial_\sigma v^\sigma)\Psi^\lambda=\mu j^\lambda. \tag{10}$$

Here we have used again the subsidiary condition

$$\chi\equiv\partial^\rho\phi_\rho-\kappa v^\sigma\partial_\sigma\phi^\rho v_\rho=0, \tag{11}$$

[1] See, for instance, W. Pauli, *Encyklopädie der math. Wiss.* (B. G. Teubner, Leipzig, 1921), V. 19, p. 655.

and for Ψ^λ we have, as in Part I,

$$\Psi^\lambda = \phi^\lambda - \kappa\phi^\sigma v_\sigma v^\lambda. \tag{12}$$

B. LAGRANGEAN FORM OF THE FIELD EQUATIONS

If we consider the current density vector j^μ as a given space-time function, then the classical field equations (9), (10) can be derived from the variational principle.

$$\delta\int L dx^0 = 0 \tag{13}$$

where

$$L = L^0 + L' = \int \mathfrak{L} d^3x. \tag{14}$$

L^0 is given by Eqs. (15), (16) of Part I. For L' we have

$$L' = \int \mathfrak{L}' d^3x, \tag{15}$$

$$\mathfrak{L}' = +\mu j_\nu \phi^\nu. \tag{16}$$

The Euler-Lagrange equations which follow from (13) are

$$\partial^\lambda(\partial/\partial\partial^\lambda\phi^\mu) - (\partial/\partial\phi^\mu) = 0$$

or

$$\partial^\lambda G_{\mu\lambda} - \partial^\lambda(g_{\lambda\mu} - \kappa v_\lambda v_\mu)\chi = \mu j_\mu. \tag{17}$$

These equations are identical with (10). If we impose the subsidiary condition (11), they become identical with (6). From (17) and the continuity equation (8) follows

$$(\partial^\lambda\partial_\lambda - \kappa\partial^\lambda v_\lambda \partial^\mu v_\mu)\chi = 0, \tag{18}$$

exactly as for the radiation field. Just as in the latter case one concludes from this that the subsidiary condition (11) is identically satisfied if it is valid together with its time derivative at a given value of the time $t=0$.

C. HAMILTONIAN FORMALISM

The canonically conjugate variables Π_μ are defined by

$$\Pi_\mu = \frac{\partial\mathfrak{L}}{\partial(\partial_0\phi^\mu)} = G_\mu{}^0 - (g_\mu{}^0 - \kappa v^0 v_\mu)\chi \tag{19}$$

and the Hamiltonian is then

$$H = \int \mathfrak{H} d^3x$$

with

$$\mathfrak{H} = \Pi_\mu\dot{\phi}^\mu - \mathfrak{L}. \tag{20}$$

We may decomposite it into the two

$$H = H^0 + H', \tag{21}$$

where H^0 is the expression given by Eq. (25), Part I, and

$$H' = -\mu\int d^3x\, j_\nu\phi^\nu. \tag{22}$$

The Eqs. (7), (9), and (17) are then equivalent with the Hamiltonian equations

$$\dot{\Pi}_\mu = -\delta H/\delta\phi^\mu, \quad \dot{\phi}^\mu = \delta H/\delta\Pi_\mu. \tag{23}$$

Since this Hamiltonian differs from the Hamiltonian H^0 of the radiation field only through the presence of the interaction term H' (22), we may find an explicit expression for it in exactly the same way as the expression (30) in Part I was derived. Thus for the Maxwell case (that is, subsidiary condition $\chi=0$ (11) satisfied) we may write

$$\mathfrak{H}^0 = \frac{1}{2}\frac{1}{1+\kappa v_0{}^2}\Big\{\mathbf{\Pi}\cdot\mathbf{\Pi} + 2\kappa v^0(\nabla\times\mathbf{W}\cdot\mathbf{\Pi}) + \frac{\kappa}{1+\kappa}(\mathbf{\Pi}\cdot\nabla)^2 + \kappa(\nabla\times(\nabla\times\mathbf{W})\cdot\mathbf{W})\Big\} + \tfrac{1}{2}\mathbf{W}\cdot\mathbf{W} + \mathbf{\Pi}\cdot\nabla\phi_0. \tag{24}$$

The last term may be transformed in the following way. We have

$$\mathbf{\Pi}\cdot\nabla\phi_0 = \nabla\cdot(\mathbf{\Pi}\phi_0) - (\nabla\cdot\mathbf{\Pi})\phi_0.$$

Here the first term is a space divergence and may be omitted from the density function since it contributes nothing to the integrated Hamiltonian. For the second term we get from (19) and (17)

$$\nabla\cdot\mathbf{\Pi} = -\mu j^0 + 2\kappa(\nabla\cdot\nabla)v^0\chi. \tag{25}$$

Since the last term is zero, if (11) holds we may replace the last term in (24) by $\mu j_0\varphi_0$. For the total Hamiltonian density we obtain thus

$$H = H_0 + H_1, \tag{26}$$

$$H_0=\frac{1}{2}\frac{1}{1+\kappa v_0^2}\int\Big\{\Pi\cdot\Pi+2\kappa v^0(\mathbf{v}\times\mathbf{W}\cdot\Pi)+\frac{\kappa}{1+\kappa}(\Pi\cdot\mathbf{v})^2+\kappa(\mathbf{v}\times(\mathbf{v}\times\mathbf{W})\cdot\mathbf{W}\Big\}d^3x+\tfrac{1}{2}\int\mathbf{W}\cdot\mathbf{W}d^3x, \quad (27)$$

$$H_1=-\mu\int d^3x\,\mathbf{j}\cdot\boldsymbol{\phi}. \quad (28)$$

D. QUANTIZATION

The quantization procedure for the field with charges can be carried through in exactly the same way as for the radiation field. For the charge and current we shall assume here that they are described by the charge and current operators of the Dirac theory for particles of spin $\frac{1}{2}$. Furthermore, we shall introduce the Hamiltonian for the particles alone. In order to simplify the procedure and also to avoid the well-known divergence difficulties of the hole theory, we describe the particle system in configuration space.

For the charge and current density operator we have in the Dirac theory

$$\begin{aligned}\rho(\mathbf{x})&=\textstyle\sum_n e_n\delta(\mathbf{x}-\mathbf{x}_n),\\ j(\mathbf{x})&=\textstyle\sum_n e_n\boldsymbol{\alpha}_n\delta(\mathbf{x}-\mathbf{x}_n).\end{aligned} \quad (29)$$

Here the index n is the particle number with the charge e_n. $\boldsymbol{\alpha}_n$ is the Dirac matrix vector and $\mathbf{x}_n$ is the position vector of the nth particle. With these expressions we obtain for the interaction Hamiltonian (28)

$$H_1=-\mu\textstyle\sum_n e_n\boldsymbol{\alpha}_n\cdot\boldsymbol{\phi}(\mathbf{x}_n). \quad (30)$$

For the particle Hamiltonians we have the well-known expressions

$$H^P=\textstyle\sum_n(\boldsymbol{\alpha}_n\cdot\mathbf{p}_n+m_n\beta_n) \quad (31)$$

and for the total Hamiltonian of the system we write therefore

$$H=H_0+H_1+H^P. \quad (32)$$

The Schrödinger functional depends now besides the field variables q also on the particle variables which we symbolically denote with $q_1, q_2, \cdots, q_k, \cdots$. Thus the Schrödinger equation may be written

$$H\Omega(q;q_1,q_2,\cdots t)=i\dot{\Omega}(q;q_1,q_2,\cdots t) \quad (33)$$

with H defined by Eqs. (32), (31), (30), and (27).

E. ELIMINATION OF THE LONGITUDINAL FIELD

The elimination of the longitudinal components of the field in ordinary quantum electrodynamics leads to the Coulomb interaction potential between the charged particles. We shall now carry out the analogous calculation for the field in a refractive medium. To that end we go into momentum space with the transformation formula

$$\left.\begin{aligned}\Phi(\mathbf{x})&=(2\pi)^{-\frac{3}{2}}\int d^3k\mathbf{Q}(\mathbf{k})e^{i\mathbf{k}\cdot\mathbf{x}}\\ \Pi(\mathbf{x})&=(2\pi)^{-\frac{3}{2}}\int d^3k\mathbf{P}(\mathbf{k})e^{-i\mathbf{k}\cdot\mathbf{x}}\end{aligned}\right\}. \quad (34)$$

In order to distinguish the longitudinal and transverse components we introduce again the special coordinate system $\mathbf{e}_1$, $\mathbf{e}_2$, $\mathbf{e}_3$ for each $\mathbf{k}$ defined in Eq. (61) in Part I.

$$\left.\begin{aligned}\mathbf{P}&=P^{(1)}\mathbf{e}_1+P^{(2)}\mathbf{e}_2+P^{(3)}\mathbf{e}_3\\ \mathbf{Q}&=Q^{(1)}\mathbf{e}_1+Q^{(2)}\mathbf{e}_2+Q^{(3)}\mathbf{e}^3\end{aligned}\right\}. \quad (35)$$

The Hamiltonian for the field may then be written as

$$H_0=H^{\text{long}}+H^{\text{tr}} \quad (36)$$

with

$$\begin{aligned}H^{\text{tr}}=\tfrac{1}{2}\int d^3k\Big[&\frac{1}{1+\kappa v_0^2}\Big\{P^{(1)+}P^{(1)}\\ &+P^{(2)+}P^{(2)}\Big(1+\frac{\kappa v^2\sin^2\alpha}{1+\kappa}\Big)\Big\}\\ &+k^2\Big(1-\frac{\kappa^2v^2\cos^2\alpha}{1+\kappa v_0^2}\Big)Q^{(1)+}Q^{(1)}\\ &+k^2\Big(1-\frac{\kappa v^2}{1+\kappa v_0^2}\Big)Q^{(2)+}Q^{(2)}\\ &-2\kappa iv^0(\mathbf{v}\cdot\mathbf{k})(Q^{(1)}P^{(1)}+Q^{(2)}P^{(2)})\Big],\end{aligned} \quad (37)$$

$$H^{\text{long}}=\tfrac{1}{2}\int d^3k\frac{1}{1+\kappa v_0^2}\Big\{P^{(3)}+P^{(3)}\Big(1+\frac{\kappa v^2\cos^2\alpha}{1+\kappa}\Big)$$
$$-2\kappa i v^0 kv|\sin\alpha|Q^{(2)}P^{(2)}$$
$$-\frac{\kappa v^2}{1+\kappa}(P^{(2)}+P^{(3)}+P^{(3)}+P^{(2)})$$
$$\times|\sin\alpha|\cos\alpha\Big\}. \quad (38)$$

This expression may be transformed with the help of Eq. (25) which may be written (since $\chi\Omega=0$)

$$(\nabla\cdot\mathbf{\Pi}+\mu\rho)\Omega=0. \quad (39)$$

If we develop $\rho(\mathbf{x})$ into a Fourier series according to the formula,

$$\rho(\mathbf{x})=(2\pi)^{-\frac{3}{2}}\int d^3k\rho(\mathbf{k})e^{-i\mathbf{x}\cdot\mathbf{k}}, \quad (40)$$

Eq. (39) may be written

$$\{-iP^{(3)}(\mathbf{k})k+\mu\rho(\mathbf{k})\}\Omega=0, \quad (41)$$

which must hold for all values of $\mathbf{k}$. This means that for a Maxwell field we get an equivalent H^{long} if we replace everywhere $P^{(3)}(\mathbf{k})$ according to the equation

$$P^{(3)}(\mathbf{k})=i(\mu/k)\rho(\mathbf{k}). \quad (42)$$

In this way we obtain for H^{long} an expression which we conveniently separate into two parts as follows:

$$H^{\text{long}}=H_c+H_2, \quad (43)$$

$$H_c=\frac{1}{2}\frac{1}{1+\kappa v_0^2}\int d^3k\Big(1+\frac{\kappa v^2\cos^2\alpha}{\kappa+1}\Big)$$
$$\times\frac{\mu^2\rho^+(\mathbf{k})\rho(\mathbf{k})}{k^2}, \quad (44)$$

$$H_2=\frac{v\kappa}{1+\kappa v_0^2}\int d^3k\frac{|\sin\alpha|}{k}\mu\rho(\mathbf{k})$$
$$\times\Big\{\frac{i(\mathbf{v}\cdot\mathbf{k})}{k(\kappa+1)}P^{(2)+}(\mathbf{k})-kv^0Q^{(2)}(\mathbf{k})\Big\}. \quad (45)$$

The expression H_c is the generalization of the Coulomb energy for moving media. For the density corresponding to point charges we have Eq. (29) and therefore for $\rho(\mathbf{k})$ we obtain from (40)

$$\rho(\mathbf{k})=(2\pi)^{-\frac{3}{2}}\textstyle\sum_n e_n e^{i\mathbf{k}\cdot\mathbf{x}_n}. \quad (46)$$

Inserting this in (44) we obtain

$$H_c=\frac{1}{2(2\pi)^3}\frac{\mu^2}{1+\kappa v_0^2}\sum_{n,n'}e_n e_{n'}\int\frac{d^3k}{k^2}$$
$$\times\Big(1+\frac{\kappa}{\kappa+1}\frac{(\mathbf{v}\cdot\mathbf{k})^2}{k^2}\Big)\exp[i\mathbf{k}\cdot(\mathbf{x}_n-\mathbf{x}_{n'})]. \quad (47)$$

These integrals can be evaluated if we drop the divergent self-energy terms and we find thus for the Coulomb energy

$$H_c=\frac{1}{4\pi}\sum_{n>n'}\frac{e_n e_{n'}}{|\mathbf{x}_n-\mathbf{x}_{n'}|}\Big\{1+\frac{1}{2}\frac{\kappa}{1+\kappa}$$
$$\times\frac{(\mathbf{v}\times(\mathbf{x}_n-\mathbf{x}_{n'}))^2}{|\mathbf{x}_n-\mathbf{x}_{n'}|^2}\Big\}\frac{\mu^2}{1+\kappa v_0^2}. \quad (48)$$

The second term in (43) given by expression (45) is a non-static interaction term. We write it by introducing the emission and absorption operators (Eq. (70), Part I)

$$H_2=\frac{v\kappa\mu}{\sqrt{2}(1+\kappa v_0^2)}\int d^3k|\sin\alpha|\Big[\frac{1}{\beta}\frac{\mathbf{v}\cdot\mathbf{k}}{k(\kappa+1)}-\beta v^0 k\Big]$$
$$\times[a_2^*(\mathbf{k})\rho(\mathbf{k})+a_2^+(\mathbf{k})\rho^+(\mathbf{k})], \quad (49)$$

where β is given by Eq. (73), Part I.

This result differs in two respects from the corresponding result in the vacuum theory. Equation (48) shows that the Coulomb law for two particles at rest in a moving medium is modified by the presence of an angular dependent term. The second difference is the appearance of an additional interaction term H_2 which depends on the medium velocity and goes to zero with the latter. The physical significance of this term will be discussed in connection with the problem of the Čerenkov radiation.

The elimination of the longitudinal field can now be completed by introducing the Schrödinger functional

$$\Omega^{\text{tr}}=S\Omega, \quad (50)$$

with

$$S=\exp\Big[-\int\frac{\mu}{k}Q^{(3)}(\mathbf{k})\rho(\mathbf{k})d^3k\Big]. \quad (51)$$

The transformation operator S has the property that it commutes with all the variables which occur in H^{tr}, H^e, H^P, H_1, and H_2 except with the particle momentum $\mathbf{p}_n$ which occurs in H^P, the Hamiltonian for the particles. One verifies easily that this momentum operator satisfies the commutation rule

$$[\mathbf{p}_n, S] = -e_n\mu\phi^{long}(\mathbf{x}_n)S, \tag{52}$$

where ϕ^{long} is defined as

$$\phi^{long}(\mathbf{x}) = (2\pi)^{-\frac{3}{2}}\int \mathbf{e}_3 Q^{(3)}(\mathbf{k})e^{i\mathbf{k}\cdot\mathbf{x}}d^3k. \tag{53}$$

Writing further

$$\phi^{tr} = \phi - \phi^{long}.$$

We obtain finally for the Schrödinger equation for Ω^{tr}

$$H\Omega^{tr} = i\dot{\Omega}^{tr}, \tag{54}$$

$$H = H^{tr} + H^e + H^P + H_1 + H_2. \tag{55}$$

With the exception of H_1 the various terms are defined in Eqs. (37), (44), (31), and (49).

H_1 is now given by

$$H_1 = -\mu\sum e_n\alpha_n\cdot\phi^{tr}(\mathbf{x}_n). \tag{56}$$

F. THE CLASSICAL FIELD OF A POINT-CHARGE AT REST

In the following sections we shall discuss a few applications of the theory so far developed. As a first example we shall study the classical field around a particle at rest in a moving medium. Since the classical equations hold also for the expectation values of the field quantities, we may consider the Eqs. (9)–(12) as the differential equations for the problem.

Let e be the charge of a particle at rest located at the origin. The density function is then $j^0 = e\delta(\mathbf{x})$. The currents j^k vanish ($k = 1, 2, 3$). We want stationary solutions of the differential equations (1) which vanish at infinity. They are of the form $\Psi^k = 0$, $\Psi^0 \neq 0$. Ψ^0 is the solution of

$$\{-\nabla^2 + \kappa(\mathbf{v}\cdot\nabla)^2\}\Psi^0 = e\mu\delta(\mathbf{x}). \tag{57}$$

We write the solution as a Fourier integral,

$$\Psi^0 = (2\pi)^{-3}\int F(\mathbf{k})e^{i\mathbf{k}\cdot\mathbf{x}}d^3k. \tag{58}$$

From (57) follows then for $F(\mathbf{k})$

$$\{k^2 - \kappa(\mathbf{v}\cdot\mathbf{k})^2\}F(\mathbf{k}) = e\mu$$

or

$$\Psi^0 = (2\pi)^{-3}\int \frac{e\mu}{k^2 - \kappa(\mathbf{v}\cdot\mathbf{k})^2}e^{i\mathbf{k}\cdot\mathbf{x}}d^3k. \tag{59}$$

In order to evaluate the integral we assume first

$$\kappa v^2 < 1. \tag{60}$$

By a convenient choice of the coordinate system we may assume the direction of velocity to be the 3-direction. Introducing further the new variables

$$\begin{aligned} k_1' &= k_1, \quad k_2' = k_2, \quad k_3' = k_3(1-\kappa v^2)^{\frac{1}{2}}, \\ x_1' &= x_1, \quad x_2' = x_2, \quad x_3' = x_3/(1-\kappa v^2)^{\frac{1}{2}}, \end{aligned} \tag{61}$$

we obtain for (59)

$$\Psi^0 = (2\pi)^{-3}[e\mu/(1-\kappa v^2)^{\frac{1}{2}}]\int e^{i\mathbf{k}'\cdot\mathbf{x}'}/k'^2 d^3k'$$

or

$$\Psi^0 = (1/4\pi)[e\mu/(1-\kappa v^2)^{\frac{1}{2}}](1/|x'|). \tag{62}$$

For a general coordinate system this may be written

$$\Psi^0 = (e\mu/4\pi)\{x^2(1-\kappa v^2) + \kappa(\mathbf{x}\cdot\mathbf{v})^2\}^{-\frac{1}{2}}. \tag{63}$$

On the other hand, if $\kappa v^2 > 1$ the integrand of (59) has two poles for real values of $\mathbf{k}$. We shall again choose the notation (61) and carry out first the integration over k_3'. In order to make k_3' and x_3' real they are now defined as

$$k_3' = k_3(\kappa v^2 - 1)^{\frac{1}{2}}, \quad x_3' = x_3/(\kappa v^2 - 1)^{\frac{1}{2}}$$

and the integration over k_3' gives

$$I = \int dk_3' \frac{e^{ik_3'x_3'}}{k_1'^2 + k_2'^2 - k_3'^2}. \tag{64}$$

There are two different solutions possible which are real according to whether we displace the path in the upper or lower half-plane around the two poles $k_3' = \pm(k_1'^2 + k_2'^2)^{\frac{1}{2}}$. In the rest system of the medium these two solutions correspond to the advanced and retarded potentials, respectively. The principle value, on the other hand, gives a linear combination of these two solutions. Just as in the case of the advanced potentials, we must exclude the first solution on physical grounds. We obtain in this way for I

with the residue theorem

$$I=\begin{cases}0 & \text{for } x_3'<0\\ +2\pi(\sin kx_3'/k) & \text{for } x_3'>0\end{cases} \tag{65}$$

with $k=(k_1^2+k_2^2)^{\frac{1}{2}}$, and, consequently,

$$\Psi^0=(2\pi)^{-2}\frac{e\mu}{(\kappa v^2-1)^{\frac{1}{2}}}\int d^3k\frac{e^{i\mathbf{k}\cdot\mathbf{x}}\sin kx_3'}{k}. \tag{66}$$

Integrating over the angles first this gives

$$\Psi^0=(e\mu/2\pi)[1/(\kappa v^2-1)^{\frac{1}{2}}]\times\int_0^\infty J_0(kr)\sin kx_3'dk, \tag{67}$$

$$(r=(x_1^2+x_2^2)^{\frac{1}{2}}).$$

The last integral can be evaluated with the help of the formula[2]

$$\int_0^\infty J_0(at)\sin btdt=\begin{cases}0 & b<a\\ 1/(b^2-a^2)^{\frac{1}{2}} & b>a\end{cases}.$$

Hence after transforming the result back to the general coordinate system,

$$\Psi^0=\begin{cases}0 & \text{for } \mathbf{x}\cdot\mathbf{v}<vr(\kappa v^2-1)^{\frac{1}{2}}\\ (e\mu/2\pi)\{|x|^2(1-\kappa v^2)+\kappa(\mathbf{v}\cdot\mathbf{x})^2\}^{-\frac{1}{2}} & \\ & \text{for } \mathbf{x}\cdot\mathbf{v}>vr(\kappa v^2-1)^{\frac{1}{2}}\end{cases}. \tag{68}$$

We see from this, the solution Ψ^0 vanishes everywhere except inside the cone given by

$$\mathbf{x}\cdot\mathbf{v}=rv(\kappa v^2-1)^{\frac{1}{2}}. \tag{69}$$

On the cone itself the solution (68) becomes infinite.* From (68) and with the help of Eqs. (12) and (9) it is easy to obtain the field strengths. Since

$$\begin{aligned}\Phi^\lambda&=\Psi^\lambda+[\kappa/(1+\kappa)]\Psi^\sigma v_\sigma v^\lambda,\\ \Phi^i&=[\kappa/(1+\kappa)]v_0\Psi^0v^i,\\ \Phi^0&=\Psi^0[1+(\kappa/(1+\kappa))v^0v_0],\end{aligned} \tag{70}$$

the field strengths are given by

$$\begin{aligned}F_{ij}&=[\kappa/(1+\kappa)]v_0(\partial_iv_j-\partial_jv_i)\Psi^0,\\ F_{i0}&=\partial_i\Psi_0[1+(\kappa/(1+\kappa))v^0v_0].\end{aligned} \tag{71}$$

[2] See G. N. Watson, *Theory of Bessel Functions* (Cambridge University Press, 1922).

* We notice that the expression (68), insofar as it is different from zero, is twice as large as (63). This means that the field simply "folds over" to the inside of the cone (69) for velocities v larger than $\kappa^{-\frac{1}{2}}$.

G. THE SELF-FORCE ON A PARTICLE AT REST IN A MOVING MEDIUM

We consider now, still in the classical case, the net force which the field exerts on a particle at rest when the medium is moving. In vacuum electrodynamics this force is, of course, always equal to zero since the field is spherically symmetrical around a point particle. However, this is, no longer the case when the particle is at rest in a moving diffracting medium.

According to Lorentz the four-vector density of the force is given by**

$$f_\mu=\mu F_{\mu\nu}j^\nu. \tag{72}$$

For a particle at rest this reduces to

$$f_i=\mu F_{i0}\rho;\quad f_0=0. \tag{73}$$

The total force on the charge is then

$$F_i=\mu\int F_{i0}\rho(\mathbf{x})d^3x. \tag{74}$$

In order to evaluate this expression we assume a charge distribution $\rho(\mathbf{x})$ with the Fourier expansion

$$\rho(\mathbf{x})=(2\pi)^{-\frac{3}{2}}\int d^3k\rho(\mathbf{k})e^{-i\mathbf{k}\cdot\mathbf{x}}. \tag{75}$$

The field strengths are then by the obvious generalization of Eqs. (59), (71) for a continuous charge distribution

$$F_{i0}(\mathbf{x})=-\left(1-\frac{\kappa}{1+\kappa}v_0^2\right)(2\pi)^{-3}i\int d^3k\times\int d^3y\frac{k_i\mu^2}{k^2-\kappa(\mathbf{v}\cdot\mathbf{k})}e^{i\mathbf{k}(\mathbf{x}-\mathbf{y})}\rho(\mathbf{y}),$$

and hence for the force (74),

$$F_i=\left(\frac{\kappa}{1+\kappa}v_0^2-1\right)i\int d^3k\frac{k_i\mu^2}{k^2-\kappa(\mathbf{v}\cdot\mathbf{k})^2}\times\rho(\mathbf{k})\rho(-\mathbf{k}). \tag{76}$$

Since the integrand in this expression is odd, we see that $F_i=0$ if the denominator has no singularity, that is, if $\kappa v^2<1$. In the other case

** The explicit appearance of the factor μ in Eq. (72) comes from our definition of energy and momentum of the field.

($\kappa v^2>1$), we must evaluate it again with the path of integration chosen according to the solution (68). In this way we obtain again with the residue theorem the expression:

$$F_i=\frac{2\pi^2}{1+\kappa}\frac{\kappa v^2-1}{\kappa v^3}v_i I, \tag{77}$$

with

$$I=\int_0^\infty kdk\mu^2\rho(\mathbf{k})\rho(-\mathbf{k}) \tag{78}$$

for spherically symmetrical charge distribution.

For a point charge $\rho(k)=e(2\pi)^{-\frac{1}{2}}$, independent of k and the integral (78) is divergent. This means in a medium with constant ϵ and μ a point particle can never be accelerated to a velocity such that $\kappa v^2>1$. The situation is different, however, in a dispersive medium. In that case the factors in front of I will be frequency-dependent and will therefore go under the integral sign. The integral is then always convergent provided $\kappa\to 0$ for $k\to\infty$.

H. THE ČERENKOV RADIATION

With Čerenkov radiation one denotes the radiation emitted by a charged high speed particle traversing a refractive medium with a speed so high that $\kappa v^2>1$. This radiation is essentially different from and must not be confused with the bremsstrahlung. It was discovered experimentally by Čerenkov in 1934 and subsequently studied by other workers.[3] The classical theory of the radiation was given by Frank and Tamm.[4] We shall here develop the quantum-mechanical theory of the radiation by using the two representations: medium at rest, particle moving and medium moving, particle at rest.[4a]

In the first case the interaction Hamiltonian is given entirely by the term H_1 in Eq. (55). We consider an electron of rest mass m and momentum $\mathbf{p}$, such that $p^2\kappa>m$. This electron can carry out a transition to a state with momentum $\mathbf{p}'$ under emission of a photon of momentum and polarization $\mathbf{k}$, r and energy k/n. The probability per unit time for such a process is given by quantum-mechanical perturbation theory as

$$dP=2\pi d\rho_F\langle|H_1|^2\rangle_{Av}. \tag{79}$$

Here $\langle|H_1|^2\rangle_{Av}$ is the square of the matrix element of H_1 for the transition in question averaged over all the spin states of the initial and final states of the electron. $d\rho_F$ represents the density of the final states, per unit energy range for photons emitted into the solid angle $d\Omega$. By denoting the spinor amplitudes of the plane waves of the electron with $u(\mathbf{p})$ and $u(\mathbf{p}')$ for initial and final states, respectively, we obtain from Eq. (56) the following expression for the matrix element

$$\langle|H_1|^2\rangle_{Av}=[e^2\mu^2/16\pi^3k(1+\kappa)^{\frac{1}{2}}]\times\tfrac{1}{2}\sum|u^*(\mathbf{p})(\boldsymbol{\alpha}\cdot\mathbf{e}_r)u(\mathbf{p}')|^2. \tag{80}$$

The summation in this expression extends over all the spin states of the initial and final state of the electron with positive energy. This sum may be evaluated in the following way. We introduce the annihilation operators

$$\begin{aligned}\Lambda(\mathbf{p})&=[(\boldsymbol{\alpha}\cdot\mathbf{p})+\beta m+E_p]/2E_p,\\ \Lambda(\mathbf{p}')&=[\boldsymbol{\alpha}\cdot(\mathbf{k}-\mathbf{p}')+\beta m+E_{p'}]/2E_{p'},\end{aligned} \tag{81}$$

with

$$E_p=+(p^2+m^2)^{\frac{1}{2}},\quad E_{p'}=+(p'^2+m^2)^{\frac{1}{2}}.$$

We obtain then for this sum

$$\begin{aligned}S&=\tfrac{1}{2}\sum|u^*(\mathbf{p})(\boldsymbol{\alpha}\cdot\mathbf{e}_r)u(\mathbf{p}')|^2\\ &=\tfrac{1}{8}tr[(\boldsymbol{\alpha}\cdot\mathbf{e}_r)\Lambda_{p'}(\boldsymbol{\alpha}\cdot\mathbf{e}_r)\Lambda_p]\\ &=\frac{1}{2E_p'E_p}\{E_pE_{p'}-(\mathbf{p}\cdot\mathbf{p}')+2(\mathbf{p}\cdot\mathbf{e}_r)^2-m^2\}.\end{aligned} \tag{82}$$

In the applications the only case of importance is that for which the photon quanta have momentum very much smaller than the momentum of the particle $k\ll p$. For this case (82) may be developed in powers of k/p. In this way we obtain for the sum (82)

$$S=(1/E_p^2)(\mathbf{p}\cdot\mathbf{e}_r)^2. \tag{83}$$

From this expression it may be seen that the Čerenkov radiation is polarized with the electric

[3] P. A. Čerenkov, C. R. Acad. Sci. U.R.S.S. **2**, 451 (1934); **3**, 413 (1936); **14**, 99, 103 (1937); **20**, 651 (1938); **21**, 116, 319 (1938); Phys. Rev. **52**, 378 (1937). G. B. Collins and V. G. Reiling, Phys. Rev. **54**, 499 (1938). H. O. Wyckoff and J. E. Henderson, Phys. Rev. **64**, 1 (1943).

[4] I. M. Frank and Ig. Tamm, C. R. Acad. Sci. U.R.S.S. **14**, 107 (1937). Ig. Tamm, J. Phys. U.R.S.S. **1**, 439 (1938).

[4a] A quantum mechanical treatment of the Čerenkov radiation has also been given by V. L. Ginsburg, J. Phys. U.R.S.S. **2**, 441 (1940). However, the relativistic invariance and the elimination of the longitudinal field are not discussed in this paper.

vector in the plane of the vectors $\mathbf{p}$ and $\mathbf{k}$. The total photon-emission probability is then proportional to

$$S=(1/E_p^2)\{p^2-[(\mathbf{p}\cdot\mathbf{k})^2/k^2]\}. \quad (84)$$

For the density of final states we have

$$d\rho_F=k^2(dk/dE_F)d\Omega. \quad (85)$$

The conservation of energy gives for the final energy the expression

$$E_F=(k/n)+[(\mathbf{p}-\mathbf{k})^2+m^2]^{\frac{1}{2}}. \quad (86)$$

From this we get

$$dE_F/dk=(1/n)+(k-p\cos\theta)[(\mathbf{p}-\mathbf{k})^2+m^2]^{-\frac{1}{2}}, \quad (87)$$

where θ is the angle between $\mathbf{p}$ and $\mathbf{k}$. This angle is entirely determined by the conservation of momentum and energy. For we obtain for the parallel and perpendicular components of momentum the equations

$$p=p_{11}+k\cos\theta, \quad 0=p_\perp+k\sin\theta, \quad (88)$$

and for the energy

$$E_p=E_{p'}+(1/n)k. \quad (89)$$

The sum of the squares of the first two equations gives

$$p'^2=p^2+k^2-2pk\cos\theta \quad (90)$$

and the square of the last

$$p'^2=p^2-(2/n)kE_p+(1/n^2)k^2. \quad (91)$$

Equating the last two expressions gives

$$\cos\theta=[E_p/pn]+[\kappa/(\kappa+1)][k/2p], \quad (92)$$

which is the desired relationship between θ and k. We mention here that in the classical theory[4] only the first term occurs on the right-hand side of Eq. (92). That the quantum theoretical treatment leads to the additional term on the right was pointed out before by Cox.[5] Inserting (84), (85), (87), and (92) in (79) gives us the desired cross section for the photon emission per unit time into the solid angle $d\Omega$.

We shall carry out the discussion of the result in the approximation $k\ll p$ which was already used to get the result (84). In this case we obtain $[u=v/(1+v^2)^{\frac{1}{2}}]$:

$$dE_F/dk\sim[k/2E_p][\kappa/(\kappa+1)], \quad (93)$$

$$d\rho_F\sim 2kE_p[(\kappa+1)/\kappa]d\Omega, \quad (94)$$

$$S\sim u^2[1-(1/n^2)u^2], \quad (95)$$

and therefore from (79)

$$dP=E_p[(\kappa+1)/\kappa][e^2\mu^2/4\pi^2(1+\kappa)^{\frac{1}{2}}]\times u^2(1-(1/u^2n^2)). \quad (96)$$

The emission probability as a function of the angle is then obtained by expressing k as a function of θ by Eq. (92).

In order to obtain the total energy radiated per unit time dw/dt we write

$$d\Omega=\sin\theta d\theta d\varphi=-d\varphi[\kappa/(\kappa+1)](dk/2p), \quad (97)$$

$$dw/dt=\int dP\cdot(k/n)$$

$$=(e^2/4\pi)\int(kdk/n^2)\mu^2[1-(1/n^2)u^2]. \quad (98)$$

It is seen that this expression diverges if no dispersion is assumed. It can be made finite with any kind of dispersion law which assumes only $n\to 1$ for $k\to\infty$. Incidentally, the expression (98) is identical with the classical expression given by Frank and Tamm.[4]

We shall finish the discussion of the Čerenkov radiation by considering the same problem in the coordinate system for which the particle is at rest. In this case H_1 does not contribute anything for $k\ll m$ since the matrix element s of α are proportional to k/m. At first hand it seems, therefore, that no radiation will be emitted. However, the part H_2 given in Eq. (49) will now contribute the necessary interaction terms. We recall that H_2 was introduced into the Hamiltonian by the process of eliminating the longitudinal part of the field. Since in ordinary quantum electrodynamics this term does not appear, its physical significance was not immediately obvious. We see now better what its physical implications are.

The probability for the emission of a photon of momentum $\mathbf{k}$ and a corresponding change of the electron momentum from 0 to $-\mathbf{k}$ is then given by

$$dP'=2\pi\rho_F(|H_2|^2)_{Av}. \quad (99)$$

[5] R. T. Cox, Phys. Rev. 66, 106 (1944).

A straightforward calculation along the lines of the previous case leads to the following result for the probability of photon emission in a direction **k** into the solid angle $d\Omega$.

$$dP' \simeq [e^2\mu^2/2][1/(2\pi)^2] \times [(\kappa v^2-1)/\kappa][(\kappa)^{\frac{1}{2}}/(1+\kappa)]d\Omega. \quad (100)$$

The conservation of momentum and energy give for the angle α of the direction of the emitted photon with the velocity v

$$\cos\alpha \simeq -[v^0/2mv]k-[1/(\kappa v^2)^{\frac{1}{2}}].$$

Thus for $d\Omega$ we may write

$$d\Omega = \sin\alpha d\alpha d\varphi = (v^0/2vm)dkd\varphi.$$

If we calculate the total momentum transferred to the electron per unit time, we find the expression

$$F = -\int k\cos\alpha dP'$$

or for the ith component,

$$F_i = [e^2\mu^2/4\pi][1/(1+\kappa)] \times [(\kappa v^2-1)/\kappa v^3]v_i \int kdk. \quad (101)$$

This expression is identical with the classical expression obtained in Eq. (77) for the static self-force of an electron at rest in a moving medium.

PHYSICAL REVIEW VOLUME 74, NUMBER 10 NOVEMBER 15, 1948

The Application of the Bethe-Peierls Method to Ferromagnetism*

P. R. WEISS
Physics Department, Rutgers University, New Brunswick, New Jersey

(Received June 11, 1948)

The method introduced by Bethe and Peierls for treating the problem of order-disorder in alloys is applied to the problem of ferromagnetism. The method is first applied to the Ising model of the spin in which case the treatment is much the same as it is for the alloy problem, as has already been pointed out by Peierls. The correct treatment of the spin is used for spin values of ½ and 1 per atom. The critical temperatures of different types of lattices are investigated. The method gives results in agreement with the rigorous results of the Bloch spin-wave theory in that only three-dimensional lattices are found to be ferromagnetic. The values of the critical temperatures of these lattices are found to lie between the values predicted by the two Heisenberg approximations. The discontinuity of the specific heat at the critical temperature is computed for a body-centered lattice and for the two values of the spin. The magnitude of the discontinuity is larger than that predicted by Heisenberg's first approximation. The magnitude for the spin 1 is 3.4 k per atom and compares favorably with the experimental value for iron. The susceptibility is computed as a function of the temperature above the critical point. The variation of the susceptibility with temperature does not obey the Curie-Weiss Law but displays some curvature. This curvature explains qualitatively the difference between the "paramagnetic" and ferromagnetic critical temperatures and also helps remove some of the discrepancy between the number of Bohr magnetons per atom as measured at high and low temperatures.

I. INTRODUCTION

THE calculations described below are based on the physical model of ferromagnetism first introduced by Heisenberg.[1] This model can be described briefly as follows. Each atom in a domain has a spin **S** which is the resultant of the spins of individual electrons (or holes) residing in an incomplete inner shell. The orbital moment is quenched so that the magnetization arises entirely from the spins and is, in the first approximation, isotropic. The exchange interaction integral is significant only when it refers to electrons in neighboring atoms and is the same for all such pairs of atoms of the domain. The exchange integral, J, is positive. The incomplete inner shell referred to is, in iron, nickel, and cobalt, the 3-d shell and, in gadolinium, the 4-f shell. It is also assumed in this model that all

* Some of the developments reported here are contained in a thesis submitted in 1940 in partial fulfillment of the requirements for the degree of Doctor of Philosophy at Harvard University. These developments are also contained in a review article, J. H. Van Vleck, Rev. Mod. Phys. **17**, 27 (1945).

[1] W. Heisenberg, Zeits. f. Physik **49**, 619 (1928).

atoms are in the same atomic state so that the same spin quantum number applies to all atoms. Measurements at low temperatures on the saturation intensity of magnetization show the number of contributing spins per atom to be non-integral. The model, therefore, is not complete but does have the virtue of simplicity from a mathematical point of view.

The spin-dependent part of the exchange interaction can be shown to be, in vector form,

$$\mathbf{H} = -2J \sum_{i>j} \mathbf{S}_i \cdot \mathbf{S}_j, \qquad (1)$$

where J is the exchange integral, i and j refer to neighboring atoms, and the summation is taken over all N atoms of the domain. The solution of this Hamiltonian for the energy levels is practically impossible, and consequently several approximation schemes have been tried. The most notable of these are the two Heisenberg[2] approximations and the method of spin waves introduced by Bloch.[3] The latter method, which is rigorous at very low temperatures, shows that only three-dimensional lattices can display ferromagnetism. The criteria arrived at by the Heisenberg approximations can be expressed in the coordination number of lattice (the number of nearest neighbors about any one atom). In the first approximation, which neglects entirely the spread of energy levels, every lattice type becomes ferromagnetic at sufficiently low temperatures; in the second approximation, in which the energy levels are distributed according to a Gaussian distribution about the mean value, the criterion is simply that the coordination number must be equal to or greater than eight.

A different type of approximation is afforded by the method introduced by Bethe[4] and Peierls[5] in connection with the theory of order-disorder transformations in binary substitution alloys. The method can be described in terms of the present problem as follows. An arbitrary atom of a domain, the central atom, and its immediate neighbors $2n$ in number ($2n$ = the coordination number) are considered in detail. The exchange energy (1) of this cluster which consists of only a few atoms can be diagonalized in a correct fashion. The interaction of the neighbor atoms with those outside the cluster and of the remaining atoms with each other are replaced by an internal field, H_1, which acts on the atoms of the first shell alone, and not on the central atom. The internal field H_1 is determined by the condition that the average magnetic moment of the central atom in an applied magnetic field H_0 is to be the same as the average magnetic moment of an atom of the first shell in this field since, actually, there is no distinction to be made between the central atom and an atom in the first shell. The two fields are in the same direction since, in this approximation, directional effects are being neglected. The critical temperature is determined as that temperature below which the internal field does not vanish in the absence of an externally applied field.

Conceptually, this is the first of a series of approximations. At each stage an additional shell is included in the part which is treated rigorously, the remaining interactions being replaced by an internal field which acts only on the outermost shell. The second of this set has been carried through in the problem of alloys and yields results only slightly different from the first. Presumably the series converges rapidly which may be assumed to be true in the present problem as well. It should be remarked that this approach imposes the character of the transformation at the critical point, namely, that of a transformation of the second kind, in which the specific heat is discontinuous. On the other hand, the very first approximation includes more properties of the lattice than the coordination number because the structure of the first shell has a direct bearing on the exchange energy of the cluster. Moreover, the results of this method are different from those of the Heisenberg procedure since this method yields different approximations to the higher (than second) moments of the distribution function.

II. THE ISING MODEL**

The simplest application of the method lies in the use of the Ising[6] model of the spin. In this

[2] See J. H. Van Vleck, *Electric and Magnetic Susceptibilities* (Oxford University Press, Teddington, 1932), Chap. XII.
[3] F. Bloch, Zeits. f. Physik **61**, 206 (1930).
[4] H. A. Bethe, Proc. Roy. Soc. **150**, 552 (1935).
[5] R. Peierls, Proc. Roy. Soc. **154**, 207 (1936).

** After this had been submitted, a paper by U. Firgau (Ann. d. Physik **40**, 295 (1941)) came to my attention. This contains the results of Section II and uses a method identical with that of Bethe and Peierls.
[6] E. Ising, Zeits. f. Physik **31**, 253 (1925).

model the spin per atom is $\frac{1}{2}$ and the off-diagonal elements of the matrix representatives of the spin operators in (1) are equated to zero. This means that each spin is oriented either parallel to or anti-parallel to an applied field. Peierls[7] has already remarked that with this model of the spin, the mathematical problem of ferromagnetism is the exact parallel to that of order-disorder in alloys. For this reason the mathematical development of this section parallels closely the treatment of Bethe.[5]

In the presence of the applied field H_0 in the z direction, the Hamiltonian is

$$H=-2JS_{0z}S_{1z}-g\beta S_{0z}H_0-g\beta S_{1z}H_1. \quad (2)$$

Here g is the spin g-factor $(=2)$, β is the Bohr magneton $e\hbar/2mc$. S_{0z}, S_{1z} are the z-components of the spins of the central atom and of the first shell. S_{0z} has the values $\pm\frac{1}{2}$ while S_{1z} assumes the values $-(n)$, $-(n-1)\cdots+(n)$. The number of states associated with a given value of S_{1z} is just the number of ways in which $(S_{1z}+n)$ spins pointing parallel to H_0 can be arranged on the $(2n)$ sites, or

$$w(S_{1z})=(2n)!/(S_{1z}+n)!(n-S_{1z})!. \quad (3)$$

For convenience in writing we replaced $g\beta H_0$ and $g\beta H_1$ by H_0 and H_1; kT by T, and set

$$x_0=\exp-\frac{H_0}{2T}, \quad x_1=\exp-\frac{H_1}{2T}, \quad y=\exp\frac{J}{2T}. \quad (4)$$

The partition function is

$$P=\sum w(S_{1z})\left\{\frac{1}{x_0}\left(\frac{y}{x_1}\right)^{2S_{1z}}+x_0(x_1y)^{-2S_{1z}}\right\}, \quad (5)$$

with the summation taken between the limits $S_{1z}=-n$ and $S_{1z}=+n$. The summation can be performed and is

$$P=\frac{1}{x_0}\left\{\frac{x_1}{y}+\frac{y}{x_1}\right\}^{2n}+x_0\left\{yx_1+\frac{1}{yx_1}\right\}^{2n}. \quad (6)$$

The average magnetic moments of the central atom m_0 and of an atom in the first shell m_1, in the direction of H_0 are, according to the rules of statistical mechanics,

$$m_0=\beta x_0\frac{\partial}{\partial x_0}\ln P \quad \text{and} \quad m_1=\beta\frac{1}{2n}x_1\frac{\partial}{\partial x_1}\ln P, \quad (7)$$

accordingly,

$$P\frac{m_0}{\beta}=x_0\left\{yx_1+\frac{1}{yx_1}\right\}^{2n}-\frac{1}{x_0}\left\{\frac{y}{x_1}+\frac{x_1}{y}\right\}^{2n}, \quad (8a)$$

$$P\frac{m_1}{\beta}=x_0\left\{yx_1+\frac{1}{yx_1}\right\}^{2n-1}\left\{yx_1-\frac{1}{yx_1}\right\}+\frac{1}{x_0}\left\{\frac{y}{x_1}+\frac{x_1}{y}\right\}^{2n-1}\left\{\frac{x_1}{y}-\frac{y}{x_1}\right\}. \quad (8b)$$

H_1 is determined by setting

$$m_1=m_0. \quad (9)$$

In the region below the critical point it is sufficient to consider these quantities in the limit of vanishing external field, $x_0=1$. This yields

$$\left(yx_1+\frac{1}{yx_1}\right)^{2n-1}=x_1^2\left(\frac{y}{x_1}+\frac{x_1}{y}\right)^{2n-1}, \quad (10)$$

which after some manipulation can be separated to give

$$\exp\frac{J}{T}=\left[\sinh\frac{n}{2n-1}\frac{H_1}{T}\right]\Big/\left[\sinh\frac{n-1}{2n-1}\frac{H_1}{T}\right]. \quad (11)$$

This is precisely the result which Bethe[5] obtains in the case of binary alloys. As there, the critical point is evidence by the fact that as the temperature increases from very low values, where $H_1\approx(2n-1)J$, the right-hand side of (10) approaches a minimum value of $(n)/(n-1)$. At this point H_1 vanishes (i.e., the intensity of magnetization vanishes) in the absence of H_0. The temperature where this occurs is

$$J/T_c=\ln 2n/(2n-2)=\ln n/(n-1). \quad (12)$$

In the temperature region immediately below the critical point the internal field is given by

$$\left(\frac{H_1}{2T}\right)^2\approx\frac{3}{2n}(2n-1)(n-1)\left(\exp\frac{J}{T}-\exp\frac{J}{T_c}\right). \quad (13)$$

To the same degree of approximation, the relative intensity of magnetization

$$\zeta=m_0/\beta, \quad (14)$$

[7] R. Peierls, Proc. Camb. Phil. Soc. 32, 477 (1936).

is given by

$$\zeta \approx \frac{2n}{2n-1}\left(\frac{H_1}{2T}\right)$$

or,

$$\zeta \approx \frac{2n}{2n-1}\left\{\frac{3}{2n}(2n-1)(n-1) \times\left(\exp\frac{J}{T}-\exp\frac{J}{T_c}\right)\right\}^{\frac{1}{2}}, \quad (15)$$

so that the saturation intensity of magnetization increases below the critical point as the square root of the temperature departure from the critical temperature. The complete expression for ζ is

$$\zeta = \tanh(n/2n-1)(H_1/T), \quad (16)$$

as can be seen from the first of (8) and from (9). Thus ζ has the same behavior below the critical point as does the long distance order, S, in reference 5.

The consideration of the energy per atom is somewhat different in the present case since there is no convenient parameter which takes the place of that which describes the *local* order in alloys. This is to be expected since the numbers of the two different types of atoms is fixed in the alloy while here the numbers of the atoms parallel and anti-parallel to the fields change as the temperature decreases from the critical point. In view of this, it is rather surprising that, as will be shown, the discontinuities in the specific heat at the critical temperatures are the same in the two cases for the same lattice types. The total energy of a domain consisting of N atoms can be obtained as follows. Suppose there are N_1 spins which point parallel to and $N_2=N-N_1$ spins which point anti-parallel to a given direction. If n_1 is the average number of atoms neighboring a parallel type which are also parallel, and if n_2 is the average number of atoms neighboring an anti-parallel type which are also anti-parallel, then the total number of different neighboring pairs which are aligned parallel to each other is

$$\tfrac{1}{2}(N_1n_1+N_2n_2).$$

The total number of different pairs is $\frac{1}{2}Nz$ and, therefore, the number of different pairs which are aligned oppositely to each other is

$$\tfrac{1}{2}[Nz-(N_1n_1+N_2n_2)].$$

The energy for a pair which are similarly aligned is $-\frac{1}{2}J$; for a pair which are oppositely aligned $+\frac{1}{2}J$. The total energy is then

$$E=-\tfrac{1}{2}J(N_1n_1+N_2n_2)+(1/4)NzJ. \quad (17)$$

N_1 and N_2 are determined by the intensity of magnetization

$$N_1=\tfrac{1}{2}N(1+\zeta), \quad N_2=\tfrac{1}{2}N(1-\zeta). \quad (18)$$

n_1 is given by

$$n_1=\frac{\Sigma\binom{2n}{k}\exp\frac{1}{T}(J+H_1)(k-n)}{\Sigma\binom{2n}{k}\exp\frac{1}{T}(J+H_1)(k-n)}. \quad (19)$$

The limits in the summations are $k=0$ and $(2n)$. A similar expression obtains for n_2 although here the sign of H_1 is reversed. The results are

$$n_{1,2}=n\left(1+\tanh\frac{J\pm H_1}{2T}\right). \quad (20)$$

The total energy is, except for a term independent of ζ and H_1,

$$E=-\frac{n}{4}NJ\left\{(1+\zeta)\tanh\frac{J+H_1}{2T} +(1-\zeta)\tanh\frac{J-H_1}{2T}\right\}. \quad (21)$$

The energy per atom is $E/N=\epsilon$. Above the critical point the energy is

$$\epsilon_0=-(n/2)J\tanh(J/2T). \quad (22)$$

On expanding the tanh functions in $(H/2T)$ and in using (11) and (14) the energy immediately below the critical point is

$$\epsilon-\epsilon_0=\frac{2n^2(n-1)}{(2n-1)^2}J\left(\frac{H}{2T}\right)^2. \quad (23)$$

The discontinuity in the specific heat is

$$\Delta C/k=\left(\frac{\partial}{\partial T}(\epsilon-\epsilon_0)\right)_{T=T_c} =\frac{3n^2(n-1)}{(2n-1)}\left(\ln\frac{n}{n-1}\right)^2. \quad (24)$$

III. ENERGY LEVELS OF THE CLUSTER

An advantage of the present method is that the Hamiltonian of the cluster can be dealt with in a correct fashion without invoking an approximate model of the spin as was done in the previous section. The Hamiltonian is

$$\mathbf{H}_0 = -2J \sum_{i>j} \mathbf{S}_i \cdot \mathbf{S}_j - S_{0z}H_0 - S_{1z}H_1, \quad (25)$$

where we have replaced $g\beta H_0$ by H_0 and $g\beta H_1$ by H_1. The summation is taken over the $(2n+1)$ atoms of the cluster and can be written as

$$\mathbf{S}_0 \cdot \sum_{j=1}^{2n} \mathbf{S}_j + \sum_{i>j} \mathbf{S}_i \cdot \mathbf{S}_j = \mathbf{S}_0 \cdot \mathbf{S}_1 + \sum_{i>j} \mathbf{S}_i \cdot \mathbf{S}_j. \quad (26)$$

$\mathbf{S}_1$ is the spin of the combined first shell; the second summation takes account of interactions within the first shell. This interaction is absent in the linear chain, the quadratic layer lattice, the simple cubic, and body-centered lattices. In the hexagonal layer lattice, each atom of the first shell has two of its six nearest neighbors in that shell; in the face-centered lattice, each atom of the first shell interacts with four other atoms of the first shell. The simplest cases are those for which such interactions are absent and these are considered first.

The vector model yields the energy values

$$\begin{aligned} E-_{\text{exch}} &= +J(S_1+1), & S &= S_1-\tfrac{1}{2}, \\ E+_{\text{exch}} &= -JS_1, & S &= S_1+\tfrac{1}{2}. \end{aligned} \quad (27a)$$

When the spin per atom is $\frac{1}{2}$ and

$$\begin{aligned} E-_{\text{exch}} &= +2J(S_1+1), & S &= S_1-1, \\ E^0{}_{\text{exch}} &= -2J, & S &= S_1, \\ E+_{\text{exch}} &= -2JS_1, & S &= S_1+1, \end{aligned} \quad (27b)$$

when the spin per atom is 1. A system of representation is used in which the exchange energy is diagonal. m is the magnetic quantum number of the total spin $S=S_0+S_1$. When the spin per atom is $\frac{1}{2}$ the levels are:

$$W = -JS_1 \mp \tfrac{1}{2}(2S_1H_1+H_0), \quad (28a)$$

for $m=\pm(S_1+\frac{1}{2})$ and when $|m| \leq (S_1-\frac{1}{2})$ the matrix is

$$\begin{pmatrix} A_a & B \\ B & A_p \end{pmatrix}, \quad (28b)$$

with

$$\begin{aligned} A_a &= J(S_1+1) - mH_1 - \frac{m}{2S_1+1}(H_1-H_0), \\ A_p &= -JS_1 - mH_1 + \frac{m}{2S_1+1}(H_1-H_0), \quad (28c) \\ B &= \frac{1}{2}\left[1 - \frac{4m^2}{(2S_1+1)^2}\right]^{\frac{1}{2}}(H_1-H_0). \end{aligned}$$

The Hamiltonian is more complicated when the spin per atom is 1. First, it is of third rather than second order and second, there is a degeneracy in the exchange energy when $S_1=1$ for the levels $S=S_1+1$ and $S=S_1$. Because of these difficulties, a discussion of this Hamiltonian is reserved for an appendix.

The secular equation for the levels belonging to the matrix (25) is of second degree and consequently the expressions for the energy levels contain a complicated square root of a sum of terms involving J, H_1, and H_0. Numerical computations of the intensity of magnetization are difficult to perform when these expressions are used. The internal field is small in the immediate vicinity of the critical temperature and a series expansion in terms of H/J is possible in this temperature region. This expansion permits the computation of the critical temperature, of the variation of the susceptibility with temperature, and of the discontinuity in the specific heat. It is necessary to include terms in the fourth powers of H/J although the computation of the critical temperature and of the susceptibility require only terms through the second degree in H/J. The levels are, for a spin of $\frac{1}{2}$,

$$\begin{aligned} W_k(S_1 m) = {} & A_k + b_k H_1 + c_k(H_1-H_0) \\ & + d_k(H_1-H_0)^2 + e_k(H_1-H_0)^3 \\ & + f_k(H_1-H_0)^4. \quad (29) \end{aligned}$$

$k=1$, 2 corresponds to the anti-parallel and parallel alignments of the spins of the central atom and of the first shell. A corresponding expression to be given in the appendix applies as well for the case of a spin of 1. The coefficients

TABLE I. Ratio of exchange integral to critical temperature (J/kT_c) for different lattice types as computed by different approximations.

Lattice	Number of nearest neighbors	Spin per atom	Heisenberg App. I	Heisenberg App. II	Present method
Linear chain	2	½	1.000	None	None
Quadratic layer	4	½	0.500	None	None
Simple cubic	6	½	0.333	None	0.540
Hexagonal layer	6	½	0.333	None	None
Body-centered	8	½	0.250	0.500	0.3445
Modified body-centered	8	½	0.250	0.500	0.4620
Body-centered	8	1	0.0937		0.1502

here are

$$A_1=J(S_1+1);\quad A_2=-JS_1;\quad b_1=b_2=-m,$$

$$c_{1,2}=\mp\frac{m}{(2S_1+1)},$$

$$d_{1,2}=\pm\frac{1}{4J(2S_1+1)}\left(1-\frac{4m^2}{(2S_1+1)^2}\right),$$

$$e_{1,2}=\pm\frac{m}{2J^2(2S_1+1)^3}\left(1-\frac{4m^2}{(2S_1+1)^2}\right), \tag{30}$$

$$f_{1,2}=\mp\frac{1}{16J^3(2S_1+1)^3}\times\left(1-\frac{24m^2}{(2S_1+1)^2}+\frac{80m^4}{(2S_1+1)^4}\right).$$

IV. THE CRITICAL TEMPERATURE

The partition function of the cluster is

$$P=\sum w(2n,S_1)\left\{\sum\exp-\frac{1}{T}W_1(S_1m)+\sum\exp-\frac{1}{T}W_2(S_1m)\right\}. \tag{31}$$

The first summation is over S_1 from 0 to n; the first of the inner summations is over m from $m=-(S_1-\frac{1}{2})$ to $m=+(S_1-\frac{1}{2})$; the second of the inner summations is over m from $m=-(S_1+\frac{1}{2})$ to $m=+(S_1+\frac{1}{2})$. The multiplicities $w(2n,S_1)$ of the different S_1 levels are obtained from the branching rule expressed in the formula

$$w(2n,S_1)=\frac{(2n)!}{(n-S_1)!(n+S_1)!}-\frac{(2n)!}{(n-S_1-1)!(n+S_1+1)!}, \tag{32}$$

for a spin ½ and

$$w(2n,S_1)=L(S_1)-L(S_1+1),$$

with

$$L(S_1)=\text{coefficient of } X^{S_1} \text{ in } (X+1+X^{-1})^{2n}, \tag{33}$$

for a spin 1. The parts of the exponentials containing the field strengths can be expanded in power series, again preserving terms through the fourth powers. The average magnetic moments of the central atom and of an atom in the first shell are found by

$$m_0=-g\beta T\frac{\partial}{\partial H_0}\ln P.\quad m_1=-\frac{1}{2n}g\beta T\frac{\partial}{\partial H_1}\ln P. \tag{34}$$

The field H_0 can be taken to be zero in the resulting expressions in the computation of the critical temperature; both moments then have terms in H_1 and H_1^3. The consistency requirement (9) yields the equation which determines H_1

$$A+CH_1^2=0, \tag{35}$$

one factor of H_1 having been canceled from each term. This indicates that $H_1=0$ is one (an unstable one) solution. The quantities A and C are:

$$A=\sum_{k=1}^{2}\sum_{S_1}w(2n,S_1)\left\{A_k^0+\frac{A_k^1}{T}\right\}\times\exp-\frac{A_k}{T}, \tag{36}$$

$$C=\sum_k\sum_{S_1}w(2n,S_1)\left\{C_k^0+\frac{1}{T}C_k^1+\frac{1}{T^2}C_k^2+\frac{1}{T^3}C_k^3\right\}\exp-\frac{A_k}{T},$$

$$A_k^0=\sum_m(-2d_k),$$

$$(1+2n)A_k^1=\sum_m\{(b_k+c_k)^2+2nc_k(b_k+c_k)\},$$

$$C_k^0=\sum_m(-4f_k), \tag{37}$$

$$(1+2n)C_k^1=\sum_m\{2(1+2n)d_k^2+(4+6n)e_kb_k+4(1+2n)e_kc_k\},$$

$$-(1+2n)C_k^2=\sum_m\{2d_k(b_k+c_k)^2+2nd_k(b_k+c_k)(b_k+2c_k)\},$$

$$6(1+2n)C_k^3=\sum_m\{(b_k+c_k)^4+2nc_k(b_k+c_k)^3\}.$$

The sums are to be taken with $|m| \leq (S_1 - \frac{1}{2})$ for $k=1$ and $|m| \leq (S_1 + \frac{1}{2})$ for $k=2$. Only terms in even powers of m are involved because sums over odd powers vanish. The summations can be performed by using

$$\sum_{m=-T}^{+T} 1 = 2T+1;$$

$$\sum_{m=-T}^{+T} m^2 = \tfrac{1}{3}T(T+1)(2T+1);$$

and (38)

$$\sum_{m=-T}^{+T} m^4 = \frac{1}{15}T(T+1)(3T^2+3T-1).$$

The complexity of the expressions (36) and (37) arises from the off-diagonal elements of the matrix representatives of the spins. It is not possible to perform the summations over S_1 in closed form and computation shows it is not possible to neglect those terms which arise from the off-diagonal elements. In fact, it is primarily these terms which give results concerning the critical temperature which are different from the Ising model, and from the Heisenberg approximations.

The critical point is found by numerical computation as the temperature for which A of (35) and (36) changes its sign. Each lattice requires a separate computation number. The critical temperatures provided by Heisenberg's first and second approximations for a spin of $\frac{1}{2}$

$$(J/T_c)_I = 1/n, \quad (J/T_c)_{II} = \frac{1}{2}\left[1-\left(1-\frac{4}{n}\right)^{\frac{1}{2}}\right], \quad (39)$$

provide useful starting points. The results of the computation for several lattice structures are shown in Table I.

The hexagonal layer lattice and the modified body-centered lattice contain interactions between atoms in the first shell. The exchange energy for the configuration presented by the first shell of the hexagonal layer lattice has been solved by Serber.[8] The levels in units of J along with their multiplicities are:

$S_1=0$	$S_1=1$	$S_1=2$	$S_1=3$	(40)
−4.606 (1)	−4.561 (2)	−5.000 (2)	−6.000 (1)	
−2.000 (2)	−4.000 (1)	−3.000 (2)		
+2.606 (1)	−3.236 (1)	−2.000 (1)		
	−1.000 (2)			
	−0.4385 (2)			
	+1.236 (1)			

[8] R. Serber, J. Chem. Phys. 2, 697 (1934).

To these must be added the interaction of the central atom with the first shell $+(S_1+1)$ and $-S_1$ for the anti-parallel and parallel alignments respectively. The corresponding values of A_p and A_{ap} can be inserted into (36). The "modified" body-centered lattice is an imaginary one in which the eight atoms of the first shell are divided into two groups of four; in each group all atoms are nearest neighbors to each other but not to any of the atoms of the other group. This is an artificial lattice imagined in order to try to determine the effect of the interactions inside the first shell on the critical temperature. The exchange energy is

$$\mathbf{H}_{\text{exch}} = -2J\mathbf{S}_0\cdot\mathbf{S}_1 - 2J\sum_{i>j=1}^{4}\mathbf{S}_i\cdot\mathbf{S}_j - 2J\sum_{i>j=5}^{8}\mathbf{S}_1\cdot\mathbf{S}_j, \quad (41)$$

$$W_{\text{exch}} = -2JS_0\cdot S_1 - J\{S_1'(S_1'+1)-3\} - J\{S_1''(S_1''+1)-3\}.$$

Here S_1', S_1'' are the total spin numbers of the two groups of four atoms. The terms independent of spin can be dropped; the energies are:

$$A_p = -J\{S_1+S_1'(S_1'+1)+S_1''(S_1''+1)\},$$
$$A_{ap} = +J\{(S_1+1)-S_1'(S_1'+1)-S_1''(S_1''+1)\}. \quad (42)$$

The summation over the S_1 levels must be taken as

$$\sum_{S_1}^{4}\sum_{S_1'}^{S_1-S_1''}\sum_{S_1''}^{2} w(4,S_1')w(4,S_1'')\exp-\frac{1}{T}A_k, \quad (43)$$

with $S_1 = S_1' - S_1'' \cdots S_1' + S_1''$. The w factors are computed with (32) using $2n=4$, as indicated.

The results as shown in Table I are notable in that of the lattice types investigated only those which are three-dimensional display a critical temperature. This is in agreement with the rigorous results of the Bloch theory and, perhaps, attests the effectiveness of the present method. Also, the critical temperatures found lie between the two Heisenberg approximations, the second of which is known to overemphasize the dispersion of the energy levels. The method also takes into account in the first approximation the inter-

action inside the first shell. In this respect, it takes into account some terms which enter first in the moment method only in the third power of the energy. The critical temperature is found to be lower in the modified than in the actual body-centered lattice. The interaction inside the first shell serves merely to increase the *local* order and does not serve to increase the long-distance order.

V. THE DISCONTINUITY IN THE SPECIFIC HEAT

The discontinuity in the specific heat at the critical temperature is one of the properties of ferromagnetics through which the theory can be compared with experiment. Actually, this is complicated by the fact that it is not certain, on the basis of measurements of the specific heat, that the transformation is one of the second kind. Usually, the specific heat falls sharply on the high temperature side of the critical point but not in the fashion required for this type of transformation. This essential feature is easily obscured by non-uniformity of temperature in the samples. At any rate, the usual practice is to extrapolate back to the critical point from the high temperature side and to measure the discontinuity from this point to the maximum value of the specific heat reached on increasing the temperature from below the critical point.

The average energy of a domain of N atoms is, since there are N central atoms

$$E=\tfrac{1}{2}N(-2J)\langle S_0\cdot S_1\rangle_{Av}=\tfrac{1}{2}NJ\{\langle S(S+1)\rangle_{Av}-\langle S_1(S_1+1)\rangle_{Av}-S_0(S_0+1)\}. \quad (44)$$

The angular brackets denote ensemble averages and the factor of $\frac{1}{2}$ is inserted since otherwise the interaction energy of each pair would be counted twice. These expressions are valid for lattice types in which the atoms of the shell do not interact with each other; the modifications necessary to take such interactions into account are obvious. The numerical computation of the discontinuity in the specific heat have been carried through for the body-centered lattice for the two spin values $\frac{1}{2}$ and 1. The expression (44) agrees with the development in Section II when the specialization required by the Ising model of the spin is made: $S(S+1)$ and $S_1(S_1+1)$ are replaced by S^2 and S_1^2 respectively. The ensemble averages are, for the case of a spin value of $\frac{1}{2}$,

$$P(\langle S(S+1)\rangle_{Av}-\langle S_1(S_1+1)\rangle_{Av})=\sum_{S_1} w(2n, S_1)\times\{(S_1-\tfrac{1}{2})(S_1+\tfrac{1}{2})-S_1^2-S_1\}\sum_m \times\exp\frac{1}{T}W_1(m, S_1)+\sum_{S_1} w(2n, S_1)\times\{(S_1+\tfrac{1}{2})(S_1+\tfrac{3}{2})-S_1^2-S_1\}\sum_m \times\exp-\frac{1}{T}W_2(m, S_1). \quad (45)$$

In the neighborhood of the critical point, the field dependent parts of the exponentials can be expanded in series in H_1. To terms in H_1^2 (45) is, except for a constant term which can be dropped,

$$P(\langle S(S+1)\rangle_{Av}-\langle S_1(S_1+1)\rangle_{Av})=-\frac{1}{J}\{2P_0\epsilon_0+H^2P_3\}, \quad (46)$$

with:

$$2P_0\epsilon_0=\sum_k\sum_{S_1} w(2n, S_1)\sum_m A_k\exp-\frac{A_k}{T},$$

$$P_0=\sum_k\sum_{S_1} w(2n, S_1)\sum_m \exp-\frac{A_k}{T},$$

$$P_3=\sum_k\sum_{S_1} w(2n, S_1)\sum_m \times\left(\frac{J^2(b_k+c_k)^2}{2T^2}-\frac{J^2d_k}{T}\right)A_k\exp-\frac{A_k}{T}.$$

To this degree of approximation, the partition function P is

$$P=P_0+\frac{H^2}{J^2}P_2,$$

TABLE II. Values of the discontinuity in the specific heat at the critical temperature per atom in units of k. The computed values are all based on a spin of 1 per atom and are for a body-centered lattice.

Heisenberg approx. I	Present method	Experiment
2.00	3.40	3.6

with

$$P_2=\sum_k \sum_{S_1} w(2n, S_1) \sum_m \times\left(\frac{J^2(b_k+c_k)^2}{2T^2}-\frac{J^2 d_k}{T}\right)\exp-\frac{A_k}{T}. \quad (47)$$

The energy per atom is

$$\epsilon=\epsilon_0+\frac{1}{2}\frac{H^2}{J}\left(\frac{P_3}{P_0}-2\epsilon_0\frac{P_2}{P_0}\right), \quad (48)$$

numerical computation yields, for a spin of $\frac{1}{2}$,

$$\epsilon=\epsilon_0-(0.0498)\frac{H^2}{J}. \quad (49)$$

With the use of (35) one obtains, in this case,

$$\frac{H^2}{J}=221\left(\frac{J}{T}-\frac{J}{T_c}\right). \quad (50)$$

The discontinuity in the specific heat per atom is,

$$\Delta C/k=2.05. \quad (51)$$

The Ising model discussed in Section II yields the numerical value

$$\Delta C/k=1.71. \quad (52)$$

The computation for a spin 1 follows the same procedure. Here, however, the levels for $S=S_1$ make no contributions to the quantities ϵ_0 and P_3 in (46), so that in the summation over k, the term with $k=2$ must be omitted. One finds that

$$\left(\frac{H}{2J}\right)^2=404\left(\frac{J}{T}-\frac{J}{T_c}\right), \quad (53)$$

corresponding to (50) and

$$\epsilon=\epsilon_0-\left(\frac{H}{2J}\right)^2\cdot J(0.3740), \quad (54)$$

corresponding to (49). The discontinuity in specific heat per atom is

$$\Delta C/k=3.40.$$

The experimental data on the discontinuity in the specific heat is meager and not very consistent for iron. Stoner[9] quotes the values 3.4, 2.3, and 3.6 obtained by Weiss, Piccard, and Carrard, by Umino, and by Klinkhardt, respectively, and gives greatest weight to the value 3.6. The computed value of 3.4 compares very favorably with this. The Heisenberg first approximation leads to a value of 2.0 for $\Delta C/k$. The results are listed in Table II.

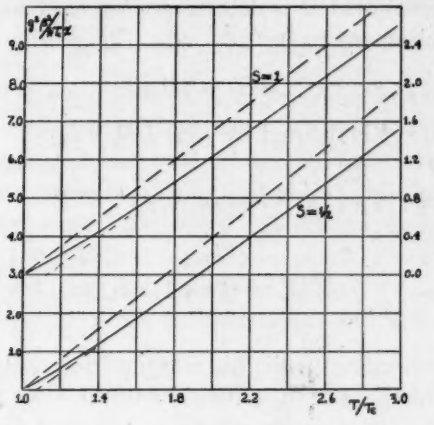

FIG. 1.

VI. THE SUSCEPTIBILITY

The internal field is zero in the temperature region above the critical temperature so long as the external field is absent. In the presence of an external field, however, the internal field is no longer zero because of the exchange interaction. It is because of this internal field that the Curie-Weiss Law is not obeyed immediately above the Curie Point. In fact, it is easily seen that the susceptibility is increased there by the exchange interactions and consequently the reciprocal of the susceptibility is decreased. Moreover, the ratio of the internal to the external field decreases with increasing temperature so that the reciprocal susceptibility *vs.* temperature curve is convex toward the temperature axis. The difference between the "paramagnetic" and "ferromagnetic" critical temperatures and the difference between the low and high temperature magneton numbers find a natural explanation in the present method.

It is legitimate to neglect saturation effects in this region and therefore the expressions for $\bar{m}_0$ and $\bar{m}_1$ as obtained from (34) need only retain first power terms in H_0 and H_1. Now, however, H_0 is not permitted to be zero. H_1 is replaced by $H_1=H_0+H$ in the expressions for $\bar{m}_0$ and $\bar{m}_1$. The

[9] E. C. Stoner *Magnetism and Matter* (Methuen and Company, Ltd., London, 1934), p. 373.

internal field H is determined by the consistency requirement to be

$$AH_0+BH=0, \tag{55}$$

where A is defined by (36) and B is

$$(2n+1)TB=\sum_{k=1}^{2}\sum_{S_1} w(2n, S_1)\sum_{m} \times\{b_k^2+(2n+1)b_kc_k\}\exp-\frac{A_k}{T}. \tag{56}$$

It is more convenient in computation to deal with the moment of the entire cluster, $\bar{m}=\bar{m}_1(2n)+\bar{m}_0$ than with the moment $\bar{m}_0$ as obtained from (34) $\bar{m}_0$ is then obtained by

$$\bar{m}_0=(1/2n+1)\bar{m}. \tag{57}$$

The susceptibility is simply $g\beta\bar{m}_0/H_0$ since saturation effects are being neglected. It is

$$\frac{1}{2n+1}\frac{X_0}{g^2\beta^2}TP_0=\sum_{k}\sum_{S_1} w(2n, S_1)\sum_{m} b_k^2 \times\exp-\frac{A_k}{T}+\frac{H}{H_0}\sum_{k}\sum_{S_1} w(2n, S_1) \times\sum_{m} b_k(b_k+c_k)\exp-\frac{A_k}{T}. \tag{58}$$

A corresponding expression is obtained when the spin per atom is 1. The computations have been carried through for the body-centered lattice for both spin values and the results are shown in Fig. 1, where $g^2\beta^2/X_0T_c$ is plotted as a function of T/T_c. The curvature is actually surprisingly small and consequently the curve could easily be taken as a straight line but with an intercept on the temperature axis different from the Curie temperature. This is called, generally, the "paramagnetic" critical temperature. In the case of a spin of $\frac{1}{2}$, the relation between the two critical temperatures is roughly $T_p\approx 1.05T_f$, the paramagnetic critical temperature is about 5 percent higher than the ferromagnetic one. For a spin 1, the curve gives $T_p\approx 1.03T_f$. If we ascribe a spin per atom of 1 for iron, this leads to a paramagnetic critical temperature which is about 30° higher than the ferromagnetic one, a value which is somewhat larger than that obtained experimentally. From the slopes of the curves, one can obtain p_B, the number of Bohr magnetons per atom. The values of p_B would be 1.73 and 2.83 for the spins $\frac{1}{2}$ and 1 respectively. The experimental value for iron[10] is higher than either of these and seems to lie between 3.5 and 4.0. The discrepancy has caused some concern, since it implies that the number of contributing spins is different in the high and low temperature regions. Some of the discrepancy is removed by the present treatment, for the values of p_B obtained from the curves are 1.87 and 3.06 for spins $\frac{1}{2}$ and 1 respectively.

VII. CONCLUSION

The method, so far as it has been applied, is seen to lead to very satisfactory results. Of the various lattice types considered, only those which are three-dimensional have been found to display ferromagnetism. This is in agreement with rigorous results of the spin-wave treatment. Moreover, in the three-dimensional lattices the critical temperature is found to lie between the two Heisenberg approximations in which the first takes no account of this dispersion of the energy about the mean value and the second overemphasizes this dispersion. The method applied to the body-centered lattice with spin 1 per atom leads to a value for the discontinuity in the specific heat of 3.40 k per atom which is in fair agreement with the experimentally determined value of 3.6 k and in far better agreement than is the value obtained by Heisenberg's first approximation. It must be remarked, however, that the method leads to a transition of the second kind at the critical temperature although this has not been established satisfactorily by experiment. Finally, the method gives some explanation of the difference between the "paramagnetic" and ferromagnetic critical temperatures as being due to the persistence of local order of the spins above the Curie Point, even though the long-distance order is zero. The difference between the high-temperature and the low-temperature magneton numbers is partly explained in the same way.

The author is indebted to Professor J. H. Van Vleck for suggesting the problem and for some discussions concerning it.

Part of this work was supported by the Rutgers

[10] See reference (9), page 379.

University Research Fund, and the Office of Naval Research.

APPENDIX

The system of representation of the Hamiltonian for a spin 1 used here is one which diagonalizes the exchange energy. When the magnetic quantum number $|m| \leq (S_1-1)$ the Hamiltonian is

$$\begin{pmatrix} A_1 & B & 0 \\ B & A_2 & C \\ 0 & C & A_3 \end{pmatrix}, \tag{59}$$

with

$$A_1=2J(S_1+1)-mH_1-\frac{m}{S_1}(H_1-H_0),$$

$$A_2=-2J-mH_1+\frac{m}{S_1(S_1+1)}(H_1-H_0),$$

$$A_3=-2JS_1-mH_1+\frac{m}{(S_1+1)}(H_1-H_0),$$

$$B=\frac{S_1+1}{S_1}\left\{\frac{S_1^2-m^2}{(S_1+1)(2S_1+1)}\right\}^{\frac{1}{2}}(H_1-H_0),$$

$$C=\frac{S_1}{S_1+1}\left\{\frac{(S_1+1)^2-m^2}{S_1(2S_1+1)}\right\}^{\frac{1}{2}}(H_1-H_0).$$

Here, as in the text, the factors $g\beta$ in the magnetic energy have been absorbed in H_0 and H_1. When $m=\pm S_1$ the matrix is of second order

$$\begin{pmatrix} A_2' & C' \\ C' & A_3' \end{pmatrix}, \tag{60}$$

with

$$A_2'=2J\mp S_1H_1\pm\frac{1}{(S_1+1)}(H_1-H_0),$$

$$A_3'=2JS_1\mp S_1H_1\pm\frac{S_1}{(S_1+1)}(H_1-H_0),$$

$$C'=\frac{1}{S_1+1}(S_1)^{\frac{1}{2}}(H_1-H_0),$$

when $m=\pm(S_1+1)$, the matrix has the one term

$$\begin{aligned} A_3''&=2JS_1\mp(S_1+1)H_1\mp(H_1-H_0) \\ &=2JS_1\mp S_1H_1\mp H_0. \end{aligned} \tag{61}$$

(59), (60), and (61) hold for all values of S_1 except $S_1=0$ and 1. When $S_1=0$, the exchange energy is zero and the total energy is only magnetic.

$$W=-mH_0, \quad m=0, \pm 1. \tag{62}$$

When $S_1=1$, there is a degeneracy in the exchange energy for the levels $S=S_1$ and $S=S_1+1$ and this case must be considered separately. S has the values 0, 1, 2 so that the Hamiltonian is of third order for $m=0$, of second order for $m=\pm 1$ and of first order for $m=\pm 2$. The energy levels can now be obtained through the fourth power terms in the field strengths and are

$$S_1=0, \qquad W=mH_0,$$

$$S_1=1, \quad m=0, \qquad W=4J+\frac{1}{9J}(H_1-H_0)^2 - \frac{1}{972J^3}(H_1-H_0)^4, \tag{63}$$

$$W=-2J\mp\frac{+1}{\sqrt{3}}(H_1-H_0) - \frac{1}{18J}(H_1-H_0)^2 \mp\frac{\sqrt{3}}{648J^2}(H_1-H_0)^3 + \frac{1}{1944J^3}(H_1-H_0)^4, \tag{64}$$

$$S_1=1, \quad m=\pm 1, \quad W=-2J\mp H_0,$$

$$W=-2J\mp H_1, \tag{65}$$

$$S_1=1, \quad m=\pm 2, \quad W=-2J\mp(H_1+H_0).$$

When $S_1>1$ the energy values are

$$\begin{aligned} W_k(S_1, m)=A_k+b_kH_1+c_k(H_1-H_0) \\ +d_k(H_1-H_0)^2+e_k(H_1-H_0)^4 \\ +f_k(H_1-H_0)^4, \end{aligned} \tag{66}$$

where

$$A_1=2J(S_1+1), \quad A_2=-2J, \quad A_3=-2JS_1, \tag{67}$$

$$b_1=b_2=b_3=-m; \quad c_1=\frac{-m}{S_1},$$

$$c_2=\frac{+m}{S_1(S_1+1)}, \quad c_3=+\frac{m}{S_1+1},$$

$$d_1=\frac{(S_1+1)}{2J(S_1+2)(2S_1+1)}\left(1-\frac{m^2}{S_1^2}\right),$$

$$d_2=\frac{1}{2J(2S_1+1)}\left\{\frac{S_1}{S_1-1}\left(1-\frac{m^2}{(S_1+1)^2}\right)-\frac{S_1+1}{S_1+2}\left(1-\frac{m^2}{S_1^2}\right)\right\},$$

$$d_3=-\frac{S_1}{2J(S_1-1)(2S_1+1)}\left\{1-\frac{m^2}{(S_1+1)^2}\right\},$$

$$e_1=+\frac{m}{4J^2S_1(S_1+2)(2S_1+1)}\left(1-\frac{m^2}{S_1^2}\right),$$

$$e_2=-\frac{m}{4J^2(2S_1+1)}\left\{\frac{1}{S_1(S_1+2)}\left(1-\frac{m^2}{S_1^2}\right)-\frac{1}{(S_1-1)(S_1+1)}\left(1-\frac{m^2}{(S_1+1)^2}\right)\right\},$$

$$e_3=-\frac{m}{4J^2(S_1-1)(S_1+1)(2S_1+1)}\times\left(1-\frac{m^2}{(S_1+1)^2}\right),$$

$$f_1=\frac{1}{8J^3(2S_1+1)(S_1+2)}\left(1-\frac{m^2}{S_1^2}\right)\times\left\{\frac{m^2}{(S_1+1)S_1^2}-\frac{(S_1+1)^2}{(S_1+2)^2(2S_1+1)}\left(1-\frac{m^2}{S_1^2}\right)+\frac{S_1(S_1+1)}{(S_1+2)(2S_1+1)^2}\left(1-\frac{m^2}{(S_1+1)^2}\right)\right\},$$

$$f_2=\frac{1}{8J^3(S_1-1)(2S_1+1)}\left(1-\frac{m^2}{(S_1+1)^2}\right)\times\left\{\frac{m^2}{S_1(S_1+1)^2}-\frac{S_1^2}{(S_1-1)^2(2S_1+1)}\times\left(1-\frac{m^2}{(S_1+1)^2}\right)\right\}+\frac{1}{8J^3(S_1+2)(2S_1+1)}\times\left(1-\frac{m^2}{S_1^2}\right)\left\{\frac{(S_1+1)^2}{(S_1+2)^2(2S_1+1)}\left(1-\frac{m^2}{S_1^2}\right)-\frac{m^2}{(S_1+2)^2(S_1+1)}\right\}+\frac{3S_1(S_1+1)}{8J^3(S_1-1)^2(S_1+2)^2(2S_1+1)^2}\times\left(1-\frac{m^2}{S_1^2}\right)\left(1-\frac{m^2}{(S_1+1)^2}\right),$$

$$f_3=\frac{-1}{8J^3(S_1-1)(2S_1+1)}\left(1-\frac{m^2}{(S_1+1)^2}\right)\times\left\{+\frac{m^2}{S_1(S_1+1)^2}-\frac{1}{(S_1-1)^2(2S_1+1)}\times\left(1-\frac{m^2}{(S_1+1)^2}\right)+\frac{S_1(S_1+1)}{(S_1-1)(2S_1+1)^2}\times\left(1-\frac{m^2}{S_1^2}\right)\right\}.$$

The summations over m where indicated are

$$\begin{aligned} m&=-(S_1-1)\cdots+(S_1-1) && \text{for } S=S_1-1,\\ m&=-S_1 \quad\cdots+S_1 && \text{for } S=S_1,\\ m&=(S_1+1) \quad\cdots+(S_1+1) && \text{for } S=S_1+1, \end{aligned}$$

and can be performed by use of (38). The entire procedure followed for a spin $\frac{1}{2}$ can be repeated for a spin 1 using the energy values given here. The multiplicities of the different S_1 levels are given by (33).

PHYSICAL REVIEW VOLUME 74, NUMBER 10 NOVEMBER 15, 1948

Theory of Rectification of an Insulating Layer

H. Y. FAN*
Research Laboratory of Electronics, Massachusetts Institute of Technology, Cambridge, Massachusetts
(Received July 9, 1948)

The problem treated is the rectification by a blocking layer of low inherent conductivity. The potential distribution is determined by the space charge due to free, current-carrying charge instead of by that due to fixed charge. The difference between this case and that treated by previous theories is pointed out. The theory is applied to copper oxide rectifiers. The result is found to agree with experimental results better than the previous theories. The applicability of the theory to other cases is also discussed.

INTRODUCTION

RECTIFICATION at the contact between different solids depends upon the existence of a blocking layer, which may be classified into two types: natural and artificial blocking layers. A natural blocking layer is one that is produced as the result of the contact. A metal and a semiconductor brought into contact may give rise to such a blocking layer in the semiconductor even when the semiconductor is homogeneous to begin with. If one of the two materials in contact has inherently a layer of different properties or if a thin layer of entirely different material exists at the boundary, then we may have an artificial blocking layer.

A conducting material in its normal state has a certain density of free charge (electrons or holes) which is balanced by an equal density of fixed charge of opposite sign. If the layer of substance playing the role of the blocking layer has a conductivity lower than its normal conductivity, then it must have a lower than normal density of free charge. This is true for all natural blocking layers. For efficient rectification the density of free charge in the blocking layer must be greatly reduced below its normal value and, therefore, becomes negligible in comparison with the density of fixed charge. The potential distribution in the blocking layer is determined by fixed space charge. We have then a simple problem of electrostatics. Most rectifier theories deal with such cases.

In the case of artificial blocking iayers the density of free charge need not be lower than its normal value. If the layer is inherently a good insulator, it may acquire a much higher than normal density of free charge when it is put in contact with two conducting materials. Mott[1] is first to treat artificial blocking layers. He assumes a straight line potential distribution neglecting space charge due to both free and fixed charges. Such an assumption cannot be a good approximation over a wide range of current. The theory of artificial blocking layers is of practical interest. A number of practical problems involve such layers. Copper oxide rectifiers are known to have near the contact a layer of much lower conductivity than that of the bulk of the oxide.[1,2] Certain oxide cathodes have been shown to possess a layer which is of different composition, has much lower conductivity, and shows rectification.[3] De Boer and van Geel[4] and Hartmann[5] have shown that a layer of good insulator (e.g., shellack, mica, sulfur) put between two conducting materials gives rise to rectification. It cannot be readily decided whether blocking layers in all these cases have higher than normal density of free charge throughout the range of operation. It is certain, however, that all artificial blocking layers have excess free charge density for large currents in the direction of easy flow. It is our purpose to treat the problem of blocking layers with excess density of free charge where the influence of the fixed charge on the potential distribution is negligible in comparison. It is immaterial for the

* On leave of absence from National Tsing Hua University, Peiping, China.

[1] N. F. Mott, Proc. Roy. Soc. **A171**, 27 (1939).
[2] W. Schottky and E. Spenke, Wiss. Veroff. Siemens-Werke **18**, 225 (1939).
[3] A. Eisenstein, Phys. Rev. **71**, 473 (1947); W. E. Mutter, Phys. Rev. **72**, 531 (1947).
[4] J. H. de Boer and W. Ch. van Geel, Physica **2**, 309 and 321 (1935).
[5] W. Hartmann, Physik. Zeits. **37**, 862 (1936).

treatment whether we have conduction by electrons or by holes. To be definite we shall assume conduction by electrons.

THEORY

Under equilibrium condition the blocking layer has a definite density of free electrons at each boundary determined approximately by the difference between the inner potential χ (energy of the bottom of the conduction band) of the layer and the work function of the material in contact at that boundary ϕ. When the work functions of the two materials in contact with the layer are different, the layer will have different densities of free electrons at the two boundaries. With a fraction of one ev's difference between the work functions the ratio of the electron densities $n_1/n_2=\exp[(\phi_2-\phi_1)/kT]$ becomes very large. It is usually assumed that the blocking layer has a constant density of free electrons at each boundary independent of the current if the material in contact is a good conductor. Actually we have the bottom of the conduction band at the boundary of the blocking layer at a constant level $(\phi-\chi)$ above the Fermi level of the conductor. This is because when two materials of different conductivities are in contact there is comparatively little potential variation in the better conducting material caused by the contact.[6] With constant $(\phi-\chi)$ the boundary density of electrons will not, however, be constant with changing current. In equilibrium the electron current crossing the boundary in either direction is the same and equal to[7]

$$en_0(kT/2\pi m)^{\frac{1}{2}},$$

where n_0 is the boundary density of electrons in the blocking layer when $i=0$. When a net current of electrons i is crossing the boundary into the blocking layer, the electron current crossing the boundary from the blocking layer is

$$en_i(kT/2\pi m)^{\frac{1}{2}},$$

where n_i is the boundary density of electrons at current i. With constant $(\phi-\chi)$ the electron current coming from the other side is the same as in equilibrium. Therefore

$$i=en_0(kT/2\pi m)^{\frac{1}{2}}-en_i(kT/2\pi m)^{\frac{1}{2}},$$
$$n_i=n_0-(i/e)(2\pi m/kT)^{\frac{1}{2}}.$$

Consequently our boundary conditions are[8]

$$\begin{aligned} n_1&=n_{10}-(i_{12}/e)(2\pi m/kT)^{\frac{1}{2}},\\ n_2&=n_{20}+(i_{12}/e)(2\pi m/kT)^{\frac{1}{2}}. \end{aligned} \tag{1}$$

For large i, n_1 reduces to zero and we have saturated emission from the conductor 1. For a given system we are given n_{10}, n_{20} and the thickness of the layer L. We can easily calculate n_1 and n_2 for each value of the current. Our problem then is to determine the potential drop across the blocking layer for given n_1, n_2, L, and i.

The Poisson equation is

$$dE/dx=(4\pi e/\kappa)n,$$

where κ is the dielectric constant of the blocking layer. We shall assume that the motion of electrons can be determined in terms of diffusion coefficient D and mobility b. In the case of natural blocking layers, sometimes the layer is so thin that it is comparable with the electron mean free path or the electric field is so high that the energy gained per mean free path is higher than the average energy exchange per collision.[9] For such cases diffusion coefficient and mobility lose their meanings. For artificial blocking layers we are not likely to have such troubles. The current is then given by

$$i=nebE-eD(dn/dx).$$

We shall take i to be the electron current and E the force on unit negative charge. Then e and b are positive and the potential is given by $V=\int Edx$. Schottky and Spenke[2] have shown that these equations can be simplified by expressing the factors involved in a system of rational units:

$$\begin{aligned} &p=n/N, \quad \gamma=i/i_0, \quad \epsilon=E/E_0,\\ &\qquad\qquad\qquad\qquad v=V/V_0, \quad \xi=x/x_0, \end{aligned} \tag{2}$$

where the unit of density of electrons N is arbi-

[6] H. Y. Fan, Phys. Rev. 62, 388 (1942).
[7] R. H. Fowler, *Statistical Mechanics* (1936), p. 347.
[8] After these results had been dreived the author came upon the work of R. G. Sachs, NDRC Div. 14 Report 129 (1942) who arrived at the same results by a more elaborate analysis.
[9] H. A. Bethe, RL Report No. 43-12 (Nov. 23, 1942).

trary and the other units are

$$\begin{aligned} i_0&=2ebN^{\frac{1}{2}}(\pi kT/\kappa)^{\frac{1}{2}},\\ E_0&=2N^{\frac{1}{2}}(\pi kT/\kappa)^{\frac{1}{2}},\\ V_0&=kT/e,\\ x_0&=(1/2e)N^{-\frac{1}{2}}(\kappa kT/\pi)^{\frac{1}{2}}. \end{aligned} \tag{3}$$

All the units depend upon the unit of density N chosen, except the unit of potential which depends upon the temperature only. We shall take N to be the smaller of the two boundary values n_1 and take the origin $x=0$ to be at this boundary. With the relation $b/D=e/kT$ the Poisson equation for current reduce to:

$$\begin{aligned} d\epsilon/d\xi&=p,\\ \epsilon p-(dp/d\xi)&=\gamma. \end{aligned} \tag{4}$$

The boundary conditions are $p=1$ at $\xi=0$ and $p=p_2=n_2/n_1$ at $\xi=L/x_0=l$. Integrating we get

$$(d\epsilon/d\xi)-(\epsilon^2/2)+\gamma\xi+\text{const.}=0, \tag{5}$$

or

$$(d\epsilon/d\xi)-(\epsilon^2/2)+\gamma(\xi+C)=0. \tag{6}$$

Let $\zeta=\xi+C$ and

$$u=\exp[-\tfrac{1}{2}\textstyle\int\epsilon d\zeta]=\exp[-\tfrac{1}{2}\int\epsilon d\xi]=\exp(-\tfrac{1}{2}v).$$

We get

$$d^2u/d\zeta^2=\tfrac{1}{2}\gamma\zeta u.$$

For $\gamma>0$, i.e., for electron current from the boundary of low electron density, $p=1$, to the boundary of high electron density, $p=p_2$, we get

$$d^2u/d\theta^2=\theta u, \tag{7}$$

where

$$\theta=\zeta[\gamma/2]^{\frac{1}{3}}=(\xi+C)[\gamma/2]^{\frac{1}{3}}. \tag{8}$$

For $\gamma<0$ it is more convenient to treat it as a current $\gamma'>0$ flowing from a boundary $p_1'=1$ at $\xi'=0$ to the boundary $p_2'=n_1/n_2$ at $\xi'=l'$. The quantities are now rationalized with $N=n_2$. Equation (7) is known as Stokes equation. When the quantities involved are all real, it is convenient to express the solution in terms of Airy integrals:

$$u=AAi(\theta)+BBi(\theta). \tag{9}$$

The values of $Ai(\theta)$ and $Bi(\theta)$ can be found elsewhere in tables.[10] The potential is given by

$$-\tfrac{1}{2}v=\ln A+\ln[Ai(\theta)+(B/A)Bi(\theta)]. \tag{10}$$

[10] *British Association Mathematical Tables* (1946), Part-Volume B.

Putting $v=0$ at $\xi=0$ we have

$$\begin{aligned} -\tfrac{1}{2}v=&\ln[Ai(\theta)+(B/A)Bi(\theta)]\\ &-\ln[Ai(\theta_0)+(B/A)Bi(\theta_0)]. \end{aligned} \tag{11}$$

The constants of integration B/A and C involved in θ and θ_0 are to be determined by the boundary values of p. The field intensity is

$$\begin{aligned} \epsilon=dv/d\xi=dv/d\zeta&=-(2/u)(du/d\zeta)\\ &=-2(\gamma/2)^{\frac{1}{3}}[[Ai'(\theta)+(B/A)Bi'(\theta)]/\\ &\qquad[Ai(\theta)+(B/A)Bi(\theta)]]. \end{aligned} \tag{12}$$

Equation (6) gives

$$p=(\epsilon^2/2)-\gamma(\xi+C). \tag{13}$$

So the boundary conditions are

$$\begin{aligned} p_1=1&=[\epsilon^2(\theta_0)/2]-\gamma C,\\ p_2=n_2/n_1&=[\epsilon^2(\theta_2)/2]-\gamma(l+C). \end{aligned} \tag{14}$$

The determination of the integration constants would involve laborious calculation. Fortunately, the properties of the functions $Ai(\theta)$ and $Bi(\theta)$ are such that for large values of v a great simplification results. Since the unit of v, kT/e, is very small, we shall be interested primarily in large values of v. The details of the method of calculation are given in the appendix.

The solution (7) is inapplicable for $\gamma=0$ because then we cannot go from (5) to (6). Equation (5) can in this case be written

$$d\epsilon/d\xi=(\epsilon^2/2)+(\kappa^2/2). \tag{15}$$

The solution is obtained by straightforward integration:

$$\begin{aligned} \epsilon&=\kappa\tan(\kappa/2)(\xi+\kappa_1),\\ p&=\kappa^2/2\cos^2(\kappa/2)(\xi+\kappa_1). \end{aligned} \tag{16}$$

The integration constants are determined by boundary values of p:

$$\begin{aligned} \cos^2(\kappa\kappa_1/2)&=\kappa^2/2,\\ \cos^2(\kappa/2)(l+\kappa_1)&=\kappa^2/2p_2. \end{aligned} \tag{17}$$

For comparison with experimental results, the slope of v *versus* γ curve at $\gamma=0$ is often important. This resistance can be calculated in the following manner. From the second of the general equations (4) we get, upon integration,

$$v=\gamma\int_0^l(d\xi/p)+\ln(p_2/p_1).$$

It follows that

$$dv/d\gamma=\int_0^l d\xi/p. \tag{18}$$

To obtain $dv/d\gamma$ at $\gamma=0$ we have only to use (16) for p in the integrand.

APPROXIMATE SOLUTION

When the current due to diffusion is very small compared with the current due to the field, $|dp/d\xi|\ll|\epsilon p|$, this term can be neglected in (4) and (5) becomes

$$\epsilon^2/2=\gamma\xi+\text{const.} \tag{19}$$

Denoting the boundary value of electron density at $\xi=0$ by p_0, we get

$$\begin{aligned}&\epsilon=[2\gamma\xi+(\gamma/p_0)^2]^{\frac{1}{2}},\\ &p=\gamma[2\gamma\xi+(\gamma/p_0)^2]^{-\frac{1}{2}},\\ &v=(\gamma^{\frac{1}{2}}/3)[(2l+(\gamma/p_0^2))^{\frac{1}{2}}-(\gamma/p_0^2)^{\frac{1}{2}}].\end{aligned} \tag{20}$$

This is essentially the solution given by Mott and Gurney.[11] They also pointed out that for

$$\gamma/p_0^2\ll 2l \quad\text{or}\quad \gamma\ll 2lp_0^2, \quad \gamma=(9/8)(v^2/l^3); \tag{21}$$

for

$$\gamma/p_0^2\gg 2l \quad\text{or}\quad \gamma\gg 2lp_0^2, \quad \gamma=vp_0/l. \tag{22}$$

We note that the solution contains only one boundary value of p, i.e., the boundary from which the electrons flow. As is shown in the appendix, for large v the influence of p at the end boundary on v becomes small. The approximate solution will thus be expected to apply for large v. In fact, comparing (19) and (5) we see that the approximate solution will apply if

$$\epsilon^2\gg d\epsilon/d\xi. \tag{23}$$

Mott and Gurney taking for the average value $d\epsilon/d\xi\sim\epsilon/l$ get from (23) the following condition for the applicability of the approximate solution:

$$v\sim l\epsilon\gg 1. \tag{24}$$

This condition may be too lenient since, strictly speaking, (23) should be true for all ξ. On the other hand, for the assumption and the result of the approximate solution to be consistent, we should have, by substituting (20) into (23),

$$[2\gamma\xi+(\gamma/p_0)^2]^{\frac{1}{2}}\gg\gamma. \tag{25}$$

This will be true for all ξ if it holds for $\xi=0$, i.e.,

$$\gamma\gg p_0^{\frac{1}{2}}. \tag{26}$$

This condition may be too stringent. If l is not too small, then for very large p_0 (25) may be satisfied for most part of the layer even though (26) is not satisfied. Let us denote $\gamma c_1=p_0^{\frac{1}{2}}$ and $\gamma c_2=2lp_0^2$. Provided (24) is satisfied, we may expect that for $\gamma<\gamma c_1$ (20) may not be good approximation, for $\gamma c<\gamma\ll\gamma c_2$ the solution should be closely represented by (21) and for $\gamma>\gamma c_1$ and $\gamma\gg\gamma c_2$ the relationship between the current and the potential drop should be very nearly a straight line (22).

RESULTS OF CALCULATION

Figures 1 and 2 show the calculated electron density p, electric intensity ϵ and potential drop

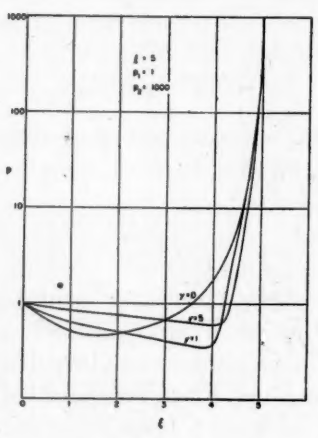

FIG. 1.

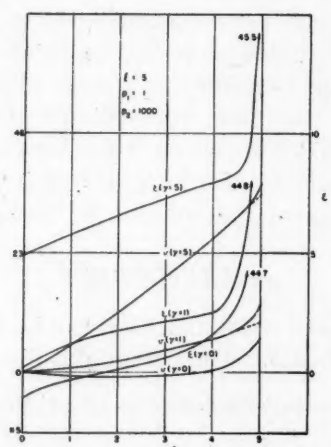

FIG. 2.

[11] N. F. Mott and R. W. Gurney, *Electronic Processes in Ionic Crystals* (1940).

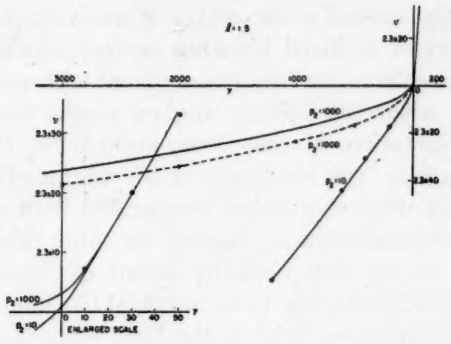

FIG. 3.

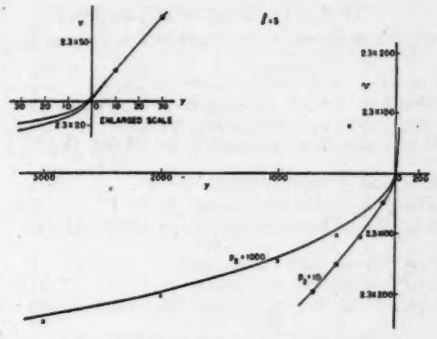

FIG. 4.

v for the equilibrium condition, $\gamma=0$, and for two values of current, $\gamma=1$ and $\gamma=5$, flowing in the direction from the boundary of $p_1=1$ to the boundary $p_2=1000$. It is seen that as the current increases, large p, due to its large value at the boundary toward which the electrons are flowing, is restricted to a smaller and smaller region. For currents in the reverse direction we will have just the opposite situation. For large currents, when the approximate solution becomes justified, the electron density over most part of the layer depends only upon its value at the initial boundary. This is basically the cause of rectification in this model. The field intensity at the initial boundary may be negative for small currents (see curve for $\gamma=0$). It becomes positive for large currents and will increase with current. It will, however, always be the lowest in the whole layer because $d\epsilon/d\xi=p>0$. The sharp rise of ϵ at the end boundary is required to balance the large gradient of electron density in this region. Although it may be quite large even at $\gamma=0$, it increases very slowly with current. The potential is not greatly affected by the sharp rise of ϵ at the end boundary as this is restricted to a small distance.

Figures 3, 4, and 5 show the relationship between current and potential drop in the blocking layer. These curves are calculated for constant p_1 and p_2. The more correct boundary conditions (1) can be written

$$p_1=1-\gamma\pi b n_{10}^{\frac{1}{3}}(2m/\kappa)^{\frac{1}{3}},$$
$$p_2=p_{20}+\gamma\pi b n_{10}^{\frac{1}{3}}(2m/\kappa)^{\frac{1}{3}}, \qquad (27)$$

taking $N=n_{10}$. When the values of n_{10} and n_{20} are known, we have no difficulty in applying these boundary conditions. In the discussion of copper oxide rectifiers below we shall see when the variations in p_1 and p_2 become important in an actual case. For not too large γ when p_1 and p_2 are approximately constant we have general curves for different values of p_2/p_1 independent of the absolute value of n_{10}. Curves of Figs. 3–5 are so calculated. They show general characteristics under this approximation. In interpreting these curves it should be borne in mind that the values of l and γ are relative only since their units depend upon n_1. The values of v are definite for a given temperature, its unit being kT/e. It should also be pointed out that v is the potential drop across the layer. The applied voltage is $v_{ap.}=v-v_{\gamma=0}$. The values of $v_{\gamma=0}$ is $\ln(p_2/p_1)$, thus for $p_2/p_1=1000$, $v_{\gamma=0}=6.9$.

It is interesting to compare these curves with the approximate solution (20). The values of γc_1 and γc_2 for these curves are given in Table I. We see from this table that in all three figures the curves for the direction of high resistance

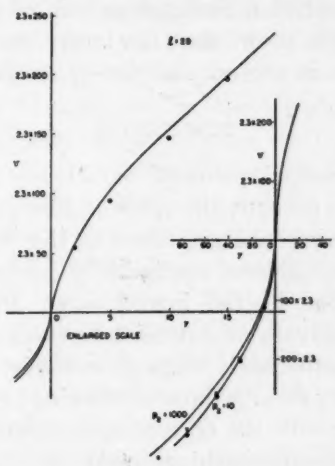

FIG. 5.

TABLE I. Values of γc_1 and γc_2.

Fig.	Curve		γc_1	γc_2
	Direction of high resistance		1	3
3	Direction of low resistance	p_2 10	31.6	300
	Direction of low resistance	p_2 1000	31600	3×10^6
	Direction of high resistance		1	10
4	Direction of low resistance	p_2 10	31.6	1000
	Direction of low resistance	p_2 1000	31600	10^7
	Direction of high resistance		1	40
5	Direction of low resistance	p_2 10	31.6	4000
	Direction of low resistance	p_2 1000	31600	4×10^7

should agree well with the approximate solution. The points shown by circles in the enlarged plots are calculated by using (20). We see that they actually check well with the curves. Most of the curves in Figs. 3 and 4 are for $\gamma>\gamma c_2$; they are accordingly approximately straight lines with slopes $l/p_0=l$. The curve in Fig. 5 approximates the square law (21) since it is in the range $\gamma c_1<\gamma<\gamma c_2$ for the most part. In the direction of low resistance the approximate solution should hold for the curves $p_2=10$. Points calculated by using (20) are shown by circles. They do agree well with the curves. According to Table I, solution (20) may not be good approximation for the curves $p_2=1000$. The points calculated according to (20) are shown by crosses. The agreement with the corresponding curves are not very good. In the case of Fig. 3 the deviation is quite large.

It is interesting to note that according to (22) for sufficiently large currents the ratio of resistances in the two directions becomes p_2/p_1, independent of l. But comparison of the calculated curves shows that the larger the thickness the poorer is the rectification at small voltages.

DISCUSSION

The essential point of our theory is that it takes into account the space charge due to current carrying charge, whereas the fixed space charge is considered negligible in comparison. As pointed out in the introduction, this theory should apply to all artificial blocking layers, at least for sufficiently large currents in the direction of easy flow. A natural blocking layer should disappear with the current approaching infinity (resistance approaching zero) as the applied voltage approaches $(kT/e)\ln(n_2/n_1)$,[2] which is usually around a few tenths of one volt. Mott's theory of artificial blocking layers,[1] which likewise neglects the free space charge, also predicts that when the voltage applied to the layer in the direction of easy flow approaches $(kT/e)\ln(n_2/n_1)$, "the resistance of the contact (layer) should drop to a value comparable with a slab of the semiconductor having the same thickness and should thus be independent of the field." Mott was referring to an artificial blocking layer of the same material as the bulk semiconductor only with fewer impurity centers; i.e., the density of free charge carriers n_2 of the blocking layer at the boundary with the semiconductor is the same as the normal n_0 of the bulk semiconductor. If the layer is of a different material, the n_2 is not necessarily the same as n_0, but the conclusions of this theory will be essentially the same: when voltage applied in the direction of easy flow approaches $(kT/e)\ln(n_2/n_1)$ the resistance of the blocking layer should drop to a value corresponding to the normal resistance of a slab of material, with free charge carrier density n_2, having the same thickness as the layer, and should thus be independent of the field. According to our theory the resistance of the layer should also reach such a stage as is shown by (22), but not necessarily at $V_{ap.}=(kT/e)\ln(n_2/n_1)$, which is only a fraction of a volt. Equation (22) becomes valid only when $\gamma\gg2lp_0^2$. In fact, all our curves for $p_2=1000$ in Figs. 3–5 cover ranges of γ far below $2lp_2^2$, although the voltages reached are considerably above $(kT/e)\ln1000$ (0.175 volt at room temperature); as high

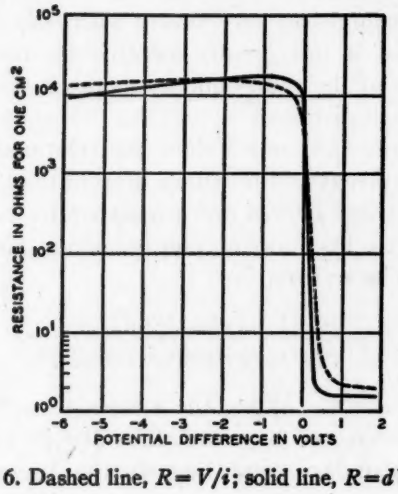

FIG. 6. Dashed line, $R=V/i$; solid line, $R=dV/di$.

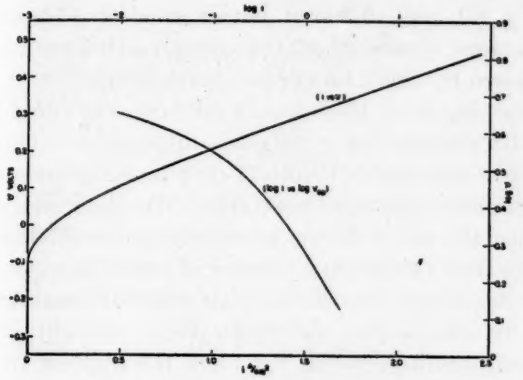

FIG. 7.

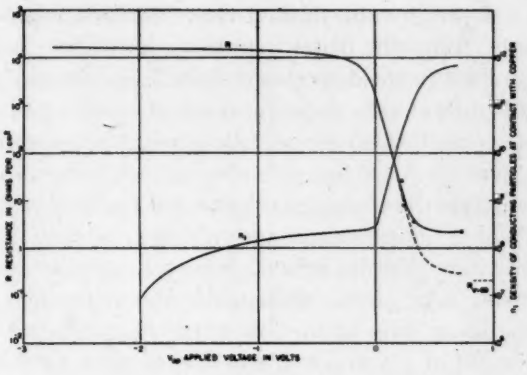

FIG. 8.

as $800kT/e$ in Fig. 5. This essential difference between the results of our theory and those of previous theories brings out the effect of the free space charge.

Thermionic oxide cathodes with coating consisting of BaO and nickel core containing a small percentage of Si have been found to form a layer of Ba_2SiO_4 between the core and the coating,[3] having a much higher resistivity than the coating. Such a layer exhibits rectification.[12] In the direction of easy flow for voltages as high as several hundred volts across the layer (interface), its resistance continues to decrease. Such behavior cannot be explained by the previous theories but can be understood in the light of our theory.

Copper oxide rectifiers have been found to have a high resistance layer near the contact due smaller concentration of excess oxygen near the contact than in the bulk oxide. This is a case for the application of our theory. Figure 6 reproduces the data given by Brattain.[13] The capacity C is given to be of the order of 2×10^{-2} microfarad/cm^2. From this the thickness of the blocking layer can be estimated:

$$L=k/4\pi C=5.3\times10^{-5}\text{ cm},$$

taking $\kappa=12$.[2] The curve shows that for the direction of high resistance the resistance becomes practically constant for $V\sim1$ volt (dashed curve). This, in the light of our theory, is the value given by (22). In terms of ordinary units

$$R_1=L/ebn_1.$$

Taking $b=80$ cm^2/sec. volt[1] and $R=1.5$ ohm for one cm^2 from the curve, we get $n_1=2.83\times10^8$ cm^{-3} at the contact with copper. The value of n_2 at the other boundary will be the same as that of the bulk oxide, the resistivity of which is given to be of the order $\rho=2\times10^3$ ohm cm. In terms of units rationalized with respect to n_1 the thickness is $l=2.22\times10^{-3}$. We shall take $n_1=3\times10^8$ per cm^3, $n_2=3\times10^{13}$ per cm^3 and $l=3\times10^{-3}$. These values give $L=7.16\times10^{-5}$ cm, $R_1=1.87\times10^4$ ohm for one cm^2 and $\rho=2.98\times10^3$ ohm cm.

The resistance at zero applied voltage, $V_{ap.}=0$, is calculated by using (18). It comes out to be 1.63×10^3 ohm for one cm^2. Referring to the experimental curve (Fig. 6) we see that this is of the correct order of magnitude. This result is reassuring. The relationship between current and potential drop across the layer for the direction of low resistance is calculated by the rigorous solution (11). Figure 7 gives the calculated curves of i *versus* V and log$i$ *versus* log$V$. It would be interesting to carry the calculation to smaller values of i, especially for the logarithmic plot. Unfortunately, we are limited by the range of the table of Airy integrals, for the direction of high resistance (20) is used for the calculation. This should be good approximation for the range covered (for $v>\ln(n_2/n_1)$ or $V_{ap.}>(kT/e)\ln(n_2/n_1)=0.292$ volt). Figure 8 gives the semilogarithmic plot of the calculated resistance of the rectifier against the applied voltage. A constant resistance of two ohms per cm^2 corresponding to the resistance of the bulk oxide, as estimated from the experimental curve, is added to the calculated resistance of the layer itself, which,

[12] W. E. Mutter, Quarterly Progress Report, Research Laboratory of Electronics, M.I.T. (April, 1947).
[13] W. H. Brattain, Bell. Lab. Record 19, 153 (1941).

as shown by the dashed curve, differs appreciably from the total resistance only for large currents in the direction of easy flow. Comparing this curve with the experimental curve (dashed curve in Fig. 6) we see the general satisfactory agreement. In the direction of low resistance, which is the important region for the test of our theory, the calculated curve drops too fast. The previous theories would, however, give an even faster drop, since they make the resistance of the layer drop to the low value $R_{V=\infty}$ (shown in Fig. 8) at a voltage $V\sim(kT/e)\ln(n_2/n_1)=0.292$ volt. In fact, the slope of our calculated curve R at $V_{ap.}=0$ corresponds to

$$d\ln R/dV=(1/1.91)(e/kT),$$

where Mott's theory gives at $V_{ap.}=0$

$$d\ln R/dV=e/kT.$$

Thus our theory gives better agreement with experiment than the previous theories. The remaining discrepancy may be due partly to some error in the choice of constants for the calculation. The thickness of the layer is determined from the given representative value of the capacity. The actual value may vary from specimen to specimen. Furthermore, the capacity really gives a measure of only a part of the blocking layer, which has low charge density. Only with sufficient voltage applied in the blocking direction will the low charge density extend to almost the whole of the layer (see Fig. 1). Therefore, depending upon how it is measured, the capacity may correspond to a much smaller thickness than the true thickness of the layer. Still there may be other more fundamental causes for the discrepancy between theory and experiment, such as non-uniformity of the blocking layer as suggested by Mott.[1]

Our curves are calculated for constant n_1 and n_2. More accurate calculation should take into account their variations according to (1). Actually the current values for the range calculated makes little change in n_2. But n_1 should change according to the curve shown in Fig. 8. Although in the direction of low resistance n_1 varies greatly, the ratio n_2/n_1 remains sufficiently large for the effect of this variation on the results of calculation to be small. For the direction of high resistance n_1 remains sensibly constant up to $V_{ap.}\approx 1$ volt. Then it begins to drop. The resistance should then rise steeply. However, as shown by Mott for copper oxide rectifiers with a blocking layer thickness of 10^{-4} cm, the effect of mirror-image force becomes appreciable at applied voltages ~ 1 volt. This effect increases n_1 and decreases the resistance. We shall not go into the effect of the mirror-image force which has been treated in a number of previous works.[14]

Schottky[15] has shown that selenium rectifiers with evaporated electrodes show straight line relationship between $1/C^2$ and the applied voltage, which indicates according to his theory uniformity of impurity (Störstellen) concentration or the absence of artificial blocking layers. According to the same author selenium rectifiers with electrodes deposited by cathode sputtering have layers (of the order of 3×10^{-5} cm in thickness) of reduced impurity concentration. For such cases our theory should apply, at least when the voltage applied in the forward direction approaches $(kT/e)\ln(n_2/n_1)$.

In conclusion we wish to point out that besides the various existing cases of application of our theory, of which copper oxide rectifiers have been discussed in detail, there is the possibility of development of rectifiers with an artificial insulating layer between two good conductors. Such rectifiers should have certain advantages, as pointed out by Torrey and Whitmer (see reference 14, p. 70). Our theory will be helpful for such development.

APPENDIX

The functions $Ai(\theta)$ and $Bi(\theta)$ are oscillatory for $\theta<0$. Only for $\theta>0$ do we get large values of v. For $\theta>0$ the function $Ai(\theta)$ decreases toward zero and $Bi(\theta)$ increases continuously. For $v>0$ we have

$$Ai(\theta_2)+(B/A)Bi(\theta_2)<Ai(\theta_0)+(B/A)Bi(\theta_0),$$

$$(B/A)[Bi(\theta_2)-Bi(\theta_0)]<Ai(\theta_0)-Ai(\theta_2)<Ai(\theta_0).$$

Since $Bi(\theta)$ increases very fast with θ we have

$$Bi(\theta_2)\gg Bi(\theta_0),$$
$$\therefore\ (B/A)Bi(\theta_2)<Ai(\theta_0),$$
$$(B/A)Bi(\theta_0)\ll Ai(\theta_0).$$

[14] H. C. Torrey and C. A. Whitmer, *Crystal Rectifiers* (1948).

[15] W. Schottky, Zeits. f. Physik **118**, 539 (1942).

Equation (13) can be written:

$$p=2(R^2-\theta)[\gamma/2]^{\frac{1}{2}},$$

where

$$R=u'/u.$$

From the condition at the initial boundary $R_0\cong Ai'(\theta_0)/Ai(\theta_0)$ can be easily calculated. θ_0 can be found then from the table. For the end boundary, $\theta_2=\theta_0+l[\gamma/2]^{\frac{1}{2}}$, we can similarly calculate $R_2=u'(\theta_2)/u(\theta_2)$ from p_2. Since

$$u'(\theta_2)/u(\theta_2)=[Ai'(\theta_2)+(B/A)Bi'(\theta_2)]/[Ai(\theta_2)+(B/A)Bi(\theta_2)],$$

taking the values of $Ai(\theta_2)$, $Ai'(\theta_2)$, $Bi(\theta_2)$, and $Bi'(\theta_2)$ from the table, the value of B/A is readily calculated. The term involving B/A is significant only in the immediate neighborhood of the end boundary. It serves to adjust the boundary value of p. Since it becomes negligible for small values of $\Delta\theta=\theta_2-\theta$ a large p_2 results only in a sharp rise of p near the very boundary. The density of electrons over most of the layer is not much affected by the value of p_2 (all this is for large v). The dashed lines joining the curves of v at the end boundary in Fig. 2 is calculated by neglecting the term involving B/A. We see that for $v>40$ neglecting this term will involve little error.

PHYSICAL REVIEW VOLUME 74, NUMBER 10 NOVEMBER 15, 1948

On the Theory of Vacancy Diffusion in Alloys

FREDERICK SEITZ
Carnegie Institute of Technology, Pittsburgh, Pennsylvania

(Received July 12, 1948)

The theory of diffusion in alloys is discussed on the basis of the migration of lattice vacancies in an attempt to interpret the experiments of W. A. Johnson on diffusion in gold-silver alloys. It is assumed that the lattice network preserves its identity during the diffusion even though there is a resultant vacancy current passing through any region. It is also assumed that two types of atom, designated as A and B atoms, are present in the lattice. The diffusion coefficients are expressed in terms of a function $p(n_{a1}, n_{a2})$ giving the probability that a vacancy in jumping from one atomic plane (designated as plane 2) to a neighboring plane (designated as plane 1) will interchange places with an A atom if there are n_{a1} A atoms per unit area of plane 1 and n_{a2} A atoms in plane 2. It is found that the chemical diffusion coefficient is related to the function p in a very different way from the diffusion coefficients for radioactive tracers if the latter migrate when no chemical gradient is present. Models of increasing complexity are employed to derive explicit expressions for the function p. It is found that Johnson's experiments can be explained only with the use of models that are more complex than those commonly used. The theory of vacancy diffusion is also employed to interpret the experiments of Smigelskas and Kirkendall concerning the relative displacement during diffusion of fiducial markers placed at the interface between copper and brass. An experiment which could provide an absolute test for vacancy diffusion is proposed.

I. INTRODUCTION

THE experiments of W. A. Johnson[1] on the diffusion in 50–50 gold-silver alloys have raised an interesting question concerning the theory of diffusion in alloys. Johnson investigated the rate at which radioactive silver and gold atoms diffuse in the alloy as well as the rate at which a minor gradient in composition is made uniform. The system studied is rather an ideal one because the constituent atoms combine substitutionally over the entire range of composition in the face-centered cubic system and do not seem to exhibit the development of long range order at particular compositions, as in the copper-gold system. The specimens on which measurements were made contained planar gradients of the diffusing atoms, so that only one Cartesian variable enters in the diffusion equation.

Figure 1 shows the measured diffusion coefficients when plotted as functions of temperature. As is conventional in the field, the logarithm of the diffusion coefficient is plotted as a function of the reciprocal of the absolute temperature. The upper curve represents D_c, the diffusion coef-

[1] W. A. Johnson, Trans. A.I.M.M.E. 147, 331 (1942).

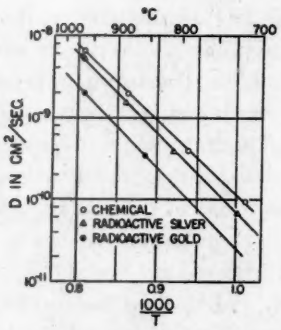

FIG. 1. The diffusion coefficients in the 50–50 silver-gold system (after Johnson). D_c is the chemical diffusion coefficient; D_{Ag} and D_{Au} are the coefficients for diffusion of radioactive tracers of silver and gold measured in a system in which there is no chemical gradient. The logarithm of the diffusion coefficient is plotted as a function of the reciprocal of the absolute temperature.

ficient that governs the rate at which a gradient in chemical composition is smoothed. In determining this Johnson used in conjunction specimens of two alloys in the 50–50 range of composition having about 14 percent of difference in concentration of the constituents. The second and the lowest curves depict the diffusion coefficients for migration of radioactive silver and gold, respectively. The coefficients were measured by using pairs of specimens which had identical chemical composition; however, one member contained a radioactive tracer.

Johnson found that the best straight lines which would fit the experimental points corresponded to the relations:

$$\begin{aligned} D_c &= 0.14 \exp(-41{,}700/RT) \text{ cm}^2/\text{sec.}, \\ D_{Ag} &= 0.39 \exp(-44{,}700/RT) \text{ cm}^2/\text{sec.}, \\ D_{Au} &= 0.12 \exp(-44{,}100/RT) \text{ cm}^2/\text{sec.} \end{aligned} \quad (1)$$

The activation energies appearing in these equations are expressed in cal./mole. R is the gas constant. The fact that the activation energies are not quite equal implies that the best straight lines passing through the points of Fig. 1 are not quite parallel.

If we were to assume that all three activation energies actually are equal, and arbitrarily chose the common value to be that for gold, namely, 44,100 cal./mole, the corresponding functions would be

$$\begin{aligned} D_c &= 0.41 \exp(-44{,}100/RT), \\ D_{Ag} &= 0.30 \exp(-44{,}100/RT), \\ D_{Au} &= 0.12 \exp(-44{,}100/RT). \end{aligned} \quad (2)$$

Thus the measured value of D_c is approximately 1.4 times larger than the value of D_{Ag} and approximately 3.5 times larger than D_{Au}. It is evident from Fig. 1 that this conclusion is quite independent of the question of whether the activation energies are equal or slightly different.

It is difficult to visualize, at first glance, the circumstances which might make it possible for the chemical diffusion coefficient to be larger than those for radioactive tracers, yet it is not apparent that this could not be the case. This topic has been discussed by several investigators,[2] most notably Darken.[3]

Darken has assumed that each atomic constituent of the lattice has its own characteristic diffusion coefficient and that the structure manages by an unspecified form of mass motion to keep the density of atoms per unit volume constant in spite of the fact that one type of atom may be diffusing in or out of a given region of the specimen more rapidly than other atoms diffuse out of or into it. If, for example, the system is a binary alloy and if A atoms are diffusing out of a given volume more rapidly than B atoms diffuse into it, the volume would contract in such a way as to maintain constant density. This type of contraction or expansion would impart a material velocity v to any atom or object in the lattice which does not participate in the diffusion. Since the local velocity of flow must be such as to compensate for the net difference in flow of atoms by diffusion, Darken is able to relate the velocity v to the diffusion currents. If D_a and D_b are the diffusion coefficients for the two constituent atoms, the velocity of flow at a given point in the specimen is

$$v = (D_a - D_b)\frac{\partial f_a}{\partial x}, \quad (3)$$

where f_a is the fractional concentration of A atoms. It is assumed that the concentration gradient is along the x axis. The axis of reference is chosen so that the velocity vanishes at regions of the specimen where the concentration gradient

[2] C. E. Birchenall and R. F. Mehl, Trans. A.I.M.E. 171 (1947); J. C. Fisher and J. H. Hollomon, Metals Tech., Tech. Pub. 2344 (1948).

[3] L. S. Darken, Metals Tech., Tech. Pub. 2311 (1948).

is zero. Darken's diffusion equation is

$$\frac{\partial f_a}{\partial t}=\frac{\partial}{\partial x}\left[(f_aD_a+f_bD_b)\frac{\partial f_a}{\partial x}\right], \tag{4}$$

so that

$$D=(f_aD_a+f_bD_b) \tag{5}$$

plays the role of the chemical diffusion coefficient.

The key assumption of Darken's treatment is that the metal can swell or shrink in a more or less plastic manner to compensate for unbalanced diffusion, maintaining constant atomic density thereby. If diffusion occurs by the migration of vacancies in the alloys of interest, it is conceivable that shrinking could occur by condensation of vacancies in a local region to form small plate-like voids which draw themselves together and disappear by inducing plastic flow in the surrounding metal in much the way that voids can be closed by pressing a ductile substance. In a polycrystalline mass the vacancies could "condense" at grain boundaries. If diffusion occurred by migration of interstitial atoms, a swelling could be induced in a region by precipitation of interstitial atoms which have diffused to the volume. The precipitate might induce a plastic expansion to compensate almost exactly for the volume of precipitated matter.

In tentative support of his viewpoint, Darken calls attention to a very interesting set of experiments of Smigelskas and Kirkendall.[4] These investigators studied the migration of the boundary between 70–30 alpha-brass and copper. An accurately shaped rectangular bar of brass was plated with a thick coating of copper on all four lateral surfaces in such a way that a number of small molybdenum wires were imbedded at the interface between the metals. It was found that after diffusion had been allowed to take place the spacing between wires on opposite rectangular faces was smaller than before diffusion by a much larger amount than could be accounted for by normal change of lattice parameter with composition. The change in spacing when plotted as a function of the square root of the time of diffusion is shown in Fig. 2. Smigelskas and Kirkendall noted that the original boundary between the two metals was clearly marked by nonmetallic inclusions which, like the molybdenum wire, presumably did not enter into the diffusion process. These inclusions moved with the molybdenum wire. The experiments also show that the amount of zinc on the copper side of the boundary after diffusion is greater than the amount of copper that has diffused into the brass side by just about the amount needed to explain the contraction if the atomic density remained constant.

From Darken's viewpoint, Smigelskas and Kirkendall's results are to be explained by assuming that zinc diffuses out of the brass more rapidly than copper diffuses into it. In consequence, the brass core shrinks in the manner described above, pulling the molybdenum wires and other fiducial marks at the initial grain boundary with it. Darken has shown that his equations give an adequate description of the effect if proper values for the diffusion coefficients for copper and zinc are assumed.

The purpose of the present paper is to attempt to shed more light on Johnson's experiments with the use of a more explicit mechanism of diffusion than that employed by Darken. It will be assumed that all of the measurable mobility in the silver-gold alloy is the result of vacancy diffusion, that is, that a given atom can move from one site to another only when a vacant lattice site appears among its neighbors and the given atom jumps into this vacant neighboring position. The calculations of Huntington[5] and

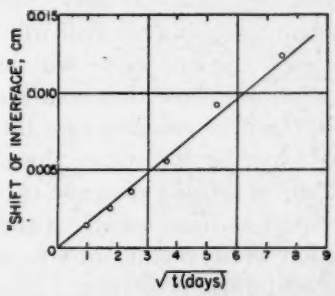

FIG. 2. The contraction of the region within the fiducial markers of molybdenum in the experiments of Smigelskas and Kirkendall. The contraction is plotted as a function of the square root of the time.

[4] A. D. Smigelskas and E. O. Kirkendall, Trans. Am. Inst. Min. Met. Eng. **171**, 130 (1947). The earliest experiments of this type of which the writer is aware were carried out by W. Shockley in 1938. Shockley observed a displacement of the type found by Smigelskas and Kirkendall.

[5] H. B. Huntington and F. Seitz, Phys. Rev. **61**, 315, 325 (1942).

the writer on this topic for the case of copper seems to leave little doubt that the vacancy mechanism is strongly preferred over the "direct interchange" or interstitial diffusion mechanisms, at least in the case of the metals having large inner shells. In any case, the vacancy mechanism is at least as complex as the other two and hence should permit as intricate processes as the other two. In fact it offers a greater range of permissible phenomena than the direct interchange mechanism, since the latter does not permit a net flow of atoms across any boundary.

We shall see that it actually is possible to envisage a model in which the chemical diffusion coefficient is larger than the diffusion coefficients for radioactive tracers. On the other hand, it is not possible to explain Johnson's results with the more obvious models of a binary alloy that might be employed to simulate an actual case.

To simplify the situation we shall assume that the concentration gradient, whether a chemical gradient or that of a tracer, depends only on one Cartesian variable which will be taken to be the x coordinate. Without loss of generality we may also assume that well defined crystallographic planes separated by distance λ lie normal to the x axis. Since we shall be primarily interested in cases of very high symmetry, we shall assume that neighboring crystallographic planes of this well defined type are symmetrically equivalent, that is, can be sent into one another by means of one of the symmetry elements of the lattice.

Whenever we discuss a practical diffusion experiment, it will be assumed that the specimen consists of two halves which individually have uniform concentration at start; however, the initial concentration in each half will differ. The two halves of the specimen will meet at an essentially infinite plane that coincides with the plane $x=0$. It will be assumed that the specimens extend for a very large distance along the x axis, so that all surfaces other than the two in contact can be treated as if at infinite distance. If the concentration of migrating atoms satisfies the conventional diffusion equation

$$\frac{\partial c}{\partial t}=\frac{\partial}{\partial x}D\frac{\partial c}{\partial x}, \tag{6}$$

the solution appropriate to the boundary conditions described above for the hypothetical experimental specimen consisting of two infinite halves in planar contact is

$$c(x,t)=c_1+\frac{(c_2-c_1)}{(\pi)^{\frac{1}{2}}}\int_{-\infty}^{x/2(Dt)^{\frac{1}{2}}}\exp(-\alpha^2)d\alpha, \tag{7}$$

when D is a constant. Here c_1 is the initial uniform concentration ($t=0$) for the half of the specimen lying on the negative side of the x axis, and c_2 is the initial concentration on the positive side of the axis. This solution depends on x and t only through the combination x^2/Dt, a fact which remains valid in the case of planar symmetry even when D in (6) is a function of concentration.

II. THE DIFFUSION CURRENTS

Let us designate the chemical species present in the alloy by A and B, and assume that in any given crystallographic plane there are n_aA atoms and n_bB atoms per unit area. If there are n atomic sites per unit area of the plane we shall have the relation

$$n_a+n_b+n_v=n, \tag{8}$$

where n_v is the number of vacant sites per unit area. We shall assume that n_v is very small compared to n_a and n_b, so that the relation

$$n_b=n-n_a \tag{9}$$

can be used to determine the density of B atoms from the density of A atoms if the latter is given. This assumption is justified by the fact that the density of vacant lattice sites is probably small even at the melting point. The calculations for copper indicate that the energy required for formation of a vacancy is of the order of 1.8 ev. In any case the fraction of vacant sites probably is not larger than 10^{-3} at the melting point in the metals of interest to us.

Let us focus attention on a region of the alloy in which there is a small gradient in concentration of A atoms (and hence of B atoms) or a gradient in a radioactive tracer. We shall assume that there is a uniform current of vacancies through this region, the direction of flow being the same as the direction of the concentration gradient, namely, the x direction. The mobility of vacancies is so much greater than the mobility of atoms

that a concentration gradient in vacancies that exists in a specimen in which diffusion is being studied will tend to decrease much more rapidly than a concentration gradient in the distribution of atoms. As a result, the vacancy current which exists in any region of the specimen after a period of time will be the result of flow of vacancies from relatively widely separated regions in which differences in concentration exist. In this connection it is to be noted that when two specimens of an alloy, which are individually uniform but contain slight differences in composition, are brought together the thermodynamic potential of the vacancies in each specimen will be equal if the specimens are individually at equilibrium. As a result there would be, at least initially, no reason for a vacancy current to flow. As the chemical diffusion takes place there may be a tendency for vacancies to diffuse to or away from the zone in which chemical interdiffusion has occurred, because the equilibrium density of vacancies in this region may be different from the density which existed there initially. This flow will presumably be small because the total number of vacancies involved will be small if the zone of interdiffusion is small. It seems safe to conclude that a large vacancy current will be present only if the vacancies are not at equilibrium initially in one or both halves of the specimen, in which case there will be a stream of vacancies moving through a large part of the system.

Consider two neighboring crystallographic planes which are normal to the x axis. We shall call the plane on the negative side number 1 and the plane on the positive side number 2 (Fig. 3). The density of A atoms in each plane will be designated by n_{a1} and n_{a2}. Now suppose that ν_{12} vacancies are jumping from plane 1 to plane 2 per unit area in unit time, and that a number ν_{21} are jumping in the reverse direction. The vacancy current in the positive x direction will then be $\nu_{12}-\nu_{21}$. If $p(n_{a1}, n_{a2})$ is the probability that a vacancy in jumping from plane 2 to plane 1 will jump into the site occupied by an A atom, and if $p(n_{a2}, n_{a1})$ is the probability that a vacancy will replace an A atom in a jump in the reverse direction, the current of A atoms between planes is

$$I_a=\nu_{21}p(n_{a1}, n_{a2})-\nu_{12}p(n_{a2}, n_{a1}). \quad (10)$$

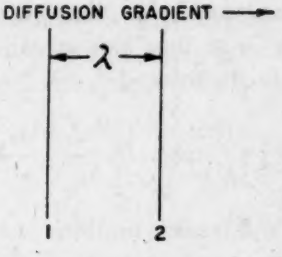

FIG. 3. Two consecutive planes in the direction normal to the diffusion gradient. The density of atoms in the planes is designated by n. λ is the spacing between planes.

Since n_{a1} and n_{a2} are nearly equal, we shall expand $p(\xi, \eta)$ in the manner

$$\begin{aligned} p(n_{a1}, n_{a2})&=p(n_a, n_a)-\frac{\partial p}{\partial \xi}\frac{\partial n_a}{\partial x}\frac{\lambda}{2}+\frac{\partial p}{\partial \eta}\frac{\partial n_a}{\partial x}\frac{\lambda}{2}, \\ p(n_{a2}, n_{a1})&=p(n_a, n_a)+\frac{\partial p}{\partial \xi}\frac{\partial n_a}{\partial x}\frac{\lambda}{2}-\frac{\partial p}{\partial \eta}\frac{\partial n_a}{\partial x}\frac{\lambda}{2}. \end{aligned} \quad (11)$$

Here $n_a=(n_{a1}+n_{a2})/2$ is the average density of A atoms in the two planes. The derivatives $\partial p/\partial \xi$ and $\partial p/\partial \eta$ are evaluated for $\xi=\eta=n_a$, and λ is the separation of the two planes. When the relations (11) are substituted in (10) we obtain

$$I_a=-I_v p(n_a)-(\nu_{12}+\nu_{21})\frac{\lambda}{2}(\alpha-\beta)\frac{\partial n_a}{\partial x}, \quad (12)$$

where

$$p(n_a)\equiv p(n_a, n_a), \quad \alpha\equiv\frac{\partial p}{\partial \xi}, \quad \beta\equiv\frac{\partial p}{\partial \eta} \quad (\xi=\eta=n_a). \quad (13)$$

Since the volume concentration of A atoms in the neighborhood of the two planes, c_a, is n_a/λ, I_a may be expressed in the form

$$I_a=-I_v p(n_a)-D_a\frac{\partial c_a}{\partial x}, \quad (14)$$

where

$$D_a=(\nu_{12}+\nu_{21})\frac{\lambda^2}{2}(\alpha-\beta). \quad (15)$$

Now

$$\frac{\partial c_a}{\partial t}=-\operatorname{div} I_a=I_v\frac{dp(n_a)}{dn_a}\frac{\partial n_a}{\partial x}+\frac{\partial}{\partial x}D_c\frac{\partial c_a}{\partial x}, \quad (16)$$

provided I_v is independent of position (but not necessarily of time) in the region considered. If the variation in concentration is relatively small

in the specimen, $dp(n_a)/dn_a$ may be treated as a constant. We note that this equation may be transformed to the form

$$\frac{\partial c_a}{\partial t}=\frac{\partial}{\partial x}D_a\frac{\partial c_a}{\partial x} \tag{17}$$

by means of the transformation

$$x'=x+vt, \quad t'=t, \tag{18}$$

where

$$v=I_v\lambda dp(n_a)/dn_a, \tag{19}$$

provided I_v is independent of time as well as position, so that v is a constant. Thus the motion of the A atoms is a superposition of a drift with uniform velocity v given by (19) in the negative x direction and diffusion with the diffusion coefficient D_a, when I_v is constant.

A similar analysis of the migration of B atoms shows that the current of B atoms, I_b, satisfies the equation

$$I_b=-I_v(1-p(n_a))+D_a\frac{\partial c_a}{\partial x}, \tag{20}$$

where $(1-p(n_a))$ is the probability that a vacancy will jump into the site occupied by a B atom when the planar density of A atoms is the same in neighboring planes and has the value n_a. Since $\mathrm{div}I_b=-\mathrm{div}I_a$ when I_v is constant, it is clear that (20) may be transformed into (16). Moreover, since the time and space derivatives of c_a are the negative of those of c_b, the volume concentration of B atoms, it follows that the migration of B atoms is also governed by the superposition of a uniform velocity v in the $-x$ direction and diffusion with diffusion coefficient D_a.

Consider next the migration of radioactive A atoms. We shall assume that the specimen has uniform chemical composition except for the fact some of the normal A atoms are replaced by radioactive atoms. If n_{a1}^* and n_{a2}^* are the concentrations of radioactive atoms in the two neighboring planes described above, the current of radioactive atoms is

$$\begin{aligned} I_a^* &= \nu_{21}p(n_a)\frac{n_{a1}^*}{n_a}-\nu_{12}p(n_a)\frac{n_{a2}^*}{n_a} \\ &= -I_v p(n_a)\frac{n_a^*}{n}-D_a^*\frac{\partial c_a^*}{\partial x}, \end{aligned} \tag{21}$$

where

$$D_a^*=(\nu_{12}+\nu_{21})\frac{\lambda^2}{2}\frac{p(n_a)}{n_a}, \tag{22}$$

and c_a^* is the volume concentration of radioactive atoms. It follows that the migration of the radioactive atoms is the superposition of a uniform motion with velocity $v^*=I_v\lambda p(n_a)/n_a$ and diffusion with the diffusion coefficient D_a^* when I_v is constant. The corresponding diffusion coefficient for radioactive B atoms is

$$D_b^*=(\nu_{12}+\nu_{21})\frac{\lambda^2}{2}\frac{(1-p(n_a))}{n_b}, \tag{23}$$

where n_b is the planar density of B atoms.

It is evident from the form of (14) and (20) that D_a is the quantity that should be designated as the chemical diffusion coefficient and may be called D_c in the following.

III. MIGRATION OF DIFFUSION BOUNDARY

Before considering the differences between the diffusion coefficients derived in the previous section, it is fruitful to contemplate the effects of a steady vacancy current in somewhat more detail.

If the mathematical framework of lattice points between which the atoms jump could be regarded as rigidly fixed, fiducial inclusions, such as the molybdenum wires employed in the experiments of Smigelskas and Kirkendall, which do not participate in diffusion would remain fixed relative to the framework and provide an origin for the stationary x coordinate. We shall keep this possibility in mind in the ensuing discussion.

The fact that the diffusing atoms experience a uniform drift as well as Brownian migration when there is a constant vacancy current is not surprising. If this current is present, the initial boundary plane between two specimens will cease to be the plane at which the concentration is just half-way between the initial values in the two halves of the specimen when D is constant (see solution (7)). Instead, this intermediate plane will be displaced by a distance vt at the end of time t in the case of chemical diffusion or by v^*t in the case of radioactive diffusion.

If the initial difference in composition of the two halves of the specimen is relatively large,

$dp(n_a)/dn_a$ in (19) will not be independent of position, and the drift motion of the atoms resulting from the vacancy current will be a function of position. We shall consider this case in conjunction with that in which I_v varies with time.

Suppose that the vacancies in the two halves of a specimen have different chemical potentials so that a vacancy current flows across the boundary when diffusion begins. We shall assume that the vacancies diffuse in accordance with Eq. (6), D being replaced by the appropriate diffusion coefficient in each half of the specimen, and c being the concentration of vacancies. We shall assume that the diffusion coefficient for vacancies is several orders of magnitude larger than D_a, D_a^*, or D_b^*, so that a uniform vacancy current is established in the boundary region where chemical or radioactive diffusion occurs before appreciable chemical or radioactive diffusion has taken place. This current, though uniform throughout the interesting region of space, will not be constant in time. It may readily be shown that the interesting solution for the concentration of vacancies depends upon position and time through a factor $x/(t)^{\frac{1}{2}}$, so that the vacancy current varies as $1/(t)^{\frac{1}{2}}$ at the boundary where chemical or radioactive diffusion is occurring. In this case, the equations of the form (16) and (21) may be written as

$$\frac{\partial c}{\partial t}=\frac{\mu\partial c}{(t)^{\frac{1}{2}}\partial x}+\frac{\partial}{\partial x}\left(D\frac{\partial c}{\partial x}\right). \tag{24}$$

As previously c is the concentration of the diffusing atoms, D is the appropriate diffusion coefficient and μ is a quantity independent of time and postion. Both D and μ may depend upon the composition. They may be treated as constants in radioactive diffusion if the two halves of a specimen have the same chemical composition. Their dependence on composition is important in chemical diffusion if the initial difference in composition of the halves of the specimen is sufficiently great. The $(t)^{\frac{1}{2}}$ appearing in the denominator of the first term on the right arises from the dependence of I_v on time described above.

Equation (24) may be expected to possess a solution that satisfies the boundary conditions of interest to us and is purely a function of the variable $s=x/(t)^{\frac{1}{2}}$. The corresponding function $c=f(s)$ satisfies the ordinary equation

$$-\frac{(s+2\mu)}{2}\frac{df}{ds}=\frac{d}{ds}\left(D\frac{df}{ds}\right), \tag{25}$$

in which D and μ may be functions of f in the general case.[6] The interesting solution of this equation when D and μ are constants is

$$f=c_1+(c_2-c_1)\int_{-\infty}^{s'/2(D)^{\frac{1}{2}}}\frac{\exp(-\alpha^2)d\alpha}{(\pi)^{\frac{1}{2}}} \tag{26}$$

in which $s'=s+2\mu$ and c_1 and c_2, as previously, are the initial concentrations in the two halves of the specimen. We see that the point at which the concentration is $(c_1+c_2)/2$ is at the position where $s'=0$ or at $x=-2\mu(t)^{\frac{1}{2}}$ at time t. Relative to a moving origin chosen at this point, the diffusion is exactly as if there were no net vacancy current.

In the more general case in which D and μ are functions of concentration, $f(s)$ will range between c_1 and c_2 as s varies from $-\infty$ to $+\infty$. As long as the concentration difference is not large we may expect to find a value of s for which $f=(c_1+c_2)/2$. If D and μ were constant so that the solution (26) were valid, this point would be $s=2\mu$. Moreover, the function df/ds would be symmetrical about this point, so that d^2f/ds^2 would be zero when $s=2\mu$. In the general case in which neither D nor μ are constants we may expect none of these simple relations to hold: usually the df/ds curve will not be symmetrical about the point for which $f=(c_1+c_2)/2$, nor will d^2f/ds^2 vanish there.

At infinitesimal times after the start of diffusion, the point at which the concentration is $(c_1+c_2)/2$ will be at the initial interface. Relative to the initial lattice network, it will be at a position $x_i=s_i(t)^{\frac{1}{2}}$ at time t. It is clear that the coefficient s_i will depend both upon the concentrations c_1 and c_2 and upon the accidental difference in initial concentration of vacancies in the two halves of the specimen.

[6] The solutions of (25) may be classified in the following manner: Given $f=a$ and $df/ds=b$ for a specified value of s, Eq. (25) may be integrated to obtain values of $f(+\infty)=c_2$ and $f(-\infty)=c_1$. These values of c_1 and c_2 may be regarded as functions of a and b, which can in turn be inverted to yield a and b in terms of c_1 and c_2.

The initial interface, for which x is zero and which, at least in principle, may be marked by fiducial material, corresponds to the point $s=0$. The concentration at this point remains constant as diffusion proceeds according to the present treatment of the problem. This result, which agrees with the experiments of Smigelskas and Kirkendall, was also obtained by Darken on the basis of his formulation of diffusion, and evidently depends only on the fact that the concentration can be expressed as a function of $x/t^{\frac{1}{2}}$.

The shift of the fiducial markers observed by Smigelskas and Kirkendall in the copper-brass remains to be discussed. If the mathematical formulation given in the preceding section were strictly correct, there would be no room for a displacement of the type found by these investigators, apart from the effect of change in lattice parameter with composition. Each atom which moves out of the central core within the initial copper-brass boundary would be replaced either by another atom or by a vacancy, which would have almost the same atomic volume as one of the atoms of the alloy. As a result the fiducial boundary would remain fixed, or two such boundaries on opposite sides of the core would not move relative to one another by more than the distance associated with change in lattice parameter. In order to explain the observed results with the use of vacancy theory, it apparently is necessary to adopt the following viewpoint: vacancies diffuse from the electroplated copper into the brass, permitting a net flow of zinc and copper atoms across the boundary separating the brass from the copper. It is possible that the copper, being an electroplated deposit, contains a high density of voids and hence of vacancies at start. In any event the vacancies could diffuse from the vacuum interface if needed. The vacancy current should vary as $1/t^{\frac{1}{2}}$ at least initially, for reasons described earlier, so that the total number of vacancies which would have flowed past the boundary at the end of time t would vary as $t^{\frac{1}{2}}$. As long as the vacancies in the brass remain atomically dispersed, the fiducial lines do not shift relative to one another. However, as the specimen is cooled, the vacancies condense to form voids. These voids close, at least in part, as a result of the action of surface tension forces and plastic flow, and the fiducial markers are drawn together. If the contraction in volume compensates for the vacancies which have diffused, this contraction should vary as $t^{\frac{1}{2}}$. Since free energy is to be gained by having zinc migrate into the copper to form a more dilute alloy of brass, it is conceivable that the vacancy current would supersaturate the brass during diffusion and that the condensation of vacancies with the consequent sintering would actually occur during diffusion.[7] These two cases could be distinguished, at least in principle, by observing whether the displacement of the boundary occurs during diffusion or subsequently.

The preceding picture of the displacement of the boundary does not appear at first sight to be substantially different from Darken's. Actually, there are several differences. Darken's formulation explicitly assumes that the contraction takes place in the region where the chemical concentration gradient is greatest. That given here permits the contraction to occur over the entire zone through which vacancies migrate. If the diffusion coefficient for vacancies is 10^3 times larger than that for atoms, this zone may be thirty times larger than the zone in which chemical diffusion has occurred. Thus the contraction within the region where the chemical gradient is large may be a negligible fraction of the whole.

In this connection, Smigelskas and Kirkendall state that after diffusion "the brass to the right of the interface is particularly susceptible to pitting. This is the side from which the zinc is diffusing to the left faster than the copper is diffusing to the right." They conclude the pitting is associated with voids induced during diffusion. Presumably these voids are the condensed gas of vacancies. Unfortunately the experimenters do

[7] In the discussion of the paper by Smigelskas and Kirkendall, C. S. Smith has suggested that the volume changes accompanying diffusion create cracks in the brass core which run normal to the interface and which promote diffusion by permitting zinc to migrate from the brass by gaseous diffusion. It is postulated that these cracks sinter together at a later period of time and thereby account for the loss of volume of the core. Although this suggestion does not explain the way in which the zinc succeeds in migrating into the copper to cause the stresses which are assumed to exist, it is possible that the presence of zinc vapor and the gradual sintering of voids would have the effect of inducing vacancies to diffuse continuously from outside the specimen, thereby creating a continuous vacancy current.

not describe the width of the zone in which the pitting occurs.

Smigelskas and Kirkendall found that the contraction of the inner core of the diffusion specimen represented about one percent of the linear dimensions at the end of 56 hours of diffusion at 785°C. The zone of chemical diffusion then represented about 20 percent of dimensions of the core. It follows that approximately one percent of the atoms of the core would have been replaced by vacancies, according to the picture presented here. It is hardly likely that all of these vacancies would have initiated in the electroplated copper —most must have come from the outer interface of the specimen. One might expect vacancies to have diffused throughout the core before 56 hours have elapsed and hence to observe a deviation from the rule that I_v varies as $t^{-\frac{1}{2}}$. The fact that this deviation does not seem to be observed (Fig. 2) remains to be explained if the vacancy mechanism is correct.

Another difference between the interpretation based on vacancies and that implied in Darken's theory is made clear by considering an experiment identical with Smigelskas and Kirkendall's, except that the copper and brass are interchanged. If Darken's viewpoint is correct the copper core should swell, since zinc atoms would diffuse into it more rapidly than copper diffuses out. On the other hand, if the vacancy mechanism of diffusion is valid the fiducial markings about the core should either remain unchanged if the vacancy current is zero, or should pull together, much as in the experiment in which there is a brass core, *provided* the only source of vacancies for an extended amount of diffusion lies outside the specimen. It would be highly interesting to see the results of an experiment of this kind.

IV. COMPARISON OF DIFFUSION COEFFICIENTS

Equations (15), (22), and (23) represent the diffusion coefficients of interest for Johnson's experiments. The following points are worthy of note:

(a) The diffusion coefficients will be influenced by any deviation of the density of vacancies from the equilibrium value for the pure alloy. This effect, which will influence $\nu_{12}+\nu_{21}$, is well known from the studies of electrolytic conduction in the salts in which the density of vacancies may be suppressed or raised by additive agents.

(b) The expressions for D_e and for the radioactive diffusion coefficients are intrinsically different in form. The first involves derivatives of the coefficient $p(\xi, \eta)$ which determines the probability that a vacancy will land on an A atom in jumping from one plane to the next, whereas the second involves $p(n_a, n_a)$ alone. In the case of 50–50 composition $(n_a=n_b=1-n_a)$ the sum of D_a^* and D_b^* is

$$D_a^*+D_b^*=(\nu_{12}+\nu_{21})\frac{\lambda^2}{n_a}, \tag{27}$$

which does not involve p.

The writer has not been able to derive relations between $p(n_a)$ and the derivatives α and β which are independent of special models that are used to describe diffusion. It appears that there are no general rules governing the behavior of $p(\xi, \eta)$ other than that it be equal to unity when $\xi=n$, where n is the density of atoms in a plane normal to the gradient, and be zero when $\xi=0$.

In principle, $p(n_a)$ could be determined as a function of n_a by measuring the diffusion of radioactive A or B atoms for various compositions. A determination of this type would require knowledge of $(\nu_{12}+\nu_{21})$; however, let us assume that this offers no problem. Three conceivable forms of $p(n_a)$ are shown in Fig. 4. These are selected somewhat arbitrarily to indicate possible situations. Curve I, which is a straight line, could occur if A and B atoms were almost identical

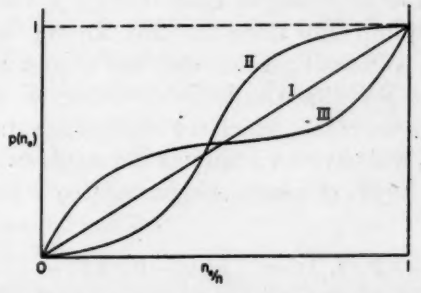

FIG. 4. Schematic representation of $p(n_a)$ in three interesting cases. Case I is that which would be valid in an ideal two-component alloy in which the atoms behaved as if chemically identical. Case II is a hypothetical one in which the slope is very steep in the 50–50 range of composition, whereas Case III is one in which the slope is small. The abscissa is n_a/n, the fraction of A atoms in each plane. The curves are constrained to pass through the points zero and unity at the two ends by definition.

chemically so that $p(n_a)=n_a/n$. Now the slope of any of these curves at a given point is readily seen to be $\alpha+\beta$ for $\xi=\eta=n_a$. Suppose that β is very small compared with α, a situation that need not occur generally, but which will obtain if the A and B atoms are very similar. In this case the slope of the $p(n_a)$ curve in Fig. 4 determines α and hence determines the quantity $(\alpha-\beta)$ appearing in D_c (Eq. (15)). A straightforward analysis of the three curves under these simplifying assumptions shows that in the vicinity of 50–50 composition $D_c=D_a^*$ in case *I*, $D_c>D_a^*$ in case *II*, and $D_c<D_a^*$ in case *III*. D_c may be larger than the sum of D_a^* and D_b^* for the 50–50 composition if the slope of the $p(n_a)$ curve is greater than 2, as is possible in case *II*.

V. A SIMPLE MODEL OF A DIFFUSING SYSTEM

It is interesting to consider the workings of a simple model of a system in which diffusion is occurring in order to visualize a case in which the radioactive and chemical diffusion coefficients are not identical. The results obtained from a specialized model evidently will lack generality. This disadvantage is compensated for by the fact that they are explicit.

Let us consider a case in which there is a constant gradient of concentration in the x direction and in which a given atom in one of the planes perpendicular to the x axis has only one neighboring site in the adjacent plane into which it could jump by vacancy diffusion. This would be the case in a simple cubic lattice if vacancies could jump only along the directions of the cube edges. We shall assume that the atoms interact in pairs and that the probability that an A atom in a given plane, which we shall designate the 1 plane, will have a vacancy in the neighboring site in an adjacent plane, designated the 2 plane, is

$$P_a(1,2)=C_{12}\exp(-V_a/kT)\frac{n_{v2}}{n}, \tag{28}$$

in which C_{12} is a coefficient which depends upon the composition, V_a is an energy parameter representing the average relative change in energy of a lattice induced by placing a vacancy next to an A atom, n_{v2} is the density of vacancies in the 2 plane, and n is the density of atoms in the planes normal to the x axis. Similarly, we shall assume that the corresponding probability for a B atom in the 1 plane is

$$P_b(1,2)=C_{12}\exp(-V_b/kT)\frac{n_{v2}}{n}. \tag{29}$$

From the condition

$$n_{a1}P_a(1,2)+n_{b1}P_b(1,2)=n_{v2}, \tag{30}$$

we find

$$C_{12}=\frac{n}{n_{a1}\exp(-V_a/kT)+n_{b1}\exp(-V_b/kT)}. \tag{31}$$

It is readily seen that under these assumptions $P_a(1,2)$ and $P_b(1,2)$ involve the energies V_a and V_b only through the factor

$$f=\exp(-(V_a-V_b)/kT). \tag{32}$$

If ν_{21} vacancies are jumping per unit time per unit area from plane 2 to plane 1, and if $p(n_{a1}, n_{a2})$, as in Section II, is the probability that a given vacancy will land on an A atom, we obtain the relations

$$\nu_{21}p(n_{a1}, n_{a2})=\nu_a n_{a1}P_a(1,2), \tag{33}$$

$$\nu_{21}(1-p(n_{a1}, n_{a2}))=\nu_b n_{b1}P_b(1,2), \tag{34}$$

in which ν_a is the probability per unit time that a vacancy which is next to an A atom will change places with it, and ν_b is the corresponding probability for interchange of a vacancy with a neighboring B atom. By adding (33) and (34) we obtain

$$\nu_{21}=C_{12}\frac{n_{v2}}{n}(\nu_a n_{a1}\exp(-V_a/kT)+\nu_b n_{b1}\exp(-V_b/kT)) \tag{35}$$

which, when substituted in (33), leads to the relation

$$p(n_{a1}, n_{a2})=\frac{\nu_a n_{a1}f}{\nu_a n_{a1}f+\nu_b n_{b1}} \tag{36}$$

that is of fundamental interest to us. The quantities ν_a, ν_b, and f appearing in this will generally be functions of both n_{a1} and n_{a2}. For simplicity we shall assume at the start that they are involved only through the combination

$$n_a=(n_{a1}+n_{a2})/2.$$

With the use of this form of $p(\xi, \eta)$ we readily find that when $\xi=\eta=n_a$

$$\frac{p(n_a)}{n_a}=\frac{\nu_a f}{\nu_a n_a f+\nu_b n_b}, \tag{37}$$

$$\alpha=\frac{\nu_a\nu_b n f+\frac{1}{2}\nu_a\nu_b n_a n_b\dfrac{df}{dn_a}+\frac{1}{2}n_a n_b f(\nu_b\nu_a'-\nu_a\nu_b')}{(\nu_a n_a f+\nu_b n_b)^2} \tag{38}$$

$$\alpha-\beta=\frac{n\nu_a\nu_b f}{(\nu_a n_a f+\nu_b n_b)^2}. \tag{39}$$

Here ν_a' and ν_b' are the derivatives of ν_a and ν_b with respect to n_a. From (37) and (39) we readily find

$$\frac{D_e}{D_a^*}=\frac{\alpha-\beta}{p(n_a)/n_a}=\frac{n\nu_b}{(\nu_a n_a f+\nu_b n_b)}. \tag{40}$$

When f is very large, so that vacancies prefer to be near A atoms, the ratio (40) is $n\nu_b/\nu_a n_a f$. This is $2\nu_b/\nu_a f$ in the case in which $n_a=n/2$.

In the opposite case in which f is small, so that vacancies prefer B atoms, the ratio is n/n_b, which is 2 for 50–50 composition.

Similarly, we find that in the case of 50–50 composition

$$\frac{D_e}{D_a^*+D_b^*}=2\frac{xy}{(x+y)^2}, \tag{41}$$

in which

$$x=\nu_a n_a f, \quad y=\nu_b n_b. \tag{42}$$

This ratio attains the maximum value of $\frac{1}{2}$ when $x=y$. Thus in the case of the simple model which we have employed, D_e can never be larger than half the sum of the radioactive diffusion coefficients.

The results (38) and (39) are definitely dependent upon the simplifying assumptions made in determining α and β from $p(n_{a1}, n_{a2})$, as given by (36). If we assume that ν_a, ν_b, and f do not involve n_{a1} and n_{a2} merely through the quantity $n_a=(n_{a1}+n_{a2})/2$, we have in place of (39)

$$\alpha-\beta=\frac{n\nu_a\nu_b f+n_a n_b f\nu_b^2\left(\dfrac{\partial r}{\partial\xi}-\dfrac{\partial r}{\partial\eta}\right)+\nu_a\nu_b\left(\dfrac{\partial f}{\partial\xi}-\dfrac{\partial f}{\partial\eta}\right)}{(\nu_a n_a f+\nu_b n_b)^2}, \tag{43}$$

where $r=\nu_a/\nu_b$.

As we have noted in the introduction, Johnson's experiments indicate that D_e is almost exactly equal to $D_a^*+D_b^*$. This result is not in accordance with the version of the foregoing model which leads to (41). On the other hand, it could arise from the extended version which leads to (43), provided the combinations of derivatives of r and f appearing in Eq. (43) are assumed to take the proper values. It is interesting to note that Johnson's results imply considerable inequality between the behavior of silver and gold atoms in the 50–50 alloy. This in turn suggests that they should show[8] pronounced short-range order, even if long-range order is absent.

The writer is particularly indebted to Professor R. J. Maurer for several valuable discussions of this paper. Maurer was apparently the first to appreciate that the problems of chemical and radioactive diffusion are basically different if radioactive diffusion takes place in the absence of a chemical gradient.

[8] The writer is indebted for conversations on this point to members of the NRC symposium group, which met at Cornell during August, 1948, to discuss "Phase changes."

Current Density of the Arc Cathode Spot*

J. D. COBINE AND C. J. GALLAGHER
Research Laboratory, General Electric Company, Schenectady, New York

(Received June 3, 1948)

New measurements of the area of the arc cathode spot from measurements of width of tracks left on metals by a cathode spot moving in a magnetic field indicate that the current density is greater than values given by previous workers. At 2.6 amperes, we find the following values in air at atmospheric pressure: Cu 124,000 amp./cm², Al 29,500 amp./cm², W 74,000 amp./cm², Hg on Cu 20,700 amp./cm².

The Cu, Al, and W electrodes were first oxidized in a bunsen flame. For an arc burning in mercury vapor with a mercury cathode at a few microns pressure we find at 2.6 amperes a current density of 50,000 to 220,000 amperes per cm². Values at currents above 5 amperes could not be obtained because of the formation of multiple spots.

ESTIMATES of the cathode current density in the electric arc have varied widely, from a few hundred amperes per cm² to several thousand.[1] The chief source of uncertainty lies in determining the effective area of the current transmitting portion of the cathode, since in general the total current can be measured easily. It has been customary to assume that the small, highly luminous area on the cathode, the "cathode spot," corresponds closely to the current-carrying region, and efforts to measure the current-density have been limited to measurements of the size of the cathode spot. This same assumption will be made in this paper. The directly measured quantity is the diameter of the cathode spot, and from this we may infer the value of the current density.

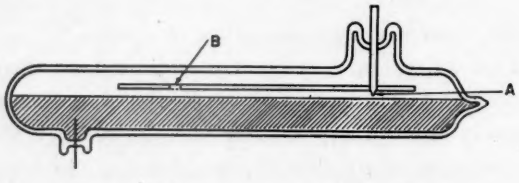

FIG. 1. Tube for mercury arc studies.

In our experiments the materials used as cathodes were mercury, copper, aluminum, tungsten, lead, brass, and mercury-copper amalgam. With the exception of the mercury, all the surfaces were lightly oxidized, and the arc was established in air at atmospheric pressure. With the mercury cathode, the arc burned in mercury vapor at low pressures of the order of 10–50 microns. It was found that the current which could be used was limited by the tendency of multiple spots to form at higher currents. The limiting current depended on the metal. For aluminum multiple spots formed at currents as low as 2 amperes, while for tungsten there was apparently but a single spot at currents up to at least 10 amperes. Other cathode materials appear to have limiting currents lying between these extremes.

The mercury cathode was studied in the tube shown in the diagram (Fig. 1). The arc was started by momentary contact between the tungsten point (*A*) and the mercury pool. An external magnetic field, perpendicular to the plane of the diagram, drives the spot to the opposite end of the tube. If the field is sufficiently strong (several hundred gauss) the spot travels in a straight line, with none of the wandering motion to the side which has limited the accuracy of observations by other experimenters. The vapor pressure is low enough that the spot moves in the retrograde direction[2] with the column trailing the spot. The spot is observed through the small hole (*B*) in the anode. If the level of the

* The material discussed here was presented in an invited paper at the New York meeting of the American Physical Society, January 1948.

[1] C. Granquist, Nova Acta Upsala **20**, 143 (1903); M. Reich, Physik. Zeits. **7**, 73 (1906); N. A. Allen, Proc. Phys. Soc. **33**, 62 (1921); A. Guntherschulze, Zeits. f. Physik **11**, 74 (1922); R. Seeliger and H. Schmick, Physik. Zeits. **28**, 605 (1927) and **31**, 691 (1930); W. G. F. Swann, J. Frank. Inst. **205**, 810 (1928); R. Tanberg and W. E. Berkey, Phys. Rev. **38**, 296 (1931); J. Slepian and E. J. Haverstick, Phys. Rev. **33**, 52 (1929); E. Nobel, Phys. Rev. **36**, 1636 (1930); L. Tonks, Physics **6**, 294 (1935); R. Holm, Arkiv. Mat. Astr. Fys. **34B**, No. 8 (1947); E. G. B. Stuckelberg, Helv. Phys. Acta. **1**, 75 (1928).

[2] N. Minorsky, J. de phys. et rad. **9**, 127 (1928).

mercury is properly adjusted, the slight random disturbances in the mercury surface will be sufficient to cause random make-and-break at the tungsten point. The average time between contacts can be adjusted by a slight tilt of the tube, so that as many as twenty new spots are formed per second.

The radiation from the spot is continuous and extends over the entire visible range. Thus, a red filter may be used to exclude most of the radiation from the mercury vapor. With a suitable microscope and filar eyepiece, the width of the trace can be measured after the observer has acquired some experience in accommodating to slight changes in position of successive traces. The moving spot may also be photographed through the microscope and the width of the resulting trace measured. Three such photographs are shown in Fig. 2, for mercury at 2.6, 5 and 10 amperes. The complicated structure of the 10-ampere trace makes it impossible to form any conclusion about the diameter of the spot. The average width of several traces at 2.6 amperes was 3.9×10^{-3} cm. For a circular spot this width would correspond to a current density of 220,000 amperes per cm^2. This value is higher than any of the values quoted in the literature by more than an order of magnitude.

The dimension of the spot along the direction of motion could be measured by means of a scanning technique. The principle is illustrated in Fig. 3. The image of the spot is focussed by means of a microscope objective onto the opaque screen. The screen has three fine slits of width considerably less than the diameter of the magnified spot. The opaque screen was a standard microscope slide coated with a thin layer of Aquadag. The slits were made by scratching the surface with a razor blade. Such slits can be made quite narrow with width of 0.005 cm easily reproducible. If the magnification of the lens is 6 or 7 diameters, the magnified spot is 10 or 15 times the slit width. The spacing between slits was large enough that the moving image had passed the first slit completely before the leading edge reached the next one.

The light passing through the slits strikes the cathode of a 931A photo-multiplier tube. The output if the multiplier is amplified in a wide-band amplifier and applied to the vertical plates

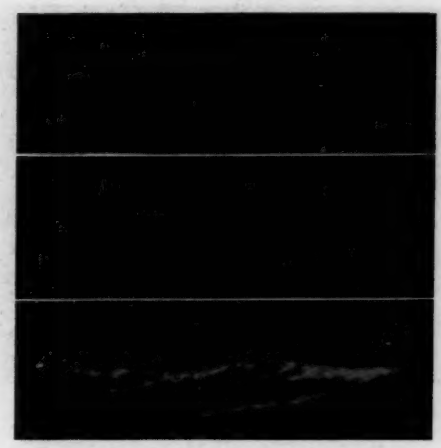

FIG. 2. Cathode tracks on mercury (direction of travel right to left).
(a) 2.6 amperes
(b) 5 amperes
(c) 10 amperes

of a Dumont 248 oscilloscope. The horizontal sweep is triggered by the signal, so that the pattern on the screen consists of three pulses. The leading edge of the first pulse is obscured by the triggering delay, but the next two pulses are the same in size and shape (Fig. 4).

From measurements of the width of the pulses and the distance between corresponding points, a value of the effective width of the spot may be deduced. As shown in the following analysis, the method is independent of the spot velocity, and depends only on the slit spacing, the lens magnification, and the geometry of the pattern on the oscilloscope screen. Let W=effective diameter of spot, MW=diameter of magnified image, d=distance between slits, L=distance on oscilloscope screen between corresponding points of pulses, S=effective width of pulse. Then, since the horizontal sweep is linear with time,

$$MW/S=d/L \quad \text{or} \quad W=Sd/ML.$$

All of the quantities on the right-hand side can be measured accurately. The limiting factor is S.

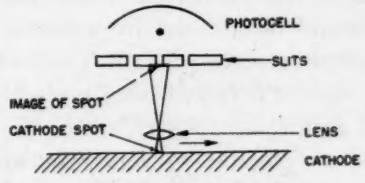

FIG. 3. Optical system for scanning the mercury cathode spot.

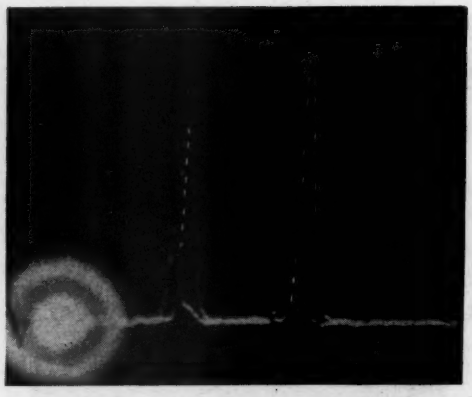

FIG. 4. Oscillograms of light distribution of cathode spots.

The width corresponding to any prescribed pulse height can be measured without difficulty, but it is uncertain which height should be chosen inasmuch as the sides of the pulse have a definite slope. The slope of the leading edge could be due to one or both of two possibilities:

1. The spot may not be uniform across its surface.
2. The gas very near the surface preceding the spot may give some contribution to the radiation.

In the latter case the intensity of the light must be far above that from the plasma in order to be seen by the photo-cell. The slope of the trailing edge of the pulse may indicate that there is a decay of activity in time after the "spot" has passed, or else there is a residual glow of high intensity in the gas. The total time for the spot to pass any point can be less than 5 microseconds. Since there appears to be no adequate way of determining how much of the radiating area is effective, it is probably best to take as an upper limit the width of the pulse across the base, corresponding to a minimum value of current density. The average diameter of the spot corresponding to the base of the pulse is 0.80×10^{-3} cm at 2.6 amperes, about twice the value obtained for the dimension perpendicular to the direction of travel. Thus, the current density would be lowered by a factor of 4, to about 50,000 amperes per cm^2, as a lower limit. The true current density is very probably greater than this figure.

It was not possible to apply the same techniques in observations of the cathode spot on solid metal cathodes. However, it was found that very interesting tracks could be obtained on metal cathodes which were traversed by a rapidly moving cathode spot. Such tracks could then be measured to give the extent of the active area at the cathode. Visible tracks could not be obtained on clean or highly polished metals, but only on electrodes having a definite layer of surface oxide. The arc was established in air at atmospheric pressure, and the spot was made to move rapidly

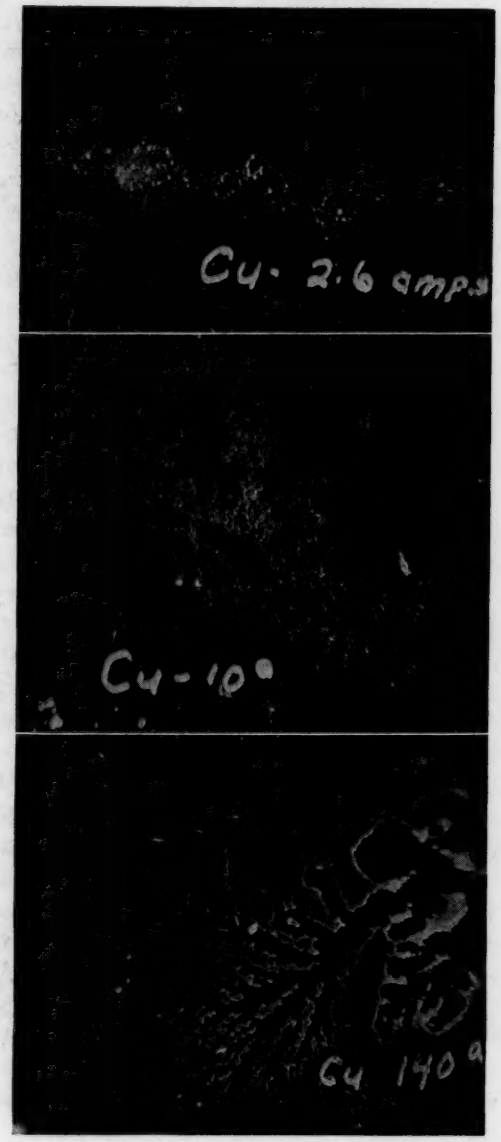

FIG. 5. Cathode tracks on copper (direction of travel right to left).

(a) 2.6 amperes
(b) 10 amperes
(c) 140 amperes

(5 to 10 meters/sec.) over the cathode by means of a magnetic field of about 2000 gauss. For these tracks the spot moved in the direction of the ponderomotive force.

Some examples of the tracks obtained are shown in Figs. 5–7. The effects of increasing the current are shown for copper, aluminum and tungsten. At low currents, single tracks are found; at higher currents multiple spots occur as in mercury. For oxidized aluminum, the tracks are very complex even at low currents, while for tungsten, there appears to be no branching for the currents observed although the track widens as the current increases.

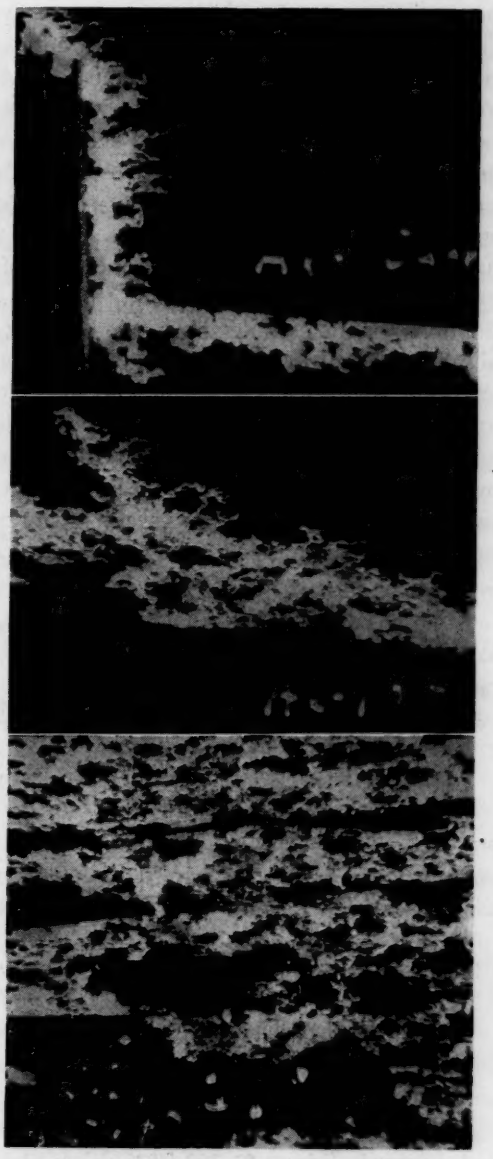

FIG. 6. Cathode tracks on aluminum (direction of travel right to left).

(a) 5 amperes
(b) 10 amperes
(c) 140 amperes

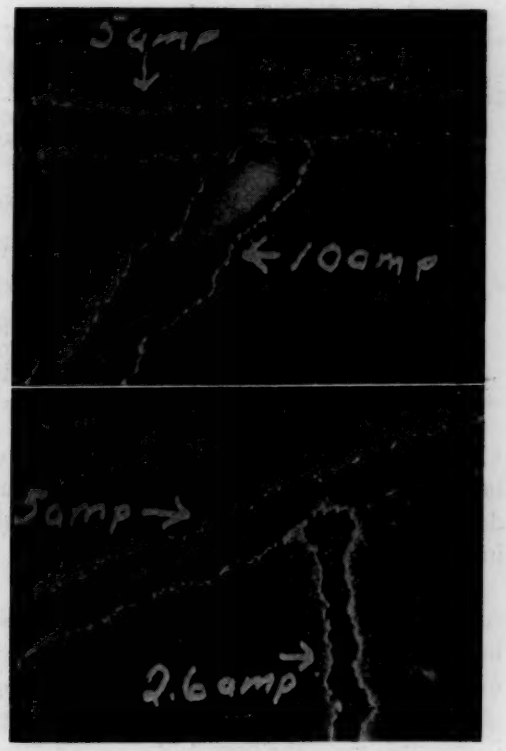

FIG. 7. Cathode tracks on tungsten.

(a) 2.6 and 5 amperes
(b) 5 and 10 amperes

It was found possible to get a non-branching track on aluminum by etching strongly in NaOH, rinsing in distilled water and alcohol, and drying. Occasionally, on all metals, short gaps were found in tracks. This does not necessarily mean an interrupting of current, since a new spot could be formed before the last one disappeared. The tracks on aluminum show some interesting features. The 5 ampere track shows that the "spot" is apparently reluctant to cross a scratch, either parallel to the direction of motion or perpendicular to it. The scratches were about 10 microns deep. The aluminum tracks appear to be much more complicated than for copper, with many of the branches apparently going in the reverse direction.

TABLE I.

Metal	Current-amp.	Width-cm	Current density amp. per cm²
W	2.6	0.0067	74,000
	5.0	0.0083	92,000
	10.0	0.0164	47,000
Pb	5.0	0.0156	26,000
Al	2.6	0.0105	29,500
Cu	2.6	0.0054	120,000
Cu-Hg	2.6	0.0127	20,700
	5.0	0.0172	21,700
	10.0	0.0275	14,700

The widths of the various tracks which could be measured and the corresponding current densities, assuming circular geometry, are shown in Table I.

It is of interest to consider what a track consists of, since the very fact of its existence indicates a change in the nature of the surface over which the spot has raced. The appearance of the track suggests that the oxide at the spot is removed from the base metal, either by direct evaporation, or by chemical reduction on the surface followed by evaporation, so that the track is just the unoxidized base metal. Apparently some material is lost from the cathode, since it is possible to make accurate replicas of the tracks with Formvar films, which indicate that the penetration below the surface is of the order of 1 micron.

From the experiments described above we conclude that the current density in the arc cathode spot is of the order of 50,000 amp. per cm² for most cathode materials. It is now necessary to inquire whether such high values can be obtained by any of the mechanisms which have been previously proposed. There have been a number of mechanisms proposed to explain the current transport at the cathode for the so-called "cold-cathode" arc. The following four seem most worthy of serious consideration: 1. Thermionic emission of electrons.[3,4] 2. Field emission of electrons.[5,6] 3. Positive ion collection, with thermal ionization in the region near the cathode producing the ions.[7,8] 4. Electron emission through insulating particles on the surface resulting from positive ions on the insulator.[9]

The first of these, thermionic emission of electrons, appears adequate to explain the current transport with highly refractory cathodes, such as tungsten and carbon under conditions where they are incandescent, but has not seemed applicable to the lower boiling point metals, for which the possible thermionic emission at the probable maximum temperature would be far too small. The high current density values quoted in this paper make the thermionic theory even less plausible, unless one can assign to the emitting surface very low values of the work function. Although the work functions of the pure metals would be too high, the true work functions for the complex electrode surfaces used are not known so that this possibility is not definitely excluded. It is well known that the arc cathode spot cannot be readily established on a very clean metal surface, so that the possible lowering of the work function by surface impurities may be sufficient to establish the necessary thermionic emission. The best values of the

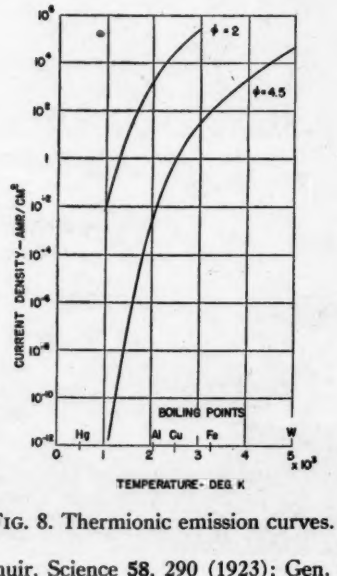

FIG. 8. Thermionic emission curves.

[3] J. J. Thomson, *Conduction of Electricity through Gases*, 3rd Edition (Cambridge Press, Cambridge, 1933), Vol. 2, pp. 596 ff.

[4] L. B. Loeb, *Fundamental Processes of Electrical Discharge in Gases* (John Wiley and Sons, Inc., New York, 1939), pp. 605 ff.

[5] I. Langmuir, Science **58**, 290 (1923); Gen. Elec. Rev. **26**, 731 (1923).

[6] S. S. Mackeown, Phys. Rev. **34**, 611 (1929).

[7] J. Slepian, Phys. Rev. **27**, 407 (1926).

[8] W. Weizel, R. Rompe, and M. Schön, Zeits. f. Physik **115**, 179 (1940).

[9] M. J. Druyvestyn, Nature **137**, 580 (1930).

photoelectric work function of the various oxides are of the order of 4 volts or higher, so that they would not be much better emitters than metals unless the boiling points were higher. The curves shown in Fig. 8 indicate what values of emission might be obtained from materials with work functions of 4.5 volts and 2 volts, respectively. The 4.5 volt curve, which may be taken as representative of most clean metals, shows that the possible current density is much too low even at the boiling point for metals such as Hg, Al, Cu, and Fe. The 2-volt curve would give considerably higher values of current density of the order of those obtained, but the presence of such low work function materials is improbable. Thus, it would appear that thermionic emission alone cannot explain the high current density, unless, as suggested by Thomson[3] and Loeb,[4] it is possible with such density of energy input to obtain local temperatures far above the boiling point.

The theory of field emission postulates that electrons are drawn out of the surface by the strong field set up at the cathode by the high density positive ion space charge outside the surface. The theory of field emission as given by Fowler and Nordheim,[10] indicates that barely measurable current density can be obtained at fields of the order of 10^5 volt/cm, but, as shown in Fig. 9, curves *A*, *B*, and *C*, the current densities we have measured would require fields of the order of 10^7-10^8 volt per cm for work functions as low as 2 volts. To explain these current densities on the field theory, one would have to assume for the work function the absurdity low value of 0.5 volt. Mackeown[6] developed a relation between the field at the cathode and the current density required to produce the field. The curves *D* and *E* of Fig. 9 were calculated from his relation, for two different ratios of positive-ion current to electron current. According to Mackeown's theory, fields of 10^7 volt/cm would require a minimum current density of more than 10^7 amp./cm^2, which is considerably higher than any measured values. Thus, for current densities such as we have measured, the field emission theory appears to be quite inadequate, even if the field be greater by a factor of ten as a result of surface irregularities.

[10] R. H. Fowler and T. Nordheim, Proc. Roy. Soc. **A118**, 229 (1928).

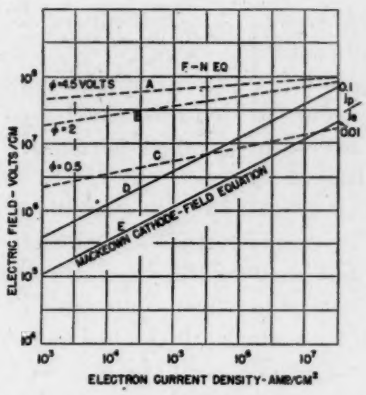

FIG. 9. Relations between cathode field and current density (electrical quantities in practical units).

------ Fowler-Nordheim equation
$j_e=6.2(10)^{-6}(E^2/\phi)\exp(-6.8(10)^7)\phi^{\frac{3}{2}}/E.$
———— Mackeown field equation
$E^2=7.57(10)^6V_e^{\frac{1}{2}}[j_p(1845W)^{\frac{1}{2}}-j_e].$
E = electrostatic field,
j_e = electron current density,
j_p = positive ion current density,
W = atomic weight.

A third theory originally advanced by Slepian[7] to apply to low current densities, and subsequently developed for higher current densities by Weizel, Rompe, and Schön,[8] attempts to show that electron emission is not necessary, but that the entire cathode current can be accounted for by positive ions generated in the gas adjacent to the surface by the various processes involved in thermal ionization. The latter authors carried through some calculations for a high pressure mercury arc in an attempt to show that the assumed mechanism would lead to correct values of voltage drop between the column and the cathode. The values calculated for the cathode drop were too high to agree with observed values, but current densities were also probably too low, by a factor of at least five. An increase in current density by this factor would lower the calculated cathode drop to some extent although not enough to give completely satisfactory agreement.

Druyvestyn[9] assumed that the "cold-cathode" spot depended on the presence of tiny insulating or semi-conducting particles, such as glass, or oxide layers Positive ions would build up these insulating particles to produce a high field, with electrons then emitted through the insulator. The theory does offer an explanation for the apparent necessity of the presence of oxides and also of the random motion of the spot, since the impurities

could be removed by the ion bombardment and a new region would then be activated. It is not at all clear from Druyvestyn's picture that the observed high current densities can be accounted for, and leaves unexplained a number of the points as listed below.

None of these theories appears really adequate. They fail to explain the observed high current densities, and offer no clue as to the reason for several phenomena which must be intimately associated with the cathode mechanism. The following are several such phenomena which at present are left without explanation: 1. The high velocity stream of vapor (or particles) coming from the cathode.[11] 2. The continuous spectrum at the cathode spot.[12] 3. The retrograde motion of the spot in a low pressure arc on application of a magnetic field.[2,13,14] 4. The increase in stability at low currents when the spot is confined to a small area.[15] 5. The difficulty of establishing a spot on a clean surface[16,**] and the random motion of the spot over the surface. 6. The failure of the mercury arc to re-ignite when interrupted for times as short as 10^{-9} second.[17]

Since none of these "classical" theories appears to give a complete picture of the cathode processes, it may well be that, as Loeb has suggested, a new approach is required, "to evolve a new physics of the microvolume with high rates of energy input."[18]

Note added in proof: Since this paper was submitted for publication Froome has reported even higher values of current density (10^6 amp/cm^2) for transient arcs of 1400 ampere peak current for copper, sodium, and mercury cathodes.[19]

[11] R. Tanberg, Phys. Rev. **35**, 1080 (1930).
[12] J. Stark, Physik. Zeits. **51**, 750 (1904).
[13] C. G. Smith, Phys. Rev. **62**, 48 (1942); Bull. Am. Phys. Soc. **18**, 5 (1943).
[14] C. J. Gallagher and J. D. Cobine, Phys. Rev. **71**, 481 (1947).
[15] C. W. Lufcy and P. L. Copeland, J. App. Phys. **16**, 740 (1945).
[16] G. E. Doan and J. L. Myer, Phys. Rev. **40**, 36 (1932).
** We have observed that a "cold cathode" arc can be established on oxidized tungsten with the typical random motion of the spot, but that no spot can be formed on clean tungsten unless the temperature is high enough that thermionic electrons can be emitted.
[17] G. Mierdel, Zeits. f. tech. physik **17**, 452 (1936).
[18] See reference 4, p. 636.
[19] See K. D. Froome, Proc. Phys. Soc. **60**, 424 (1948).

Letters to the Editor

PUBLICATION of brief reports of important discoveries in physics may be secured by addressing them to this department. The closing date for this department is five weeks prior to the date of issue. No proof will be sent to the authors. The Board of Editors does not hold itself responsible for the opinions expressed by the correspondents. Communications should not exceed 600 words in length.

On Vector Transforms

JOHN W. MILES
Department of Engineering, University of California, Los Angeles, California
September 30, 1948

THE use of integral transforms, particularly of the Fourier and Fourier-Bessel types, has proved a valuable tool in formulating solutions to the scalar wave equation.[1] Such an approach exhibits a solution as a superposition of cylindrical (or plane) waves, rather than the superposition of sources effected by the direct application of the methods of Green or Riemann. While solutions to the vector wave equation may be deduced from solutions to the scalar wave equation, thereby making use of transform theory, it is sometimes expedient to formulate direct vector solutions, in which case it is desirable to introduce transforms for the vector eigenfunctions.

The solutions to Maxwell's equations are determined by the values of the tangential electric field at the boundaries.[2] In attacking diffraction problems in cylindrical coordinates this boundary may be taken as the plane $z=0$ (plus a hemisphere at infinity), and the problem is to find a solution $\mathbf{f}(u, v, z)$ to the vector wave equation in the cylindrical coordinates (u, v, z) which reduces to a prescribed field $\mathbf{f}(u, v, 0)=\mathbf{f}(u, v)$. Such a solution is given by

$$\mathbf{f}(u, v, z)=\int_{\lambda}\int d\Lambda(\lambda)F(\lambda)\boldsymbol{\phi}_{\lambda}(u, v)\exp[\pm i(k^2-\lambda^2)^{\frac{1}{2}}z], \quad (1)$$

where k is the wave number. Equation (1) represents only the transverse field, but the axial (z) component may be determined directly from Maxwell's equations. The branch points $|\lambda|=k$ must be circumvented in such a way as to satisfy a Sommerfeld radiation condition at infinity. $\boldsymbol{\phi}_{\lambda}$ is an eigenvector satisfying the two-dimensional vector, Helmholtz equation

$$\nabla^2\boldsymbol{\phi}_{\lambda}(u, v)+\lambda^2\boldsymbol{\phi}_{\lambda}(u, v)=0, \quad (2)$$

where λ is an eigenvalue which may be distributed discretely or continuously over a two-dimensional spectrum, an element of which is $d\Lambda(\lambda)$.

It is found that the desired transform $F(\lambda)$ may be written

$$F(\lambda)=\int_{z=0}\int dS(\xi, \eta)\mathbf{f}(\xi, \eta)\cdot\langle\boldsymbol{\phi}_1\rangle_{Av}(\xi, \eta), \quad (3a)$$

and its inversion yields

$$\mathbf{f}(u, v)=\int_{\lambda}\int d\Lambda(\lambda)F(\lambda)\boldsymbol{\phi}_{\lambda}(u, v). \quad (3b)$$

(ξ, η) are coordinates of integration, the bar denotes the complex conjugate, and the dot denotes the scalar product.

In Cartesian coordinates $(u=x, v=y)$ it is found that Eqs. (3) are consistent for the choice

$$\boldsymbol{\phi}_{\lambda}(x, y)=(2\pi)^{-1}(\mu^2+\nu^2)^{-\frac{1}{2}}(\mathbf{i}\mu+\mathbf{j}\nu)\times\exp[i(\mu x+\nu y)], \quad (4)$$

$$\lambda^2=\mu^2+\nu^2, \quad (5)$$

where μ and ν are Cartesian coordinates in the λ-spectrum, and $d\Lambda=d\mu d\nu$.

Equations (3) then become

$$\mathbf{f}(x, y)=\frac{1}{2\pi}\int_{-\infty}^{\infty}d\mu\int_{-\infty}^{\infty}d\nu F(\mu, \nu)(\mu^2+\nu^2)^{-\frac{1}{2}}\times(\mathbf{i}\mu+\mathbf{j}\nu)\exp[i(\mu x+\nu y)], \quad (6a)$$

$$F(\mu, \nu)=\frac{1}{2\pi}\int_{-\infty}^{\infty}d\xi\int_{-\infty}^{\infty}d\eta(\mu^2+\nu^2)^{-\frac{1}{2}}(\mathbf{i}\mu+\mathbf{j}\nu)\cdot\mathbf{f}(\xi, \eta)\times\exp[-i(\mu\xi+\nu\eta)]. \quad (6b)$$

In polar coordinates $(u=r, v=\theta)$ the results are

$$\boldsymbol{\phi}_{\lambda}(r, \theta)=(2\pi)^{-\frac{1}{2}}\lambda^{-1}[\mathbf{r}_1J_n'(\lambda r)+in(\lambda r)^{-1}\boldsymbol{\theta}_1J_n(\lambda r)]\times\exp[i(n\theta-\pi/2)], \quad (7)$$

$$\mathbf{f}(r, \theta)=(2\pi)^{-\frac{1}{2}}\sum_{n=-\infty}^{\infty}\exp[i(n\theta-\pi/2)]\int_0^{\infty}\lambda d\lambda F_n(\lambda)\times[\mathbf{r}_1J_n'(\lambda r)+in(\lambda r)^{-1}\boldsymbol{\theta}_1J_n(\lambda r)], \quad (8a)$$

$$F_n(\lambda)=(2\pi)^{-\frac{1}{2}}\int_0^{2\pi}d\eta\exp[-i(n\eta-\pi/2)]\int_0^{\infty}\xi d\xi\times\mathbf{f}(\xi, \eta)\cdot[\boldsymbol{\xi}_1J_n'(\lambda\xi)+in(\lambda\xi)^{-1}\mathbf{n}_1J_n(\lambda\xi)]. \quad (8b)$$

[1] J. A. Stratton, *Electromagnetic Theory* (McGraw-Hill Book Company, Inc., New York, 1941), Chap. V and VI.
[2] H. M. MacDonald, *Electric Waves* (Cambridge University Press, Teddington, 1902), p. 16; Proc. London Math. Soc. (2) **10**, 91 (1911); Phil. Trans. Roy. Soc. London (**A**)**212** (1916). Also, A. E. H. Love, Phil. Trans. Roy. Soc. London (**A**)**197** (1901).

The Relative Abundance of the Zinc Isotopes*

D. C. HESS, JR., M. G. INGHRAM, AND R. J. HAYDEN
Argonne National Laboratory, Chicago, Illinois
September 24, 1948

IN the course of an examination of a sample of zinc for possible alterations in its isotope abundances,[1] we were led to revise the values for the normal abundances, in the same direction as was later reported in the letter by W. T. Leland and A. O. Nier.[2] Our measurements were carried out both on samples of zinc prepared by chemical reduction of the ore and on samples of electrolytic zinc, and extend the results reported in the letter referred to.

We were at first surprised to find that our samples, and even samples of commercial zinc, showed a large apparent enrichment of the heavy isotopes over the light when compared with Dr. Nier's values of 1936. We learned from the metallurgists that most zinc is now made by an electrolytic process, while twelve years ago, when Dr. Nier's determinations were made,[3] commercial zinc was almost

TABLE I. Abundance of the zinc isotopes.

Mass	64	66	67	68	70
Nier, 1936	50.9	27.3	3.9	17.4	0.5
Electrolytic, I & H	48.89	27.82	4.14	18.54	0.617
Chemical, I & H	48.90	27.82	4.17	18.48	0.623
Leland and Nier, 1948	48.89	27.81	4.07	18.61	0.620

exclusively made by chemical reduction of the ore, followed by a purification by evaporation. We investigated the possibility that this earlier process might have produced the apparent enhancement of the light isotopes. This proved not to be the case; a sample of chemically reduced zinc and a sample of electrolytic zinc could not be distinguished within the accuracy of our measurements as shown in the values given in Table I, lines 2 and 3.

It should be pointed out that the 1936 values of Nier for the abundances of the zinc isotopes have been used as standards for photometric measurements by Ewald[4] and by Duckworth and Hogg[5] for the isotope abundances in copper, which gave a ratio of 2.330 ± 0.032 and 2.277 ± 0.017, respectively. These values, when corrected for the change in the zinc standards, give 2.163 for Ewald's measurements and 2.092 for Duckworth and Hogg's. Our direct electrical comparison of the copper isotopes[6] in connection with the study of meteoritic copper gave a ratio of 2.235 ± 0.010.

* The work described in this article was performed under the auspices of the Atomic Energy Project.

[1] Report ANL-4012, p. 11, July, 1947.
[2] W. T. Leland and A. O. Nier, Phys. Rev. **73**, 1206 (1948).
[3] Alfred O. Nier, Phys. Rev. **50**, 1041 (1936).
[4] H. Ewald, Zeits. f. Physik **122**, 487 (1944).
[5] H. E. Duckworth and B. G. Hogg, Phys. Rev. **71**, 212 (1947).
[6] D. C. Hess, Jr., M. G. Inghram, and R. J. Hayden, Phys. Rev. **72**, 347 (1947).

Space-Charge Wave Amplification Effects

ANDREW V. HAEFF
Naval Research Laboratory, Washington, D. C.
October 5, 1948

A SEARCH for better methods of generation and amplification of microwave energy has led to a conception and a successful development of an entirely new method based on space-charge wave amplification effects occurring as a result of interaction between streams of charged particles. A full account of the theory of the new method, and of the design and performance of special amplifier tubes based on the new method, will be given elsewhere.[1] It is the purpose of this letter to bring early to the attention of physicists the fact that this mechanism of interaction between particles and the associated space-charge waves plays an important part in many natural phenomena. The author believes that such effects as the abnormally intense bursts of solar radio noise associated with sun spot activity, the excess noise in electron beam tubes and magnetrons, the abnormally high temperature of electron clouds in magnetrons, and other effects will find a satisfactory explanation in terms of the new theory, the salient features of which are given below.

If a stream of charged particles of space-charge density ρ_1 and velocity v_1 is injected into the space occupied by another stream of density ρ_2 and velocity v_2, then, in addition to energy interchanges between particles in the two streams caused by scattering, there occurs a partial conversion of kinetic energy of the particles into the energy of electromagnetic fields associated with space-charge fluctuations.

If only the first-order effects of perturbation of space-charge streams are considered, and it is assumed that the density, velocity, current and voltage vary with distance z and time t as

$$V=V_0\exp(\Gamma z+j\omega t),$$

where Γ is the propagation constant and ω is the frequency of the disturbance, then by the use of the Poisson equation, the equation of conservation of charge, and the force equation, the following expression for Γ can readily be derived in terms of velocities v_i of the i components of the stream and the corresponding plasma frequencies $\omega_i=\left(\frac{e}{m}\cdot\frac{\rho_i}{\epsilon}\right)^{\frac{1}{2}}$.

$$\sum_1^i \frac{\omega_i^2}{(\omega+j\Gamma v_i)^2}=1. \tag{1}$$

For a stream consisting of only two components of velocities v_1 and v_2, the real component of Γ, for a special case $\omega_1=\omega_2$ is given by:

$$\Gamma_{\text{real}}=\pm j\frac{\omega_1}{v}\left(\left(\frac{\delta\omega}{v\omega_1}\right)^2+1-\left(4\left(\frac{\delta\omega}{v\omega_1}\right)^2+1\right)^{\frac{1}{2}}\right)^{\frac{1}{2}}. \tag{2}$$

where $\delta=\frac{1}{2}(v_1-v_2)$ and $v=\frac{1}{2}(v_1+v_2)$.

Amplification of space-charge waves occurs only over a limited range of the factor $(\delta\omega/v\omega_1)$ which has been named the inhomogeneity factor. The initial amplitude of the disturbance (V_0) increases exponentially as the space-charge waves travel with the particles in the stream so that the gain in energy of the original disturbance after it traveled a distance z is given by $e^{2\Gamma z}$. Even with moderate charge densities very high energy gain per unit length of the particle stream can be realized. Experimental tubes based on this principle and called the "electron wave tubes" have produced at a frequency of 3000 megacycles electronic gains as high as 80 decibels with electron streams only 20 cm in length and average currents of a few milliamperes. At the same time, the frequency range over which effective amplification takes place is very wide and is approximately given by

$$\Delta\omega\approx\omega\frac{2.32}{(\text{Gain})^{\frac{1}{2}}}. \tag{3}$$

The frequency ω_m corresponding to maximum gain is given by $\omega_m=(\sqrt{3}/2)\cdot(v/\delta)\cdot\omega_1$ and can be much higher than the plasma frequency ω_1.

It is a most striking feature of the new mechanism of energy amplification that it occurs entirely because of interaction of the different components of the stream through their space-charge fields without the presence of any field-supporting resonant or wave-guiding structures. Because of this feature, the electron wave tube offers a

very promising solution to the problem of generation and amplification of energy at millimeter wave-lengths. This feature also makes it easy to understand how electromagnetic radiation over limited frequency bands is produced in nature whenever there exist inhomogeneous streams of charged particles. For example, streams of charged corpuscles emerging from sun spots during solar flares present just such conditions where enormous amplification of space charge fluctuations can occur over a limited frequency range determined by the composition of the streams. The associated space-charge fields radiate the electromagnetic energy in this frequency band, and it is usually observed in radio telescopes as intense bursts of solar noise. Application[2] of the above theory made it possible to estimate the expected spectral energy distribution of radio noise associated with solar flares which agrees well with measurements such as those of Appleton and Hey.[3]

The excess noise in electron-beam tubes and in magnetrons can also be explained in terms of the new theory. The inhomogeneity of the electron stream in beam tubes is caused by d.c. space-charge field and the excess noise is then the result of amplification of the original shot noise due to interaction of the different velocity components of the stream. In magnetrons the original fluctuations of cathode current create fluctuations of space-charge field. These fluctuating fields or waves interact with electrons in such a manner that original fluctuations increase in amplitude and some electrons gain and some lose energy. Since at cut-off fields many electrons return to the cathode, the space-charge waves also travel in both directions and the amplification proceeds to a saturation level determined by the anode potential, the magnetic field, and the density of the electron cloud. Some electrons can thus attain high excess energy proportional to anode potential so that the final energy distribution of the electron cloud may correspond to an apparent temperature of millions of degrees.[4] The flow of current to the anode at magnetic fields exceeding cut-off value can thus be understood.

[1] The author's paper on "The electron wave tube—A novel method of generation and amplification of microwave energy" has been submitted to the Proc. I. R. E.

[2] A fuller account of the theory of generation of abnormal solar radio noise is the subject of a paper now in preparation.

[3] E. Appleton and J. S. Hey, "Solar radio noise," Phil. Mag. **37**, 73–84 (1946).

[4] E. G. Linder, "Excess-energy electrons and electron motion in high-vacuum tubes," Proc. I.R.E. **26**, 346–71 (1938).

Disintegration of Deuterium by Gamma-Rays from ^{24}Na

N. O. LASSEN
Institute for Theoretical Physics, University of Copenhagen, Denmark
September 28, 1948

ACCORDING to theory, the angular distribution of protons created by the process $^2_1D+h\nu\rightarrow{}^1_1H+{}^1_0n$ can be described by the formula $n_\theta=a+b\sin^2\theta$, where n_θ is the number of protons emitted per unit solid angle in a direction making an angle θ with the direction of the incident γ-rays, and a and b are constants. The first constant term is caused by the so-called photomagnetic effect, the second term to the photoelectric effect. The ratio σ_m/σ_e between the cross sections for the two processes can be derived when the ratio $n_{0°}/n_{90°}=a/(a+b)$ is measured, and such measurements have been performed by several investigators.[1–5] However, since the various results do not agree with each other and, furthermore, since mainly the angles $\theta=0°$ and $\theta=90°$ have been examined, measurements of the angular distribution were undertaken by means of a new method.

The instrument used was a battery of proportional counters arranged in parallel and filled with pure deuterium. Each counter was cylindrical, having a length ten times the diameter. The photo-protons created in the gas inside the tubes were recorded by means of a proportional amplifier and a cathode-ray oscillograph which was photographed on a moving film. The magnitude of the pressure inside the counters was such that the range of the protons was about $\frac{3}{4}$ the counter diameter. Hence, protons traveling perpendicularly to the axis of the counters will hit the walls and only a small part of their tracks will lie inside the counters; consequently, these protons will give rise to much smaller pulses on the oscillograph than those moving parallel to the counter axis. Only protons moving in directions deviating from the axis by less than a certain small angle, the magnitude of which is determined by the range and the counter diameter, will end their paths inside the counters and produce pulses of maximum size. A simple calculation shows that the pulse-size distribution curve falls off with increasing pulse sizes, except in the very end where a peak occurs, the height of which is determined by the accuracy of the pulse-size measurements. In order to get reasonably good statistics it was necessary to use a rather strong γ-irradiation (~500 millicuries at a distance of 30 cm), which caused a high background ionization in the counters and consequently a background noise on the oscillograph, which involved a rather high spread in the pulse size measurements. Nevertheless, a pulse size distribution curve with a peak was actually obtained, as shown in Fig. 1. The protons corresponding to this peak will have tracks deviating but little from the counter axis, and hence the angular distribution of the protons can be obtained by measuring the number corresponding to the peak for varying values of the angle θ between the γ-rays and the counter axis. For small values of θ two peaks corresponding

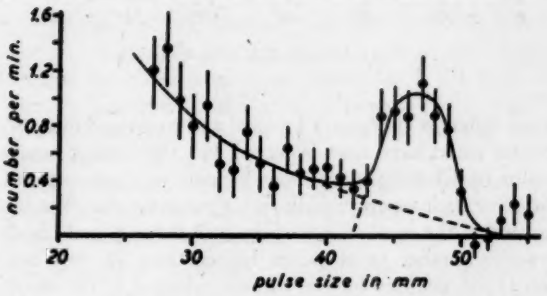

FIG. 1. Pulse-size distribution curve obtained for $\theta=90°$.

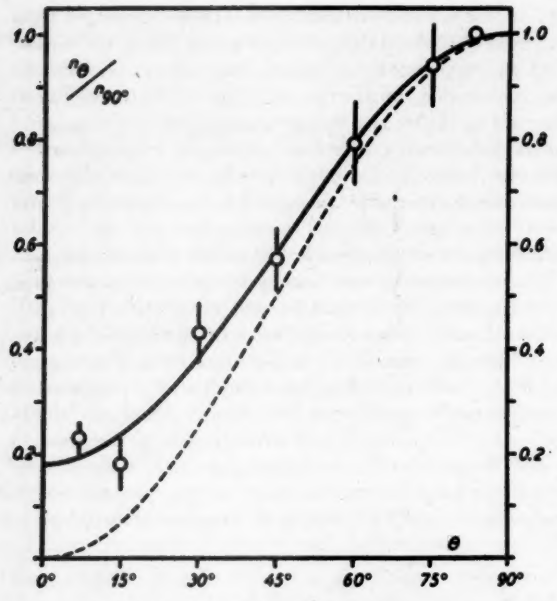

FIG. 2. Angular distribution of photo-protons.

to the different energies of forward and backward directed protons could have been expected, but the limited statistical material and the mentioned spread in pulse sizes did not allow their separation. In fact, for small values of θ the position of the peak was not very well defined, and therefore the number n_θ of pulses higher than 40 mm (see Fig. 1) was counted for the various values of θ. The result of the measurements, in which ^{24}Na was used as a γ-ray source, is given in Fig. 2, where the full-drawn curve corresponds to the formula

$$n_\theta/n_{90°}=a+b\sin^2\theta=0.18+0.82\sin^2\theta.$$

The ratio $a/(a+b)$ is found to be 0.18 ± 0.03, the ratio a/b to be 0.22 ± 0.04, in good agreement with the value 0.26 ± 0.08 given by Graham and Halban.[5] The present experiments give $\sigma_m/\sigma_e=0.33$ and $\sigma_m/\sigma_{\text{total}}=0.25$. The dotted curve in Fig. 2 corresponds to $\sigma_m=0$, and the figure clearly shows that there can be no doubt that both the photomagnetic and the photoelectric effect exist for the γ-energy concerned.

When determining the absolute cross section it is necessary to know the absolute strength of the γ-source and the range ρ of the protons. The author is indebted to Mr. Koefoed-Hansen for measuring the absolute strength of a weak sample of ^{24}Na by means of a special counting arrangement. Unfortunately, ρ is not known very accurately and, hence, the result may be given as follows, where a correction of +20 percent resulting from the absorption of the γ-rays and a correction of −20 percent resulting from the foot on the pulse-size distribution curve are included:

$$\sigma_{\text{total}}=0.8\cdot10^{-27}\cdot\frac{9\rho^2}{11-3\rho}\ \text{cm}^2\pm20\ \text{percent},$$

where ρ is the range in cm deuterium. Putting $\rho=1.5$ cm we get $\sigma_{\text{total}}=2.5\cdot10^{-27}$ cm^2 but, as we have seen, the result depends strongly on the value of ρ chosen.

A more detailed account of the work will soon be published in the Communications of the Danish Academy of Science.

[1] Chadwick, Feather, and Bretcher, Proc. Roy. Soc. **A163**, 366 (1937).
[2] Halban, Nature **141**, 644 (1938).
[3] R. J. Richardson and L. Emo, Phys. Rev. **53**, 234 (1938).
[4] F. E. Meyers and L. C. Van Atta, Phys. Rev. **61**, 19 (1942).
[5] G .A. R. Graham and H. Halban, Jr., Rev. Mod. Phys. **17**, 297 (1945).

Multiple Scattering with Energy Loss

LEONARD EYGES
University of Birmingham, Birmingham, England
September 23, 1948

FERMI[1] has found the distribution function for the lateral and angular displacements of charged particles which undergo multiple elastic scattering in passing through a layer of matter. In his treatment the energy loss which the particles suffer due to ionizing collisions is neglected. In this note we show that energy loss can be taken into account to a good approximation, and that this leads to a simple generalization of Fermi's distribution function.

The diffusion equation for the distribution function $F(t, y, \theta)$ is, in Rossi and Greisen's[1] notation and units,

$$\frac{\partial F}{\partial t}=-\theta\frac{\partial F}{\partial y}+\frac{1}{W^2}\frac{\partial^2 F}{\partial\theta^2}, \tag{1}$$

where $W=2p\beta/E_s$. *We assume that* p *and* β *are functions of* t, i.e., we neglect the fact that a particle at t has traveled a somewhat greater distance than t due to the deviations caused by scattering. For the multiple scattering of high energy particles these deviations will be small and the approximation will be a good one. In (1) then we assume that W^2 is some known function of t, although not necessarily one for which there is an analytic expression. If we apply the Fourier transforms

$$F(t, y, \theta)=\frac{1}{2\pi}\int_{-\infty}^{\infty}\int_{-\infty}^{\infty}G(t, x, \zeta)\exp(i(xy+\zeta\theta))dxd\zeta, \tag{2}$$

$$G(t, x, \zeta)=\frac{1}{2\pi}\int_{-\infty}^{\infty}\int_{-\infty}^{\infty}F(t, y, \theta)\exp[-i(xy+\zeta\theta)]dyd\theta, \tag{3}$$

to (1) we are led to the equation for $G(t, x, \zeta)$,

$$\frac{\partial G}{\partial t}=x\frac{\partial G}{\partial\zeta}-\frac{\zeta^2}{W^2(t)}G. \tag{4}$$

After introducing the two new variables

$$\xi=t+\zeta/x, \tag{5}$$
$$t'=t,$$

Eq. (4) becomes:

$$\frac{\partial G}{\partial t'}=-\frac{x^2(\xi-t')^2}{W^2(t')}G. \tag{6}$$

The solution of (6) is

$$G=H(\xi)\exp\left[-x^2\int_k^{t'}\frac{(\xi-\eta)^2}{W^2(\eta)}d\eta\right], \tag{7}$$

where $H(\xi)$ is the "constant" of integration, and for convenience we have taken the lower limit in the integral to be some fixed number K. The boundary condition is that at $t=0$ there is one particle incident normally at $y=0$, i.e.,

$$F(0, y, \theta)=\delta(y)\delta(\theta). \tag{8}$$

The condition on G is then from (3)

$$G(0, x, \zeta)=1/2\pi. \tag{9}$$

If we write out (7) in terms of the original variables x, ζ, t, we get

$$G(t, x, \zeta)=H(t+\zeta/x)\exp\left[-x^2\int_k^t \frac{(t+\zeta/x-\eta)^2}{W^2(\eta)}d\eta\right]. \tag{10}$$

From (9) we see that

$$H(\zeta/x)=\frac{1}{2\pi}\exp\left[x^2\int_k^0 \frac{(\zeta/x-\eta)^2}{W^2(\eta)}d\eta\right]. \tag{11}$$

Equation (11) gives the functional form of H, and therefore G is completely determined from (10) as

$$G(t, x, \zeta)=\frac{1}{2\pi}\exp\left[-x^2\int_0^t \frac{(\zeta/x+t-\eta)^2}{W^2(\eta)}d\eta\right]. \tag{12}$$

If we define three new functions of t by

$$A_0(t)=\int_0^t \frac{d\eta}{W^2(\eta)}, \tag{13a}$$

$$A_1(t)=\int_0^t \frac{(t-\eta)d\eta}{W^2(\eta)}, \tag{13b}$$

$$A_2(t)=\int_0^t \frac{(t-\eta)^2}{W^2(\eta)}d\eta, \tag{13c}$$

we can write G in the simple form

$$G(t, x, \zeta)=\frac{1}{2\pi}\exp[-(A_0\zeta^2+2A_1\zeta x+A_2x^2)].$$

This expression for G can be put into (3) and the integrations with respect to x and ζ carried out, with the result

$$F(t, y, \theta)=\frac{1}{2\pi(B(t))^{\frac{1}{2}}}\exp\left(-\frac{\theta^2A_2-2y\theta A_1+y^2A_0}{4A_0B}\right), \tag{14}$$

where $B(t)=A_0A_2-A_1^2$. If we assume that W^2 is constant, it is easy to see that (4) reduces to the Fermi solution as given by Rossi and Greisen. If we integrate over y, we get for the angular distribution irrespective of displacement

$$\int_{-\infty}^{\infty} F(t, y, \theta)dy=\frac{1}{2(\pi A_0)^{\frac{1}{2}}}\exp\left(-\frac{\theta^2}{4A_0}\right). \tag{15}$$

Similarly, for the lateral distribution independent of angle

$$\int_{-\infty}^{\infty} F(t, y, \theta)d\theta=\frac{1}{2(\pi A_2)^{\frac{1}{2}}}\exp\left(-\frac{y^2}{4A_2}\right). \tag{16}$$

We can gain a little insight into our formula by comparing (15) and (16). The angular distribution defined by (15) depends on t through A_0, i.e., through $\int_0^t (d\eta/W^2(\eta))$, whereas the radial distribution (16) depends on t through $\int_0^t [(t-\eta)^2/W^2(\eta)]d\eta$. Because of the factor $(t-\eta)^2$ large values of $t-\eta$ are weighted more heavily in the last integral than in the preceding one. This is caused by the fact that a given angular deflection produces a larger *radial* displacement at t the farther from t that it occurs, whereas all angular deflections at any intermediate thickness contribute equally to the total angular deflection at t.

In general the integrals A_1, A_1, A_2 which determine the distribution can be obtained by simple numerical integrations using the range *vs.* momentum curves given, e.g., in Rossi and Greisen's article. In some special cases the A's can be found by direct integration. If, for example, we consider particles with energy much greater than their rest energy, it is a good approximation to assume the rate of momentum loss is independent of the momentum and that $\beta=1$. Then the momentum p of a particle at depth t radiation lengths is $p_0-\epsilon t$, where ϵ is the constant momentum loss per radiation length. Then $W^2(t)=[4(p_0-\epsilon t)^2/E_s^2]$ and the A's become:

$$A_0(t)=\frac{E_s^2t}{4p_0(p_0-\epsilon t)}, \tag{17a}$$

$$A_1(t)=\frac{E_s^2}{4\epsilon^2}\left[\ln\frac{p_0}{p_0-\epsilon t}-\frac{\epsilon t}{p_0}\right], \tag{17b}$$

$$A_2(t)=\frac{E_s^2}{4\epsilon^2}\left[2t-\frac{t^2\epsilon}{p_0}-2\frac{(p_0-\epsilon t)}{\epsilon}\ln\frac{p_0}{p_0-\epsilon t}\right]. \tag{17c}$$

It is interesting to note that if one wished to take energy loss roughly into account using Fermi's original distribution function by taking some *mean* value for $W^2(t)$ that this mean value could not be simultaneously correct for both (15) and (16), i.e., for both the angular and radial distributions.

It is a pleasure to thank Dr. Max Krook for a discussion on the first part of this work and Professor R. E. Peierls for criticizing the manuscript.

[1] B. Rossi and K. Greisen, Rev. Mod. Phys. 13, 267 (1941).

Isotope Effect in the Spectrum of Ne II

K. MURAKAWA AND S. SUWA
Institute of Science and Technology, Komaba, Meguroku, Tokyo, Japan
October 4, 1948

THE spectrum of Ne II was excited in an alumnum hollow cathode discharge tube which was filled with neon of a few mm Hg pressure. It was found that, when the neon was quite free from impurities, the energy of the discharge was spent mainly in exciting the spectrum of the cathode material and only a very weak spectrum of Ne II was obtained, so the experimental arrangement which was finally adopted contained a purifying equipment that absorbed impurity gases only loosely. Under this condition the doublet spectrum[1] was strong, while the quartet spectrum was relatively weak. The fine structure was examined

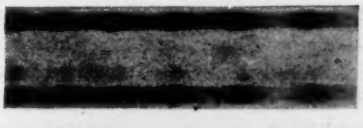

FIG. 1. Enlargement of interference patterns of Ne II λλ3378 and 3393 taken with a quartz Lummer plate of thickness 4.4 mm.

by the use of two glass Lummer plates (thickness = 10 mm and 4.7 mm) as well as of two quartz Lummer plates (thickness = 5.6 mm and 4.4 mm).

Every strong Ne II line was found to consist of two components, the weaker one lying always on the short wave-length side of the stronger one. The intensity ratio of the two components was found by eyes' estimates to be about 1:9. As in the case of the Ne I spectrum,[2] the weaker component can be ascribed to the less abundant isotope Ne^{22} and the other component to the isotope Ne^{20}. Measured isotope effects in some typical lines are given in Table I, and the structure of the lines λλ3378 and 3393 is reproduced in Fig. 1.

TABLE I. Isotope effect in the Ne II spectrum.

λ(A.U.)	Allocation	Isotopic displacement $\Delta\nu$ (cm^{-1})
3727.1	$3s\ ^2P_{1/2}(^3P) - 3p\ ^2D_{3/2}(^3P)$	0.22_7
3713.1	$3s\ ^2P_{3/2}(^3P) - 3p\ ^2D_{5/2}(^3P)$	0.23_3
3392.8	$3s\ ^2P_{1/2}(^3P) - 3p\ ^2P_{3/2}(^3P)$	0.25_7
3378.3	$3s\ ^2P_{1/2}(^3P) - 3p\ ^2P_{1/2}(^3P)$	0.25_1
3323.8	$3s\ ^2P_{3/2}(^3P) - 3p\ ^2P_{3/2}(^3P)$	0.26_0
3694.2	$3s\ ^4P_{5/2}(^3P) - 3p\ ^4P_{5/2}(^3P)$	0.15
3568.5	$3s\ ^2D_{5/2}(^1D) - 3p\ ^2F_{7/2}(^1D)$	0.13_5
3345.5	$3s\ ^2D_{5/2}(^1D) - 3p\ ^2P_{3/2}(^1D)$	0.15_4
3319.8	$3s\ ^2D_{3/2}(^1D) - 3p\ ^2P_{1/2}(^1D)$	0.16_6

All the lines of the doublet system belonging to the combination $3s(^3P) - 3p(^3P)$ that were measured showed a distinctly larger isotope effect (of the order of 0.25 cm^{-1}) than the other lines, especially than the combination $3s(^3P) - 3p(^3P)$ of the quartet system. This situation seems to be somewhat analogous to the Mg I spectrum[3] where the $3p\ ^1P_1 - ns\ ^1S_0$ combination has a larger isotope effect than the $3p\ ^3P - n\ ^3S_1$ combination.

It is hoped to measure in the near future the structure of the lines of other combinations than those here reported and to obtain a more quantitative conclusion.

[1] The Ne II spectrum was classified by T. L. de Bruin and C. J. Bakker, Zeits. f. Physik 69, 19 (1931).
[2] H. Nagaoka and T. Mishima, Sci. Pap. Inst. Phys. Chem. Research (Tokyo) 25, 223 (1934); R. Ritschl and H. Schober, Physik. Zeits. 38, 6 (1937); H. Schober, Physik. Zeits. 40, 77 (1939).
[3] L. G. Mundie and K. W. Meissner, Phys. Rev. 65, 265 (1944).

Photo-Induced Reactions at 20 Mev

DANA L. MOCK, RAMOND C. WADDEL, LAWRENCE W. FAGG, AND RALPH A. TOBIN
Naval Research Laboratory, Nucleonics Division, Washington, D. C.
October 1, 1948

CALCULATED binding energies of neutrons and protons in nuclei indicate that it is energetically possible to remove one neutron or proton from all nuclei with 20-Mev photons. Because of the Coulomb barrier it can be expected that the cross sections for (γ, n) reactions will be larger than those for (γ, p) reactions at the above energy. This letter reports on results obtained when various elements were irradiated with x-rays from a 20-Mev betatron using a platinum target.

The energy spectrum of the x-rays is not known exactly, but the number of photons having a given energy is probably approximately inversely proportional to their energy, up to the maximum energy limit.

The elements investigated were placed about one meter from the x-ray source, and were irradiated for times governed by the half-lives expected or found. Each sample was then transferred to a position close to a thin mica-window counter tube. Pulses from the counter were fed through a scaling unit of suitable scaling factor and the scaler output was recorded on paper tape. Half-lives of less than about two minutes or more than a few months would probably not be detected by the techniques used in this survey.

The elements and compounds irradiated were of C.P. grade and were spectrographically analyzed for impurities. A list of half-lives, together with probable associated reactions, is shown in Table I.

The reactions were assigned to the half-lives, where possible, by a consideration of the following factors: the periods resulting from known $(n, 2n)$ and other reactions, relative abundances, amount and kind of impurities, and initial activities. Long periods not shown in the table are still under measurement.

Of particular interest is the fact that rhodium has a relatively large cross section, judged from the fact that the 205-day period was excited to an activity greater than 1000 counts per minute with an x-ray irradiation of only 120 hours at an intensity of about 40 roentgens per minute.

TABLE I. Reactions and half-lives resulting from irradiation with x-rays generated by a 20-Mev betatron.

Probable reaction	Half-life	Probable reaction	Half-life
$As^{75}+\gamma \rightarrow As^{74}+n$	(16.8±0.8)d	$Ag^{109}+\gamma \rightarrow Ag^{108}+n$[a]	(2.3±0.1)min.
$Cb^{93}+\gamma \rightarrow Cb^{92}+n$	(9.8±0.7)d	$Ag^{107}+\gamma \rightarrow Ag^{106}+n$[a]	(24.3±0.1)min.
$Hg+\gamma \rightarrow Hg^{*}$(a)	(44.4±0.5)min.	$Pd^{110}+\gamma \rightarrow Pd^{109}+n$	(14.1±0.3)hr.
$I^{127}+\gamma \rightarrow I^{126}+n$[a]	(13.1±0.5)d	$Pd+\gamma \rightarrow ?$[e]	(26±5)min.
$Sn^{114}+\gamma \rightarrow Sn^{113}+n$	~100d[c]	$Pd+\gamma \rightarrow ?$[d]	(4.9±1)min.
$Sn+\gamma \rightarrow ?$[e]	(45±1)hr.	$Rh^{103}+\gamma \rightarrow Rh^{102}+n$	~210d[c]
$Sn^{124}+\gamma \rightarrow Sn^{123}+n$[a]	(41.5±0.5)min.	$Cd^{116}+\gamma \rightarrow Cd^{115}+n$	(57.5±2)hr.
$Ru^{104}+\gamma \rightarrow Ru^{103}+n$	(45±1)d	$Cd+\gamma \rightarrow ?$[e]	(19.8±0.5)hr.
$Ru^{98}+\gamma \rightarrow Ru^{97}+n$	(2.8±0.1)d	$Cd^{110}+\gamma \rightarrow Cd^{109}+n$	(38±5)min.
$Ru^{96}+\gamma \rightarrow Ru^{95}+n$	(1.6±0.1)hr.	$Pt^{196}+\gamma \rightarrow Pt^{*}$	(87±5)min.
$Ru^{102}+\gamma \rightarrow Tc^{101}+H^1$[a]	(16.5±0.5)min.	$Bi+\gamma$	no measurable activity
$Ba^{134}+\gamma \rightarrow Ba^{133}+n$[b]	(38±1)hr.		
$Ba+\gamma \rightarrow Ba+?$[b]	(5±0.5)hr.		

[a] Indicates reaction has been previously reported.
[b] Indicates active product followed a barium chemical separation.
[c] Indicates half-life is estimated, measurements not yet complete.
[d] Indicates activity possibly due to copper contamination.
[e] ? or absence of mass number indicates that evidence is insufficient for an assignment.

It may also be noted that only one (γ, p) reaction was encountered. Other such reactions may have been masked by the more prolific (γ, n) activities.

The 26-minute palladium activity could have been produced by a small neutron component in the radiation. However, samples irradiated for equal times with and without paraffin and borax neutron shielding showed similar specific activities.

The authors thank Mr. S. H. Cress and Mr. D. I. Walter of this laboratory for assistance in preparing and analyzing samples.

The Rotational Spectrum of Ethylene Oxide

G. L. CUNNINGHAM, W. I. LEVAN,* AND WILLIAM D. GWINN
Department of Chemistry and Department of Electrical Engineering, University of California, Berkeley, California
September 27, 1948

ELEVEN strong lines of the rotational spectrum of ethylene oxide have been observed by us in the microwave region. The spectrograph used is similar to that described by Hughes and Wilson,[1] employing Stark effect modulation of the energy levels. The voltage applied to the electrode was a 40-kilocycle square wave with a maximum height of 600 volts/cm. In order to resolve all the components of the lines, an added d.c. bias voltage was used. In this way, fields up to 3000 volts/cm were obtained. Frequencies were measured by comparison with a crystal-controlled oscillator, standardized by comparison with *WWV*. The frequencies of the lines observed are given with an accuracy of ± 1 megacycle or better. The inability of our unbiased modulation voltage to separate the components of low M values from the unperturbed line limits the precision.

The assignments of the $3_{-1}-3_1$, 3_1-3_3 and 4_0-4_2 lines were determined by resolution of the Stark components and application of the method of analysis of Golden and Wilson.[2] From these it is possible to calculate κ and $(a-c)$[3] and predict the frequencies of all other transitions for which $\Delta J=0$. While the tables of King, Hainer, and Cross[3] are invaluable for interpretation and preliminary calculations, interpolation with their tables does not give sufficiently precise values for our purposes, so that our final calculations of the energy levels were made from the equations given by Nielsen.[4]

TABLE I.

Frequency observed	Assignment	$\frac{(a-c)^*}{2}$	Δ
39,582	0_0-1_0	—	—
24,924.4 mc	$2_{-2}-2_0$	5692.9	—
23,134 mc	3_1-3_3	5692.6	0.3
23,610 mc	$3_{-1}-3_1$	5692.4	0.5
39,677 mc	3_0-3_2	5692.2	0.7
24,834.3 mc	4_0-4_2	5692.2	0.7
29,688 mc	5_1-5_3	5692.0	0.9
37,781 mc	$5_{-1}-5_1$	5692.0	0.9
35,791 mc	6_0-6_2	5691.6	1.3
38,702 mc	6_2-6_4	5691.2	1.7
37,329 mc	7_1-7_3	5690.7	2.2

* Values of $(a-c)/2$ calculated, using $\kappa=0.40932$.

The value of κ best fitting the $2_{-2}-2_0$, $3_{-1}-3_1$, 3_1-3_3, and 4_0-4_2 lines was found to be 0.40932 ± 0.00002, and from this the value of $(a-c)/2$ for each line was calculated. These are shown in Table I along with the values for the other lines which were also measured. It may be observed that the value of $(a-c)$ decreases regularly as J increases. This decrease is undoubtedly due to centrifugal distortion. We select the value of 5693.0 ± 0.5 mc as the probable ground state value of $(a-c)/2$. A calculation of the effect of centrifugal distortion on the variation of $(a-c)$ and κ is in progress.

The precise value of $(a+c)$ cannot be calculated if no line with $\Delta J=1$ is observed. The lowest such line of reasonable intensity is the 0_0-1_0 transition, whose frequency is exactly equal to $(a+c)$. This transition has been observed at 39,582 mc. From the values of $(a+c)$, $(a-c)$, and κ, we can calculate the moments of inertia to be:

$$I_A=32.921\times10^{-40}\ \text{g-cm}^2$$
$$I_B=37.926\times10^{-40}\ \text{g-cm}^2$$
$$I_C=59.510\times10^{-40}\ \text{g-cm}^2.$$

We have observed about five lines attributable to natural isotopic species in the 23,000–25,000-mc region and are engaged in a search for further transitions and in the synthesis of isotopic molecules in order to determine the bond distances. The following lines have been predicted,

TABLE II.*

Transition	$A\times10^6$	$B\times10^6$
$2_{-2}-2_0$	−1.56	−0.375
$3_{-1}-3_1$	−0.287	1.24
3_1-3_3	0.385	0.797
4_0-4_2	−0.120	1.05
0_0-1_0	14.0	

* Coefficients in the equation $\Delta\nu_M=(A+BM^2)E^2$, where $\Delta\nu$ is in mc/sec. and E is in volts/cm.

and lines in the proper region observed, but not measured because of experimental difficulties:

$2_{-1}-2_1$ 34,157 mc
4_2-4_4 34,088 mc.

The Stark coefficients of the lines which have been resolved are shown in Table II. The value of A for the 0_0-1_0 line is calculated to be 12×10^{-6}. The observed values are rather uncertain because of the broadness of the components at high voltages and difficulty of sufficiently precise control of electrode spacing. The value for the 0_0-1_0 line is particularly uncertain, as a result of the difficulty of working at the higher frequency.

We wish to express our appreciation to the Research Corporation for a grant-in-aid in support of this research.

* Department of Electrical Engineering.
[1] R. H. Hughes and E. B. Wilson, Jr., Phys. Rev. 71, 562 (1947).
[2] S. Golden and E. B. Wilson, Jr., J. Chem. Phys. 16, 669 (1948).
[3] King, Hainer, and Cross, J. Chem. Phys. 11, 27 (1943).
[4] Harold H. Nielsen, Phys. Rev. 38, 1432 (1931); corrected by Randall, Dennison, Ginsburg, and Weber, Phys. Rev. 52, 160 (1937).

Proposed Method for Measuring Scattering of Particle Tracks*

S. A. GOUDSMIT
Brookhaven National Laboratory, Upton, New York
AND
W. T. SCOTT
Smith College, Northampton, Massachusetts
September 23, 1948

DETERMINATIONS of range, grain or droplet count, and curvature of particle tracks have lately been supplemented by measurement of the scattering.[1] Because of the wide spread of the scattering data, they do not give

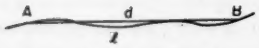

FIG. 1. Scattering of particle track.

precise information but only occasional confirmatory evidence as to the nature or energy of the particle. The measurement itself is rather crude and too involved for the little knowledge gained from it.

The present method.[2] The track of length l is divided in a number of equal segments ΔS. The small angles α_k between the chords of consecutive segments k, $k+1$ are measured and multiplied by the kinetic energy E_k of the particle at the end of the segment k. The square of this product is summed. Thus, a measure for the scattering is essentially given by

$$q=(1/l)\,\Sigma\, E_k^2\alpha_k^2. \tag{1}$$

The average value of q can be compared with theory. If the segments have a length ΔS, one has[3]

$$\langle\alpha^2\rangle_{Av}=\tfrac{2}{3}G(E)\Delta S.$$

The theoretical expression for $G(E)$ changes somewhat with derivation and interpretation and is of the form (non-relativistic)[4]

$$G(E)=(a/E^2)\,\log(bEM)^{\frac{1}{2}}.$$

Approximating the sum by an integral, we have

$$\langle q\rangle_{Av}=(2/3l)\int_0^l dS E^2(S)g(S);\quad g(S)=G(E(S)). \tag{2}$$

For the evaluation of $\langle q\rangle_{Av}$ it is necessary to know the dependence of E upon S, that is, the range-energy relation. One assumes in the measurement that the track is produced by a proton, and a comparison of the measured and theoretical values of q indicates whether this assumption is probably correct, or what the probable mass might have been.

The proposed method. Essentially the same information can be obtained in a simpler way. Consider in Fig. 1 the portion AB of a track. We now take as a measure of the scattering the difference $(l-d)$ of the lengths of the track and of the line AB. The length l can easily be measured on a projection or an enlargement by means of a map measure, a little wheel with connected dial. The geometry is simple and for the average value we find

$$\langle l-d\rangle_{Av}/l=\frac{1}{2}\int_0^l S(l-S)g(S)ds/l^2. \tag{3}$$

We see that result (3) is very similar to (2) except for the weight factor of $g(S)$.

Far from the end of the track, where the energy is roughly constant, one can put $G(E)$ outside the integral and obtain

$$\langle l-d\rangle_{Av}/l=(1/12)G(E)l. \tag{4}$$

The old method gives for this case

$$\langle q\rangle_{Av}=\tfrac{2}{3}E^2G(E). \tag{5}$$

Evaluation near end of track. A semi-empirical range-energy relation for photographic emulsions is[5]

$$E=\kappa M^{\frac{1}{2}-\epsilon}r^{\frac{1}{2}+\epsilon}.$$

The residual range r is the same as our $(l-S)$ if the end portion of the track is taken. Substituting in the integrals (3) and (2) gives

$$\langle l-d\rangle_{Av}/l=a\left[\log b\kappa M^{\frac{1}{2}-\epsilon}l^{\frac{1}{2}+\epsilon}-\frac{(3-4\epsilon)(1+2\epsilon)}{4(1-2\epsilon)(1-\epsilon)}\right]\Big/ 8(1-2\epsilon)(1-\epsilon)\kappa^2M^{1-2\epsilon}l^{2\epsilon}, \tag{6}$$

$$\langle q\rangle_{Av}=(E_p^2/l)\times a[\log b\kappa M^{\frac{1}{2}-\epsilon}l^{\frac{1}{2}+\epsilon}-\tfrac{1}{2}(1+2\epsilon)]\times 3\kappa^2M^{1-2\epsilon}l^{2\epsilon}. \tag{7}$$

In the last expression, we assume that the scattering has been measured as if the particle were a proton, so that E_p is the energy of a proton of range l. We notice that both expressions are essentially inversely proportional to $M^{1-2\epsilon}$.

For Ilford plates, one has $a=2.48\times10^{-4}$, $\log b=16.58$. This gives for the last 200 microns of a track a value for $\langle l-d\rangle_{Av}$ of 3.9 microns for π-mesons, 5.6 microns for μ-mesons, and 1.2 microns for protons.

Accuracy. The objection might be raised that the proposed method is not accurate. For an arc of a circle, for example, it seems easier to measure the angle between two chords than the difference of arc and chord. If, however, we divide the arc into several small segments and have to measure several very small angles, it soon becomes easier to measure the difference between chord and total arc length. Besides the limitation set by the inaccuracy of the measurements themselves, it is also essential to consider the expected statistical distribution. It will be shown in a later note by one of us (W.T.S.) that for both methods these distributions have a very wide spread and are, moreover, quite skew. Large deviations from the above given average values are highly probable. The angle method may become more accurate under experimental conditions for which the mean scattering becomes unusually large. In general, however, high precision is definitely out of place here and great care must be taken in the determination of masses by use of scattering measurements.

* Research carried out at Brookhaven National Laboratory under the auspices of the Atomic Energy Commission.

[1] S. Lattimore, Nature 161, 518 (1948).

[2] E. O. Salant, private communication.

[3] The factor $\frac{2}{3}$ arises from using angles between chords instead of the tangent angles.

[4] $a=1.23Z^2z^2e^4N\times10^8$ (Mev)^2/micron,
$b=1.615\times10^8/Z^{\frac{1}{3}}$ (proton mass $\times$Mev)$^{-1}$.

Ze is the charge of the scatterer, N the number of scatterers per cc, ze the charge of the incident particle. For a mixture one must take the average of $G(E)$. The numerical factor of b is not quite certain. The value used here is obtained from Eq. (4) of S. Goudsmit and J. L. Saunderson, Phys. Rev. 58, 36 (1940). It has to be multiplied by $(181\theta_{max}/150)^2$ to agree with the expression of B. Rossi and K. Greisen, Rev. Mod. Phys. 13, 240 (1941).

[5] From a graph of proton measurements by C. F. Powell as given by B. T. Feld, Tech. Report 8, T.O. VI, Navy Contract N5ori-78, M.I.T. (1948), we find using the interval 100 to 1000 microns, $k\simeq0.21$, $\epsilon\simeq0.10$, when M is in proton masses, r in microns and E in Mev.

On the Relative Yields of (γ, n) Reactions

W. A. BOWERS
University of North Carolina, Chapel Hill, North Carolina
September 23, 1948

MEASUREMENTS of (γ, n) yields for a number of different nuclei made recently by Perlman and Friedlander[1] using the G. E. 100-Mev betatron have indi-

cated a sudden and rather surprising increase in yield around mass 60. Thus the $Ni^{58}(\gamma, n)$ yield is about 6 as compared with about 30 for Cu^{63}.

It may be pointed out that these figures are not necessarily inconsistent with the statistical theory of nuclear reactions (evaporation model). According to the statistical theory,[2] the yield will depend quite sensitively on the binding energy of a neutron to the nucleus in question. New thresholds of (γ, n) reactions have been measured by Baldwin and Koch,[3] who find a threshold of 10.9 ± 0.3 Mev for the Cu^{63} reaction. Although no data seem to be available on Ni^{58}, the same authors find 14.2 ± 0.4 Mev for the $Fe^{54}(\gamma, n)$ reaction. Since $_{28}Ni^{58}$ and $_{26}Fe^{54}$ both have a neutron excess of two, and in fact differ from each other by just an alpha-particle, whereas $_{29}Cu^{63}$ has a neutron excess of five, differing from $_{28}Ni^{58}$ by the addition of one proton and four neutrons, it is perhaps reasonable to suppose the binding energy of a neutron in the Ni^{58} nucleus to be about the same as that in Fe^{54}. With this assumption one can calculate the ratio of Cu^{63} to $Ni^{58}(\gamma, n)$ yield, using the level density formula $\exp(aE)^{\frac{1}{2}}$,[2] with $a=15$ Mev^{-1}, and taking the betatron spectrum to be inversely proportional to the energy.[1] One finds a ratio of about 4 using the neutron binding energies 10.9 Mev and 14.2 Mev, respectively, for Cu^{63} and Ni^{58}. By going to the extreme values consistent with the experiments quoted above, namely, 10.6 Mev and 14.6 Mev, respectively, one raises the ratio to slightly over 5, which is about the same as the experimental value.

Thus the experimental (γ, n) yields for the heavier nuclei can probably be understood within the framework of the statistical theory, considering all the uncertainties in the theoretical formulae (level densities, binding energies, etc.). For the lighter nuclei (mass <50), the statistical treatment is not expected to hold.

[1] M. L. Perlman and G. Friedlander, Phys. Rev. **74**, 442 (1948).
[2] V. F. Weisskopf and D. T. Ewing, Phys. Rev. **57**, 472 (1940).
[3] G. C. Baldwin and H. W. Koch, Phys. Rev. **67**, 1 (1945).

The Melting Pressure of Helium II

J. E. Haggenmacher
Commonwealth Color and Chemical Company, Brooklyn, New York
October 4, 1948

TAMMANN[1] proposed the equation

$$T-1=\log(P_{\text{atmos}}-24.0),$$

for representing the melting pressure of helium up to 2.5°K. The equation, however, does not account for the singularity in the curve on meeting the λ-line.

The elliptic function,

$$p=a-[r-n(T-l)^2]^{\frac{1}{2}}, \quad (1)$$

$$dp/dT=[n(T-l)/a-p], \quad (2)$$

reproduces the values given by Keesom and Keesom[2] from 1.15 to 1.78°K with an average deviation of 0.1 percent and a maximum deviation of 0.3 percent.

TABLE I.

T, °K Scale 1937	p, atmos. K.K.	p, atmos. Eq. (1)	dp/dT Eq. (2)
1.15	25.27	25.29	0.13
1.20	25.32	25.32	0.89
1.30	25.50	25.49	2.46
1.40	25.81	25.82	4.20
1.50	26.32	26.34	6.36
1.60	27.13	27.12	9.43
1.70	28.39	28.31	15.2
1.75	29.30	29.21	21.1
1.78	29.96	29.99	31.8

With $a=32$, $r=45$, $n=100$, and $b=1.14$, the results of the calculations are shown in Table I.

[1] W. H. Keesom, *Helium* (Elsevier Publishing Company, Inc., Amsterdam, 1942), p. 202.
[2] Reference 1, p. 203.

Discrepancies Caused by Source Charging in Beta-Spectrometers

C. H. Braden, G. E. Owen, J. Townsend, C. S. Cook, and F. B. Shull
Department of Physics, Washington University, St. Louis, Missouri
September 27, 1948

A STUDY is being made of the radiations from Na^{22}, which emits positrons and gammas with a half-life of about three years. A small 180° spectrometer, a thin lens, and a large double-focusing spectrometer[1] have been used for this purpose. Each instrument employs G-M tubes whose thin Zapon windows have a low energy cut-off of less than five kilovolts.

The purpose of this letter is to report on a somewhat disturbing phenomenon which became apparent early in the investigation. A measurement of the positron spectrum with the lens spectrometer, which does not resolve positrons and negatrons, indicated the presence of a strong low energy peak at about 9 kev. Further work with the 180° instrument uncovered a strong negatron peak at 8 kev, whose intensity is roughly half that of the positron spectrum. This disagreement on the energy of the peak led us to seek a further check using the double-focusing spectrometer. The strong negatron peak was again found, but at about 25 kev. In all three instruments the same sodium chloride source was used. It was deposited in a thin layer upon a thin backing of Zapon.

It has been found that this enormous discrepancy stems from the fact that the sources are Zapon-mounted, and are therefore well insulated electrically from the body of the spectrometer. The sodium source and the spectrometer body form, in effect, a small capacitance, with a very high resistance leakage path between them. The magnitude of the capacitance will vary from instrument to instrument. The excess of positron emission develops a negative charge on the source, thus gradually establishing a considerable potential difference between source and vacuum chamber. As a result, positrons are decelerated and negatrons are accelerated.

To substantiate the above explanation, further experiments were carried out. In one, the source was backed by a grounded aluminum foil and a search was made for the negatron line with the lens spectrometer. No peak was observed, indicating that the unaccelerated negatrons have an energy below the cut-off energy of the window. In a second experiment, this time with the double-focusing spectrometer, the negatron peak from a Zapon-mounted, ungrounded, originally uncharged source was followed over a period of about eleven days.

The results are shown in Fig. 1, where the energy of the

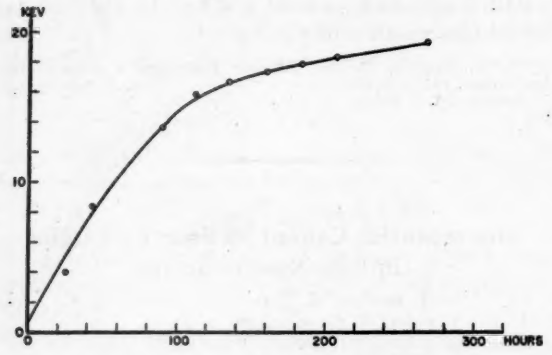

FIG. 1. Plot showing charging of an insulated beta-source. The circles indicate the measured energy of a monochromatic negatron line at different times following the insertion of an uncharged source.

negatron line is plotted as a function of time. The peak was unobservable during the first few hours, being completely stopped by the counter window. Thereafter, its energy was found to increase as a roughly exponential function of time, approaching an asymptotic value of about 21 kev. Extrapolation back to zero time indicates that the unaccelerated negatron energy is probably less than one kev, but the exact value is very uncertain. It is perhaps conceivable that these negatrons are Auger electrons which follow a K-capture process, but this is only a hypothesis at present. Further work is under way in search of a more positive identification.

The importance of these findings lies in the fact that a considerable number of recent studies of beta-spectra and internal conversion lines have been performed with sources which were supported on non-conducting backing-foils such as Zapon, Nylon, Cellophane, and the like. In such cases, the experimental data must be viewed with suspicion, since it seems altogether possible that source-charging effects similar to those described here may have been involved. Not only are energy measurements affected, but it seems quite likely that the effective solid angle of the spectrometer for beta-particles of low energy is altered, thus distorting the spectrum shape.

It is possible that the phenomenon discussed in this letter has contributed largely to the discrepancies noted in results reported by different workers in the field.

This work has been assisted by the joint program of the Office of Naval Research and Atomic Energy Commission.

[1] F. N. D. Kurie, J. S. Osoba, and L. Slack, Rev. Sci. Inst. 19, 771 (1948).

Half-Life of UX_1 (Th_{234})*

G. B. KNIGHT AND R. L. MACKLIN
K-25 Research Laboratories, Carbide and Carbon Chemicals Corporation, Oak Ridge, Tennessee
September 29, 1948

THE half-life of UX_1 has recently been redetermined in this laboratory. Several values are reported in the literature including 24.5 days by Curie *et al.*[1] in 1931 and more recently 24.1±0.2 days by Sargent[2] in 1939. The present work was undertaken to reduce the uncertainty in this constant and thereby allow a more accurate calculation of the quantities of U_{234} grown from samples of UX_1. As a preliminary step, the data of Sargent[2] were re-evaluated statistically. The estimate of the half-life arrived at by applying the method of least squares to the logarithm of Sargent's observed activities and associated decay times was 24.03±0.27 days. The error here forms the limits of the 95 percent confidence belt. The half-life was then redetermined independently.

Samples of uranium largely freed of the U_{235} and U_{234} isotopes and other radioactive contaminants were used as a source of UX_1 for half-life determinations. The UX_1 was isolated after a suitable growth period by precipitating zirconium iodate as a carrier in a uranyl nitrate solution. The first precipitate so formed was dissolved in concentrated hydrochloric acid, and a second precipitation then made to further reduce the traces of occluded uranium present.

The final precipitate was mounted for counting in a thin film on a one-inch filter paper disk. Two such samples were prepared and counted.

Two standard thin-walled (0.006-inch) Geiger counters (Technical Associated Model GS-4 mountings and circuits) were used, each sample being counted on both. The first sample had an initial counting rate of some eleven hundred counts per minute and was counted for seventy-one hour periods on each counter during the 1700 hours (3 half-lives) immediately following sample preparation. The second sample had an initial rate near three thousand and was counted for about one hundred one-hour periods on each counter during the 2200 hours (4 half-lives) immediately following its preparation.

A close check on counter sensitivity was maintained by overnight counts of high purity U_3O_8 samples which had had two years to approach equilibrium with UX_1 and UX_2.

All sample counts were corrected for counter shift, coincidence losses (never over 1.5 percent), and background (determined by counting zirconium iodate blanks).

The decay curve of each of the four samples was found by the usual method of fitting a least squares line to the collection of points formed by the logarithms of the corrected counting rates with the associated time of measurement of each rate, assuming the time as precisely known. Each point was weighted as the reciprocal of the total variance of its logarithm. From the slope of this least squares line, an estimate of the half-life may be readily computed.

The data for each sample on each counter were tested for curvature (the expected effect of a long-lived contami-

nant such as U_{238}) in two ways. The deviation of the logarithm of each sample count from its least squares line was calculated and shown not to be preponderantly positive or negative near either the middle or the ends of the periods of measurement of the sample. The variances of these deviations were compared, using the F test, with the internally predicted variances. In only one of the four cases did the deviations show a significantly larger variance than that due to the counting statistics alone.

Using the larger variance in each case, the following four estimates of half-life were calculated:

Sample	*Counter A*	*Counter B*
I	24.14±0.10 days	24.04±0.07 days
II	24.13±0.04 days	24.09±0.04 days

There being no evidence of significant differences among these values they were averaged and the error of the mean (95 percent confidence interval limits) determined by propagation of the individual errors. The final value thus arrived at is 24.101±0.025 days. These data support Sargent's earlier data and give a tenfold decrease in the uncertainty of the half-life of uranium X_1.

* This document is based on work performed under Contract No. W-7405-Eng-26 for the Atomic Energy Commission by Carbide and Carbon Chemicals Corporation, at Oak Ridge, Tennessee.

[1] Curie, Debierne, Eve, Geiger, Hahn, Lind, Meyer, Rutherford, and Schweidler, Rev. Mod. Phys. **3**, 427 (1931).
[2] B. W. Sargent, Can. J. Research **A17**, 103 (1939).

Angular Correlation of Successive Gamma-Ray Quanta. II*

EDWARD L. BRADY AND MARTIN DEUTSCH
Massachusetts Institute of Technology, Cambridge, Massachusetts
September 23, 1948

SINCE our first communication on this subject[1] the use of Kallmann scintillation counters has greatly increased the accuracy of the experiments. The approximately tenfold gain in efficiency over G-M counters permits useful coincidence counting rates about a hundred times greater than formerly. Figure 1 shows the angular correlation observed by this improved method for six radioactive substances indicated in the figure. The gamma-rays are, of course, emitted by the product nuclei Ni^{60}, Ti^{46}, Mg^{24}, Ba^{134}, Sr^{88}, and Pd^{106}, respectively, all of which are of even-even type and have presumably $J=0$ in the ground state. The abscissa in Fig. 1 is the angle θ between the directions of emission of the two successive gamma-rays and the ordinate is the ratio of the coincidence rate observed at the angle θ to that observed at $\theta=\pi/2$. The vertical lines indicate standard deviations for the points indicated. The errors for the other points are of comparable magnitude. All results are corrected for the finite angular resolution of the instrument, determined by observations on annihilation radiation.

The solid line in Fig. 1a represents the calculated[2] distribution for two quadrupole quanta and angular momenta $J=4, 2, 0$, respectively, for the three states involved. The solid line in Fig. 1b has the shape calculated[2] for two quadrupole quanta, $J=0, 2, 0$ but with the coefficients R/Q and S/Q only half as big as calculated from theory. The dotted line represents a distribution calculated by Ling[3] from a proposed disintegration scheme for Y^{88} by Peacock[3] considering interference between electric quadrupole and magnetic dipole radiation for $J=2, 1, 0$.

In every case investigated an anisotropic correlation was found. In every case except Y^{88} the probability is greatest for the two quanta to be emitted in opposite directions. The

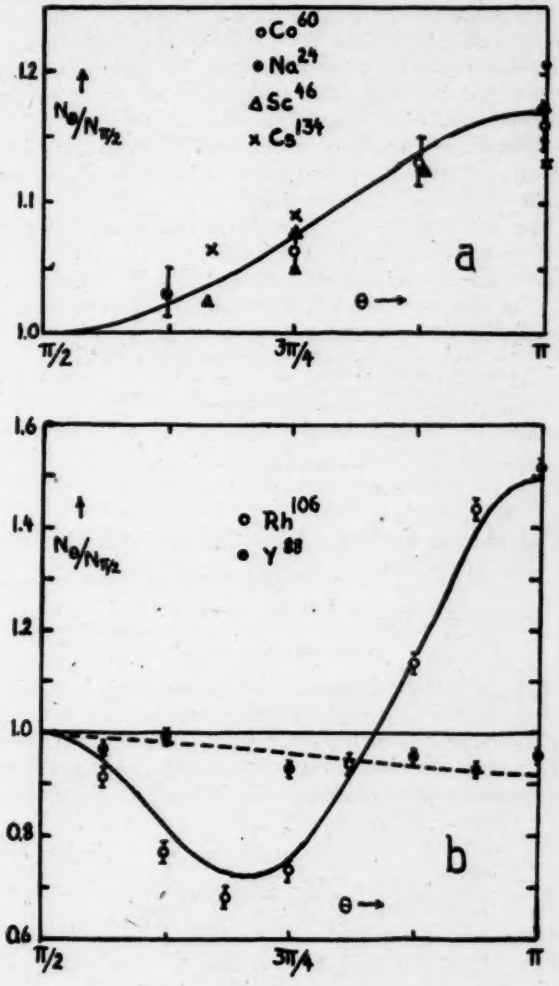

FIG. 1. Angular correlation of successive quanta. Note the different scales in (a) and (b).

results for the four substances shown in Fig. 1a are consistent with two quadrupole quanta and $J=4, 2, 0$ but other interpretations are possible. The distribution for Y^{88} is best explained by interference between electric and magnetic radiations. The particularly high coincidence rate at exactly $\theta=\pi$ for Na^{24} and Y^{88} might be explained by the presence of a few positrons, perhaps from internal pair conversion. Both rays of Rh^{106} must be at least quadrupole and the first excited state of Pd^{106} must therefore have

$J \geqslant 2$. The assignment $J=0, 2, 0$ to the three states concerned which is suggested by the shape of the curve could be accepted only if a reason could be found for the reduction of the coefficients by a factor of two. Obvious possibilities of instrumental causes were ruled out by appropriate tests. The possibility of interference by other gamma-rays seems unlikely because the curve remained unchanged by lead absorbers around the source. It is possible that the coefficients of the angular anisotropy are reduced by some perturbation destroying the constancy of the magnetic quantum numbers of the intermediate state, particularly the hyperfine structure interaction. However, a magnetic field of about 10^4 gauss did not affect the correlation in Rh^{106} or any of the other substances. The experiment was performed only with moderate precision, and may not be entirely conclusive. The assignment of J values to Pd^{106} is important because Peacock[4] has based a strong argument for the validity of Gamow-Teller selection rules on evidence that the second excited state does *not* have $J=0$.

A complete discussion of the experimental method and of the results and their interpretation will be given in a paper to be submitted soon for publication in this journal.

The sources, except Y^{88}, were obtained from Oak Ridge.

* Supported in part by the Office of Naval Research.
[1] E. L. Brady and M. Deutsch, Phys. Rev. **72**, 870 (1947).
[2] Donald R. Hamilton, Phys. Rev. **58**, 122 (1940).
[3] Private communication.
[4] W. C. Peacock, Phys. Rev. **72**, 1049 (1947).

Correlation between Direction and Polarization of Successive Gamma-Ray Quanta*

MARTIN DEUTSCH AND FRANZ METZGER
Massachusetts Institute of Technology, Cambridge, Massachusetts
September 23, 1948

HAMILTON[1] has calculated the expected correlation between the polarization of one quantum and the direction of emission of the other for two successive gamma-rays. We have succeeded in observing this effect. The apparatus is shown schematically in Fig. 1. A, B, C represent the naphthalene crystals of three Kallmann counters. Counters A and B, connected in coincidence, form the polarimeter determining the polarization of γ_1, while γ_2 emitted simultaneously at the angle θ with respect to γ_1 is counted in counter C. If γ_1 experiences a Compton encounter in A, a scintillation is counted due to the recoil electron e. The scattered quantum γ_e is most likely to move in the plane perpendicular to the electric vector of γ_1; if γ_e is in or near the common midplane of A and B, it is very likely to cause a count in B because of the high efficiency of the Kallmann counter for soft quanta. Thus A and B define the "ϕ-plane" making an angle φ with the "θ-plane" formed by the two rays γ_1 and γ_2. Coincidences are most likely to occur between A and B when the electric vector of γ_1 is perpendicular to the ϕ plane. Exactly the same argument is valid if γ_1 strikes crystal B and γ_e enters A.

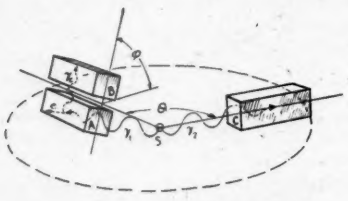

FIG. 1. The coincidence polarimeter.

The polarimeter was tested with gamma-rays of Co^{60} and Cs^{134} scattered through 90° by an aluminum scatterer. The observed difference in counting rate when the polarimeter was rotated through 90° indicated that for perfectly plane polarized radiation the ratio of the counting rates in the two perpendicular positions would be $D=2.1\pm0.3$. D measures the effectiveness of the polarimeter.

The actual experiments consisted of observing the triple coincidence rate $N(ABC)$ for $\varphi=0°$ and $\varphi=90°$ for various values of θ. The single counting rates and the twofold coincidences $N(AB)$, $N(AC)$, and $N(BC)$ were also counted to correct for slight asymmetries due to the difference in the effective value of θ in the two positions and to evaluate the chance coincidence rate. $\varphi=90°$ corresponds to the electric vector of γ_1 being in the θ-plane and the counting rate $N(ABC)$ in this position is denoted by $N_{\parallel}$. The counting rate for $\varphi=0°$ is denoted by $N_{\perp}$. Typical values of $N(ABC)$ are between 5 and 15 c.p.m. It follows from the Klein-Nishina formula that the polarimeter should be most efficient for low energy gamma-rays. Also strong polarization effects are expected in general when[1] the angular correlation between the gamma-rays is very anisotropic. Thus our first significant results have been obtained with Rh^{106}, which shows very anisotropic angular correlation[2] and emits rather soft gamma-rays.[3] Figure 2 shows the ratio $N_{\parallel}/N_{\perp}$ as a function of θ.

The dotted line is calculated from Hamilton's paper[1] (Eq. 12b) on the assumption that both quanta are electric quadrupole. The experimentally observed coefficients[2] of the angular correlation were used in the calculations. The eeffectiveness of the polarimeter was assumed to be that determined as described above, i.e., $D=2.1$. The solid line

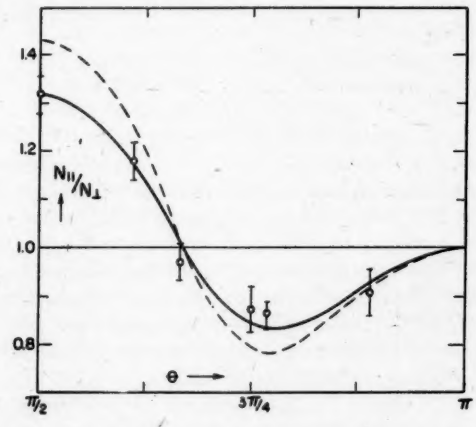

FIG. 2. Polarization of Rh^{106} gamma-rays. Solid line: $D=1.76$. Dotted line: $D=2.1$.

was constructed in the same manner except that D was adjusted to give the best fit. The value $D=1.76$ is not inconsistent with the uncertainty in our calibration. Our results indicate that the parity of the second excited state of Pd^{106} is the same as that of the ground state. If the two transitions are quadrupole, they are electric. The radioactive material was obtained from Oak Ridge.

* Assisted by the joint program of the Office of Naval Research and the Atomic Energy Commission.

[1] Donald R. Hamilton, Phys. Rev. **74**, 782 (1948).
[2] E. L. Brady and M. Deutsch, Phys. Rev. **74**, 1541 (1948).
[3] W. C. Peacock, Phys. Rev. **72**, 1049 (1947).

Decay Times of Scintillations

GEORGE B. COLLINS*
Brookhaven National Laboratory, Upton, Long Island, New York
September 23, 1948

MANY investigators have reported the effectiveness of phenolic compounds when used as phosphors in scintillation counters, but because of their extreme speed only an upper limit has been set for the decay times of these substances. The purpose of the work reported here was to obtain quantitative values for these decay times which could serve as a basis for the use of these phosphors in extremely high speed counting circuits.

The phosphor under investigation was attached to the envelope of a selected 931-A photo-multiplier tube, the output of which was connected directly to the deflecting plates of a microoscillograph.[1]

This instrument was an essential part of the experiment. By virtue of the fact that the electron beam traces are recorded directly on a photographic plate the oscillograph has ample writing speed, and more important, it has the very high voltage sensitivity of 2 volts per line width. This high sensitivity plus operation of the 931-A at 150 volts per stage made unnecessary any amplifier and the time resolution of the equipment was limited only by the photomultiplier tube and leads to the oscillograph.

The voltage divider for the 931-A was made up of 100,000-ohm resistors and 0.001-μf condensers were connected across the last two dynodes. The anode to deflecting plate connection was less than 10 cm long over all, and had a total capacity of 1.1×10^{-11} farad. The combination was connected to ground by a 100,000-ohm resistor. The time constant ($RC\sim10^{-6}$ sec.) was thus long compared to the events to be measured and the deflection of the trace represented the time integral of the current. In most of the work the 931-A and phosphor were near liquid nitrogen temperatures as this reduced the noise current and permitted stable operation of the 931-A at higher voltages.

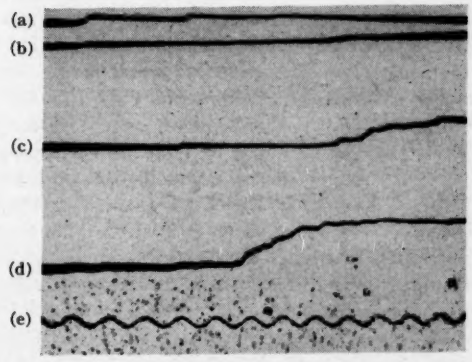

FIG. 1. Representative traces showing steps (a, b) resulting from thermal emission and deflections (c, d) resulting from light pulses from anthracene.

The use of delay lines would have reduced the signal voltage to an unreadable level and thus triggered sweeps could not be employed. Instead it was necessary to establish a random counting rate sufficient to insure a satisfactory pulse from the 931-A at least once every 10 to 20 sweeps. A counting rate of about 2 million counts/sec. with amplitude in excess of 20 volts was required and this was obtained by placing a 10-mc radium source about 4 cm from the phosphor. Sweeps with over-all time durations of between 0.15 μsec. to 1.0 μsec. were used. Sweep speeds were calibrated by connecting the deflecting plates to a 130 Mc/s signal generator and relying on uniformity of performance from sweep to sweep. This was found to be better than 3 percent.

The resulting traces show steep, short steps and slowly rising larger deflections (Fig. 1). The slowly rising deflections result from light emitted by the phosphor and the steps seem to result from single (or at most a few) electrons leaving the cathode of the 931-A. These steps are found with no source present and the 931-A at room temperature, or with the source next to a cooled 931-A without phosphor. They are absent when the 931-A is cooled and no source present. Examination of these steps permits the time response of the 931-A plus associated circuit to be determined. Figure 2 shows one of these steps enlarged together

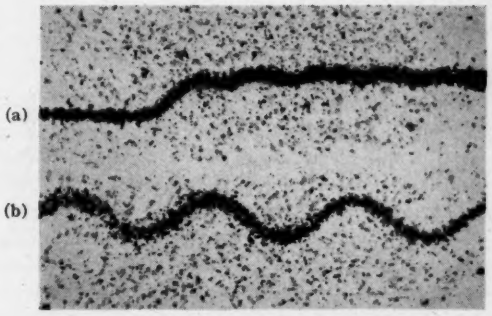

FIG. 2. Highly enlarged step showing ringing.

with its 130 Mc/s timing trace. The rise time is about 2×10^{-9} sec. This is considerably slower than the rise time of 6×10^{-10} sec. as calculated by Sard.[2] This slow rate of rise is probably set by the constants of the output circuit corresponding to the ringing frequency of 200 Mc/s seen in Fig. 2. Space-charge limitation at the last dynode is also not far from limiting the rise time. The step shown corresponds to about 10 volts and with $C=1.1\times10^{-11}$ farad and $t=2\times10^{-9}$ sec. the peak current must be about 50 ma, which is within a factor of two of the expected saturation

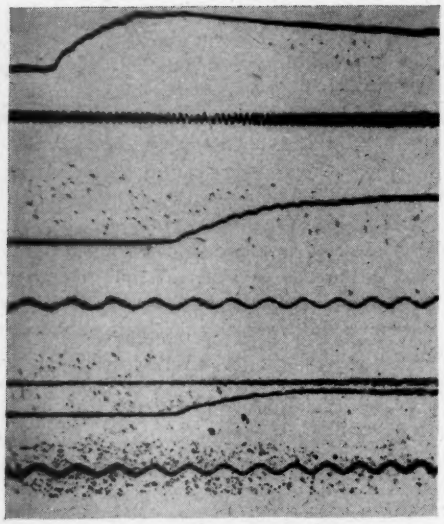

FIG. 3. (a) Naphthalene. (b) Anthracene with evidence of ringing. (c) Phenanthrene.

current. If this step originated from a single electron, the gain of the 931-A for this pulse was $7\times10^{+8}$. Figures 3a, 3b, 3c show deflected traces due to naphthalene, anthracene, and phenanthrene, respectively, together with their 130 Mc/s timing traces.

Plots of the logarithm of the deflections against time for all three substances showed that their pulse shape is consistent with the charging up of the output circuit by a current which is of the form $I=I_0e^{-t/\tau}$, where τ is defined as the time constant of the phosphor. Even for the same substance the slopes of the semilog plots varied considerably from pulse to pulse, presumably because of the irregular character of many of the traces. On the basis of these plots an estimate was made for each substance of the decay constant and the probable error of these estimates. The results are shown in Table I.

Traces for naphthalene and anthracene were obtained at both room and near liquid nitrogen temperatures with no observable difference in the decay constants. Commercial naphthalene and a sample of carefully purified naphthalene showed similar decay constants.

It is to be expected that the maximum intensity of light emitted should follow immediately the passage of the ionizing particle through the phosphor. Evidence of this is seen in the shock excitation of some of the phosphor events (see Fig. 3b) indicating a rise time of the order of 2×10^{-9} sec. To summarize, it appears that the passage of an electron of around 1 Mev through any of the phosphors produces enough light to result in the production of a few ($\sim$10) electrons from the cathode of the photo-multiplier tube, that the build up of this emission is quite fast ($\sim2\times10^{-9}$ sec.) and that in the case of phenanthrene 95 percent of the light is emitted in a time less than 3×10^{-8} sec.

TABLE I. Estimates of decay constants.

Substance	τ
Naphthalene	$5.7\pm0.5\times10^{-8}$ sec.
Anthracene	$1.3\pm0.2\times10^{-8}$ sec.
Phenanthrene	$0.9\pm0.2\times10^{-8}$ sec.

I am indebted to Dr. Martin Deutsch for samples of phenanthrene and purified naphthalene, and to Doctors W. C. Elmore and J. B. H. Kuper for many helpful suggestions.

* Research carried out at Brookhaven National Laboratory under the auspices of the Atomic Energy Commission while the author was on leave from the University of Rochester.
[1] G. M. Lee, Proc. I.R.E. **34**, 121W (1946).
[2] R. D. Sard, J. App. Phys. **17**, 768 (1946).

Irreversible Processes in Liquid Helium II

C. J. GORTER
Kamerlingh Onnes Laboratorium, Leyden, Holland
September 23, 1948

THE transport phenomena in liquid helium may find a simple description on the basis of the two-fluid model of London,[1] Tisza,[2,3] and Landau.[4] According to that model helium II is a mixture of two fluids: the normal or gas-like phase and the superfluid phase with densities ρ_n and ρ_s, respectively. The entropy of the superfluid phase is zero or anyhow very small. The ratio ρ_n/ρ_s is very small at 1°K and becomes infinite at the λ-temperature.

In considering the heat flow and the fountain effect in a slit or capillary it is necessary to distinguish between the gradient of the hydrostatic pressure, grad$p$, and the gradient of the internal osmotic pressure, ρS grad$T$, where S is the entropy.[3] We have also to distinguish between two kinds of energy dissipation.

First there is the internal friction η_n of the normal phase which transmits the hydrostatic force to the walls of the slit or the capillary. In case of laminar flow

$$\text{grad}p=\eta_n\Delta v_n, \tag{1}$$

where v_n is the velocity of the normal phase, leads to proportionality between the average velocity of the normal phase and the grad$p$ in agreement with Poiseuille's laws.

Secondly there is a mutual friction between the two phases, of as yet obscure nature, depending on the relative velocity of the two phases v_s-v_n.

The heat flow in a slit or capillary being proportional to the average of v_n is, according to (1), proportional to grad$p$. This accounts for the remarkable proportionality between the heat flow and the fountain pressure.[5] From the proportionality coefficient obtained for slits of 5, 10, and 15 microns[6] the viscosity η_n may be calculated. Its absolute value as well as its dependence on temperature is found to be in good agreement with that calculated according to Tisza[3] from Keesom and Mac Wood's viscosity measurements with an oscillating disk.[7] In slits of 1 micron and narrower,[4] however, large discrepancies occur, especially at the lower temperatures. Perhaps these discrepancies are caused by a mean free path effect, which might also account for the high extinction coefficient[8] for ultrasonic waves at the lower temperatures.

In wide capillaries the energy dissipation by mutual friction is predominant over that by internal friction of the

normal phase. In order to explain the proportionality of the heat flow with the cube root of the temperature gradient[9] the force of mutual friction M per unit of volume has to be taken as

$$M = A\rho_s\rho_n(v_s - v_n)^3 + \cdots, \quad (2)$$

where A is about 50 cm sec./gram and decreases with decreasing temperature. Approximately the same value of A is found from the analysis of heat transport and fountain effects in the slits of 5, 10, and 15 microns.

There are very few data on the flow of matter at known values of grad$p$ and grad T. In narrow slits this flow should also be conditioned by the mutual friction and the order of magnitude of the flow agrees satisfactorily with (2).

A detailed comparison with the experimental data will be published in Physica in cooperation with Dr. J. H. Mellink.

[1] F. London, J. Phys. Chem. **43**, 49 (1939).
[2] Laszlo Tisza, J. d. phys. et rad. **1**, 164, 350 (1940).
[3] Laszlo Tisza, Phys. Rev. **72**, 838 (1947).
[4] L. D. Landau, J. Phys. Sowjetunion **5**, 71 (1941).
[5] J. F. Allen and J. Reekie, Proc. Camb. Phil. Soc. **35**, 114 (1939).
[6] W. H. Keesom and G. Duyckaerts, Physica **13**, 153 (1947); J. H. Mellink, Physica **13**, 180 (1947); L. Meyer and J. H. Mellink, Physica **13**, 197 (1947); J. H. Mellink, Thesis, Leyden, 1948.
[7] W. H. Keesom and G. E. Mac Wood, Physica **5**, 737 (1938).
[8] J. R. Pellam and C. F. Squire, Phys. Rev. **72**, 1245 (1947).
[9] W. H. Keesom, B. F. Saris, and L. Meyer, Physica **7**, 817 (1940).

Interaction Energy in Quantum Field Theory

ALEX E. S. GREEN
Department of Physics, University of Cincinnati, Cincinnati, Ohio
September 29, 1948

IN Focks treatment of quantum electrodynamics[1] the auxiliary conditions are eliminated by means of a transformation which when followed by the single time formulation results in the explicit appearance of the Coulomb interaction energy.[2] The purpose of this note is to point out that an extension of this mathematical method will also give the dynamic interaction energy. Thus the solution $\psi = (\exp\chi)\Omega$ where

$$\chi = 1/c\hbar \int d\mathbf{k}[2k_iA_i^*\phi + \Sigma_v (\phi f^{v*}/k - k_iA_i^* f^v/k^2 - \Sigma_w f^w f^{v*}/4k^3 + \alpha_i^v A_i^* f^v/k - \alpha_i^v k_i k_j A_j^* f^v/k^3)],$$

and

$$f^v = (1/2\pi)^{\frac{1}{2}} e^v \exp[i(ckt^v - k_i x_i^v)]$$

leads to a transformed wave equation which does not contain any photon creation operators. Summing the set of wave equations for the various particles, applying the single time formulation, and evaluating the integrals yields Breit's formula,[3] which is good for first-order processes. As is well known it is necessary in the electrodynamic case to discard the infinite self-energies and to evaluate the integrals with care. The first four terms above are equivalent to those used by Fock. The last two replace the perturbation method used to find the dynamic interaction.

The present method is relatively simple, it points out clearly the nature of the approximations, and it avoids the objectionable resolution of the vector potential into longitudinal and transverse components. An analogous procedure may be used to obtain the total interaction energy in vector meson theory, in generalized electrodynamics, and in generalized meson theory.[4]

[1] V. Fock, Physik. Zeits. Sowjetunion **6**, 449 (1934).
[2] P. A. M. Dirac, *The Principles of Quantum Mechanics* (Oxford University Press, London, 1947), 3d ed., Sect. 80.
[3] Gregory Breit, Phys. Rev. **34**, 553 (1929).
[4] Alex E. S. Green, Phys. Rev. **73**, 26 (1948).

On the Range of Decay Electrons from Mesons*

M. H. SHAMOS AND A. RUSSEK
Physics Department, New York University, New York, New York
September 23, 1948

THE slow meson detector described earlier[1] has been used to obtain information regarding the range of decay electrons in carbon. The wide range of energies reported to date[2-8] lends considerable doubt to the hypothesis of a unique decay energy. Moreover, two of the experiments described recently[9,10] showed evidence for a continuous distribution in the range of the decay particles. One of these,[9] in fact, seemed to indicate a continuous distribution superimposed upon a unique range.

The counter telescope is shown in Fig. 1 for reference. The method employed consists in comparing the observed yield (number of electrons detected by "D" per stopped meson) from the cylindrical carbon absorber with the yield calculated on the basis of an assumed range. It was necessary to evaluate the yield numerically, taking into account the distribution of stopped mesons in the absorber. Runs were taken with six absorbers, ranging in radius from $\sim$2 to $\sim$13 g/cm^2, and with $\sim$32 cm of Pb above the telescope. Background runs were taken without absorber and the data corrected accordingly. Only those electrons which were delayed more than 0.95μsec. were recorded, and these numbers were than extrapolated to zero time on the basis of a 2.15-μsec. mean life. In determining the number of mesons stopped in each case, the decay electrons which passed through the anticoincidence set "E" were recorded

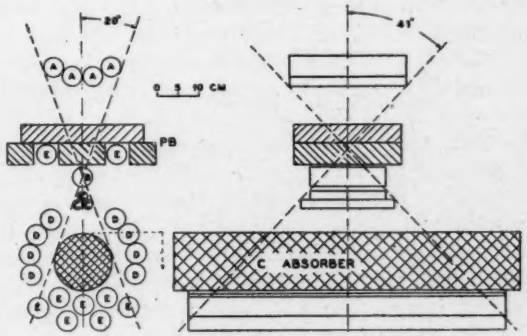

FIG. 1. Counter telescope.

by a separate delay discriminator. This also served to establish the fact that the distribution of decay electrons about the absorber was isotropic.

The results are shown in Fig. 2. Here are plotted the

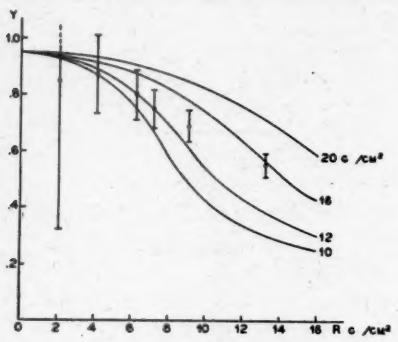

FIG. 2. The yield Y as a function of the absorber radius with range as the parameter.

yield Y as a function of the absorber radius R, with range as the parameter. The indicated deviations are standard statistical errors, and the solid curves show the results to be expected for *unique* ranges of 10, 12, 16, and 20 g/cm². It is assumed that the electrons escape through the surface of the absorber with sufficient energy to penetrate the counter walls, which are 0.7 mm of brass or equivalent to ~0.5 g/cm² of carbon. This correction is taken into account later in translating range into energy.

In computing the theoretical yield curves, it was necessary to know the fraction of mesons which decay in carbon. Assuming Wheeler's[11] fourth-power relation to hold, only 89 percent of the negative mesons should decay in carbon (for $Z_0 \approx 10$), or 95 percent of the total (for a 20 percent positive excess). The fact that the experimental points do not tend toward unit yield as R decreases was taken to indicate some capture of negative mesons. Consequently, the yield curves have been adjusted to a maximum yield of 0.95.

It will be observed that the data are not consistent with a unique range. Instead, the *mean* range tends to increase with increased radius of absorber. For absorber radii up to ~8 g/cm², the apparent range is ~12 g/cm², increasing to ~16 g/cm² for an absorber radius of 13 g/cm². The increase in mean range with absorber radius is a consequence of the non-linear dependence of the yield upon the range for the particular geometry employed here; were this dependence linear, a constant mean range should be found regardless of absorber size, and the effect of a distribution in range, if any, would be masked. The energies corresponding to the ranges 12 and 16 g/cm² are about 25 and 33 Mev, respectively, taking into account both the ionization and average radiation losses, but neglecting scattering. Here the ionization losses have been computed on the basis of the Halpern-Hall[12] calculation. These values would be increased some 20 percent if the losses were calculated on the Bethe-Bloch theory. In computing the energy, an allowance of 2 Mev was made for the counter walls. This was considered a reasonable average for the oblique paths since the minimum path through the walls corresponds to an energy loss of ~1 Mev. The decrease in range due to scattering was calculated in a manner similar to that employed by Koenig[13] for mesons. The effect was found to be small, requiring that the above energies be increased by ~2 Mev. In addition, a rough calculation was made of the spread in range to be expected as a result of fluctuations in the radiation loss,[14] assuming a unique decay energy of 40 Mev. The results indicated that this effect could not account for the observed yields, although the fluctuations are not negligible. The same conclusions apply to the assumption of a lower unique energy.

The experimental results are in agreement with those reported by Steinberger[9] and by Hincks and Pontecorvo[10] insofar as they indicate an apparent distribution of electron energies. Unfortunately, it is not possible to draw accurate conclusions regarding the mean range or the form of the distribution, due primarily to the uncertainty in the fraction of negative mesons which are captured in carbon. For example, if only 90 percent of the total mesons decay in carbon, the mean range indicated would correspond to about 40 Mev at the largest radius. It is interesting to note that the results would be consistent as well with a spectrum consisting of two discrete energies, one of the order of 20 Mev and the other about 45 Mev.

We are indebted to Dr. I. S. Lowen for his continued support, and to Mr. M. G. Levy and Miss E. Karasak for their valuable assistance in carrying out the experiment.

* Assisted by the Joint Program of the Office of Naval Research and the Atomic Energy Commission.

[1] M. H. Shamos and M. G. Levy, Phys. Rev. **73**, 1396 (1948).
[2] M. Conversi and O. Piccioni, Phys. Rev. **70**, 874 (1946).
[3] Anderson, Adams, Lloyd, and Rau, Phys. Rev. **72**, 724 (1947).
[4] Adams, Anderson, Lloyd, Rau, and Saxena, Rev. Mod. Phys. **20**, 334 (1948).
[5] Zar, Hershkowitz, and Berezin, Phys. Rev. **74**, 111 (1948).
[6] Fowler, Cool, and Street, Phys. Rev. **74**, 101 (1948).
[7] J. G. Retallack, Phys. Rev. **73**, 921 (1948).
[8] Robert W. Thompson, Phys. Rev. **74**, 490 (1948).
[9] J. Steinberger, Phys. Rev. **74**, 500 (1948).
[10] E. P. Hincks and B. Pontecorvo, Phys. Rev. **74**, 697 (1948).
[11] John Wheeler, Phys. Rev. **71**, 320 (1947).
[12] O. Halpern and H. Hall, Phys. Rev. **73**, 447 (1948).
[13] Henry Paul Koenig, Phys. Rev. **69**, 590 (1946).
[14] H. Bethe and W. Heitler, Proc. Roy. Soc. **A146**, 83 (1934).

A Boundary Value Condition for Proton-Proton Scattering

G. BREIT AND W. G. BOURICIUS
Yale University, New Haven, Connecticut*
September 27, 1948

IT has been found that the values of the phase shift for the ^1S state of two protons, derivable from experiments[1] on the scattering of protons by protons in the energy range 0.2–14 Mev, can be interpreted by means of a boundary condition requirement with about the same accuracy as by means of a potential energy curve description. The requirement is that of keeping the logarithmic derivative $d(rR)/Rdr = Y$ constant at a value of the interparticle distance $r \sim 0.47\ e^2/mc^2$. Here R is the radial wave function in

a Coulomb field. At this distance $Y \sim 0.08$. Similarly, if one interprets the scattering of protons by neutrons in the ^1S state as explicable by means of a potential energy of constant value in a distance of e^2/mc^2, then one can also approximately interpret the data by requiring that $Y \sim 0.06$. It is also possible to interpret the phase shifts in terms of an approximately linear variation of Y with energy. There is a connection between the boundary condition view and the velocity dependent potentials.[2] Even though experimental values can be represented by means of potential energy curves, the conclusion that the interaction between nucleons is adequately pictured by means of potentials is now somewhat more seriously in doubt. It is not proposed to substitute for the potential energy concept a requirement that Y be strictly energy independent at a fixed distance, but the fact that experiment agrees with this requirement about as well as with the more conservative one suggests that the interaction may be taking place in a manner which has some aspects resembling either of the two viewpoints. Since the ratio of proton to meson mass is about 6, the meson's velocity is roughly 1/2.5 of that of the proton for the same energy and the usual conditions of the Born-Oppenheimer approximation are not satisfied. It is realized that the usual meson theory does not bear a close resemblance to theories of molecular binding. On the other hand, meson theory is far from final either in structure or mathematical consistency. It appears appropriate, therefore, to call attention to the possibility of describing experimental values by means of a boundary condition which, in an extreme case, would suggest that the shape of the wave function of the protons in the part of configuration space, within which dissociation becomes definite, is affected mainly by other factors than the kinetic energy of relative motion at a large distance.

* Assisted by contract N6ori-44, Project NR 024-055.

[1] M. A. Tuve, N. P. Heydenburg, and L. R. Hafstad, Phys. Rev. **50**, 806 (1936); L. R. Hafstad, N. P. Heydenburg, and M. A. Tuve, Phys. Rev. **53**, 239 (1938); R. G. Herb, D. W. Kerst, D. B. Parkinson, and G. L. Plain, Phys. Rev. **55**, 247 (1939); L. R. Hafstad, N. P. Heydenburg, and M. A. Tuve, Phys. Rev. **56**, 1078 (1939); G. L. Ragan, W. R. Kanne, and R. F. Tashek, Phys. Rev. **60**, 628 (1941); R. R. Wilson and E. C. Creutz, Phys. Rev. **71**, 339 (1947); Robert R. Wilson, Phys. Rev. **71**, 384 (1947); R. R. Wilson, E. J. Lofgren, J. R. Richardson, B. T. Wright, and R. S. Shankland, Phys. Rev. **72**, 1131 (1947); I. H. Dearnley, C. L. Oxley, and J. E. Perry, Jr., Phys. Rev. **73**, 1290 (1948); J. M. Blair, G. Freier, E. E. Lampi, W. Sleator, Jr., and J. H. Williams, Phys. Rev. **74**, 553 (1948).

[2] G. Breit, H. M. Thaxton, and L. Eisenbud, Phys. Rev. **55**, 1018 (1939).

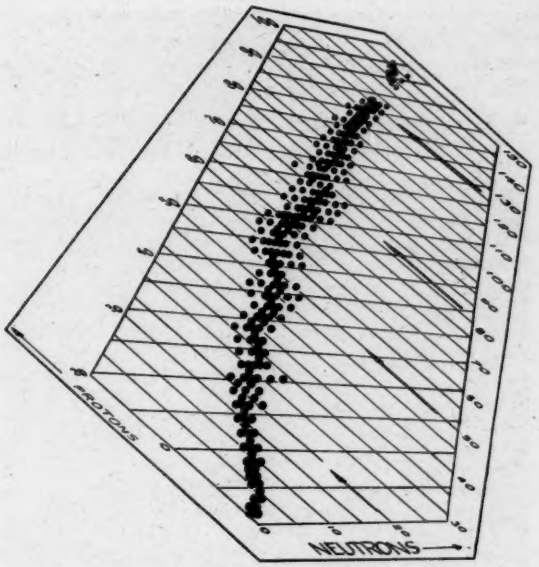

FIG. 1. Photograph taken at an oblique angle of a rectangular chart of the stable isotopes (together with the heavy long-lived radioactive ones). Each isotope is indicated by a small round-headed pin. The group at the far end represents those heavy radioactive nuclei having half-lives greater than 10 years; the remainder are stable. The arrows are at 20, 50, 82, and 126 neutrons.

of neutrons *vs.* protons, whereon the stable (and heavy long-lived) isotopes are represented by small round-headed pins. The four arrows point to the neutron values listed above.

Other discontinuities occur at around 32, 60, and possibly 100 neutrons. The three sections 20–32, 50–60, and 82–100 neutrons give the appearance of regions of transition between stability regimes.

Most of Fig. 1 might also be considered as displaying a competition between two possible slopes of the stability curve. Regions where the tendency is to add one neutron for every added proton alternate with regions where two neutrons, on the average, are added for every added proton.

[1] Maria G. Mayer, Phys. Rev. **74**, 235 (1948). See also the earlier summary and theoretical discussion in H. A. Bethe and R. F. Bacher, Rev. Mod. Phys. **8**, 82 (1936), par. 34.

On Closed Shells in Nuclei

CECIL B. ELLIS
Office of Naval Research, Washington, D. C.
September 7, 1948

RECENTLY, Maria G. Mayer[1] has summarized the evidence for particular stability of nuclei with 20, 50, 82, or 126 neutrons or protons. It may be pointed out that discontinuities at approximately these and other neutron values become obvious to the eye if the usual rectangular chart of the isotopes is viewed from the proper direction. Figure 1 is a photograph from an oblique angle of a chart

On the Disintegration of Mesotrons*

KAN-CHANG WANG AND STANLEY B. JONES
Department of Physics, University of California, Berkeley, California
September 24, 1948

WE have been performing a cloud-chamber experiment at sea level to observe what occurs when cosmic-ray mesotrons are brought to rest. The cloud chamber has an 11-inch inner diameter and an 11-inch depth. The illuminated region is about 4 inches deep. Two lead plates, each 0.63 cm thick, and five aluminum sheets, each 0.081 cm thick, are placed inside the chamber. One of the lead plates

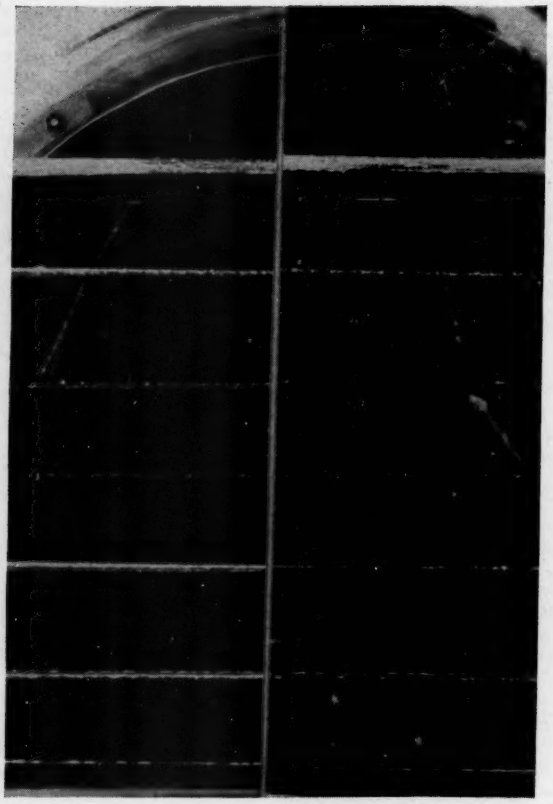

FIG. 1. Mesotron stopping in one of the aluminum sheets with the emission of a decay electron.

FIG. 2. One case which might be interpreted as a mesotron stopping in the second aluminum plate and causing the emission of a proton, or the stopping of a mesotron in the third plate without producing secondaries.

is put above the five aluminum sheets and the other one below them. The chamber is triggered by two vertically separated coincidence counters placed above the chamber and a set of anticoincidence counters placed beneath it. This method of triggering favors the detection of those charged particles which stop in the chamber. A lead block 11 inches thick is inserted between the two coincidence counters to filter out the electron component. The photographing is done with a stereoscopic type camera.

Up to the present, we have observed 40 mesotrons stopping within the cloud chamber. Of the 20 which stopped in the aluminum sheets, 12 showed decay particles of electronic character. Of the 20 mesotrons stopping in the lower lead plate, 7 showed decay particles of electronic character.

Figure 1 shows a mesotron stopping in one of the aluminum sheets with the emission of a decay electron. This decay electron penetrates through three aluminum sheets suffering scattering, which yields projected angles of 1.6°, 1.3°, and 1.5°, respectively. From the formula connecting the mean square of the projected scattering angles, the energy of the electron, and the thickness of the material through which the electron passes, we get from the above data an approximate value of the energy of the electron. The calculated energy is found to be 52 ± 10 Mev. In another case the decay electron passes through the first aluminum sheet and the upper lead plate and then goes out of the chamber. We calculate the lower limit of its energy to be about 10 Mev. These values are to be compared with those recently found by different authors.[1–6] For the rest of the decay electrons observed in our experiment, the visible tracks are shorter and are more unfavorable for energy estimation.

Figure 2 shows the one case which might be considered as the emission of a proton from the end of the mesotron track which stops in the second aluminum sheet. However, it might also be regarded as a mesotron stopping in the third aluminum sheet without producing any secondaries. From this and the 7 cases in which the mesotron is stopped in an aluminum sheet with no visible emission of a secondary, we conclude that either the probability of a mesotron producing a star after it stops in an aluminum sheet is rather small, or the energies of the prongs of the star are so small that the prongs have very little chance of getting out of the 0.081 cm of aluminum. This is in agreement with the result of Chang.[7] It is also in agreement with the recent results of Occhialini and Powell,[8] who have found no definite evidence for the production of stars by μ-mesons.

It is clear that our result does not support the hypothesis of the accelerated decay of the negative mesotrons but rather favors the hypothesis that some of the negative mesotrons are captured by the aluminum nuclei,[9] since of the 20 mesotrons stopping in the aluminum sheets, we have observed 8 giving no decay electrons.

The writers wish to express their thanks to Professor R. B. Brode for his encouragement and continuous interest in this work. They are also indebted to Professor W. B. Fretter and Dr. J. G. Retallack for their suggestions and help.

* This work was supported in part by the Atomic Energy Commission and the Office of Naval Research.

[1] Anderson, Adams, Lloyd, and Rau, Phys. Rev. **72**, 724 (1947).
[2] Adams, Anderson, Lloyd, Rau, and Saxena, Rev. Mod. Phys. **20**, 334 (1947).
[3] E. C. Fowler, R. L. Cool, and J. C. Street, Phys. Rev. **74**, 101 (1948).
[4] J. L. Zar, J. Hershkowitz, and E. Berezin, Phys. Rev. **74**, 111 (1948).
[5] Robert W. Thompson, Phys. Rev. **74**, 490 (1948).
[6] J. Steinberger, Phys. Rev. **74**, 500 (1948).
[7] W. Y. Chang, Phys. Rev. **74**, 1236 (1948).
[8] G. P. S. Occhialini and C. F. Powell, Nature **162**, 168 (1948).
[9] John A. Wheeler, Phys. Rev. **71**, 320 (1947); G. E. Valley and B. Rossi, Phys. Rev. **73**, 177 (1948); J. G. Retallack, Phys. Rev. **73**, 921 (1948); Harold K. Ticho, Phys. Rev. **74**, 492 (1948).

On Feenberg's Perturbation Formula

HERMAN FESHBACH
Brookhaven National Laboratory, Upton, Long Island, New York*
September 20, 1948

IN two recent papers,[1] Feenberg has derived perturbation formulas in which there are no repetitive matrix elements in the construction of a term of given order. Feenberg's calculation proceeded by effecting summations and regroupings of various infinite processes occurring in the Brillouin[2]-Wigner[3] formulation of perturbation theory. The purpose of the present note is the derivation of Feenberg's

formula directly from the eigenvalue problem by a method of successive approximations. The derivation also has the advantage of simplicity.

The equations to be solved for the coefficients are:

$$(E-H_{mm})a_m=\sum_{m\neq n} H_{mn}a_n, \tag{1}$$

where the original eigenvalue problem is $H\psi=E\psi$ expanded in an orthonormal set of functions, a_m are the amplitudes in the expansion, and H_{mn} are the matrix elements of H.

Suppose now that the principal state in question is the k^{th} so that it is convenient to take

$$a_k=1, \tag{2}$$

then

$$(E-H_{mm})a_m=H_{mk}+\sum_{n\neq mk} H_{mn}a_n. \tag{3}$$

To set up the method of successive approximations, we must now write the equation determining $a_n(n\neq m, k)$. To avoid repetitive matrix elements, we separate the m and k terms in the expression for a_n

$$(E-H_{nn})a_n=H_{nk}+H_{nm}a_m+\sum_{p\neq nmk} H_{nk}a_p. \tag{4}$$

To determine a_p

$$(E-H_{pp})a_p=H_{pk}+H_{pm}a_m+H_{pn}a_n+\sum_{q\neq pnmk} H_{pq}a_q. \tag{5}$$

For a_q

$$(E-H_{qq})a_q=H_{qk}+H_{qm}a_m+H_{qn}a_n+H_{qp}a_p+\sum_{r\neq qpnmk} H_{qr}a_r, \tag{6}$$

etc. To obtain a_m to first order we need only drop the summation in (3). To obtain to second order we need only drop the summation in (4) and solve for a_n, etc. We shall give the second- and third-order formulas obtained in this way. It is convenient to define the symbols

$$(\mathcal{E}_{km}^*)_1=H_{mm}\qquad (\mathcal{E}_{km}^*)_2=H_{mm}+\sum_{n\neq km}\frac{H_{mn}H_{nm}}{E-(\mathcal{E}_{kmn}^*)_1},$$

$$(\mathcal{E}_{km}^*)_3=H_{mm}+\sum_{n\neq km}\frac{H_{mn}H_{nm}}{E-(\mathcal{E}_{kmn}^*)_2}+\sum_{\substack{n\neq km\\ p\neq kmn}}\frac{H_{mn}H_{np}H_{pm}}{[E-(\mathcal{E}_{kmn}^*)_2][E-(\mathcal{E}_{kmnp}^*)_1]}. \tag{7}$$

Then to *second order*

$$a_m[E-(\mathcal{E}_{km}^*)_2]=H_{mk}+\sum_{n\neq mk}\frac{H_{mn}H_{nk}}{E-(\epsilon\mathcal{E}_{mn}^*)_1}. \tag{8}$$

To *third order*

$$a_m[E-(\mathcal{E}_{km}^*)_3]=H_{mk}+\sum_{n\neq mk}\frac{H_{mn}H_{nk}}{E-(\mathcal{E}_{kmn}^*)_2}+\sum_{\substack{n\neq mk\\ p\neq nmk}}\frac{H_{mn}H_{np}H_{pk}}{[E-(\mathcal{E}_{kmn}^*)_2][E-(\mathcal{E}_{kmnp}^*)_1]}. \tag{9}$$

These formulas are precisely those of Feenberg's to the order indicated. The general formula obtained by him is given by replacing $(\epsilon_k\ldots^*)_i$ by $(\epsilon_k\ldots^*)_\infty$. Feenberg uses $\epsilon_k\ldots^*$ for this symbol. The general expression may be derived here but the details are lengthy and uninformative. It may be noted that the procedure rather obviously yields an exact expansion for any finite secular equation.

The writer is greatly indebted to Dr. Eugene Feenberg for pointing out the relevance of this particular derivation. This work was done while serving as a consultant at the Brookhaven National Laboratory, whose hospitality is hereby gratefully acknowledged.

* Research carried out at Brookhaven National Laboratory under the auspices of the Atomic Energy Commission while author was on summer leave from the Massachusetts Institute of Technology.

[1] E. Feenberg, Phys. Rev. **74**, 206 (1948); E. Feenberg, Phys. Rev., in press.
[2] L. Brillouin, J. de phys. et rad. **III**, 373 (1932).
[3] E. P. Wigner, Mathu-Naturwirs. Anzerg. d. Ungar Akad Wiss **LIII**, 475 (1935).

Penetrating Power of Extensive Shower Particles*

G. T. Reynolds and W. D. Hardin
Palmer Physical Laboratory, Princeton University, Princeton, New Jersey

October 4, 1948

An experiment has been performed to measure the penetrating power in lead of extensive shower particles. This experiment differed from others of a similar purpose in that an extensive shower was first selected by two Geiger counter trays which had nothing to do with the measurement of penetration, and then the behavior of the particles in the shower was analyzed by means of six other Geiger counter trays under various thicknesses of lead. This procedure guaranteed that a decrease in counting rate observed with increasing thickness of lead was a true measure of particle penetrating power, and not an effect due to the exclusion of certain classes of showers. Thus, the only requirement imposed on a particle was that it be associated with an extensive shower.

This method of observation had the experimental advantage that it allowed simultaneous sampling under several different thicknesses of lead, an advantage because of the low counting rate encountered in extensive shower detections. The counter array is shown in Fig. 1. Trays M_1 and M_2 are the master coincidence trays which selected the shower. They are separated by about 4.5 meters. Trays 1 through 6 were in lead boxes, spaced evenly along the

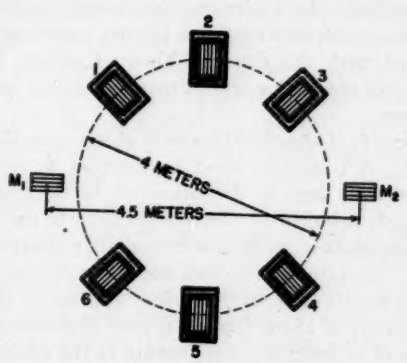

Fig. 1. Disposition of counter trays.

circumference of a circle of diameter approximately 4 meters, and were covered with lead of thickness ranging from 0 to 30 centimeters in the present experiment. The thickness of the lead in the side wall and bottom of the box was at least one-half the thickness of the lead covering the box. Each Geiger counter tray consisted of four counters of 6-inch effective length and 1-inch diameter arranged in parallel.

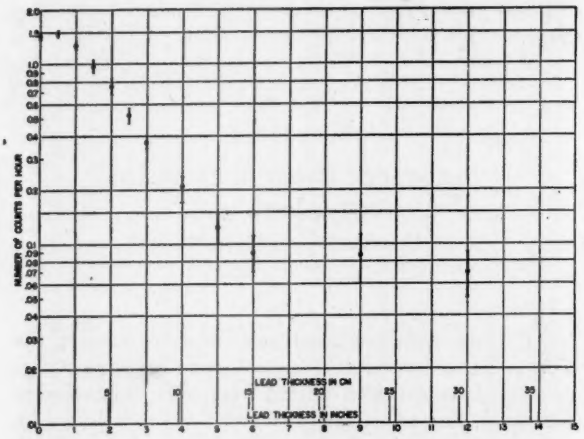

FIG. 2. Number of counts per hour observed in counter trays 1 through 6 as a function of the thickness of lead above these trays.

The method of sampling extensive showers was made possible by the incorporation of a cathode-gate circuit[1] in the following manner. When a "master coincidence" was registered by the two master coincidence trays, each of the circuit channels associated with the other trays was gated electronically so that any other tray experiencing a count in coincidence with the master coincidence could register on a paper tape by means of a spark. Thus, any count in any of the trays 1 through 6 was recorded if and only if a master coincidence was observed at the same time, and therefore if and only if the count corresponded to a particle in an extensive shower. The resolving time of the circuit was measured to be 6 microseconds, so that chance coincidences were unimportant. The present experiments were conducted with the counters about 4 meters below a wooden roof containing approximately 8 grams per square centimeter.

The results of about 650 hours of observation are shown in Fig. 2. A transition effect is observed as the lead is increased from zero to 2 centimeters in thickness. This corresponds to increased effective efficiency of the counters due to local shower production immediately above the tray. The counting rate with no lead above the tray agrees well with the results of Singer.[2] A break appears in the curve in the vicinity of 15 centimeters of lead, demonstrating the presence of at least two components in the showers. The ratio of the number of particles penetrating 15 centimeters to the number penetrating zero centimeters of lead is about 1/17.

Light weatherproof boxes are being prepared so that the measurements can be continued away from the laboratory building. An analysis of the data is in progress to determine an upper limit to the cross section for the photo-meson process produced by the gamma-rays in extensive air showers.

* Assisted by the Joint Program of the Office of Naval Research and the Atomic Energy Commission.
[1] Jerome Kurshan, Rev. Sci. Inst. 18, 647 (1947).
[2] S. F. Singer, private communication.

The Hyperfine Structure and Quadrupole Moment of Al^{27}*

HIN LEW
Physics Department and Research Laboratory of Electronics, Massachusetts Institute of Technology, Cambridge, Massachusetts
September 30, 1948

THE hyperfine structure of the metastable state of aluminum has been measured by the atomic beam method of radiofrequency spectroscopy. From the observed hyperfine separations the quadrupole moment of the nucleus has been calculated.

The atomic beam system used in the study of aluminum is essentially that employed by Zacharias[1] in the study of K^{40}. A slight departure from the system as used by Zacharias occurs at the detector. The aluminum atoms are ionized by the usual hot tungsten filament but, after ionization, the aluminum ions are accelerated into a mass spectrograph and are there separated from the other ions which are given off by the impure tungsten. This scheme has been used by Davis, Feld, Zabel, and Zacharias[2] in the study of Cl^{35} and Cl^{37}. For aluminum, the tungsten ribbon is operated at about 1780°K. The detection end of the mass spectrograph consists of an electron multiplier, the electrodes of which are patterned after the RCA-931A and made of commercial beryllium-copper alloy.[3] The source of aluminum atoms is an oven containing about 0.2 gram of aluminum wire and operated at about 1650°K. The oven is an assembly consisting of an aluminum oxide crucible around which is wrapped a layer of tantalum foil and the unit placed inside a graphite jacket with a slit in it. Heating is accomplished by the passing of 800 watts of electrical power directly through the graphite.

The spin and magnetic moment of aluminum have been determined with reasonable certainty through the efforts of three pairs of workers.[4] The values are $I=(5/2)\hbar$, $\mu=+3.630$ nuclear magnetons, and $g_I=1.452$. The spin of 5/2 has been verified by the present writer. The hyperfine structure of the $^2P_{3/2}$ metastable state of aluminum therefore consists of four levels corresponding to total angular momentum quantum numbers $F=1$, 2, 3, and 4. One Zeeman line between the $F=4$ and $F=3$ levels and eleven Zeeman lines between the $F=3$ and $F=2$ levels have been observed. From the observations, the following hyperfine separations are found:

$$\Delta\nu(F=4-F=3)=392.0+0.2 \text{ megacycles per second}$$
$$\Delta\nu(F=3-F=2)=274.4\pm0.1 \text{ megacycles per second.}$$

The Hamiltonian of the atomic beam system in the $^2P_{3/2}$ state may be written, in the absence of an external mag-

netic field and neglecting perturbations due to neighboring levels,

$$\mathcal{H}=a\frac{K}{2}+b'\frac{(3/8)K(K+1)-(1/2)I(I+1)J(J+1)}{I(2I-1)J(2J-1)},$$

where $K=F(F+1)-J(J+1)-I(I+1)$. The first term gives the dipole-dipole interaction between the nucleus and the electrons, and the second term gives the interaction between the electric quadrupole moment of the nucleus and the gradient of the electric field at the nucleus due to the electrons. In terms of the interaction constants a and b', the hyperfine separations are

$$\Delta\nu(F=4-F=3)=4a+(4/5)b',$$
$$\Delta\nu(F=3-F=2)=3a-(9/20)b',$$
$$\Delta\nu(F=2-F=1)=2a-(4/5)b'.$$

From these relations and the observed separations, the constants a and b' are found to be

$$a=94.27\pm0.04 \text{ megacycles per second},$$
$$b'=18.66\pm0.25 \text{ megacycles per second}.$$

Following the method of Davis, Feld, Zabel, and Zacharias,[2] we find the quadrupole moment of the nucleus to be

$$Q=+(0.156\pm0.003)10^{-24} \text{ cm}^2.$$

The perturbation of the $F=3$ and $F=2$ levels by the corresponding levels of the ground $^2P_{\frac{1}{2}}$ term can be shown to be too small by a factor of a hundred to account for the observed deviation from the interval rule of the hyperfine separations of the metastable state.

In the identification of aluminum as the substance on which the above measurements have been made, primary dependence has been placed on the mass spectrograph. Using the positions of Na^{23} and K^{39} as the reference points, the peak of the substance studied occurs at mass number 27 and does not occur at mass number 54. At mass numbers 26 and 28, the only particles observed are those due to scattering. Further confirmation is afforded by the fact that a rough determination of the hyperfine separation of the ground state yields $\Delta\nu=1500\pm50$ mc/sec., which overlaps the spectroscopic value of 1440 ± 30 mc/sec. found by Jackson and Kuhn.[4]

* This work has been supported in part by the Signal Corps, the Air Materiel Command, and the Office of Naval Research.

[1] Jerrold R. Zacharias, Phys. Rev. 61, 270 (1942).
[2] L. Davis, Jr., B. T. Feld, C. W. Zabel, and J. R. Zacharias, Phys. Rev. 73, 525(L) (1948).
[3] James S. Allen, Rev. Sci. Inst. 18, 739 (1947).
[4] S. Millman and P. Kusch, Phys. Rev. 56, 303 (1939); M. Heyden and R. Ritschl, Zeits. f. Physik 108, 739 (1938); Jackson and Kuhn, Proc. Roy. Soc. A164, 48 (1938).

Light Scattering in Supersonic Streams*

J. H. McQueen, J. W. Beams, and L. B. Snoddy
University of Virginia, Charlottesville, Virginia
September 30, 1948

In a previous note[1] experiments were briefly described in which light was scattered from a supersonic free stream of dried dust-free air. The observed light scattering by various regions of the stream was interpreted by the well-known theory of light scattering[2] as indicating density variations in the respective regions. In extending these light scattering experiments it has been found that in addition to density variations in the supersonic stream itself a number of other phenomena connected with supersonic streams or jets may contribute to the observed light scattering. Under certain special conditions the intensity of the light scattered due to the density variations alone is small in comparison to the other scattering so the various phenomena therefore may be studied.

If dried dust-free air at a pressure, say, of 70 lb./in.^{2} (gauge) is allowed to expand through a de Laval nozzle into the ordinary atmosphere containing moisture, and a beam of parallel light is directed perpendicularly through the resulting supersonic stream, very intense light scattering is observed where the supersonic stream or free jet mixes with the atmosphere, i.e., along the boundary of the stream the amount of light scattering is many times greater than that which can be accounted for by density variations alone.

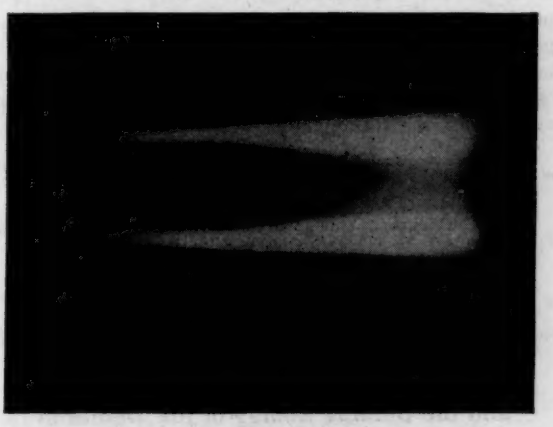

Fig. 1. Photograph of light scattered from a one-inch supersonic cylindrical jet emerging into the undried atmosphere.

However, if the atmosphere into which the supersonic stream expands is carefully dried, the amount of light scattering is very greatly reduced. It is believed that the intense scattered light is due to small water droplets formed by the mixing of the cold supersonic stream with the undried air of the atmosphere. If this is the case, the light scattering caused by the small droplets gives an outline of the mixing region around the supersonic stream as well as an indication of the magnitude of the mixing. Also since the size of the droplets can be determined by the relative amount, color, polarization, etc., of the scattered light, the heat transfer from the stream may be studied by observing the growth of the droplets. Clearly if a small amount of another condensible vapor is substituted for the water vapor in the atmosphere, the rate of growth of droplets other than water can be studied. Figure 1 shows a photograph taken of scattered light from a one-inch supersonic cylindrical jet Mach No. about 1.8 emerging into the undried atmosphere. The stream was illuminated by a beam

FIG. 2. Short spark shadowgraph of a supersonic jet taken under conditions similar to those of Fig. 1.

of sunlight with rectangular cross section $\frac{3}{8}$ inch wide and 3.5 inches long with the 3.5-inch dimension parallel to the stream. The plane of the beam passed through the axis of the stream. The photograph is a snapshot taken perpendicular to both the stream and incident light. For comparison, Fig. 2 shows a short spark shadowgraph[3] taken under approximately the same conditions. The thickening of the mixing boundary layer of the stream is shown as it extends into the atmosphere.

* This work was supported by Contract NOrd-7873 with the Bureau of Ordnance of the Navy.

[1] McQueen, Beams, and Snoddy, Phys. Rev. **73**, 260 (1948).
[2] See Bhagavantam, *Scattering of Light and Raman Effect*.
[3] Beams, Kuhlthau, Lapsley, McQueen, Snoddy, and Whitehead, J. Opt. Soc. Am. **37**, 868 (1947).

Gamma-Rays from the Reaction $H^1(n, \gamma)D^2$ and the Binding Energy of the Deuteron

R. E. BELL AND L. G. ELLIOTT
Chalk River Laboratories, National Research Council of Canada, Chalk River, Ontario
October 5, 1948

THE γ-ray accompanying the capture of a neutron by a proton has been studied in a magnetic lens β-ray spectrometer by photoelectric conversion in a thin U radiator.

The γ-rays were produced in a slab of pure paraffin 5″×25″×25″ placed in the thermal column of the Chalk River pile. A Pb collimator limited the γ-rays to a solid angle having the shape of a thin conical shell of 15° half-angle, converging to a small region outside the thermal column at the end of the β-ray spectrometer. A boron shield prevented the escape of neutrons from the thermal column. By placing a radiator in the γ-ray flux at the end of the β-ray spectrometer, secondary electrons ejected by the γ-rays could be studied. Figure 1 shows the momentum distribution of the photoelectrons and Compton recoil electrons ejected from a U radiator of 142 mg/cm². The counting rate taken with a spectrometer line width of 2.4 percent in momentum is plotted as a function of the focusing current in the lens coil, which is an accurate relative measure of the electron momentum. The effect due to the γ-rays from the paraffin is superposed on a background due to the γ-rays from the graphite in the thermal column. This background is constant over the energy range of this experiment. The peak at 4.800 amp. is due to photoelectrons ejected from the K-shell of U by the γ-rays from the paraffin. The general shape of the Compton background taken with a brass radiator is shown in this region as a broken line. The γ-ray energy deduced from the position of the photoelectron line is 2.236±0.005 Mev, using the ThC″ 2.620-Mev γ-ray as a standard to calibrate the spectrometer. The position of the paraffin γ-ray photoelectron line was determined accurately relative to the standard γ-ray photoelectron line by placing a source containing ThC″ in the Pb collimator behind the radiator and

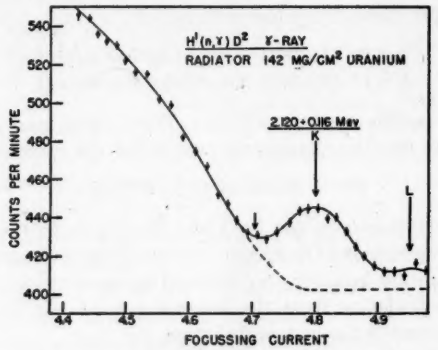

FIG. 1. The momentum distribution of the secondary electrons ejected from a U radiator. The standard deviations of the experimental points are indicated by vertical bars.

carefully determining the position of each line without any change in the arrangement of the apparatus. Any error due to the effect of finite radiator thickness is small because the paraffin γ-ray is close to the standard γ-ray in energy, and is further reduced by calculating the relative position of the two photoelectron lines from their high energy edges.

By adding the nuclear recoil energy to the above γ-ray energy, we obtain 2.237±0.005 Mev for the binding energy of the deuteron, using the ThC″ 2.620-Mev γ-ray as standard. This is surprisingly different from the previously accepted value of the deuteron binding energy.[1] The magnitude of the discrepancy is illustrated in Fig. 1 by the small arrow at 4.704 amp., marking the position the photoelectron peak would occupy were the deuteron binding energy as low as the previously accepted value. As a further check the ThC″ source was replaced by a Ra source and the RaC 2.198-Mev γ-ray was shown to have an energy about 1.5 percent lower than that of the paraffin γ-ray. This precludes the disintegration of the deuteron by that particular γ-ray of RaC and invalidates Kimura's[2] argument leading to a low value of the deuteron binding energy. The low value quoted by Myers and Van Atta[3] could be due either to voltage instability in the electrostatic generator or to non-linearity of the generating voltmeter calibration.

Taking the $H^1H^1-D^2$ separation[4] as 1.433±0.002 Mev together with the value of the deuteron binding energy

reported here, we obtain 1.008992 ± 0.000010 amu for the mass of the neutron. The probable error given includes an uncertainty of 0.3 percent in the absolute energy value for the ThC'' γ-ray. This neutron mass value is 0.051 mmu greater than the value quoted by Stephens[1] and gives a value for the $n - H^1$ difference of 0.804 ± 0.009 Mev. The theoretical lifetime of the neutron is reduced by a factor of 1.3 when this new value for the $n - H^1$ difference is used.

[1] W. E. Stephens, Rev. Mod. Phys. **19**, 19 (1947).
[2] K. Kimura, Kyoto Coll. Sci. Mem. **22**, 237 (1940).
[3] F. E. Myers and L. C. Van Atta, Phys. Rev. **61**, 19 (1942).
[4] R. Cohen and W. R. Hornyak, Phys. Rev. **72**, 1127 (1947).

On the Radioactivity of K^{40}

O. Hirzel and H. Wäffler
Swiss Federal Institute of Technology, Zurich, Switzerland
September 13, 1948

SOME years ago we published measurements of the quantum energy and the upper limit of the beta-ray spectrum of K^{40}. The values found by us are, respectively,[1]

$$E_\gamma = 1.54 \pm 0.1 \text{ Mev}, \quad E(\beta_{max}) = 1.41 \pm 0.02 \text{ Mev}.$$

These data are in good agreement with later measurements by Meyer *et al.*,[2] Gleditsch and Gráf,[3] Dželepow *et al.*,[4] and Henderson.[5] Recently, Franchetti and Giovanozzi,[6] using the cloud-chamber method, obtained a much higher value for the maximum beta-ray energy of K^{40}, namely, 1.7 ± 0.1 Mev. We believe that with respect to our measurements such a high beta-ray energy is rather improbable. Figure 1 gives the absorption curves obtained by us with P^{32} ($E_{max} = 1.71$ Mev), Na^{24} ($E_{max} = 1.41$ Mev), and K^{40} in the same geometrical arrangement. The points for K^{40} are taken up to 1/500 of the initial intensity and are all lying on the Na^{24} curve.

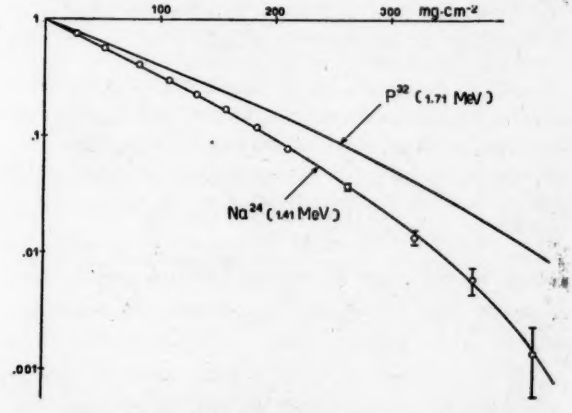

FIG. 1. Absorption curves in aluminium of P^{32} and Na^{24}. The points refer to K^{40}.

In addition we have determined the number Γ of quanta emitted per 100 beta-rays. For this purpose, the radiation from a thick KCl sample (cylindrical arrangement) was measured (a) with a thin-walled (27 mg/cm² Al) G-M counter and (b) with a cylindrical absorber, thick enough to absorb all the beta-rays, between the sample and the counter. The same measurements were performed with Al^{28}, which is known to emit one quantum of 1.8 Mev per beta-ray. The ratio of the sensitivities for γ-rays of 1.54- and 1.8-Mev quantum energies is 0.84 for Al counters, as computed by Bleuler and Zünti[7] and obtained experimentally by Bradt *et al.*[8] Taking into account the self-absorption of the beta-rays in the samples and their absorption in the counter wall, we obtain for Γ

$$8.7 \pm 1.2 \ \gamma\text{-quanta per 100 beta-rays.}$$

Furthermore we have determined the half-life of the transition $K^{40} \rightarrow Ca^{40}$. The number of counts from a thin sample (4 mg/cm²) of purified KCl (cylindrical arrangement) was compared with a very thin (<1 mg/cm²) U_3O_8 sample. The back-scattering from the holder (0.01-mm Al foil) was determined to be smaller than 1 percent. Taking into account the somewhat different absorption of the two beta-spectra in the wall of the G-M counter, as well as the very weak intensity of UX_1 and UY radiation passing through the counter wall, we get

$$T_{\frac{1}{2}}(K^{40}) = T_{\frac{1}{2}}(U^{238}) \times 0.246$$
$$T_{\frac{1}{2}}(K^{40}) = (11.1 \pm 1.9) \times 10^8 a.$$

The greatest contribution to the error in $T_{\frac{1}{2}}$ is given by the incertainty in the relative abundance of K^{40} (0.011 ± 0.001 percent).[9]

We are very indebted to Professor P. Scherrer for his stimulating interest in this work.

[1] O. Hirzel and H. Wäffler, Helv. Phys. Acta **19**, 216 (1946).
[2] H. A. Meyer, G. Schwachheim, and M. D. de Souza Santos, Phys. Rev. **71**, 908 (1947).
[3] E. Gleditsch and T. Gráf, Phys. Rev. **72**, 640 (1947).
[4] B. Dželepow, M. Kopjava, and E. Vorobjov, Phys. Rev. **69**, 538 (1946).
[5] W. J. Henderson, Phys. Rev. **71**, 323 (1947).
[6] S. Franchetti and M. Giovanozzi, Phys. Rev. **74**, 102 (1948).
[7] E. Bleuler and W. Zünti, Helv. Phys. Acta **19**, 375 (1946).
[8] Bradt, Gugelot, Huber, Medicus, Preiswerk, and Scherrer, Helv. Phys. Acta **19**, 77 (1946).
[9] Alfred O. Nier, Phys. Rev. **50**, 1041 (1936).

Observations of Naphthalene Scintillations Caused by Tritium Beta-Rays*

R. F. Taschek and H. T. Gittings
Los Alamos Scientific Laboratory, Los Alamos, New Mexico
September 27, 1948

IT seems desirable to report here some preliminary observations on the scintillations produced in commercial naphthalene by the beta-rays from tritium and by the bremsstrahlung coming from tritium occluded in tantalum. Of immediate interest is the lower limit set on the conversion efficiency from beta-ray to visible light energy.

A small amount of gaseous tritium was put in direct contact with finely powdered naphthalene crystals in a 15-cm³ glass Kjeldahl flask, an identical flask but without tritium being used as a control, to find the direct action of the betas. A tantalum disk containing tritium occluded throughout its volume was placed near a solid piece of

naphthalene to investigate the effect of soft x-rays since this is almost a pure source of such radiation. Both sources produced scintillations which were observed with a 1P21 photo-multiplier, the pulse samplified by a Los Alamos Model 501 amplifier. The photo-multiplier was not refrigerated. The rise-time and total pulse-length, easily observed on a 248A Dumont scope were, respectively, 0.05 μsec. and 0.2 μsec. The gas concentration was not well

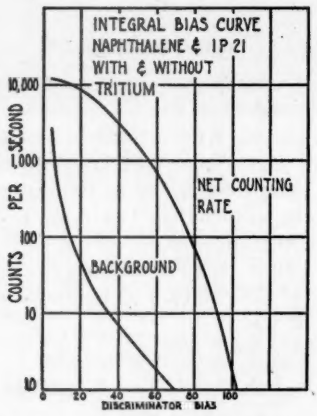

FIG. 1. Representative bias curve together with a background using the dummy naphthalene cell.

known because the initially too high counting rates necessitated two depletions.

Only integral pulse-height data have been taken and a representative bias curve is shown in Fig. 1, together with a background using the dummy naphthalene cell. The "no naphthalene" background is considerably lower, presumably a result of a low gamma-intensity about the laboratory. For at least the higher half of the pulse-height curve the pulses are definitely not caused by "pile up" and must be considered true individual counts.

If one assumes that the maximum energy of betas from tritium is 15 kev, then, very conservatively, individual pulses down to at least 10-kev beta-energy are being observed. Since experiments are being designed to determine the absolute conversion efficiency with accelerated electrons of about this energy, detailed calculations are not worth while at present, but an estimate leads to the following numbers. We can assume roughly one electron going through the multiplier and making a pulse for about twenty photons on the average striking the cathode. In the geometry used by us, somewhat less than 10 percent of all photons produced could be seen by the photo-multiplier cathode; if these photons are of about 3 ev and are produced by a 10-kev beta, then a lower limit on the conversion efficiency is 6 percent. This seems to us to be a conservative limit.

The comparatively large energy conversion and the possibility of increasing the light collected by a factor of five or more raised the interesting question of the possibility of using this method to study beta-ray spectra, in particular that of tritium. Over a short energy interval, say 15 or 20 kev, it seems reasonable to suppose that the conversion efficiency should vary only slowly, and this can be checked experimentally. The immediate attraction for low energy betas is that for gases or finely divided solids the source is always "thin." The greatest difficulty arises from the expected large output-pulse-height spread from a fixed number of incident photons. For single particles incident on a first stage, this is known to be large[1] and a lower limit on the dispersion is undoubtedly set by the statistics of the multiplication process which gives a mean pulse-height spread of about $(2/n)^{\frac{1}{2}}$ instead of $(1/n)^{\frac{1}{2}}$ where n is the number of electrons made in the first stage. Clearly, if a large number of particles (photons) simultaneously initiate a pulse, this statistical spread can be greatly reduced. The spread introduced by the photo-multiplier design itself is as yet unknown but may render the method worthless. Experimental effort is presently directed toward maximizing the solid angle of observation to make use of as many photons as possible and toward the use of anthracene[2] and other scintillating materials for increasing the conversion efficiency. It is planned to study the pulse-height distribution arising from monoenergetic electrons incident on anthracene.

* This document is based on work performed under government Contract Number W 7405 Eng 36 for the Los Alamos Scientific Laboratory of the University of California.

[1] James S. Allen, Rev. Sci. Inst. 18, 739 (1947).
[2] P. R. Bell, Phys. Rev. 73, 1405 (1948).

Proceedings of the American Physical Society

MINUTES OF THE MEETING AT THE CALIFORNIA INSTITUTE OF TECHNOLOGY, PASADENA, CALIFORNIA

THE 287th meeting of the American Physical Society was held at the California Institute of Technology, Pasadena, on June 24–26, 1948. This meeting followed the Symposium on Cosmic Rays, which was held in honor of Professor R. A. Millikan's eightieth birthday and, as a consequence, The Physical Society meeting was attended by an unusually large number of distinguished physicists from the East and from foreign lands. The Division of Fluid Dynamics presented its first Symposium on the Pacific Coast as part of the Heat Transfer and Fluid Mechanics Institute. The American Physical Society dinner was held on Friday, June 25, at the Athenaeum, with Dr. J. R. Oppenheimer presiding, and Professor and Mrs. R. A. Millikan as honored guests. About two hundred and fifty attended the dinner. Doctors Pierre Auger, G. D. Rochester, M. S. Vallarta, J. Clay, and I. I. Rabi paid tribute to Dr. Millikan's achievements during a short program following the dinner.

The opening session of the meeting attracted the largest audience of about 500. Two papers by I. I. Rabi and Julian Schwinger resulted in one of the best meetings ever held on the Pacific Coast. Dr. Millikan presided. The attendance at the other sessions varied from about 200 to 400. Outstanding invited papers attracted these large audiences. At the second session, presided over by C. D. Anderson, the speakers were E. H. Krause, Marcel Schein, and W. B. Fretter. The third session for invited papers brought together C. M. G. Lattes and E. Gardner on the experimental side of the observation of mesons in the 184-inch cyclotron, and R. Serber on the theoretical side. A fourth session was made up of papers by H. W. Babcock, A. C. Helmholz, and W. M. Powell, and the final session on problems of interest to the fluid dynamics group was made up of papers by R. W. Ladenburg and I. Estermann.

Post-deadline papers were presented by Luke C. L. Yuan on the "Neutron density in the free atmosphere up to 67,000 ft.," and by Kan-Chang Wang and S. B. Jones on the "Disintegration of cosmic-ray mesotrons."

J. KAPLAN, *Local Secretary for the Pacific Coast.*

Invited Papers

A1. Recent Experiments on the Dynamics of the Electron in Atoms. I. I. RABI, *Columbia University.*

A2. (Subject to be announced.) JULIAN SCHWINGER, *Harvard University.*

B1. Cosmic Rays above the Atmosphere. E. H. KRAUSE, *Naval Research Laboratory.*

B2. The Problem of Low Energy Mesotrons in the Cosmic Radiation. MARCEL SCHEIN, *University of Chicago.*

B3. Penetrating Showers in Lead. W. B. FRETTER, *University of California, Berkeley.*

D1. Observation of Mesons Produced by the 184-Inch Cyclotron. C. M. G. LATTES AND E. GARDNER, *University of California, Berkeley.*

D2. Interpretation of the Radiation Laboratory Meson Experiments. R. SERBER, *University of California, Berkeley.*

E1. Stellar Magnetic Fields. H. W. BABCOCK, *Mount Wilson Observatory.*

E2. Nuclear Isomerism. A. C. HELMHOLZ, *University of California, Berkeley.*

E3. Cloud-Chamber Measurements of Recoil Protons in the Neutron Beam of the 184-Inch Cyclotron. W. M. POWELL, *University of California, Berkeley.*

G1. (Subject to be announced.) R. W. LADENBURG, *Princeton University.*

G2. The Interaction of Molecules with Solid Substances. I. ESTERMANN, *Carnegie Institute of Technology.*

Contributed Papers

B4. The Altitude Dependence of Auger Showers. M. M. MILLS, *California Institute of Technology.*—Assuming primary electrons, the variation of shower counting rate with altitude has been computed and compared with Kraybill's[1] observations. The theory gives a weaker maximum (ratio: maximum to sea level is 24 *vs.* 63 for experiment) at a greater depth (10.5 radiation units *vs.* 8.5 for experiment). The theoretical zenith angle distribution of showers which are detected by Kraybill's counters at 31,000 feet has been compared with one observed by E. W. Cowan utilizing a counter-controlled cloud chamber. The observed distribution has a different shape and is narrower (half-angle 17 degrees *vs.* 30 degrees for theory) than the theoretical. It is difficult to reconcile this discrepancy with the observed altitude dependence. The multiple production of second-

aries by primary protons proposed by Lewis, Oppenheimer, and Wouthuysen[2] should lead to a more pronounced maximum at higher altitudes, and therefore should lead to an altitude dependence in better agreement with experiment than the present computation.

[1] H. L. Kraybill, Phys. Rev. 73, 632 (1948).
[2] H. W. Lewis, J. R. Oppenheimer, and S. A. Wouthuysen, Phys. Rev. 73, 127 (1948).

B5. East-West Asymmetry of Cosmic Rays at 33,000 Feet.* W. C. BARBER, *University of California, Berkeley.*—By means of counter telescopes mounted in a B-29 plane, the east-west asymmetries of the total and hard components of the cosmic rays are being measured. The apparatus consists of six similar triple coincidence telescopes, three with 14 cm of lead and three with no lead. Preliminary measurements give the following results for a zenith angle of 45°.

$2\frac{(I_W-I_E)}{I_W+I_E}$	Probable error	Hard or total	Geomagnetic latitude	Altitude
0.11	±0.019	Total	~35°N	Average of 25,000 and 33,000 ft.
0.07	±0.034	Hard	~35°N	Average of 25,000 and 33,000 ft.
0.04	±0.015	Total	41°N	33,000 ft.
0.06	±0.034	Hard	41°N	33,000 ft.

The data indicate a predominance of positive primary particles for both the hard and total components. The soft component, which comprises about four-fifths of the total at these altitudes, must, therefore, also arise from primaries which are mostly positive. The statistical accuracy of the results for the hard component is poor, but since the hard is only a small fraction of the total intensity, errors here will not greatly affect the conclusion that the soft component has a positive east-west asymmetry.

* The research described in this abstract was supported in part by the Office of Naval Research.

B6. Energy Spectrum and Altitude Dependence of Slow Protons and Stars up to 30,000 Feet.* HARRIET H. FORSTER, *University of California, Berkeley.*—The nuclear emulsion technique has been used to obtain information on the energy distribution of low energy protons and stars at sea level and 30,000 feet. High altitude exposures were made on a series of B-29 flights at Inyokern, California. Between 30,000 feet and sea level, single proton trajectories with energies between 2.3 and 35 Mev decrease exponentially by a factor of $\exp(-P/1.3)$, where P is measured in meters of water equivalent. The exponential decrease of the star producing radiation is of the same order of magnitude. The integral energy spectrum of slow protons is found to be proportional to $\exp(-E/\epsilon)dE$, where ϵ is approximately 3 Mev. Calculations based on the above spectrum indicate that slow protons in the lower atmosphere can be accounted for by star production alone, as suggested by Bagge.[1]

* The research described in this abstract was supported in part by the Office of Naval Research.
[1] E. Bagge, Ann. d. Physik 521 (1941).

B7. Capture of Sea Level Negative Mesons by Nuclei. L. I. SCHIFF, *Stanford University.*—The rare appearance of ionizing radiation following the capture of a sea level (light or μ-type) negative meson by a nucleus suggests that "capture" consists of the conversion of μ^- into a neutral meson (μ^0), accompanied by the change of a nuclear proton into a neutron. The energy transferred to the nucleus would usually be small, and μ^0 would be easily detected only if it were to disintegrate into a pair of photons or charged particles. Capture will occur if heavy ($\pi^\pm$) mesons are strongly coupled to nucleons and can disintegrate into $\mu^\pm$ and μ^0; its probability is approximately proportional to Z^4. The intermediate step in the capture process then contains P, π^-, μ^0, or N, π^+, μ^-. The lifetime of $\pi^\pm$ for μ-decay can be related to the known rate of μ^- capture and the strength of nuclear forces. If $\pi^\pm$, $\mu^\pm$, and μ^0 are scalar mesons with masses 313 m, 200 m, and 100 m, respectively, this lifetime is about 4×10^{-8} sec., and the resulting $\mu^\pm$ has a few Mev energy. The lifetime of $\pi^\pm$ for β-decay, assuming that nucleons have no direct interaction with the electron-neutrino field, is significantly shorter than this, about 10^{-9} sec.

C1. Quantitative Relations for the Thresholds of Pre-Onset Positive Burst Pulse Corona and of Positive Streamer Advance. LEONARD B. LOEB AND ROBERT A. WIJSMAN, *University of California, Berkeley.*—Loeb[1] has suggested that the form of threshold equations for onsets of self-sustaining discharges, including sparks by positive streamer mechanism, must bear a formal analogy to the Townsend low pressure criterion for a spark, e.g., $\gamma \exp \int \alpha dx = 1$. Here α is the first Townsend coefficient for ionization by collision and γ a coefficient representing the probability of electron emission by some secondary mechanism. With this approach it has been possible to derive expressions for the threshold of the pre-onset burst pulse corona from positive points, and for the threshold of streamer propagation and streamer conditioned spark breakdown, both processes involving photo-ionization of the gas near atmospheric pressure. Quantitative test is at present precluded as a result of ignorance of such quantities as photon production, photoelectric ionization probabilities, and absorption coefficients. The streamer equation replaces the Meek criterion for spark breakdown by streamer mechanism and supplies the deficiencies caused by omission of photo-ionization in that theory. These relations clearly indicate to the experimentalist the kind of data needed in order quantitatively to calculate various breakdown thresholds.

[1] L. B. Loeb, Rev. Mod. Phys. 20, 151 (1948).

C2. Effect of Point Material on Corona Onset.* W. N. ENGLISH, *University of California, Berkeley.*—Several observers have remarked on the near equality of the positive and negative intermittent corona onset potentials, V_0^+ and V_0^-, in a point-to-plane gap in air, as contrasted to values of V_0^- far below V_0^+ in pure hydrogen and nitrogen. In an article on the "Mechanisms of positive and negative coronas in air," submitted to the Journal of Applied Physics, L. B. Loeb concludes that the equality is fortui-

tous, and can be due only to an exceptionally high negative point work function in the presence of O_2. Accordingly, a study of the effect of a wide variety of point materials and conditions on corona onset seemed urgent. Roughly shaped points of CuO, FeS, and As have shown V_0^- considerably below V_0^+ at atmospheric pressure. Treatment of a Pt point by hydrogen ion bombardment in a glow discharge immediately before onset determination gave no significant change. A comparison of carefully formed 1-mm diameter points of C, Al, Zn, and Cu, and the effect of gradual oxidation and reduction of Cu points will be reported on.

* Work supported by the Office of Naval Research.

C3. Factors Affecting the Determination of Particles Size by the Hopper-Laby Stokes' Law Method.* WULF KUNKEL, *University of California, Berkeley. (Introduced by Leonard B. Loeb.)*—Most electrified particles observed by Hopper-Laby method in a study of dust electrification[1] appeared much larger than individual particle sizes present in the powders. Calculations on aggregation due to electrostatic attractive forces indicated that particle growth is negligible unless either the cloud density exceeds a million particles per cm³ or the average charge of one sign exceeds 1000 electrons per particle. Deviations from Stokes' law by the particle shape might be considered responsible for such discrepancies. Experiments on the rate of fall of various models in a heavy oil showed that all shapes fall *more slowly* than the spheres of equal weight, thus appearing smaller than their true size in a Stokes' law estimate. The amount of particle surface seems the predominant parameter. The error in size estimate was rarely found to exceed fifty percent. Thus the dust particles observed were actually at least as large as estimated, and they must have existed as such before they started settling out.

* Work supported by the Office of Naval Research.
[1] Refer to J. W. Hansen, Phys. Rev. **73**, 532 (A) (1948).

C4. Point-to-Plane Impulse Corona.* D. B. MOORE AND W. N. ENGLISH, *University of California, Berkeley.*—A study of point-to-plane impulse corona in air at atmospheric pressure has been carried out, with a view to applying the impulse method to the determination of photo-ionization by positive corona streamers. Photographs of positive and negative corona from a 0.1-mm diameter point with two microsecond square pulses at potentials up to 12000 volts, show interesting peculiarities. With positive point burst pulse corona can be seen, and pre-onset streamers are particularly well developed, proceeding radially from the point, as a result of the absence of inhibiting space charge. Small groups of superimposed streamers are clearly seen, giving the corona a coarse streaked appearance. Attempts to photograph a single streamer have not yet succeeded. The negative point corona has a remarkable appearance. In addition to the normal brush-like structure associated with a steady negative potential, there is a concentrated central "streamer" spike and at higher impulse voltage, two side spikes. Tests have indicated no appreciable positive transient on the negative high voltage pulse. It is considered that the effect is due to a positive streamer discharge between the intense positive space charge near the point, left by an interrupted Trichel pulse, and the negative space charge further out in the gap.

* Work supported by the Office of Naval Research.

C5. Potential and Field Distribution in the Hemispherically Capped Cylindrical Point to Plane Corona Gap. JAMES M. PARKER AND LEONARD B. LOEB,* *University of California, Berkeley.*—Experience shows that hemispherically capped cylindrical point-to-plane electrode systems are the most satisfactory geometry for corona studies. Quantitative investigation of mechanisms requires that field distributions along the axis be known. As these are not amenable to computation, distribution was studied by large electrolytic model tank. Within limits of accuracy, a unique curve was observed for constant ratio of point radius r to gap length L. The ratio of gap length to plane radius R must be less than unity and large ratio L/r is desirable, thus setting a practical limit of 160. With this value the ratio of potential V at distance x from point surface to the applied potential V_0 was measured. Curves for V/V_0 as function (x/r) and $(dV/dx)(r/V_0)$ as function (x/r) have been determined which permit dV/dx to be evaluated as function of x for any radius. Applied to positive burst pulse onset corona threshold, $r=0.019$ cm in 760 mm air, the field at the point is exceedingly high, with very steep decline, throwing the ionization coefficients near the point into the Morton-Johnson[1] regime and making calculation of the Townsend integral difficult.

* Work supported by the Office of Naval Research.
[1] G. W. Johnson, Phys. Rev. **73**, 284 (1948).

C6. Point-to-Plane Corona Characteristics.* H. W. BANDEL AND W. N. ENGLISH, *University of California, Berkeley.*—A standard set of consistent corona data for point-to-plane geometry in air, covering variation in potential, point size and pressure, with current, oscilloscope, visual and photographic observations, has been urgently needed for the development of corona calculations and theory. These studies are being done in a brass chamber 30 cm in diameter by 30 cm with quartz windows. The ratio of the gap length to the radius of the platinum points has been kept constant at 160, as recommended by Loeb.[1] Positive and negative current-voltage curves with 0.5-mm diameter point in air at atmospheric pressure have been obtained from below 1000 volts to just under the sparking potential. Saturation currents caused by collection of externally caused ionization are observed below electron multiplication by collision and range around 10^{-13} ampere. A marked change in slope indicates the beginning of electron multiplication by collision near the point, and the curve is nearly linear up to intermittent onset, where the slope again becomes steeper and the current increases by a factor of 1000 in a few hundred volts. Above onset the corona currents are at first linear and then curve upward to the sparking potential as noted by previous observers.

* Work supported by the Office of Naval Research.
[1] See abstract C1 by Loeb and Parker.

D3. The Detection of Positive Mesons Produced by the 184-in. Cyclotron. A. S. BISHOP, JOHN BURFENING,* EUGENE GARDNER, AND C. M. G. LATTES, *University of California, Berkeley.*—Positive mesons have been produced by the 184-in. cyclotron and detected with photographic plates. The method of production is similar to that used for negative mesons.[1] Two methods of exposure to positive mesons are available: (1) Plates are placed below the circulating beam at a smaller radius than that of the target. Positive mesons emitted from the target with the proper energy in a forward direction are 180° focused upon the plates. (2) Plates are placed in the position initially used for exposure to negative mesons, but the shielding is modified to admit those positive mesons which are emitted from the target in the backward direction. Plates exposed in this way thus contain positive meson tracks which start at one edge and negative meson tracks which start at the opposite edge. In about half of the cases tracks of positive secondary mesons are observed to originate from the above-mentioned positive primary mesons. It is believed that all of the primary positive mesons decay into secondary mesons, but that in some cases the secondary meson is not seen because of unfavorable angle or bad background of neutron knockons, or both. This paper is based on work performed under Contract W-7405-eng-48 with the Atomic Energy Commission in connection with the Radiation Laboratory, University of California, Berkeley, California.

* Lieutenant Colonel, U. S. Army.
[1] Eugene Gardner and C. M. G. Lattes, Science **107**, 270 (1948).

D4. Meson Mass Estimation by Grain Counting in Photographic Emulsions. WALTER H. BARKAS,* EUGENE GARDNER, AND C. M. G. LATTES, *University of California, Berkeley.*—Negative mesons produced by the 184-inch Berkeley cyclotron have been studied by means of Ilford C.2 photographic plates of emulsion thickness 50μ. The meson tracks lie approximately parallel to the plane of the emulsion, and often end in the emulsion. The track grains are about 0.35μ in diameter. For particles carrying one unit of charge, the number of grains, $N(R)$, in a residual range R is assumed to be given by $N(R)=Mf(R/M)$, where M is the mass of the particle. By counting grains in meson tracks and proton tracks found in the same plate, the mass ratio of meson to proton can be found. A consistent convention for estimating the number of grains which occur in clumps reduces subjective errors. Comparisons of masses obtained by grain counting and by magnetic deflection on the same particle are made. Results of different observers are also related. Masses of star producing and non-star producing mesons are compared. Assuming that just two types of mesons are represented, the observed values are 305 and 202 electron masses for the heavy and light mesons, respectively. This paper is based on work performed under contract with the Atomic Energy Commission in connection with the Radiation Laboratory, University of California, Berkeley, California.

* Office of Naval Research, San Francisco, California.

D5. The Detection of Light and Heavy Mesotrons outside the Tank of the 184-in. Cyclotron. WOLFGANG K. H. PANOFSKY, *University of California, Berkeley.*—The mesotrons artificially produced by the 184-in. cyclotron* have been brought out of the cyclotron tank by means of a specially designed magnetic channel which brings mesotrons of $H\rho=148{,}000$ gauss$\pm$cm out of the field of 14,000 gauss at the target into a region of 4000 gauss in a re-entrant chamber in the cyclotron wall. Both light and heavy mesotrons have been detected in this chamber. A measurement of the lifetime of the heavy meson appears possible in this arrangement. The writer is indebted to L. W. Alvarez for suggesting the magnetic channel method. This work was sponsored by the Atomic Energy Commission.

* E. Gardner and C. M. G. Lattes, Science **107** (March 12, 1948).

D6. High Frequency Proton Source. R. N. HALL, *California Institute of Technology.*—An ion source and gun capable of producing beams of several hundred microamperes of 120-kev protons will be described. A 50-watt, 450-mc/sec. oscillator maintains an electrodeless discharge inside a barrel-shaped Pyrex discharge chamber of $\frac{1}{2}$-cc volume. An axial magnetic field of 1000 gauss greatly improves the performance. The r-f voltage is applied between the ends of the discharge chamber which contain holes through which the hydrogen and ions pass. The ions which diffuse out through the 0.040-in. diameter exit hole are accelerated without the use of a probe. A differential pumping arrangement removes most of the hydrogen which would otherwise enter the accelerating column. Typical operating conditions are: gas flow, 35 cc/hr. (N.T.P.); total beam current collected by 2-in. aperture, 420 μa; mass one (proton) current collected by $\frac{5}{8}$-in. aperture, 210 μa; mass two current, 115 μa; mass three current, 40 μa; ratio of mass one protons to hydrogen molecules consumed, 0.005; current density at the exit hole due to mass one protons, 0.027 amp./cm^2. The source operates well at reduced rates of gas flow with the ratio of mass one protons to hydrogen molecules increasing to 0.01. This work was assisted by the Office of Naval Research.

D7. Low Energy $C^{12}(p, \gamma)$ Cross Section. W. A. FOWLER AND R. N. HALL, *California Institute of Technology.*—The low voltage accelerator and high frequency ion source described in the previous abstract have been used to measure the cross section of the reaction $C^{12}(p\gamma, \beta^+)C^{13}$ in the 100- to 120-kev energy range. Preliminary results indicate that at 100 kev the thick target yield is 7×10^{-17} positrons per proton corresponding to a cross section of approximately 10^{-34} cm^2. A special thin-walled bell jar beta-ray counter obtained from the Radiation Counter Laboratories with a sensitive volume 1.2 cm in length and 2.8 cm in diameter was employed to measure this low yield. A belt of ten conventional counters in anticoincidence was used to reduce the background counting rate under $4\frac{1}{2}$" of lead from 10 counts/min. to 6 counts/min. The cross section calculated using the dispersion formula, including barrier penetration factor from the characteristics of the 453 kev resonance ($\Gamma_p=35$ kev, $\Gamma_\gamma=0.63$ ev),[1] is 0.4×10^{-34}

cm^2. The theoretical expression used by Bethe[2] in the absence of experimental data in calculating cross sections at stellar temperatures gives a cross section at 100 kev of 1.2×10^{-30} cm^2. The results at 100 kev and at resonance indicate that the stellar cross section may be 100 times as great as that employed by Bethe. This work was assisted by the Office of Naval Research.

[1] Fowler, Lauritsen, and Lauritsen, Rev. Mod. Phys. 20, 275 (1948).
[2] H. A. Bethe, Phys. Rev. 55, 434 (1939).

D8. Energy Production in the Sun. J. O'REILLY AND R. F. CHRISTY, *California Institute of Technology.*—The experiments described in the previous abstract show that the cross section for the reaction $C^{12}(p, \gamma)N^{13}$ for protons of about 100-kev energy is approximately 100 times larger than that used[1] in calculating the energy production of stars. Under the assumption that the carbon cycle is responsible for the energy production of the sun, this implies that the central temperature of the sun must be much smaller than assumed heretofore. Preliminary calculations indicate a value of about 15×10^6°C. This low temperature, combined with the stability and luminosity equations, implies a mean molecular weight in the neighborhood of 0.6 and a heavy element concentration (Russel mixture, for example) of only about 1 percent by weight. The ratio of hydrogen to helium, which together account for about 99 percent of the mass, is thus fairly large but not as yet well determined. Detailed calculation of these questions is being carried through. This work was supported in part by the Office of Naval Research.

[1] H. A. Bethe, Ap. J. 92, 118 (1940).

E4. Radioactive Potassium. R. V. LANGMUIR, *General Electric Company.*—During a search for short lived nuclear isomers with the 70 Mev synchrotron a new activity was observed in the bombardment of several potassium salts. The observed half-life was 1.3 (±0.1) seconds. It is suggested that this is one of the mirror nuclei,[1] and that the reaction is $K^{39}(\gamma, 2n)K^{37}$. A calculation of $tF(e_0)$ shows this interpretation to be possible. No short lived isomers with half-lives between 100 microseconds and 1 second were observed in the 55 elements bombarded. This work has been supported by the Office of Naval Research.

[1] E. Konopinski, Rev. Mod. Phys. 15, 209 (1943).

E5. The Half-Lives of Aluminum^{25} and Aluminum^{26}. HUGH BRADNER AND J. D. GOW, *University of California.*—The availability of separated isotopes of Mg makes it easy to determine the half-life of Al^{25}, a member of the Wigner series which has long been suspected to have a half-life of approximately 7 seconds, but which has not been confirmed because of the masking 7-second activity of Al^{26}. Mg^{24}, Mg^{25}, and Mg^{26} (in the form of MgO) have been bombarded with protons from the Berkeley linear accelerator, with the following results: Mg^{24} yields an activity of approximately 20 seconds half-life, presumably due to Na^{21} from the reaction $Mg^{24}(p, \alpha)Na^{21}$. The Mg^{25} yields an activity of 7.3-seconds half-life, which we assign to the reaction $Mg^{25}(p, n)Al^{25}$. The Mg^{26} yields an activity of 6.3-second half-life, assigned to Al^{26} according to a similar reaction. It seems probable, therefore, that the 7-second half-life normally given for Al^{26} is a mixture of these two activities. This paper is based on work performed under contract with the Atomic Energy Commission in connection with the Radiation Laboratory, University of California, Berkeley, California.

E6. Assignment of 48-Min. and 2-Min. Isomers of Cd. A. C. HELMHOLZ AND C. L. MCGINNIS, *University of California, Berkeley.*—The assignment of the 48-minute isomerism to Cd^{111} by Goldhaber[1] has been verified by bombardment of enriched isotopes with fast neutrons. The activity has also been produced by high energy alphas (>20 Mev) on Ag ($Ag(\alpha, pn)$), and Pd^{108} (α, n). Attempts to separate this activity from the 2.7-d In^{111} have failed, showing that the γ-ray of energy 173 kev observed in its decay[2] is not the same as that of energy 145 kev reported in the 48-min. isomerism by Hole.[3] Further work on these γ-rays will be reported. The 2-minute isomerism in Cd has been assigned to Cd^{113} also by bombardment of separated isotopes with fast neutrons. Initial measurements have given 2.3 min. as the half-life. This paper is based on work performed under contract with the Atomic Energy Commission in connection with the Radiation Laboratory, University of California, Berkeley, California.

[1] Abstracts of Washington Meeting.
[2] J. L. Lawson and J. M. Cork, Phys. Rev. 57, 982 (1940).
[3] Hole, N. Ark. Mat. Ast. Fys. 345, No. 19 (1947).

E7. Radioactive Products of High Energy Deuteron Bombardment of Cu. DOROTHY BOCKHOP, A. C. HELMHOLZ, AND J. M. PETERSON, *University of California, Berkeley.*—Serber[1] has suggested inelastic collisions in which only a fraction of the available energy is lost as the initial step in the formation of nuclei by high energy particle bombardment. The nucleus thus excited subsequently boils off particles and energy. This theory differs from that of the compound nucleus, which holds at low energies, in that the incident particle is not captured. Serber's theory has been applied with success to several cases.[2] The characteristic feature of the excitation function is the large value of cross section at high energies (~5 times the threshold) relative to that predicted by the theory of the compound nucleus. The formation of atomic number $Z+1$ from target of atomic number Z cannot proceed by this process since it requires the capture of a proton, although another possibility would be an exchange collision between incident proton and a neutron. The excitation functions of a number of radioactive species from the bombardment of Cu with 190-Mev deuterons have been measured. Chemical separation of a number of fractions, including Zn, Cu, Co, and Ni, were performed. The Zn^{65} and Zn^{62} activities which must be formed as mentioned above show maxima at less than 50 Mev, and steady decreases to the highest energy measured (140 Mev) where the values are less than ½ those of the maxima. This is in accord with considerations of the compound nucleus. However, Ni and Co activities show maxima at low energies, minima and

subsequent increases at higher energies, such as are characteristic of Serber's theory. This work is based on work performed under contract with the Atomic Energy Commission in connection with the Radiation Laboratory, University of California, Berkeley, California.

[1] R. Serber, Phys. Rev. **72**, 1114 (1947).
[2] R. L. Thornton and R. W. Senseman, Phys. Rev. **72**, 872 (1947); W. W. Chupp and E. M. McMillan, Phys. Rev. **72**, 873 (1947).

E8. Excitation Curves of $C^{12}(p, pn)C^{11}$ and $B^{11}(p, n)C^{11}$ up to 32 Mev. ROBERT PHILLIPS AND WOLFGANG K. H. PANOFSKY, *University of California, Berkeley.*—The excitation curves of $C^{12}(p, pn)C^{11}$ and $B^{11}(p, n)C^{11}$ have been obtained by the stacked foil technique using accurately molded boron carbide and polystyrene sheets. 32-Mev protons from the linear accelerator were used as the bombarding particle. Because of the homogeneity of the linear accelerator beam, very accurate resolution near the threshhold has been obtained. The shape of the curve will be discussed. This work was sponsored by the Atomic Energy Commission.

F1. The Ratio (e/m_0) for Free Electrons by Use of a Resonant Cavity. CHARLES H. WILTS, *California Institute of Technology.*—A deflection method for measuring (e/m_0) for free electrons is described. A beam of electrons is directed along the axis of a cylindrical cavity excited in the TM_{110} mode. A null in the subsequent deflection of the beam occurs when the transit time is nearly equal to an integral number of cycles of the cavity oscillation. Three quantities must be measured: a distance, a frequency, and a difference of potential; two very small corrections must be made. An accuracy of 1 part in 10,000 seems to be achievable Preliminary apparatus gave a value: $e/m_0 = 1.759 \pm .007(10)^7$ e.m.u. per gram.

F2. Wave-Guide Fast Counter. R. F. POST, *Stanford University.*—The theory is given for a fast counter which would operate by measuring the change in phase velocity of propagation in a gas-filled wave guide induced by primary ionization from a high energy charged particle. It is shown that increased sensitivity can be achieved by applying a longitudinal magnetic field sufficient to make the Larmor frequency of the electrons equal to the applied radiofrequency. This effect is similar to the critical phenomena associated with the propagation of radio waves in the ionosphere. Such a counter should have short response and resolving time, but this can only be obtained at the expense of sensitivity and solid angle. Thus the device will probably be useful only for the counting of heavily ionizing particles for which the path direction is accurately known. Possible methods for increasing counter sensitivity are discussed.

F3. Method of Measuring Cavity Impedance.* W. W. HANSEN AND R. F. POST, *Stanford University.*—In the design of a linear electron accelerator it has become necessary to measure the normalized value of the line integral of electric field along the axis of an accelerator cavity. An experimental method has been developed which gives results accurate to 3 or 4 percent. The method consists of measuring the shift of resonant frequency produced by perturbing the wall of the cavity on the axis at one end by means of a movable cylindrical plunger, and of taking the slope of the frequency *vs.* plunger height curve at the point where the plunger is flush with the cavity wall, for which case the perturbation theory surely applies. From this measurement the normalized value of E at one point on the axis is obtained, and a separate simple experiment yields the variation of E along the axis. This enables one to compute the value of the desired integral. The method has been checked by applying it to simple cylindrical cavities for which the integral may be evaluated analytically. In these cases it gave results accurate to less than 2 percent.

* This work was supported by Office of Naval Research.

F4. Continuous Spectrum of X-Rays to 13A.* S. T. STEPHENSON AND F. D. MASON, *Washington State College.*—Previous work on the continuous spectrum of x-rays ends at 2.8A as an upper limit for wave-length and 7 kv as the lower limit for voltage. The present paper describes results obtained up to 13A in wave-length and down to 1.2 kv. A vacuum Geiger counter x-ray spectrometer[1] was used with a mica crystal. A counter of special window design to allow for either excess pressure from without or, after evacuation of the spectrograph, from within was used with windows of Al as thin as 0.0003 inch. Corrections are made for background, the absorption of tube windows, counter efficiency, and for the reflecting power of mica (although this latter correction is an extrapolated correction gotten by comparing mica with calcite out to 4.5A). The intensity of radiation appears to depend, as at the shorter wave-lengths, on the first power of the atomic number and the square of the voltage. The shape of the curve, however, quite definitely changes at long wave-lengths. The maximum in the curve of intensity against wave-length comes closer to the short wave cut-off than at shorter wave-lengths, and the general pattern approaches the one to be expected from a thin target.

* Assisted by the Office of Naval Research.
[1] S. T. Stephenson and F. D. Mason, Phys. Rev. **72**, 744 (1947).

F5. Properties of Cerenkov Radiation Near the Threshold. JOHN M. HARDING AND JOSEPH E. HENDERSON, *University of Washington.*—A study has been made of Cerenkov radiation from mica in the vicinity of the threshold predicted classically when the incident electron travels with a velocity equal to the velocity of the light which it produces in the medium. The electrons were directly accelerated by means of a Van de Graaff generator and passed through a transverse magnetic field. The magnetic field served not only to provide velocity selection and focusing, but also eliminated the direct light from the filament of the tube from confusing the interpretation of the light from the mica. It is found that: (1) A threshold does exist very close to the conditions predicted by simple theory. (2) The light at the threshold is unpolarized and rapidly becomes polarized as the electron energy exceeds the threshold and the cone of radiation expands. (3) The total radiation increases approximately linearly with energy above the threshold energy over the region investigated,

which is about twice the threshold. This information at the larger values of electron energy becomes increasingly uncertain due to larger angles of emission, introducing internal reflection problems within the mica.

G3. Precision Spectroscopy of Nuclear Gamma-Rays with a Focusing Curved Quartz Crystal.* JESSE W. M. DUMOND, DAVID LIND, AND BERNARD B. WATSON, *California Institute of Technology.*—A newly developed precision instrument and technique is described which has permitted the extension of the methods of the focusing curved crystal x-ray spectrometer into the nuclear gamma-ray region. The range of the instrument, 500 x.u. to 8 x.u. or less, permits *establishment of a precision link between the well established scale of x-ray wave-lengths and the wave-lengths of nuclear gamma-rays.* The wave-length of the 0.41-Mev gamma-ray line from Au^{198} has been measured with a precision better than two parts in 10000. The chief limitation comes from the weak crystal reflection at short wave-lengths (see a companion abstract in this program). The proposed program includes the establishment with strong neutron activated sources of a number of precisely defined gamma-ray wave-lengths to serve as easily reproducible *fixed points* in this region of the spectrum. Since these gamma-ray lines can in turn be used to eject photoelectrons in β-ray spectrometers, the precision thus made available can be used in the calibration of β-ray spectra to increase the precision of our knowledge there also. Therefore, it is hoped that this technique of direct spectroscopy of gamma-rays ushers in a new era of precision in nuclear energy measurements.

* Assisted by the Office of Naval Research.

G4. The Reflecting Power of the (310) Planes of a Curved Quartz Crystal for X-Rays and Gamma-Rays from 494 x.u. (Sn $K\alpha$ X-Rays) to 30 x.u. (Au^{198} Gamma-Rays). Experimental Results and Theoretical Interpretation.* DAVID LIND, BERNARD B. WATSON, AND JESSE W. M. DUMOND, *California Institute of Technology.*—Using the 2-meter focusing curved quarts crystal spectrometer[1] with (1) concentrated sources of nuclear gamma-rays and (2) secondary fluorescent sources of x-rays placed at the focus we have measured, as a function of λ, by means of a multicellular gamma-ray counter,[1] the ratio Γ of counts reflected to counts of wave-length λ incident on the (310) planes of the quartz crystal. Γ, to some extent an instrumental constant, depends on the overlapping of four distribution functions: (1) The pattern produced by the geometrical aberrations of focus. (2) The distribution of source intensity. (3) The diffraction pattern curve of the (310) planes of the quartz crystal at the wave-length used. (4) The "natural line profile" of the radiation, λ. At 500 x.u. Γ, in our instrument, is nearly 18 percent while at 30 x.u. it has fallen to 0.3 percent. The "integrated reflection coefficient" R (the integral of curve (3) above) has been calculated from our measurements of Γ. R we find is quite closely proportional to the square of the wave-length. This is explicable if one assumes that the curved quartz lamina behaves in this spectral range like a mosaic of domains small compared to the primary extinction length.

* Supported by the Office of Naval Research.
[1] See companion abstract in this programme; also Rev. Sci. Inst. 18, 626 (1947).

G5. A Method of Studying the Gamma-Ray Spectrum of the Annihilation Radiation from a Source of Positrons Using the Focusing Curved Crystal Spectrometer.* BERNARD B. WATSON, DAVID A. LIND, AND JESSE W. M. DUMOND, *California Institute of Technology.*—Behind a deep jawed lead slit placed at the focus of the gamma-ray spectrometer[1] there is placed a strong source of positrons of considerably greater dimensions than the slit. The spectrum of the annihilation radiation coming from the recombination of the positrons with negative electrons in that region of the source material which is directly behind the slit is then studied with the spectrometer both for spectral distribution and precision wave-length determinations.

* Assisted by the Office of Naval Research.
[1] This instrument is described in a companion abstract on this programme. See also Rev. Sci. Inst. 18, 626 (1947).

H1. Counting Efficiency of Scintillation Counter. A. V. TOLLESTRUP, *California Institute of Technology.*—Efficiency curves for a scintillation type counter for low energy protons, deuterons, and alpha-particles will be presented. The counter consists of a 931A multiplier tube, and a zinc sulfide phosphor obtained from the Radio Corporation of America.[1] A conventional amplifier which has a gain of 500 is used. The counter can be sealed directly onto the vacuum system of the accelerators used in the study of nuclear reactions. Thus the problems associated with thin windows are eliminated. Protons of energy as low as 17 kev have been counted. The background due to dark current in this case was 300 counts per minute. Protons whose energy is 80 kev give pulses large enough to allow complete discrimination against the dark current pulses. This work was assisted by the Office of Naval Research.

[1] J. W. Coltman and Fitz-Hugh Marshall, Nucleonics 1, No. 3 (November 1947).

H2. Design and Performance of a 15-cm Electrostatic Analyzer. SAMUEL K. ALLISON AND HAROLD V. ARGO, *University of Chicago.*—An electrostatic deflector for high energy ions, intended for use with an electron multiplier tube, has been designed, constructed, and is in operation. The ions are deflected through 90° between two cylindrical plates 5 millimeters apart with average radius of 15 cm. Both plates are mounted on a heavy quartz post at the axis of the instrument and each plate can be charged to high voltage independently. Tolerance on the diameter of the quartz post has been held to ± 0.0001 inch and on the radii of the plates to ± 0.001 cm. Slits of adjustable width are incorporated in the design and can be moved from outside the vacuum wall transversely to the ion beam and parallel to it, thus allowing the experimental location of conjugate foci. It is computed that the fraction of the particles focused from a monoenergetic source emitting in all direc-

tions is 1.7×10^{-4}. At the present time singly charged ions up to 600-kv energy have been deflected and detected with negligible background in the multiplier tube by charging one of the plates to 40 kv, and indications are that the upper energy limit of the instrument is still higher than this. The resolution is a function of the slit width which can be readily adjusted without breaking the vacuum, and the instrument has been operated at a resolving power of 0.3 percent in energy.

H3. An Improved Lock-In Amplifier. WALTER C. MICHELS AND ESTHER D. REDDING, *Bryn Mawr College.*—The design of the lock-in amplifier previously used in this laboratory[1] has been modified to produce a semiportable instrument of increased sensitivity and selectivity. One stage of pentode amplification has been added, the stability has been improved, and the phase shifter has been transferred from the input to the lock-in circuit. With these changes and with a 19.5-ohm type H.S. galvanometer as the final detector, sensitivities up to 2.5×10^{5} mm/volt have been obtained at 800 cycles. The amplifier operates successfully with an inductive input of 2×10^{6} ohms impedance at this frequency so that the maximum current sensitivity is of the order of 10^{12} mm/ampere. The selectivity has also been improved, largely because the increased stability has allowed the use of a longer period (7 sec.), more sensitive galvanometer. The measured response is fifty percent of the maximum at 0.1-cycle/sec. deviation from the lock-in frequency and drops to one percent if the frequency departs by 0.6 cycle/sec.

[1] Walter C. Michels and Norma L. Curtis, Rev. Sci. Inst. **12**, 444 (1941).

H4. Reaction Time of Parallel-Plate Counters. J. W. KEUFFEL, *California Institute of Technology.*—The uncertainty in the reaction time of the parallel-plate counters described previously[1] is being studied. The uncertainty is measured by placing one counter directly above another and observing by means of a 10-detector chronotron[2] the distribution of time lags of one counter relative to the other. Preliminary results show that half the relative lags fall within $\pm12\times10^{-9}$ sec. at an overvoltage of 500; at an overvoltage of 1000 the uncertainty is $\pm4\times10^{-9}$ sec. By varying the voltage on one counter some idea as to the absolute value of the lags may be obtained. Such tests indicate that better parallelism may improve the precision attainable, as the present lags could be due to variations in field strength from point to point. The lifetime of the counters at 1000 volts overvoltage seems to be about a month of background rate counting.

[1] J. W. Keuffel, Phys. Rev. **73**, 531 (1948).
[2] Neddermeyer, Althaus, Allison, and Schatz, Rev. Sci. Inst. **18**, 488 (1947).

H5. On Diffraction under Small Angles by Three-Dimensional Lattices. OTTO HALPERN AND EDWARD GERJUOY, *University of Southern California.*—We have continued the investigation[1] of small angle diffraction by crystals, taking into account lattice errors and interference between perfect crystal blocks. Results of a rather general nature have been obtained under diverse assumptions about the structure of the crystal or polycrystal. We find, e.g., for a representative case that the integral cross section σ_s of scattering into angles lying between the zero'th and first Laue spot (Debye ring) is given by $\sigma_s=C\sigma_0N(\lambda/\pi a)^2$. Here σ_0 is the atomic differential cross section for forward scattering multiplied by 4π, a the lattice distance, λ wavelength, N number of atoms in scatterer, C a numerical constant of order $\frac{1}{2}$. Various applications to the scattering of light ($\lambda\gg a$) as well as to that of neutrons ($\lambda\sim a$) and hard radiations ($\lambda\ll a$) will be discussed.

[1] Otto Halpern, Phys. Rev. **73**, 653 (1948).

H6. The Average Negative Gradient of Potential Energy. F. W. WARBURTON, *University of Redlands.*—Methods of developing the Lagrangian equations are applied to the variation in potential energy V of two bodies to verify the general equation,

$$\cdots-(d^2/dt^2)(\partial V/\partial\ddot{q})+(d/dt)(\partial V/\partial\dot{q})-(\partial V/\partial q)=F_q.$$

Use is made of the integral $\int(F_q\delta q)dt$ divided by the time interval t_2-t_1, as expressing the average work done by the variable force F_q exerted by one body on the other. As the forces concerned are functions of relative velocity which are not bound by the classical Lorentz force, the contention that "magnetic forces do no work" does not affect the validity of this extended concept of potential energy. An advantage of replacing the Lagrangian function $L=T-V$ by V and the kinetic energy T separately, is that F_q may be determined from V alone or may be expressed in terms of T alone, when one considers the mechanical energy gained by the electron as the result of *all* the external forces.

H7. Modes of Vibration in Contoured Quartz Plates.* RENATE S. BEVER, VIRGIL E. BOTTOM, AND LOUIS R. WEBER, *Colorado A. & M. College.*—The admittance spectrum of flat quartz plates vibrating in thickness shear shows numerous inharmonic overtones having frequencies within a few percent of the fundamental frequency. These overtones seem to be spaced at random; many are coupled together. Making the major surfaces of the plate convex causes dispersion of the overtone modes and decreases the coupling between them. Chladni patterns of such contoured plates show the vibrations to be restricted to a small area and independent of the remaining peripheral portion; the frequencies are determined by the thickness of the outermost loop of the individual patterns. Moreover, these inharmonic overtones may be grouped into series associated with standing waves along X, Z', or one of the "diagonal" directions, since the difference between the frequencies of the modes of each series is very nearly constant and depends upon the curvature of the surfaces and the elastic modulus in the direction of the standing wave train. Thus the overtone spectrum of a contoured quartz plate vibrating in thickness shear may be resolved into a set of series having a definite regularity.

* This work supported by Signal Corps Contract.

H8. High Frequency Loading. NICHOLAS BEGOVICH, *California Institute of Technology.*—An interesting high frequency loading phenomena occurring in very closed spaced vacuum tubes has been reported.[1] The experimental set-up is the measurement of the shunt conductance at 3.0×10^9 c.p.s. of a diode as a function of the retarding voltage on the anode. With large values of retarding voltage the impedance is the same whether the cathode is operating or turned off. With the cathode operating and decreasing the retarding voltage, the conductance sharply increases and reaches a maximum value before any electrons are collected at the anode. A calculation of the to and fro electron transit time, taking into account the Maxwellian velocity distribution, indicates that

$$G\cong 3.44\times10^{-4} I_e T V_a^{-2} h^{-1} \times\{(h+2)\exp(-1/h)_1F_1(1/2;\,3/2;\,1/h)-h\}\ \text{mhos/cm}^2,$$

where I_e is the emission current density, T the absolute temperature of the cathode, ${}_1F_1(1/2;\,3/2;\,1/h)$ the confluent hypergeometric function, V_a the anode retarding voltage, d the diode spacing in cm, ω the angular frequency, and $h=1.021\times10^{19} V_a^2 T^{-1}(\omega d)^{-2}$.

[1] Hamilton *et al.*, *Klystrons and Microwave Triodes* (McGraw-Hill Book Company, Inc., New York), p. 156.

H9. On the Theory of a New Magneto-Electric Effect. ELLIOT T. BENEDIKT, *North American Aviation, Inc., Los Angeles.*—It is the purpose of the present paper to show the possibility of producing electrostatic effects by means of unhomogeneous magnetic fields. Consider a system of particles having a magnetic moment and subjected to an unhomogeneous magnetic field. The particles will be subjected to a force which will alter their space distribution. If the particles have, furthermore, an electric charge, this space distribution will, in general, produce an electric field. Such an effect can be expected with ferromagnetic colloidal particles, ions, electrons in a metal, and particles (nuclei, electrons) belonging to atoms or molecules. In the latter case, an electric polarization of the atoms or molecules should be obtained for magnetic fields strong enough to remove the coupling between the magnetic moments of the various constituents of the particle. It is interesting to notice the different results which can be expected according to whether the laws of classical or quantum electrodynamics are assumed to be valid. In the former case, the particles will be in stable rotational equilibrium if their magnetic moment is parallel to the field; consequently, all the particles will be forced to move toward the region of greatest field intensity. In the latter case, a number of stable orientations or the moment of the particles is possible, and therefore some of them will be forced to move toward the region of greatest field intensity, and some in the opposite direction. The electron density will therefore have a minimum inside the metal. The detailed theory of the effect for an ionized medium and an electron gas will be given from the classical and quantum-mechanical point of view, respectively.

H10. The Quantization of Unitary Field Theories. R. J. FINKELSTEIN, *Institute for Advanced Study.*—In a unitary field theory particles appear not as singularities but as small volumes of the field in which charge and energy are concentrated. In a theory of this nature, which is necessarily non-linear, all particle properties, such as their equations of motion, follow from the field equations. We have studied the quantization of such a theory without specializing the Lagrangian. Momentum (G_α) and angular momentum ($M_{\alpha\beta}$) of particles appear naturally and a relativistic definition of the position (X_α) of a particle may be given in terms of $M_{\alpha\beta}$ and G_α. The commutators of these particle observables (X_α, G_α, $M_{\alpha\beta}$) agree with current theory if the fields are quantized according to the usual (Einstein-Bose or Fermi-Dirac) rules. (The Born-Infeld theory did not meet this requirement because it was not strictly unitary.) The connection between velocity and momentum and the equation of motion of particles which follow from the field equations are the usual ones. Operators for mass, charge, and spin may be defined; these mutually commute and permit the usual classification of the elementary particles according to charge, mass, and spin. Mass and position are not simultaneously observable, even if knowledge of momentum is given up. External fields cannot be measured with arbitrary accuracy at the position of a particle. Magnetic moment and charge, on the other hand, commute with external fields. The non-linearity present in the usual field theories is sufficient to permit the existence of particle-like solutions under certain conditions. Hence we may derive from the current field theories a class of non-trivial unitary theories by postulating that only those solutions of the current theory which are free from singularities are physically admissible.

H11. Behavior of Spherically Tipped Bodies in the Early Stage of Water Entry. HAROLD WAYLAND AND SAUL BAKER, *Naval Ordnance Test Station, Pasadena.*—The behavior of large spherically tipped bodies projected obliquely into water is examined both theoretically and experimentally, particularly during the stage in which the body is balanced on its nose in the cavity. The theory is based on the assumption that the only hydrodynamic force acting on the body in the cavity can be represented by a force acting through the center of the spherical tip in the direction of motion of the c.g. of the body, and that the force is proportional to the square of the velocity of the body. The agreement between theory and experiment confirms the validity of these assumptions within practical limits. Equipment for precise measurement and recording of angular positions is described which is capable of withstanding the shocks occurring at water entry and recording throughout the entry phase.

H12. A Family of Rotational Corner Flows. R. C. PRIM, *Naval Ordnance Laboratory, White Oak, Maryland.*—A formally simple family of truly rotational solutions for the equations governing steady plane flow of an ideal gas in the absence of body forces is discovered. This family of

solutions is rotational with respect to both the reduced velocity field and the actual velocity field. These rotational flows are related to the irrotational Prandtl-Meyer corner flow, which is included in the family as a special case. The equations of the streamlines and isobars and equations for the distribution of velocity components, pressure, density, and Mach number are given. General properties of the flows are discussed and examples of flow patterns exhibited.

I1. A Non-Homogeneous Cosmological Model with a Finite Cosmological Constant. GUY C. OMER, JR., *California Institute of Technology.*—The cosmological models described earlier[1] have been generalized to include a finite cosmological constant. In the neighborhood of the assumed observer in the model we take the average density as 10^{-29} g/cc at the present time, the cosmological constant as 8.78×10^{-19} (lt. yr.)$^{-2}$, and the radius of curvature as 10^{10} lt. yr. Then we find the total time elapsed in this neighborhood since the beginning of the expansion to be 3.64×10^{9} yr. This is in agreement with the probable range of astronomical time given by Bok[2] and with the estimated age of the earth stated by Holmes.[3] The calculated red shifts, except for the two Ursa Major clusters, agree with the observed red shifts given by Hubble[4] to within 0.1 magnitude. The calculated values of $\log N$, the nebular counts, depart from the observed values presented by Hubble[4] by 0.002 or less.

[1] G. C. Omer, Jr., Phys. Rev. 72, 744(A) (1947).
[2] B. J. Bok, M.N.R.A.S. 106, 61 (1946).
[3] A. Holmes, Nature 159, 127 (1946).
[4] E. Hubble, Astrophys. J. 84, 517 (1936).

I2. Existence of Tensor Interactions between Nucleons. ROY THOMAS,* *St. Louis University.*—Various meson theories predict exchange and tensor nuclear interactions. The angular dependences of the neutron-deuteron and the proton-deuteron cross sections for elastic collisions are calculated. The interaction between nucleons is assumed to be:

$$V(r_{ij})=G_{ij}[1+\alpha S_{ij}]J(r_{ij}).$$

S_{ij} is the tensor operator and G_{ij} represents the exchange nature of the interaction. α and $J(r_{ij})$ are adjusted to give the binding energy and a four percent D state to the deuteron, and G_{ij} is normalized to unity for the deuteron. Calculations show that for relative energies to 10 Mev only S and P waves contribute to the scattering. the tensor terms contributing little. For much higher relative energies the D wave contributes and in this case the tensor terms dominate the scattering. The angular dependence of the scattering produced by the tensor terms shows a significant difference from the non-tensor terms.

* Now at Oregon State College.

I3. A Double-Focusing Magnetic Spectrograph. C. W. SNYDER, C. C. LAURITSEN, W. A. FOWLER, AND S. RUBIN *California Institute of Technology.*—A magnetic spectrograph for analyzing charged particles emitted in nuclear reactions has been built, adapted from the design of Svartholm and Siegbahn[1] for electrons. Particles are deflected through 180° between steel pole pieces shaped to give a field decreasing radially approximately as $r^{-\frac{1}{2}}$ so that two-directional focusing is obtained. The central path has a radius of 28 cm, and the maximum field is 7600 gauss with a 4.5-cm gap. Protons of 2 Mev can be analyzed. With the present field shape, there is some astigmatism when source and image are placed symmetrically, but it can be minimized so that a nearly point focus is obtained by moving the source farther away from the end of the pole pieces. The field is measured by a torsion-type magnetometer calibrated by elastic scattering at known bombarding voltages. The effective angle, relative to the bombarding beam, of the particles entering the spectrograph is also determined by elastic scattering, and the consistency of results with various bombarding energies and targets indicates a precision of approximately 0.1 percent in measuring momenta. This work was supported in part by the Office of Naval Research.

[1] Svartholm and Siegbahn, Arkiv f. Astro., Mat., Fys. 33A, No. 21 (1946).

I4. Inelastic Scattering of Protons from Li^7. S. RUBIN, C. W. SNYDER, C. C. LAURITSEN, AND W. A. FOWLER, *California Institute of Technology.*—The energy of the lowest excited state of Li^7 has been measured with the double-focusing magnetic spectrograph by measuring the energy of the group of inelastically scattered protons from a thin lithium target bombarded by 1222-kev protons. The spectrograph was calibrated by elastic scattering of 1222-kev protons from gold, beryllium, carbon, and oxygen. The bombarding proton energy is fixed to better than 1 kev by an electrostatic analyzer,[1] calibrated at 440 kev with the γ-ray resonance from $Li^7(p,\gamma)$.[2] The chief sources of error are in the shape of the peak obtained with the inelastically scattered protons, and in the calibration of the electrostatic analyzer. Both amount to 0.3 percent in terms of energy. The result of this determination is 480 $\pm$2 kev, in good agreement with the measurement of Hornyak and Lauritsen on the γ-ray accompanying the decay to the ground state, discussed in an accompanying abstract. These two results can be combined to locate the resonance in $Li^7(p,\gamma)$ conventionally taken at 440 kev on the nuclear energy scale[3] at 439$\pm$3 kev with respect to annihilation radiation at 510.8 kev. This work was assisted by the Office of Naval Research.

[1] W. A. Fowler, C. C. Lauritsen, and T. Lauritsen, Rev. Sci. Inst. 18 818 (1947).
[2] W. A. Fowler, C. C. Lauritsen, and T. Lauritsen, Rev. Mod. Phys. 20, 236 (1948).
[3] L. R. Hafstad, N. P. Heydenburg, and M. A. Tuve, Phys. Rev. 50, 504 (1936).

I5. Short-Range Repulsion as a Mechanism for Nuclear Saturation. G. PARZEN AND L. I. SCHIFF, *Stanford University.*—Nuclear saturation can be explained by a short range repulsion and a longer range attraction between each pair of nucleons.[1] An attempt has been made to fit the density of heavy nuclei, deuteron binding energy, ortho-para and crystal scattering data, proton-proton scattering, and neutron-proton scattering at 90 Mev, by

means of a square potential of this type. For parameters that give the correct deuteron energy, the magnitude of the scattered triplet amplitude at zero energy is greater than for a square well of the same over-all range; thus the range is so small that the density of heavy nuclei is excessive. Introduction of the repulsion worsens the agreement of the square well potential with the proton-proton scattering below 1 Mev. At 90 Mev, the new potential tends to make the phase shift δ_1 larger than δ_0 and δ_2, but the effect is not pronounced enough to give the observed backward maximum in the neutron-proton scattering. It is concluded that a short-range repulsion is not an adequate substitute for an exchange interaction.

[1] H. A. Bethe and R. F. Bacher, Rev. Mod. Phys. 8, 161 (1936); H. A. Bethe, *Elementary Nuclear Theory* (John Wiley & Sons, Inc., New York, 1947), p. 81; see also P. M. Morse, J. B. Fisk, and L. I. Schiff, Phys. Rev. 50, 748 (1936).

I6. On Neutron-Proton Scattering Models. L. GOLDSTEIN AND D. W. SWEENEY, *Los Alamos Scientific Laboratory.*—Using semi-empirical square well interaction forms of the "central force" type, differential and total $n-p$ scattering cross sections have been obtained for neutrons of absolute kinetic energy extending to 90 Mev, with a variety of well radii. The total $n-p$ cross-section data of the Minnesota group, up to 6-Mev neutron energy, when compared with the computed cross sections, seem to favor well radii smaller than the classical electron radius. In the intermediate energy range, 10–25 Mev, data on differential cross sections might help in choosing the most appropriate well radius and the type of interaction representing best the data. Available total cross-section data in this range are insufficient for this purpose, on account of the relative insensitivity of total cross sections to well ranges, at smaller radii and to types of force (ordinary, exchange, or symmetrical). The Berkeley results at 90-Mev neutron kinetic energy, while excluding "ordinary" interaction, are incompatible with either "exchange" or "symmetric" type of interactions for wells with radii from 1.5×10^{-13} cm upward. Empirical "mixtures" of different types of interactions might lead though to a satisfactory representation of these data.

I7. On the Failure of Beta-Decay Theory at Low Energies. EUGENE P. COOPER, *University of Oregon.*—The Fermi theory of beta-decay predicts the energy distribution of electrons (or positrons) in any particular nuclear disintegration over the whole range of energies. At high kinetic energy (say above 200 kev), where the predominant energy dependence is in the statistical factor, agreement with unambiguous experiments in excellent. Serious disagreement is encountered, however, at low energies where the Coulomb factor is important. Such disagreement has frequently been attributed to instrumental scattering. However, the recent measurements of Cook and Langer on the electrons and positrons from Cu^{64} are largely free from scattering errors but show definitely too few electrons and too many positrons at low energies. The so-called proof of the Fermi theory given by Scherrer *et al.* with respect to their data on the positrons and K-captures from $Cd^{107,109}$ is shown to be incomplete as their positron spectrum, at low energies, deviates from the theory in the same manner as that of Cu^{64}. In an attempt to explain these low energy discrepancies it is assumed that electromagnetic radiation (x-rays) plays an essential role in the beta-process. The resulting modification of the Coulomb factor is discussed.

I8. Neutron Spectra from Proton Recoils in Photographic Emulsions. F. REINES, *Los Alamos Scientific Laboratory.*—With the coming of nuclear reactors, it becomes interesting to determine neutron spectra for isotropic neutron fluxes. The proton recoil technique rising photographic emulsions may be adapted to this case. Criteria, based on geometrical probability, are provided for the treatment of all tracks which do not touch an emulsion boundary. Emulsion shrinkage is considered. The range energy relation for protons in photographic emulsion is applied to the tracks to yield the neutron spectrum which is related to the proton recoil spectrum by the equation:

$$n(E)=C\lambda(E)E^{\frac{1}{2}}[dm(E)/dE],$$

where C is a constant, $\lambda(E)$ is the mean free path for neutron proton collisions in the emulsion at neutron energy E, $m(E)$ represents the recoil proton spectrum, and $n(E)$ is the desired neutron spectrum. This equation is valid when $\lambda(E)$ is large compared with the dimensions of the photographic plate employed. Work is progressing on a method which considers all tracks independently of whether they penetrate the emulsion.

I9. Radiations from Gold (199).* C. E. MANDEVILLE AND M. V. SCHERB, *Bartol Research Foundation of the Franklin Institute.*—Au^{199} was grown from its 30-minute platinum parent when platinum was irradiated by neutrons in the pile at Oak Ridge. Aluminum absorption and Feather analysis gave a maximum beta-ray energy of 0.38 Mev, and lead absorption indicated the presence of a single gamma-ray of energy 0.18 Mev. The beta-gamma coincidence rate was constant, independent of the beta-ray energy, and beta-beta coincidences were also present. No gamma-gamma coincidences were found. These data suggest that the 0.38-Mev beta-rays are followed by a single 0.18-Mev gamma-ray which is partially converted. The 1.01-Mev beta-rays, the 0.45-Mev gamma-rays, and the 2.6-day half-period assigned to Au^{199} by Krishnan and Nahum[1] are now attributed to Au^{198} formed in the reaction $Pt^{198}(D, 2n)Au^{198}$.

* Assisted by the Office of Naval Research.
[1] Krishnan and Nahum, Proc. Camb. Phil. Soc. 37, 422 (1941).

I10. The First Excited State of Li^7. W. F. HORNYAK AND T. LAURITSEN, *California Institute of Technology.*—A determination of the energy of the γ-ray accompanying the decay of the lowest excited state of the nucleus Li^7 to the ground state has been made using a magnetic lens type spectrometer. The excited level was reached by non-capture excitation, using 1.2-Mev protons on a LiOH target

mounted in the spectrometer. Photoelectrons were ejected from a 0.001" thick thorium converter. Using the same spectrometer geometry, and source assemblies matching as nearly as possible, the Li^7 γ-ray was compared directly with the 411.1-kev γ-ray[1] from Au^{198} and the 510.8-kev[2] annihilation radiation from N^{13}. With the aid of a calibration based on an internal conversion line in Th B, a study of the energy shift due to the thickness of the converter was made. A shift of 7.0 ± 0.8 kev for the Li^7 γ-ray was found and the energy determined as 479 ± 2 kev. The present value is in good agreement with recent determinations of the γ-radiation from Be^7 by S. Rubin[3] and by A. C. G. Mitchell,[4] but disagrees markedly with the value of 453 ± 5 kev reported by K. Siegbahn.[5] This work was assisted by the Office of Naval Research.

[1] J. W. M. DuMond and D. Lind, in publication.
[2] J. W. M. DuMond and E. R. Cohen, Rev. Mod. Phys. 20, 82 (1948). We are indebted to Professor DuMond and Dr. Lind for the Au source and for advance information on the γ-ray.
[3] S. Rubin, Phys. Rev. 69, 134 (1946).
[4] Private communication.
[5] K. Siegbahn, Arkiv. f. Astro., Math., Fys. 34B, No. 6 (1946).

I11. Gamma-Radiation from $Be^9(d,n)B^{10}$. T. LAURITSEN, C. B. DOUGHERTY, AND V. K. RASMUSSEN, *California Institute of Technology.*—Previously reported work[1] on the $Be+d$ gamma-rays has been extended to the upper limit of the spectrum. Using a magnetic lens spectrometer with a resolution of three percent, secondary electrons ejected from Th and Be converters have been studied from <100 kev to 4 Mev. Calibrations were made at 147.6 kev ("F" line from Th B), 411.1 kev (Au^{198}), 510.8 kev (annihilation radiation) and 2.620 Mev (Th C''). At a deuteron bombarding energy of 1.2 Mev the following gamma-ray lines are observed (energies in kev):

411 ± 5	1435 ± 20
475 ± 6	2170 ± 25
718 ± 3	2924 ± 25
1024 ± 10	3425 ± 25

The values obtained agree reasonably well with those derived from neutron groups.[2,3] The most reasonable level scheme would suggest states in B^{10} at 411-, 718-, 1435-, 2170-, and 3425-kev excitation, although the existence of levels at 1024 and 2924 kev cannot be excluded. This work was assisted by the Office of Naval Research.

[1] Lauritsen, Fowler, Lauritsen, and Rasmussen, Phys. Rev. 73, 636 (1948).
[2] Bonner and Brubaker, Phys. Rev. 50, 308 (1936).
[3] Staub and Stephens, Phys. Rev. 55, 131 (1939).

I12. Analysis of the Be^9+p Resonances at 0.988 and 1.077 Mev. E. RICHARD COHEN AND R. F. CHRISTY, *California Institute of Technology.*—An attempt has been made to determine the level assignments of the energy levels in B^{10} indicated by the 0.988- and 1.077-Mev resonances of protons on beryllium previously reported by this laboratory.[1] The observed total scattering cross sections and angular distributions for protons cannot be explained purely on the basis of Coulomb scattering and the two observed resonances, but require the inclusion of a non-resonant nuclear scattering cross section whose magnitude is comparable to that of the Coulomb term. Using a non-resonant cross-section term which, for simplicity, is assumed to be independent of energy or angle, best agreement at the 0.988-Mev resonance is obtained by the assignment $J=1$. The 1.077-Mev resonance seems to be due to incident d-wave protons and the possible assignments to this level will also be considered. This work was supported in part by the Office of Naval Research.

[1] R. G. Thomas, W. A. Fowler, and C. C. Lauritsen, Phys. Rev. 73, 536 (1948); C. C. Lauritsen, T. Lauritsen, and W. A. Fowler, Phys. Rev. 72, 739 (1947).

SUPPLEMENTARY PROGRAMME

SP1. The Protected Multicellular Geiger Counter for Short-Wave-Length X-Rays and Gamma-Rays for Use in the Curved Crystal Spectrometer.* DAVID A. LIND, *California Institute of Technology.*[1]—A Geiger counter is described for use in the gamma-ray spectrometer[2] consisting of a series of electrically negative metallic gauze septa placed transversely in a tube together with an alternating series of electrically positive four-pronged "spiders" of 10-mil tungsten wire supported on an axial rod passing through central holes in the septa. The radiation whose photons are to be counted passes axially through this system and ejects electrons from each septum by photoelectric absorption, Compton scattering, and pair formation. The background counting rate from cosmic radiation is markedly reduced by placing above the multicellular counter a battery of six conventional Geiger counters connected in an anticoincidence circuit which suppresses counting by the main counter when any one of the protective counters is excited. This entire system is protected from local radiation other than the beam to be measured by a lead shield 3 to 4 inches in thickness. A mixture of argon with three percent of petroleum ether at 20 cm Hg gives a counting threshold at 1100 volts with a plateau of 200 volts and excellent stability. At 1 Mev a counting efficiency of eight percent of all incident photons is indicated with a counter of five septa and four spiders.

* To be given at the end of Session G if the chairman considers that time permits.
[1] Assisted by the Office of Naval Research.
[2] See companion abstract on this program and also Rev. Sci. Inst. 18, 626 (1947).

Author Index to Abstracts of Papers Presented at the Pasadena Meeting

Allison, Samuel K. and Harold V. Argo—No. A2
Babcock, H. W.—No. E1
Bandel, H. W. and W. N. English—No. C6
Barber, W. C.—No. B5
Barkas, Walter H., E. Gardner, and C. M. G. Lattes—No. D4
Begovich, Nicholas—No. H8
Benedikt, Elliot T.—No. H9
Bever, S., Virgil E. Bottom, and Louis R. Weber—No. H7
Bishop, A. S., John Burfening, E. Gardner, and C. M. G. Lattes—No. D3
Bockhop, Dorothy, A. C. Helmholz, and J. M. Peterson—No. E7
Bradner, Hugh and J. D. Gow—No. E5
Cohen, E. Richard and R. F. Christy—No. I12
Cooper, Eugene P.—No. I7
DuMond, Jesse W. M., David Lind, and Bernard B. Watson—No. G3
English, W. N.—No. C2
Estermann, I.—No. G2
Finkelstein, R. J.—No. H10
Forster, Harriet H.—No. B6
Fowler, W. A. and R. N. Hall—No. D7
Fretter, W. B.—No. B3
Goldstein, L. and D. W. Sweeney—No. I6
Hall, R. N.—No. D6
Halpern, Otto and Edward Gerjuoy—No. H5
Hansen, W. W. and R. F. Post—No. F3
Harding, John M. and J. E. Henderson—No. F5
Helmholz, A. C.—No. E2
Helmholz, A. C. and C. L. McGinnis—No. E6
Hornyak, W. F. and T. Lauritsen—No. I10
Keuffel, J. W.—No. H4
Krause, E. H.—No. B1
Kunkel, Wulf—No. C3
Ladenburg, R. W.—No. G1
Langmuir, R. V.—No. E4
Lattes, C. M. G. and E. Gardner—No. D1
Lauritsen, T., C. B. Dougherty, and V. K. Rasmussen—No. I11
Lind, David—No. SP1
Lind, David, Bernard B. Watson, and Jesse W. M. DuMond—No. G4
Loeb, Leonard B. and Robert A. Wijsman—No. C1
Mandeville, C. E. and M. V. Scherb—No. I9
Michels, Walter C. and Esther D. Redding—No. H3
Mills, M. M.—No. B4
Moore, D. B. and W. N. English—No. C4
Omer, Guy C., Jr.—No. I1
O'Reilly, J. and R. F. Christy—No. D8
Panofsky, Wolfgang K. H.—No. D5
Parker, James M. and Leonard B. Loeb—No. C5
Parzen, G. and L. I. Schiff—No. I5
Phillips, Robert and Wolfgang K. H. Panofsky—No. E8
Post, R. F.—No. F2
Powell, W. M.—No. E3
Prim, R. C.—No. H12
Rabi, I. I.—No. A1
Reines, F.—No. I8
Rubin, S., C. W. Snyder, C. C. Lauritsen, and W. A. Fowler—No. I4
Schein, Marcel—No. B2
Schiff, L. I.—No. B7
Schwinger, Julian—No. A2
Serber, R.—No. D2
Snyder, C. W., C. C. Lauritsen, W. A. Fowler, and S. Rubin—No. I3
Stephenson, S. T. and F. D. Mason—No. F4
Thomas, Roy—No. I2
Tollestrup, A. V.—No. H1
Warburton, F. W.—No. H6
Watson, Bernard B., David A. Lind, and Jesse W. M. DuMond—No. G5
Wayland, Harold and Saul Baker—No. H11
Wilts, Charles H.—No. F1